THE EFFECT OF CALCIUM ON THE GASIFICATION REACTIONS OF CARBON

VOL. 1

Joachim K. Floess

B.S., Rensselaer Polytechnic Institute (1972)
M.E., Rensselaer Polytechnic Institute (1973)

SUBMITTED IN PARTIAL FULFILLMENT
OF THE REQUIREMENTS FOR THE DEGREE OF

DOCTOR OF PHILOSOPHY
IN CHEMICAL ENGINEERING

at the
MASSACHUSETTS INSTITUTE OF TECHNOLOGY
December 1985

Signature of Author _____
Department of Chemical Engineering
December 10, 1985

Certified by _____
John P. Longwell
Thesis Supervisor

Certified by _____
Adel F. Sarofim
Thesis Supervisor

Accepted by _____
William M. Deen
Chairman, Departmental Committee on Graduate Students

THE EFFECT OF CALCIUM ON THE GASIFICATION REACTIONS OF CARBON

Joachim K. Floess

Submitted to the Department of Chemical Engineering in December, 1985 in partial fulfillment of the requirements for the degree of Doctor of Philosophy from the Massachusetts Institute of Technology

ABSTRACT

A study was conducted to determine the catalytic effect of calcium on the intrinsic reactivity of a high surface area microporous char. The chars used in this study were made from sucrose to which calcium was added in various amounts and degrees of dispersion. Rate data were obtained, using a thermogravimetric analyzer, for both the oxygen and carbon dioxide reactions, over the complete carbon conversion range, and at reaction rates where intra-particle diffusion begins to become significant.

The results show that only when the calcium is atomically distributed and presumably forms a cation-carbon bond are the gasification reactions catalyzed. One atomic percent calcium increases the oxygen reaction rate by almost two orders of magnitude and the carbon dioxide reaction rate by almost three orders of magnitude. The catalyst tends to depress the activation energy by about 15%. Calculations using absolute rate theory demonstrate that this decrease in activation energy can exactly account for the greater reactivity of the catalyzed char. Analysis of the rate versus conversion data indicates that, at least up to 50% conversion, the calcium remains with the carbon and does not deactivate. The reaction rate increases directly with the increase in the calcium to carbon ratio of the char as carbon is removed over this conversion range. Heat treatment of the char prior to reaction showed that catalyst deactivation becomes important at temperatures above 1060 K.

In a complementary study, the rate versus conversion data of the chars were analyzed using the random pore model and an extension of the random pore model that includes the opening of initially inaccessible porosity as carbon conversion progresses. Measurements obtained in these experiments suggest that a microporous char particle reacts preferentially near the particle surface. The particles apparently decrease in size as well as in density as carbon conversion takes place.

The low temperature carbon-oxygen reaction is observed to be first order, even though large quantities of surface oxides are con-currently present on the carbon. The surface oxide concentration is about equivalent to monolayer coverage. The surface oxides remain on the carbon at the reaction temperature in the absence of oxygen. These observations are inconsistent with any simple adsorption-desorption mechanism. A mechanism is proposed in terms of a reaction between the oxygen and the surface oxides on the carbon.

Thesis Supervisors: John P. Longwell
Professor of Chemical Engineering

Adel F. Sarofim
Professor of Chemical Engineering

ACKNOWLEDGEMENTS

I wish to express my gratitude to Professor Adel F. Sarofim and Professor John P. Longwell for their suggestions and helpful criticisms during the course of this thesis. Their guidance and encouragement are gratefully acknowledged. I would also like to thank the members of my committee, Professor J.B. Howard and Dr. W.A. Peters for their suggestions and support during my stay at M.I.T.

The friendships and the inevitable technical discussions with my fellow students will long be remembered. Although this list is far from complete, I wish to especially acknowledge the discussions I have had with Bob Hurt, as well as with the other members of my research group, Tom Hastings, C.K. Lai, C.S. Chang, Mike Serio, Mike Snow, Judy Wornat, Derek Mess, Tony Modestino, Lyle Timothy, and Rowena Torres-Ordonez. Thanks also to Joel Plawsky, Gail Gamboa, and Mark Manton.

A special thank you to Reiner Musier for his assistance with the modeling work and to Ohene Kwapong who diligently ran some of the dullest experiments imaginable (and always with a smile).

Financial support for myself and for the work presented in this thesis was provided by the Exxon Corporation and is gratefully acknowledged.

I want to express my gratitude to my Mother and Father and my special aunt (Amalie Oexle) for their support and encouragement of my studies. I wish to also acknowledge my brother Carsten, who preceeded me in such an undertaking, at a time when I could not understand what was taking him so long to finish, and my cousin Gunther for many uplifting thoughts.

Finally, I wish to thank my wife, Patricia, for her constant support, encouragement, and love throughout this undertaking. Her cheerful spirit is a joy for all. The final manuscript is as much the result of her efforts and interest in this work as they are mine. It is to her that I dedicate this thesis.

TABLE OF CONTENTS

LIST OF FIGURES

LIST OF TABLES

CHAPTER ONE. SUMMARY

1.1. INTRODUCTION

The reaction rate of carbon with oxidizing gases will often be two to four orders of magnitude higher if the carbon contains small amounts of inorganic impurities. This striking increase in reactivity, either because of the presence of inherent inorganic elements in the carbon or upon the addition of certain inorganic compounds, has led to many investigations of this phenomena. These studies, which have been summarized and reviewed by McKee, 1981; Wen, 1980; and Walker et al., 1968, have demonstrated that a broad range of inorganic elements can act as catalysts for carbon gasification. However, an understanding of the catalysis is so far largely empirical because of the few systematic studies that have been made and a lack of understanding of the carbon gasification reactions themselves, which could provide some insight into alternative catalytic reaction pathways. Attempts to explain the catalyst action in terms of a chemical mechanism have been directed at establishing a broad ranging explanation that encompasses the numerous species that act as catalysts. The two most widely supported explanations are the electron transfer and the oxygen transfer mechanisms. The electron transfer mechanism (Long and Sykes, 1950) postulates that the catalyst interacts with the π electrons of the carbon and thereby affects the overall energy level of the solid. One version of the oxygen transfer mechanism proposed by McKee

(1981) suggests that the catalyst undergoes oxidation-reduction cycles with the reactant and the carbon and thereby acts as an intermediate to supply oxygen to the carbon. In an alternative explanation, Mims and Pabst (1980) assume that the catalyst increases the number of active sites on the carbon at which carbon-oxygen complexes are formed.

In this study, only the catalytic activity of calcium was investigated. Previous studies have shown that many of the Group IA and IIA elements are effective catalysts for carbon gasification by all three of the major oxidants, O_2, CO_2, and H_2O, although calcium is not generally considered to be one of the more active catalysts of this group. The effectiveness of calcium as a catalyst appears to depend strongly on the method of addition to the carbon. Results reported in a number of investigations (McKee, 1980; Tomita et al., 1977) show the effectiveness of calcium to be quite variable, which is presumably a function of the method of addition and of the dispersion of calcium on the carbon. Studies by Radovic (1982) and Hippo (1977) have shown that calcium ion-exchanged onto demineralized lignites will increase the reactivity of the lignite greatly and that the reactivity will increase linearly with calcium loading. They also conclude that it is principally calcium that is responsible for the higher inherent reactivity of certain coal chars. In neither case, however, are possible mechanisms for the catalysis carefully considered, although Radovic suggests an oxidation-reduction cycle as a probable mechanism and attempts to relate the activity of the

catalyst to calcium dispersion measurements obtained by x-ray diffraction line broadening.

In this study, a systematic investigation of the intrinsic kinetics of a pure and a calcium-added high surface area amorphous char was made. Insight into the mechanism of carbon catalysis was obtained by analysis and comparison of the kinetic data of the catalyzed and non-catalyzed chars. The principal objectives of this thesis were:

1. To determine how the relative effectiveness of calcium as a catalyst depends on the method and amount of calcium addition and the degree of dispersion.
2. To determine the effect of reaction conditions on catalyst activity by measuring char reactivity over a wide range of conditions. Previous studies have usually compared reactivities only at very low reaction rates to insure completely intrinsic kinetics. In this study, measurements were made with both O_2 and CO_2, over the entire conversion range, and up to rates where intra-particle diffusion begins to become significant.
3. To critically evaluate proposed catalytic mechanisms by comparison with the data obtained in these experiments.
4. To compare the rate versus conversion data with the surface area and porosity variations with conversion of the chars. In a complementary study, the rate versus conversion data were compared to theoretical models that predict surface area variations with respect to conversion.

1.2. EQUIPMENT AND EXPERIMENTAL PROCEDURES

A model char was used in these studies to allow control over the mineral matter content and the chemical composition of the char. The char was manufactured from sucrose, and it is a high surface area carbon that has no measureable porosity in pores larger than 100 Å. The lack of hetero-atoms (except oxygen) and other inorganic elements in the char eliminated any secondary reactions between the calcium and these compounds, and the narrow pore size distribution provided a material with a relatively well characterized porosity. Some additional experiments were conducted with Spherocarb because this carbon has been used by a number of investigators as a model material. Spherocarb is a commercially available high surface area carbon (Analabs, New Haven, CT).

The char was manufactured by pyrolysis of sucrose at 925 K in a small furnace. Three methods of calcium addition were used: calcium was added before pyrolysis by dissolution of CaO in a sucrose solution and by incorporation of approximately 1 μm size $CaCO_3$ particles into the sucrose during recrystallization of the sucrose from solution. Calcium was also added directly onto the char by ion-exchange.

Although calcium oxide is practically insoluble in water, it is highly soluble in a sucrose solution. A mixture of calcium oxide and sucrose forms what is known as a saccharate (Honig, 1953). It is likely that the behavior of the sucrose as a weak acid towards the hydroxide results in the extensive solubility of CaO. Upon evaporation of excess water at

approximately 90°C, the saccharate forms a residue in which the calcium is atomically dispersed. Subsequent pyrolysis of the saccharate results in a char with highly dispersed calcium. In comparison to calcium oxide, calcium carbonate is not soluble in a sucrose solution. In this case, small calcium carbonate particles will form a uniform dispersion in the solution when it is agitated. Upon evaporation of excess water from the solution, the sucrose will recrystallize and incorporate the calcium carbonate. Pyrolysis of the sucrose-calcium carbonate mixture gives a char in which the calcium is present primarily in a separate solid phase. Calcium was ion-exchanged onto the char by stirring the char in a 0.1 M calcium acetate solution. Pre-oxidation of the char to 6% conversion at 673 K was necessary to obtain a significant amount of ion-exchange.

The calcium content and elemental composition of the chars are listed in Table 1.2-1. The maximum calcium content of the chars is 3.6 wt% except for the char with the $CaCO_3$ particles. All chars were heat treated to 1100 K prior to the analysis. The nominal particle size used in these experiments was 90-106 μm.

Surface areas were determined from nitrogen adsorption isotherms at 77K. Except for the char at 0% conversion, the time required to reach equilibrium at each adsorption step was less than 15 seconds. Equilibrium was not achieved for the unreacted char even after 60 minutes. The measurements for the char at 0% conversion are based on a 20 minute adsorption time. Although the amount that would have been adsorbed at a longer

Table 2-1. ELEMENTAL ANALYSIS OF THE CHARS[1]
(Chars Heat Treated at 1100 K)

(wt%, dry ash free)	C-0 (sucrose)	C-1 (saccharate)	C-3.6 (saccharate)
C	95.9	-	93.65
H	1.08	-	1.28
O (by difference)	3.02	-	5.07
Ca[2]	0.0	0.97	3.6

	C-ion (sucrose char with ion-exchanged calcium)	C-$CaCO_3$ (sucrose char with particulate $CaCO_3$)	Spherocarb
C	91.45	-	96.84
H	1.06	-	0.73
O (by difference)	7.49	-	2.43
Ca	2.3	6.8	-

[1] All chars were heat treated at 1100 K in the TGA in the same manner used prior to a run. Before analysis, the samples were dried under vacumn at 600 K, and any subsequent transfers were done under dry nitrogen.

[2] Calcium content is also reported on an ash free basis, i.e. wt Ca/wt calcium-free char.

equilibrium time is not negligible, the adsorption rate is highest initially and decreases with time. Experiments with partially reacted chars showed that approximately 5% conversion is necessary to open up the pore structure so that the nitrogen adsorption is rapid.

The monolayer coverage was calculated using the n-layer BET equation. The data are usually best fit by the equation for n (the number of layers) less than three. Desorption measurements demonstrated that not all of the nitrogen would desorb from the char at 77 K. In all experiments, the desorption measurements came to a distinct end point. This is shown in Figure 1.2-1, in which the adsorption and desorption isotherms of the sucrose char at 25% conversion are presented. The remaining nitrogen corresponds to a quantity just less than the amount at which the isotherm bends over. The amount of nitrogen remaining on the solid after the last desorption step is in approximate agreement with the mono-layer nitrogen volume calculated by the n-layer BET equation. In fact, because the surface area calculated from the remaining nitrogen is lower than the surface area calculated by the BET equation, it is felt that the desorption end point may provide a more accurate estimate of the surface area of the char. In addition, except for the data point at 0% conversion, the surface areas determined by the nitrogen end point technique are comparable to surface areas determined by CO_2 adsorption measurements (Hurt, 1985). Surface areas were calculated from the monolayer volume using an area of 16.2 $Å^2$/molecule. Because the char is

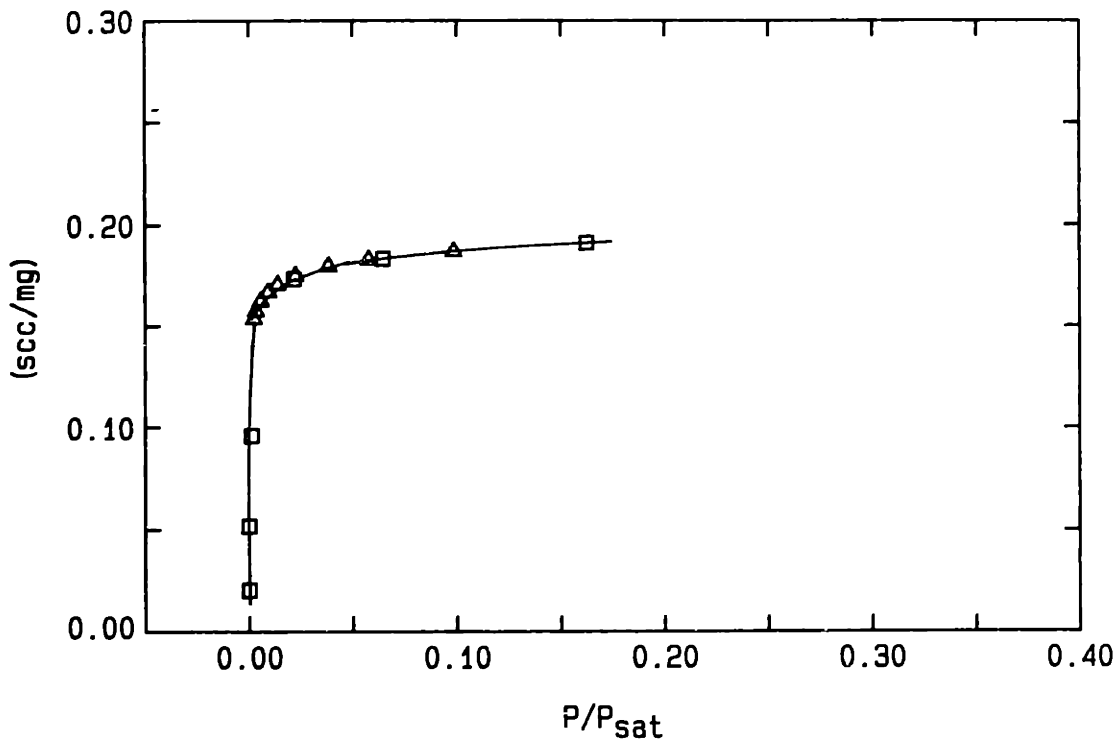

Figure 1.2-1. Nitrogen adsorption and desorption isotherms at 77 K. C-O char at 24.4% conversion reacted in air at 760 K. (□) adsorption; (△) desorption.

predominantly microporous, it is also possible to determine the total porosity of the char from the nitrogen adsorption measurements using the Dubinin-Polanyi equation. The data are summarized in Table 1.2-2. The surface area is about 640 m^2/g for the sucrose char and 550 m^2/g for the calcium-added char, and for both chars is approximately constant between 10 and 70% conversion.

Reaction rate data were obtained by measuring the change in weight of the solid as a function of time with a Cahn Model 113 thermogravimetric analysis system (TGA). Modifications of the gas flow system of the TGA were made which allowed accurate measurement of weight changes on sample amounts as small as 50 µg.

The effects of external heat and mass transfer on the reaction rate of the sample on the TGA sample pan were determined both experimentally and theoretically. Figure 1.2-2 shows the effect of sample weight on the reaction rate per unit mass of sample. Theoretical calculations are presented for different values of emissivity; the best fit to the data is obtained for an emissivity of 0.45, which is in good agreement with the expected value of emissivity for platinum with some carbon on one side at 875 K. Because with small amounts of sample the char does not completely cover the sample pan, the model includes a factor that changes the projected surface area of the sample on the pan with the amount of char. Based on the results of this analysis, all experiments were conducted at a reaction rate less than .25 mg/min. At higher reaction

Table 12-2. SURFACE AREA AND POROSITY OF THE C-O and C-3.6 CHARS[1] AS A FUNCTION OF CONVERSION.

C-O Char
(0 wt% Ca)

CONVERSION	SURFACE AREA		POROSITY
	n-layer BET equation	desorption end point	
(%)	(m^2/g of reacted char)		(cc/g of reacted char)
0	(1.5)[2]	282	318	0.129
6.4	(1.5)	580	531	0.232
22.0	(1.5)	753	645	0.30
24.4	(1.5)	778	664	0.306
54.5	(2.0)	870	627	0.343
C-3.6 Char				
(3.6 wt% Ca)				
0		104	114	0.050
7.0	(1.3)	510	374	0.192
22.0	(3.0)	700	553	0.278
58.0	(3.0)	660	478	0.272

[1] Chars were heat treated at 1100 K and reacted in air at 760 K for the C-O char and 610 K for the C-3.6 char.

[2] value of n

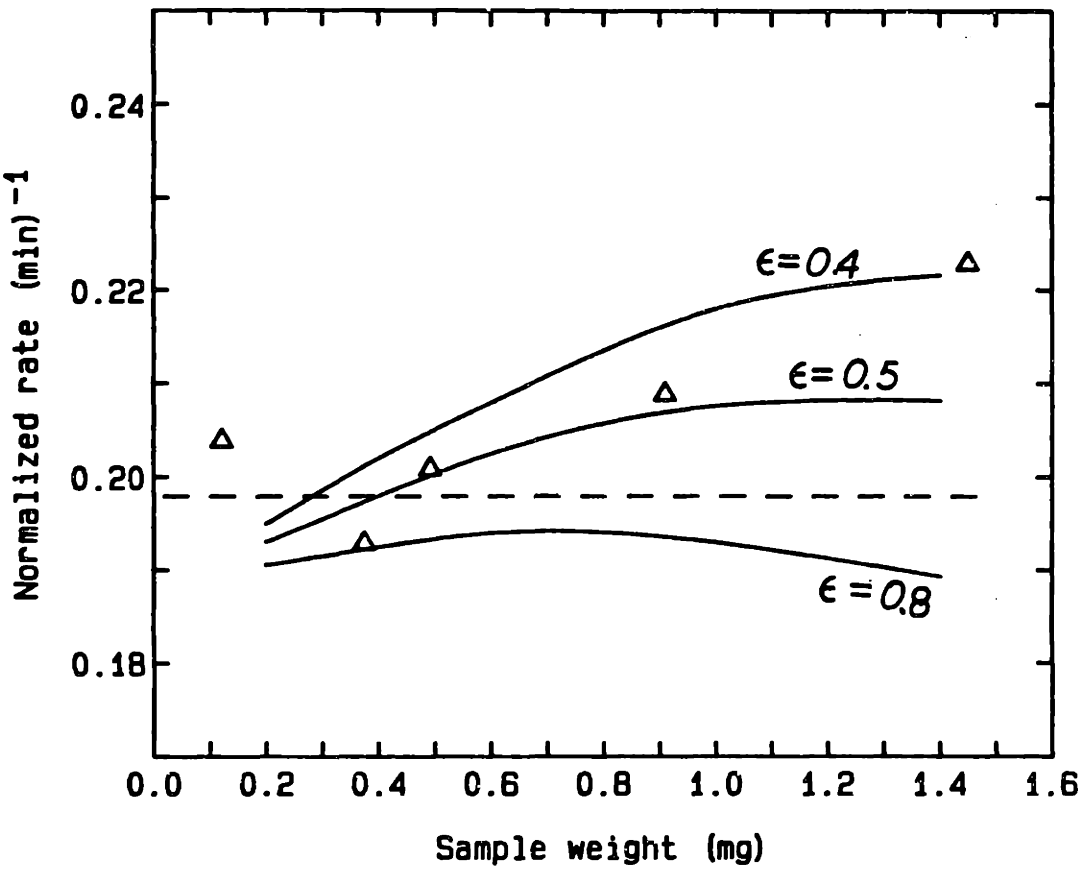

Figure L2-2. Reaction rate as a function of sample weight. (——) calculations at 875 K; (Δ) experimental data (C-O char; 875 K in air; heat treatment temperature 1100 K).

temperatures, the sample weight was decreased as required to keep the rate within this limit.

The experimental procedure was as follows. After the sample was placed on the sample pan and the reactor reassembled, the sample was heated at 25 C/min in nitrogen to a pretreatment temperature (1100 K or 1300 K for the carbon-oxygen runs; or the reaction temperature itself for the carbon-carbon dioxide runs) and then brought to the reaction temperature without any intermediate exposure to air at room temperature. The run was started by switching the gas from nitrogen to the reactant. Runs were made in air, and at oxygen partial pressures below 0.21 atm, and in 100% CO_2.

1.3. RESULTS

The rate data for the oxygen reaction at 40% conversion for the C-O, C-1, and C-3.6 chars (sucrose and saccharate with 1 and 3.6 wt% calcium chars) are presented in Arrhenius form in Figure 1.3-1. The rate constant is defined as:

$$k = \frac{r}{m_o P_{O_2}}$$

where r is the measured rate of weight loss (mg/min), m_o is the initial sample weight (mg ash-free char) and P_{O_2} is the oxygen partial pressure. P_{O_2} is equal to 0.21, unless otherwise noted. The activation energies and pre-exponential factors of the rate constants for the individual chars are summarized in Table 1.3-1. The activation energies for the catalyzed chars are lower than for the non-catalyzed char.

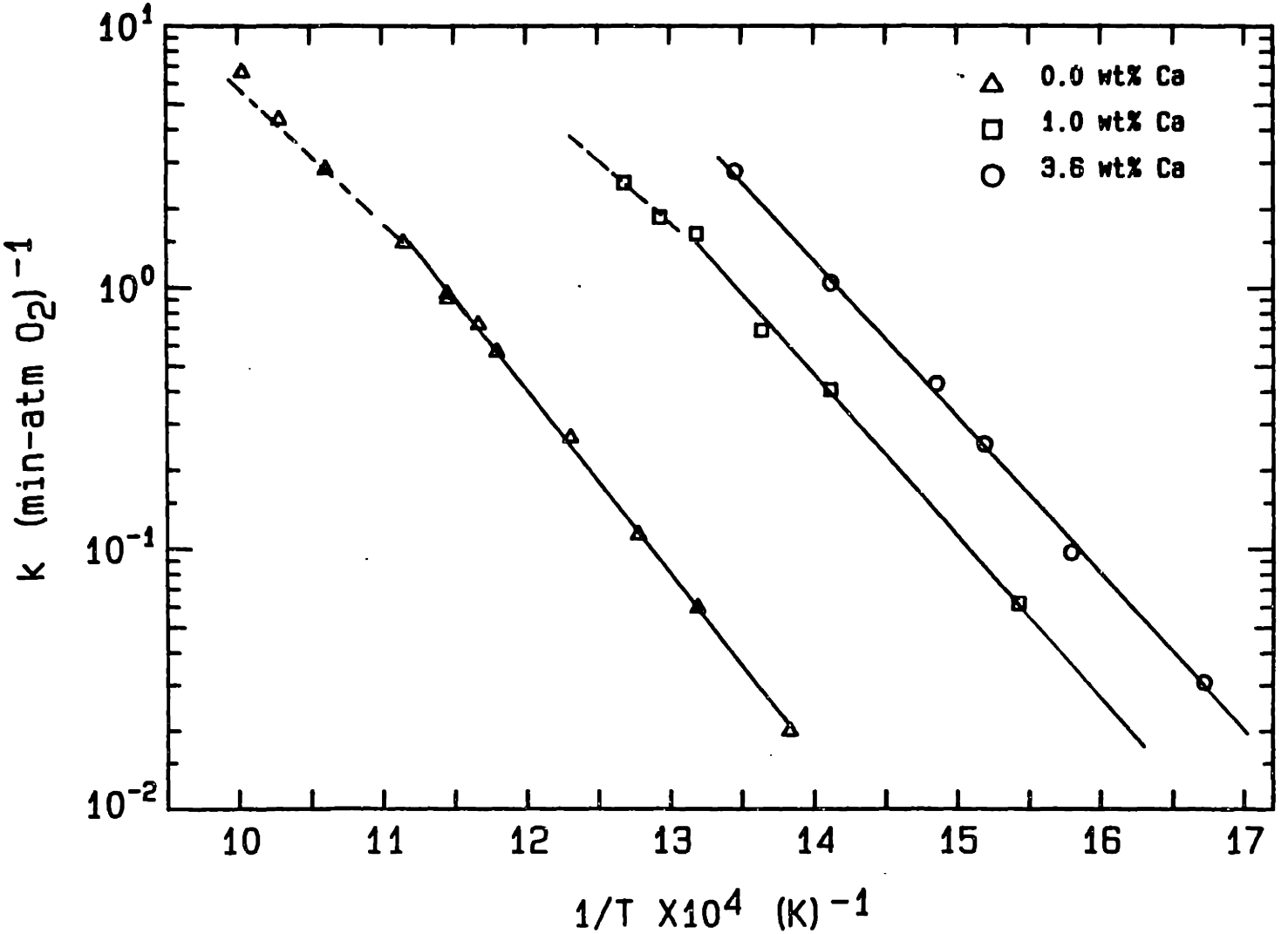

Figure L.3-1. Arrhenius Diagram for the C-O, C-1, and C-3.6 chars at 40% conversion; reaction with oxygen (0.21 atm); 90-106 μm particles; heat treatment temperature 1100 K.

Table 13-1. PRE-EXPONENTIAL FACTORS AND ACTIVATION ENERGIES OF THE RATE CONSTANTS AT 40% CONVERSION

Char - Reactant	Pre-Exponential Factor (cc/gmole-sec)	Activation Energy (cal/mole)
C-O - air	3.44×10^{11}	34,000
C-1 - air	5.75×10^{11}	29,700
C-3.6 - air	7.24×10^{11}	28,600
C-ion - air	9.61×10^{12}	31,100
C-$CaCO_3$ - air	5.20×10^{11}	33,000
C-O - CO_2	4.26×10^{13}	70,700
C-3.6 - CO_2	9.59×10^{13}	58,000

The change in slope of the rate versus reciprocal temperature data at high reaction rates indicates the onset of intra-particle diffusion in the chars. This change in slope occurs at approximately the same reaction rate for each of the three chars, and in terms of a first-order reaction diffusion model, this can only arise if the effective diffusivity is the same for each char. This result implies that the catalyst must be active in all pores and, therefore, must be uniformly distributed throughout the char.

Figure 1.3-2 presents the reaction rate of the C-O char for three particle sizes, 45-53 μm, 90-106 μm, and 177-212 μm. In general, the reaction rate is about 20% higher relative to the next larger size in each case. For the different sizes, the data lie on a straight line spanning over two orders of magnitude indicating the reaction rate to be intrinsic. Because the data lie on practically parallel lines, it is not possible to interpret the particle size effect in terms of a classical reaction-diffusion model. No particle size effect was observed with the C-3.6 char.

In Figures 1.3-3 to 1.3-5, the reaction rates (normalized to the maximum rate) are plotted as a function of conversion. All three chars show a maximum reaction rate at some intermediate conversion; however, for the catalyzed chars, the maximum occurs at a higher conversion. Also, the difference between the initial and maximum rate is more pronounced for the catalyzed than the non-catalyzed char. For the catalyzed chars, the rate versus conversion data beyond the maximum rate all lie on approximately straight lines.

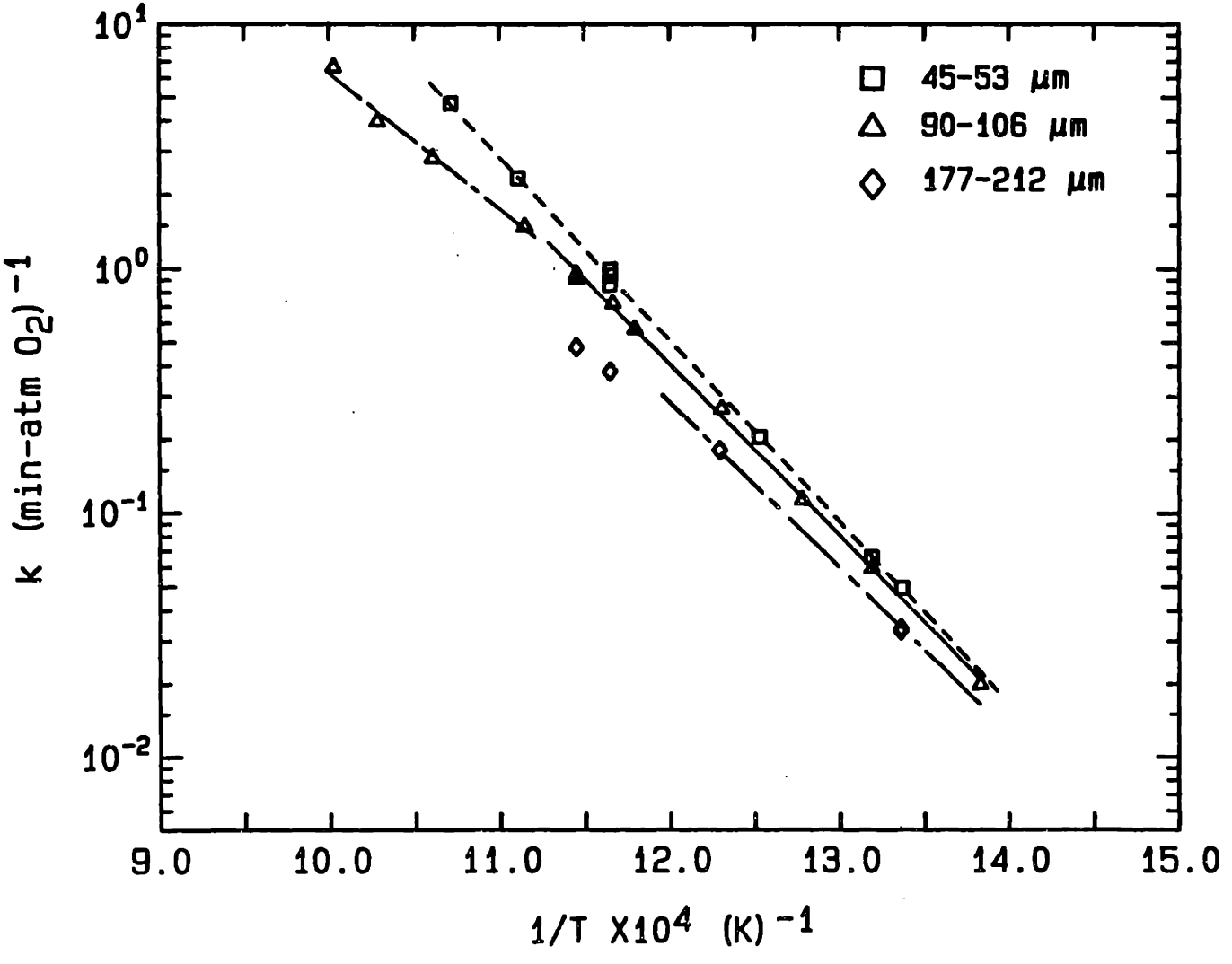

Figure 1.3-2. Arrhenius diagram for the C-O (0 wt% Ca) char at 40% conversion for three particle sizes; oxygen (0.21 atm); heat treatment temperature 1100 K.

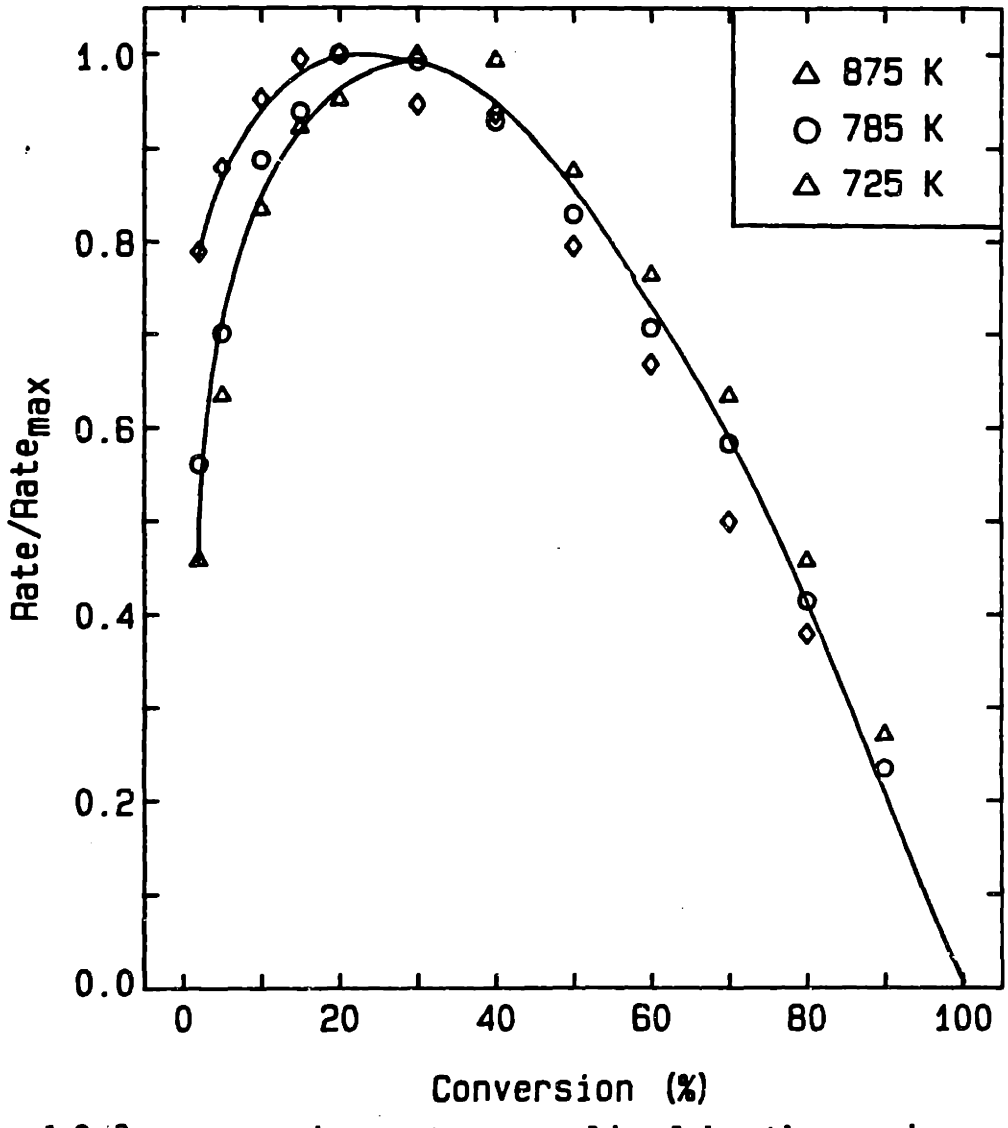

Figure 1.3-3. Reaction rate normalized by the maximum rate versus conversion. C-O char - oxygen (0.21 atm) reaction; 90-106 μm particles; 1100 K heat treatment temperature.

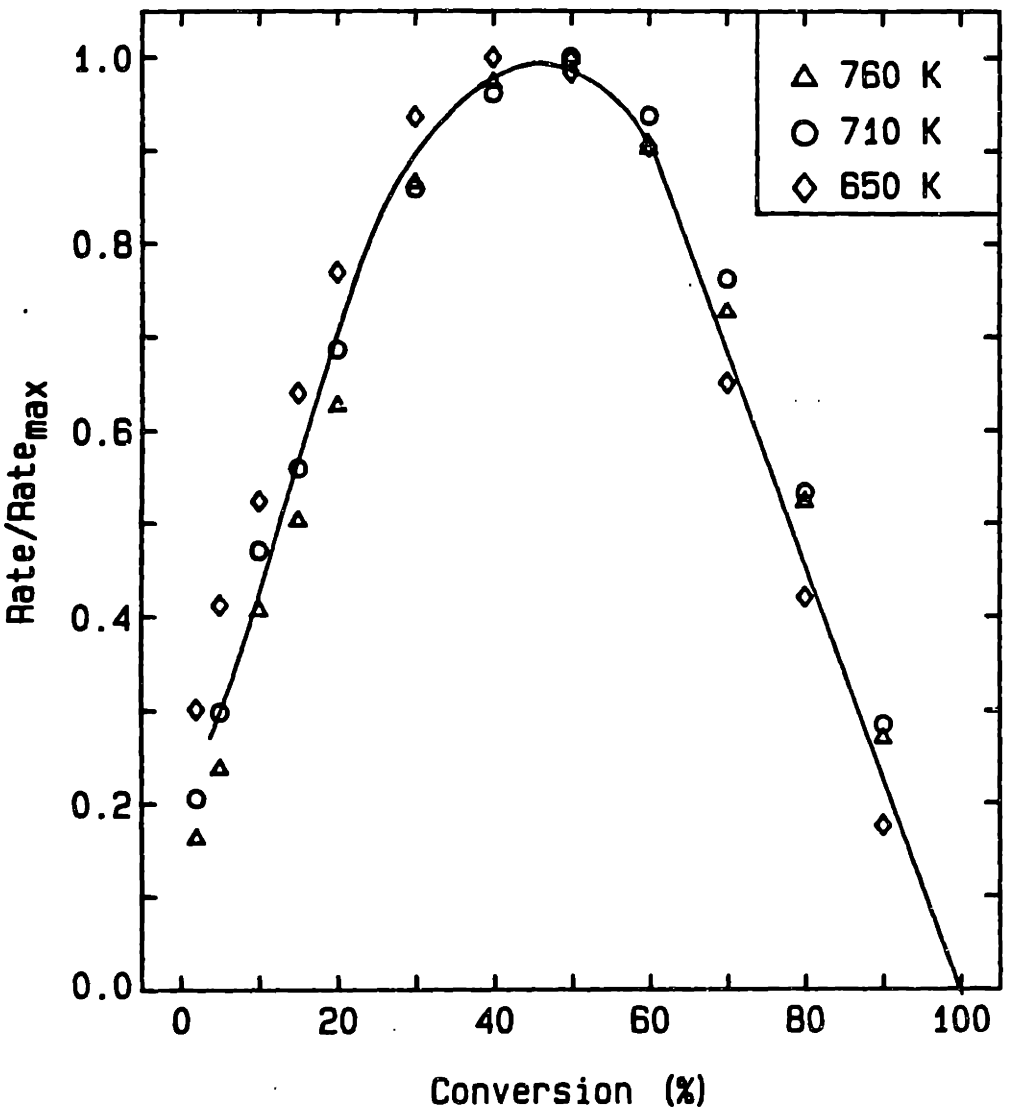

Figure 13-4. Reaction rate normalized by the maximum rate versus conversion. C-1 char - oxygen (0.21 atm) reaction; 90-106 μm particles; 1100 K heat treatment temperature.

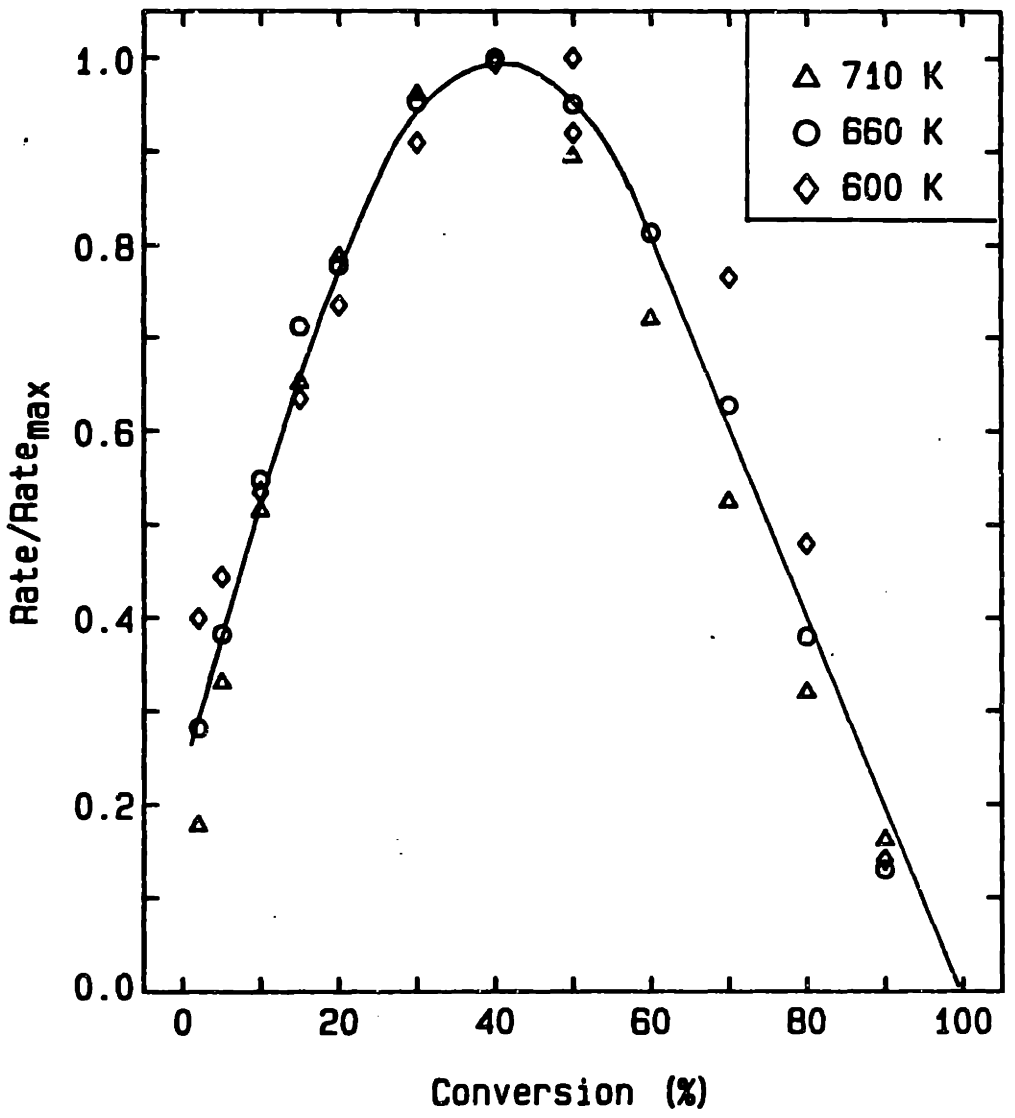

Figure 1.3-5. Reaction rate normalized by the maximum rate versus conversion. C-3.6 char - oxygen (0.21 atm) reaction; 90-106 μm particles; 1100 K heat treatment temperature.

The effect of oxygen concentration on the reaction rate of the C-O and C-3.6 chars is summarized in Figure 1.3-6. The first order rate dependence on oxygen concentration extends to at least 0.21 atm for the catalyzed char but only to 0.16 atm for the non-catalyzed char. The reaction order of the non-catalyzed char is identical at the two temperatures that were investigated.

The rate data at 40% conversion for the C-ion (ion exchange char) and C-$CaCO_3$ (sucrose char with $CaCO_3$ particles) chars are presented in Arrhenius form in Figure 1.3-7. The activation energies and pre-exponential factors of the rate constants are summarized in Table 1.3-1.

The rate versus conversion data of the ion exchange char are shown in Figures 1.3-8. In general, the shape of the rate versus conversion curve is quite similar to the C-3.6 char.

The relative reactivity of the catalyzed chars as a function of calcium loading is shown in Figure 1.3-9. The rate increases linearly with calcium loading up to a calcium content of at least 6%. The ion-exchange char is a factor of two more reactive than the calcium-added char at the same calcium content. The C-$CaCO_3$ char, however, exhibits hardly any catalytic effect; it is about twice as reactive as the non-catalyzed char.

Reaction rate data of the C-O and C-3.6 chars with carbon dioxide are presented in Figure 1.3-10. The experiments were conducted at 1 atm. CO_2. Activation energies and pre-exponential factors are also summarized in Table 1.3-1. The

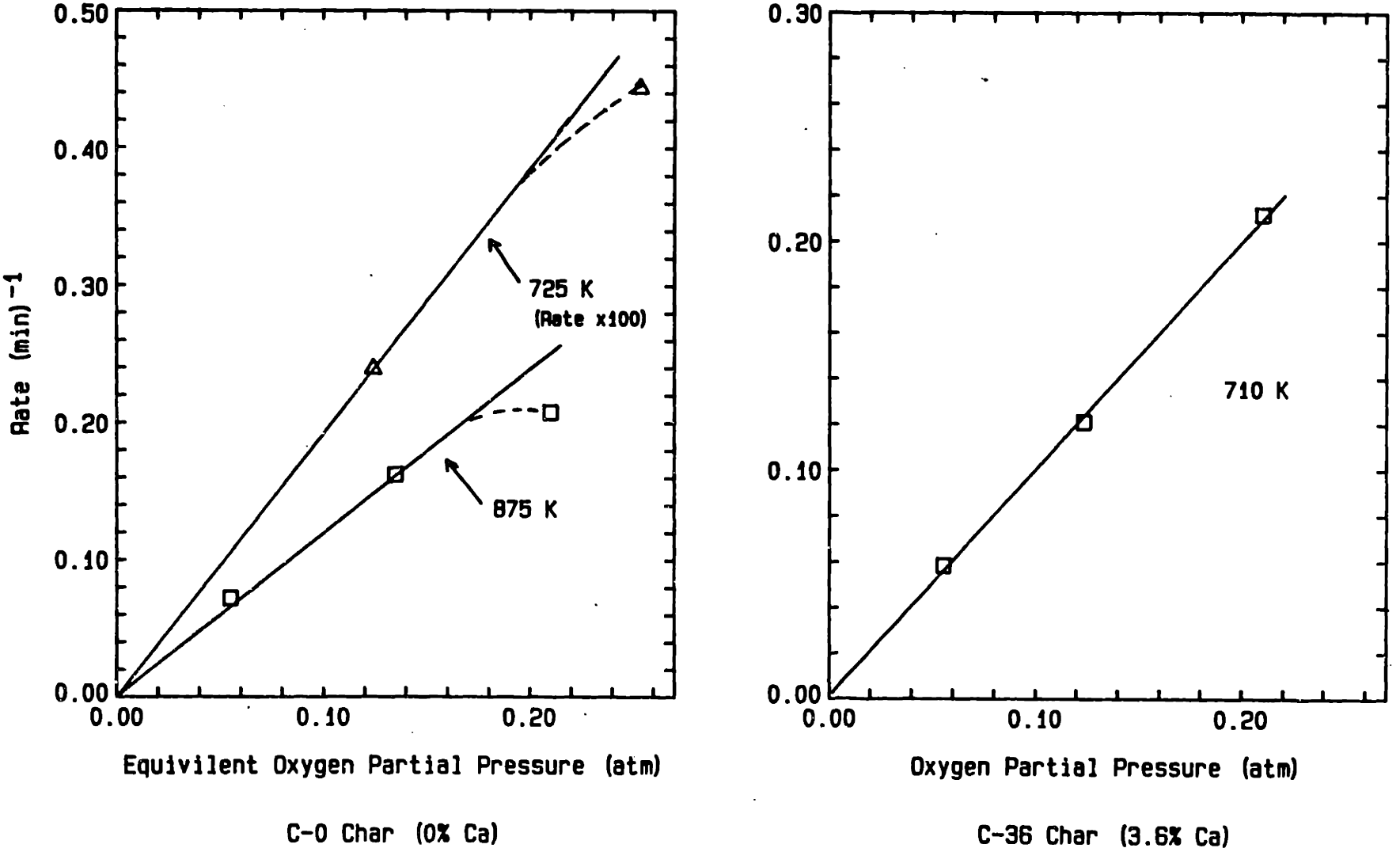

Figure 1.3-6. Reaction order for the C-0 and C-3.6 chars. The oxygen partial pressure for the C-0 char is corrected to account for the higher oxygen concentration at 725 K. Rates are at 40% conversion.

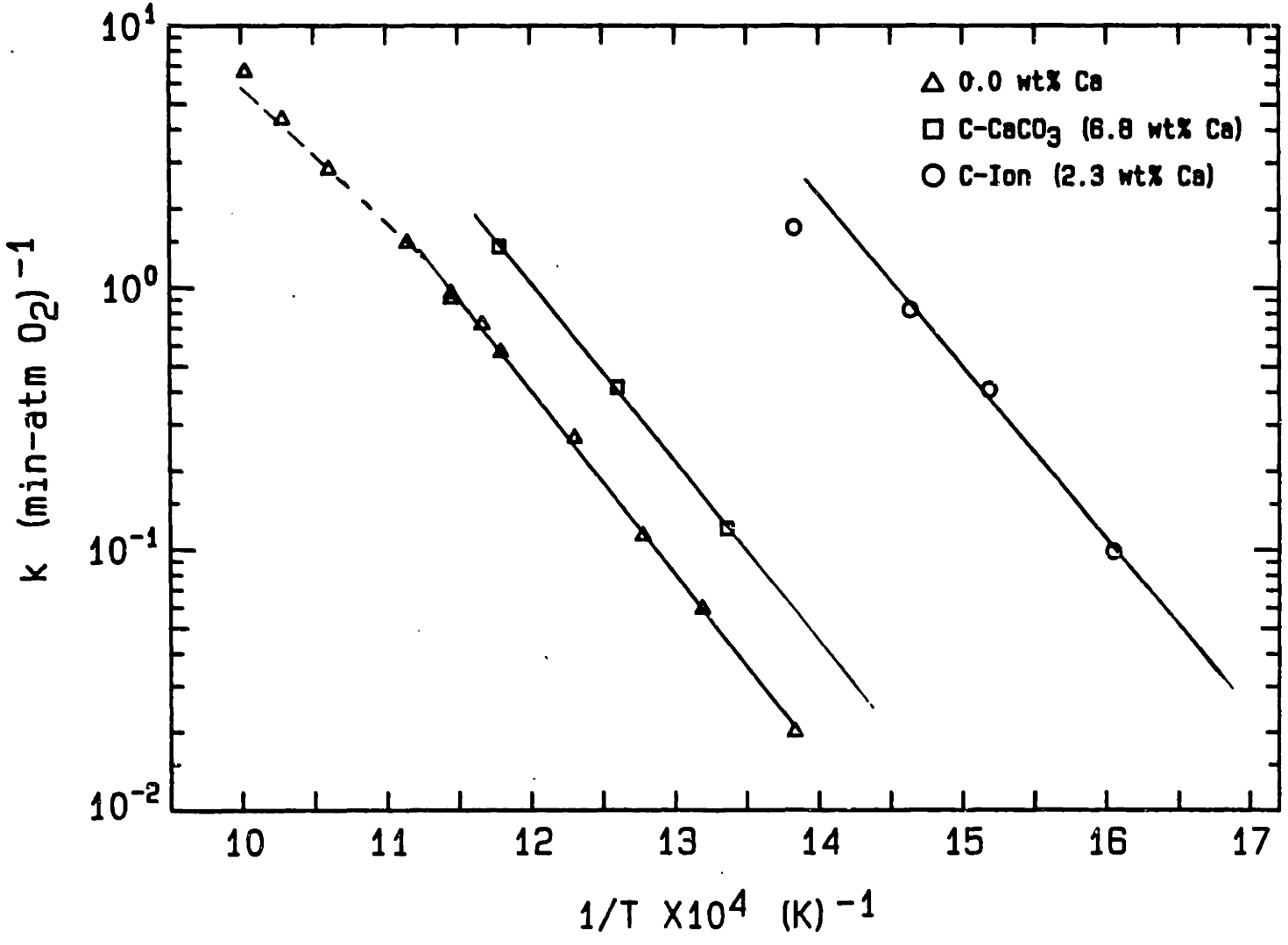

Figure 3-7. Arrhenius diagram for the C-ion and C-$CaCO_3$ chars at 40% conversion; 0.21 atm oxygen; particle size 90-106 μm; heat treatment temperature 1100 K.

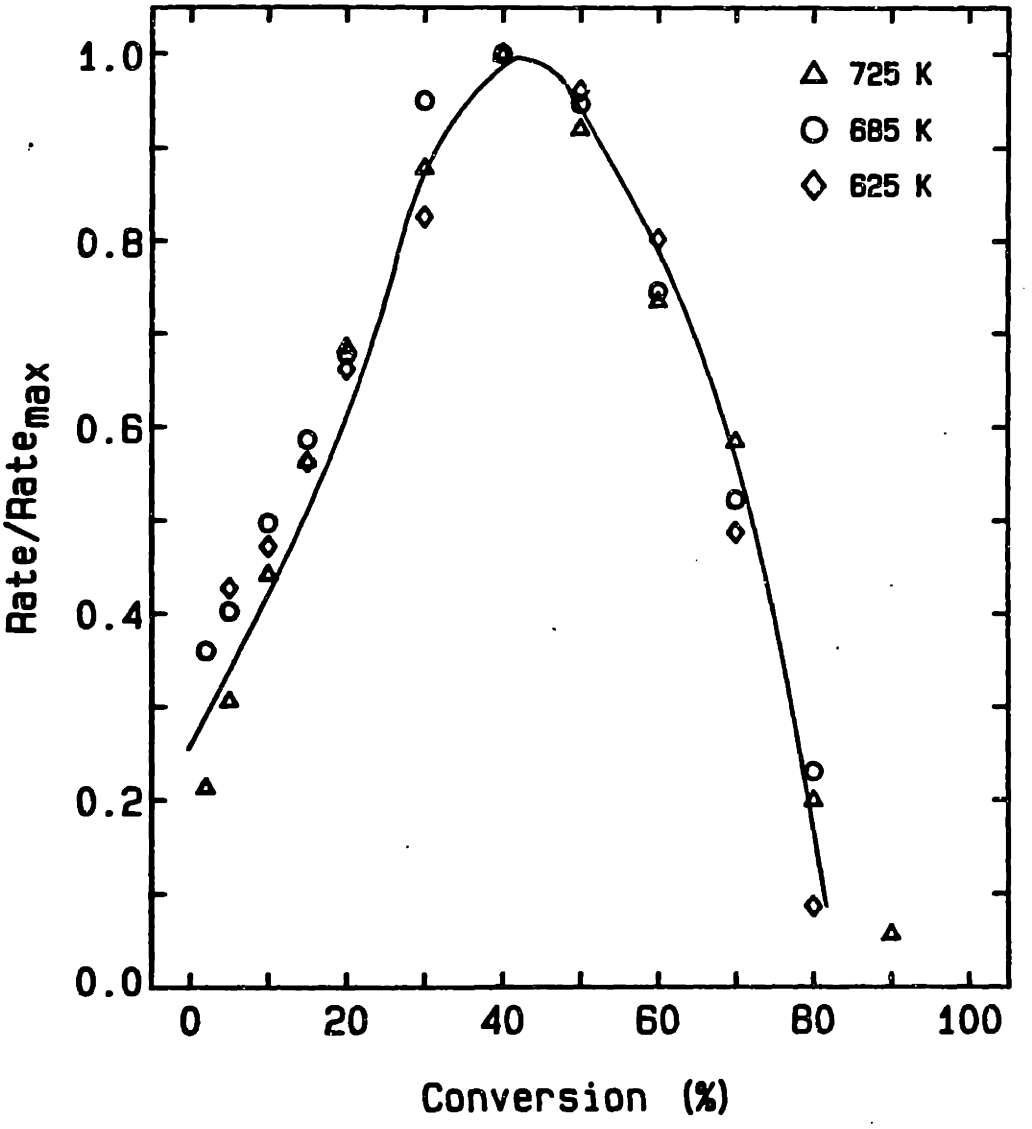

Figure 1.3-8. Reaction rate normalized by the maximum rate versus conversion. C-ion (2.3 wt% Ca) - oxygen (0.21 atm) reaction; 90-106 μm particles; heat treatment temperature 1100 K.

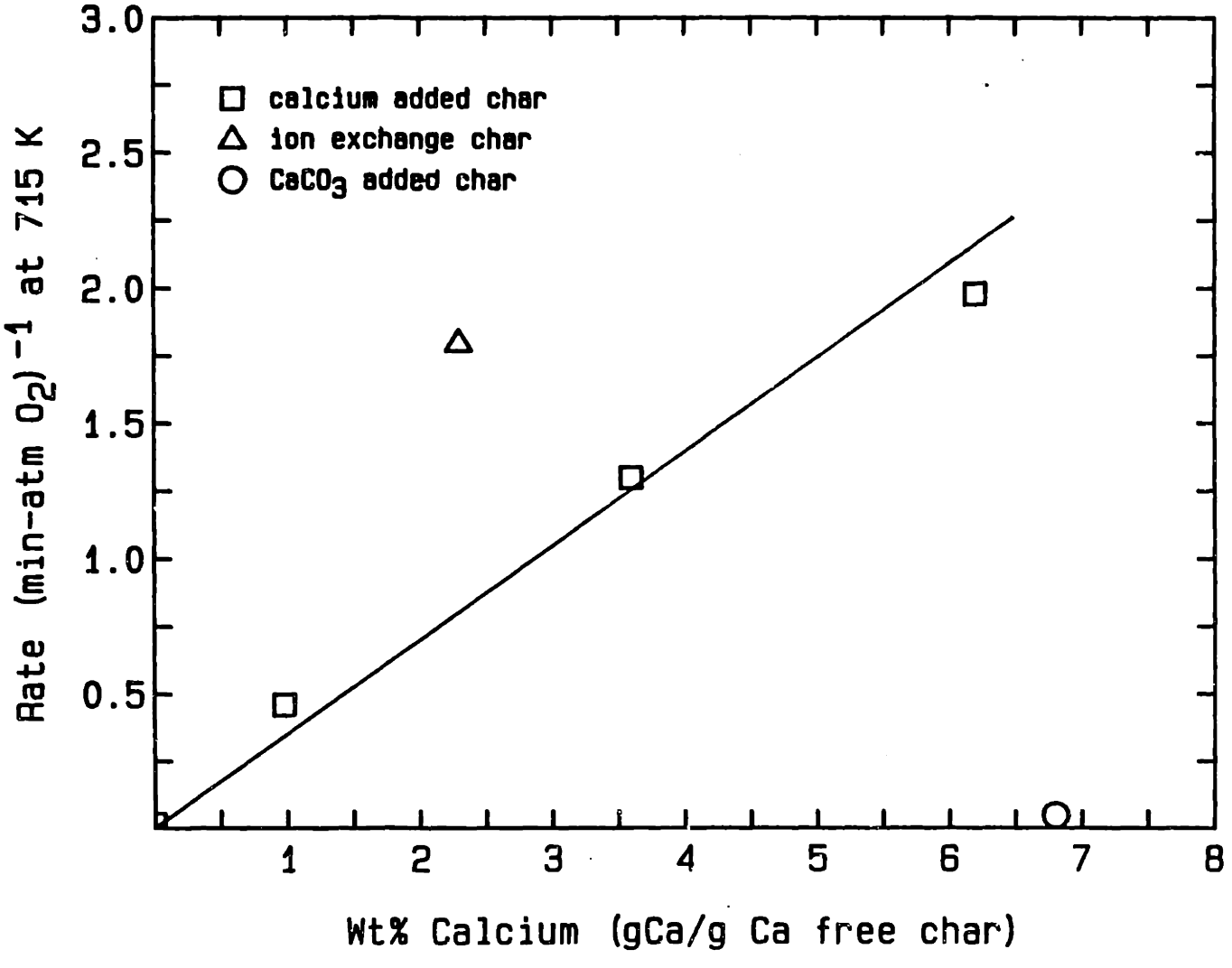

Figure 13-9. Reaction rate versus calcium content at 715 K, 40% conversion, carbon-oxygen (0.21 atm) reaction.

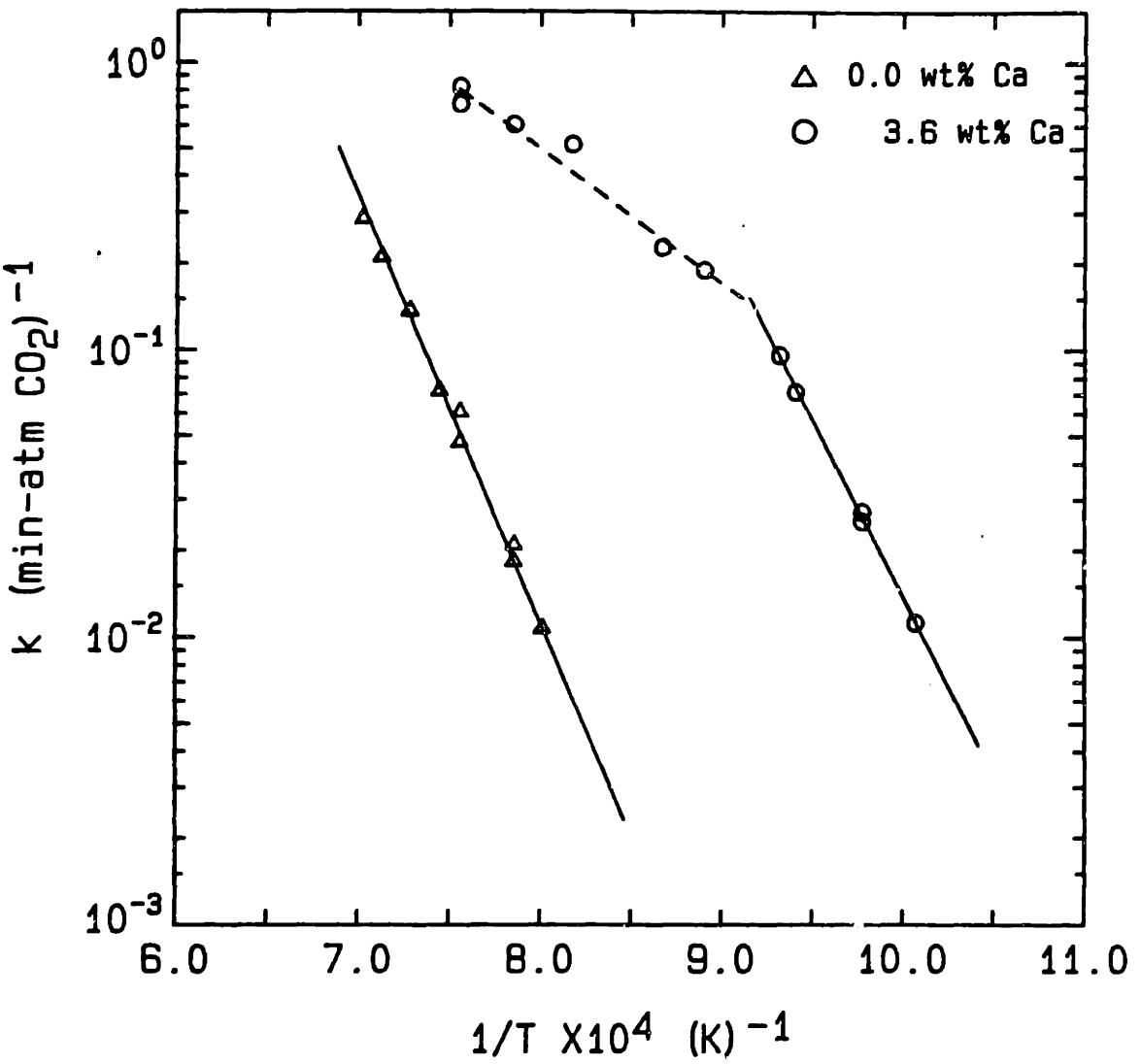

Figure 13-10. Arrhenius diagram for the C-O and C-3.6 chars at 40% conversion; carbon dioxide reaction (1.0 atm); 90-106 μm particles.

change in slope of the rate data in the Arrhenius diagram for the C-3.6 char at 1080 K is not believed to be due to intra-particle diffusion, since no change in the slope is observed with the non-catalyzed char and since the rate is below the rate at which intra-particle diffusion is observed in the oxygen runs. Rather, the fall-off in reactivity of the catalyzed char is apparently due to more rapid catalyst deactivation at elevated temperatures. As shown in Figure 1.3-11, the reaction rate of the catalyzed char decreases rapidly with heat treatment at 1100 K, whereas at 1025 K no significant decrease in reactivity is observed.

Rate versus conversion data for the carbon dioxide reaction are presented in Figures 1.3-12 and 1.3-13. Unlike the oxygen data, the maximum rate is almost constant between 20 and 60% conversion for the catalyzed char. In addition, the initial rate is higher relative to the maximum rate. This is observed with the non-catalyzed char also.

1.4. DISCUSSION

A. Catalysis of the Gasification Reactions by Calcium

The char containing 3.6% calcium increases the reaction rate of the carbon-oxygen reaction by almost two orders of magnitude and the carbon-carbon dioxide reaction rate by almost three orders of magnitude. Such a reactivity increase for the carbon dioxide reaction is comparable to the increase in reactivity obtained with potassium (Freund, 1984), which is commonly assumed to be a much more effective catalyst, at an

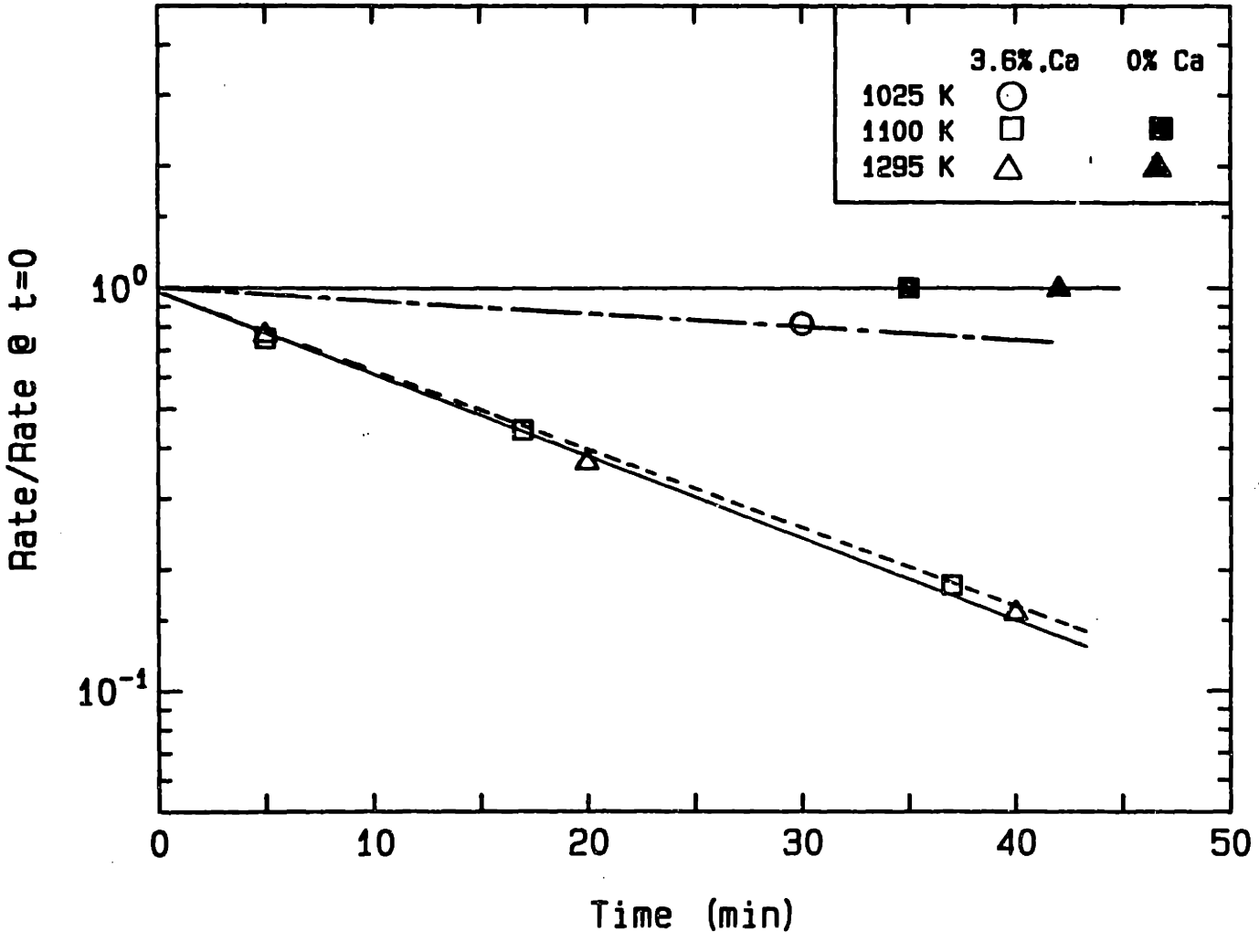

Figure 1.3-11. The effect of heat treatment time on the reactivity of the C-0 and C-3.6 chars. Reaction rate is normalized to the rate at 0 minutes heat treatment time.

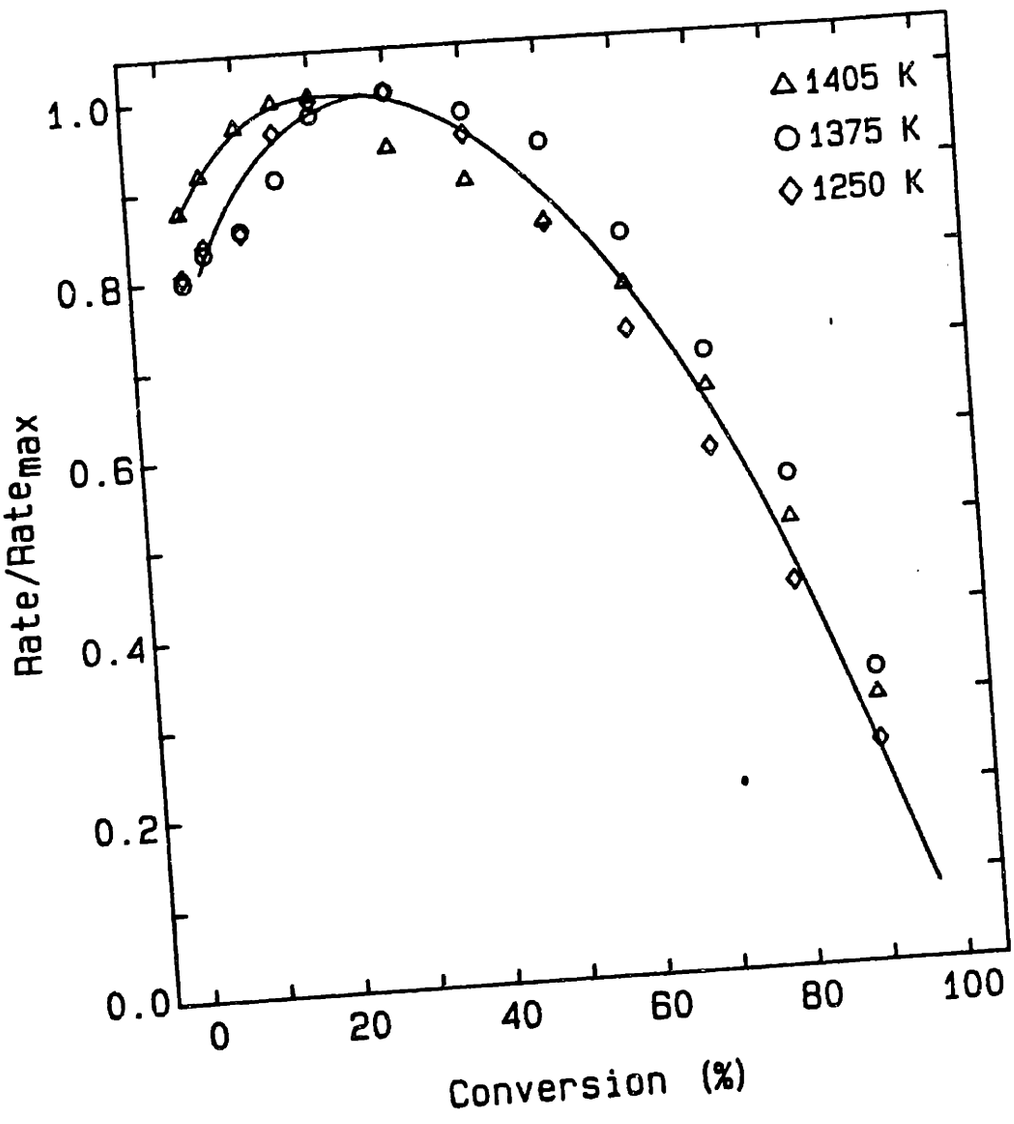

Figure L.3-12. Reaction rate normalized by the maximum rate versus conversion. C-O char - carbon dioxide (1 atm) reaction; 90-106 μm particles.

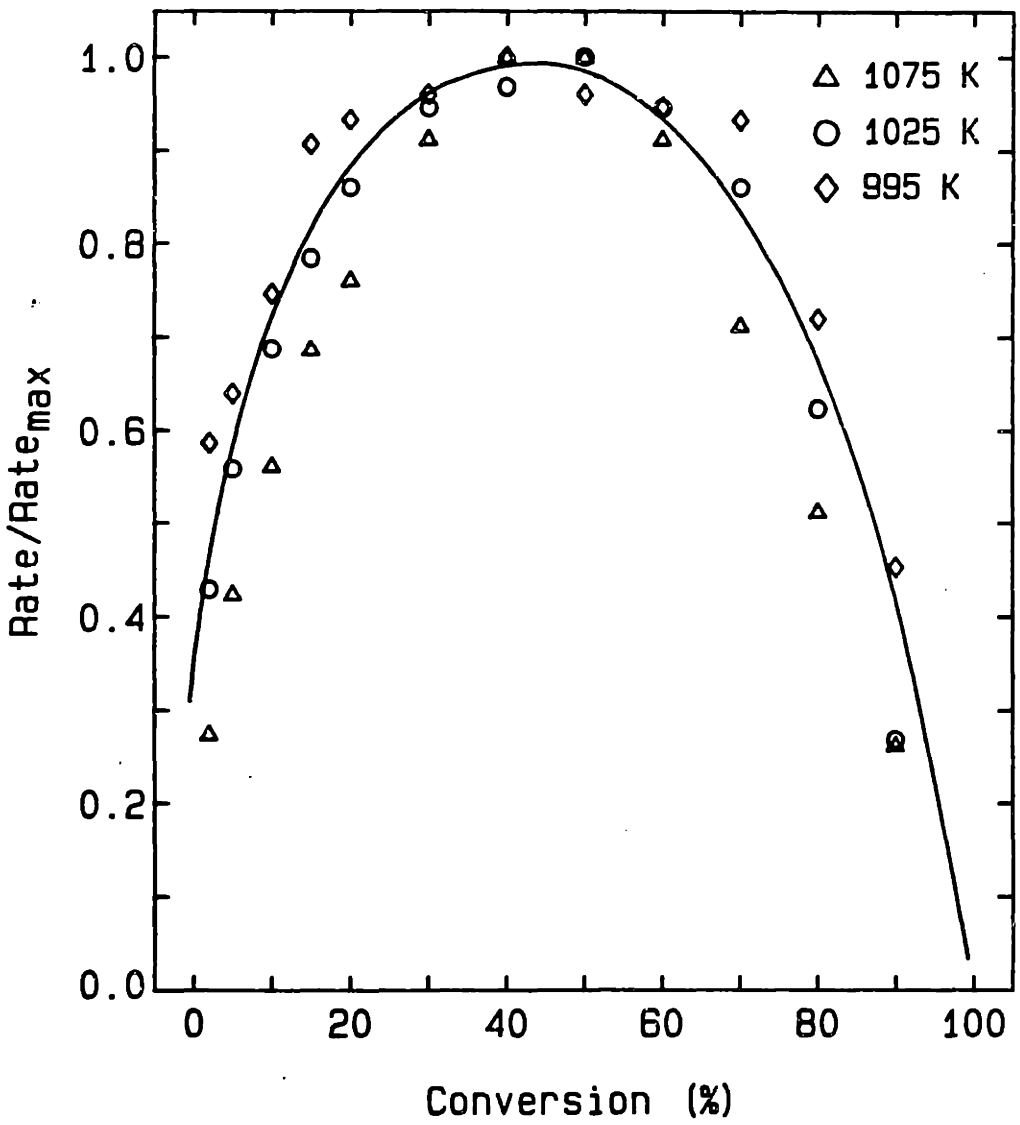

Figure 13-13. Reaction rate normalized by the maximum rate versus conversion; C-3.6 char - carbon dioxide (1.0 atm) reaction; 90-106 μm particles.

equivalent atomic loading. For the oxygen reaction, the increase in reactivity is comparable to the results obtained by Radovic (1982) in his study with calcium ion exchanged lignites.

In order to obtain catalysis of the gasification reactions, however, the calcium must be dispersed in the char on an atomic scale. Incorporation of the calcium as a separate solid phase (either as CaO or $CaCO_3$) directly into the char results in only a minor increase in reactivity. (This small increase in reactivity is possibly due to a slight solubility of $CaCO_3$ in a sucrose solution, thereby providing some atomic dispersion.) Evidence obtained in this study indicates that calcium in a separate solid phase (i.e., the surface molecules of a $CaCO_3$ or CaO crystallite) does not promote higher carbon reactivity. If catalysis indeed occurs at the calcium carbon phase boundary, one would expect the catalytic activity to be a function of the calcium crystal structure. However, the catalytic activity is unaltered whether CaO or $CaCO_3$ is the stable phase. Figure 1.3-10 shows that the catalysis of the Boudouard reaction does not change at temperatures above or below the decomposition temperature of calcium carbonate (1160 K) at 1 atm CO_2. Likewise, catalytic activity in the carbon-oxygen reaction is not altered if the char at the reaction temperature is initially exposed to carbon dioxide and the reaction is conducted in air and a CO_2 partial pressure above the calcium carbonate decomposition pressure. Furthermore, in a discrete site model of catalysis by small crystallites the reactivity of

the catalyzed char should be governed solely by the action of the catalyst. Therefore, the reactivity of the char should be correlative by models that describe the dispersion of supported metal catalysts. Such models predict that the change in exposed surface area of the catalyst is (Ruckenstein and Pulvermacher, 1973):

$$\frac{dS}{dt} = -kS^n \qquad (1.4.1)$$

where S is a measure of the exposed catalyst surface area. Ruckenstein and Pulvermacher state that the exponent, n, equals 2 or 3 if the reaction is controlled by particle sintering and $n > 4$ if the reaction is controlled by surface migration. Such dispersion models, with $n > 2$, would predict catalyst deactivation to be a function of the catalyst loading, yet the rate versus conversion data for the C-0 and C-1 chars are approximately proportional over the complete conversion range. In addition, it would have been expected that the rate versus conversion data for the ion exchange char should not have exhibited such a large difference between the initial and maximum rates for such a dispersed site model of catalysis.

As a result, it must be that calcium will act as a gasification catalyst only when the calcium forms a solution or a direct chemical bond with carbon and not when it is present as a separate solid phase. This is consistent with the results of Mims and Pabst (1983) who have demonstrated that potassium will form a carbon-potassium surface complex and that the

number of such complexes correlates with the catalytic activity. Mims and Pabst propose that the complex is similar to a phenolate species. The analogous chemistry of the Group IA and IIA elements makes it likely that such complexes are also formed with calcium, although no direct evidence for a surface complex was obtained in this study. However, in contrast to potassium, a cation-carbon solution is not formed by simply heating calcium carbonate with the carbon. Rather, the calcium-carbon solution (or surface complex) must be formed in a prior reaction step. (It is possible that a small number of surface complexes may be formed directly at the interface between the calcium and carbon when the sample is heated; however no extensive spreading of the calcium on the char takes place. Either this route or calcium dispersion during sample preparation or both are probably responsible for the slightly higher reactivity of the C-$CaCO_3$ char.)

The detailed chemical mechanism by which the catalyst increases carbon reactivity cannot be determined from these data. However, the results obtained in this study suggest that the action of the catalyst apparently is to sufficiently alter the electron distribution within the solid to affect the kinetics of reactions involving the solid. Overall the behavior of the catalyzed and non-catalyzed chars is almost the same. The rate versus conversion data, although not identical, are similar for both the catalyzed and non-catalyzed chars and, in each case, can be scaled by a single rate constant over practically the entire conversion range. The reaction order

for the oxygen reaction is not substantially altered by the catalyst. In addition, the catalyst is effective for both the oxygen and carbon dioxide reactions, even though the rate mechanism for each of these reactions is probably different. The primary effect of the catalyst is to lower the temperature at which the reaction takes place. In addition, the activation energy in all cases is slightly lower for the catalyzed char than for the non-catalyzed char. If this lower activation energy is interpreted in terms of the energy necessary to decompose a reaction complex into products, one finds that the decrease in activation energy gives exactly the higher reactivity that was measured with the catalyzed char. This result is shown in Table 1.4-1, where calculations using absolute rate theory as applied to surface reactions at the conditions of adsorption control and desorption control are summarized. In each case, the pre-exponential factor is given in terms of the partition functions of the reactant and the reaction complex, and the activation energy is a measure of the probability that the reaction complex will decompose to the products in a particular reaction step. The pre-exponential factors were evaluated for adsorption and desorption control using the assumptions suggested by Laidler (1965). The experimentally measured reaction rate for the oxygen reaction is as fast as the rate predicted for mobile adsorption control (the pre-exponential factor for mobile adsorption is identical to the Hertz-Knudsen equation) which suggests that the rate controlling step is probably not adsorption control. This is

Table 1.4-1. COMPARISON OF MEASURED REACTION RATES TO THEORETICAL CALCULATIONS.

	ABSOLUTE RATE THEORY			EXPERIMENTAL
	ADSORPTION		DESORPTION	
C-O Char-Oxygen	Mobile[1]	Immobile		
Temperature (K)	873	873	873	873
Activation Energy (E^*) (cal/mole)	-	-	-	34,000
Pre-Exponential Factor (molecules/cm^2-sec)	3.3×10^{22}	1.3×10^{17}	3.63×10^{28}	-
exp (E^*)	3×10^{-9}	3×10^{-9}	3×10^{-9}	-
Rate (molecules/cm^2-sec)	9.9×10^{13}	3.9×10^{8}	1.1×10^{20}	3.4×10^{13} [3]
C-3.6 Char-Oxygen				
Temperature (K)	700	700	700	700
Activation Energy	-	-	-	28,600
Pre-exponential Factor	3.7×10^{22}	2.2×10^{17}	2.9×10^{28}	-
exp (E^*)	1.2×10^{-9}	1.2×10^{-9}	1.2×10^{-9}	-
Rate(molecules/cm^2-sec)	4.4×10^{13}	2.6×10^{8}	3.5×10^{19}	3.4×10^{13}

[1] Equivalent to the Hertz-Knudsen Equation.

[2] Calculations assume a site density of 2×10^{15} sites/cm^2 (Blyholder and Eyring, 1957).

[3] Surface area for C-O char 640×10^4 cm^2/g; C-3.6 char 550×10^4 cm^2/g; stoichiometry: 0.75 mole O_2/mole C.

Table 1.4-1 (continued):

	ABSOLUTE RATE THEORY		EXPERIMENTAL
	ADSORPTION	DESORPTION	
C-O Char-CO_2	Mobile		
Temperature (K)	1,360	1,360	1,360
Activation Energy (E^*) (cal/mole)	-	-	70,700
Pre-Exponential Factor	1.1×10^{23}	5.7×10^{28}	-
exp (E^*)	4.3×10^{-12}	4.3×10^{-12}	-
Rate (molecules/ cm^2/sec)	4.7×10^{11}	2.5×10^{17}	2.0×10^{13}
C-3.6 Char-CO_2			
Temperature (K)	1,075	1,075	1,075
Activation Energy	-	-	58,000
Pre-exponential Factor	1.2×10^{23}	4.5×10^{28}	-
exp (E^*)	1.6×10^{-12}	1.6×10^{-12}	-
Rate (molecules/ cm^2/sec)	2.0×10^{11}	7.2×10^{16}	2.0×10^{13}

in contrast to the observation that the carbon oxygen reaction is first order, and thus usually assumed to be under adsorption control. The rate of the carbon dioxide reaction is considerably greater than the rate predicted for adsorption control, and therefore, the assumption that the controlling step of this reaction is product desorption is probably correct. However, the principal result of this calculation is that the change in activation energy between the catalyzed and non-catalyzed char is exactly the amount necessary to account for the increased reactivity.

A decrease in activation energy with respect to greater catalyst loading is observed with all the chars. The activation energy of the ion-exchanged char is slightly higher than expected relative to the increased reactivity. It is felt that this discrepancy is most likely due to an uncertainty in the determination of the activation energy from only three data points.

An alternative explanation of the catalyst action, which is frequently proposed, is that the catalyst changes the number of mono-energetic active sites on the char at which the reaction takes place. However, this is inconsistent with the observed change in activation energy. Rather, the catalyst must change the energy distribution of the sites.

B. Modelling of Rate Versus Conversion Data

In a complementary study, the rate versus conversion data were analyzed using the random pore model and an extension of

the random pore model that includes progressive pore opening as carbon conversion proceeds. The extended random pore model provides a better fit to the experimental data, albeit at the expense of additional model parameters. However, the main reasons for including pore opening were the observations that the surface area of the microporous char initially increases faster than the random pore model predicts, the char porosity does not increase directly with conversion, and the particle size effect illustrated in Figure 1.3-2.

The random pore model assumes that the pores of the solid can be modeled as randomly orientated capillaries. The model gives the total porosity of the solid, ϵ_o in terms of a parameter, λ, that is directly related to the pore size distribution (Gavalas, 1980) as:

$$\epsilon_o = 1 - \exp[-2\pi \int_{r_*}^{r^*} r^2 \lambda(r)\, dr] \qquad (1.4.2)$$

where $\lambda(r)$ is defined as the number of intersections of pores with radius in $(r, r+\Delta r)$ with any surface element; and r_* and r^* are the upper and lower bounds of the distribution.

The model assumes that surface receeds in all pores at a constant rate and that the initial porosity of the solid determines the development of surface area with conversion. Since the recession distance in a micropore is small relative to the particle diameter, the conversion is therefore directly related to the porosity of the solid:

$$1 - x = \frac{1 - \epsilon}{1 - \epsilon_o} \qquad (1.4.3)$$

where ϵ_o is the initial porosity and ϵ the porosity at conversion x. The final equation obtained with this model is (Gavalas, 1980):

$$\frac{S(x)}{S_o} = (1-x)[1 - \beta \ln(1-x)]^{1/2} \qquad (1.4.4)$$

where S(x) is the surface area at conversion, x; S_o is the surface area at 0 conversion; and β is a parameter of the model. Note that because of the assumption of a constant reaction rate, the surface area is directly proportional to the reaction rate. The parameter, β, is not an independent parameter but is related to the initial pore size distribution of the solid through the zeroeth and first moments of $\lambda(r)$. This parameter was evaluated for the sucrose char based on an initial porosity of 0.3 and a 1/r pore size distribution. The model predictions compared to the measured nitrogen surface area and the rate versus conversion data of the C-O oxygen reaction are presented in Figure 1.4-1. The model gives an adequate representation of the data; however, it cannot predict the initial rapid increase in rate (or surface area), and it tends to overpredict the rate at high conversion. Besides the incomplete match between the data and the model, examination of the char porosity data show that the particle density does not

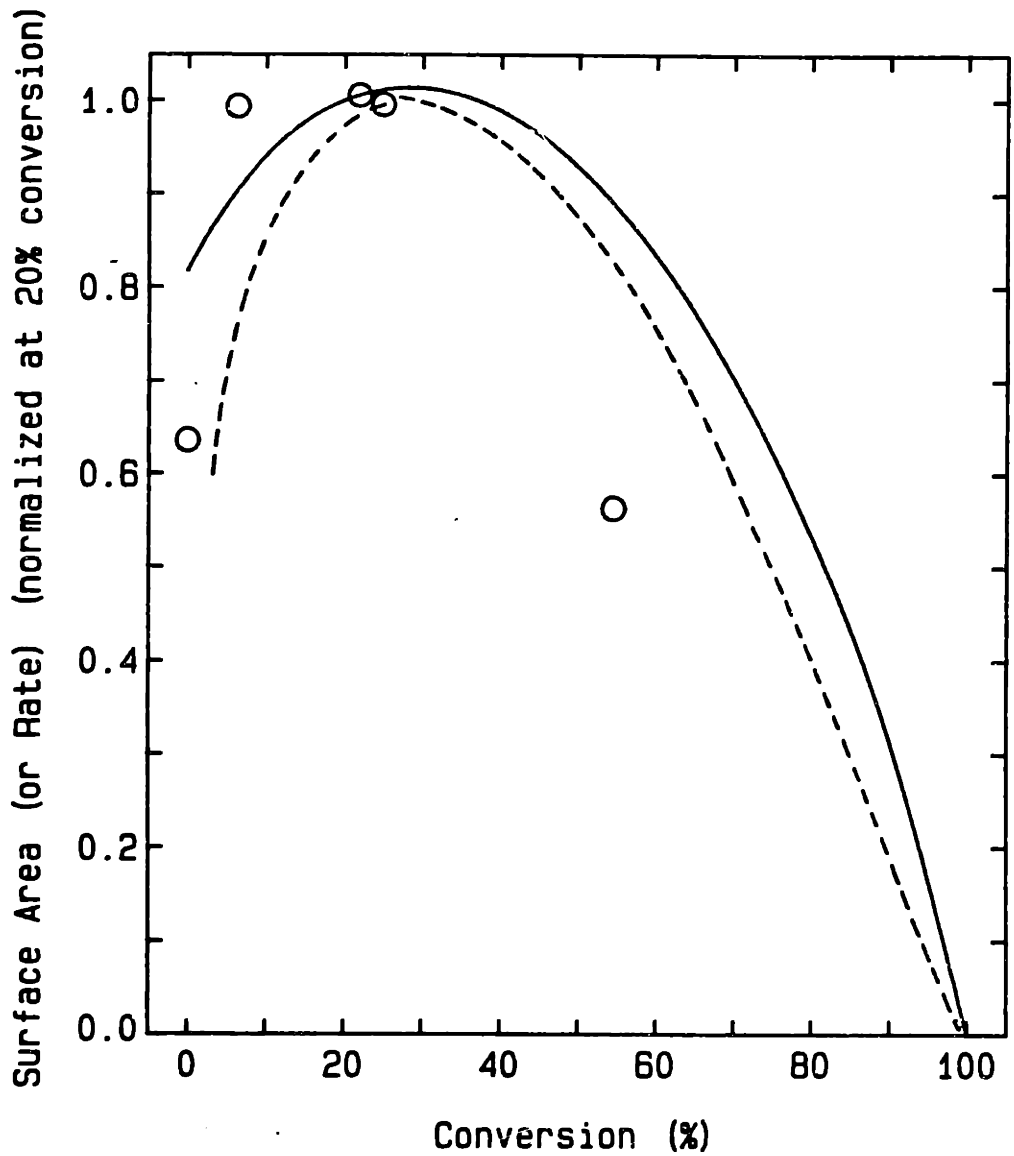

Figure 1.4-1. Normalized rate (or surface area) versus conversion; (—) random pore model; (---) experimental data C-O char-oxygen reaction; (o) surface area measurements.

in actuality decrease as (1-x). The particle density evaluated from the pore volume data (Table 1.2-2) and with the assumption of a constant true solid density is compared to carbon conversion in Figure 1.4-2. It is clear that the changes in porosity do not completely account for the carbon conversion. This discrepancy between particle density and conversion implies that either some nitrogen (or even helium) inaccessible porosity exists that is not accounted for in the calculations because of the assumption of a constant true solid density, or that the reaction occurs preferentially near the surface of a microporous particle so that the particle diameter decreases during reaction. The latter explanation is also consistent with the observed particle size effect. However, it is not possible to discriminate between these alternatives without additional experimental data. Nonetheless, both explanations involve the fact that additional reactive surface area in a microporous char particle becomes available with increasing carbon conversion.

The modified version of the random pore model includes the progressive opening of pores with conversion to account for these experimental observations. In the extended random pore model, it is assumed that not all the pores participate in the reaction initially. It is assumed that $\lambda(r)$ can be divided into two parts: one part represents the pores on which the reaction takes place initially and the other represents those pores that participate in the reaction only at a later carbon conversion. It is assumed that the opening of inaccessible

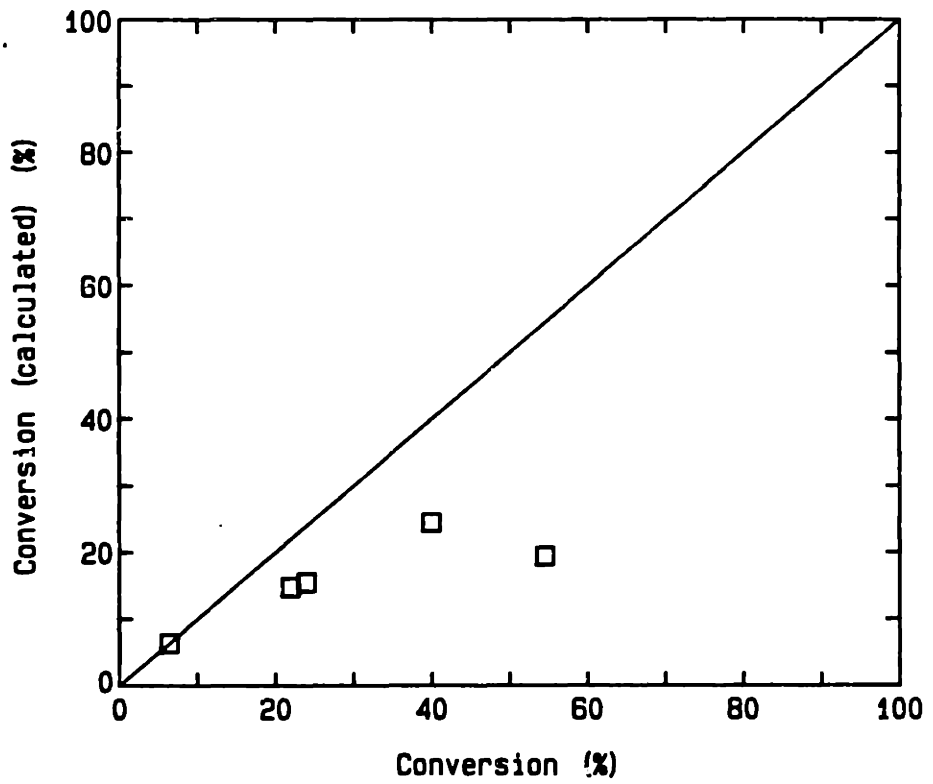

Figure 1.4-2. Conversion calculated from porosity data versus conversion by reaction in air at 760 K (C-O char).

pores can be described by an empirical function, $(1-e^{-q\tau})$, where τ is a constant and q is the distance the surface of an initially accessible pore has receeded.

The porosity of the solid is then given as:

$$-\ln(1-\epsilon(q)) = 2\pi\int_{r_*}^{r^*}(r+q)^2\lambda(r)dr + 2\pi\int_{o}^{q}\int_{r_*}^{r^*}\phi(r+q-s)^2\,\lambda(r)e^{-\tau s}\,drds$$

$$+ 2\pi\int_{q}^{q_\infty}\int_{r_*}^{r^*}\phi r^2\,\lambda(r)\,e^{-\tau s}\,drds \qquad (1.4.5)$$

where $\epsilon(q)$ is the porosity of the solid as a function of q, the recession distance and ϕ is a fraction of the initially accessible pores that are closed. The first term on the RHS is the contribution to the porosity of pores initially accessible, the second term is the contribution of pores opening at a later conversion and the third term includes those pores not yet accessible.

Evaluation of the integrals and additional algebraic simplification yields:

$$-\ln\left(\frac{1-\epsilon(q)}{1-\epsilon_T}\right) = 2\pi\left[\,2q\,B_1\left(1+\gamma-(\gamma/q\tau)(1-e^{-\tau q})\right)\right.$$

$$\left. + q^2\,B_o\left(1+\xi-(2\gamma/q\tau)(1-1/q\tau(1-e^{-\tau q}))\right)\right] \qquad (1.4.6)$$

where ϵ_T is the initial total porosity, including the

contribution of all initially inaccessible pores; $\zeta = \phi/\tau$; and B_o and B_1 are the zeroeth and first moments of $\lambda(r)$. Differentiation of Equation 1.4-6 and simplification yields the surface area (or reaction rate since the rate is assumed to be directly proportional to the surface area) in terms of the variable q:

$$\frac{S(x)}{S_o} = (1-x)\left[(1+\zeta-\zeta e^{-\tau q}) + B_o/B_1\left(q(1+\zeta) - \zeta/\tau\,(1-e^{-q\tau})\right)\right] \tag{1.4.7}$$

where S_o is defined as either the initial surface area or rate. The model was fitted numerically to the non-catalyzed char oxygen rate versus conversion data. The results are presented in Figure 1.4-3. The model gives an improved fit to the data, although the empirical pore opening function cannot quite match the initial reaction rate increase. If a mono-sized pore distribution is assumed, the parameters of the model can be related to an initial porosity of 0.35 and an inaccessible porosity equal to 23% of the total porosity. The parameter τ is equal to about 0.1 of the pore radius. The initial porosity predicted by the model is in good agreement with that of the C-O char, and the fraction inaccessible is a quite reasonable value. If it is assumed that the difference in reaction rate between the smallest particle size and the 90-106 μm particles represents an initially inaccessible porosity, the predicted value agrees quite well with measurements.

For the catalyzed chars, it was not possible to fit the

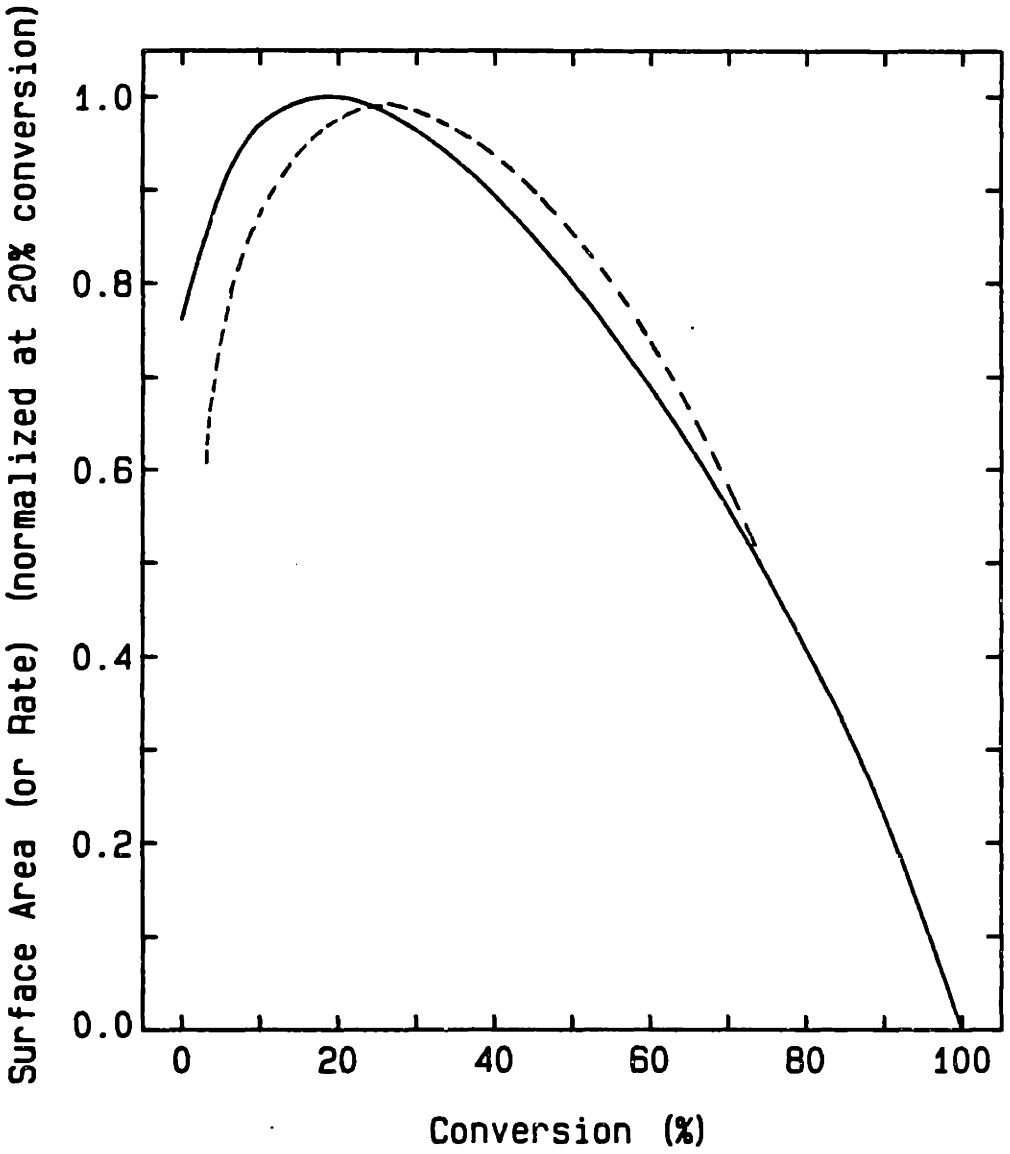

Figure 1.4-3. Comparison of the C-O char rate versus conversion data (---) to the extended random pore model (——).

data directly because of the large difference between the initial and maximum rates. However, if it is assumed that the rate constant for the catalyzed reaction is proportional to the calcium to carbon ratio of the char, one obtains:

$$r = m_o S(x) \cdot k_o \frac{Ca}{C_o(1-x)} \qquad (1.4.8)$$

where r is the rate, m_o is the initial sample weight, k_o is a rate constant, S(x) is the surface area as a function of conversion, and $Ca/C_o(1-x)$ is the calcium to carbon ratio of the char with respect to conversion. Normalization by the maximum rate yields:

$$\frac{(1-x)r}{(1-x_m)r_m} = \frac{S(x)}{S_m} \qquad (1.4.9)$$

where S_m is the surface area at the maximum rate and x_m is the conversion at the maximum rate. Values for $S(x)/S_m$ corrected for the calcium/carbon ratio are compared to the rate versus conversion data of the noncatalyzed char in Figure 1.4-4. Correction of the reaction rate by this factor brings the rate versus conversion curve of the catalyzed char into good agreement with the data of the non-catalyzed char. This result implies that the important factor in catalysis is the total calcium to total carbon ratio rather than the calcium to surface area ratio of the catalyzed char. Furthermore, it shows that the calcium remains with the carbon and does not deactivate at least over the first half of the carbon

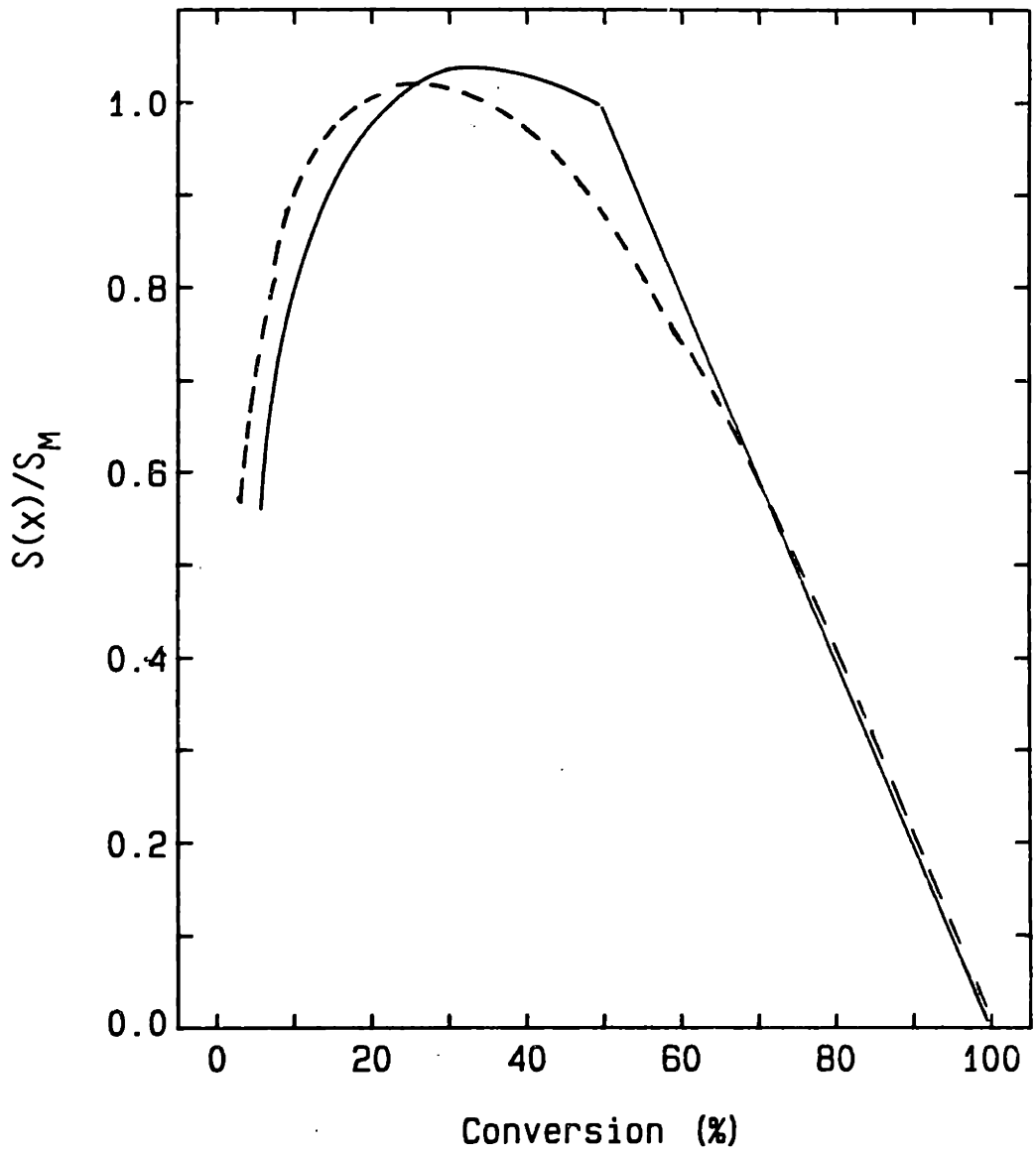

Figure 1.4-4. Rate versus conversion data of the C-3.6 char (——) adjusted to a constant calcium to carbon ratio at x = 0.4. Rate normalized to the rate at x = 0.4 for the C-O char (----).

conversion range. The reason the rate of the catalyzed char reaches a maximum at 40% conversion is uncertain. Possibly further increases in the calcium to carbon ratio beyond this point provides no additional increases in reactivity, although other factors must also affect catalyst deactivation at progressively higher carbon conversions. For example, although the maximum rate for the 1% calcium char is displaced to a slightly higher conversion ($\sim$ 50%), this displacement cannot quantitatively account for deactivation only because of calcium saturation.

1.5. CONCLUSIONS

1. Calcium is an effective catalyst for carbon gasification when it is present as a complex (or in solution) with the carbon. Calcium in a separate solid phase is inactive.

2. Approximately 1%(mole/mole) calcium increases carbon reactivity by almost two orders of magnitude for the oxygen reaction and three orders of magnitude for the carbon dioxide reaction. This is comparable to the increase in reactivity obtained with potassium for the Boudouard reaction. For the oxygen reaction, the higher reactivity is comparable to the results obtained by Radovic with calcium ion exchanged lignite chars. The reaction rate increases linearly with calcium content.

3. Calcium increases reactivity over practically the entire carbon conversion range. The catalyst affects the reactivity of the carbon in all pores in approximately an equal manner. Intra-particle diffusion becomes evident at approximately the same reaction rate for both the catalyzed and non-catalyzed chars. At least up to 1050 K, the activity of the catalyst is not adversely affected by extensive heat treatment of the char.

4. The catalyst depresses the overall activation energy of the intrinsic reaction. Calculations, using absolute rate theory, show that the decrease in the activation energy gives exactly the higher reactivity observed with the catalyzed char. It is inferred that the catalyst acts through an alteration of the electron distribution in the solid, thereby changing the overall energy level of the solid.

5. Experimental measurements show that for microporous chars new reaction surface area must become available with increasing carbon conversion. An extension of the random pore model in which pore opening takes place as carbon conversion proceeds is used to model the rate versus conversion data of microporous chars.

6. The reaction rate of the catalyzed char increases directly with the increase in the calcium to carbon ratio of the char as carbon is removed. This implies that the calcium tends to remain with the carbon and not deactivate at least over the first 50% of the carbon conversion range.

CHAPTER 2. INTRODUCTION, LITERATURE REVIEW, AND THESIS OBJECTIVES

2.1 INTRODUCTION

The gasification reactions refer to the reactions of carbon with oxygen, steam, or carbon dioxide. The industrial importance of these reactions in a broad range of processes has resulted in many fundamental studies of carbon gasification with carbons ranging from graphite to numerous different types of non-structured chars. Certainly in terms of the number of investigations and of our basic understanding of the gasification reactions, this is a well developed research area. However, an approximate understanding of the surface reaction mechanism has not yet been obtained, and a quantitative understanding of the primary variables that determine the reactivity of a specific carbon and how this reactivity changes with conversion are still unknown. The determination of a reaction mechanism is difficult because of the inability to measure surface intermediates during reaction and to unambiguously interpret the limited data available. In comparison, the measurement of overall char reactivity as a function of the physical properties or chemical composition of the solid is much more amenable to engineering studies. Such studies have recently focused primarily on the effect of inorganic elements or compounds on carbon reactivity because of the large increase in reactivity often obtained by the addition of small amounts

of certain compounds to carbon. This increase may approach three or four orders of magnitude in some cases.

The large catalytic effect of certain inorganic elements has resulted in studies to determine such factors as the chemical state of the inorganic elements and the degree of dispersion on the carbon substrate in an effort to understand the mode of action of the catalyst. So far, however, there has been limited success in explaining why many inorganic elements can have such a significant effect on carbon reactivity. Studies of carbon catalyis have also attempted to quantify the increase in reactivity resulting from catalyst addition; however, almost all of the studies have been conducted over a limited carbon conversion range and at quite slow reaction rates to insure completely intrinsic kinetics. As a result, there still exists an uncertainty about the range of conditions for which catalysis is effective.

For the class of non-structured microporous chars, which includes coal chars and petroleum cokes, the two elements that have been principally studied as catalytic additives are potassium and, to a much lesser extent, calcium. The main reason for the current interest in the role of potassium during carbon gasification was the development of the Exxon catalytic coal gasification process (Lang and Neavel, 1982; Nahas, 1983). This process utilizes potassium salts both to catalyze the methanation reaction and to increase the gasification rate of the carbon. It was largely this

development that provided the impetus to study the fundamentals of a solid catalyzed gas-solid reaction and to consider how to exploit either the catalytic behavior of inorganic species towards carbon or any secondary reactions of the inorganic species with the reaction products in a coal conversion process. Calcium is of interest because it is this element that contributes to the formation of inherently more reactive chars. It is widely present in many coals and oil shales, either as calcium carbonate or ion exchanged onto the organic matrix. In addition, calcium is potentially an inexpensive additive for the modification of reactivity or other properties of the char.

Although much emphasis has been placed on increasing carbon reactivity in the literature, it is not obvious exactly what advantages this will provide in a specific process. From an engineering standpoint, the carbon-oxygen reaction generally occurs under conditions where the rate of mass tranport of the gas to the solid will largely govern the design of reactors. An increase in carbon reactivity, unless it is quite large, may not greatly alter the regime of mass transfer control. For the steam and carbon dioxide-carbon reactions the reaction kinetics can affect the reactor size or the process design. These reactions are endothermic, and therefore, the rate with which heat is converted to chemical energy will be a function of the char reactivity.

Beyond any direct application for improving the efficiency of a gasification process, a basic understanding

of intrinsic carbon reactivity is necessary for the development of mechanistic models that can accurately predict the reaction rate under complex conditions where mass transport effects are important.

Finally, it is possible that the presence of certain inorganic elements may be beneficial in a manner independent of any effect they may have as catalysts for the gasification reactions. For instance, the inorganic elements may act as a methanation catalyst as in the Exxon process, or they may possibly be very active for sulfur removal or NO_x reduction.

This study was undertaken to determine the effect of calcium on the intrinsic reactivity of a non-structured high surface-area carbon and to study the details of a gas-solid reaction involving a highly microporous solid. The kinetic measurements were obtained over the entire conversion range, over a wide temperature range, and at various reactant gas concentrations.

2.2 BACKGROUND AND LITERATURE REVIEW

2.2.1 The Reactivity of Carbons

Many of the quantitative kinetic studies that have been made over the past two decades are summarized in a number of reviews (Essenhigh, 1981; Smith, 1982; Laurendeau, 1978). These compilations show that there is a significant variation in reactivity among chars. The differences in reactivity are usually attributed to char properties such as the extent of graphitization, the pore structure of the solid, and the

presence of inorganic species. In particular, the measured activation energy and reaction order for graphite and microporous chars are often significantly different. To date, the differences in the kinetic parameters of these two types of carbon have been inadequately characterized with respect to the physical properties of the two carbons; however, it is the inclusion of both graphite and microporous chars in a common list of carbon reactivity data that has amplified the variations in reactivity among carbons.

Except for the difference in reactivity between graphite and microporous chars, catalysis of the carbon reaction by inorganic species may well be the primary factor responsible for variations in reactivity. Within either class of carbons, reactivity can be altered by a few orders of magnitude when catalysts are present. For example, Hastings (1984), Jenkins et al. (1973), and Hippo (1975) all emphasize the importance of mineral matter in determining the reactivity of coal chars.

2.2.2 Catalysis of the Carbon Gasification Reactions

The substantial literature in which the catalytic effect of many different elements on char and graphite reaction rates has been investigated has been reviewed by Walker et al. (1968); Wen (1980); McKee (1981); and Wood and Sancier (1984). Although the term catalysis is usually applied to this phenomena, the situation is different from the usual catalytic reaction system, since one is already dealing with

a heterogeneous reaction system. In addition, the catalysts may be altered or undergo severe changes as the carbon is removed.

What is evident from these reviews is the wide range of elements that can act as gasification catalysts. Many of the catalysts accelerate char reactivity under both reducing and oxidizing conditions. (Hydrogenation catalysts were not considered in this study.) Catalytic studies usually compare the differences in reactivity between a specific carbon both with and without a catalyst. Thus, differences in carbon structure (e.g. Spiro et al., 1983) are usually not strongly considered by investigators when the catalytic effect of a specific element is evaluated or when a mechanistic explanation for the catalytic effect is established. McKee has summarized the experimental data by categorizing the results with respect to elements of the same groups in the periodic table. He notes that the alkali and alkaline earth elements, transition elements, noble metals, and certain miscellaneous compounds are all effective oxidation catalysts. For the gasification reactions, the alkali and alkaline earth elements and the metals of the iron and platinum group are identified as the most active.

Attempts to explain the catalytic activity in terms of a chemical mechanism have been directed toward establishing a broad ranging explanation that encompasses the numerous species that act as catalysts. The two most widely supported explanations to date are the electron transfer and the oxygen

transfer mechanisms. The electron transfer mechanism, the details of which were originally proposed by Long and Sykes (1950), postulates that the catalyst affects the general energy level of the solid. It proposes that the catalyst acts by withdrawing a π-electron from the graphitic structure. Calculations with molecular orbital theory show that such an electron deficient ring would induce a stronger carbon-oxygen bond and weaken the adjacent carbon-carbon bonds. Long and Sykes suggest that transition elements, which have unfilled d-bands, could withdraw a π-electron from the ring structure and that the alkali and alkaline earth elements could form covalent bonds at points of high electron density and thereby withdraw a π-electron. This mechanism does not require the catalyst to be situated directly at a reactive site; the catalyst only alters the electron distribution of the carbon substrate.

The oxygen transfer mechanism proposes that the catalyst undergoes oxidation reduction cycles with the reactant and the carbon and thereby acts as an intermediate to supply oxygen to the carbon. McKee (1981) lists as support for this mechanism the observation of Amariglio and Duval (1966) who suggest that only metals that can oscillate between two or more oxidation states can act as oxidation catalysts. McKee also notes that transition elements that can be reduced by carbon at temperatures below 1000C are active catalysts, whereas stable oxides such as those of aluminum, silica, and tungsten are not. Further evidence for this mechanism are

the CAEM (controlled atmosphere electron microscopy) experiments, which usually show mobile catalyst particles on the carbon surface and extensive pitting of the carbon near the particle. This phenomena is interpreted as evidence of cyclic oxidation and reduction of the catalyst particle as it migrates across the carbon surface (McKee, 1983). For the alkali and alkaline earth elements, evidence for this mechanism are the observations that carbon accelerates the decomposition of the carbonate to the oxide and that the oxide form is the active species during the catalyzed carbon-oxygen reaction. McKee (1981; 1983) suggests that a possible reaction sequence involving these elements could be:

$$M_2CO_3 + C + O_2 \rightarrow M_2O + 2CO_2$$
$$M_2O + 1/2\ O_2 \rightarrow M_2O_2$$
$$2\ M_2O_2 + C \rightarrow 2\ M_2O + CO_2$$

where the active intermediary compound is a peroxide or higher oxide. M is assumed to be any group IA element.

It is proposed that the oxygen transfer mechanism is also operative during the catalyzed carbon dioxide and steam reactions. Walker et al. (1968) in their study of graphite gasification by group VIII metals (Fe, Ni, Co) present a phenomenological argument for a mechanism that involves dissociative chemisorption of CO_2 at the metal surface to form CO and a labile oxygen atom that can react with the carbon to form CO. McKee (1981; 1983) suggests a similiar type of mechanism for the group IA elements based on the

observation of alkali metal vapor during the carbon catalyzed reaction. The proposed sequence involves the carbothermic reduction reaction to form metal vapor:

$$M_2CO_3 + 2\ C \longrightarrow 2\ M + 3\ CO$$

The alkali can then participate in a dissociative chemisorption mechanism in the same manner as the group VIII metals. Wood et al. (1983) have verified the occurrence of the carbothermic reduction reaction using Knudsen cell mass spectrometry.

Based on experimental data which show the alkaline earth elements to behave analogously to the group IA elements as carbon catalysts, McKee (1979; 1980) suggests that an analogous mechanism applies to these elements. However, extension of the mechanism is problematic since reduction to the metal is unlikely to occur for the group IIA elements because of the greater stability of the oxide.

Wood and Sancier (1984) point out that much of the recent experimental data support a mechanism whereby the catalyst acts to supply oxygen to the carbon but indicate that there is insufficient data to establish a possible reaction sequence. Evidence for a mechanism involving oxygen transfer is based to a large extent on Wood's study of the carbon-alkali reaction and on the work of Mims and Pabst (1980). Mims and Pabst have clearly demonstrated that K_2CO_3 will react with the carbonaceous substrate to form a stable

and distinct surface salt complex, which is assumed to be analogous to a phenolate salt (Mims et al., 1982):

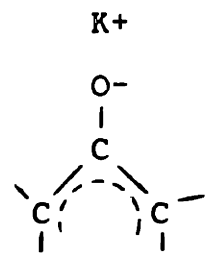

Their data provide strong evidence that the surface complexes participate directly in the catalytic reaction. They postulate that these surface salts accelerate the reaction by acting as oxygen transfer sites. Mims and Pabst argue that catalysis occurs because the catalyst increases the number of active sites on the carbon. Their studies, however, were concerned only with the steam and carbon dioxide reactions.

Objections to the oxygen transfer mechanism have been pointed out by a number of researchers. Walker et al. (1968) note that the mechanism tacitly assumes that the rate-controlling step for the non-catalyzed reaction is oxygen chemisorption or that the catalyst particle acts as an active site center. Long and Sykes (1950) conclude that since this mechanism consists of a series of steps completely different from those occurring in the non-catalyzed reaction, it would be expected that the kinetic parameters of the catalyzed reaction be widely different. This is usually not observed.

2.2.3 Calcium as a Gasification Catalyst

Most of the recent studies of carbon catalysis with microporous chars have involved the group IA elements, principally potassium. (Fuel 62, February, 1983 and Fuel 63, August, 1984 present a summary of the papers presented at the International Symposium, "Fundamentals of Catalytic Coal and Carbon Gasification", Amsterdam, The Netherlands, Sept. 1982 and at the Conference on "Carbon and Catalysis", London, Dec. 1983, respectively.) The interest in potassium is probably related to the potential commercial application of this element in coal conversion processes. In addition, potassium catalyzed chars are relatively simple to prepare. Mims and Pabst (1980) have demonstrated that the catalytic activity is relatively independent of the method of preparation. Whether potassium addition is by wet impregnation, dry mixing, or ion exchange, the linear relationship between potassium loading and reactivity is about the same.

In contrast, studies with calcium have been much more infrequent. In part, this is due to the uncertainty in the past of the effectiveness of calcium as a catalyst. Marsh and Adair (1975) added various metal nitrates, including $CaNO_3$, to solutions of furfuryl alcohol, which were subsequently polymerized and charred. No increase in the reactivity of the calcium-added char is observed although the other metal nitrates all cause an increase in char reactivity. Tomita et al. (1977) added $CaCO_3$ as a dry powder to a char and found no effect. Haynes et al. (1973)

have investigated many different compounds for catalytic potential and found that $Ca(OH)_2$ has only a minor effect. However, a number of investigators (Hippo, 1977; Radovic, 1982; and Lang and Neavel, 1982) ion-exchanged calcium onto a carbon substrate or removed calcium by demineralization of coal char and found a significant change in reactivity. Otto et al. (1978) also have found an increase in reactivity after impregnating graphite and chars with a calcium acetate solution. (This method of impregnation, however, may have resulted in ion exchange occurring with the carbon surface.) In another study, McKee (1979; 1980) mixed $CaCO_3$ with graphite and observed an increase in reactivity. CAEM investigations (Cairns et al., 1977) indicate that calcium oxide particles are mobile on a graphite surface and that accelerated pitting of the surface occurs in the vicinity of the particle.

In summary, these studies indicate that calcium is an active catalyst, but that the method of impregnation and the degree of dispersion are important in determining the extent of activity. Furthermore, it is the ion-exchanged calcium that is responsible for the inherently higher reactivity of some coal chars. Potassium is usually present in much smaller amounts than calcium in coals, and when present, it is usually tied up in an inactive state with the alumina-silicate minerals in the ash (Lang and Neavel, 1982). Hippo (1977) has shown that carbon reactivity responds linearly to the amount of ion-exchanged calcium.

Calcium oxide can react with carbon dioxide to form calcium carbonate, or the carbonate can readily decompose to form calcium oxide:

$$CaCO_3 \rightleftharpoons CaO + CO_2$$

The direction of the reaction depends on the temperature and the local CO_2 partial pressure. The equilibrium diagram for this reaction is given in Figure 2.2-1. The variance of this system is one (Meissner, 1971); therefore fixing both the temperature and CO_2 pressure below the equilibrium line results in the formation of only a single phase, $CaCO_3$, whereas above the line only CaO is present.

2.2.4 Properties of the Carbon Surface Oxides

Surface oxides on the carbon may be important to the interaction between the carbon and the alkali or alkaline earth elements. Sears et al. (1980) show that the reactivity of certain lignites correlates with the oxygen content of the char as well as with the calcium content, and Lang and Neavel (1982) also present evidence that the ability of calcium to enhance carbon reactivity depends on the oxygen content of the char. In addition, surface oxides are important in the ion exchange properties of the carbon surface (Schafer, 1970).

Puri (1970) has extensively studied the surface oxides of sugar charcoal and has identified two types of surface oxide complexes. H surface complexes are formed by exposing chars

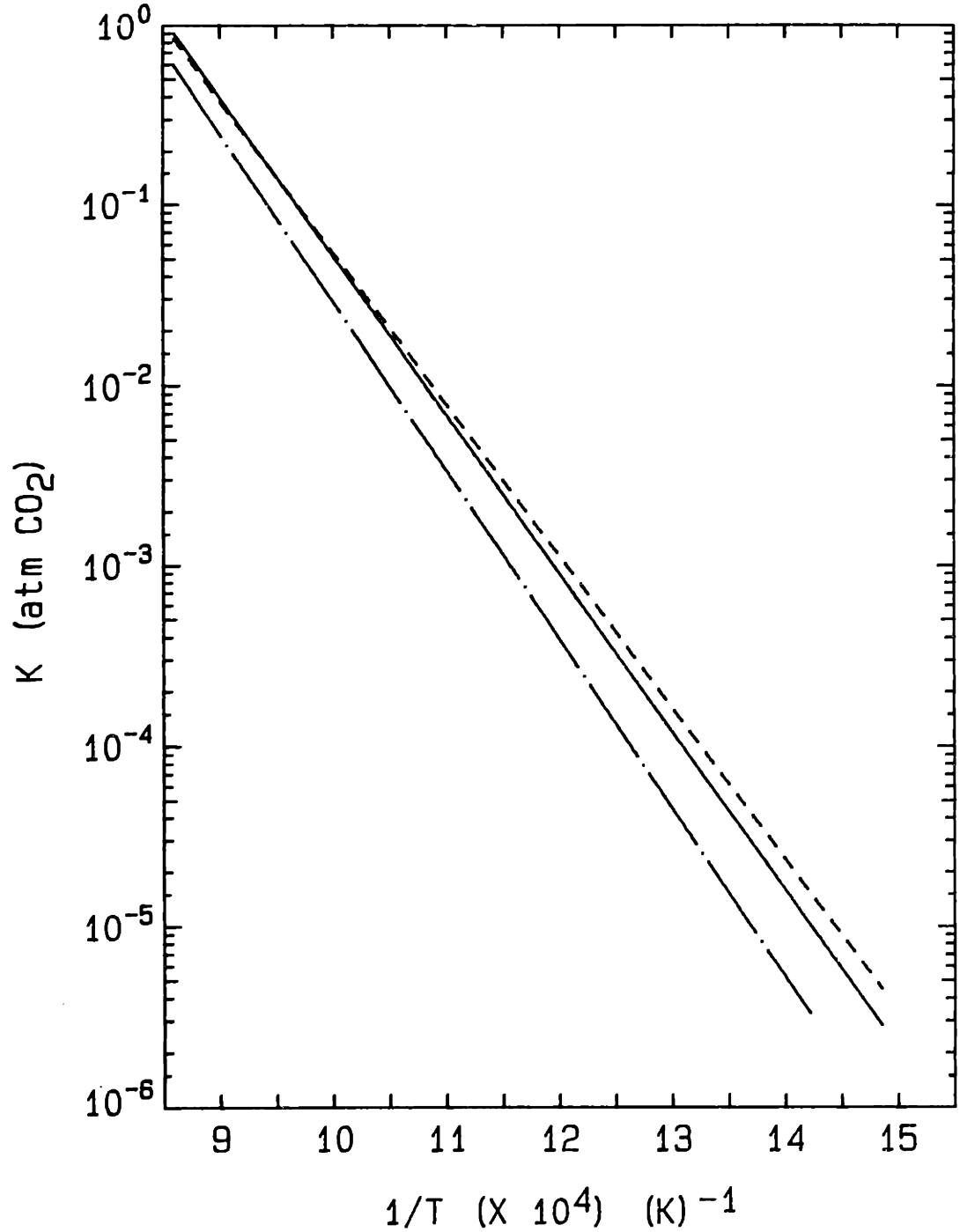

Figure 2.2-1. Effect of temperature on the equilibrium constant for the reaction $CaCO_3 \rightleftarrows CaO + CO_2$. (——) Squires, 1967; (---) Turkdogan et al, 1973; (-·-) Campbell, 1978, experimental data.

that had been previously heated to 1000C to oxygen at room temperature. L complexes are formed by exposure of the char to oxygen at 200-400C or with aqueous oxidizers. These two surface oxides show quite different behaviors: H carbons can raise the pH of a neutral solution and are hydrophobic, L carbons lower the pH of a solution and are hydrophillic (Mattson and Mark, 1971).

Puri (1957) has shown that the L carbon behave like insoluble acids and that they react with alkalis in a neutralizing reaction where the salt is associated with the insoluble solid phase. The results of his work have shown that the acid behavior of the carbon is associated with an oxygen complex on the carbon surface that is released as CO_2 upon heating. Alternatively, oxides that leave the surface as CO or H_2O do not contribute to the acidic behavior of the solid. Furthermore, since one mole of CO_2 is released for every two equivalents of base neutralized, he asserts that the CO_2 cannot be associated with a carboxylic acid group because in that case one mole of CO_2 would be formed for each equivalent of base that is neutralized (Puri, 1965).

In summary, his data indicate that the oxygen is present in distinctly different functional groups and that it is only the oxygen released as CO_2 upon heating, which is responsible for the acidic and thus ion exchange property of the char. Furthermore, the presence of an adequate number of these acidic oxygen groups is probably necessary to obtain significant loadings of a self dispersing catalyst such as

potassium. Puri (1957) also shows that the acid sites on the surface can bring about the decomposition of $CaCO_3$ in a manner analogous to other aqueous acids. By refluxing a solution of CaCO3 and sugar char, he has found that the amount of $CaCO_3$ that is decomposed corresponds closely to the acidic value (CO_2 complex equivalent) of the char.

2.2.5 The Gasification Reactions of Carbon

The gas reactions of carbon and the effect of diffusion in the porous solid on the reaction rate have been summarized and reviewed in a number of articles. The review by Walker, Rusinko, and Austin (1959) is still considered a classic in this field. More recent reviews by Essenhigh (1981) and Laurendeau (1978) include the numerous investigations and developments reported in the field since Walker's publication.

The gasification reactions refer to the reactions of carbon with oxygen as well as with carbon dioxide or steam. In all cases, the reactions transfer oxygen to the carbon, even though in terms of the gas phase one condition is oxidizing and the other is reducing. Although the thesis title refers to this entire group of reactions, in general usage the term gasification refers only to the carbon dioxide or steam reactions. The principal gasification reactions are summarized in Table 2.2-1. The two reactions of interest in this study are the carbon oxygen and the carbon-carbon dioxide (Boudouard) reactions.

Table 2.2-1. The Gasification Reactions of Carbon

Carbon-Oxygen

$$C + O_2 \longrightarrow CO_2 \qquad \Delta H = -94.0 \text{ kcal}$$

$$C + 1/2\ O_2 \longrightarrow CO \qquad = -26.6 \text{ kcal}$$

Carbon-Water

$$C + H_2O \longrightarrow CO + H_2 \qquad \Delta H = +31.1 \text{ kcal}$$

Carbon-Carbon Dioxide
(Boudouard)

$$C + CO_2 \longrightarrow 2\ CO \qquad \Delta H = +40.8 \text{ kcal}$$

Carbon dioxide and carbon monoxide are apparently both primary products of carbon oxidation. The CO/CO_2 ratio seems to increase sharply with temperature, but there is still much uncertainty about the fundamental aspects of this reaction and the carbon oxide ratio of the primary reaction products. Walker et al. (1967) has made a number of studies of surface oxide formation during the carbon-oxygen reaction and have concluded that oxygen is dissociatively adsorbed and that product formation upon desorption could probably be represented by the following reactions:

$$C(O) \longrightarrow CO$$

$$C(O) + C(O) \longrightarrow CO_2 + C_f$$

where C(O) is an adsorbed oxygen atom and C_f is an active site. The concept of an active site proposes that the reaction (adsorption or desorption) occurs at specific favored sites on the surface. Laurendeau (1978) suggests that these sites are associated with carbon edges or dislocations, inorganic impurities, or hydrogen or oxygen functional groups.

The Boudouard reaction is a reversible reaction and under appropriate conditions disproportionation of CO to carbon and CO_2 can occur. The equilibrium diagram for this reaction is presented in Figure 2.2-2. The rate of reaction, however, generally becomes appreciable only at temperatures above about 1100K.

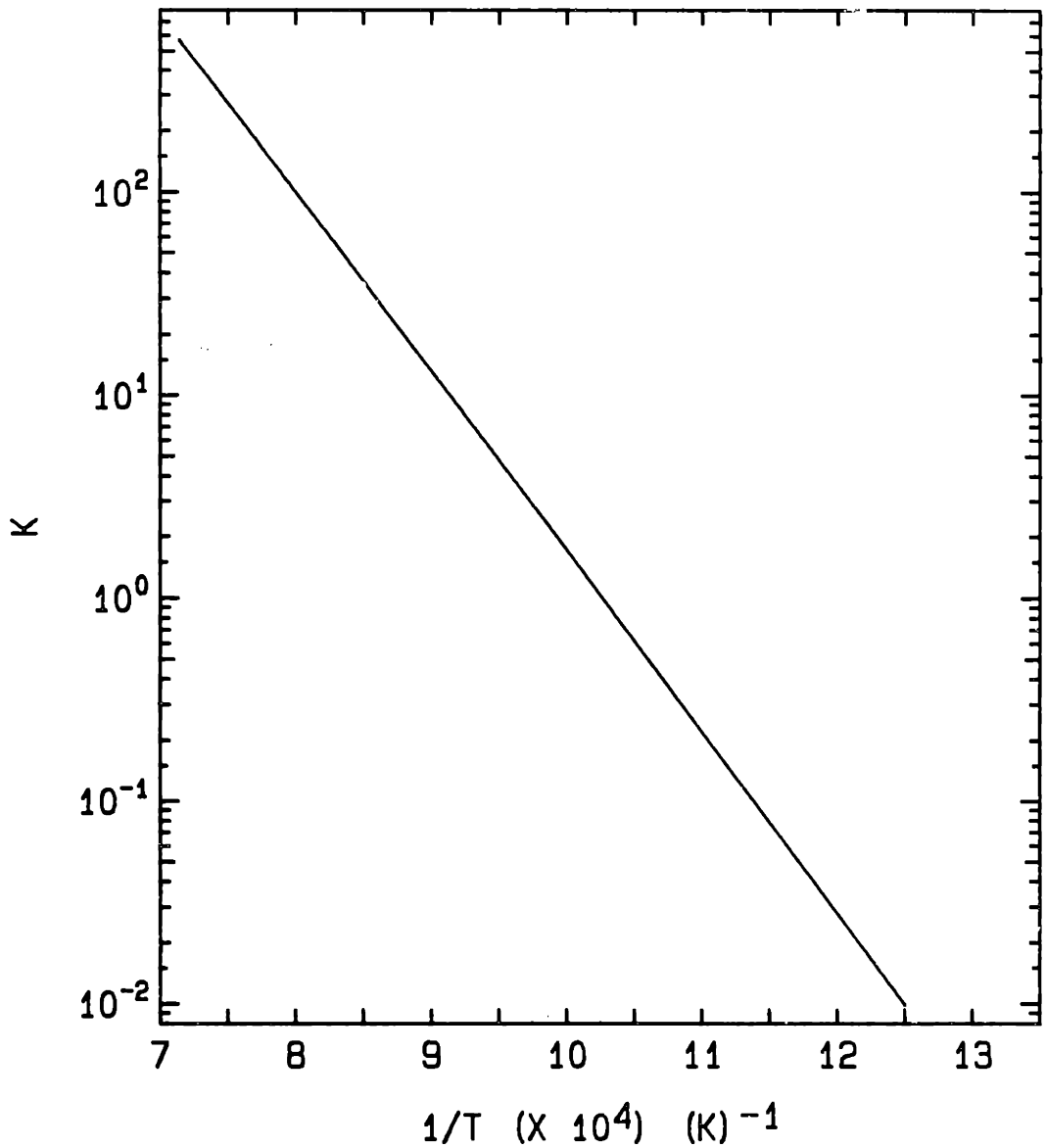

Figure 2.2-2. Effect of temperature on the equilibrium constant for the reaction $C + CO_2 \rightarrow 2\ CO$.

The overall reaction rate of carbon is usually described in terms of the intrinsic reactivity of the carbon surface and the total surface area of the solid:

$$r = \eta A_g [\rho(C_i, C_T, T)]$$

where: r is the rate of reaction (gmole C/sec - gmole C); η is an effectiveness factor defined in an analogous way to the effectiveness factor used in heterogeneous catalysis; A_g is the surface area of the solid (cm^2/gmole); and $\rho(C_i, C_T)$ is an intrinsic rate expression (gmole/cm^2-sec) that is a function of the local gas concentration (C_i), the number of active sites on the carbon surface (C_T), and temperature. Its functional form may be either a power law or a Langmuir-Hinshelwood expression.

The functional form of ρ is determined from a mechanistic model for the surface reaction. For the oxidation reaction, no generally agreed upon mechanism exists, and therefore, a power law expression is generally used. Laurendeau (1978) suggests that the reaction order lies between 0 and 1 and that it is a function of temperature. The stoichiometry of the reaction is usually determined experimentally, or it can be calculated from some correlation (e.g. Arthur, 1951).

The kinetic data for the Boudouard reaction can be successfully correlated by a Langmuir-Hinshelwood rate expression (Walker, 1968):

$$\rho = \frac{k_2 k_1 [C_T] [CO_2]}{k_2 + k_{-1}[CO] + k_1 [CO_2]}$$

where the k's are rate constants for the individual reaction, C_T is the concentration of active sites, and the brackets denote concentration. Although there are a number of different mechanistic formulations that will give the same kinetic expression, experimental evidence has accumulated to indicate that oxygen exchange is one of the steps in the mechanism. Inhibition of the reaction does not seem to be due to CO adsorption on active sites. A simple two step model that will give the appropriate rate expression is:

$$CO_2 + C_f \underset{k_{-1}}{\overset{k_1}{\rightleftharpoons}} CO + C(O)$$

$$C(O) \xrightarrow{k_2} CO$$

Application of the usual steady state assumption to C(O) yields the general form of the rate equation:

$$C(O) = \frac{k_1 [CO_2]}{k_2 + k_{-1}[CO] + k_1 [CO_2]}$$

Ergun and Mentser (1965) have shown that at typical experimental reaction conditions $k_1[CO_2] > k_2$. For some conditions, the $k_{-1}[CO]$ term dominates, and one obtains a relatively simple form for the rate expression:

$$\rho = \frac{k_1 k_2 [C_T][CO_2]}{k_{-1} [CO]}$$

2.2.6 Surface Area Measurements of Chars and Surface Area Models

The rate expressions presented in Section 2.2.5 are a

function of the surface area of the solid on which the reaction takes place. The determination of the intrinsic reactivity from experimental data, therefore, requires knowledge of the reactive surface area of the solid. The calculation of char surface areas is at present not a routine analysis. The basis of the analysis is usually an experimental isotherm, but the determination of the monolayer coverage from the adsorption data is usually not straight forward and cannot be made without regard to prior experience and consistency of value as determined from different adsorption isotherms. Complications arise because chars often tend to exhibit either micropore filling or activated diffusion (Lamond and Marsh, 1964; Marsh and Wynne-Jones, 1964). These two opposite phenomena generally do not both occur within a class of other materials. Pore filling results when molecules fill the micropores at low relative pressures. Analysis of the adorption data will then result in the determination of pore volume rather than surface area. Activated (or restricted) diffusion occurs when the adsorbate requires extra energy to pass through a restriction or into a very narrow pore. Activated diffusion can be checked for experimentally by measuring the time to achieve adsorption equilibrium; however, micropore filling will only become apparent when unrealistically high values for the surface area are calculated.

It has been shown experimentally that CO_2 adsorption isotherms will not exhibit either of these phenomena as

strongly as nitrogen adsorption isotherms, presumably because the carbon dioxide isotherms can be obtained at temperatures between 195 and 295 K rather than at 77 K. Calculation of the monolayer coverage from the adsorption data at very low relative pressures (i.e. from isotherms obtained at 273 or 295 K at CO2 pressures below 1 atm.) requires analysis by the Dubinin-Polanyi equation (Gregg and Sing, 1976). That the Dubinin-Polanyi equation will yield a value for the micropore surface area rather than the pore volume when applied to the low pressure CO2 adsorption data at 273-295 K has been demonstrated by Lamond and Marsh (1964). They also give some phenomenological arguments as to why this could be expected. Application of both the BET equation and the Dubinin-Polanyi equation to the nitrogen and CO_2 adsorption isotherms obtained with various polymeric chars was demonstrated in their study. The standard BET equation (Adamson, 1976) is usually used to calculate surface areas from adsorption data obtained at relative pressures up to about 0.3. More recently, Nenninger (1982) and Hurt (1985) have calculated surface areas from carbon dioxide and nitrogen adsorption data using these two equations.

A number of theoretical models have been formulated to predict changes in the internal surface area of a porous solid with conversion, and thus to determine the variation in reactivity of the solid with conversion. This of course assumes that the changes in reactivity are caused only by variations in the surface area of the solid. In all cases,

the models assume that the reaction rate on all pore surfaces is uniform and that the porosity of the particle is uniform.

The pioneering effort in the development of a surface area model for a porous solid that is consumed during reaction is the random capillary model of Petersen (1957). This random pore model approach to predicting surface area evolution and the frequency of pore intersections has been placed on a firm mathematical basis by Gavalas (1980), who developed a model using a Poisson process to describe the probability density function of randomly orientated lines in space that represent the pores of a solid. The model is discussed in detail in Section 5.1-3. An identical random pore model has been developed by Bhatia and Perlmutter (1980) who use the relationship of Avrami (1940) to relate the pore volume of a non-overlapped system of pores to the pore volume of an actual solid in which overlap will occur.

Another statistical model is the pore tree model of Simons and Finson (1979) and Simons (1982). This model also considers a distribution of pores in space, but it assigns an aspect ratio to the pores. This results in a model where constant downsizing of pores occurs, and a pore structure resembling a tree or river system is envisioned.

Hashimoto and Silveston (1973) have developed a model using the population balance equations to describe pore formation, pore intersections, and pore coalescence. The resulting model equations, however, can only be solved numerically, and the system of equations have a number of

adjustable parameters. As a result, it is difficult to apply the model in a discriminating manner in practice.

These structural models have also been used to determine the pore diameter and thus the effective diffusivity of a solid when intra-particle diffusion is significant (regime II kinetics). Application of the random pore model to this case is considered by Gavalas (1981).

2.3 OBJECTIVES AND OUTLINE OF THE THESIS

The principal objective of this thesis was to investigate the effect of calcium on the intrinsic reactivity of a non-structured microporous char and to obtain insight into the mode of action of the catalyst by comparing the catalyzed and non-catalyzed reaction rate data. The study also considered, in some detail, the change in reaction rate with conversion of a microporous char particle.

The experimental basis of this study was the measurement of reaction rates with a thermogravimetric analyzer (TGA) over a wide range of conditions. The TGA is described in detail in Chapter 3. A novel modification of the reactant flow system in the TGA allowed the measurement of weight changes smaller than 1.0 μg at typical operating conditions.

The char used in this study was manufactured from sucrose to provide an ash free material to which calcium could be added in a controlled manner. A model char was used in this investigation to eliminate any effects on the catalyst that could be attributed to the mineral matter or hetero-atom

content of the char.

The specific experimental tasks of this study included:

1. The manufacture of model chars from polymeric precursors and the development of techniques for the inclusion of calcium in these chars in different amounts and in various states of aggregation. The primary reason for using model compounds was to obtain some control over the properties of the solid and to allow the composition of the solid to be systematically varied.

2. The determination of the effectiveness of calcium as a catalyst for different initial dispersions and amounts of calcium in the char.

3. The measurement of reaction rate data for both the calcium-free and calcium-added chars over a wide range of conditions to ascertain the effectiveness of the catalyst. Measurements were made both at intrinsic reaction conditions and at conditions where intra particle diffusion begins to become significant. Reaction rates were measured over the complete conversion range to compare changes in reactivity with conversion of both the catalyzed and non-catalyzed chars. Kinetic data were obtained with carbon dioxide and oxygen and at different oxygen partial pressures.

4. The measurement of changes in catalyst dispersion with respect to conversion from an analysis of the rate data and

from carbon dioxide chemisorption measurements at 25 and 425 C.

5. The measurement of surface area and char porosity as a function of conversion. These values were determined from nitrogen adsorption and desorption isotherms obtained at 77 K.

6. The determination of the chemical (carbon, hydrogen, and oxygen) composition of the char as a function of conversion.

The results of the experimental measurements are summarized and presented in Chapter 4. The results are discussed in Chapter 5 and cover the main objectives of this thesis:

1. To determine how the relative effectiveness of calcium as a catalyst depends on the method and amount of calcium addition and the degree of dispersion.

2. To determine the effects of reaction conditions on the activity of calcium as a catalyst for the gasification reactions by measuring char reactivity over a wide range of conditions.

3. To critically evaluate proposed catalytic mechanisms against the data obtained in these experiments. The results indicate that the catalyst probably affects the energy distribution of the electrons in the solid, thereby making it more reactive; neither a mono-energetic active site model of

the catalyst nor an oxidation-reduction cycle involving the catalyst are consistent with the experimental data.

4. To compare the rate versus conversion data with the surface area and porosity variations of the char with respect to conversion. In a complementary study, the rate versus conversion data were compared to theoretical models that predict surface area variations with conversion. An extension of the random pore model is described that includes the opening of inaccessible porosity during the reaction of a microporous char. Experimental measurements showed that new surface area must become available as carbon conversion proceeds.

The conclusions are summarized and recommendations for further research are listed in Chapter 6.

Chapter 3. EXPERIMENTAL EQUIPMENT AND PROCEDURES

Reaction rate data were obtained by measuring the change in weight of the solid as a function of time with a Cahn Model 113 thermogravimetric analysis system. Modifications of the analyzer's gas flow system were made which allowed the acccurate measurement of weight changes smaller than 1 μg. This made operation possible with sample amounts as small as 50 μg. As a result, it was possible to obtain true kinetic data for characteristic reaction times approaching 30 sec. without the need to correct for bulk phase heat or mass transfer effects. These modifications and the thermo-gravimetric analyzer (TGA) are described in Sections 3.3.1 and 3.3.2. In Section 3.3.3, the experimental procedures are described.

The chars used in these experiments were manufactured from polymeric precursors and were a high surface area non-structured carbon. The surface area and total porosity of the model chars are similar to values typical of many coal chars. Char manufacture and characterization are discussed in detail in Section 3.1 of this chapter.

3.1 MANUFACTURE, PREPARATION, AND ANALYSIS OF THE CHARS

3.1.1 Introduction

Chars were made from a number of different organic precursors to provide a model substance with respect to the mineral matter content and chemical composition of the char.

The chars were made from sucrose, polyvinyl chloride (PVC), and furfuryl alcohol. Experimental techniques were developed for the addition of calcium in various states of aggregation to either the precursor or directly onto the char.

Kinetic measurements, however, were only made with the sucrose char both with and without calcium addition. A number of rate measurements were also made with Spherocarb because this carbon has been used by other investigators as a model material. Spherocarb (Analabs Inc., North Haven, CT) is a commercially available high surface area carbon molecular.

3.1.2 Sucrose Char

The sucrose char was made by pyrolyzing reagent grade sucrose (Mallinckrodt, Inc., Paris, KY), which contained less than 70 ppm residue after ignition, in a small stainless steel furnace under a steady flow of nitrogen. The pyrolysis furnace is described in Section 3.1.6. Between 50 and 75 g of sucrose (~1 mm size particles) were pyrolyzed in each run. The sucrose was heated at a rate of 7 K/min to approximately 925 K and then held isothermally for 15-30 minutes at the maximum temperature. Char yield was approximately 30%. Pyrolysis of the sucrose resulted in the formation of large but thin and brittle cenospheric char structures that completely filled the reactor volume. Individual char particles, generally less than 250 μm in size, were obtained by lightly crushing the expanded char. The crushed char

particles from a number of pyrolysis runs were subsequently heat treated for a second time in the furnace. The char was heated to 900 K in 1 hr but not held isothermally at the maximum temperature during the second heat treatment. The heat treated char was dry sieved to narrow size cuts using standard Tyler sieves and a Roto-tap machine. Oversized particles were crushed by mortar and pestle to increase the yield of the desired size fraction. The nominal particle size used in these experiments was 90-106 μm.

3.1.3 PVC char.

The PVC char was made from PVC powder obtained from Aldrich Chemical Co., Milwaukee, WI. Pyrolysis of the PVC was accomplished in two steps. The sample was initially heated to 500 K and held at that temperature for about 120 minutes to complete the initial decomposition of PVC, which results primarily in the evolution of HCl. Over 90% of the chlorine content of the PVC is lost as HCl at this temperature (Winslow et al., 1956). The residue was then heated to 900 K in 60 minutes and held isothermally at 900 K for an additional 30 minutes. This results in the evolution of the residual chlorine, some of the hydrogen, and various volatile hydrocarbons including tars (Gilbert and Kipling, 1962). Final char yield was about 13%. The resulting char consisted of small individual particles; swelling and agglomeration of the char was minimal. The char composition

is carbon and hydrogen; it contains only trace quantities of oxygen and chlorine.

3.1.4 PFA Char

Polyfurfuryl alcohol polymer (PFA) was made by adding 0.6 ml of 0.1 N nitric acid to 100 ml of furfuryl alcohol in a stainless steel beaker and heating the alcohol in a forced convection oven at 420 K overnight. Subsequent removal of the resinous polymer from the beaker was best done by cooling the beaker in liquid nitrogen and fracturing the polymer with a small hammer. The polymer chips (~60 μg) were pyrolyzed in the furnace at a heating rate of 5°C per minute to 900 K and held at that temperature for 30 minutes. Char yield was about 40%. The char had a rather glassy appearance; no significant swelling of the char precursor occurred during pyrolysis.

3.1.5 Sucrose Char, Calcium Added

Three different techniques were used to incorporate calcium into the sucrose char. Calcium was added prior to pyrolysis by dissolution of CaO in a sucrose solution and by incorporation of $CaCO_3$ particles in sucrose recrystallized from solution. Calcium was also added directly to the char by ion exchange.

Although calcium oxide is practically insoluble in water, it is highly soluble in a sucrose solution. A mixture of calcium oxide and sucrose forms what is known as a saccharate (Honig, 1953). It is likely that the behavior of the sucrose

as a weak acid towards the hydroxide results in the extensive solubility of CaO in a sucrose solution. Upon evaporation of excess water at a temperature of 360 K, the saccharate residue forms a caramel-like substance in which the calcium is atomically dispersed. Experimentally, calcium oxide (reagent powder, MCB, Cincinati, OH) was added to 150 ml of a 40 weight percent sucrose solution and the solution was stirred until the calcium oxide was completely dissolved. Dissolution of the CaO was slow. Between 0.3 and 2.0 g of calcium oxide were added depending on the desired calcium loading in the char. The mixture was then heated on a hot plate and continuously stirred until sufficient water had evaporated to form a syrup-like residue. At this point, the mixture was stirred manually and further heated until a very viscous caramel-like residue was obtained. This residue was readily removed from the beaker by freezing it with liquid nitrogen. The saccharate was pyrolyzed in the same manner as the sucrose; however, the saccharate did not swell as severely as the sucrose during pyrolysis. The saccharate char was not pyrolyzed a second time.

In comparison to calcium oxide, calcium carbonate is not soluble in a sucrose solution. Small calcium carbonate particles in a sucrose solution will form a uniform dispersion when the solution is agitated. Experimentally, 12 g of calcium carbonate (primary standard powder, Mallinkcrodt) were added to a solution of 250 ml distilled water and 200 g of sucrose. The mixture was continuously

stirred and heated until all the water was evaporated. The dispersed calcium carbonate particles became incorporated in the sucrose as it recrystallized from solution. The recrystallized sucrose was pyrolyzed in the same manner as the sucrose. Its behavior during pyrolysis was the same as that of the sucrose.

The final method of calcium addition was ion exchange of calcium onto the char. Data reported by Puri (1957) indicates that the ion-exchange capacity of the sucrose char should be quite high; however, in the present experiments it was only possible to exchange small amounts of calcium onto the pyrolyzed char. Pre-oxidation of the pyrolyzed char at 675 K for 90 minutes in 1 atm air (6% conversion) was necessary to obtain sufficient exchange capacity. A previous attempt to pre-oxidize the char at 325 K for 12 hours did not result in a significant increase in the number of exchangeable sites on the original pyrolyzed char. The experimental procedure was as follows: 180 mg of the pre-oxidized char were added to 230 ml of a 0.1 M calcium acetate solution to which a small amount of calcium hydroxide had been added to raise the initial pH to 10. The mixture was continuously stirred on a hot plate unit, and the approximate rate of exchange was monitored by measuring the pH of the solution (see Appendix 1). The reaction was conducted with a large excess of calcium acetate so that appreciable exchange could occur before the solution pH decreased significantly. The calcium ion exchange reaction

is apparently facilitated at pH values between 7 and 8.5 (Schafer, 1970). The reaction was conducted at 298 K. The char was kept in solution for about 6 hours, but even after that time, a small fraction of the char did not wet completely. At the end of the reaction, the mixture was vacuum filtered across a medium grit (30 μm) fritted glass funnel and rinsed with 0.7 ℓ of distilled water. The exchange solution was saved and back titrated with 0.1 N sodium hydroxide to determine the amount of calcium exchanged onto the char. The pH of the rinse solution was monitored to assure complete removal of the calcium acetate solution from the char. The char and the the fritted disc funnel were vacuum dried in a small oven at 310 K.

3.1.6 Low Temperature Pyrolysis Furnace

The pyrolysis furnace is shown schematically in Figure 3.1-1. The stainless steel vessel is approximately 8 cm in diameter and 20 cm high and is fitted with a quick release cap. A stainless steel screen retainer is mounted inside the vessel to prevent the sucrose char from expanding into the cooler upper section of the chamber during pyrolysis and plugging the gas outlet. The char precursor was placed in a crucible inside the vessel. The gaseous and condensable pyrolysis products exiting the vessel were passed through a glass wool filter, bubbled through a water scrubber, and passed through another glass wool filter before being vented. The nitrogen flow rate through the pyrolysis vessel was

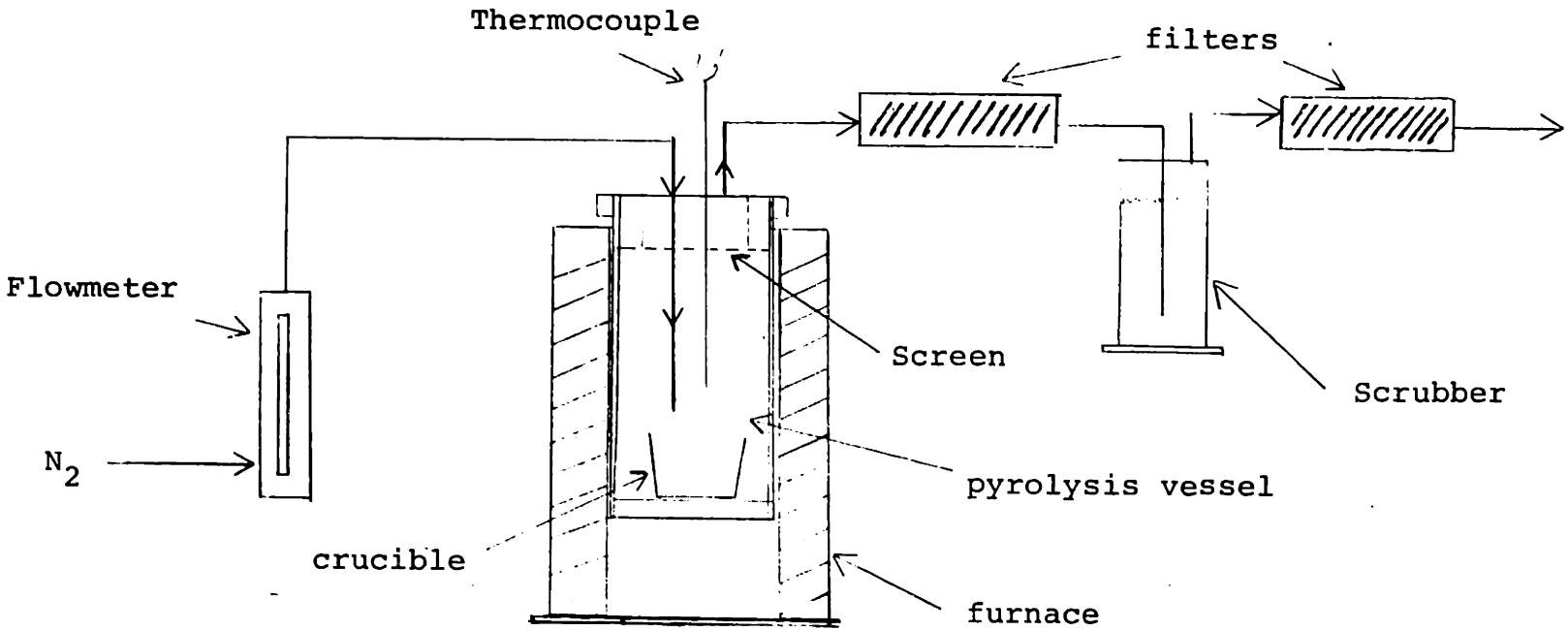

Figure 3.1-1. Low Temperature Pyrolysis Furnace.

approximately 0.7 ℓ/min. The furnace was constructed from four half circular high temperature electric heating elements. The temperature was monitored with a type K thermocouple and was controlled manually with two variacs.

3.1.7 Elemental Analysis

The elemental composition and the calcium content of the chars were determined by a commercial analytical laboratory (Huffman Laboratories, Wheatridge, CO and Galbraith Laboratories, Knoxville, TN). The calcium content of the chars was also determined using a Perkin Elmer Model 360 Atomic Adsorption Spectrophotometer from samples prepared from the ash residue at the conclusion of a TGA run. In general, the analysis technique developed in-house gave more consistent results than the results reported by the commercial laboratories.

A. Carbon, Hydrogen, and Oyxgen Analysis

Carbon, hydrogen, and carbonate carbon analyses were performed by Huffman Laboratories. It was requested that the samples be vacuum dried at 600 K for 15 minutes prior to analysis, and that all subsequent sample transfers be done under dry nitrogen. A temperature of 600 K was chosen to assure decomposition of any calcium hydroxide (Mess, 1985) and to remove any physically adsorbed gases on the char but to minimize the decomposition of chemisorbed oxygen. The carbon, hydrogen, and oxygen contents (oxygen was determined by difference) are based on the weight of the vacuum dried

sample. The oxygen content of the calcium added char was determined as follows:

$$x_o = 1 - \left[(x_c - x_{cc}) + x_H + x_{CO_2} + \frac{1.4\, x_{Ca}}{(1 - x)}\right] \qquad (3.1.1)$$

where x_o is the weight fraction of oxygen; x_c is the weight fraction of total carbon; x_{cc} is the weight fraction of carbonate carbon; x_H is the weight fraction of hydrogen; x_{CO_2} is the weight fraction carbonate carbon dioxide; x_{Ca} is the original weight fraction calcium in the (unreacted) char; and x is conversion.

B. Calcium Analysis

For the in-house method, the residue remaining on the sample pan after a TGA run was dissolved in 5 ml of 1 N HCl. The sample pan was removed from the solution using pre-cleaned tweezers and rinsed with 5 ml of distilled water, which was added directly to the HCl solution. The sample jar was a glass stoppered weighing jar that had been carefully cleaned and rinsed with dilute HCl and distilled water. Prior use of regular capped jars found that the HCl could leach calcium from the cap liner and that fingerprints could cause significant contamination of the glassware. The calcium content of the solution was determined with a Perkin-Elmer Atomic Adsorption Spectrophotometer in an air-acetylene flame at 422.7 nm. The instrument was calibrated with a blank solution and with a 20 µg/ml standard solution diluted by 50% in 1 N HCl. All measurements were

made at calcium concentrations less than 10 μg/ml, for which the instrument signal was linear.

Analysis by the commercial laboratories was done on the char, which required decomposition of the sample prior to analysis. This was done by the analytical laboratory using their standard techniques.

3.1.8 X-ray Diffraction Analysis

X-ray diffraction patterns were measured on selected char samples to determine the presence of calcium crystallites and the size of these crystallites. The diffraction measurements were made with a Diano vertical axis x-ray diffractometer using CuKa radiation (35 KV, 15 ma, and a nickel filter), a 0.1 degree receiving slit, and a 1.0 degree source slit. Peak intensity measurements were made at a step-through rate of 0.02 2θ degrees every 15 sec. The integral peak widths of the $K\alpha_1$ peak were obtained from the intensity versus 2θ degree data using the x-ray diffraction data interpretation program of Snow (1985). Instrument broadening was determined by a silicon standard. Crystallite size was calculated from the Scherrer equation (Azaroff and Buerger, 1958): $t = k\lambda/(B\cos\theta)$, where t is the grain size; θ is the position of the 2θ peak; λ is the radiation wavelength; B is the peak width in radians; and K is a constant with a value close to unity.

3.2 GAS ADSORPTION MEASUREMENTS

Nitrogen adsorption isotherms were obtained at 77K for various chars that had been heat treated or reacted to

different extents of conversion. Measurements were obtained with a volumetric gas adsorption apparatus. It was possible to obtain adsorption data with samples as small as 6 mg. Accuracy with such small samples depended primarily on a correct weighing of the sample; the volumetric measurements had sufficient accuracy provided the samples had a relatively high surface area.

3.2.1 Volumetric Adsorption Apparatus

The volumetric apparatus is shown schematically in Figure 3.2-1. It consists of a calibrated volume (A) that is connected to a gas storage volume (C) and the vacuum manifold (D) via a three way stopcock (V-1). Connected to the known volume is a pressure transducer (E), a second calibrated volume (F) and the sample bulb (B). The pressure in the system was maintained below 0.005 torr by a small mechanical vacuum pump and a liquid nitrogen trap. No diffusion pump was utilized in this system. The system vacuum was monitored by a McLoed Gauge (G). The pressure in the calibrated volume and sample bulb was measured by a Barocell Type 590 pressure transducer (Datametrics, Wilmington, MA). The transducer has an accuracy of +/- .005 mm Hg plus 0.15% of the reading when the transducer is maintained at a constant temperature. The output is linear over the pressure range of 0 to 500 mm Hg. The volume displacement of the diaphragm is 0.16 cc at 500 mm Hg. (This volume change was not taken into account in the volumetric calculations.) Helium and nitrogen from gas

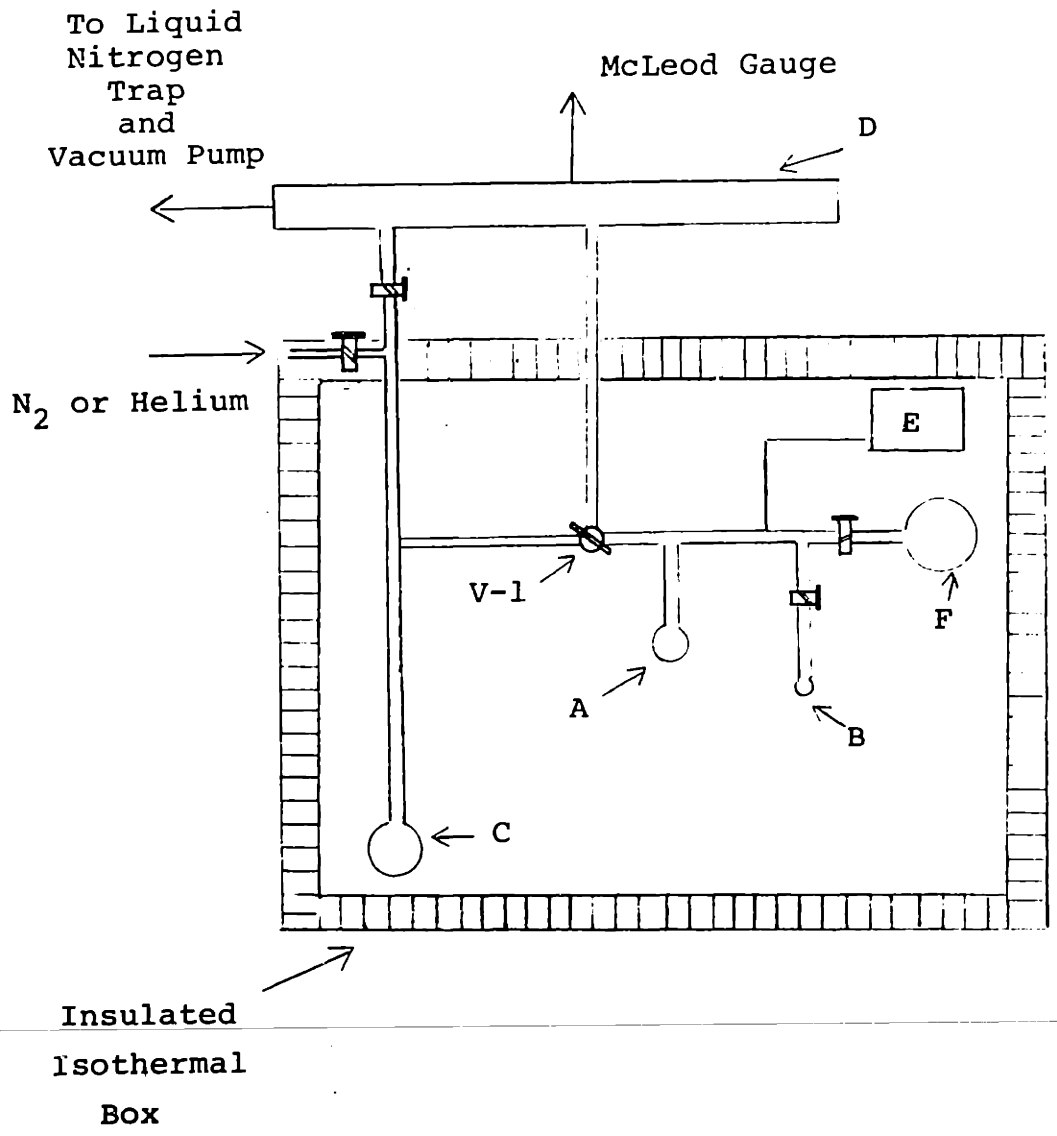

Figure 3.2-1. Volumetric Gas Adsorption Apparatus.

cylinders (Matheson, ultra high purity) were delivered via two low pressure (pancake-type) regulators to a manifold from which either gas could be admitted to the evacuated storage volume (C). Prior to each run, the manifold and regulators were carefully purged to displace any air that may have diffused into the system. This generally involved flushing nitrogen and helium through the lines and regulators for 5 minutes and then evacuating the connecting lines between the manifold and the volumetric apparatus. The volumetric adsorption apparatus is mounted inside an insulated constant temperature box that is based on the design of Mahajan and Walker (1978). Two light bulbs are used to supply heat and the temperature is controlled by a thermo-regulator. A small fan circulates air in the box to maintain temperature uniformity. A constant temperature within 0.1°C can be maintained in the box even after repeated door openings.

3.2.2 Experimental Procedure

Volume changes as small as 0.1 cc can be accurately measured with the apparatus. This allows surface area measurements with less than 10 mg of sample, provided the material has a high surface area. Accuracy with such small samples depends primarily on a precise weighing of the sample. Sample weights were obtained both before and after the adsorption measurements, since it was observed that the sample weight was slightly less after the sample was outgassed. Outgassing the char under vacuum was a tedious

procedure that required many more outgassing steps than the number calculated based on the dead volume of the sample bulb. Apparently the chars will physically adsorb a substantial amount of gas at room temperature. Outgassing needed to be done carefully and slowly to avoid blowing the char out from the sample bulb. Prior to an adsorption measurement the sample was heated under vacuum at 160 C for about four hours. During this time, it was necessary to keep liquid nitrogen in the cold trap to prevent back diffusion of vacuum pump oil to the heated sample bulb. After the sample was placed in the sample bulb, which was weighed before and after a run, the operating procedure was as follows. A small amount of nitrogen (or helium in the dead volume measurements) from the storage volume was admitted into the calibrated volume (A). After an equilibration time of approximately 5 minutes, valve (V-2) was opened and the gas was admitted to the sample bulb. From the pressure reading after a suitable equilibration time and the previously determined dead volume, the amount of gas adsorbed can be calculated:

$$N_{ads} = \frac{P_1 V_1}{RT_1} - \frac{P_2 (V_1 + V_2)}{RT_2} + N_r \qquad (3.2.1)$$

where V_1 is the calibrated volume; V_2 is the dead volume of the sample bulb; P_1 is the initial pressure; P_2 is the final pressure; T_1 and T_2 are the temperatures at each pressure measurement; R is the gas constant; N_r is the number of moles of gas remaining in the sample bulb, if any, from the

previous adsorption measurement and N_{ads} is the number of moles of gas adsorbed.

The adsorption measurements as a function of pressure were made in a cummulative manner. Desorption measurements were obtained by reducing the pressure in the calibrated volume to below the equilibrium pressure in the sample bulb and thereby outgassing the sample. Use of the larger (F) or both calibrated volumes allowed a greater amount of gas to be desorbed with each step. The liquid nitrogen level in the dewar surrounding the sample bulb was maintained at a constant level throughout the experiment by monitoring the temperature near the top of the dewar with a type T thermocouple. When the liquid nitrogen level dropped just enough to completely expose the thermocouple, a rapid increase in temperature was observed. This point was taken as the set point for the liquid nitrogen level.

3.3 REACTION RATE MEASUREMENTS BY THERMOGRAVIMETRIC ANALYSIS

3.3.1 The Thermogravimetric Analyzer

The kinetic measurements were obtained with a Cahn thermogravimetric analyzer (TGA). A schematic of the TGA system is shown in Figure 3.3-1. The microbalance is mounted inside a Pyrex glass housing. The balance is an electro-mechanical transducer that measures the force applied onto the balance beam by the current a motor coil needs to counterbalance the applied torque. The ultimate sensitivity of the balance is about 0.1 μg. The cylindrical glass

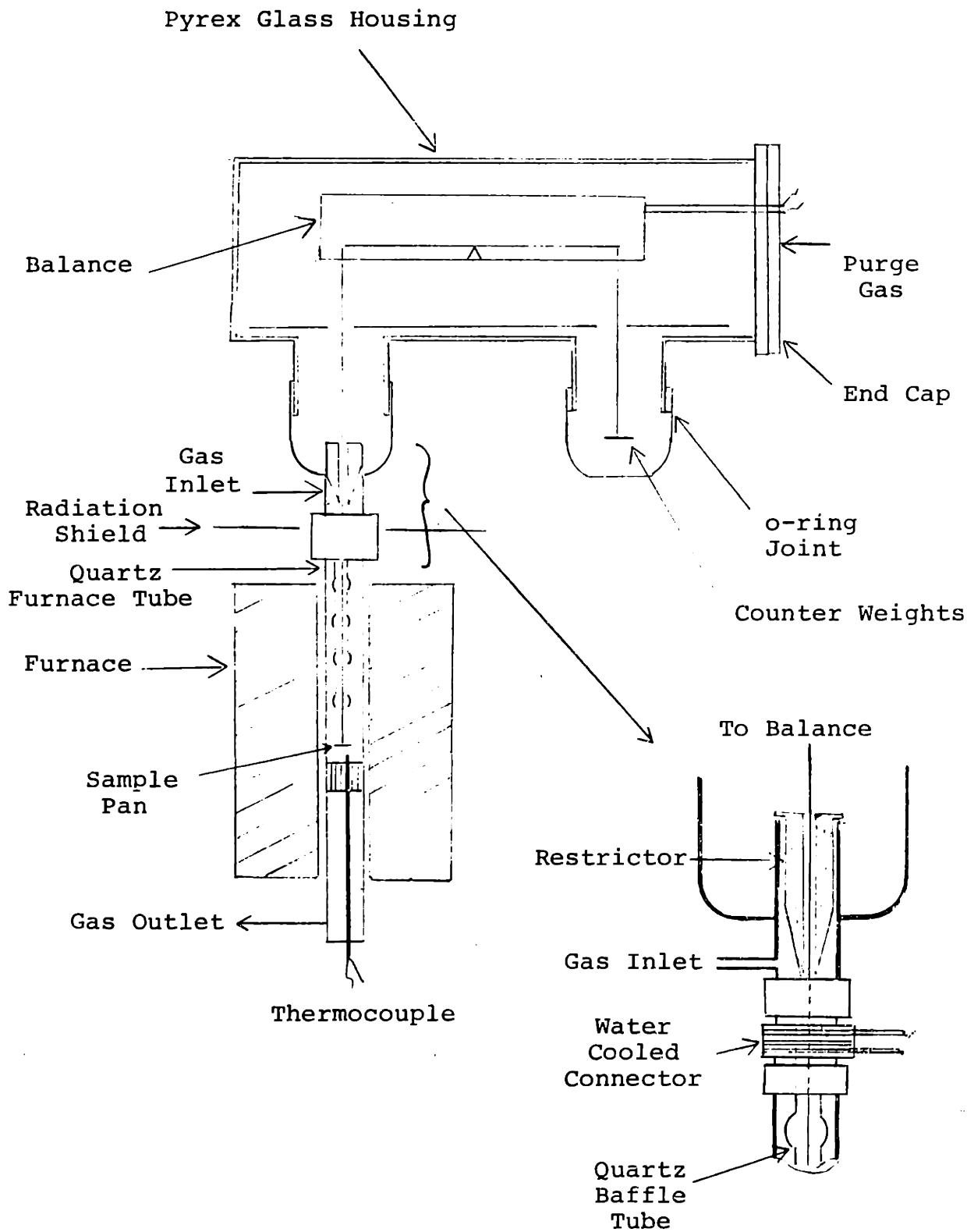

Figure 3.3-1. Thermogravimetric Analyzer.

chamber housing the balance is approximately 13 cm in diameter and 30 cm long. It is fitted on one end with an aluminum end cap with an o-ring seal. Electrical connections to the balance and a port for a purge gas are provided on this cap. Underneath the balance chamber are two large o-ring glass joints that allow either end caps or the reactor tube assembly to be connected to the housing. An endcap, which encloses the counterbalance pan, is attached to the right hand side o-ring joint underneath the balance chamber. Connected to the left-hand o-ring joint is a transition piece that provides a connection between the o-ring joint and a section of 1" heavy wall glass tubing. The inlet port for the reactant gases is attached onto this transition piece and an alternative inlet for the purge gas is available at the top of the transition piece. A flow restrictor is situated around the hangdown wire to minimize mixing by free convection of reactant gases with the large volume of gas in the balance chamber. The transition piece is shown in detail in the enlargement in the figure. The quartz tube is connected directly to the 1" glass tubing of the transition piece by a water-cooled Cajurn o-ring vacuum connector. The connector is cooled by 1/8" copper tubing wrapped around and soldered to the body of the fitting. Both the water cooled connector and the radiation shield between the furnace and the balance are needed to prevent thermal gradients caused by the hot furnace from affecting the performance of the balance inside the housing. The quartz furnace tube is 1" in

diameter with a 1 1/2" section of heavy wall 26 mm quartz tubing attached to one end. This end was precision ground and polished to the correct outside diameter to provide a tight connection to the o-ring fitting. Inside the furnace tube is a quartz glass baffle. This baffle is supported by a lip inside the body of the fitting. The baffle was supplied by Cahn and is intended to minimize free convection currents inside the vertical furnace tube. Two thermocouples are mounted through the bottom of the furnace tube. The type K thermocouple provides the input signal for the temperature controller. The type S thermocouple is used solely as a check. The alumina protection tube for the thermocouple wires is used to support a honeycomb ceramic baffle located just below the sample pan. The purpose of this baffle is also to minimize free convection currents in the furnace tube and to assure that the section of tube near the sample pan remains isothermal. The sample pan is supported by a hang-down wire of 0.1 mm nichrome. Before installation, the wire was straightened and stiffened by passing an electric current through the wire until the wire glowed a bright red to almost yellow color. The 8 mm diameter sample pan was constructed from a thin piece of platinum. In some runs an alumina pan (an 8 mm disc of alumina paper) was used instead.

The gas flow system is shown schematically in Figure 3.3-2. It consists of a reactant gas mixing system and a separate inert gas line. Both of these lines are directed to the inlet port of the TGA via a 4-way ball valve. Switching

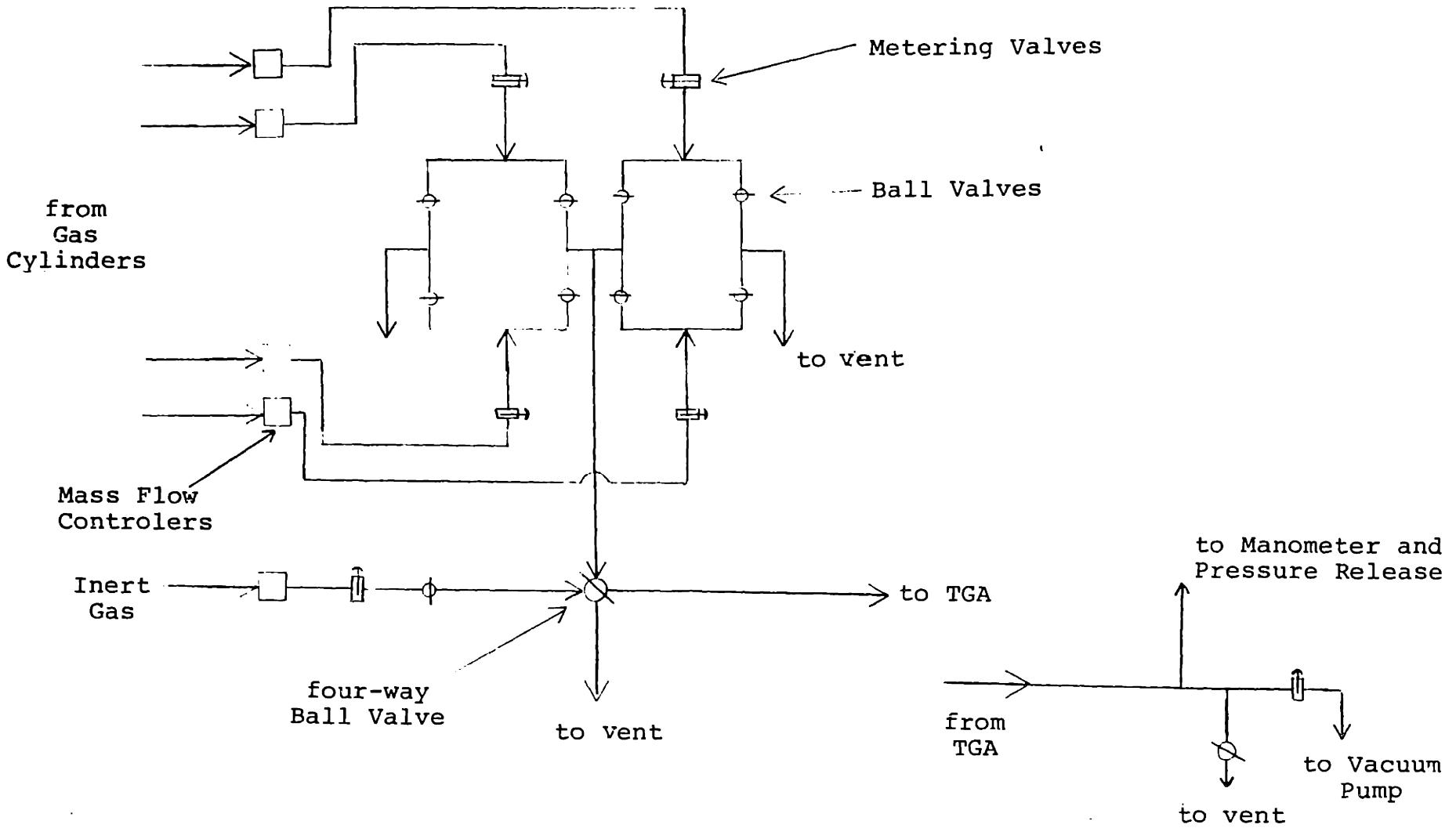

Figure 3.3-2. Reactant Flow System.

the valve directs either the reactant gas or the inert gas to the TGA while the alternate gas is vented. Product gases exit the TGA at the bottom of the furnace tube. (The TGA reactor can be considered a differential reactor.) The gases leaving the TGA are vented across a critical flow orifice to a hood. The pressure downstream of the valve is maintained at a sufficiently low pressure by a mechanical vacuum pump to achieve critical flow. Since the inlet gas flow is also metered across an orifice at critical flow conditions, this arrangement effectively isolates the gas flow in the reactor from any ambient aerodynamic disturbances. The pressure in the TGA is monitored with a water manometer that has a safety release at 24 cm H_2O.

The gas mixing system consists of four ports that are connected into a mixing tee and four alternate bypass lines that are connected to a vent. The entire system is constructed from 1/8" stainless steel tubing; the on-off valves are ball valves, and the control valves are Nupro fine metering valves. Flow rates are adjusted manually and are measured with Brooks Model 5810 thermal mass flowmeters located on the high pressure side of each control valve. The flowmeters were calibrated against a standard laboratory bubble meter. Reactant gases were obtained from Matheson and were ultra-high purity nitrogen (<3 ppm O_2; <3 ppm H_2O); Anaerobic grade carbon dioxide (<10 ppm O_2); and air, CO_2 free. Except for the CO_2, no additional purification of the gases is made. The CO_2, however, was passed through a silica

gel column. Two stage (except CO_2) high purity regulators were used with each cylinder.

The furnace tube is heated with a standard resistance furnace. The temperature is controlled with a Micricon 823 process controller. Up to 40 individual ramp and isothermal steps can be programmed into the controller. The controller is able to maintain a steady state temperature within 1°C of the set point.

The weight versus time data were recorded on a Bascom-Turner model 4110 digital recorder and data storage system. The maximum data acquisition rate is 100 milliseconds per datum point. The derivative of the TGA data (weight vs. time) was calculated using software available in the Bascom-Turner operating program. Smoothing of the derivative data was done using a 5 point moving average routine also available in the software. A visual best fit curve was drawn through the smoothed data and numerical values for the rate were determined directly from the graph paper.

The TGA system described above was modified from the factory design. The original connection between the furnace tube and the transition piece was a ground glass joint. Ambient air was able to infuse through this joint into the reactor vessel even when the pressure in the system was slightly above ambient ($\sim$10 cm H_2O above atmospheric). Leakage can occur when the system pressure is above ambient if the pathways for diffusion are in the Knudsen regime or if

surface diffusion is significant. Replacement of this joint with the o-ring fitting eliminated this problem. No leaks could be detected at any connection in the system with a helium-leak detector after this connection was changed.

The addition of the critical flow orifice at the gas outlet significantly improved the stability of the balance by isolating the gas flow in the reactor tube from any ambient pressure fluctuations. During initial testing of the balance, it was observed that minor change in the ambient pressure of the laboratory were primarily responsible for the low frequency but high amplitude noise in the output signal. Isolation of the flow system between two critical flow orifices resulted in a dramatic improvement in the performance of the balance.

3.3.2 Characterization of the TGA Reactor

Kinetic experiments were made with samples weighing from 0.1 to 3.0 mg, depending on the temperature (i.e., the reaction rate) at which the measurement was made. Sample size was modulated to minimize the effects of bulk phase heat and mass transfer at different reaction rates. The nominal sample size was 0.3 mg. The char sample was dispersed as much as possible over the area of the sample pan so that the bed depth at any single point was less than 3 particles. Calculations presented in Appendix 2 show that heat and mass resistances are minor at reaction rates below ~ 0.2 mg/min. Therefore, with a 0.1 mg sample, it is possible to obtain

kinetic data at a characteristic reaction time of 0.5 minutes.

Gas flow through the vertical furnace tube is in a mixed laminar free-convection regime. At 1000 K and a flowrate of 200 cc/min of air, the Reynolds number based on the inside tube diameter, is 5.4. Because of the baffle in the furnace tube, exact calculation of the Raleigh number is difficult. The characteristic length and the temperature differential over the distance is not easily estimated. If one assumes a temperature differential of 100 C and a length of 5 cm, Ra = 8000. These values place the flow well within the mixed laminar free-convection regime (Eckert and Drake, 1972). Thus, small changes in the gas velocity will not significantly alter the mass transfer between the solid and the fluid. This was observed experimentally by Wigmans et al., (1983) who report that the mass transfer rate does not change significantly if the flow direction in the reactor tube is changed.

It was noted in the previous section that small pressure fluctuations in the laboratory result in a significant increase in the signal noise from the TGA. The pressure changes cause small changes in gas velocity in the reactor tube. This in turn alters the aerodynamic drag (.3 μg/cc/min) on the hang-down wire and sample pan thus changing the effective weight. Because of the large capacitance in the system (due to the gas volume of the balance housing) the gas velocity fluctuations will have a low frequency. The

signal noise is accentuated when the TGA is operated at elevated temperatures. As a result, venting the exit gas across a critical flow orifice gave a much more significant improvement in performance at high temperatures than at room temperature. The output signals obtained with and without the critical flow orifice are compared in Figure 3.3-3.

The temperature in the reaction zone near the sample pan is nearly isothermal. Temperature measurements with a dual bead thermocouple assembly (ratio of bead diameters = 5) showed that the effective wall temperature and the gas temperature are approximately the same at gas velocities below 300 cc/min. The data are presented in Figure 3.3-4. Figure 3.3-4 also presents the axial temperature profile in the sample pan region.

3.3.3 Experimental Procedure

The general experimental procedure was as follows: the furnace tube was carefully removed at the o-ring connection and the sample pan was removed from the support stirrup with a pair of tweezers. A small amount of sample was dispersed on the pan by either lightly tapping the pan or with the aid of a small needle or brush. The end of the furnace tube that fits into the o-ring connector was carefully cleaned with acetone, and any electrostatic charge on the glassware was removed with a small ionization strip. Care was taken to not directly touch any of the glassware to prevent electrostatic charges from affecting the hangdown wire. While the furnace

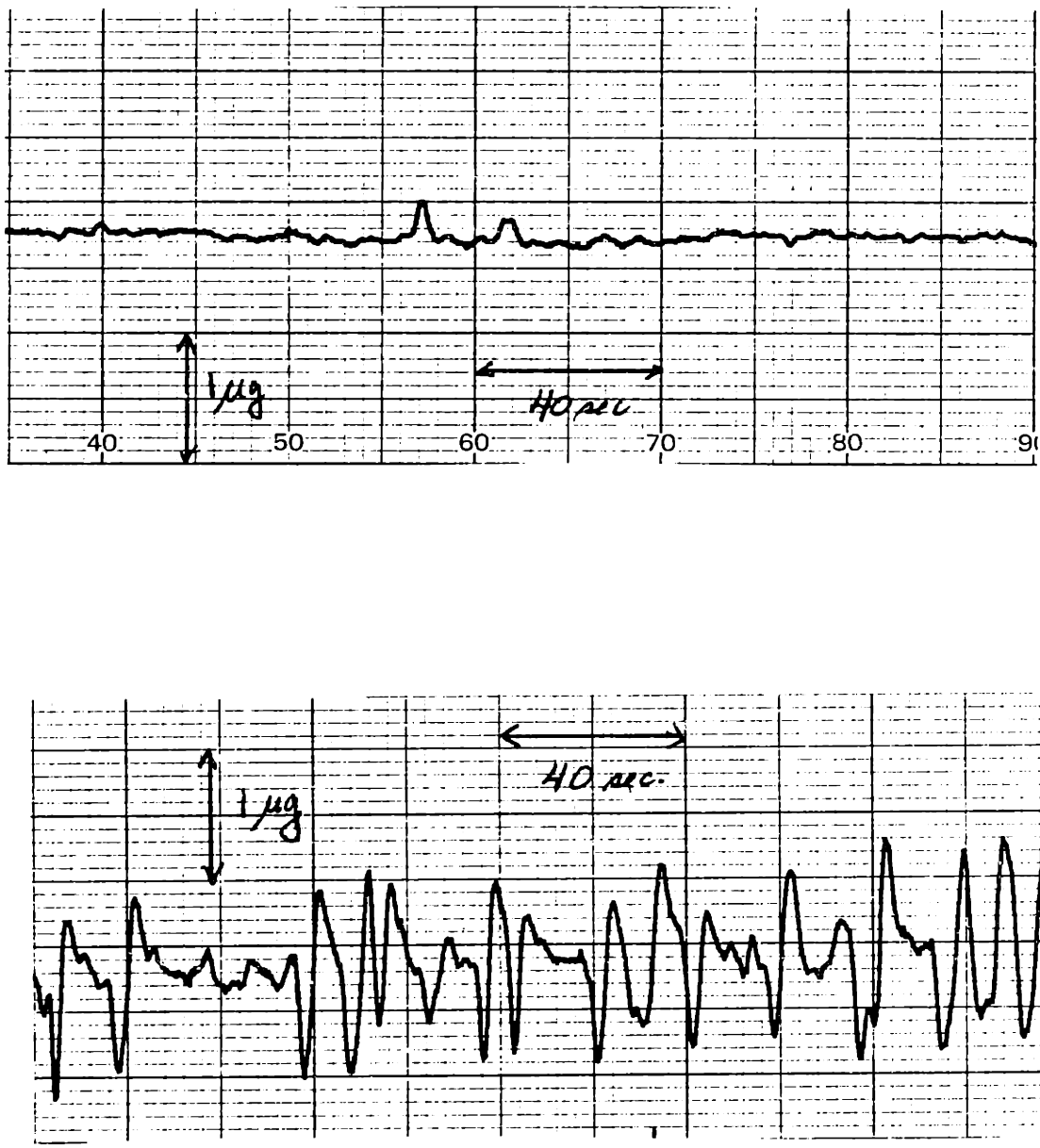

Figure 3.3-3. TGA signal with (top) and without (bottom) critical flow orifice in place at the gas exit port. Gas flow 200 cc/min; signal obtained at 298 K.

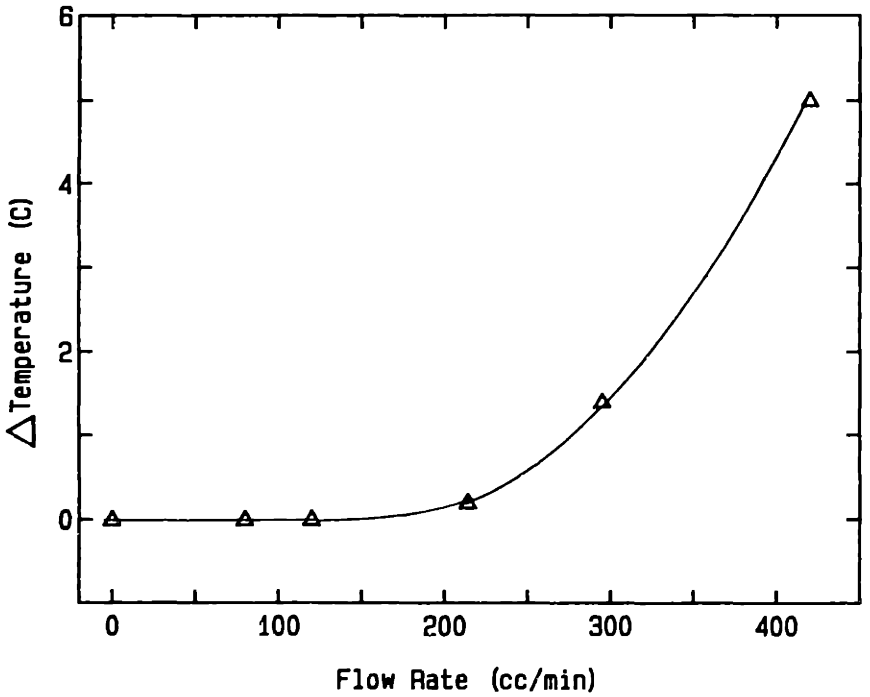

Figure 3.3-4a. The effect of gas velocity on the temperature difference measured by a dual bead thermocouple assembly.

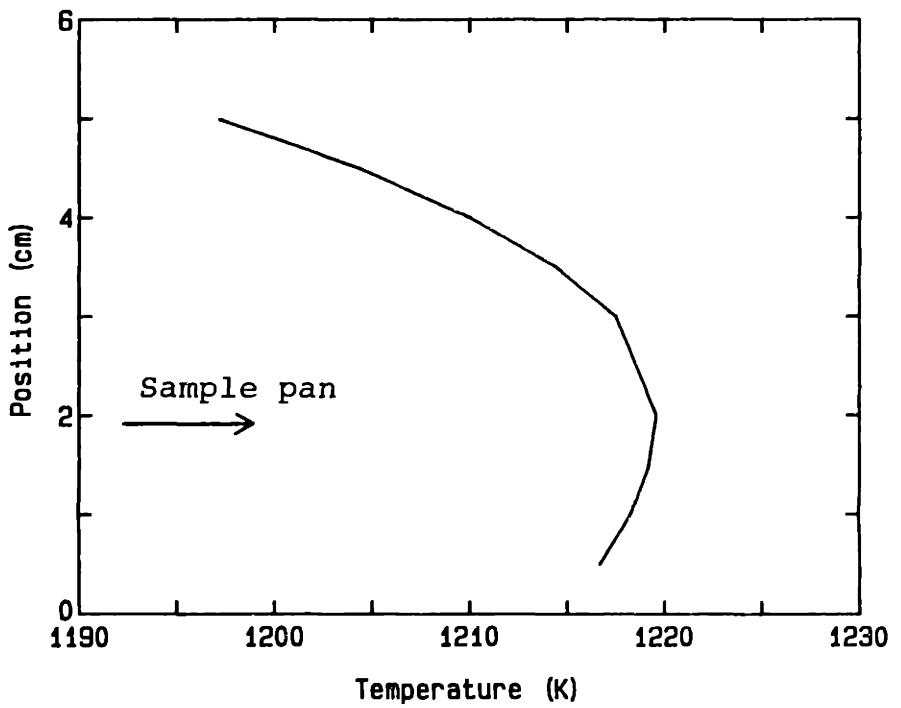

Figure 3.3-4b. Axial temperature profile in the reaction zone of the TGA.

tube was removed, the purge gas flowrate was set at about 300 cc/min and the flow of inert gas to the inlet port was left on to prevent any air from diffusing into the large volume of the balance housing. This gas flow was continued through the TGA system for 30-40 minutes after the system was reassembled and before a run was started. At the start of a run, the purge gas flow was stopped and the inert gas flowrate was set at about 200 cc/min. The sample was heated to the pretreatment temperature and then brought directly to the reaction temperature. The samples were always reacted immediately after heat treatment; the samples were never exposed to air between heat treatment and reaction. Heat treatment of the samples prior to an oxidation reaction rate measurement followed one of two modes: the sample was heated to 1100 K in 20 minutes and held isothermally at 1100 K for 8 minutes, or the sample was heated to 1300 K in 27 minutes and held at that temperature for 5 minutes. If the reaction temperature is widely different from the heat treatment temperature, it is necessary to wait approximately 5 minutes to reach an effective equilibrium weight once the furnace is cooled to the reaction temperature. The run was started by switching the 4-way valve from the inert gas to the reaction gas.

Heating the sample causes a change in the effective weight of the sample by about 0.2 mg. This is the result of a change in the aerodynamic drag on the hang-down wire and sample pan. Switching the gas composition from nitrogen to

air results in a small 35 sec. transition in the effective sample weight. The maximum weight change of this transient is +3 μg. The difference in the effective weight at steady state is approximately +1 μg. Switching from nitrogen to carbon dioxide results in a transient of about the same duration but with an amplitude of -5 μg. However, there is no steady state difference in weight.

The char samples used in these experiments are listed in Table 3.3-1. The calcium content is based on a number of analyses, and it has an accuracy of about +/- 5%. The calcium in the calcium added chars reacted with carbon dioxide during the reaction to form calcium carbonate. Carbon conversion for these chars was calculated based on the assumption that recarbonation increased linearly with conversion:

$$x = \frac{w + x(w_{cc})}{w_c} \quad \text{or} \quad x = \frac{w}{w_c - w_{cc}} \tag{3.3.1}$$

where w is the measured weight change; w_c is the total weight of the ash free char, w_{cc} is the total amount of CO_2 added by the end of the run; and x is conversion. The total ash free char weight was calculated as follows:

$$w_c = \frac{w_t + w_r}{(1 + 1.4\, x_{Ca})} \tag{3.3.2}$$

where w_t is the total weight change during a run; w_r is the sample weight remaining at the end of a run; and x_{Ca} is the calcium content of unreacted char.

Table 3.3-1 Char Samples

DESIGNATION	DESCRIPTION	Ca CONTENT wt Ca/wt Carbon (%)
C-0	sucrose char	0
C-1	saccharate char	0.97
C-3.6	saccharate char	3.6
C-6.2	saccharate char	6.2
C-$CaCO_3$	sucrose, with 1 μm calcium carbonate particles, char	6.8
C-ion	sucrose char - ion exchanged in a calcium acetate solution	2.3
Spherocarb		0

Section 4. RESULTS

The experimental results are summarized as follows: Section 4.1, kinetic data for the carbon-oxygen reaction; Section 4.2, kinetic data for the carbon-carbon dioxide reaction. In Section 4.3, physical property and chemical composition data are summarized. Section 4.4 contains the results of the carbon dioxide chemisorption and x-ray diffraction experiments that were made to measure calcium dispersion in the char.

4.1 Carbon-Oxygen Reaction

Most experiments were conducted in 79% nitrogen and 21% oxygen; additional experiments were made with oxygen concentrations between 5 and 21% and with 2-10% carbon dioxide in the gas. All experiments were conducted at 1 atmosphere total pressure. Reaction rates were determined directly from the derivative of the TGA data. The measured sample weight, however, is the difference between weight loss due to reaction and any weight gain because of oxygen chemisorption on the char and the reaction of carbon dioxide with the calcium oxide of the catalyzed chars. In the conversion range of 5-90%, chemisorption and recarbonation have a negligible effect on the rate of weight loss since the rates of these two processes are small in comparison to the rate of carbon gasification. As a result, the rate of total weight loss as measured by the TGA will be equivalent to the rate of char oxidation in this conversion range. At the beginning of a run, however, oxygen

chemisorption is rapid compared to carbon conversion. Although the weight increase at the start of a run is small, the initial rate of oxygen chemisorption is sufficiently fast to obtain an induction period in the weight versus time curve. Complete conversion curves, which illustrate the initial induction period, are presented in Appendix 4. After this initial increase in oxygen level, the oxygen content of the char continues to increase but at a slower rate. Calculation of the exact reaction rate and the correct carbon conversion from TGA data during the initial reaction time will require additional information on the rate of oxygen adsorption. For the calcium-added chars, the induction time at the start of a run was generally somewhat longer.

All samples were heat treated in situ at 1100 K for 8 minutes or at 1300 K for 5 minutes prior to a run. The samples were heated at a rate of 25 C/min to the final heat treatment temperatures. Samples were not exposed to air at room temperature between heat treatment and reaction.

Any calcium initially present as calcium carbonate will decompose to calcium oxide at those temperatures. At reaction conditions, the calcium oxide can recarbonate if the local CO_2 partial pressure exceeds the equilibrium CO_2 pressure for the recarbonation reaction. Also, calcium that is initially atomically dispersed on the carbon will remain as either calcium oxide or calcium carbonate as the carbon is gasified away. At temperatures below 725 K, the equilibrium CO_2 partial pressure for the calcination reaction is less than 20×10^{-6} atm (see

Figure 2.2-1). The local CO_2 concentration during combustion of the char was probably greater than this in most of the runs, and indeed, calcium carbonate was present at the conclusion of nearly all runs.

Gas concentrations were measured in a few runs, but because of the low product gas concentrations, analysis was problematic. In all measurements that were made, both carbon monoxide and carbon dioxide were present. Data were not collected over a sufficient range of conditions to determine whether the CO_2 is a primary reaction product or the result of secondary CO oxidation.

Carbon conversion is defined on an ash free basis. For the calcium added chars, conversion is calculated as:

$$x = 1 - \frac{w}{w_c - w_{CO_2}} \qquad (4.1.1)$$

where w_c is the initial amount of char (ash free); w_{CO2} is the total weight of CO_2 added by the end of the run; and w is the sample weight at conversion x. This equation assumes that if recarbonation of CaO occurs during reaction, the amount of carbonate formed increases linearly with conversion. The sample weight, w, was not corrected for any variation in oxygen content of the char with conversion.

4.1.1 Reaction Rate of the C-O, C-1, and C-3.6 Chars

Figures 4.1-1 through 4.1-6 present Arrhenius plots of log k vs. 1/T for the reaction of the sucrose and saccharate chars

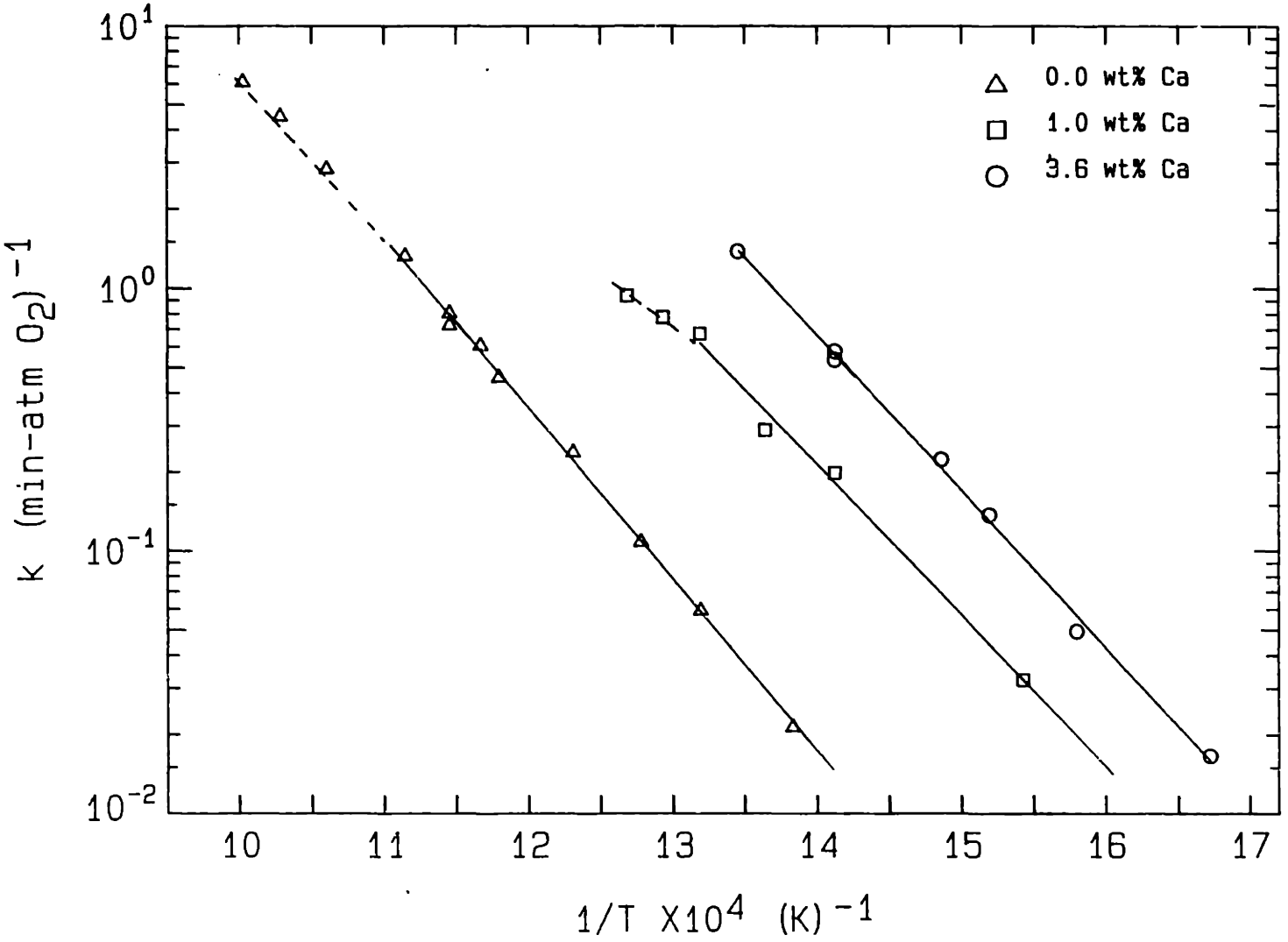

Figure 4.1-1 Arrhenius Diagram for the C-0, C-1, and C-3.6 chars at 10% conversion; reaction with oxygen (0.21 atm); 90-106 μm particles; heat treatment temperature 1100 K.

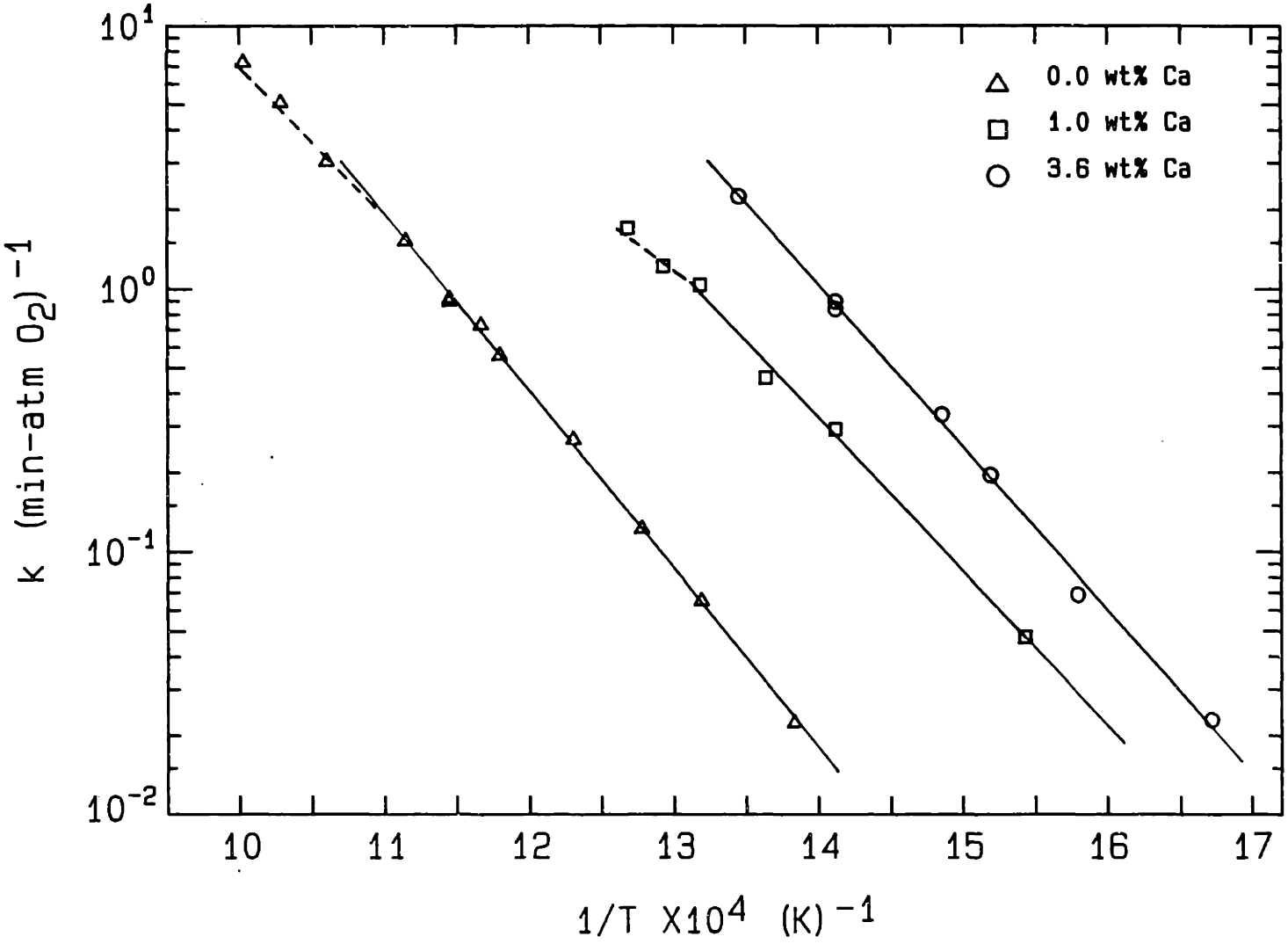

Figure 4.1-2 Arrhenius Diagram for the C-0, C-1, and C-3.6 chars at 20% conversion; reaction with oxygen (0.21 atm); 90-106 μm particles; heat treatment temperature 1100 K.

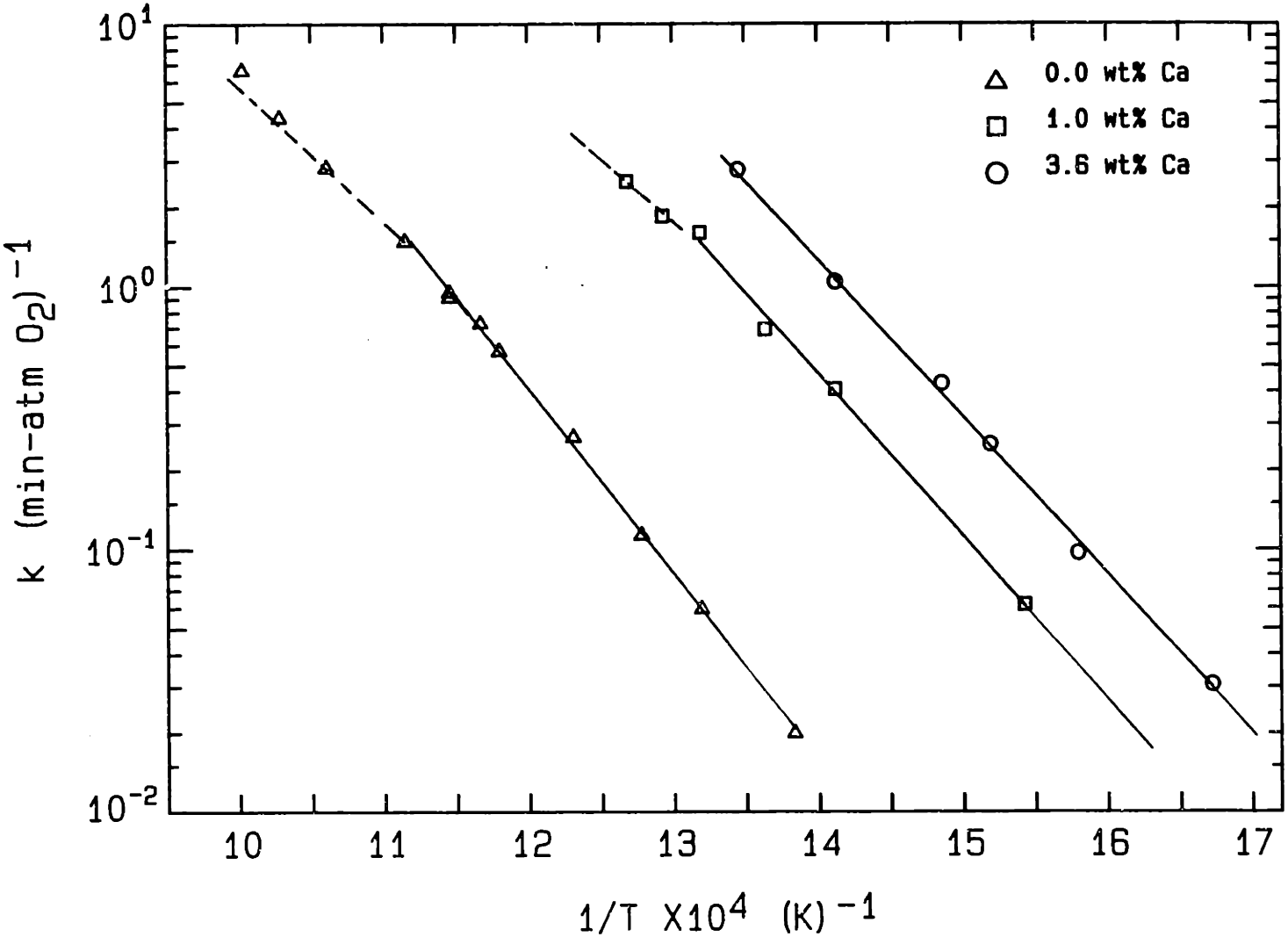

Figure 4.1-3 Arrhenius Diagram for the C-0, C-1, and C-3.6 chars at 40% conversion; reaction with oxygen (0.21 atm); 90-106 μm particles; heat treatment temperature 1100 K.

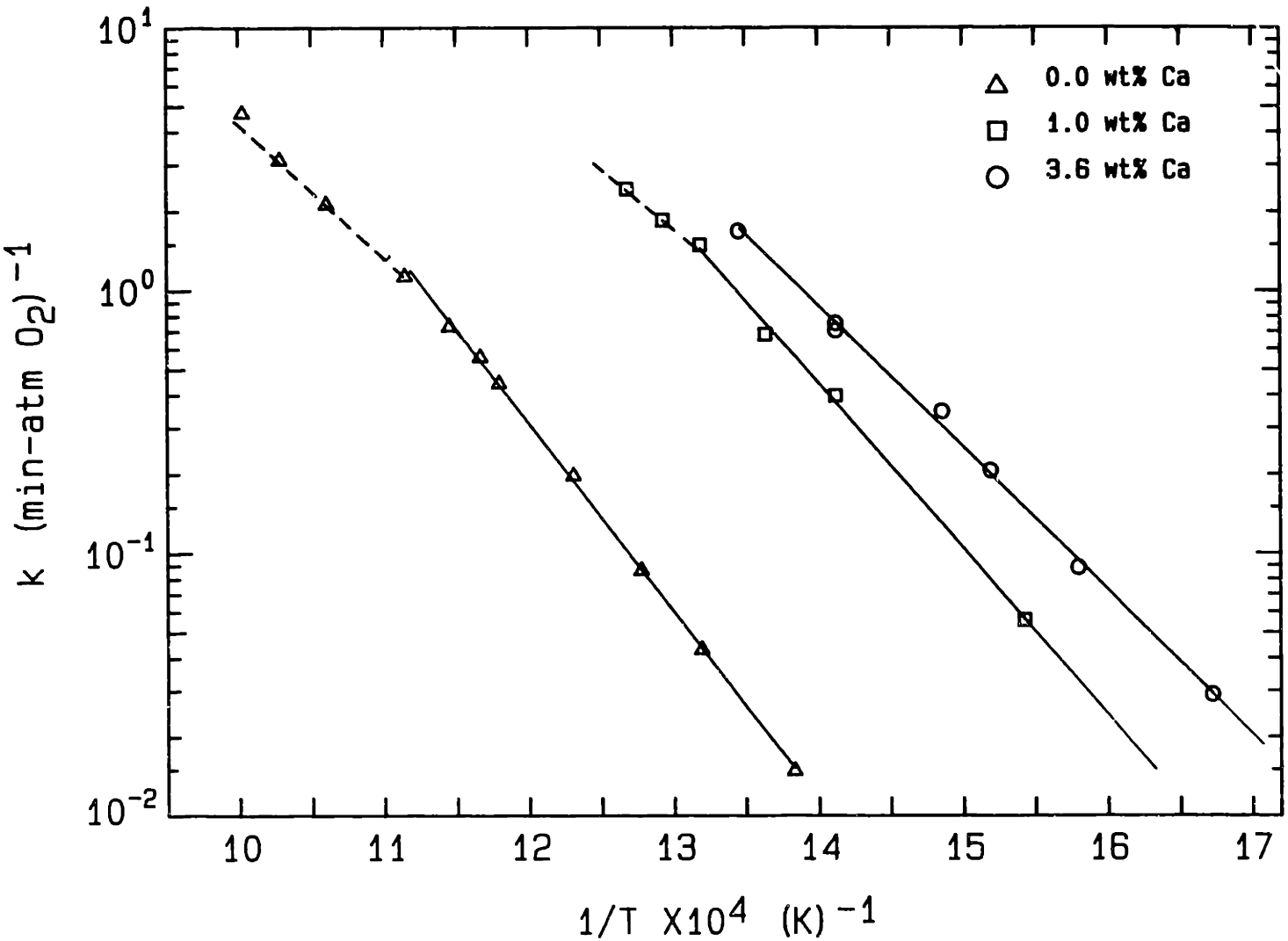

Figure 4.1-4 Arrhenius Diagram for the C-O, C-1, and C-3.6 chars at 60% conversion; reaction with oxygen (0.21 atm); 90-106 μm particles; heat treatment temperature 1100 K.

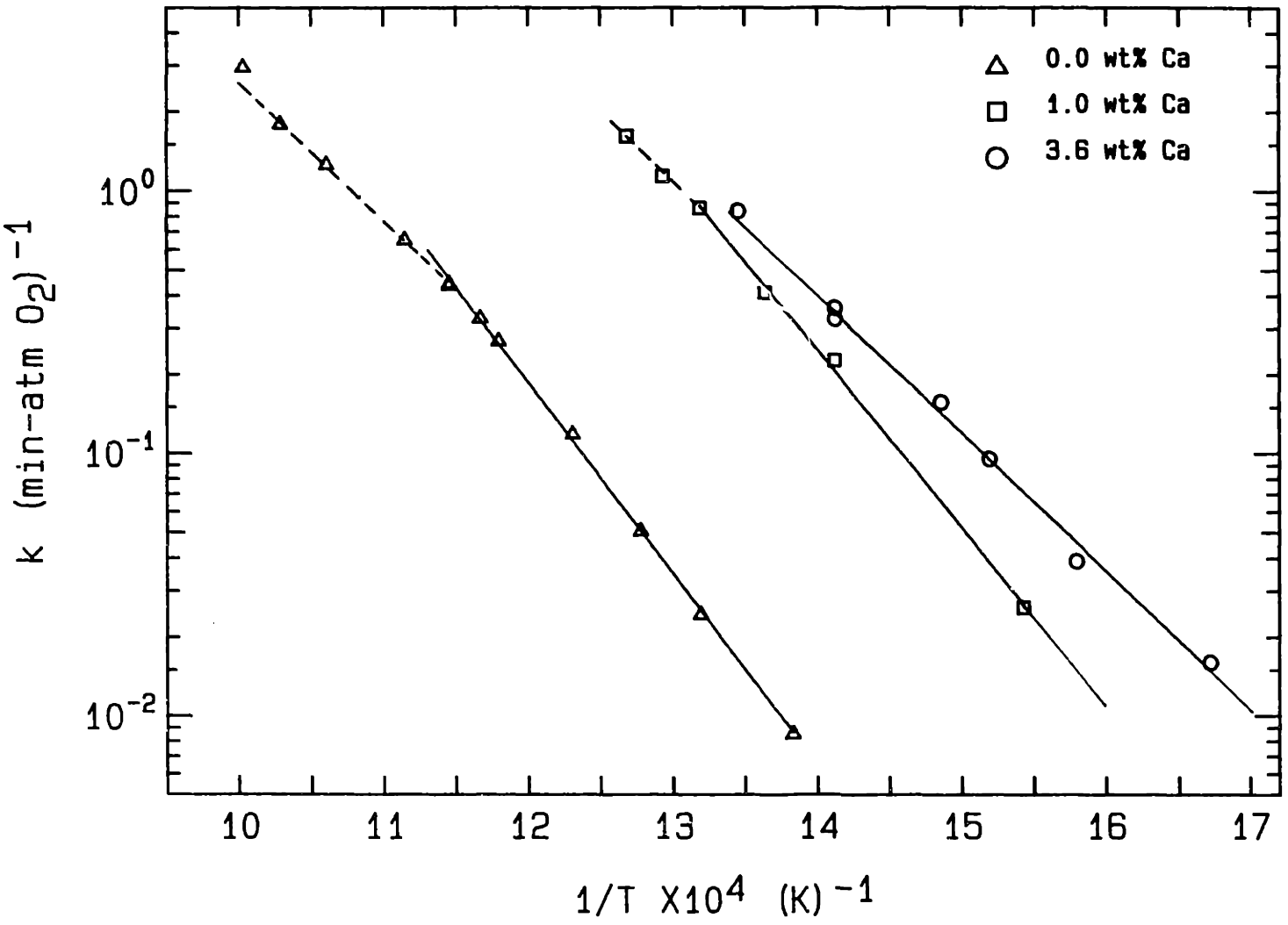

Figure 4.1-5 Arrhenius Diagram for the C-0, C-1, and C-3.6 chars at 80% conversion; reaction with oxygen (0.21 atm); 90-106 μm particles; heat treatment temperature 1100 K.

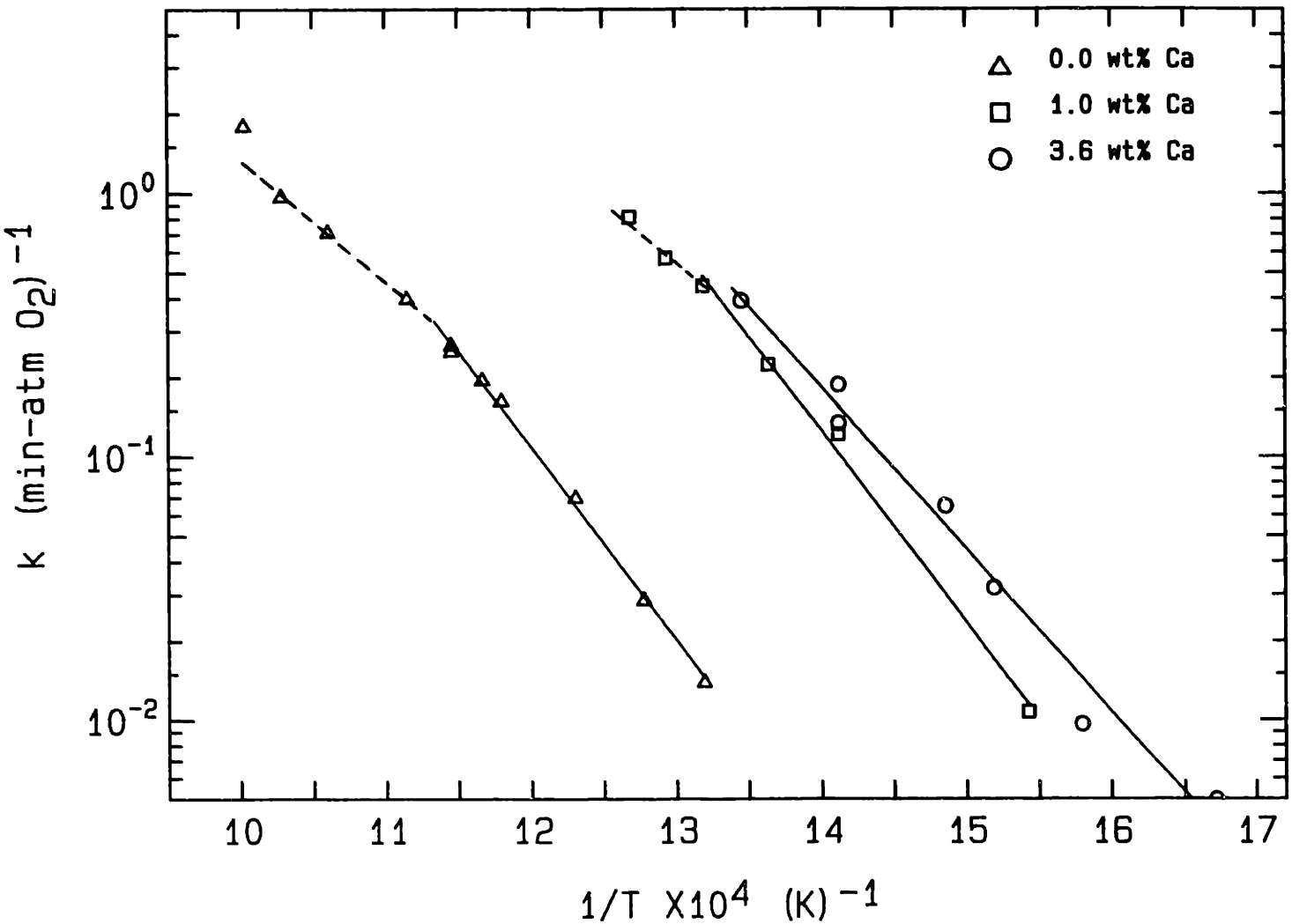

Figure 4.1-6 Arrhenius Diagram for the C-0, C-1, and C-3.6 chars at 90% conversion; reaction with oxygen (0.21 atm); 90-106 μm particles; heat treatment temperature 1100 K.

containing 0 wt% calcium (C-0), 1 wt% (C-1), and 3.6 wt% (C-3.6) with air at conversions of 10, 20, 40, 60, 80, and 90%. The rate constant is defined as:

$$k = \frac{r}{m_o P_{O_2}} \qquad (\text{min - atm } O_2)^{-1} \qquad (4.1.2)$$

where r is the measured rate of weight loss (mg/min), m_o is the initial sample weight (mg - ash-free char), and P_{O_2} is the oxygen partial pressure (atm). P_{O_2} is equal to 0.21, except if stated otherwise. The data are presented on a mass basis rather than a surface area basis; however, because the total surface area of the catalyzed and non-catalyzed chars differ by about 15%, a comparison on such a basis, if desired, will not be significantly different. Surface area data are presented in Section 4.3.2. The reactivity of the sucrose char is similar to the reactivity of a demineralized lignite char (Radovic, 1982) on either basis. The surface areas of typical lignite chars are comparable to the surface areas of the sucrose and saccharate chars used in this study.

Activation energies and pre-exponential factors calculated by a linear least squares regression of the data are summarized in Table 4.1-1. The reported values are for the low temperature portion of the data. The line drawn through the data points that deviate from the straight line representing the low temperature data only indicates the trend of the data. The kinetic parameters are reported in units of concentration rather than partial pressure. The activation energy for the reaction decreases slightly with increasing calcium content. Variations

Table 4.1-1. Activation Energies and Pre-Exponential Factors for the Carbon-Oxygen (0.21 atm) Reaction; 90-106 μm particles; 1100 K heat treatment temperature.

Conversion (%)	Pre-Exponential Factor (cc/gmole-sec)	Activation Energy (cal/mole)
C-O Char (0 wt% Ca)		
10	7.42×10^{10}	31,500
20	1.67×10^{11}	32,604
40	3.44×10^{11}	33,811
60	3.76×10^{11}	34,402
80	2.98×10^{11}	34,872
90	2.075×10^{11}	35,161
C-1 Char (1.0% Ca)		
10	5.90×10^{10}	27,600
20	1.29×10^{11}	28,412
40	5.75×10^{11}	29,739
60	7.40×10^{11}	30,165
80	1.97×10^{12}	32,283
90	4.66×10^{12}	34,575
C-3.6 Char (3.6% Ca)		
10	3.90×10^{11}	28,700
20	1.19×10^{12}	29,641
40	7.24×10^{11}	28,655
60	8.81×10^{10}	26,175
80	2.19×10^{10}	25,329
90	1.70×10^{11}	29,350

in activation energy with respect to conversion are almost negligible for the calcium-free char but are significant for the catalyzed char. This must reflect a change in the activity of the catalyst over the course of the reaction. At conversions above 80%, the catalyzed char data exhibit more scatter than the data of the C-O char.

The change in slope at a rate of 1.5 (min-atm O_2)$^{-1}$ is assumed to indicate the onset of intra-particle diffusion in the chars. This change in slope persists to 90% conversion, which is unexpected since the pores of the solid should widen with conversion and thereby decrease diffusion resistance. The data are analyzed with an isothermal first order reaction-diffusion model in Appendix 3 and the results are further discussed in Section 5.1.4. The change in slope of the Arrhenius diagram occurs at approximately the same reaction rate for both the catalyzed and non-catalyzed chars. In terms of a first order reaction-diffusion model, this can only occur if the effective diffusivity for each char is the same. This implies that the catalyst must be active in all the pores of the char and must be uniformly distributed throughout the char particle.

In Figures 4.1-7 through 4.1-9, the rate normalized to the maximum rate during conversion is plotted with respect to time normalized by the time at 50% conversion. Plotted in this manner, it is possible to follow the relative changes in rate with reaction time at different temperatures. As shown in Section 5.1.2, all the data should lie on a single common curve if the kinetics can be characterized by a single rate constant

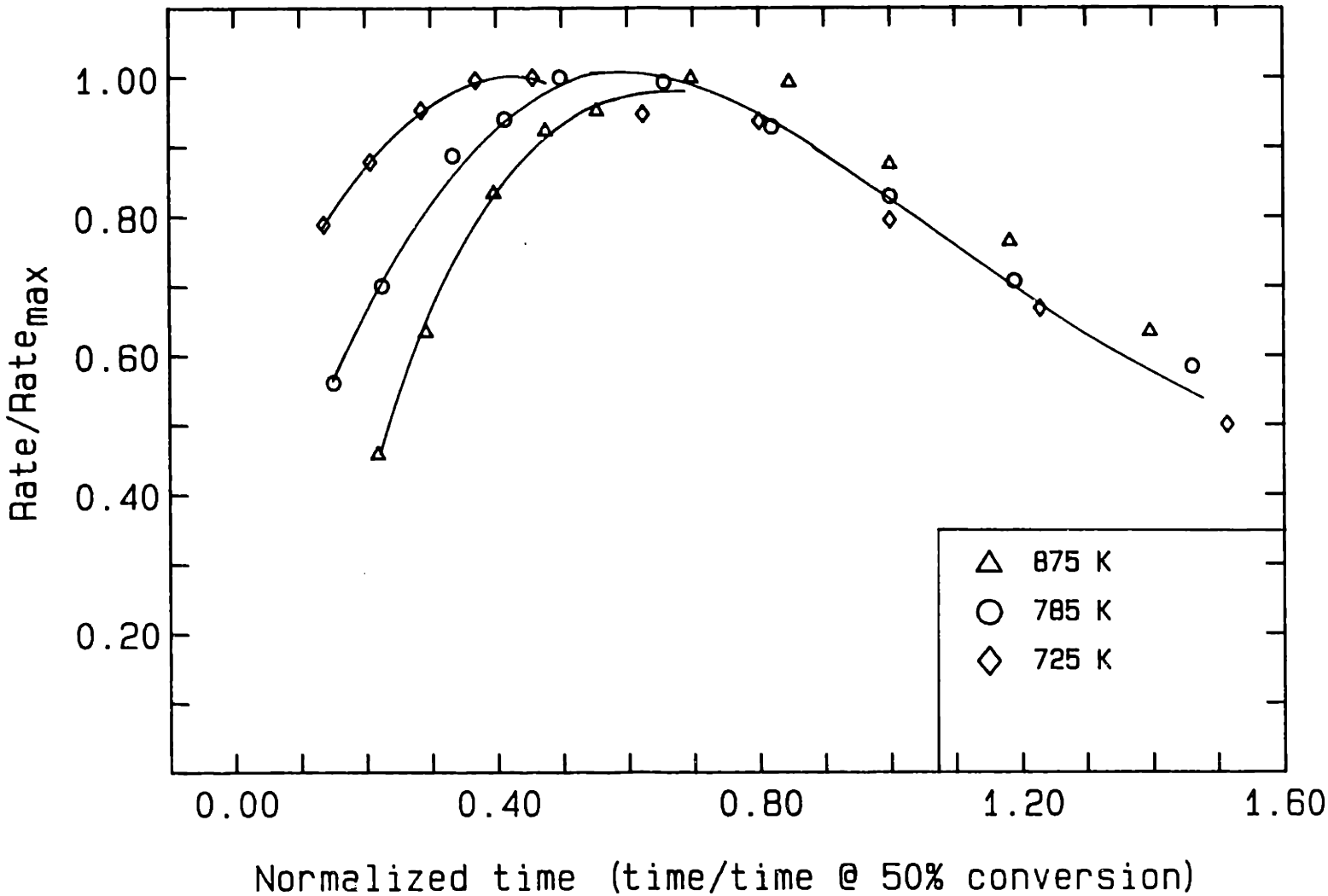

Figure 4.1-7 Reaction rate normalized by the maximum rate plotted against normalized time. C-O char (0 wt% Ca) - oxygen (0.21 atm) reaction; 90-106 μm particles; 1100 K heat treatment temperature.

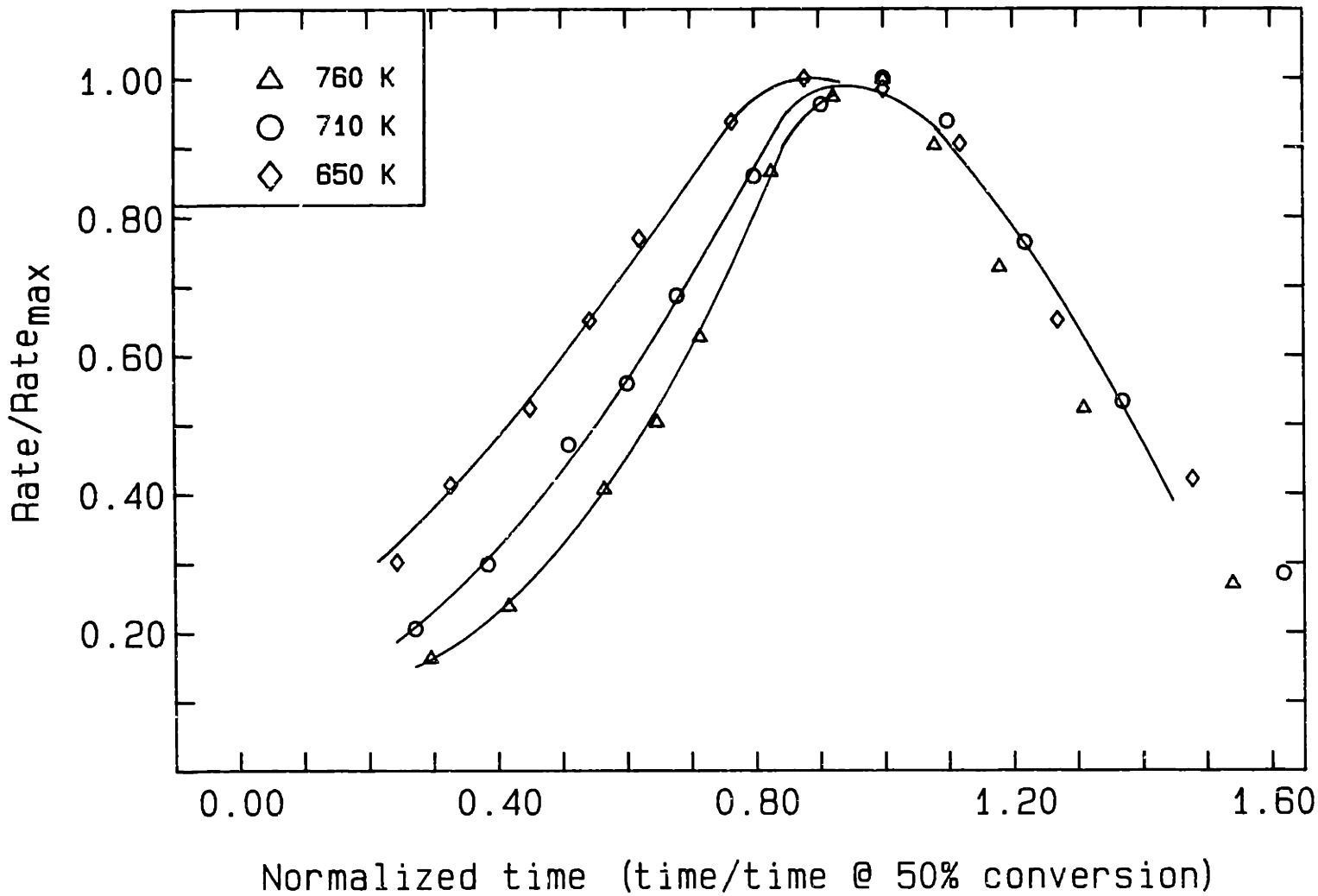

Figure 4.1-8 Reaction rate normalized by the maximum rate plotted against normalized time. C-1 char (1 wt% Ca) - oxygen (0.21 atm) reaction; 90-106 μm particles; 1100 K heat treatment temperature.

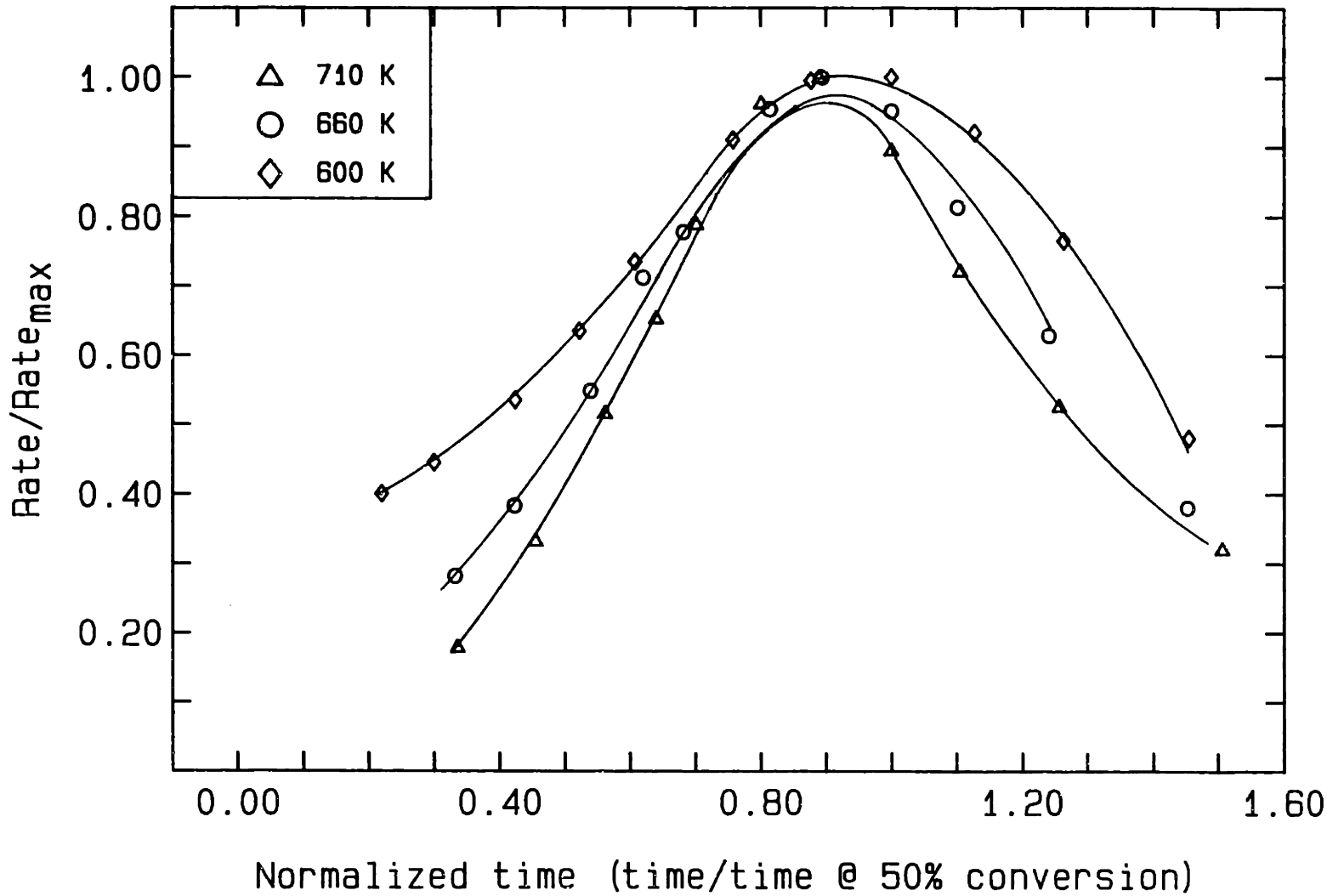

Figure 4.1-9 Reaction rate normalized by the maximum rate plotted against normalized time. C-3.6 char (3.6 wt% Ca)-oxygen (0.21 atm) reaction; 90-106 μm particles; 1100 K heat treatment temperature.

over the entire conversion range. The shape of the curve, however, will depend on the specific properties of each char. The data, in general, do conform approximately to a single curve. With respect to temperature, the curves for the C-O char are shifted to the right, and the maximum rate occurs at a later relative time with increasing temperature. A similar shift is observed for the calcium added chars at $t_{0.5}$ below 0.8. Above $t_{0.5}$ equal to 1.2, all the data approximately coincide. The rate versus time curves for the catalyzed chars are not greatly different from those of the calcium-free char although there is some difference in detail. The maximum rates for the C-1 and C-3.6 chars occur at a later relative time and are shorter in duration than for the C-O char. The slight concave shape of the catalyzed char data reflects the more pronounced sigmoidal shape of the weight loss curves obtained with the catalyzed char. In general, the data do not extrapolate through the origin reflecting the induction time at the start of a run. All the normalization factors are listed in Appendix [8].

Data of rate versus conversion are presented in Figures 4.1-10 to 4.1-12. All the data should likewise fall on a single curve if the kinetics can be characterized by a single rate constant. Plotted in this more conventional manner, variations in the burn-out curves at different temperatures become less distinct since the conversion is the integral of the rate versus time data. On the other hand, differences between the catalyzed and non-catalyzed chars are easier to compare when the data are summarized in this manner. For the C-O char, above

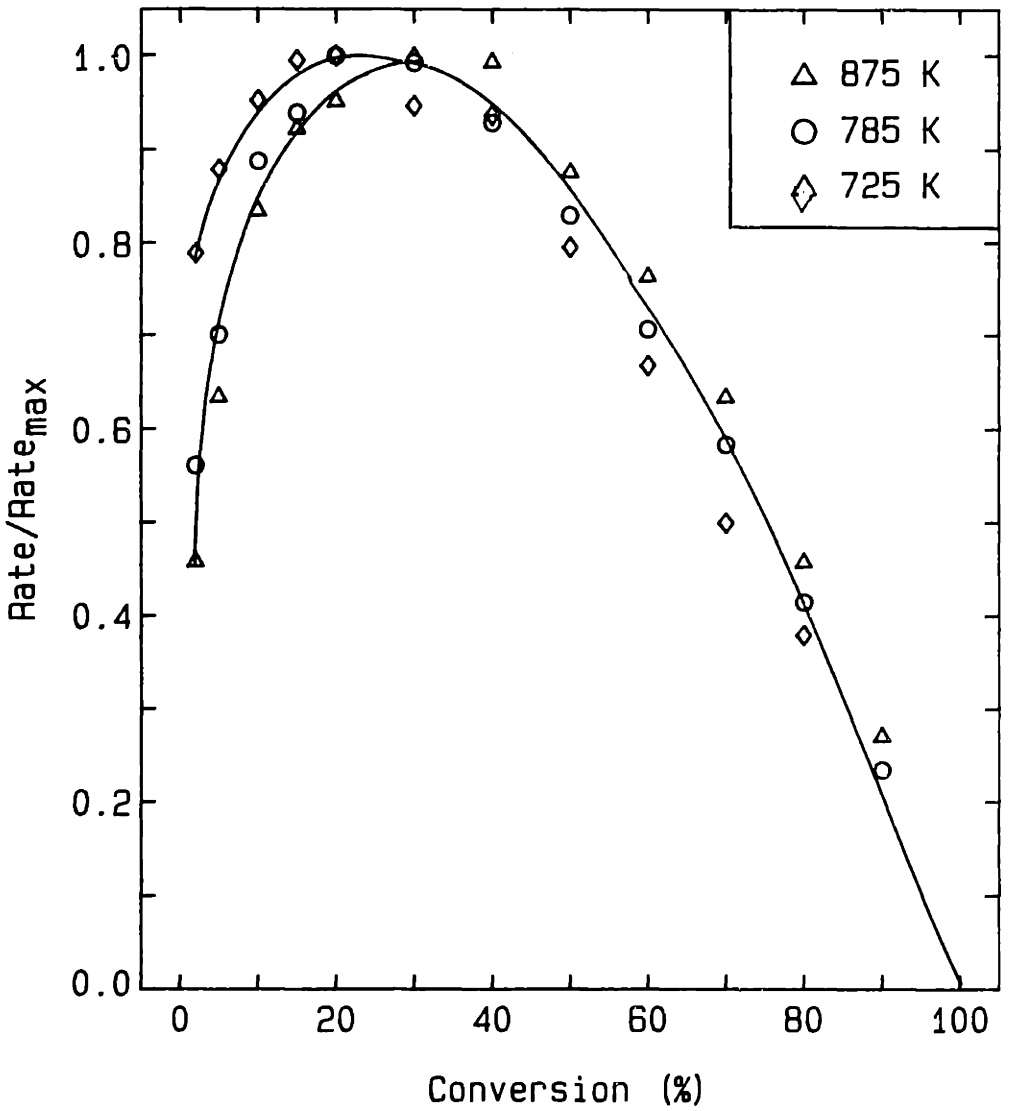

Figure 4.1-10 Reaction rate normalized by the maximum rate versus conversion. C-O char - oxygen (0.21 atm) reaction; 90-106 μm particles; 1100 K heat treatment temperature.

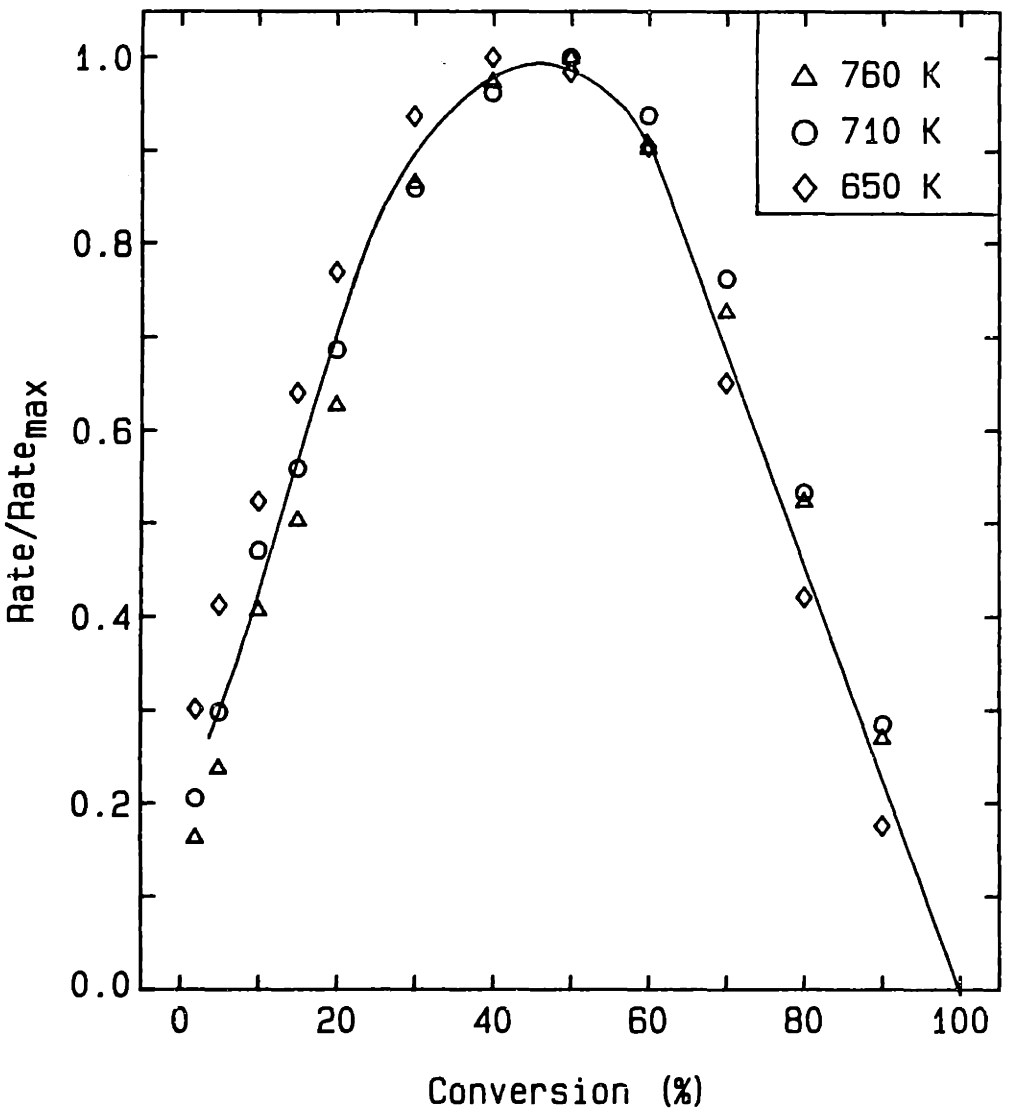

Figure 4.1-11 Reaction rate normalized by the maximum rate versus conversion. C-1 char - oxygen (0.21 atm) reaction; 90-106 μm particles; 1100 K heat treatment temperature.

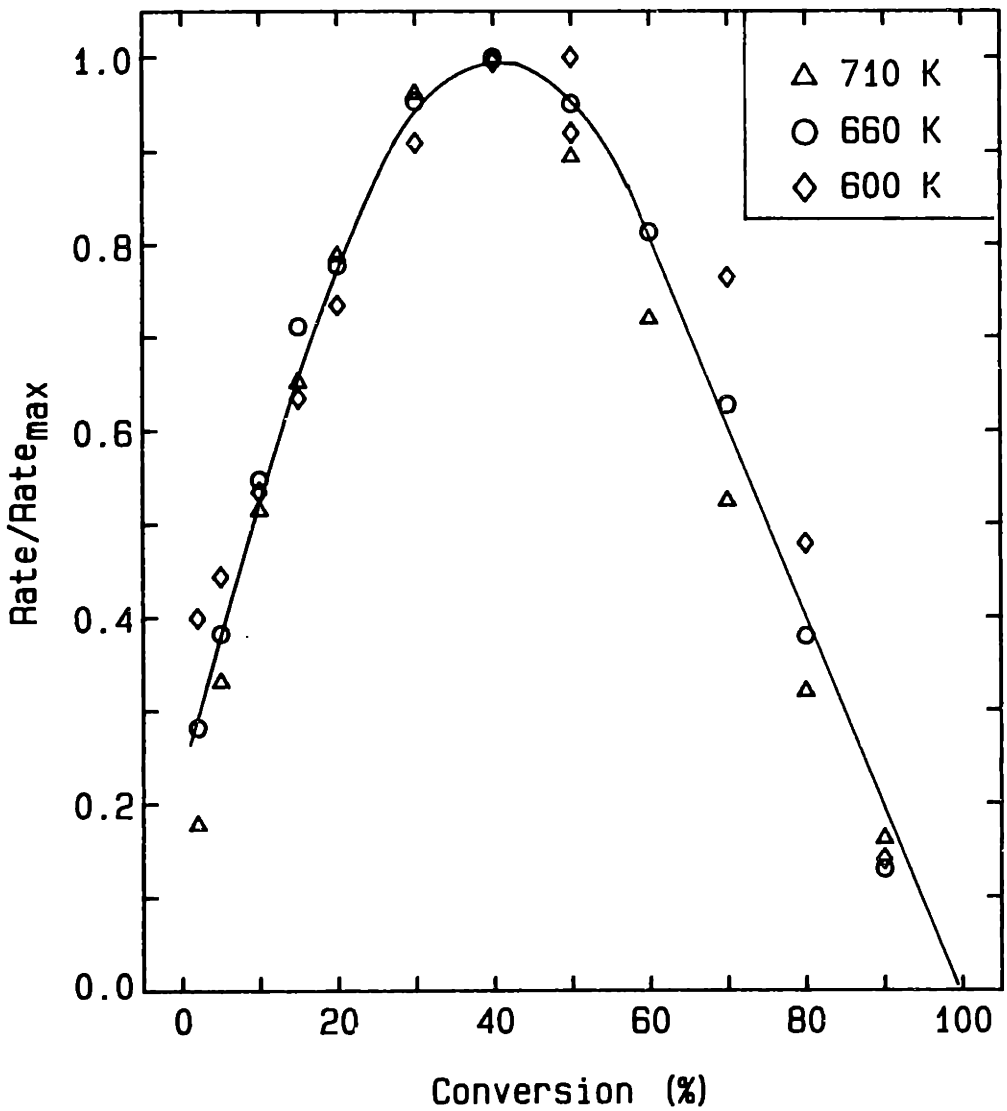

Figure 4.1-12 Reaction rate normalized by the maximum rate versus conversion. C-3.6 char - oxygen (0.21 atm) reaction; 90-106 μm particles; 1100 K heat treatment temperature.

approximately 5% conversion the difference between the maximum and initial rates is less than 50%; this difference is even smaller for the data obtained at the lowest reaction temperature (725 K). Between 15 and 40% conversion, the rate is approximately constant. For the catalyzed chars, the difference between the initial and maximum rates is much greater, the maximum rate occurs at a higher conversion, and an extended period of constant rate is not observed. Above 60% conversion, the data for the catalyzed chars all fall on approximately straight lines that pass through 100% conversion.

4.1.2 Reaction Order of the C-O and C-3.6 Chars

The effect of oxygen concentration on the reaction rate of the C-O and C-3.6 chars is summarized in Figure 4.1-13. All experiments were conducted at 1 atm. total pressure with nitrogen as the diluent gas. For the C-O char, the rate dependence on oxygen concentration is the same at both 725 and 875 K. The rate increases nearly linearly with oxygen partial pressure up to a pressure of about 0.18 atm; at higher partial pressures, the rate deviates from a first order dependence. The C-3.6 char, however, is first order in oxygen concentration over the entire range of oxygen pressures investigated. Graphs of rate versus normalized time are presented in Figures 14.1-14 to 14.1-16. The rates for the C-O char are proportional over the entire time scale; if the data had been normalized with respect to the maximum rate, all the points would coincide. For the catalyzed char, the rates are identical over the entire

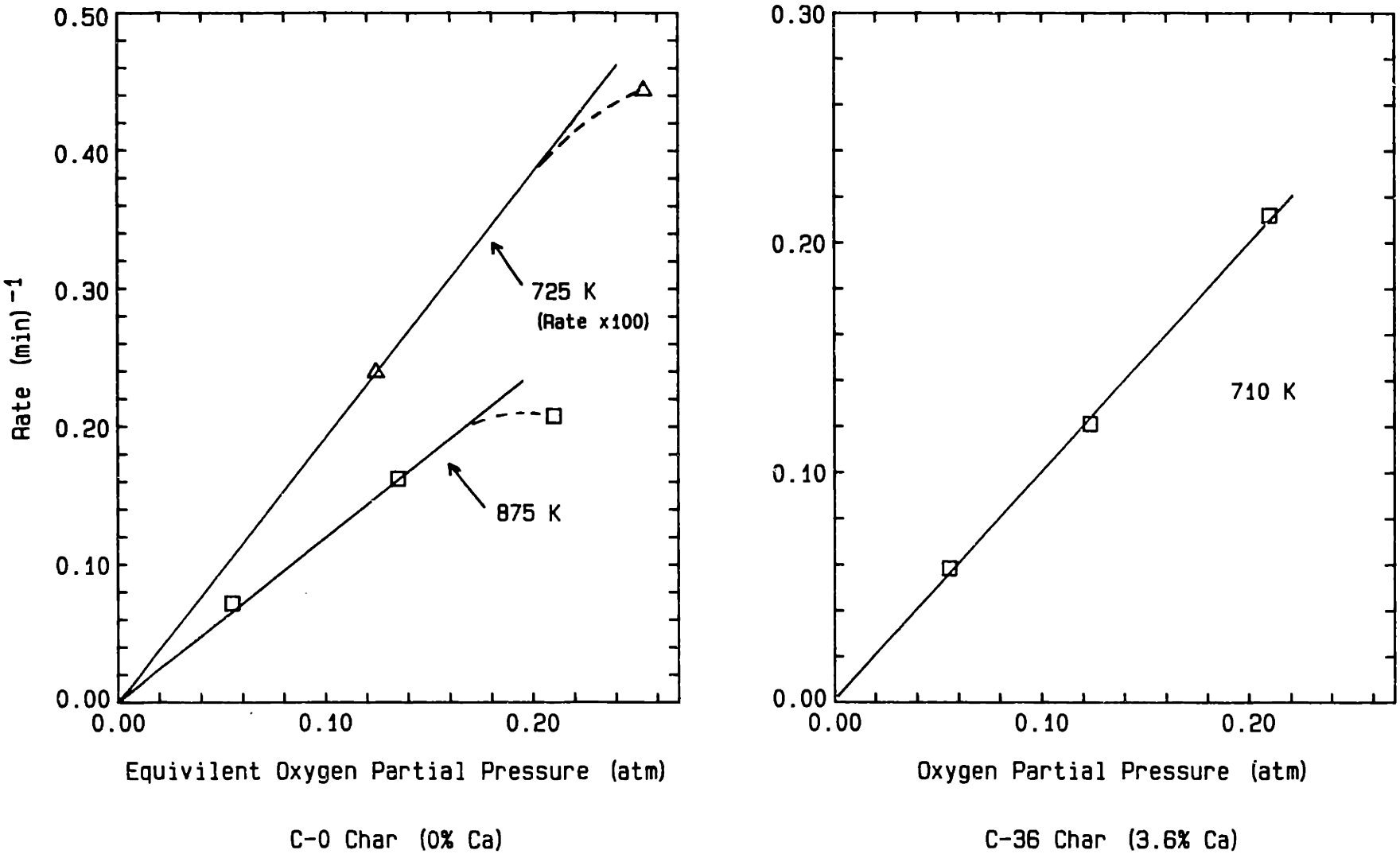

Figure 4.1-13. Reaction order for the C-O and C-3.6 chars. The oxygen partial pressure for the C-O char is corrected to account for the higher oxygen concentration at 725 K compared to 875 K. Reaction rates are at 40% conversion. (90-106 μm particles; heat treatment temperature 1100 K)

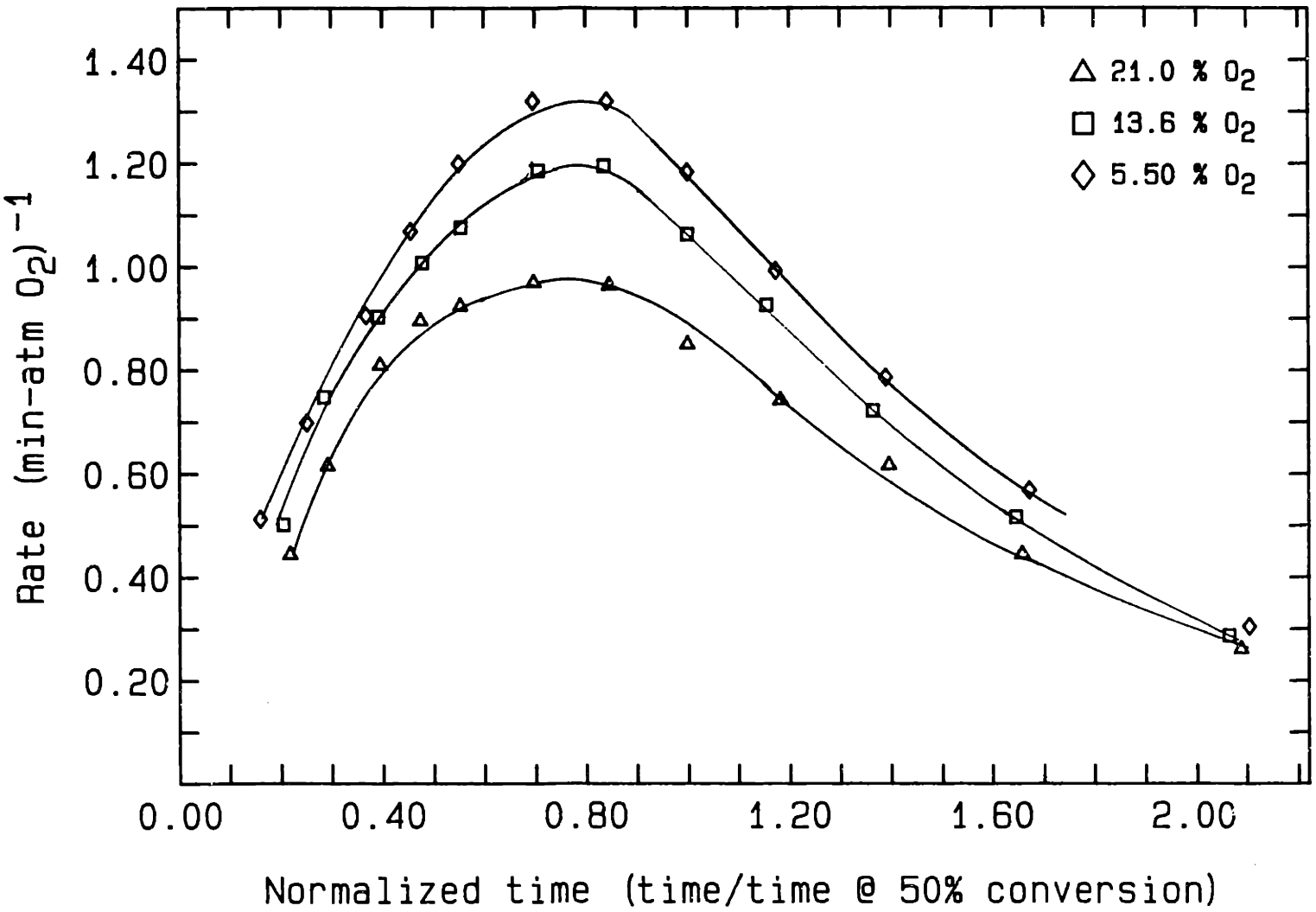

Figure 4.1-14. Reaction rate versus normalized time for the C-O char at different oxygen partial pressures; 875 K reaction temperature.

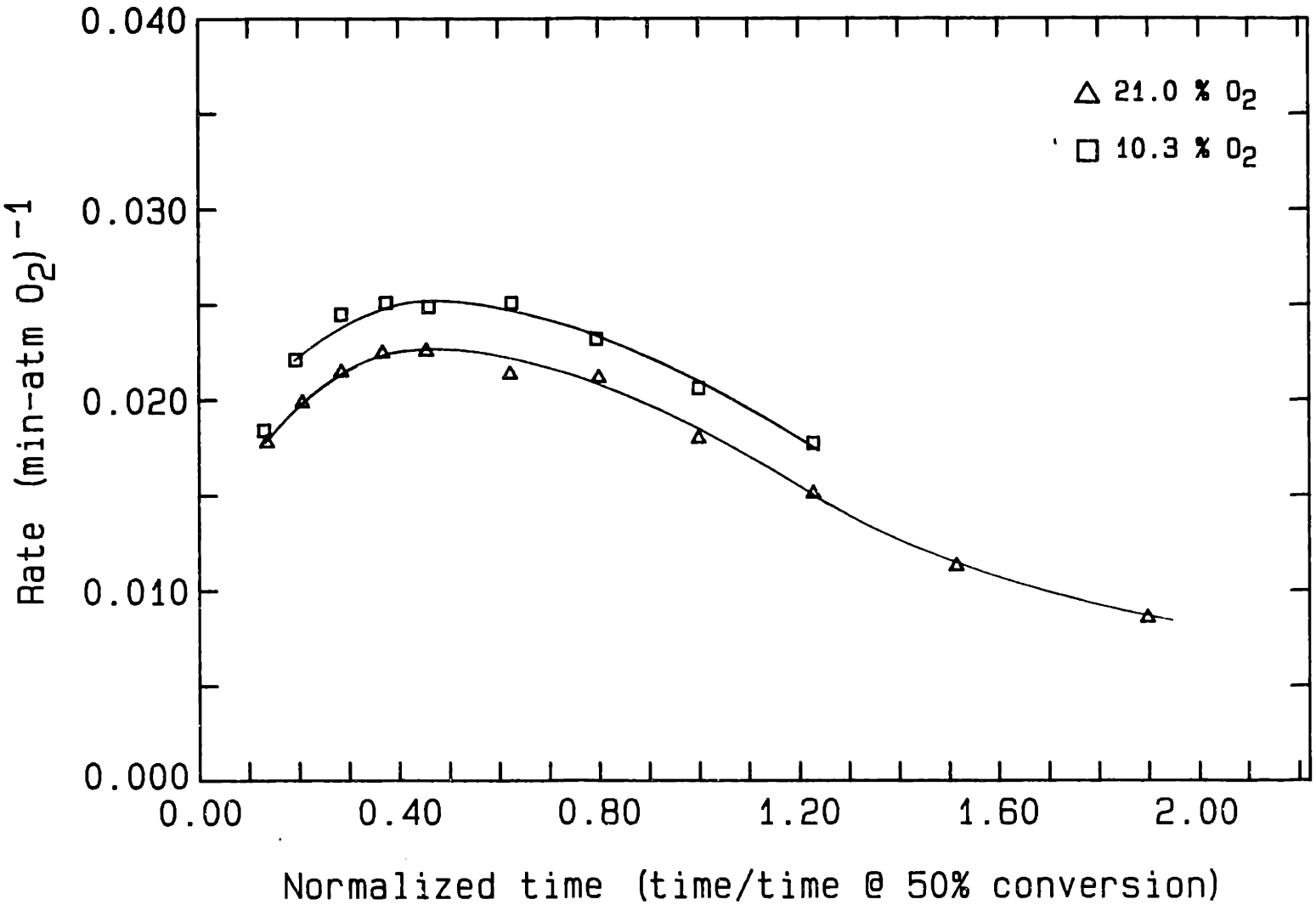

Figure 4.1-15. Reaction rate versus normalized time for the C-O char at different oxygen partial pressures; 725 K reaction temperature.

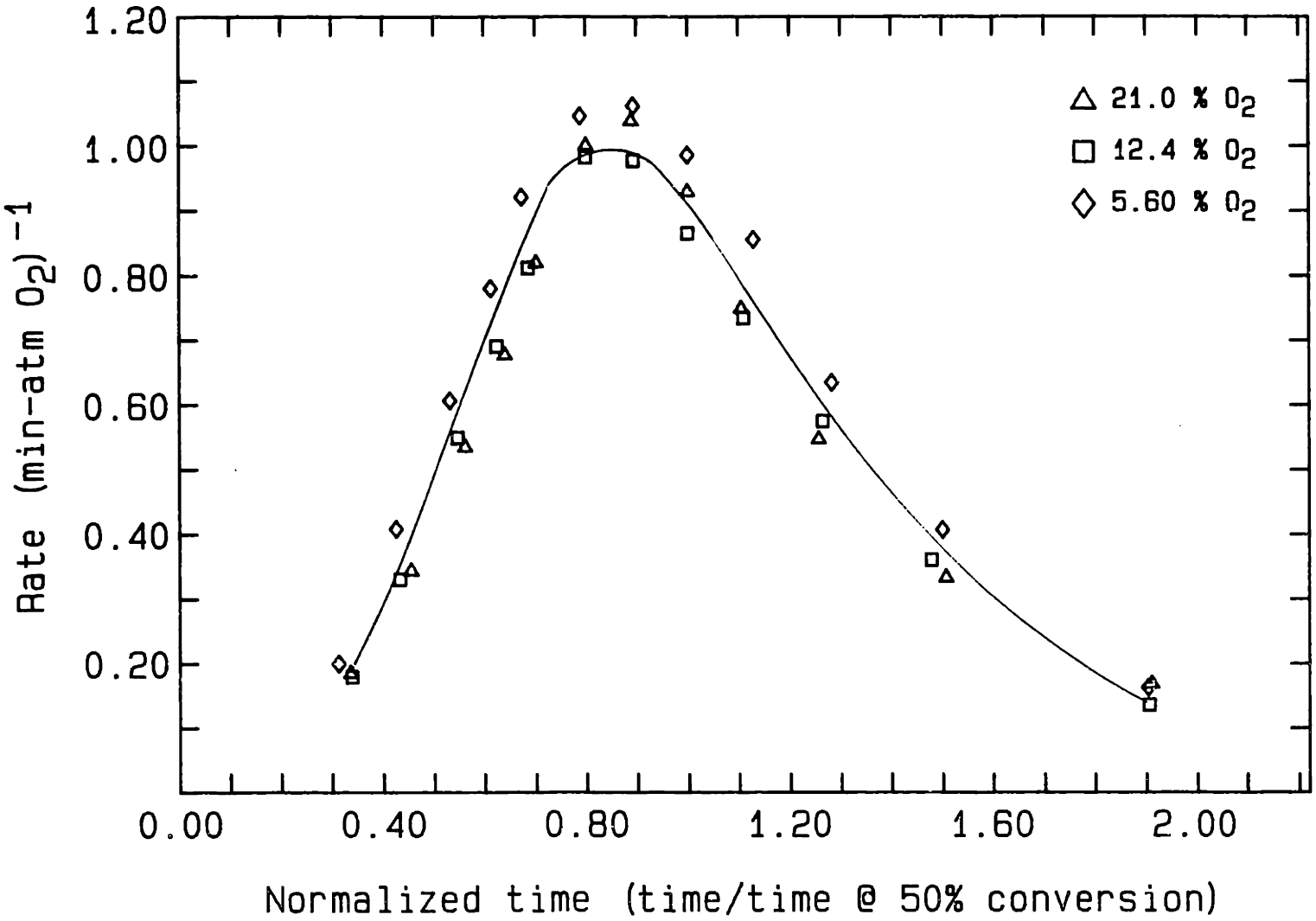

Figure 4.1-16 Reaction rate versus normalized time for the C-3.6 char at different oxygen partial pressures.

conversion range. This result suggests that the kinetic mechanism for the oxidation reaction does not depend in a complex manner on the oxygen partial pressure. The rate data can be scaled by a single constant that is a product of a rate constant and a concentration term over the complete conversion range. In a few experiments, 2 - 10% carbon dioxide was added to the gas. The addition of CO_2 had no effect on reactivity.

4.1.3 Reaction Rate of the C-ion and C-$CaCO_3$ Chars

Arrhenius diagrams for chars in which calcium is added by ion exchange (C-ion) or by incorporation of 1 μm $CaCO_3$ particles (C-$CaCO_3$) are shown in Figures 4.1-17 to 4.1-22 at conversions of 10, 20, 40, 60, 80, and 90%. The C-O char data are included in these figures for reference. The addition of micron-size calcium particles promotes char reactivity very little. This char is about twice as reactive as the non-catalyzed char. However, the ion-exchange char is about 100 times as reactive. The single datum point at 725 K suggests that intra particle diffusion in the C-ion char may become important at a lower reaction rate than for the C-3.6 char. This implies that the calcium was not as uniformly distributed in all the pores of the ion exchange char as in the C-3.6 char.

Activation energies are summarized in Table 4.1-2. Above 70% conversion, accurate activation energies could no longer be obtained because the log k versus 1/T data showed appreciable scatter.

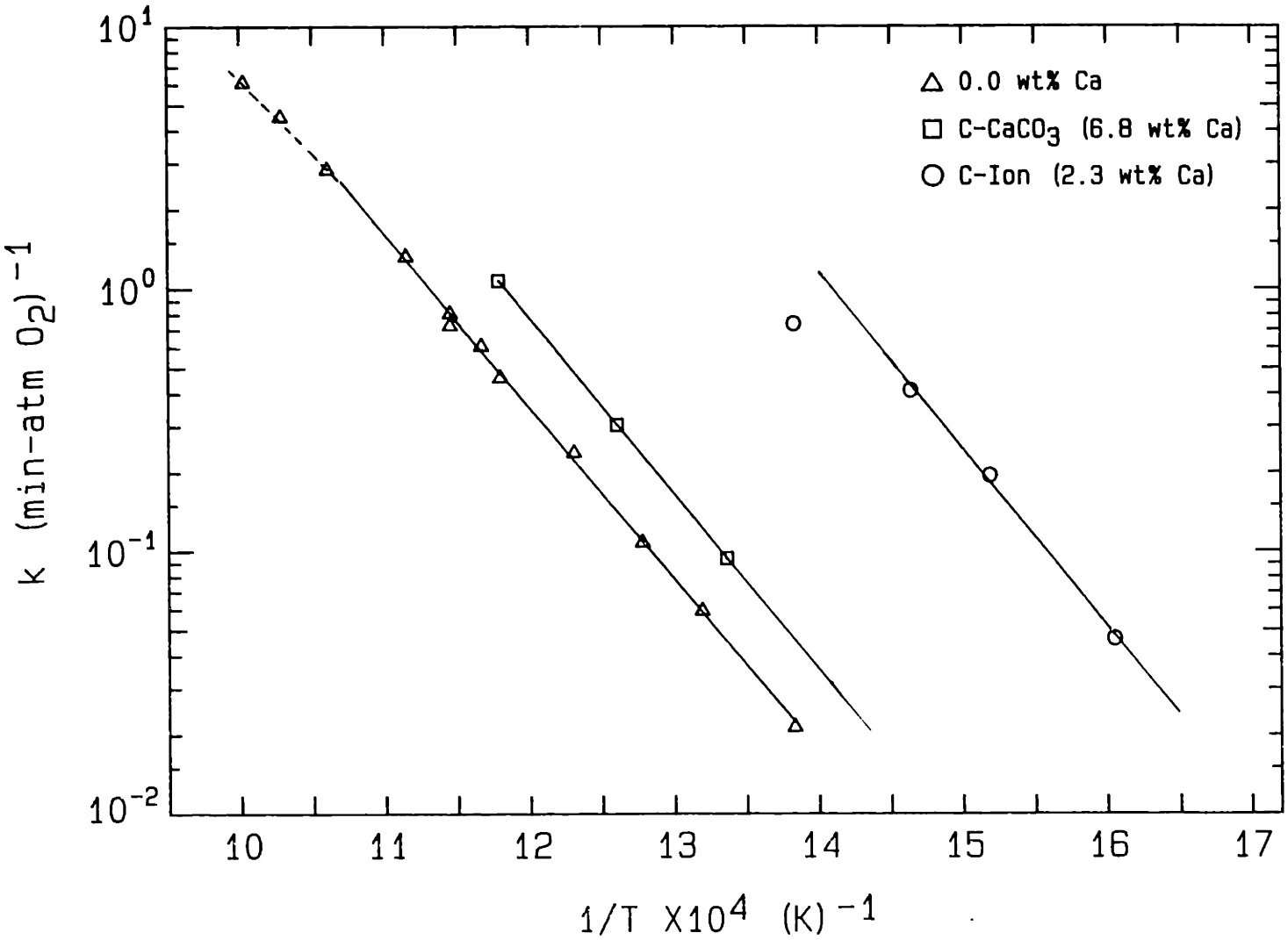

Figure 4.1-17. Arrhenius diagram for the C-ion and C-$CaCO_3$ chars at 10% conversion; 0.21 atm oxygen; particle size 90-106 μm; heat treatment temperature 1100 K.

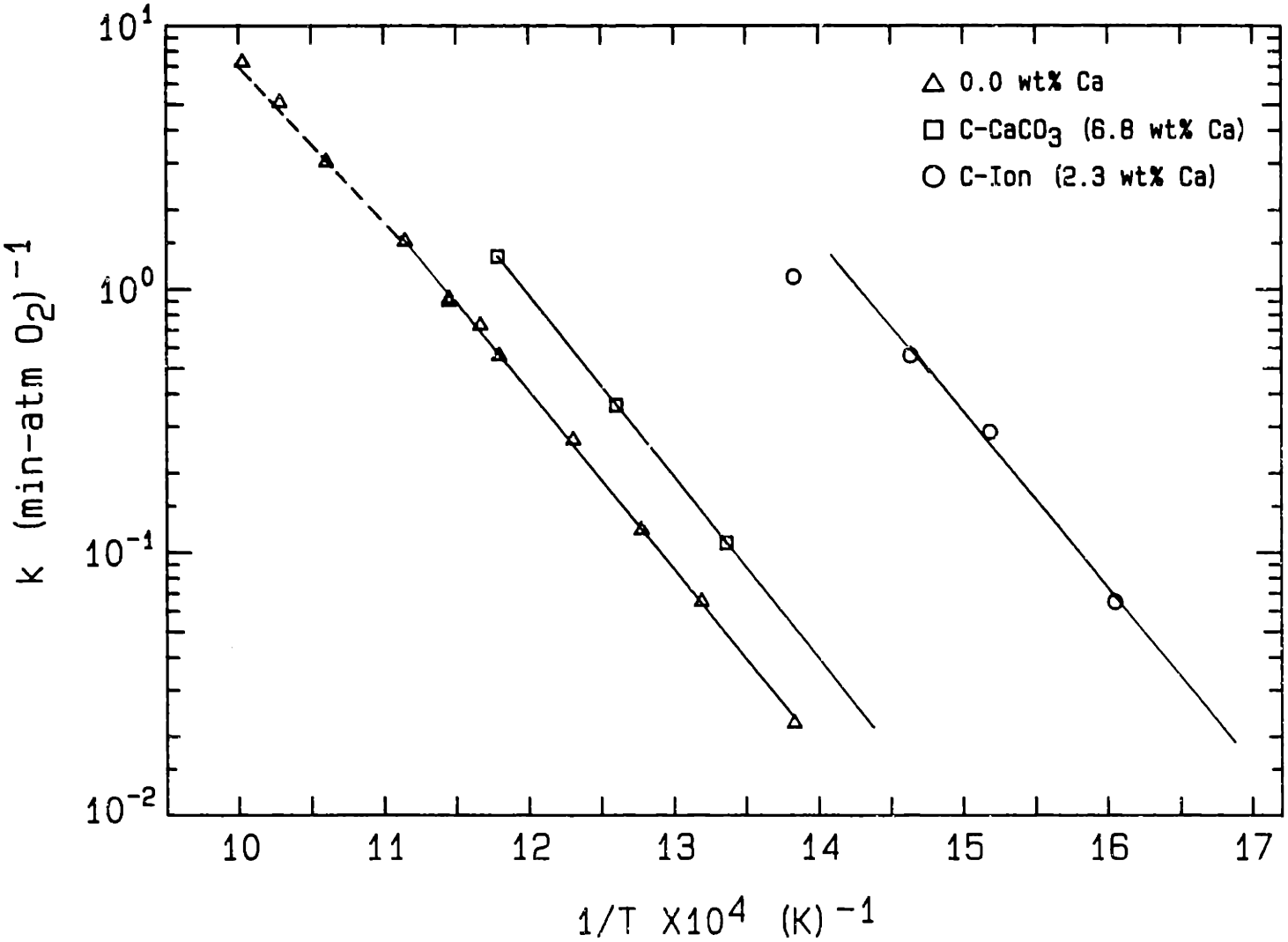

Figure 4.1-18 Arrhenius diagram for the C-ion and C-$CaCO_3$ chars at 20% conversion; 0.21 atm oxygen; particle size 90-106 μm; heat treatment temperature 1100 K.

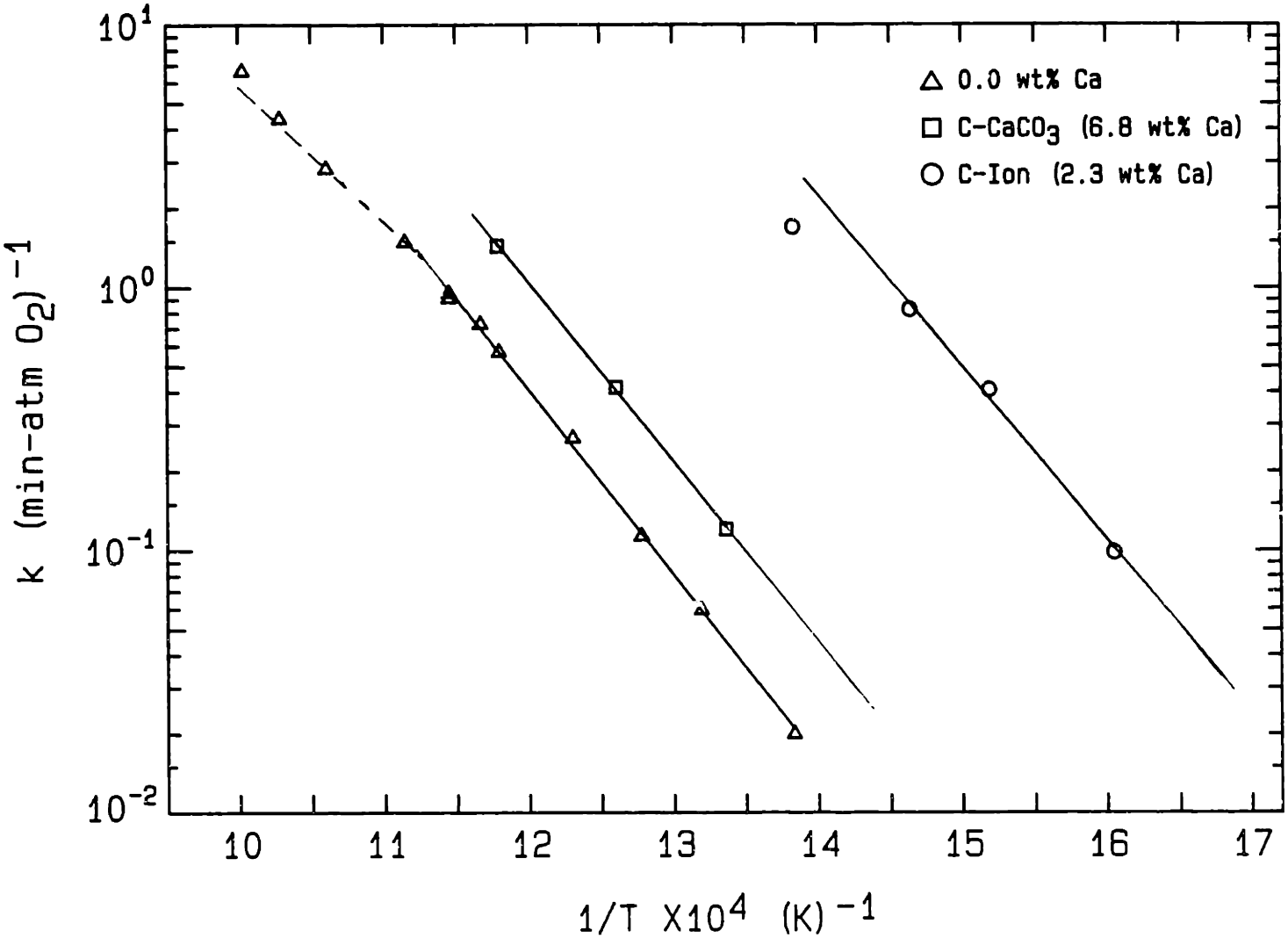

Figure 4.1-19 Arrhenius diagram for the C-ion and C-$CaCO_3$ chars at 40% conversion; 0.21 atm oxygen; particle size 90-106 μm; heat treatment temperature 1100 K.

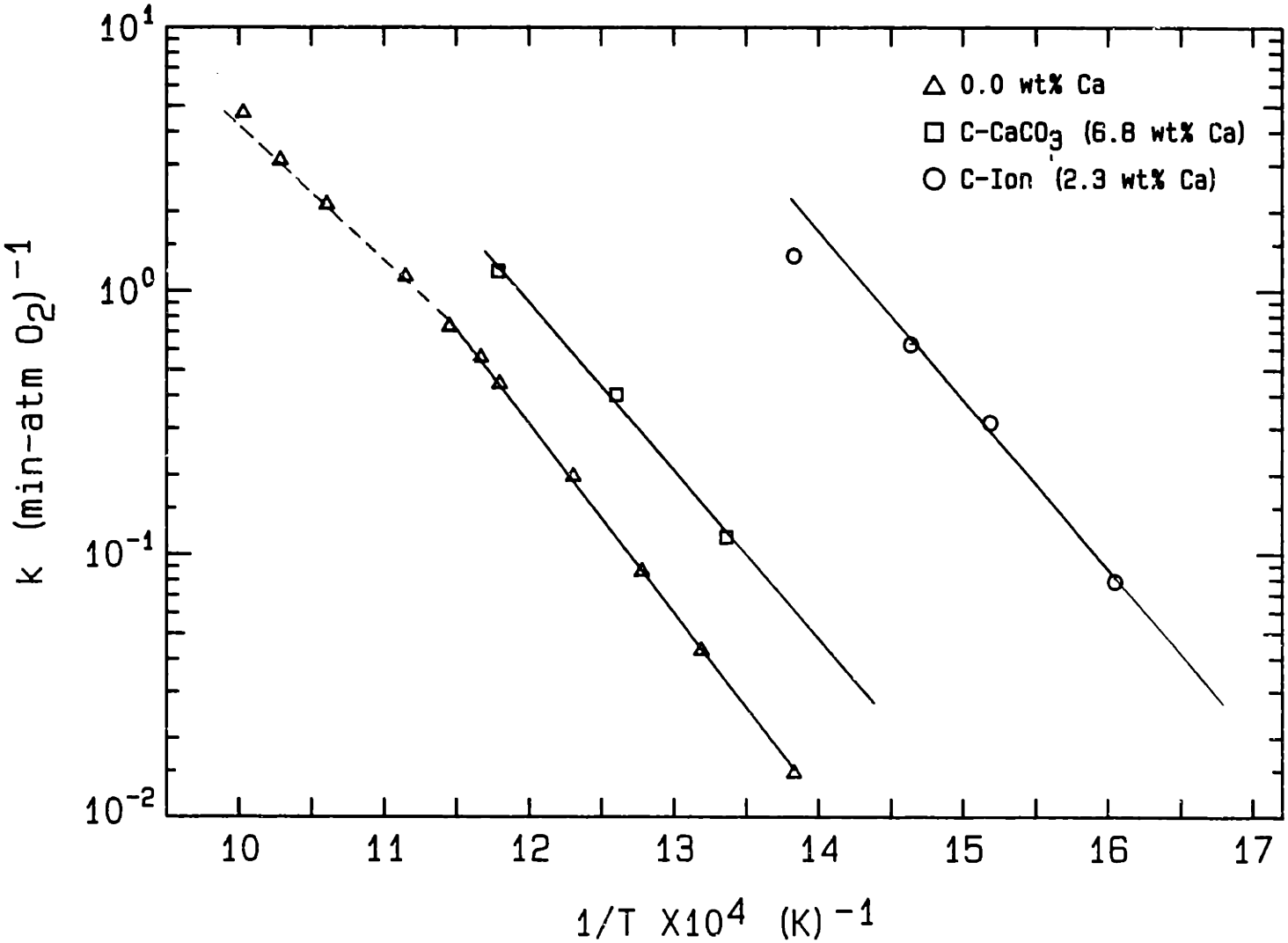

Figure 4.1-20 Arrhenius diagram for the C-ion and C-$CaCO_3$ chars at 60% conversion; 0.21 atm oxygen; particle size 90-106 μm; heat treatment temperature 1100 K.

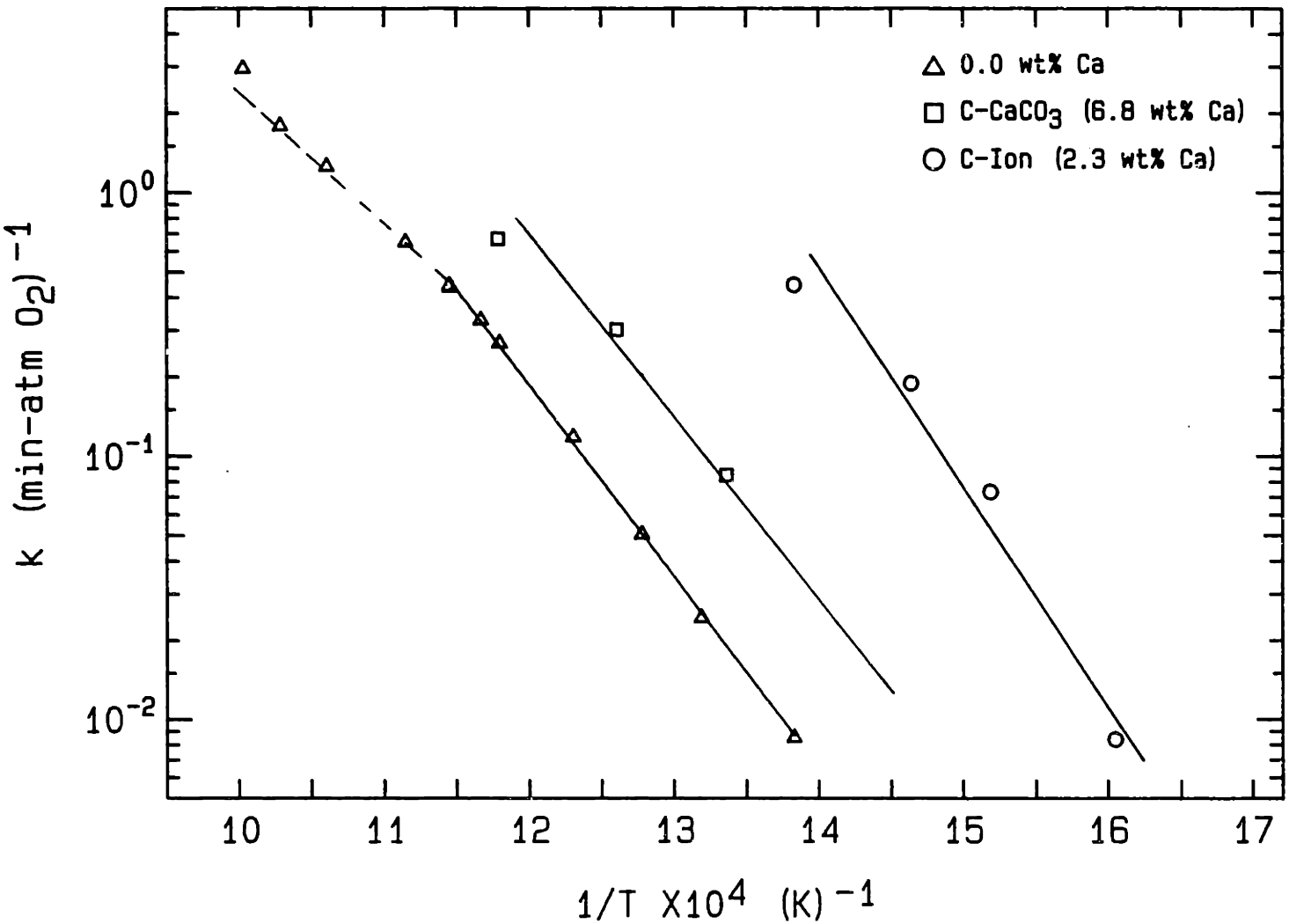

Figure 4.1-21 Arrhenius diagram for the C-ion and C-$CaCO_3$ chars at 80% conversion; 0.21 atm oxygen; particle size 90-106 μm; heat treatment temperature 1100 K.

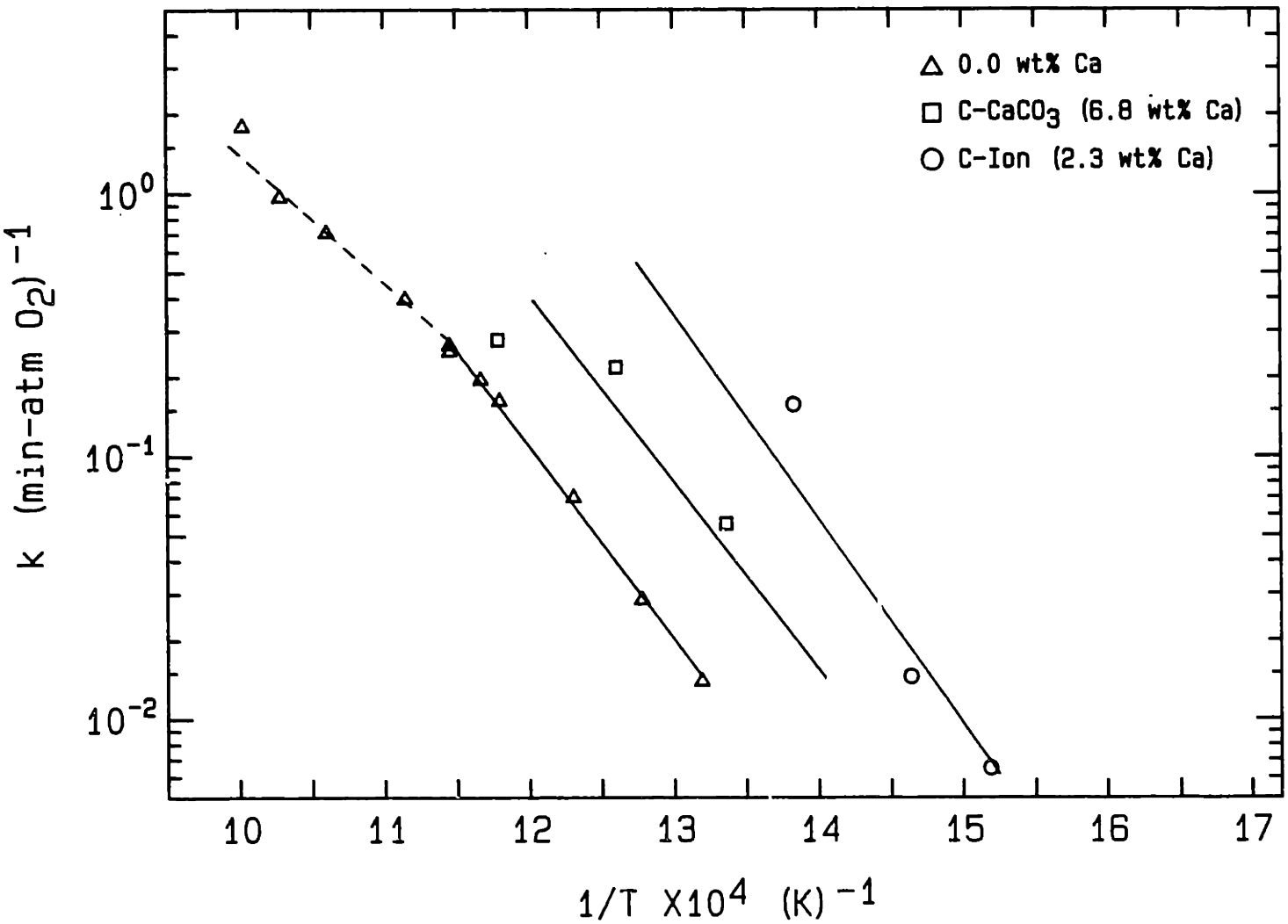

Figure 4.1-22 Arrhenius diagram for the C-ion and C-$CaCO_3$ chars at 90% conversion; 0.21 atm oxygen; particle size 90-106 μm; heat treatment temperature 1100 K.

Table 4.1-2. Activation Energies and Pre-Exponential Factors for the Carbon-Oxygen Reaction.

Conversion (%)	Pre-Exponential Factor (cc/gmole-sec)	Activation Energy (cal/mole)
C-ion Char (2.3 wt% Ca)		
10	8.04×10^{12}	32,200
20	9.12×10^{12}	31,900
40	9.70×10^{12}	31,100
60	4.16×10^{12}	30,700
C-$CaCO_3$ Char (6.8 wt% Ca)		
10	2.57×10^{11}	32,300
20	5.79×10^{11}	33,300
40	5.23×10^{11}	33,000
60	1.34×10^{11}	31,000
Spherocarb		
20	1.30×10^{13}	41,600
40	1.94×10^{13}	42,000
60	1.34×10^{13}	41,400
80	5.36×10^{12}	40,200

Normalized rate versus normalized time data for the C-ion and normalized rate versus conversion data for both the C-ion and C-$CaCO_3$ chars are presented in Figures 4.1-23 to 4.1-25. In general, the ion exchange char data are quite similar to the C-3.6 data, whereas the C-$CaCO_3$ and C-O data are more similar to each other.

The similarity between the C-ion and C-3.6 chars suggests that the catalytic effect is largely independent of the method of calcium addition, provided the calcium is atomically dispersed on the char. This result was unexpected, however, because a fraction of the calcium in the C-3.6 char is presumably bound up within the solid and therefore not accessible until after some carbon conversion has occurred. This may imply that the catalyst does not necessarily have to be on the surface to promote the reaction. Just as with the C-3.6 char, the C-ion data show a low initial rate and the maximum rate is reached only at about 40% conversion. However, the reaction rate of the C-ion char falls off sharply above $t_{0.5} = 1.4$ or, when plotted against conversion, at 80% conversion. The rate appears to approach zero at 80% rather than 100% conversion. Why the rate falls off so precipitously before complete conversion was not investigated. Loss of contact between the calcium and carbon is perhaps greater for the ion exchange char at high conversions. This loss in reactivity is probably responsible for the scatter in the ln k versus 1/T data at and above conversions of 80%.

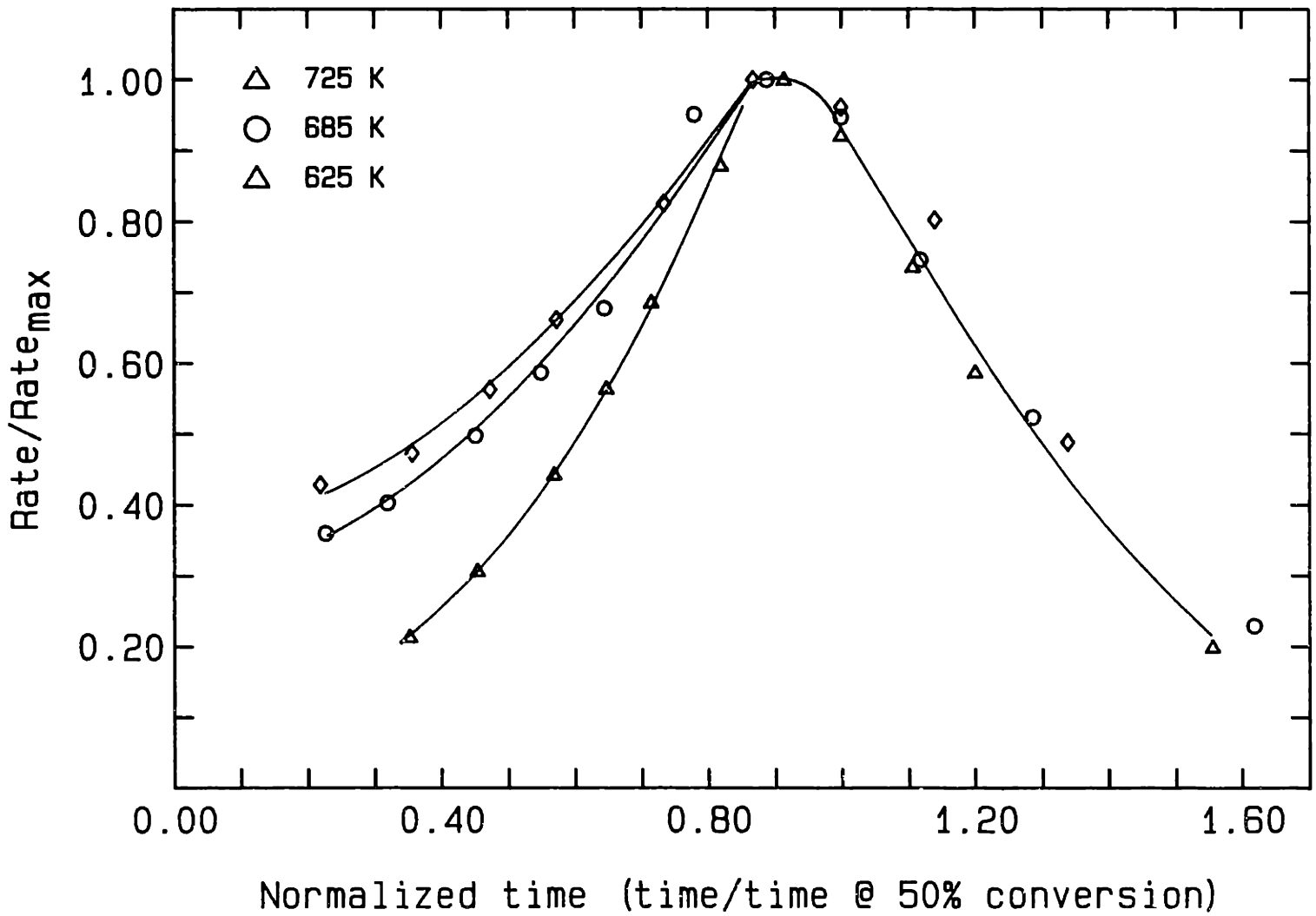

Figure 4.1-23 Reaction rate normalized by the maximum rate plotted against normalized time. C-ion char (2.3 wt% Ca) - oxygen (0.21 atm) reaction; 90-106 μm particles; heat treatment temperature 1100 K.

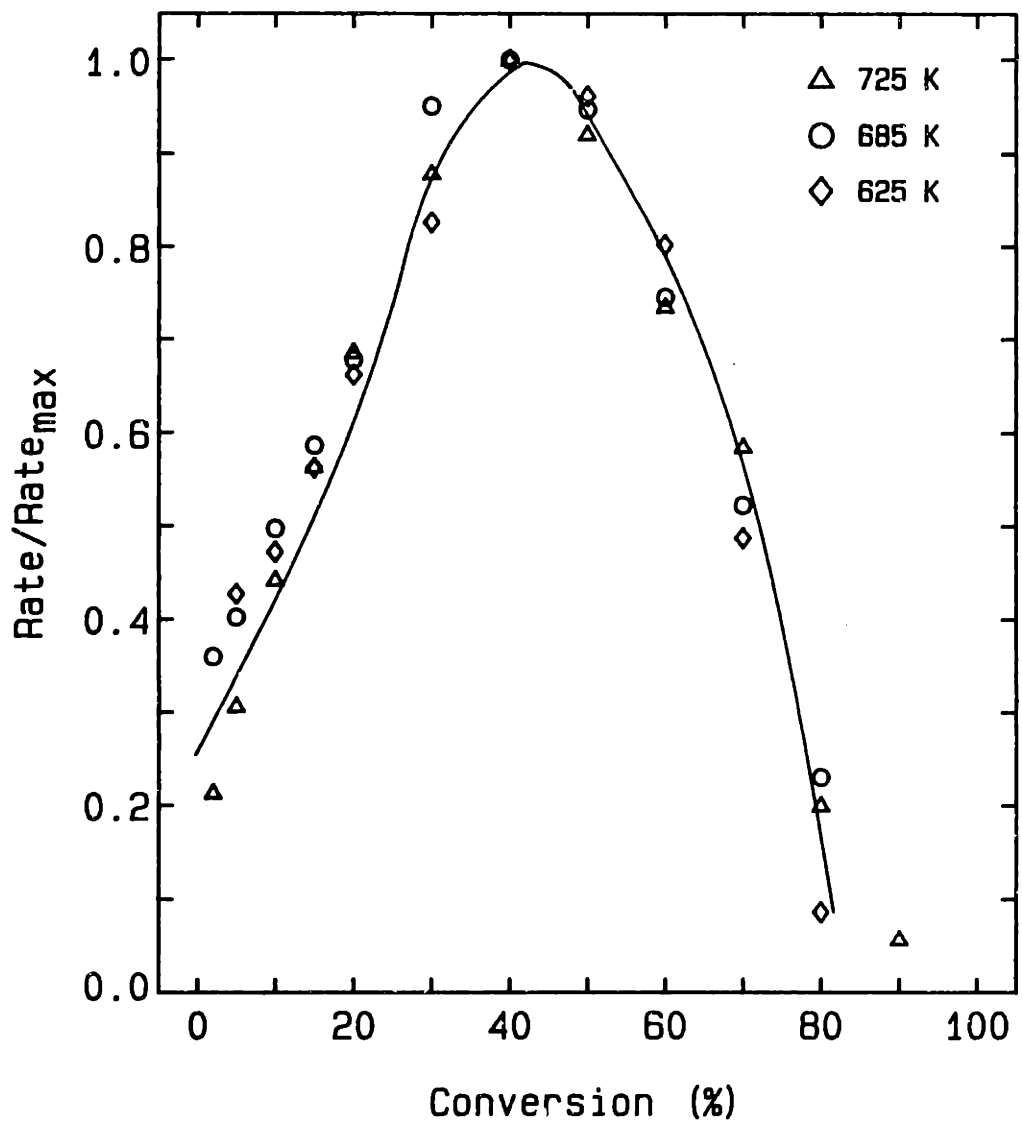

Figure 4.1-24 Reaction rate normalized by the maximum rate versus conversion. C-ion (2.3 wt% Ca) - oxygen (0.21 atm) reaction; 90-106 μm particles; heat treatment temperature 1100 K.

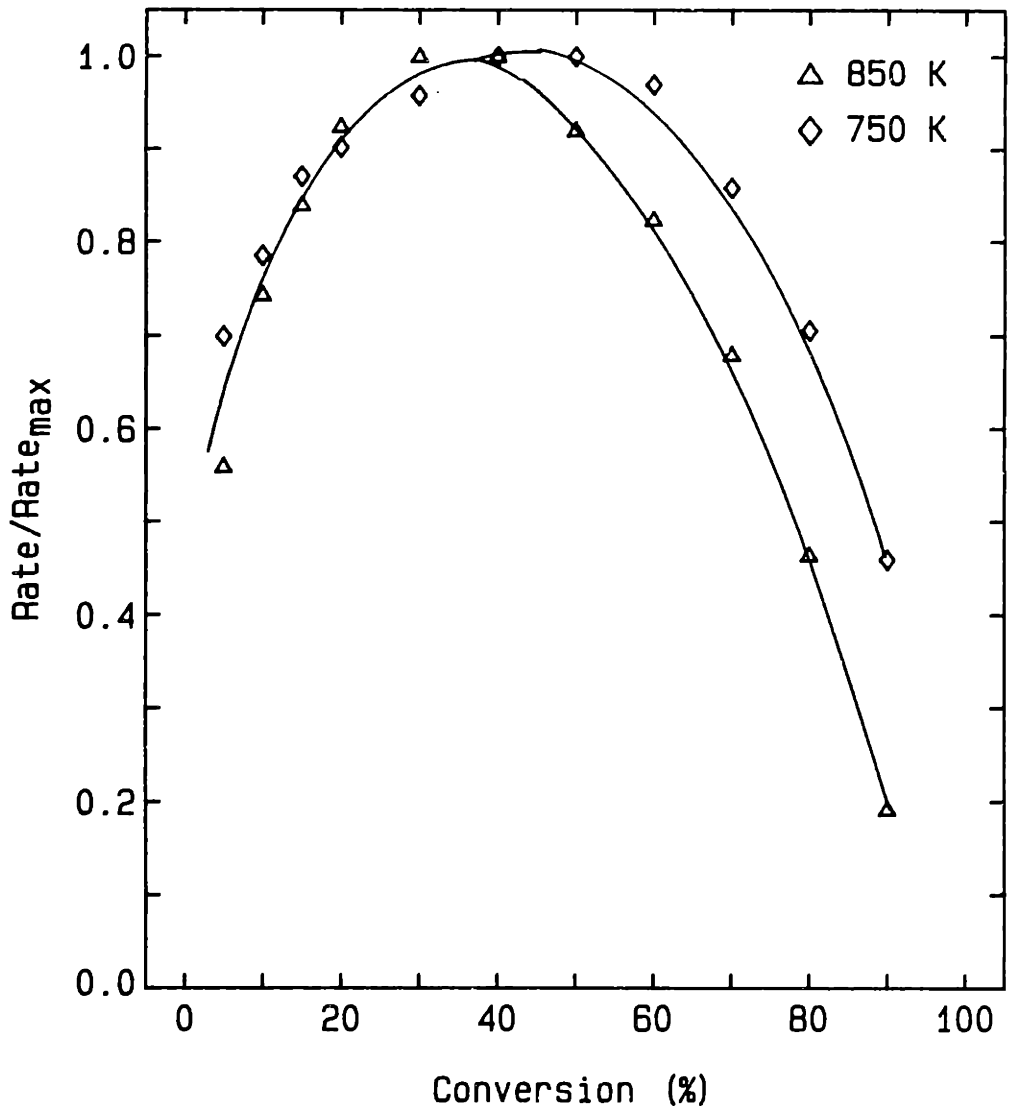

Figure 4.1.25 Reaction rate normalized by the maximum rate versus conversion. C-$CaCO_3$ char (6.8 wt% Ca) - oxygen (0.21 atm) reaction; 90-106 μm particles; heat treatment temperature 1100 K.

4.1.4 Effect of Calcium Content on Reaction Rate

Reaction rate at 715 K versus calcium content of the chars at 40% conversion is shown in Figure 4.1-26. The rate increases linearly with calcium loading up to a calcium content of at least 6%. The ion-exchange char is a factor of two more reactive than the calcium added char with the same calcium content.

The increase in reactivity with calcium loading is comparable to the results obtained by Radovic (1982) for ion exchanged calcium on lignite char.

4.1.5 Reaction Rate of Spherocarb

The oxidation rate of Spherocarb was also determined in this thesis. Spherocarb has been used by Mims and Pabst (1980) and Lang and Neavel (1982) as a high surface area, non-structured carbon substrate in studies of catalytic gasification. Thus, the spherocarb data provide a reference for comparison to data reported by other investigators. The spherocarb was also heat treated at 1100 K prior to reaction. Figures 4.1-27 to 4.1-31 compare the reactivity of spherocarb with the C-O char. Data are presented in Arrhenius form at conversions of 20 through 90%. The reactivity of spherocarb is lower at conversions below 60% but becomes comparable to the reactivity of the C-O char at conversions above 60%. Activation energies as a function of conversion are presented in Table 4.1-2. The activation energy decreases considerably at conversions above 80%; however, they are still about 20% higher than for the C-O char.

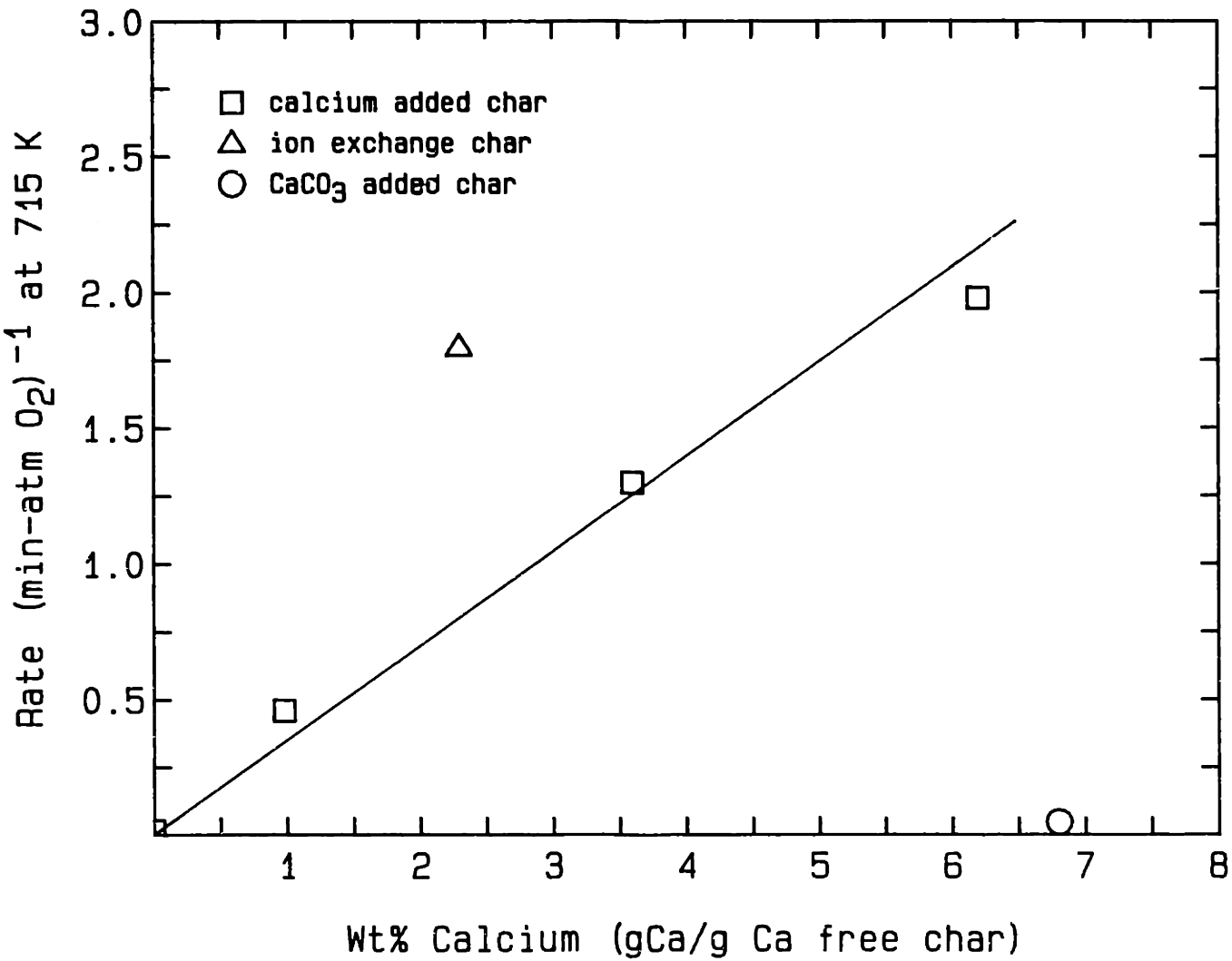

Figure 4.1-26 Reaction rate versus calcium content at 715 K, 40% conversion, carbon-oxygen (0.21 atm) reaction. (90-106 μm particles; heat treatment temperature 1100 K)

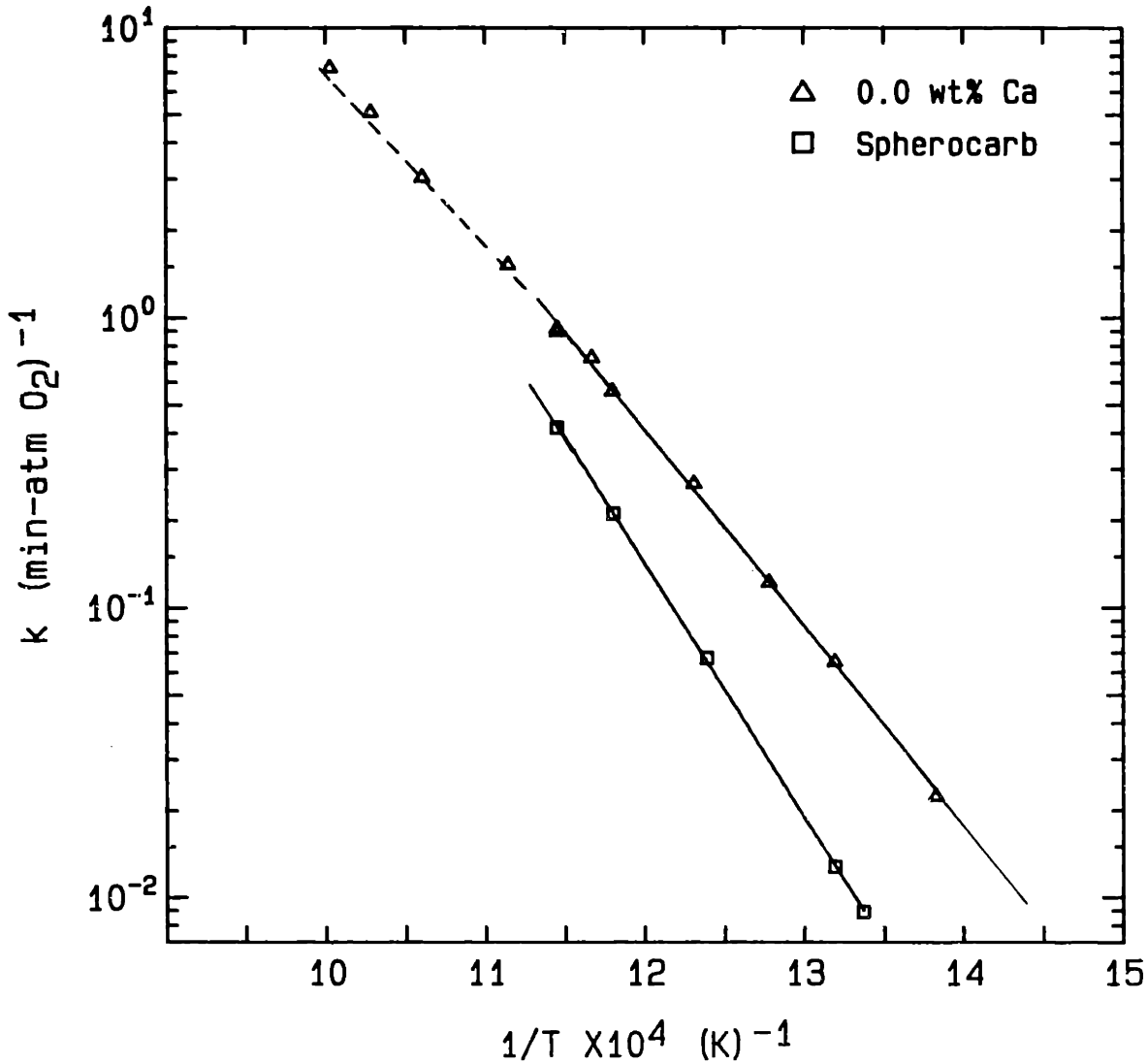

Figure 4.1-27 Arrhenius diagram for the spherocarb-oxygen reaction (0.21 atm) at 20% conversion.

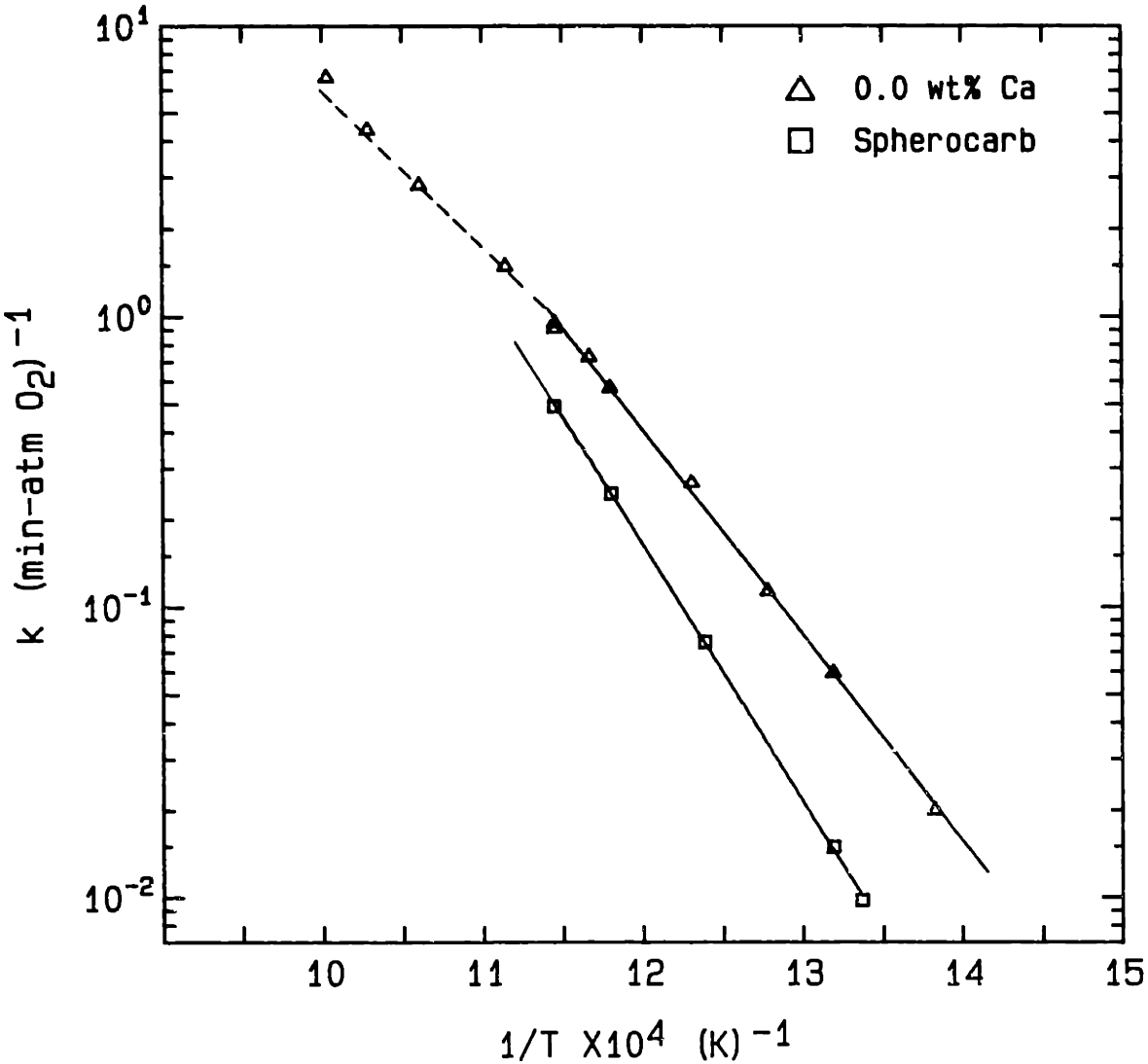

Figure 4.1-28 Arrhenius diagram for the spherocarb-oxygen reaction (0.21 atm) at 40% conversion.

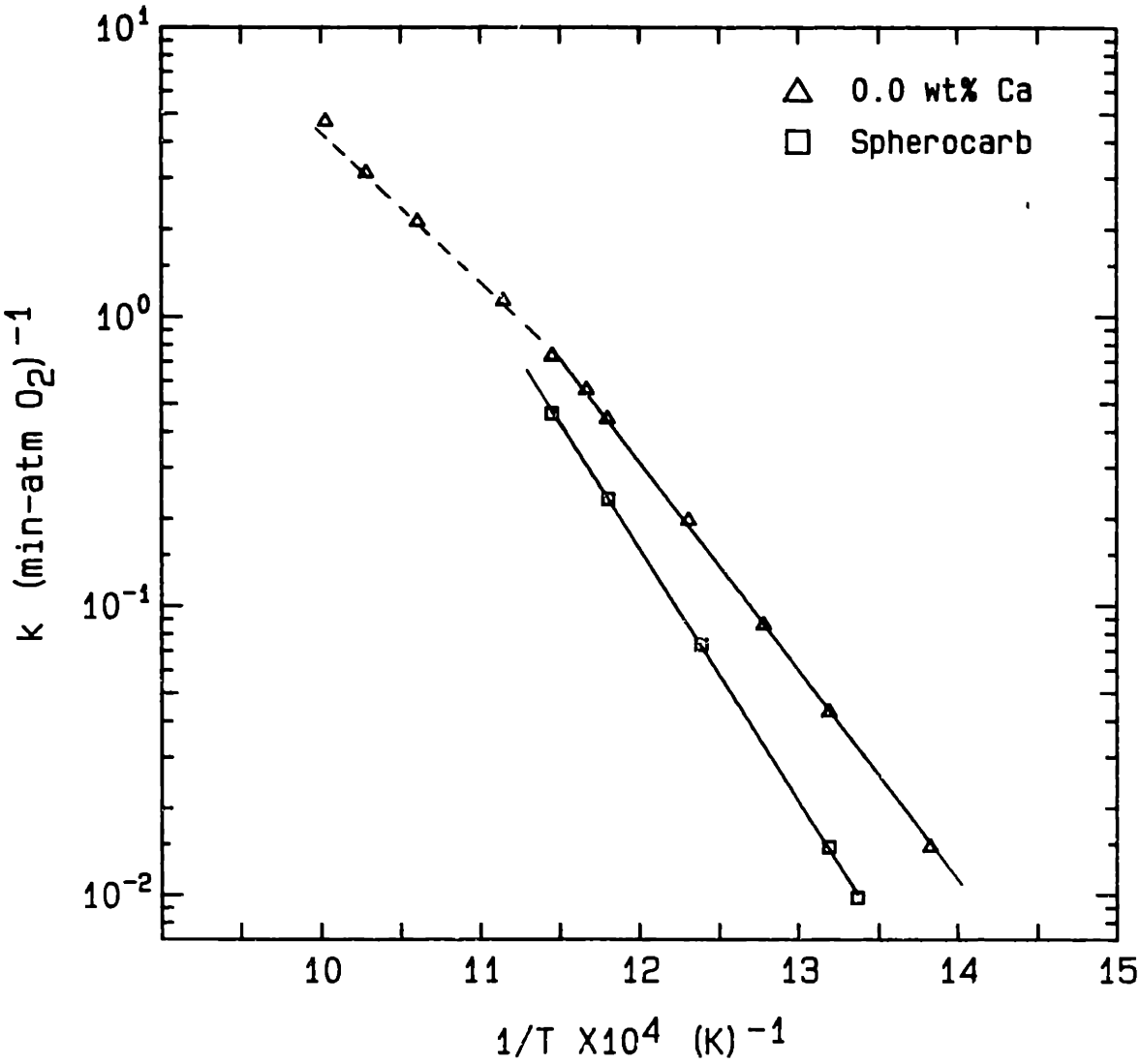

Figure 4.1-29 Arrhenius diagram for the spherocarb-oxygen reaction (0.21 atm) at 60% conversion.

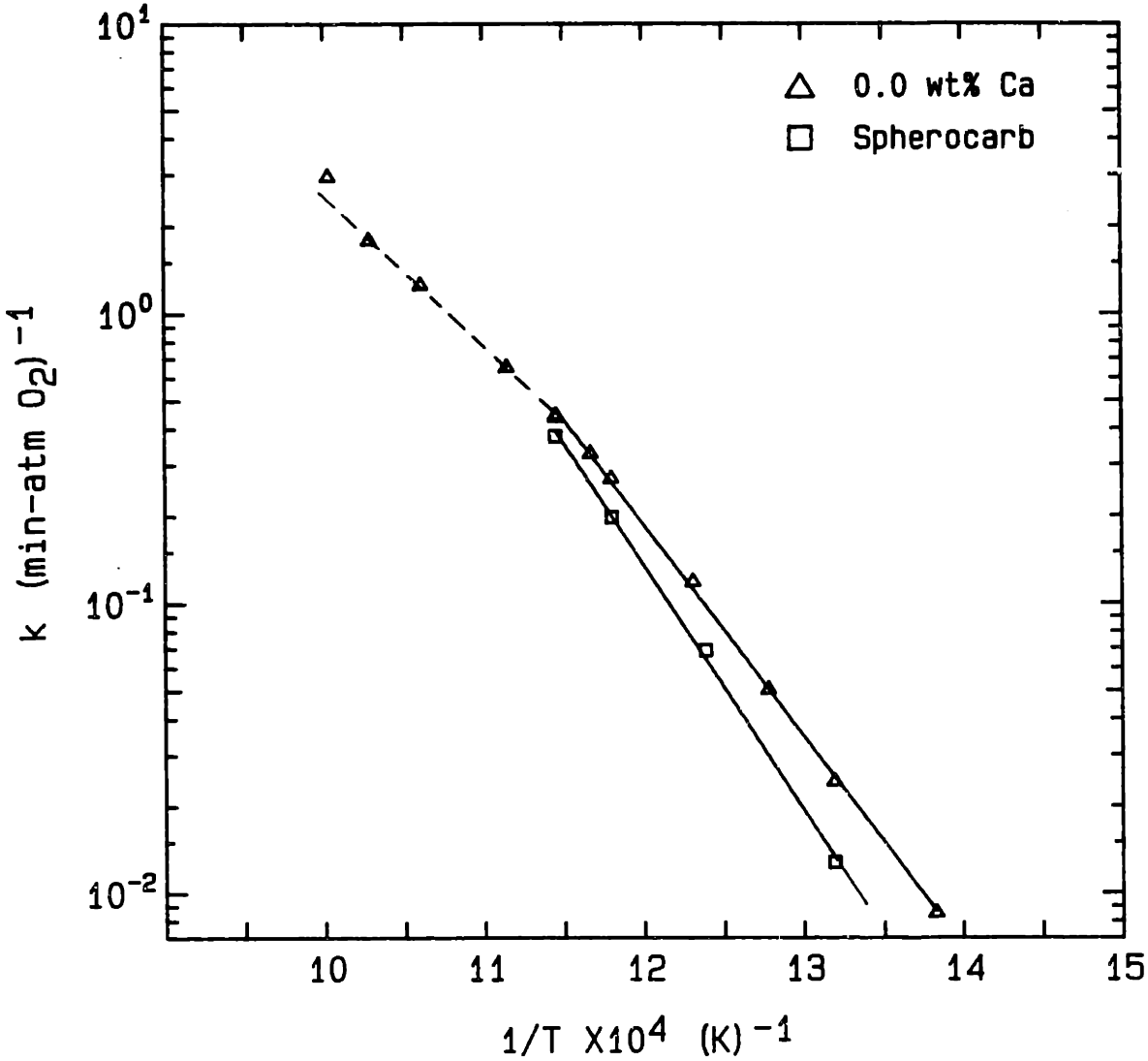

Figure 4.1-30 Arrhenius diagram for the spherocarb-oxygen reaction (0.21 atm) at 80% conversion.

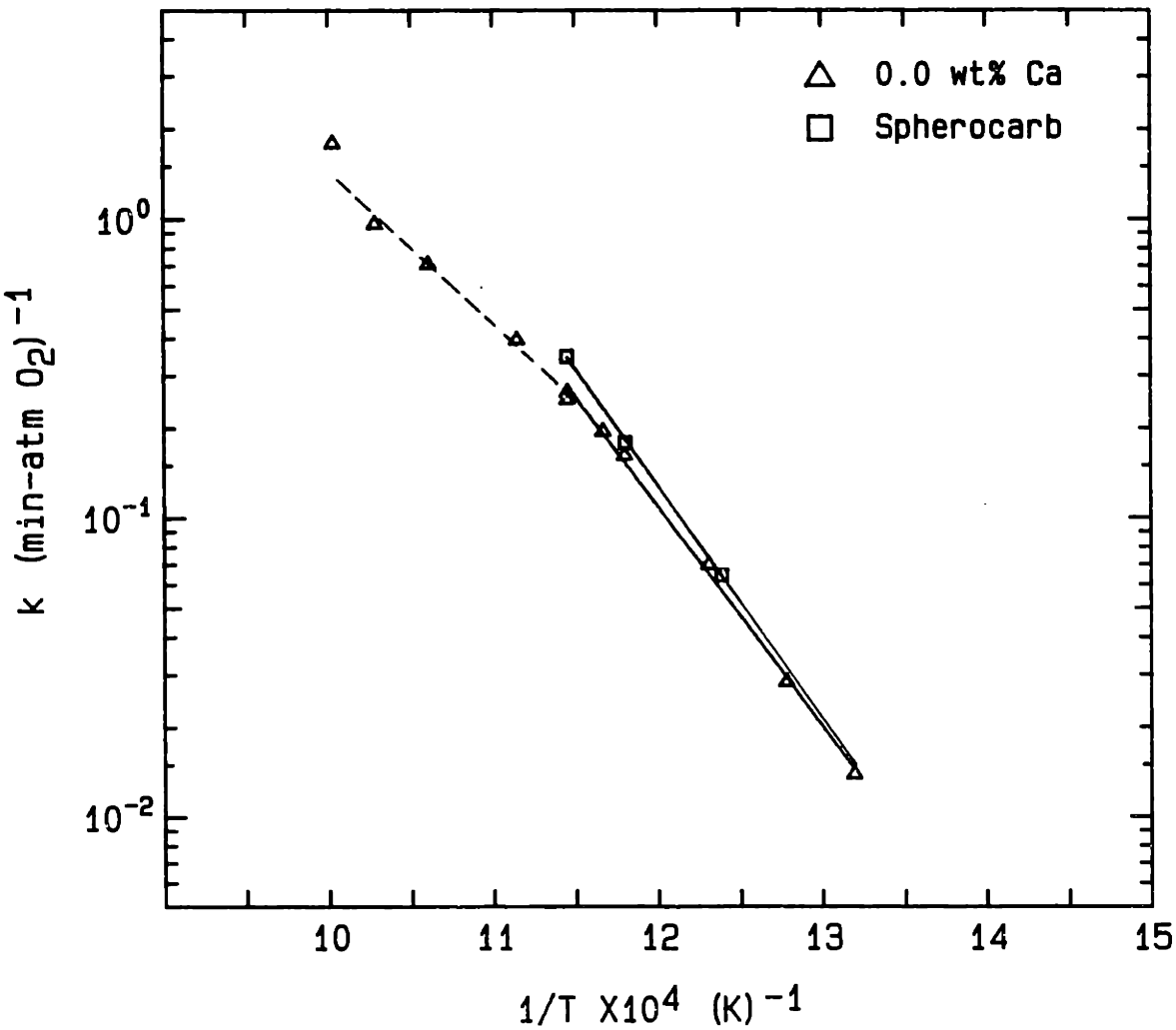

Figure 4.1-31 Arrhenius diagram for the spherocarb-oxygen reaction (0.21 atm) at 90% conversion.

Normalized rate versus conversion and versus normalized time are given in Figures 4.1.32 and 4.1.33. The normalized rate data below 80% conversion all coincide almost exactly onto a single curve. The maximum rate occurs at a conversion of about 30%, and it is over twice the initial rate. The reaction rate remains high even as complete conversion is approached; the residual spherocarb is apparently extremely reactive.

4.1.6 The Effect of Heat Treatment on Reactivity

Reactivity data were obtained with chars that had been heat treated for various time periods and at different final temperatures. To reach the final heat treatment temperature the samples were heated at a rate of 25 C/min from room temperature. Heat treatment for 5 minutes at 1300 K instead of 8 minutes at 1100 K resulted in a significant reduction in reactivity. The reduction in reactivity is greater for the catalyzed chars than for the calcium free char, and it is greater for the ion-exchange char than for the C-1 or C-3.6 chars. The results are summarized in Table 4.1-3.

The effect of heat treatment time, after the sample was heated (25 C/min) to the final heat treatment temperature, on reactivity is shown in Figure 4.1-35. The logarithm of the rate relative to the rate for the char at 0 minutes heat treatment at the same temperature plotted against time gives a linear correlation. Heat treatment time did not have an effect on the reactivity of the calcium free char. Therefore, changes in the char structure of the non-catalyzed char that results in a

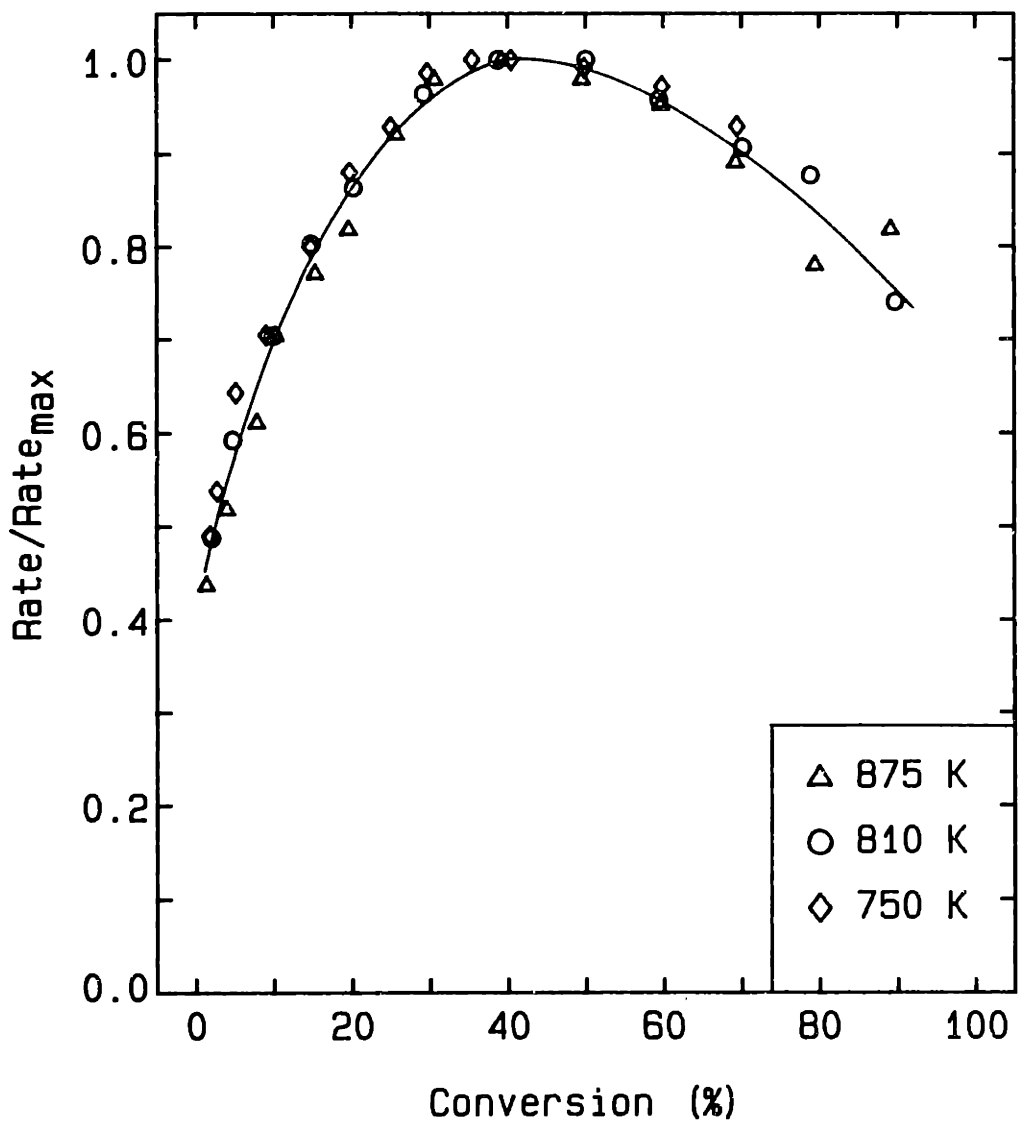

Figure 4.1-32 Reaction rate normalized by the maximum rate versus conversion; spherocarb-oxygen (0.21 atm) reaction.

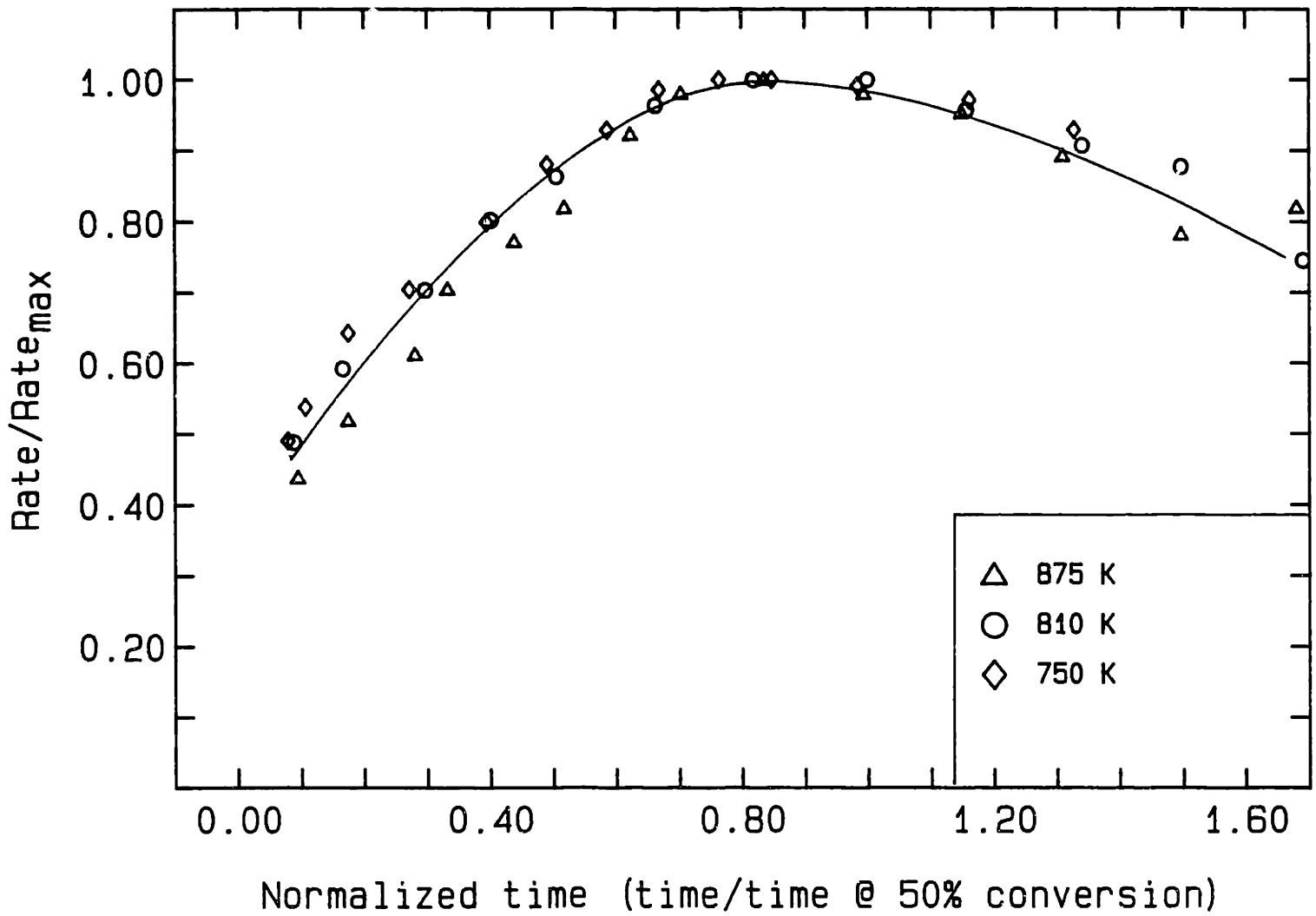

Figure 4.1-33 Reaction rate normalized by the maximum rate versus normalized time; spherocarb-oxygen (0.21 atm) reaction.

Table 4.1-3. Relative Reactivity of the Chars at Two Heat Treatment Conditions.

Char	$\left[\frac{\text{Rate}^{(1)}\ (\text{heat treatment at } 1300\ K)}{\text{Rate}\ (\text{heat treatment at } 1100\ K)}\right]$
C-0 (0 wt% Ca)	0.50
C-1 (1 wt% Ca)	0.17
C-3.6 (3.6 wt% Ca)	0.21
C-ion (2.3 wt% Ca)	0.081

(1) Oxygen reaction (0.21 atm) at 775 K; 40% conversion.

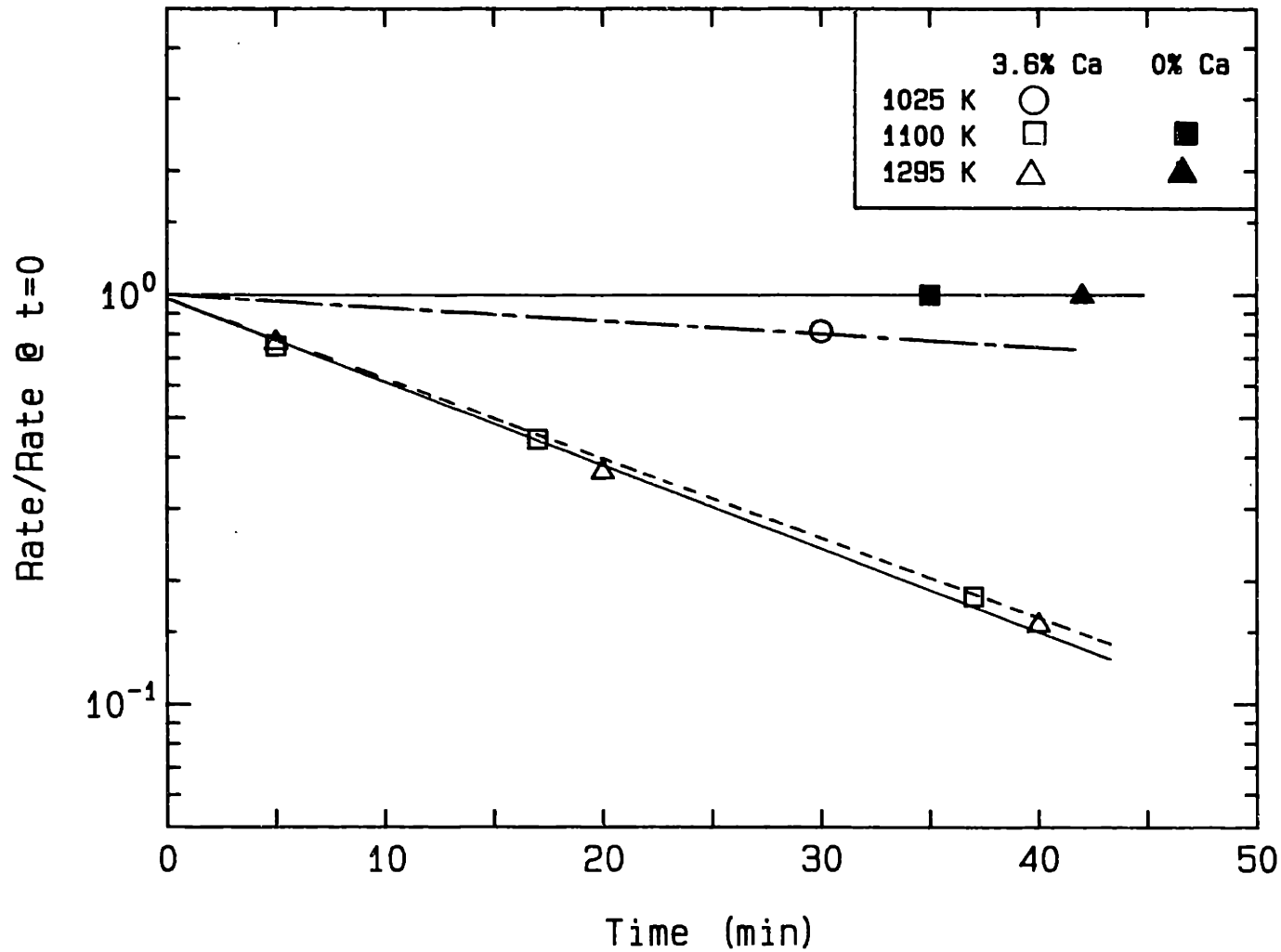

Figure 4.1-34 The effect of heat treatment time on the reactivity of the C-O and C-3.6 chars. Reaction rate is normalized to the rate at 0 minutes heat treatment time.

decrease in carbon reactivity must occur on a time scale that is shorter than the heating rate used in these experiments. Further isothermal heat treatment thereafter does not affect the char's reactivity. For the catalyzed char, heat treatment at 1025 versus 1100 K affects reactivity very differently. A temperature of 1070 K seems to represent a thermal deactivation point for the catalyzed char. The failure of the rate constant to have an Arrhenius temperature dependence, however, suggests that the presentation of the data in this manner must be an essentially empirical correlation.

Reaction rate data of the C-O and C-3.6 chars heat treated at 1300 K for 5 minutes are presented in Figures 4.1-35 to 4.1-39. Activation energies are summarized in Table 4.1-4; they are similar to the values obtained at the lower heat treatment temperature. At conversions above 80%, it was not possible to accurately determine the activation energy of the C-3.6 char because of scatter in the data points about a straight-line correlation.

4.1.7 The Effect of Particle Size on Reactivity

Experiments were conducted with particles 177-212 μm, 90-106 μm, and 45 - 53 μm in size. Experiments were conducted with particles that were crushed directly from the next larger size as well as with the particle sizes obtained in the original classification of the sucrose char directly after manufacture. The results were the same in all cases. The particle shape can best be described as angular. Electron

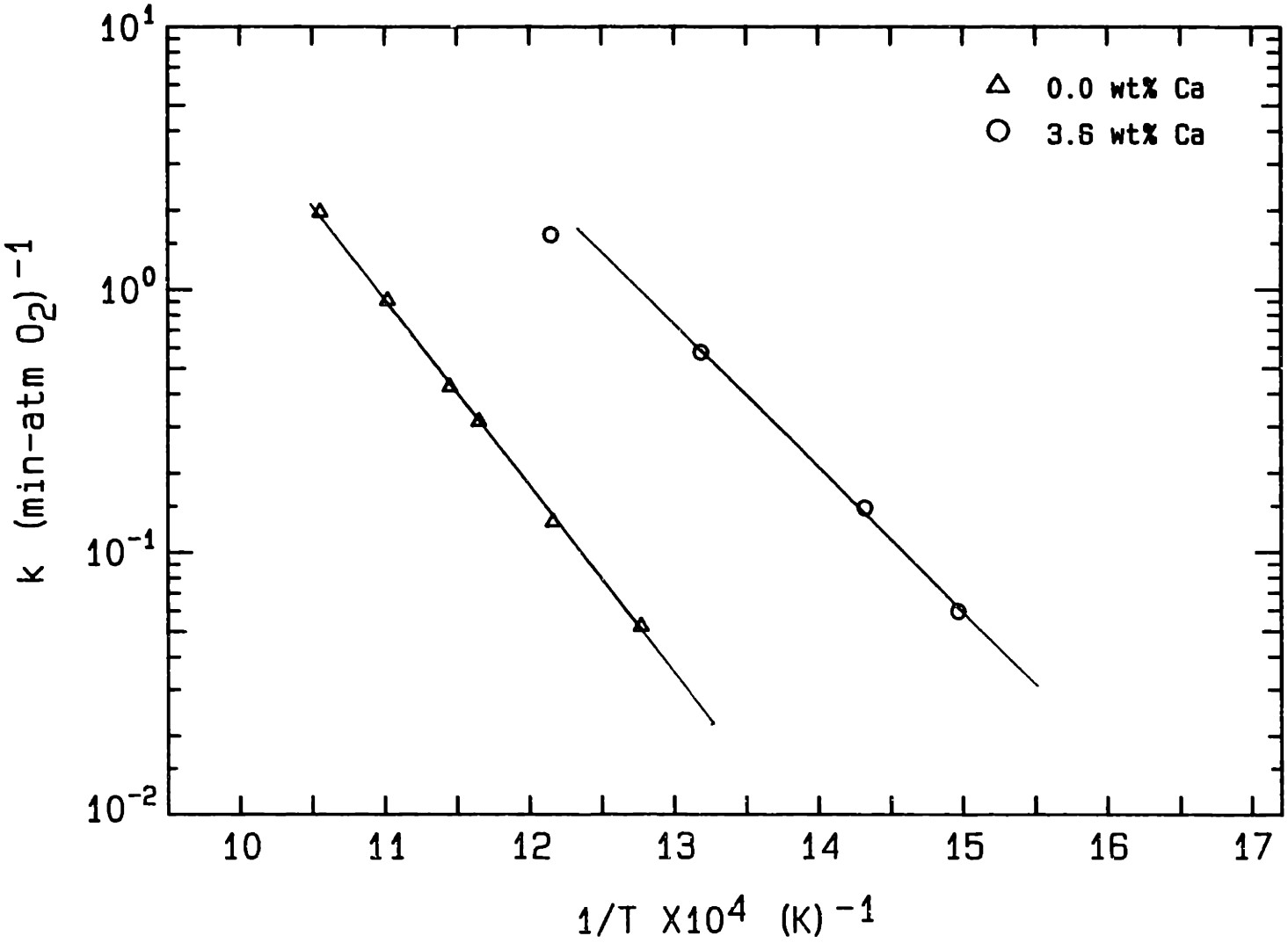

Figure 4.1-35 Arrhenius diagram for the C-O (0 wt% calcium) and the C-3.6 (3.6 wt% Ca) chars at 20% conversion. Heat treatment temperature is 1300 K; 0.21 atm oxygen; 90-106 μm particles.

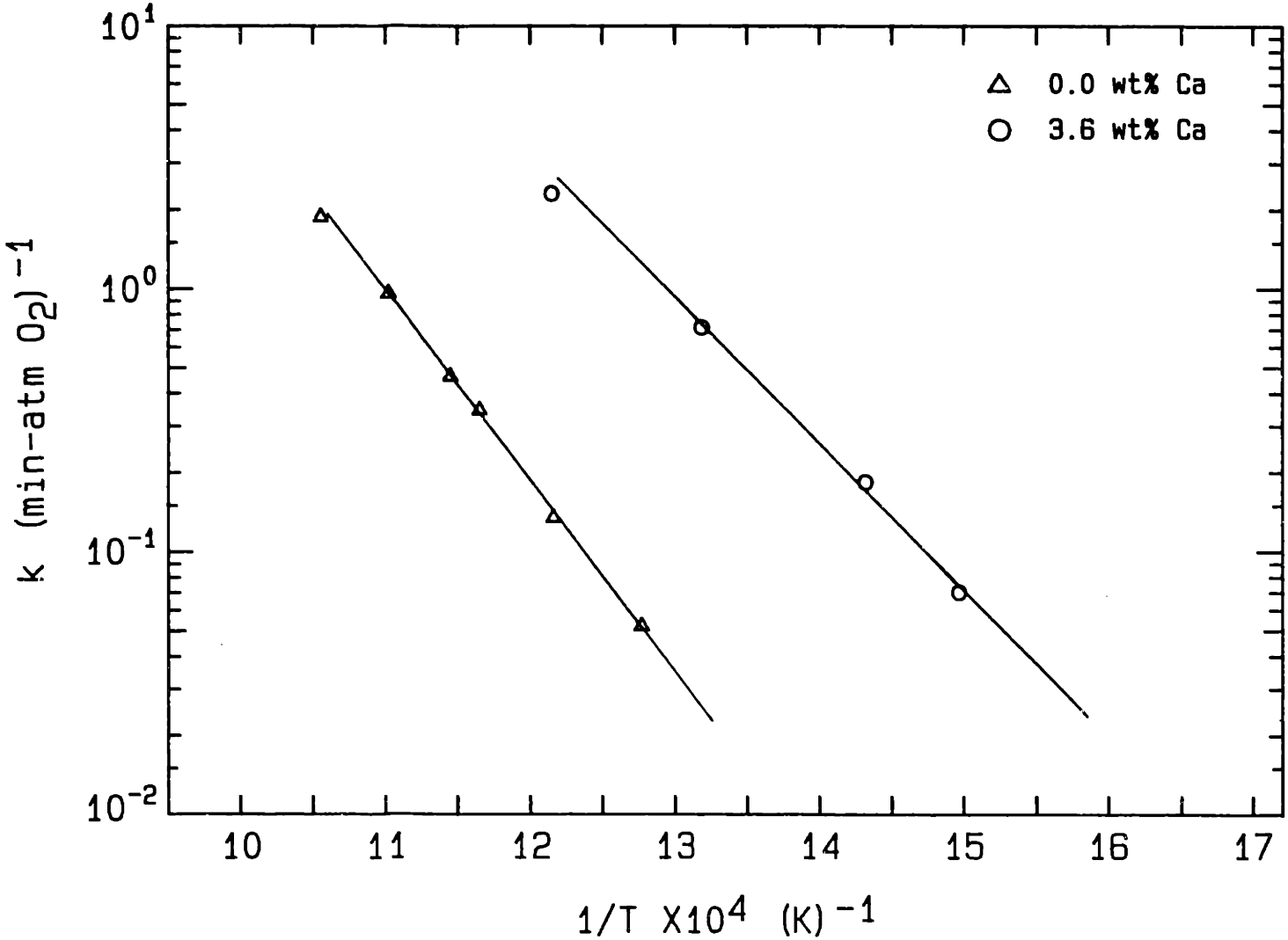

Figure 4.1-36 Arrhenius diagram for the C-O (0 wt% calcium) and the C-3.6 (3.6 wt% Ca) chars at 40% conversion. Heat treatment temperature is 1300 K; 0.21 atm oxygen; 90-106 μm particles.

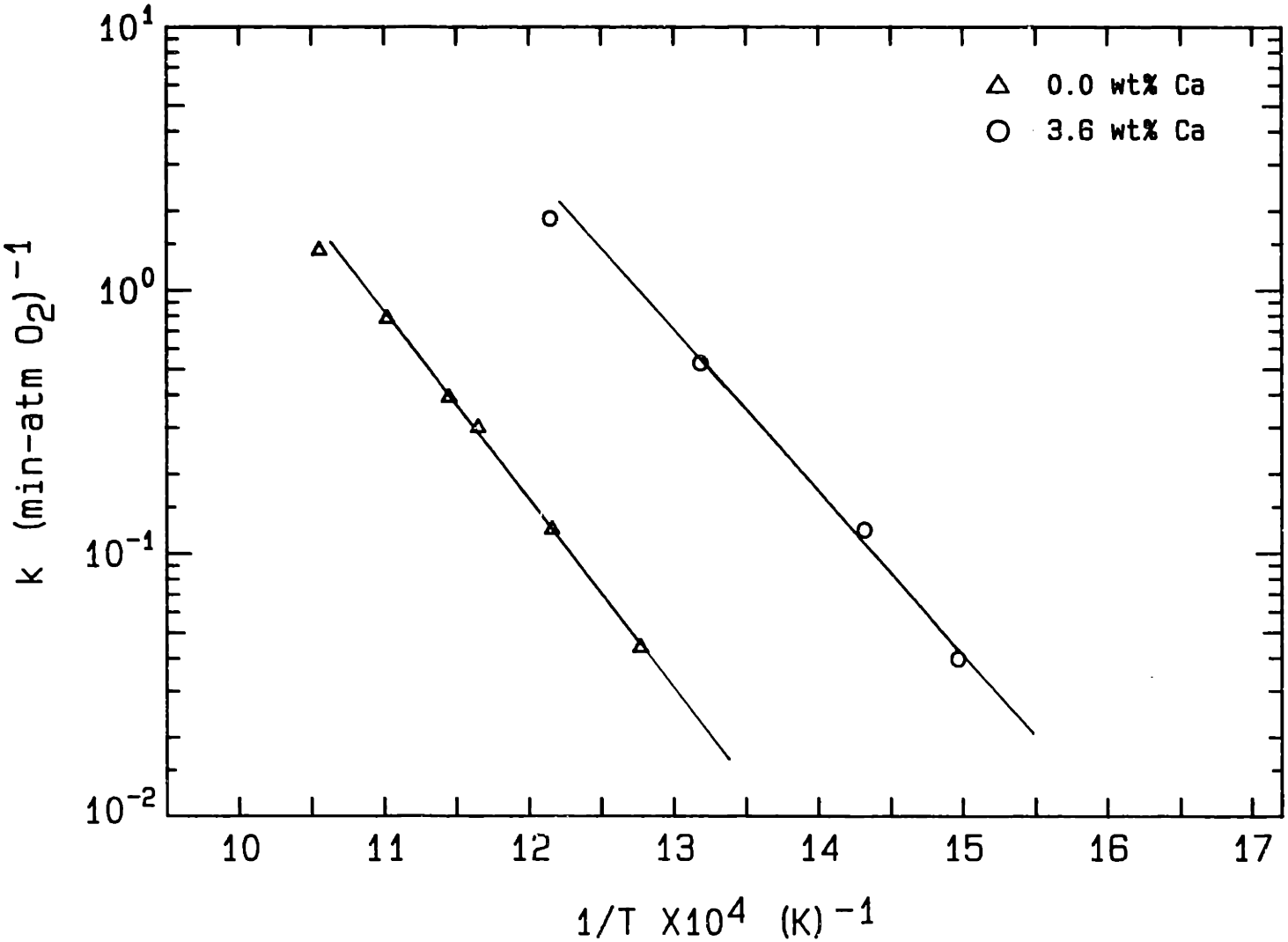

Figure 4.1-37 Arrhenius diagram for the C-O (0 wt% calcium) and the C-3.6 (3.6 wt% Ca) chars at 60% conversion. Heat treatment temperature is 1300 K; 0.21 atm oxygen; 90-106 μm particles.

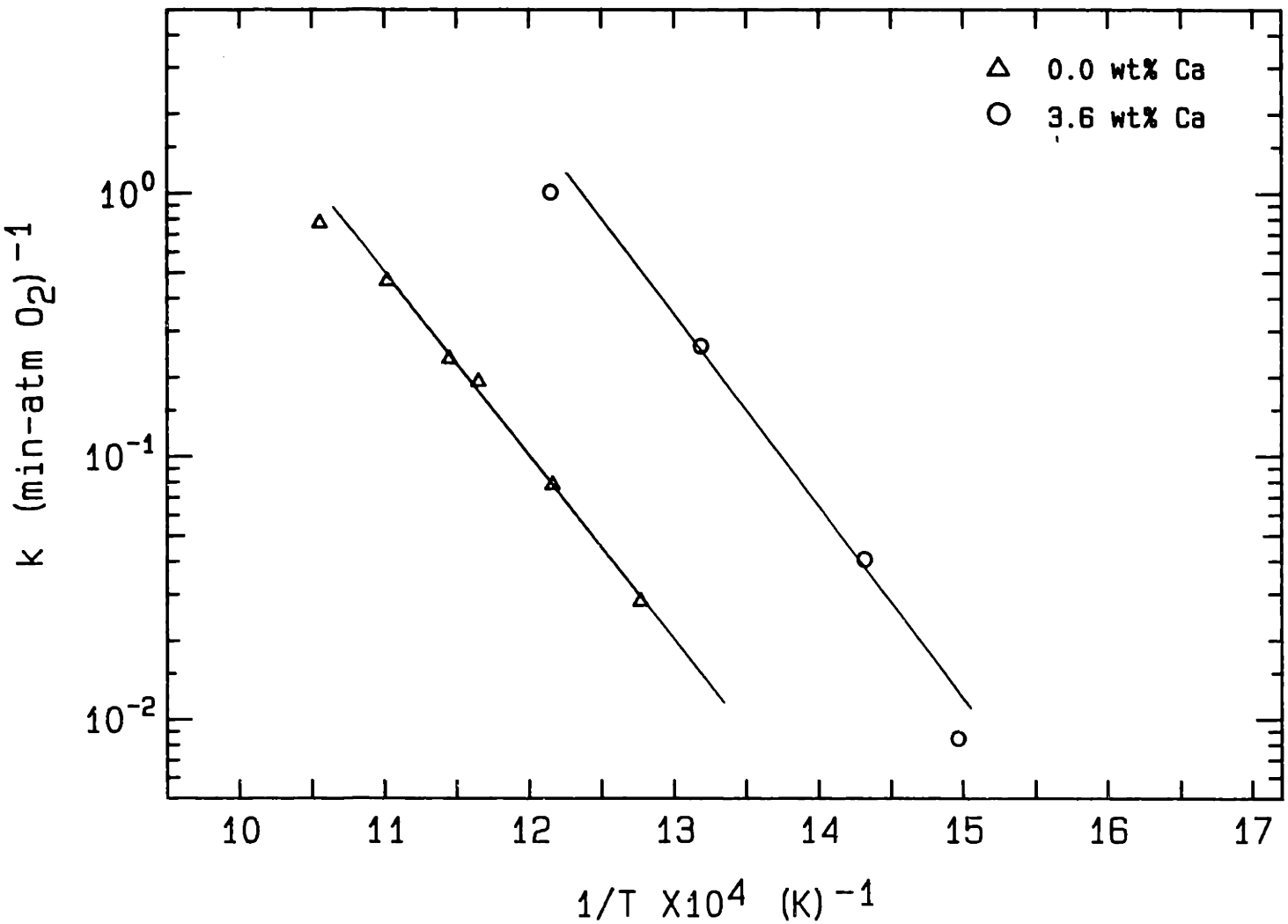

Figure 4.1-38 Arrhenius diagram for the C-O (0 wt% calcium) and the C-3.6 (3.6 wt% Ca) chars at 80% conversion. Heat treatment temperature is 1300 K; 0.21 atm oxygen; 90-106 μm particles.

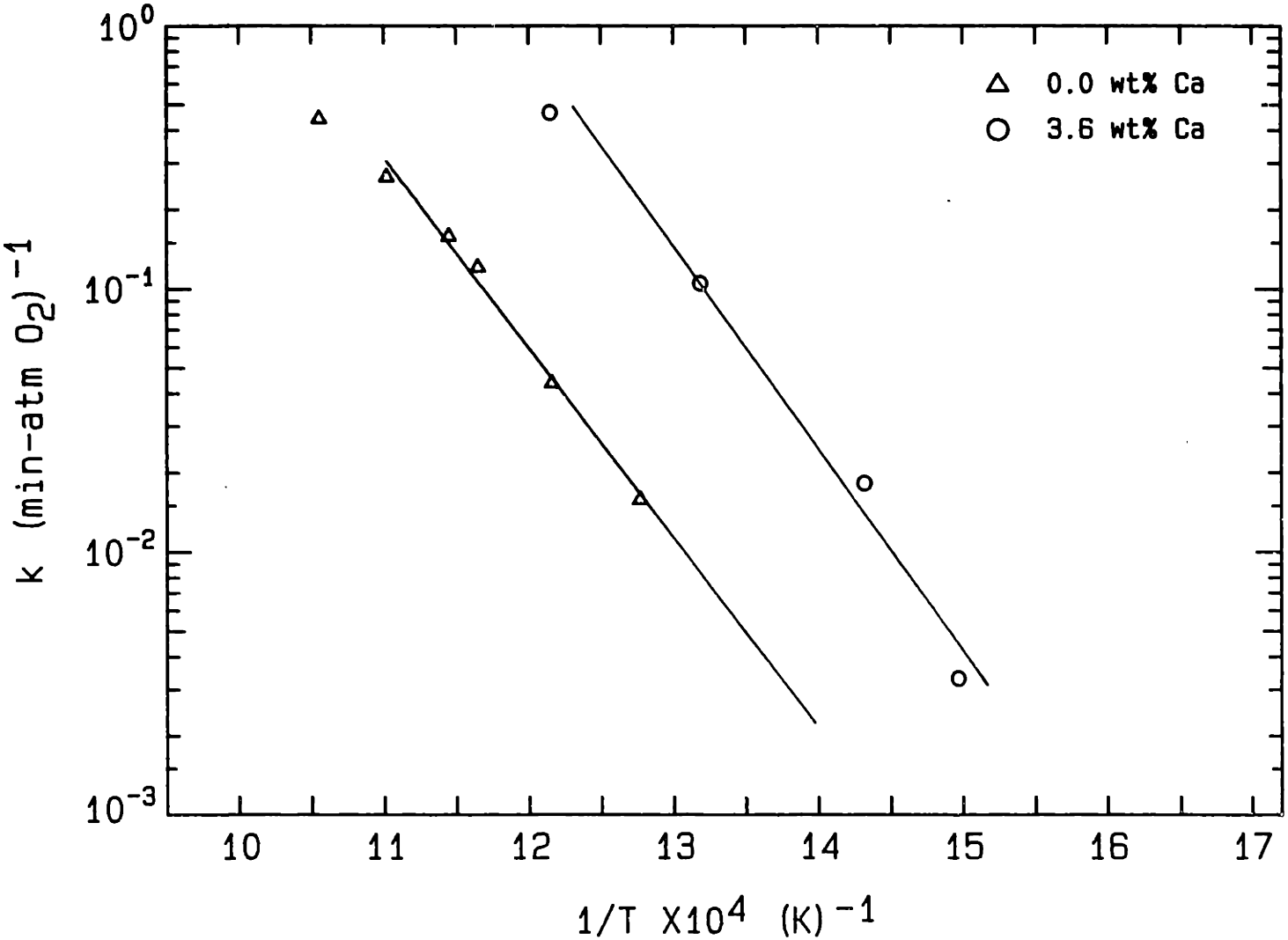

Figure 4.1-39 Arrhenius diagram for the C-O (0 wt% calcium) and the C-3.6 (3.6 wt% Ca) chars at 90% conversion. Heat treatment temperature is 1300 K; 0.21 atm oxygen; 90-106 μm particles.

Table 4.1-4. Activation Energy and Pre-Exponential Factor for the Carbon-Oxygen Reaction; 90-106 μm particles.

Conversion (%)	Heat Treatment Temperature 1300 K Pre-Exponential Factor (cc/gmole/sec)	Activation Energy (cal/mole)
C-O Char (0 wt% Ca)		
20	1.88×10^{11}	34,200
40	3.33×10^{11}	35,000
60	2.04×10^{11}	34,500
80	7.80×10^{10}	33,700
90	9.00×10^{10}	34,800
C-3.6 Char (3.6 wt% Ca)		
20	2.90×10^{10}	26,600
40	5.04×10^{10}	27,100
60	2.40×10^{11}	30,000
80	5.70×10^{13}	39,000
90	2.50×10^{13}	39,200

micrographs of the char particles are presented and described in Section 4.3.8.

The reaction rates of the different sized C-O char particles are not the same even at the lowest temperature at which measurements were made. The data are summarized in Figures 4.1-40 to 4.1-44. The rate data fall on three straight lines that tend to separate slightly with increasing reactivity; the lines are not strictly parallel to each other. The maximum difference in rate between the smallest particles and the 100 μm particles is about 20%. With increasing conversion, the particle size effect remains evident. Since the smaller particles were obtained by crushing larger particles, these results indicate that the entire char volume probably does not participate uniformly in the reaction. However, because the Arrhenius diagrams are straight lines over almost two orders of magnitude for each of the particle sizes, a true intrinsic rate regime apparently does exist. Such a regime is defined as one where no concentration gradient of the reactant exists inside the particle. Although not generally considered, a no flux boundary condition inside the solid will meet this criterion. If reaction only occurs in a spherical volume of a certain thickness, the reactivity will be a function of the particle diameter. The relative reactivities of the three particle sizes as a function of the thickness of the reactive volume (measured from the particle surface) are shown in Figures 4.1-45. A comparison of the data in this figure to the reactivity data

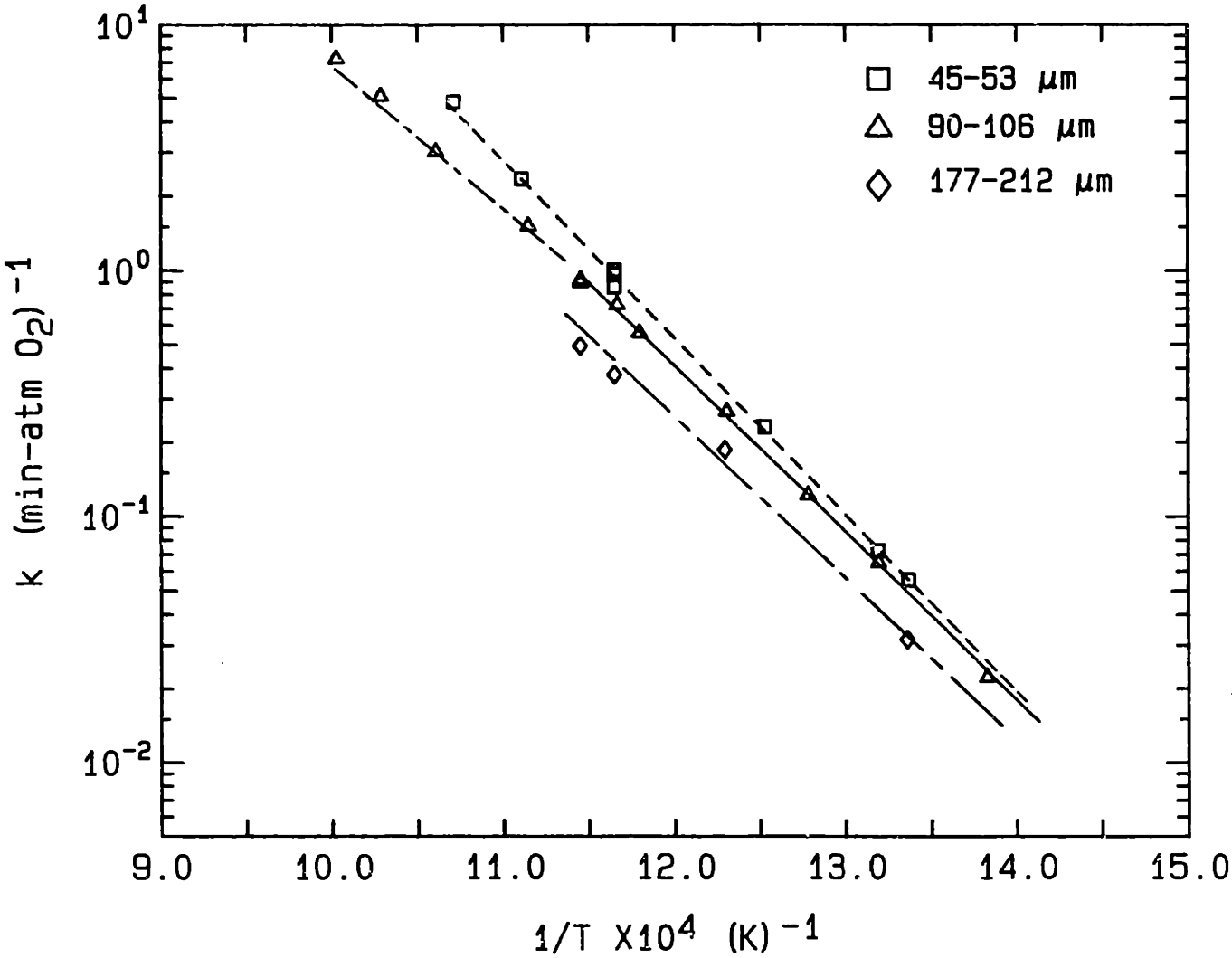

Figure 4.1-40 Arrhenius diagram for the C-O (0 wt% Ca) char at 20% conversion for three particle sizes; oxygen (0.21 atm); heat treatment temperature 1100 K.

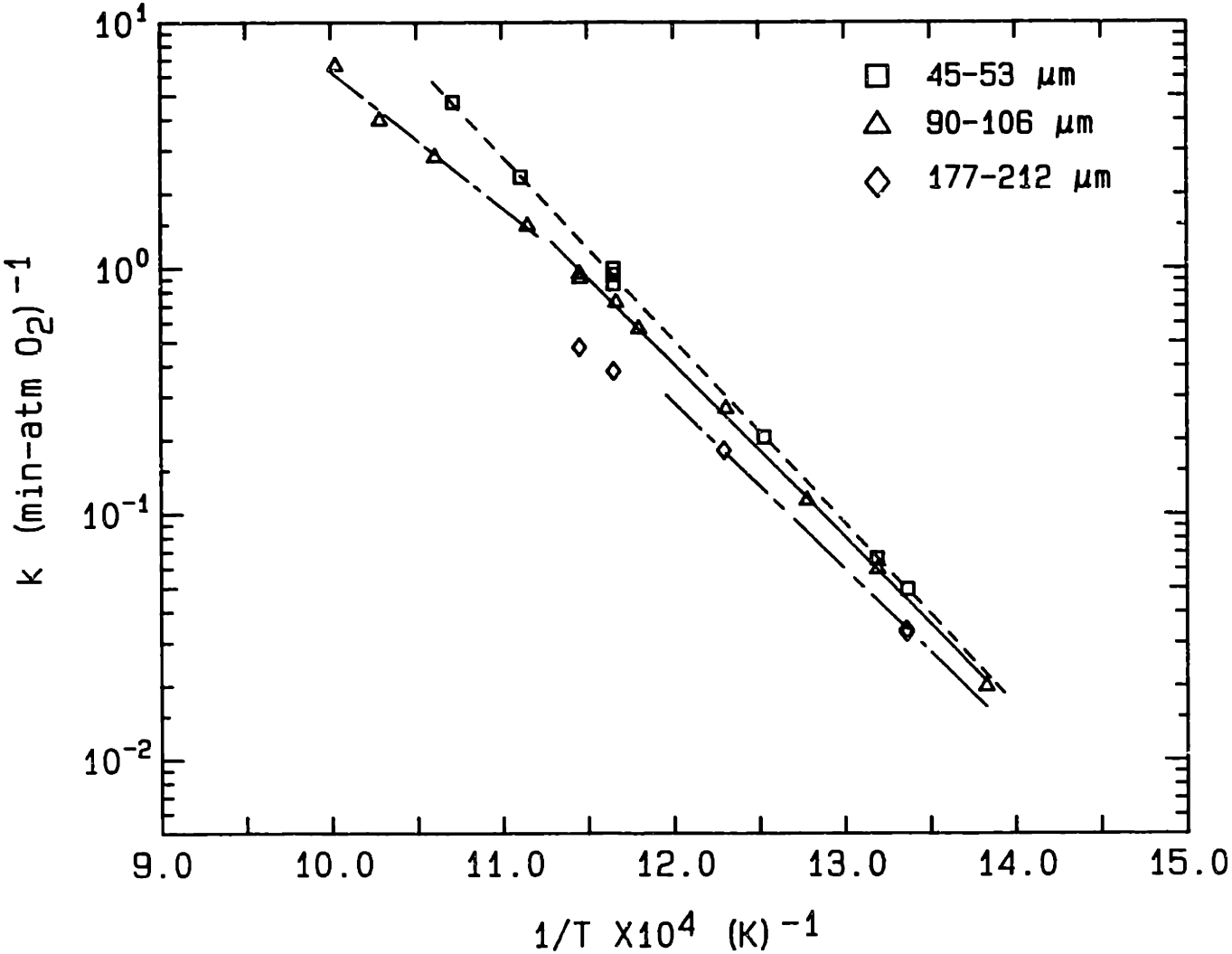

Figure 4.1-41 Arrhenius diagram for the C-O (0 wt% Ca) char at 40% conversion for three particle sizes; oxygen (0.21 atm); heat treatment temperature 1100 K.

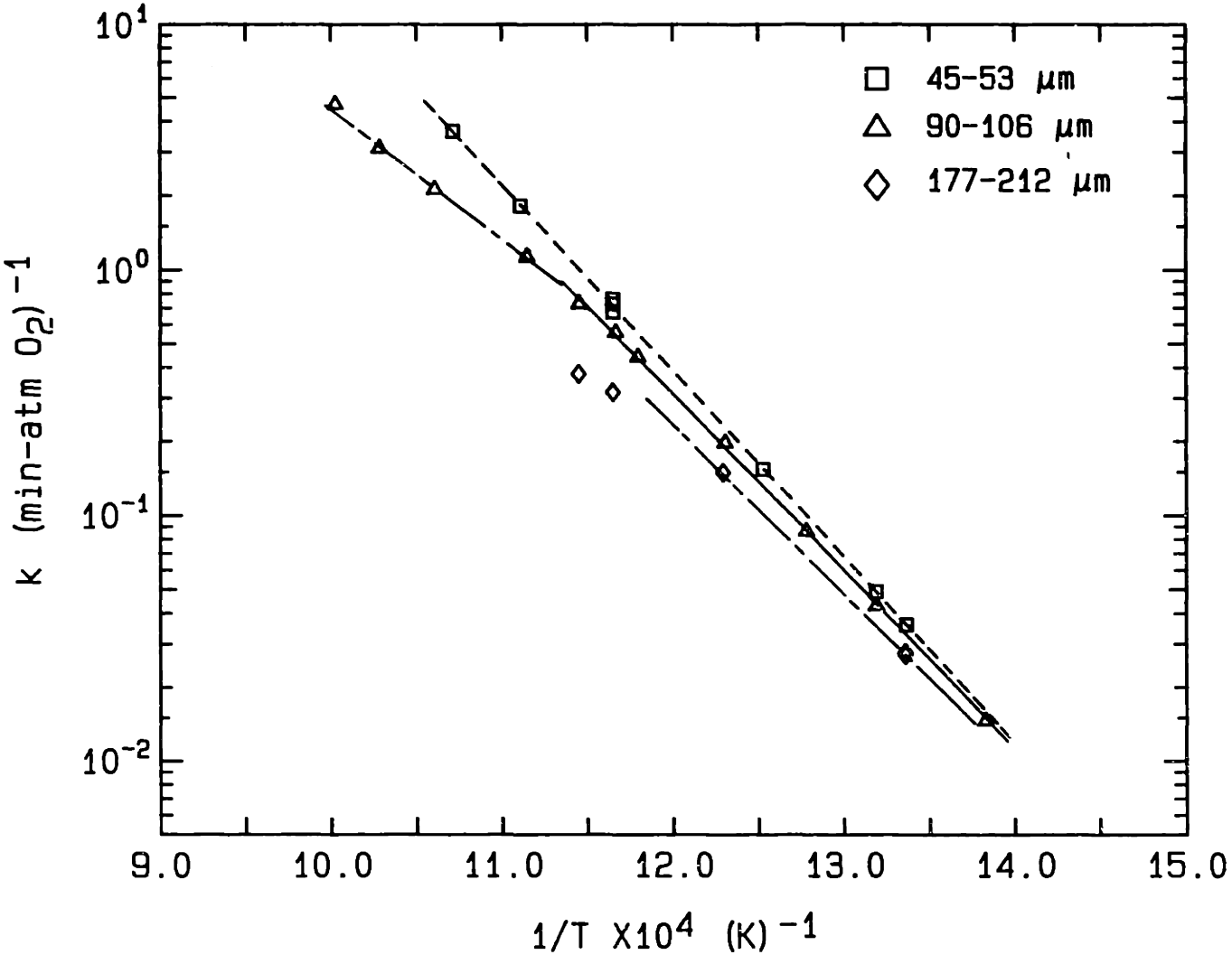

Figure 4.1-42 Arrhenius diagram for the C-O (0 wt% Ca) char at 60% conversion for three particle sizes; oxygen (0.21 atm); heat treatment temperature 1100 K.

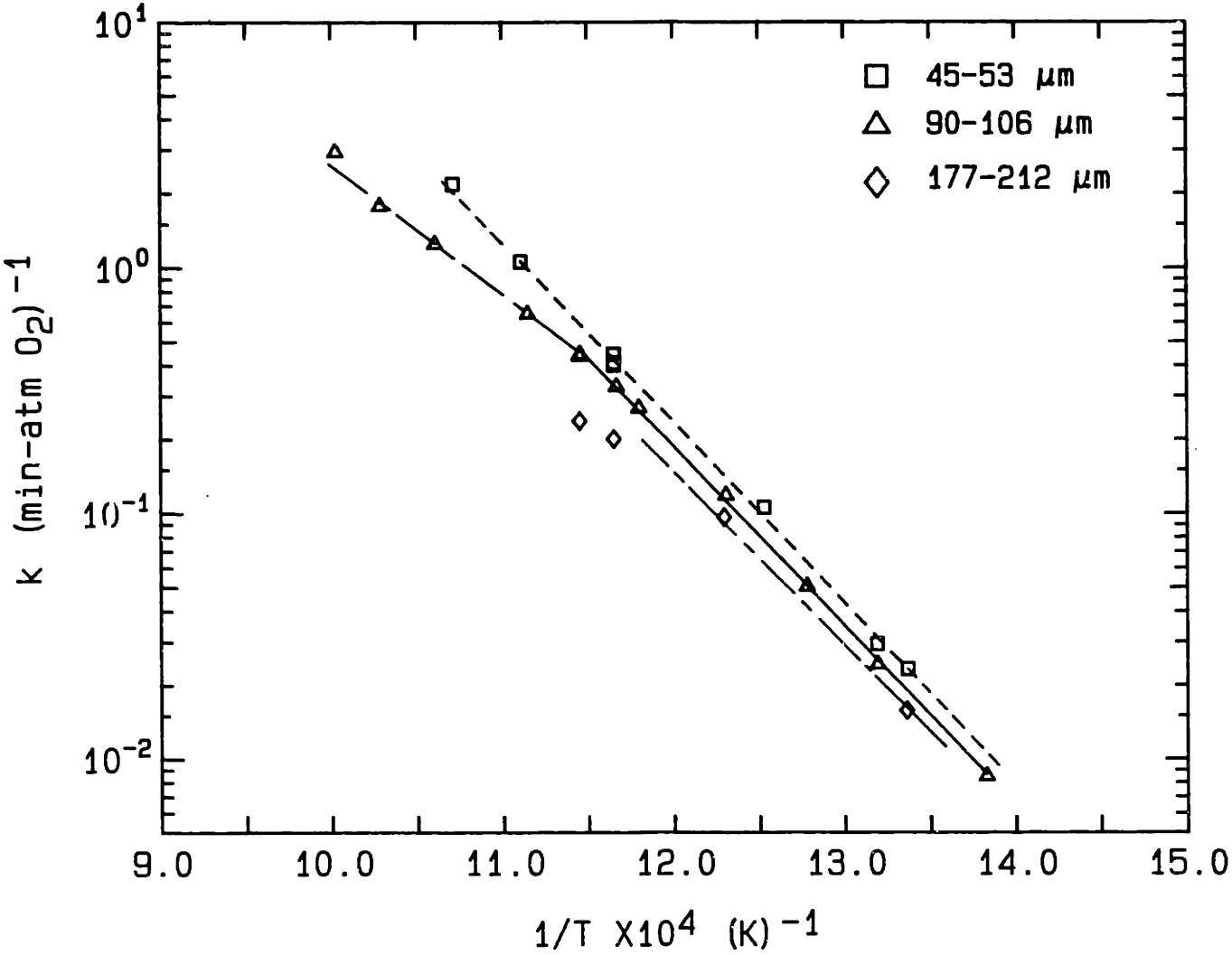

Figure 4.1-43 Arrhenius diagram for the C-O (0 wt% Ca) char at 80% conversion for three particle sizes; oxygen (0.21 atm); heat treatment temperature 1100 K.

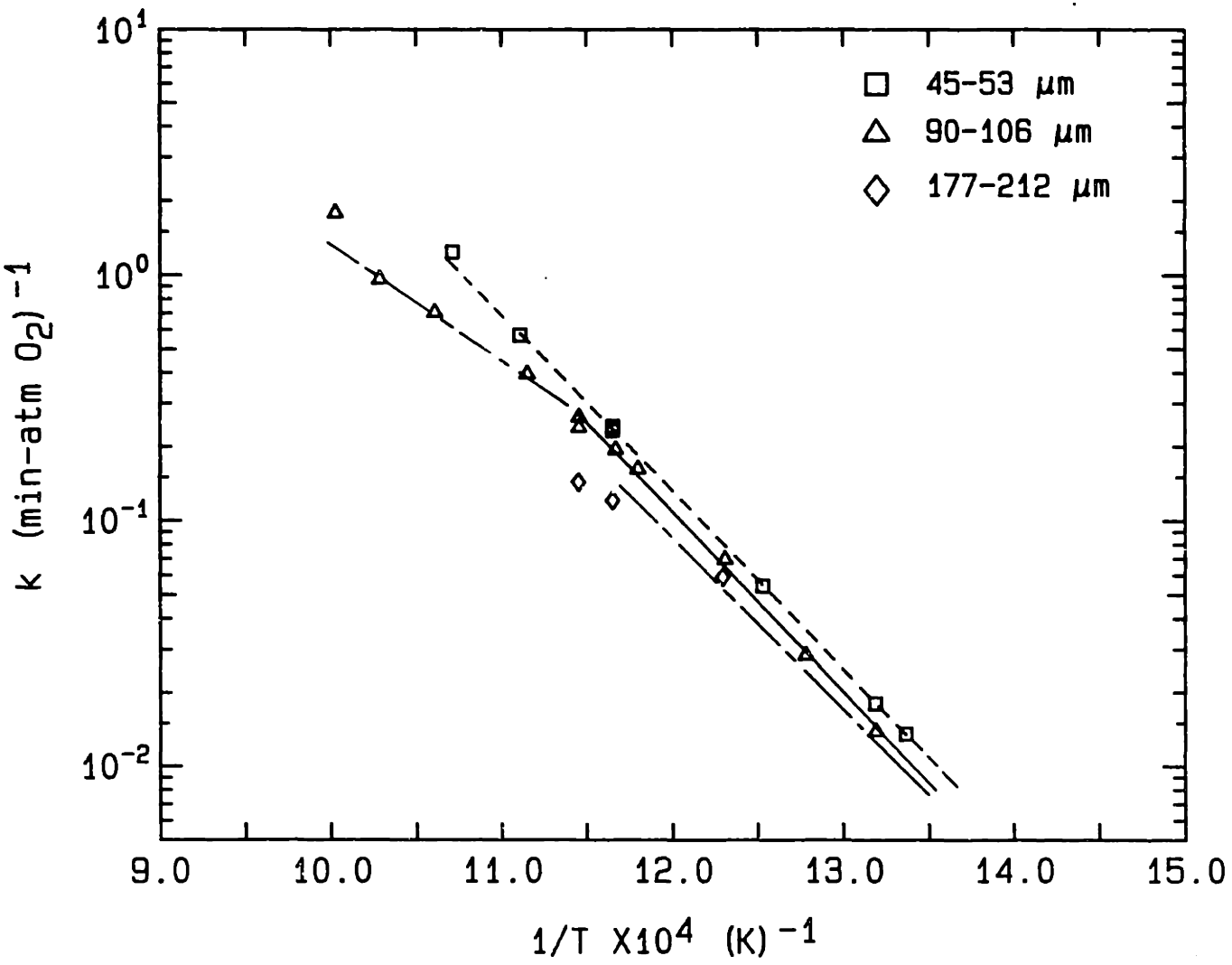

Figure 4.1-44 Arrhenius diagram for the C-O (0 wt% Ca) char at 90% conversion for three particle sizes; oxygen (0.21 atm); heat treatment temperature 1100 K.

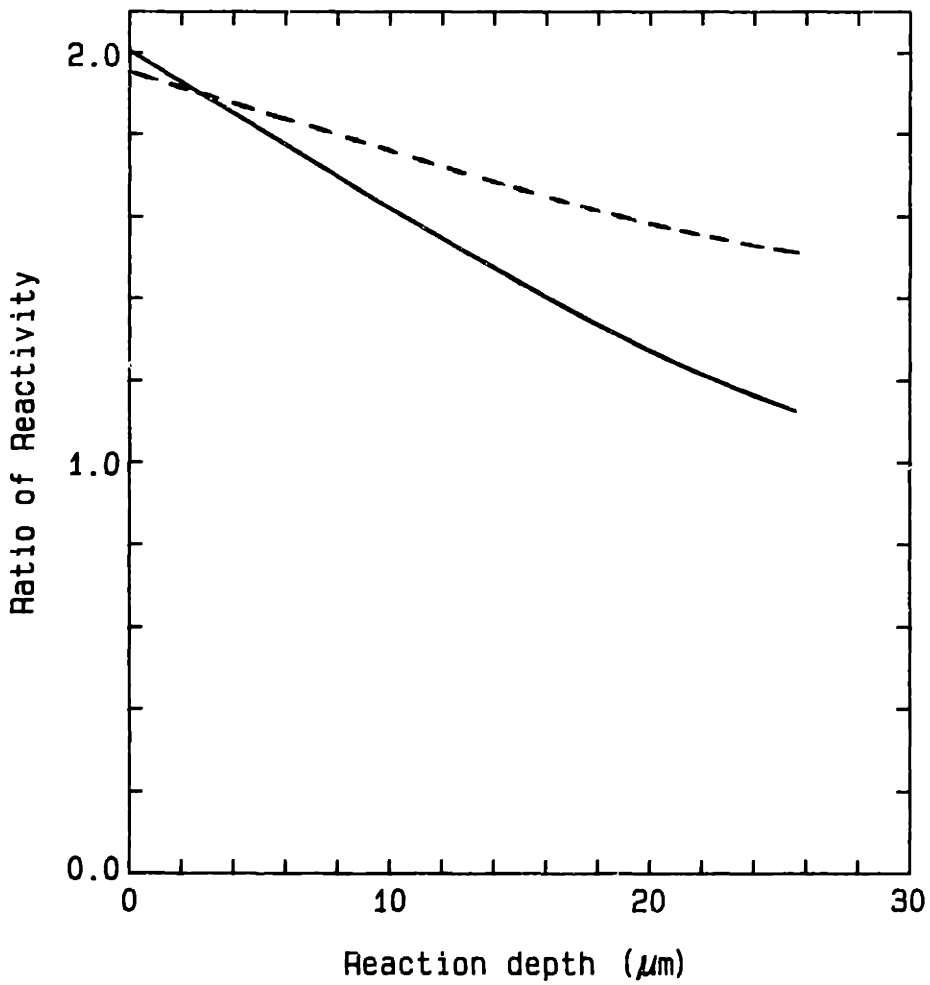

Figure 4.1-45 Relative reactivity of three different particle sizes as a function of the reaction depth from the particle surface;
(——) - 50 μm/100 μm;
(----) - 100 μm/195 μm.

suggests that reaction takes place primarily in an outside spherical volume, the thickness of which is about 20 μm.

Activation energies for the 45-53 μm size particles are presented in Table 4.1-5. The activation energies are less than 5% higher for the smaller particle.

Reaction rates at 860 K versus conversion and versus normalized time for the different particle sizes are plotted in Figures 4.1-46 to 4.1-47. The rate versus conversion data are a function of the particle size; however, normalization of the rate data with respect to the maximum rate for each curve would tend to obscure the differences.

No particle size effect was observed with the C-3.6 char. Reaction rates for the 45-53 μm size particles are presented in Arrhenius form at conversions of 20-90% in Figures 4.1-48 to 4.1-51. Rate versus time data at 660 K are presented in Figure 4.1-52. The data of the larger particle are shifted slightly to the right because a slightly longer induction time is observed with the larger particle at the beginning of the run. However, the rate is the same for both particle sizes when compared at identical conversions.

Spherocarb, crushed to a smaller size, did not react at a different rate from the orginal particle. This was not completely unexpected since spherocarb is activated during manufacture and therefore the original particle is already extremely porous.

Table 4.1-5. Activation Energy and Pre-Exponential Factors for the Carbon-Oxygen Reaction; heat treatment temperature 1100 K.

45-53 μm particle size

Conversion (%)	Pre-Exponential Factor (cc/gmole-sec)	Activation Energy (cal/mole)
10	7.53×10^{11}	34,700
20	2.29×10^{11}	32,900
40	1.41×10^{12}	35,800
60	1.51×10^{12}	36,300
80	5.11×10^{11}	35,300
90	1.93×10^{11}	34,700

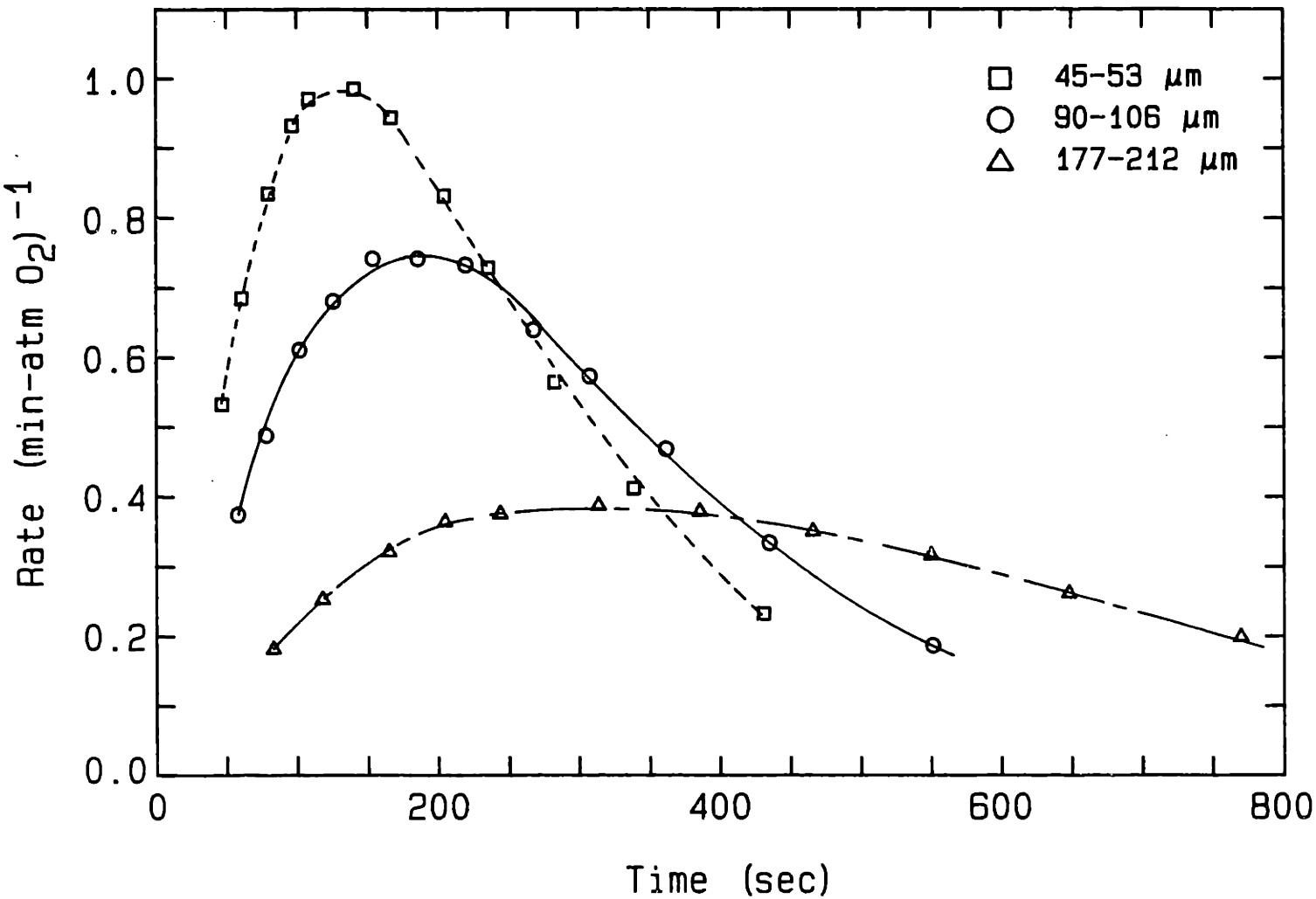

Figure 4.1-46 Effect of particle size on the reaction rate versus normalized time data of the C-O (0 wt% Ca) char, 0.21 atm oxygen; 860 K; heat treatment temperature 1100 K.

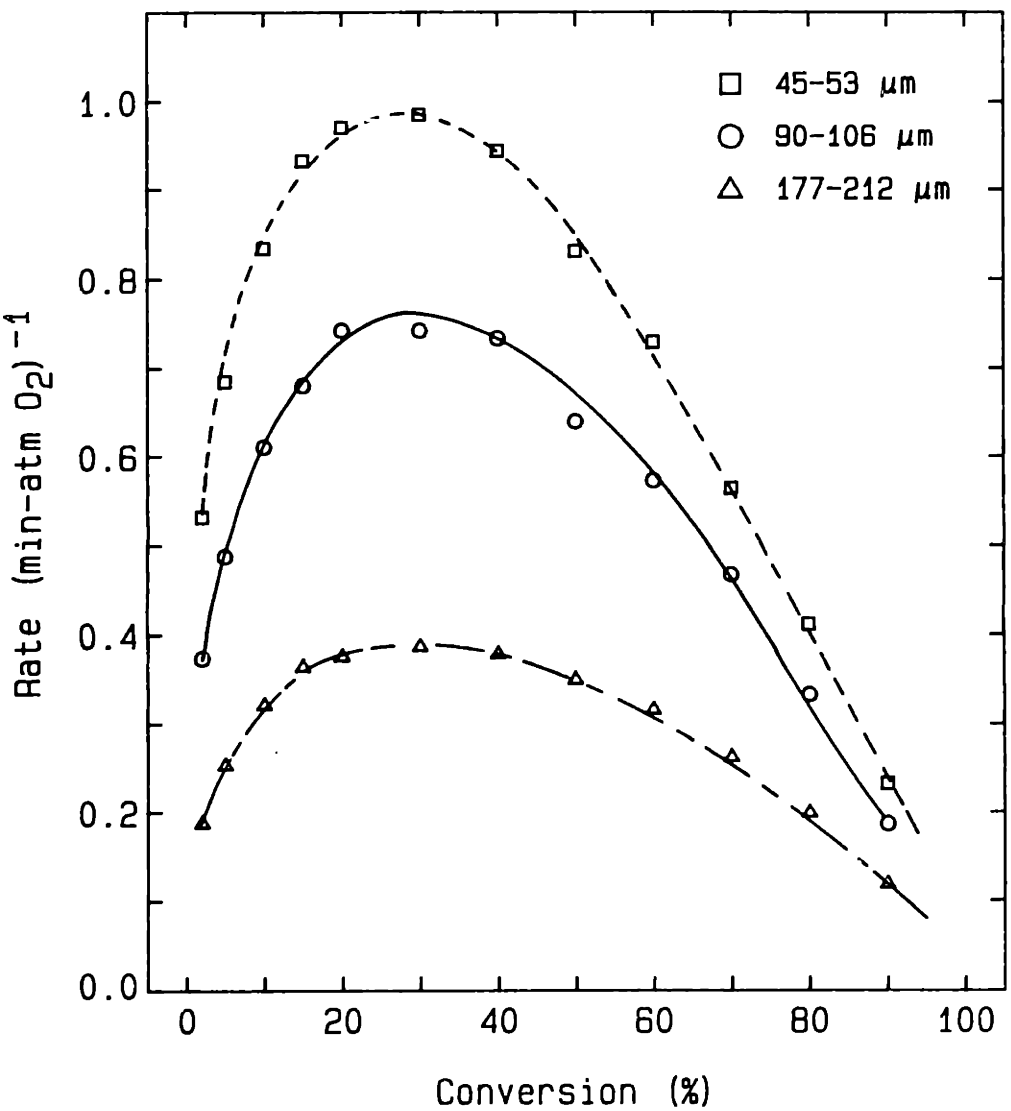

Figure 4.1-47 Effect of particle size on the rate versus conversion data of the C-O char; 0.21 atm oxygen; 860 K; heat treatment temperature 1100 K.

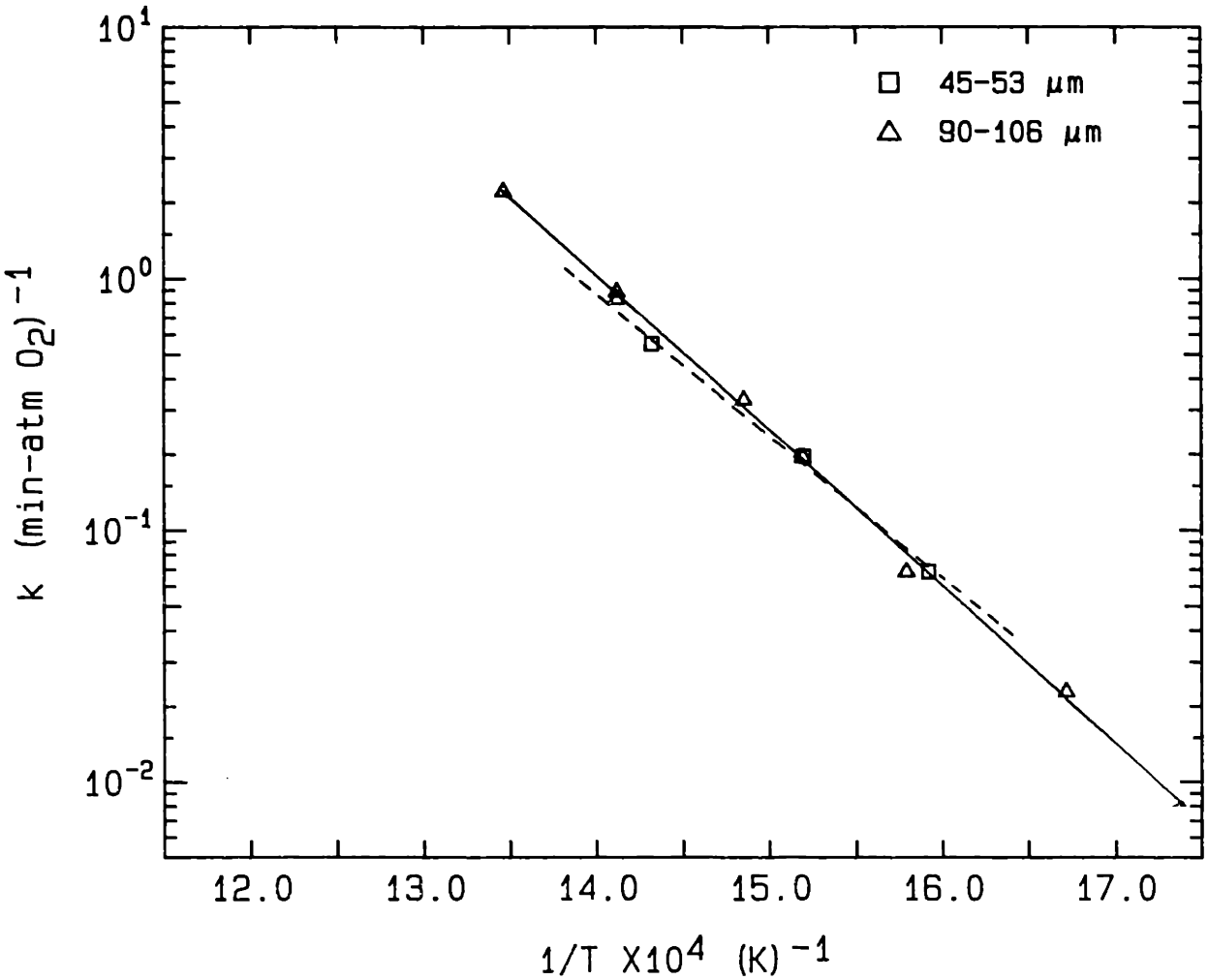

Figure 4.1-48 Arrhenius diagram for the C-3.6 (3.6 wt% Ca) char, two particle sizes at 20% conversion; 0.21 atm oxygen; heat treatment temperature 1100 K.

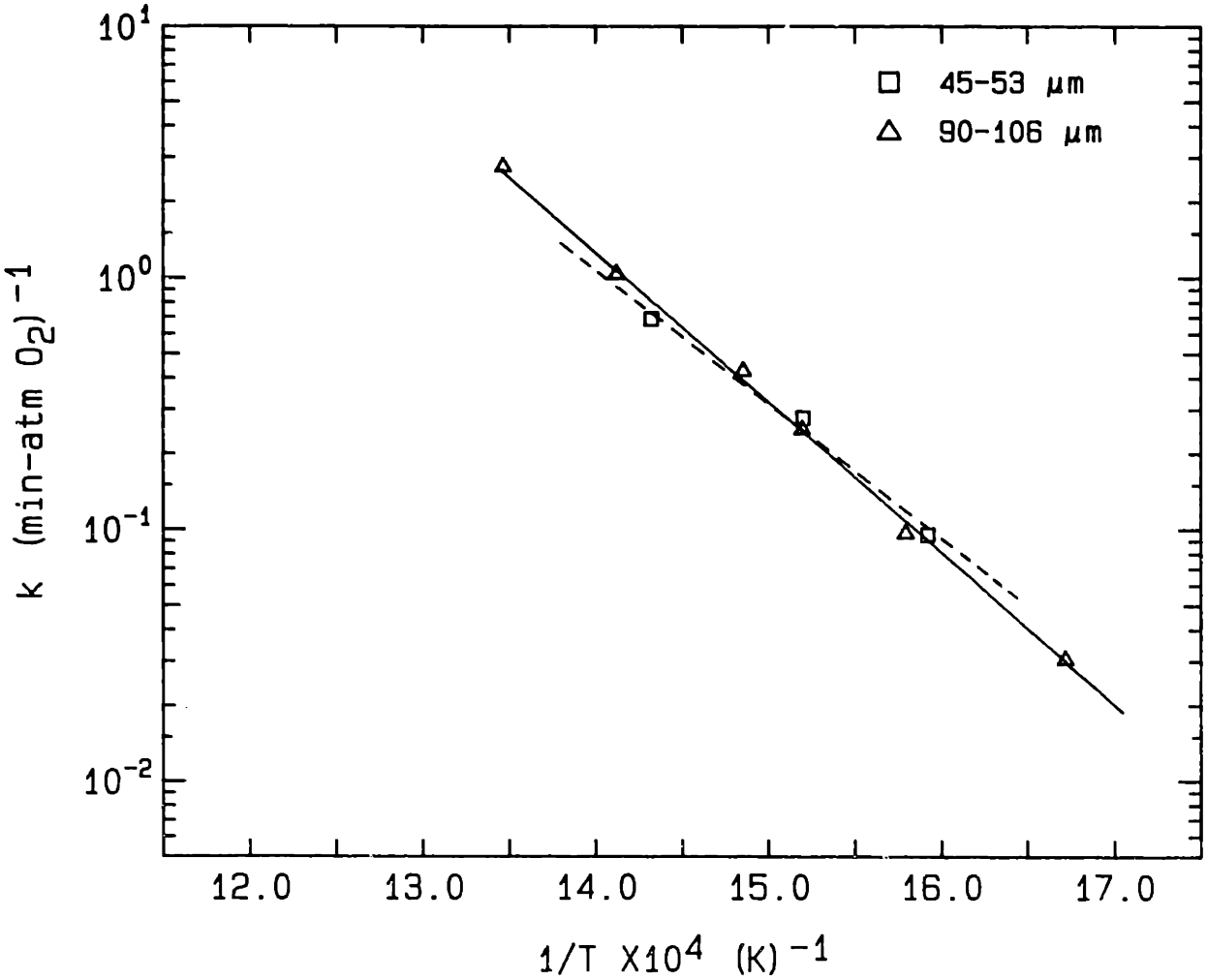

Figure 4.1-49 Arrhenius diagram for the C-3.6 (3.6 wt% Ca) char, two particle sizes at 40% conversion; 0.21 atm oxygen; heat treatment temperature 1100 K.

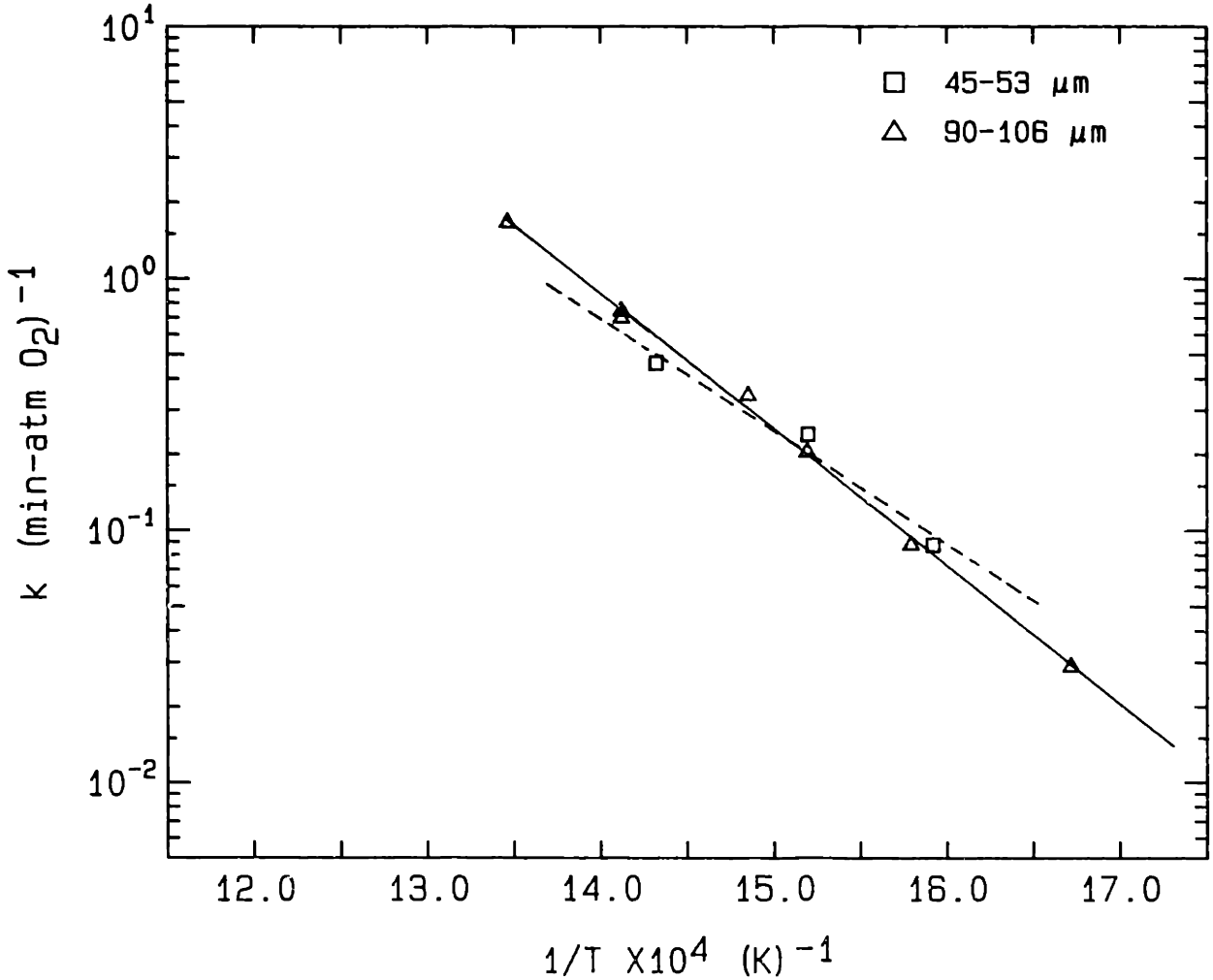

Figure 4.1-50 Arrhenius diagram for the C-3.6 (3.6 wt% Ca) char, two particle sizes at 60% conversion; 0.21 atm oxygen; heat treatment temperature 1100 K.

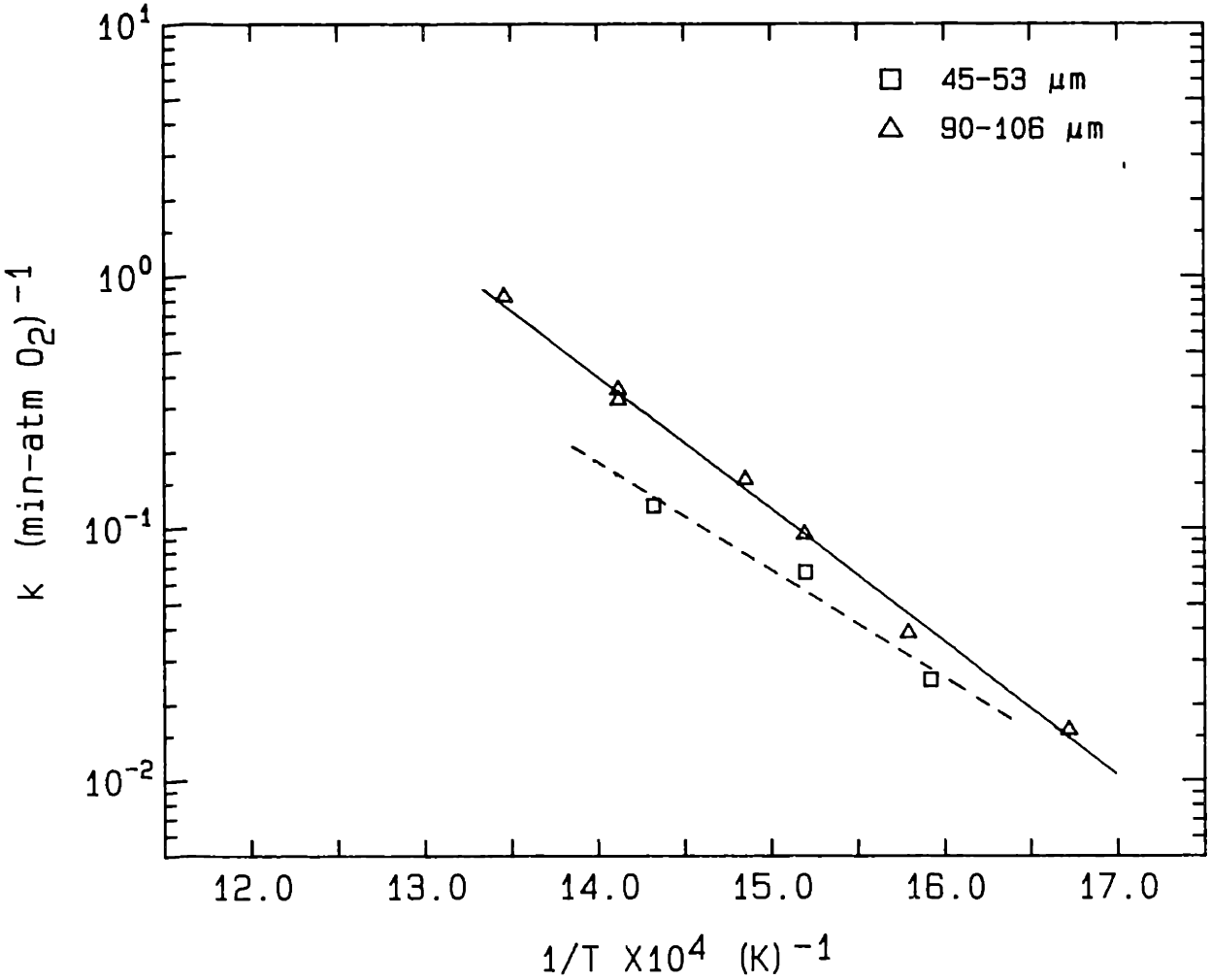

Figure 4.1-51 Arrhenius diagram for the C-3.6 (3.6 wt% Ca) char, two particle sizes at 90% conversion; 0.21 atm oxygen; heat treatment temperature 1100 K.

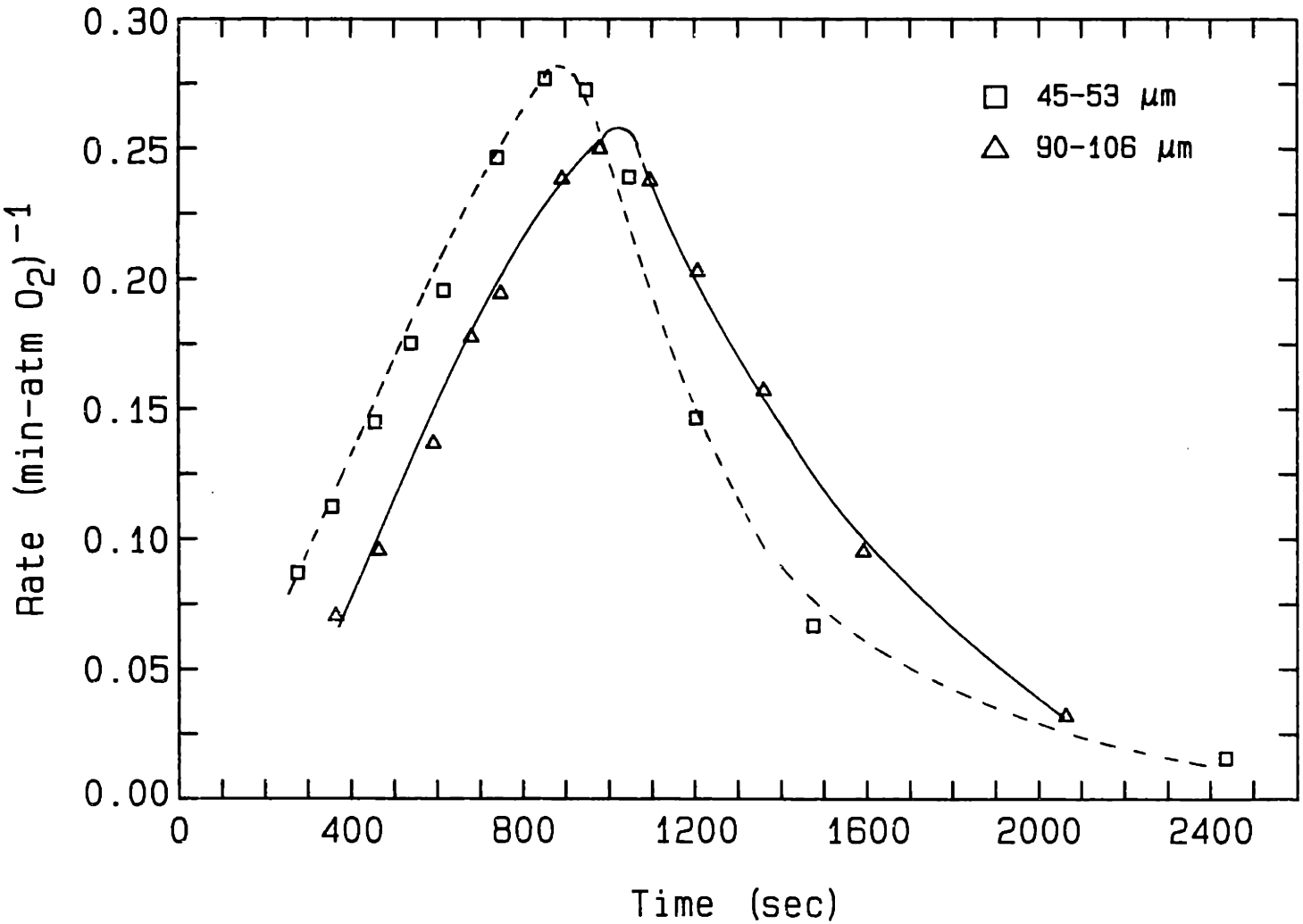

Figure 4.1-52 Effect of particle size on the reaction rate versus normalized time data of the C-3.6 (3.6 wt% Ca) char; 0.21 atm oxygen; 660 K; heat treatment temperature 1100 K.

4.2 Carbon-Carbon Dioxide Reaction

All experiments were conducted in pure CO_2 at a nominal pressure of 1 atm. The rate constant reported in this section is defined as:

$$k = \frac{r}{m_o P_{CO_2}} \qquad (\text{min-atm } CO_2)^{-1} \qquad (4.2.1)$$

where r is the measured rate of weight loss (mg/min) at 1 atm CO_2 pressure (P_{CO_2}) and m_o is the initial sample weight (mg). In the CO_2 experiments, the heat treatment procedure prior to a run was different from that used in the oxidation runs. Samples were heated (at 25 C/min) only to the reaction temperature. The samples were kept at this temperature for about 20 minutes before the reaction was started to allow the apparent sample weight (on the 100 µg TGA range) to equilibrate. The run was started by switching from an inert gas (nitrogen) to carbon dioxide. In comparison to the oxygen data, no induction period or weight gain at the start of a run was observed. The reaction rate went immediately to or almost immediately to the maximum rate of weight loss.

4.2.1 Reaction Rate of the C-O and C-3.6 Chars

Arrhenius diagrams of log k versus 1/T for the C-O and C-3.6 chars are presented in Figures 4.2-1 to 4.2-6. The C-O char data lie on a straight line that spans almost 1 1/2 orders of magnitude. The reaction rate at the maximum operating temperature of the TGA is well below the rate at which a change in slope of the Arrhenius diagram is observed in the oxygen

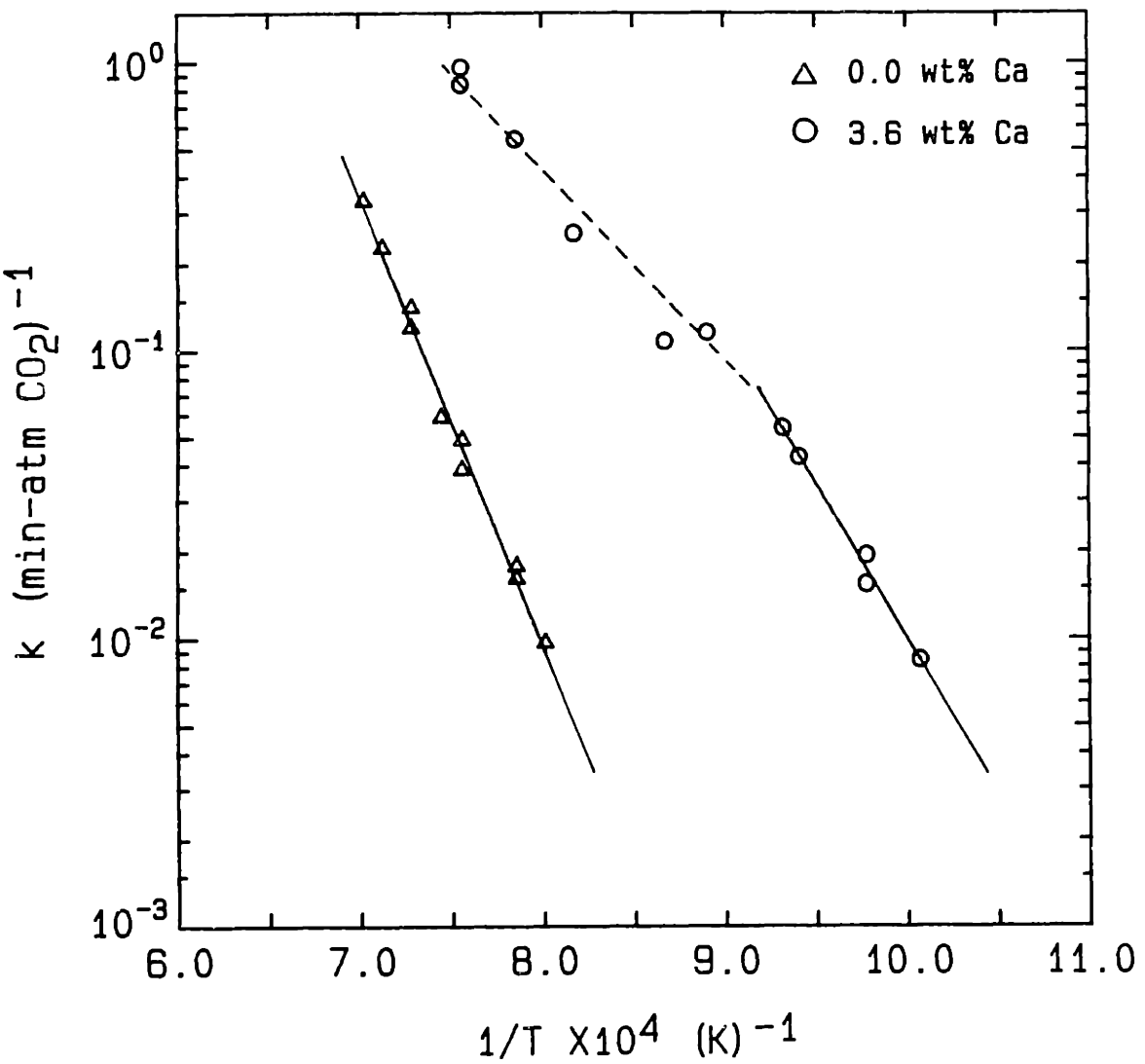

Figure 4.2-1 Arrhenius diagram for the C-O and C-3.6 chars at 10% conversion; carbon dioxide reaction (1.0 atm); 90-106 μm particles.

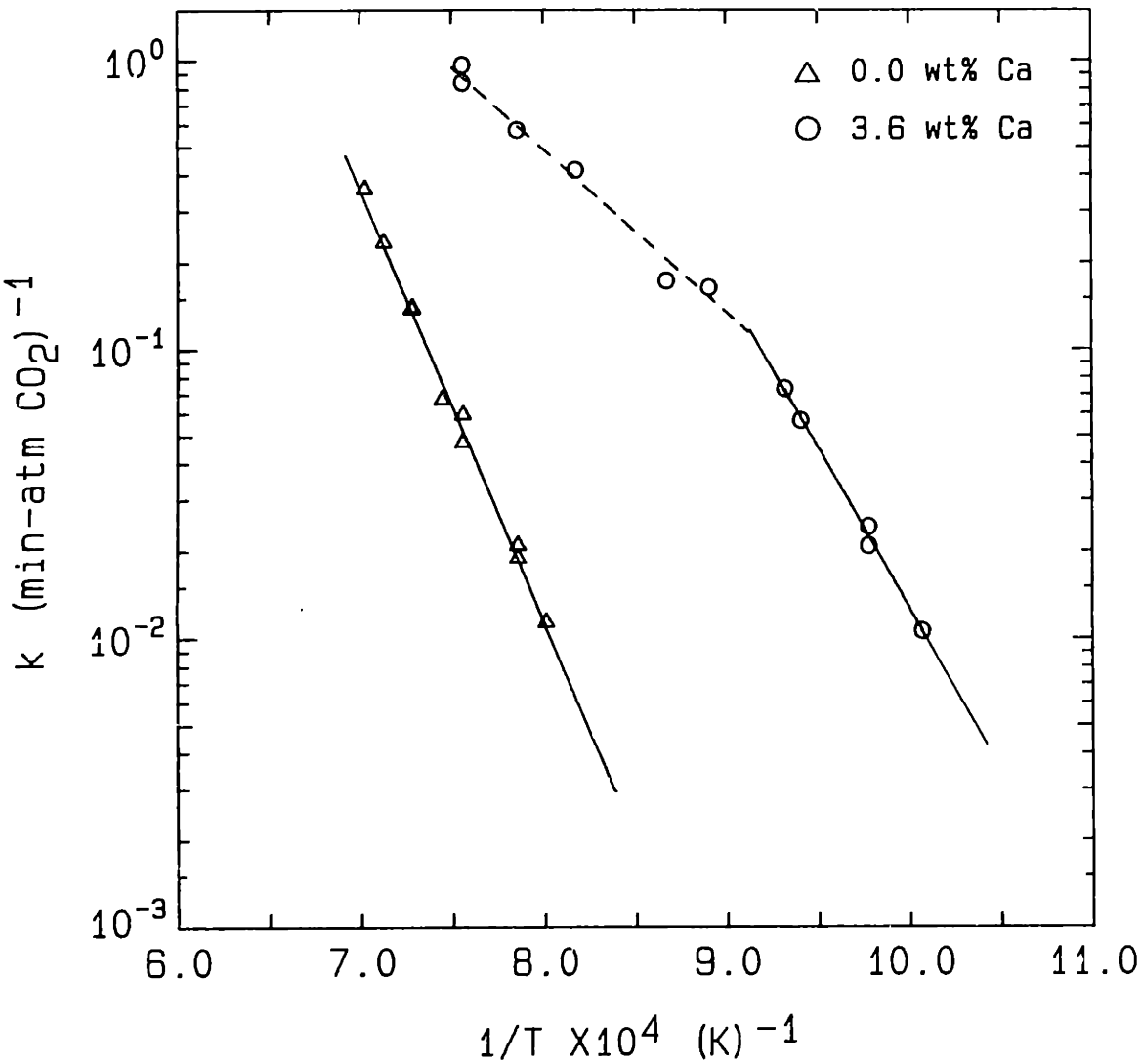

Figure 4.2-2 Arrhenius diagram for the C-O and C-3.6 chars at 20% conversion; carbon dioxide reaction (1.0 atm); 90-106 μm particles.

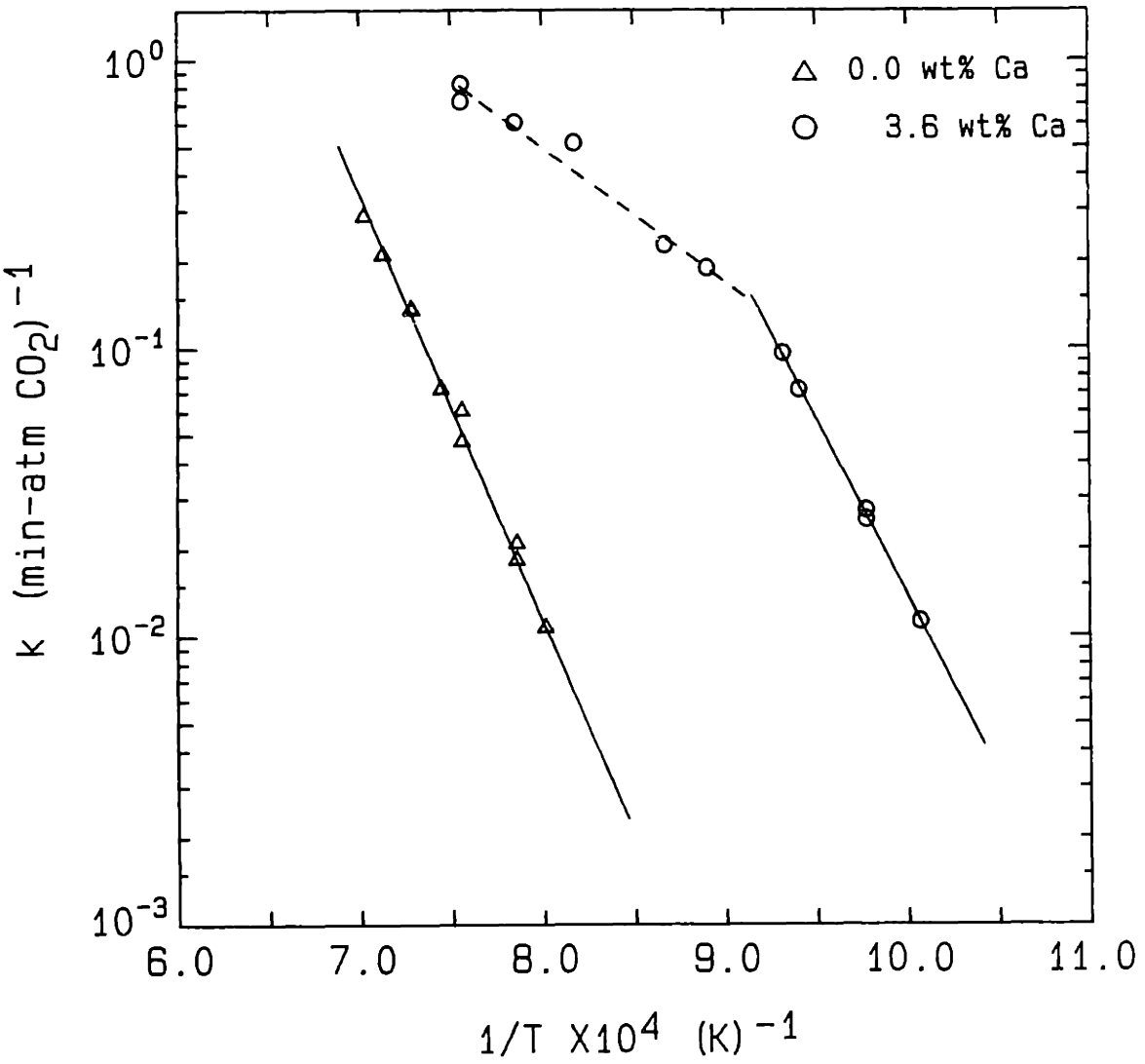

Figure 4.2-3 Arrhenius diagram for the C-O and C-3.6 chars at 40% conversion; carbon dioxide reaction (1.0 atm); 90-106 μm particles.

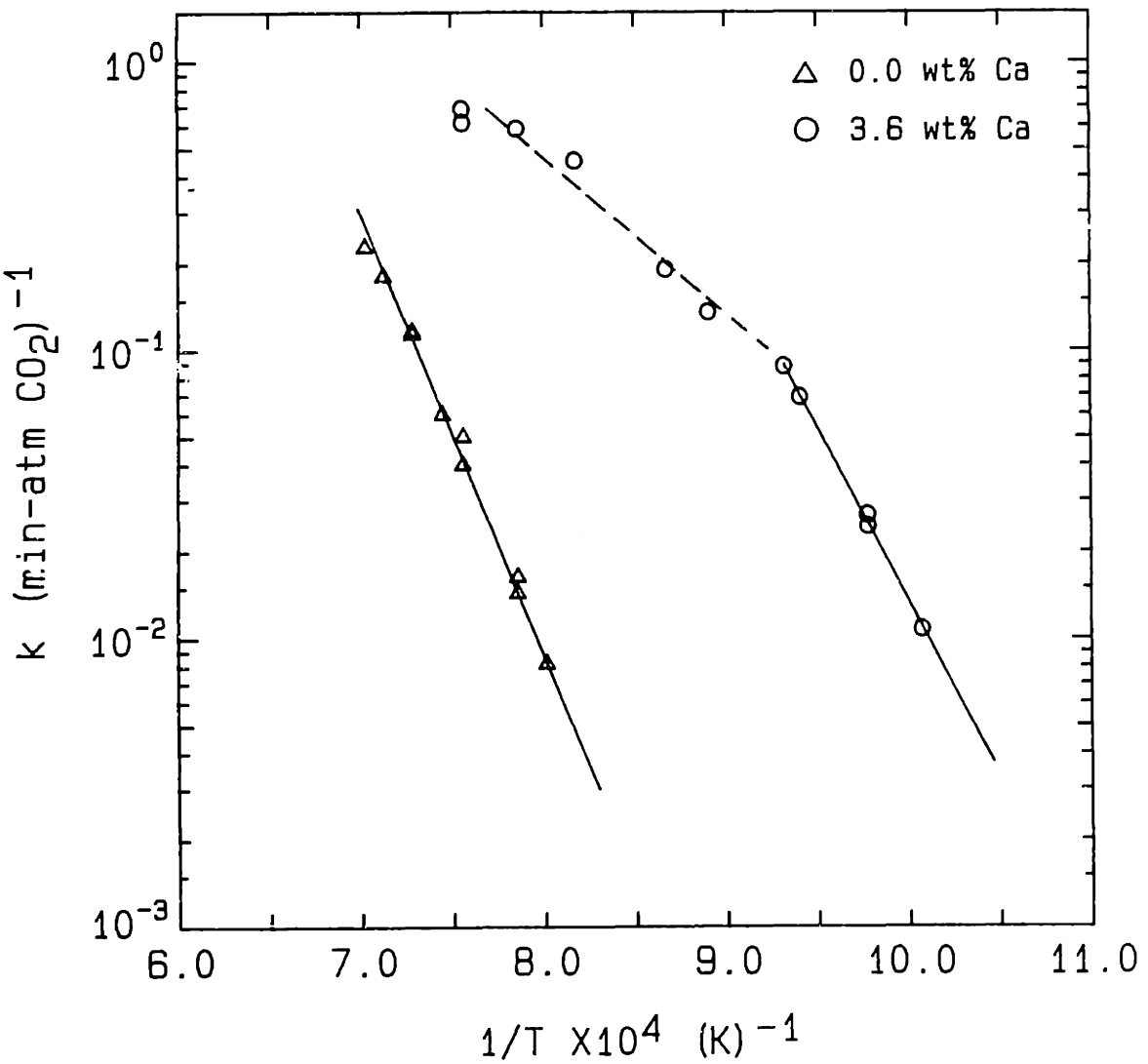

Figure 4.2-4 Arrhenius diagram for the C-O and C-3.6 chars at 60% conversion; carbon dioxide reaction (1.0 atm); 90-106 μm particles.

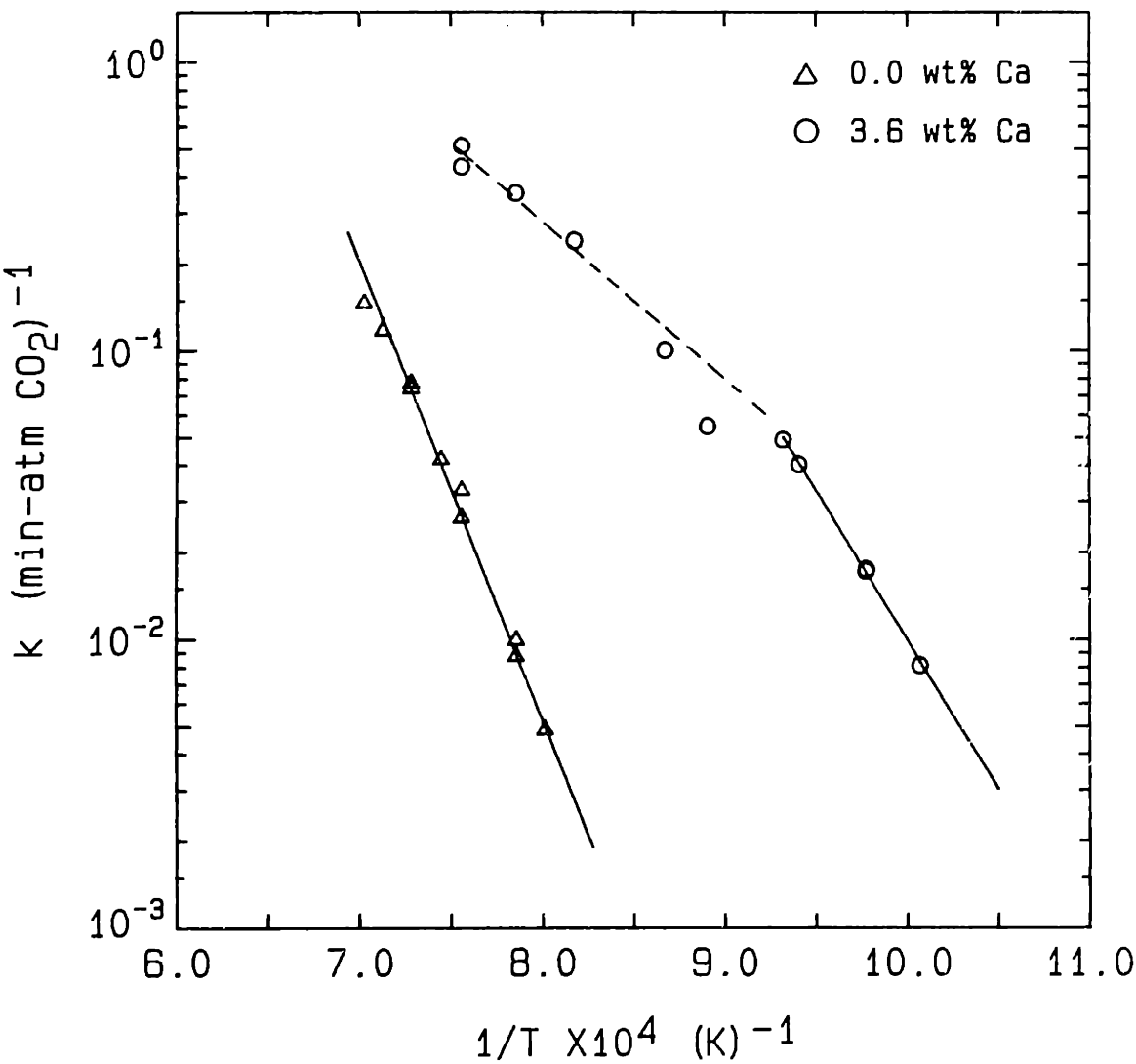

Figure 4.2-5 Arrhenius diagram for the C-O and C-3.6 chars at 80% conversion; carbon dioxide reaction (1.0 atm); 90-106 μm particles.

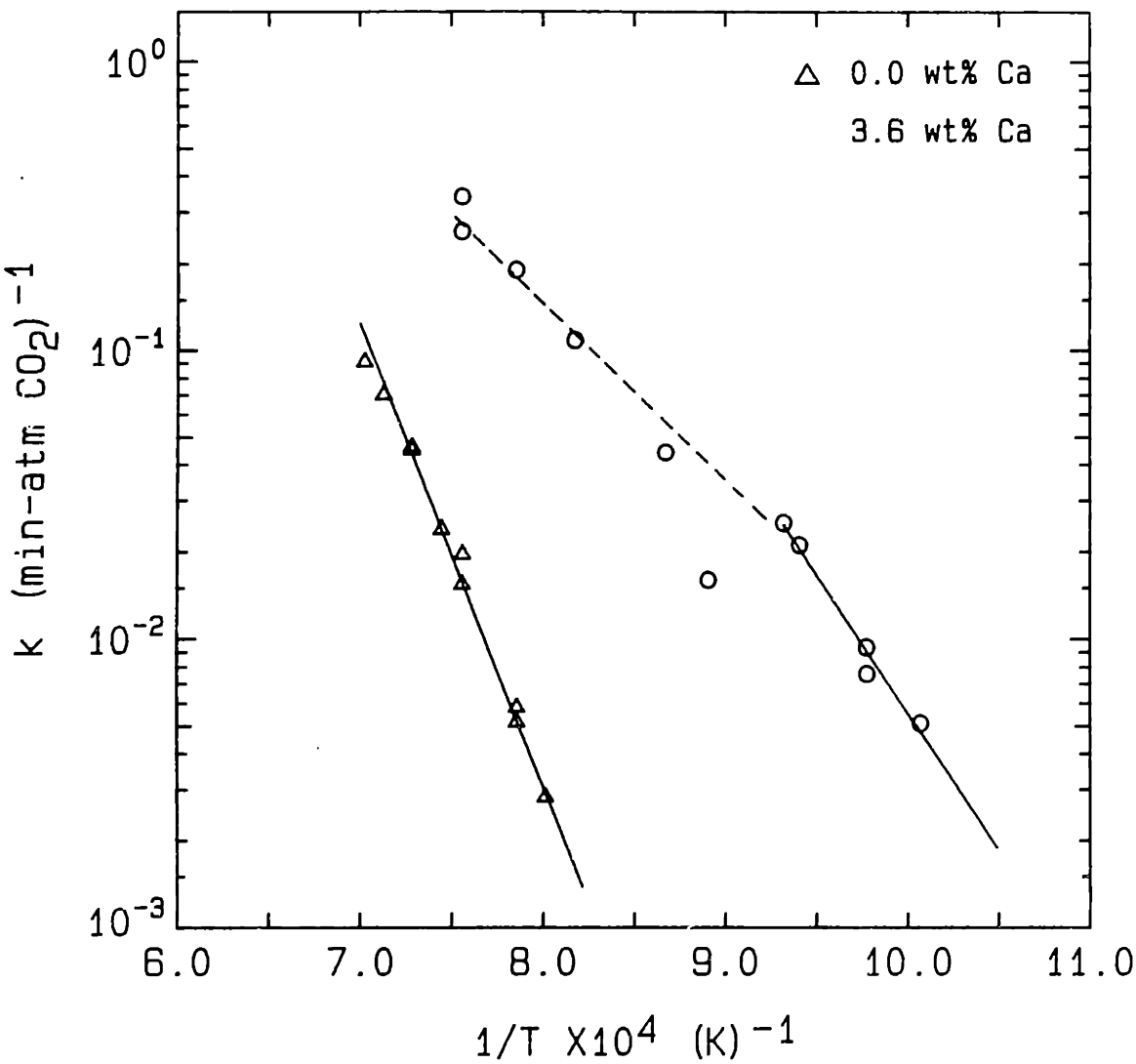

Figure 4.2-6 Arrhenius diagram for the C-O and C-3.6 chars at 90% conversion; carbon dioxide reaction (1.0 atm); 90-106 μm particles.

runs. Therefore, the change in slope in the Arrhenius diagram of the C-3.6 char is probably not due to the onset of intra-particle diffusion. Rather, the falloff in reactivity at temperatures above 1070 K could be the result of more rapid catalyst deactivation. As previously discussed in Section 4.1.6, heat treatment time causes a significant decrease in the reactivity of the catalyzed char only at temperatures above approximately 1060 K. The close agreement between these two temperatures indeed suggests that catalyst deactivation is responsible for the change in slope of the Arrhenius line.

At 1 atm. CO_2, calcium carbonate decomposes at approximately 1170 K. This temperature is well above the temperature at which the change in slope occurs on the Arrhenius diagram. No abrupt change in reactivity coincidental to this temperature is observed.

Activation energies and the pre-exponential factors calculated by a least squares regression are summarized in Table 4.2-1. The activation energies for the C-3.6 char are for the low temperature data. The line drawn through the upper points is only to indicate the trend of the data. The activation energy is approximately 20% lower for the C-3.6 char than for the C-O char. The activation energies show considerable variation with respect to conversion, particularly for the C-3.6 char.

Graphs of normalized rate versus time and versus conversion are presented in Figures 4.2-7 and 4.2-8 for the C-O char and in Figures 4.2-9 and 4.2-10 for the C-3.6 char. For the C-O char,

Table 4.2-1. Activation Energy and Pre-Exponential Factors for the Carbon Dioxide Reaction; 90-106 μm particles.

Conversion (%)	Pre-Exponential Factor (cc/gmole-sec)	Activation Energy (cal/mole)
C-O Char (0 wt% Ca)		
10	1.35×10^{14}	73,900
20	2.29×10^{13}	70,800
40	4.26×10^{13}	70,600
60	9.55×10^{13}	73,300
80	1.51×10^{14}	75,600
90	1.20×10^{14}	76,400
C-3.6 Char (3.6 wt% Ca)		
10	2.00×10^{12}	51,000
20	6.41×10^{12}	52,900
40	9.59×10^{13}	58,100
60	5.62×10^{13}	57,100
80	7.98×10^{11}	49,300
90	7.90×10^{10}	45,800

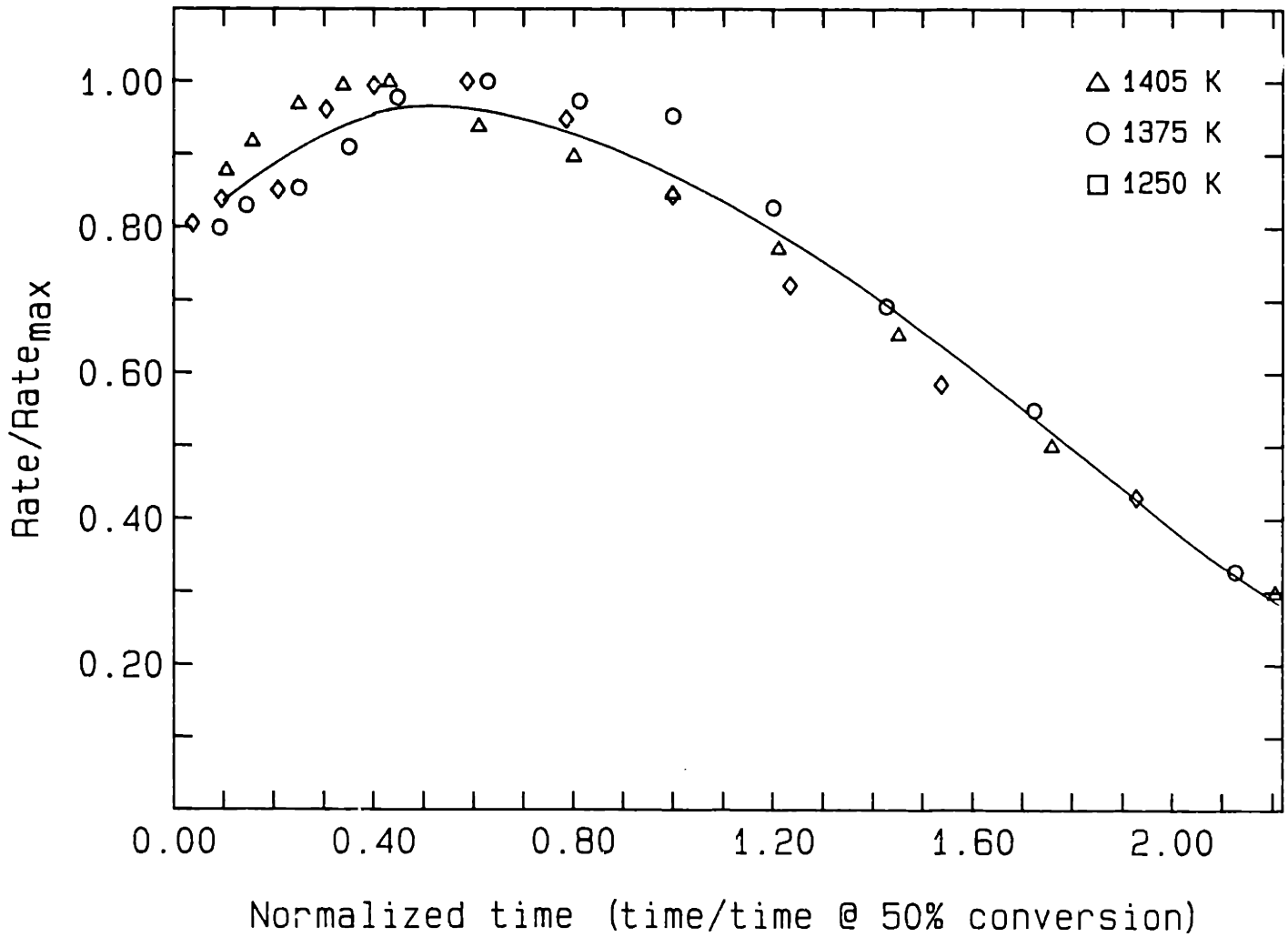

Figure 4.2-7 Reaction rate normalized by the maximum rate plotted against normalized time; C-O char - carbon dioxide reaction (1 atm); 90-106 μm particles.

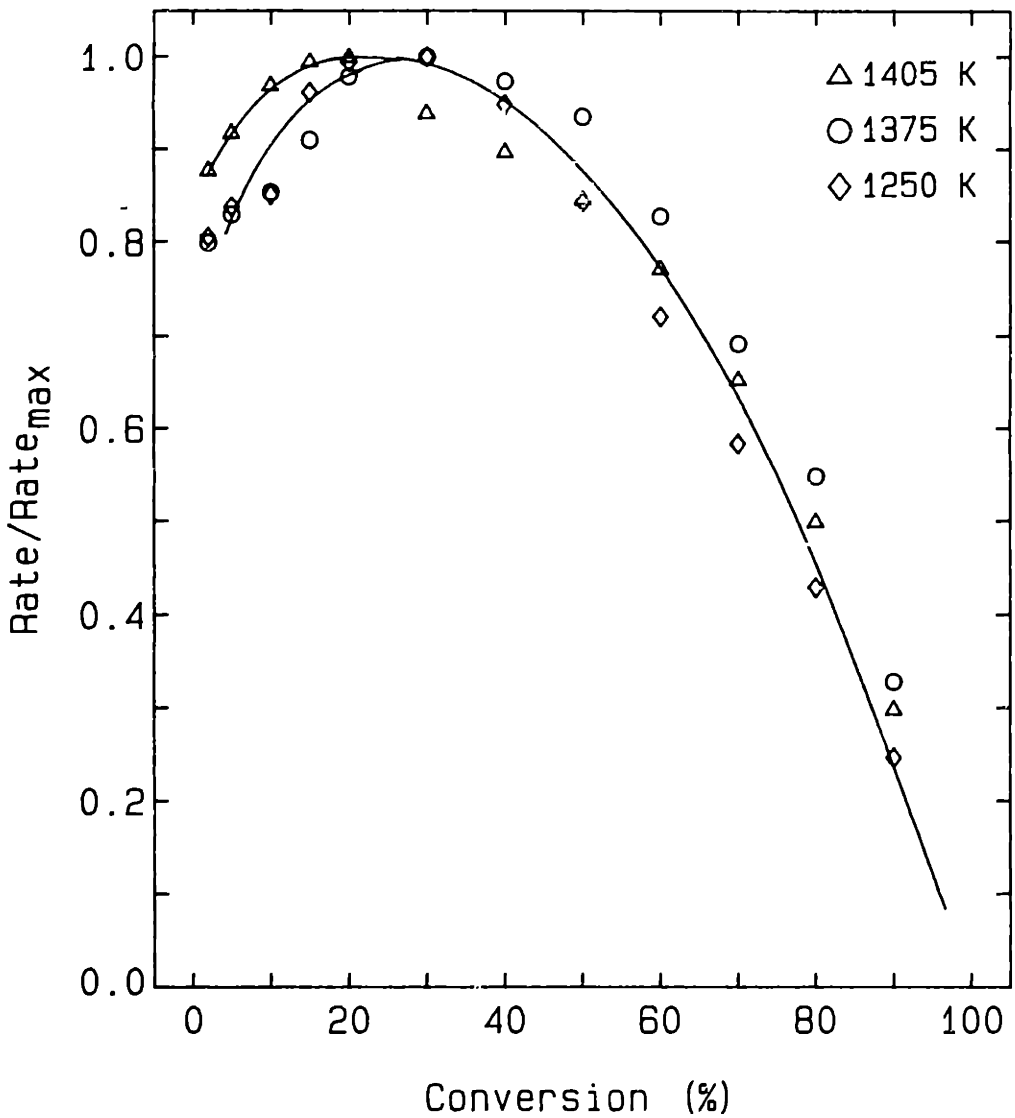

Figure 4.2-8 Reaction rate normalized by the maximum rate versus conversion. C-O char - carbon dioxide (1 atm) reaction; 90-106 μm particles.

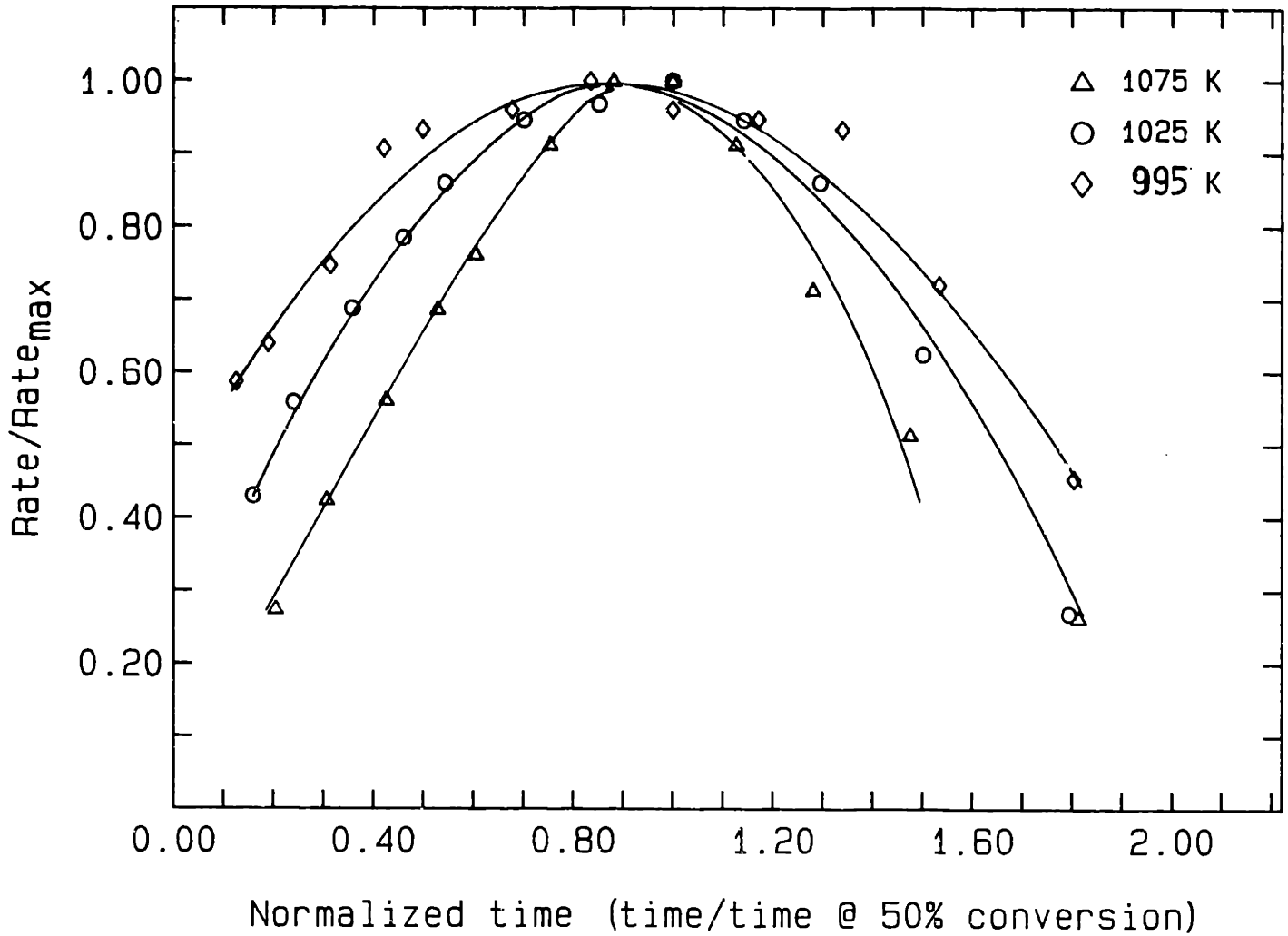

Figure 4.2-9 Reaction rate normalized by the maximum rate plotted against normalized time; C-3.6 (3.6 wt% Ca) char - carbon dioxide (1 atm) reaction; 90-106 μm particles.

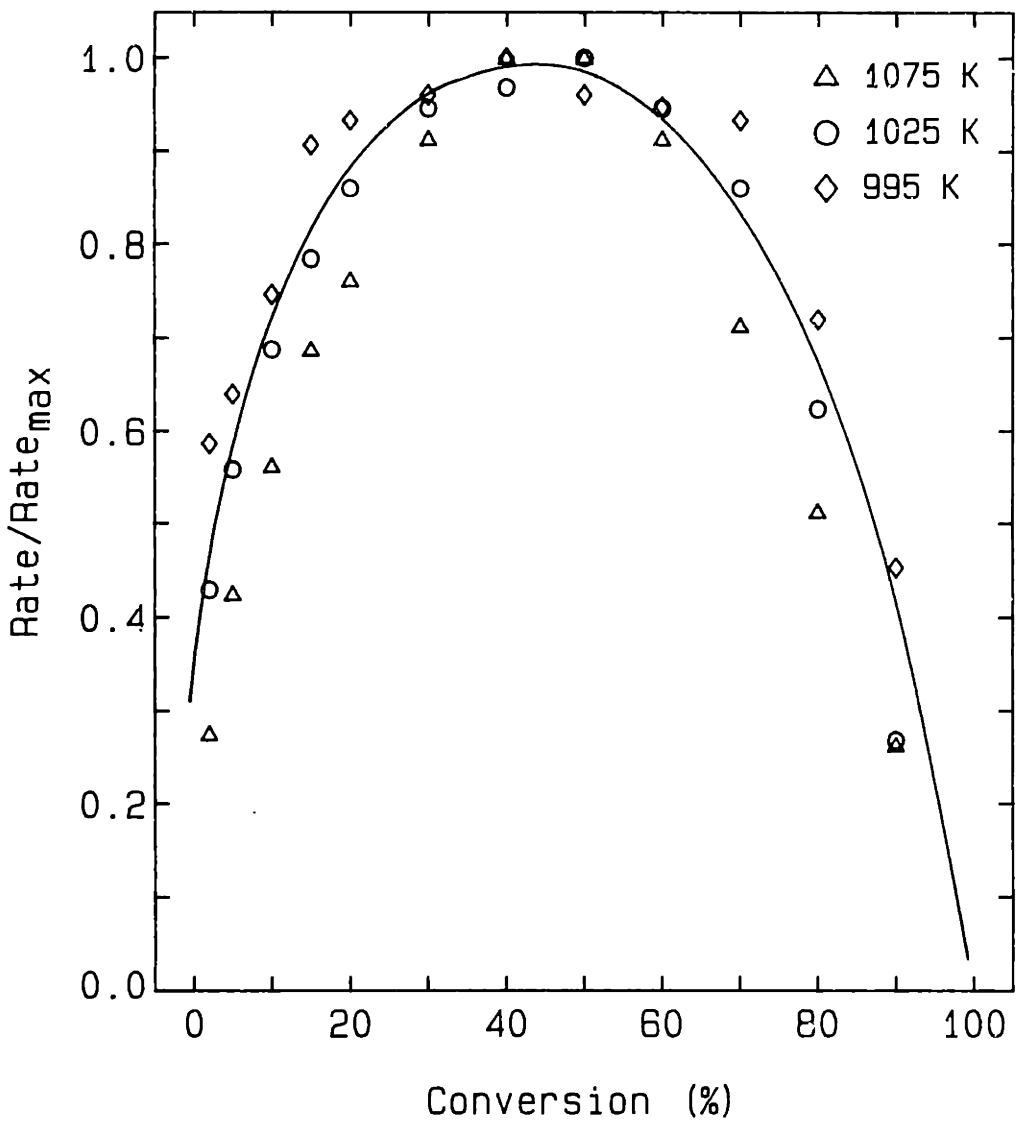

Figure 4.2-10 Reaction rate normalized by the maximum rate versus conversion; C-3.6 char - carbon dioxide (1.0 atm) reaction; 90-106 μm particles.

the data at different temperatures all coincide approximately onto one common curve. The initial rates are approximately 20% below the maximum rates, and the rate remains relatively constant between approximately 10 and 40% conversion. For the catalyzed char, the data at different reaction temperatures do not coincide as well onto a single curve. The data show a consistent shift in position with respect to increasing temperature. In comparison to the non-catalyzed char, there is a larger difference between the initial and maximum rates, and the maximum rate is reached at a later conversion. The reaction rate is constant between about 25 and 60% conversion. The rate versus conversion or time curves are different in detail from the curves obtained with oxygen. This is particularly true for the calcium added char. For the C-O char, the difference between the two sets of data occur principally at low conversion. However, the data must be compared with caution. The TGA data from the carbon-oxygen runs at conversions below approximately 5% are not precisely identical to the carbon gasification rate because of oxygen chemisorption on the char at the start of a run. No appreciable amounts of oxygen are apparently chemisorbed on the char during CO_2 gasification (Freund, 1984), so for this reaction the TGA data are equivalent to the gasification rate.

Reactivity measurements were also made with 177-212 μm particles and with Spherocarb. The data are presented in Figures 4.2-11 to 4.2-15 at conversions of 20-90%. The reactivity of Spherocarb is similar to that of the C-O char.

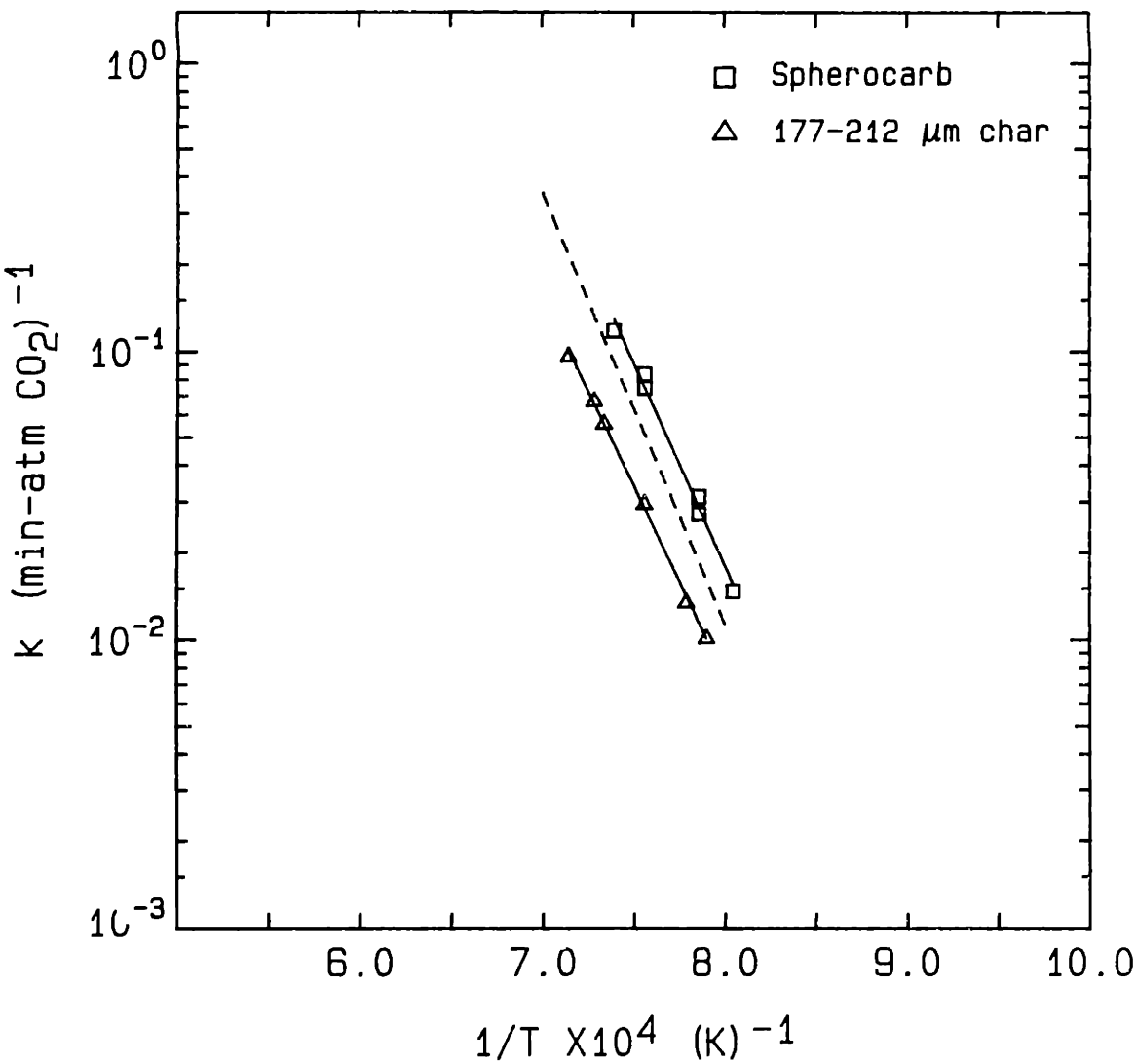

Figure 4.2-11 Arrhenius diagram for the reaction of the C-O char and spherocarb with carbon dioxide (1 atm) at 20% conversion.

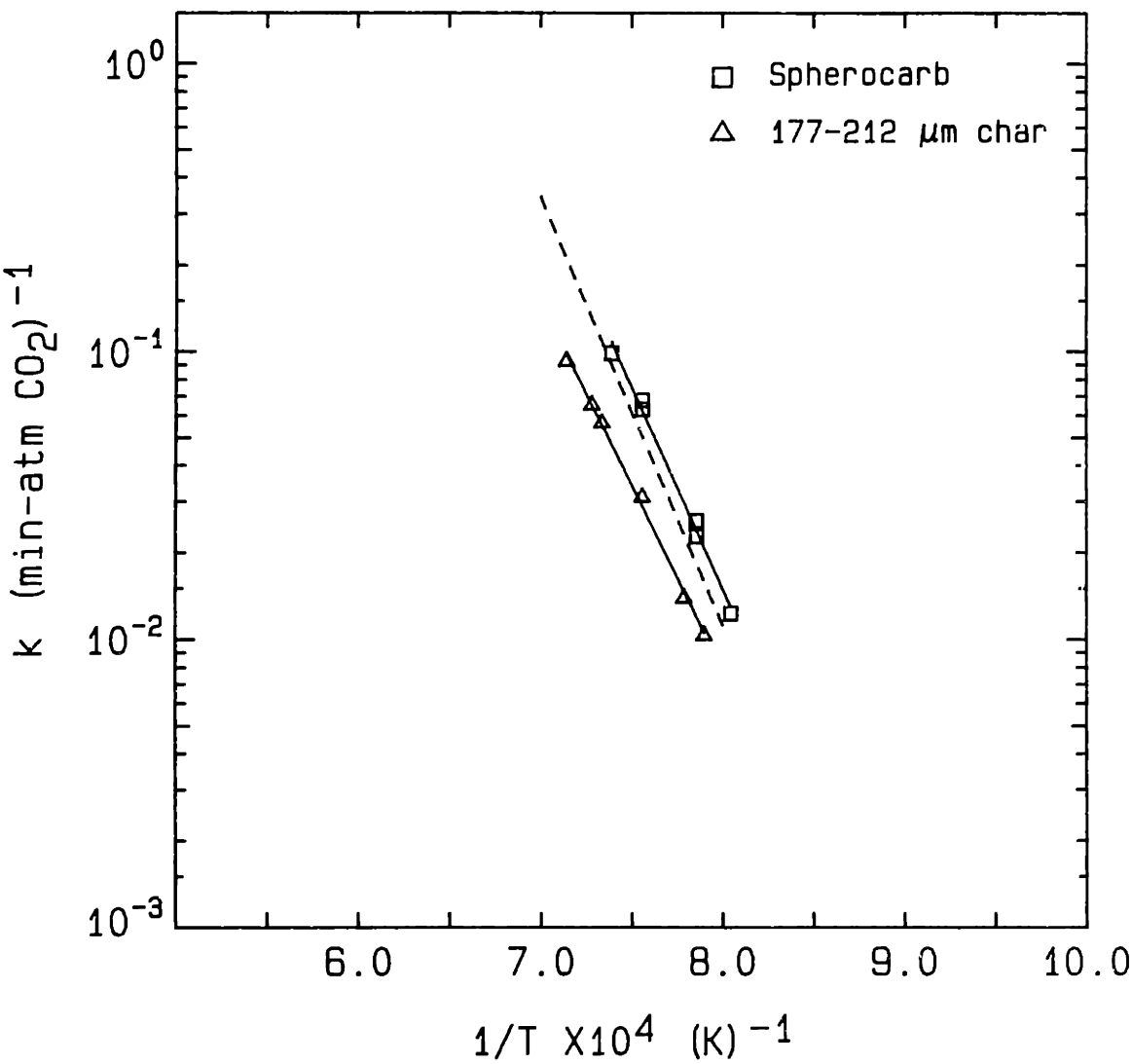

Figure 4.2-12 Arrhenius diagram for the reaction of the C-O char and spherocarb with carbon dioxide (1 atm) at 40% conversion.

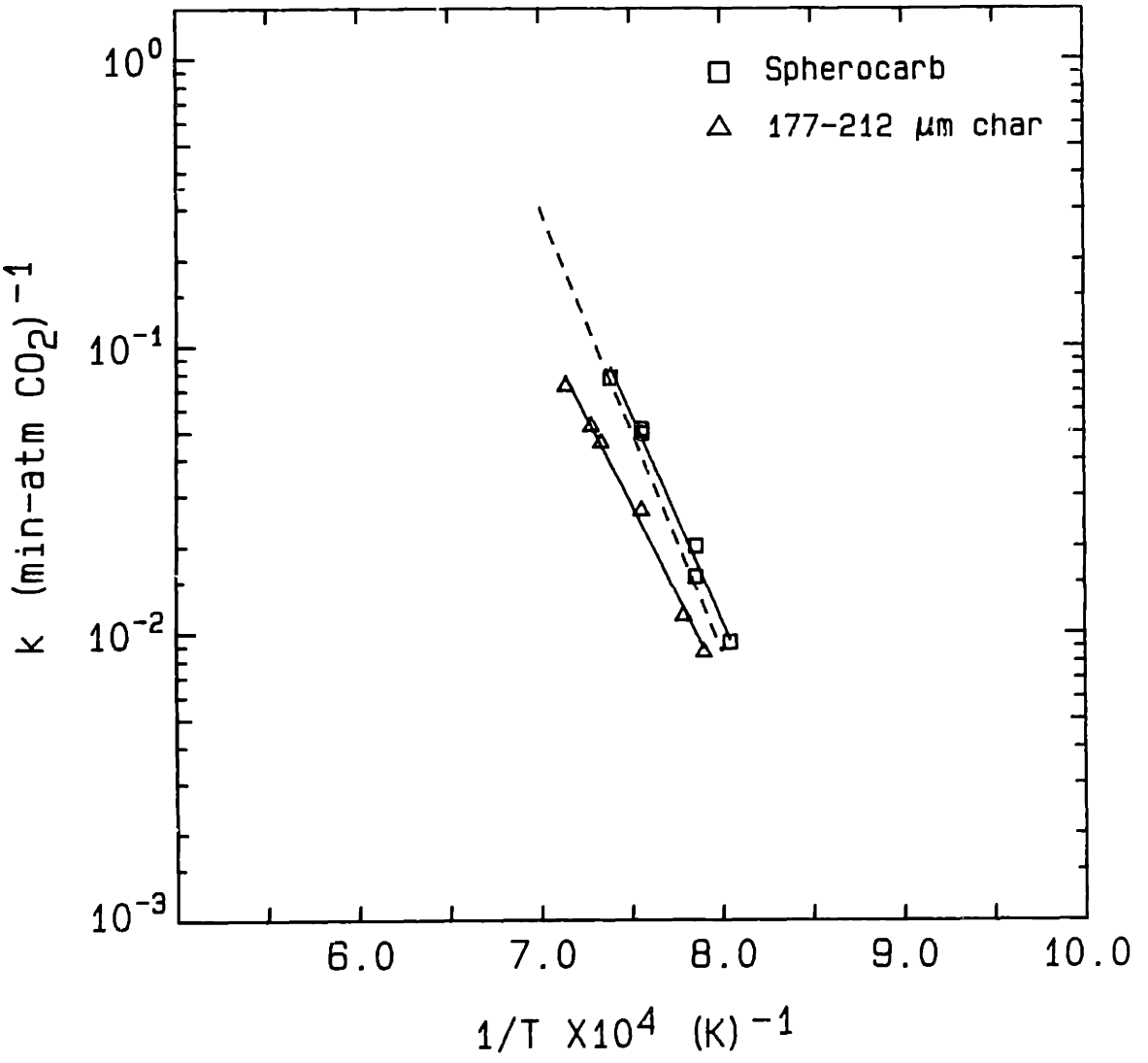

Figure 4.2-13 Arrhenius diagram for the reaction of the C-O char and spherocarb with carbon dioxide (1 atm) at 60% conversion.

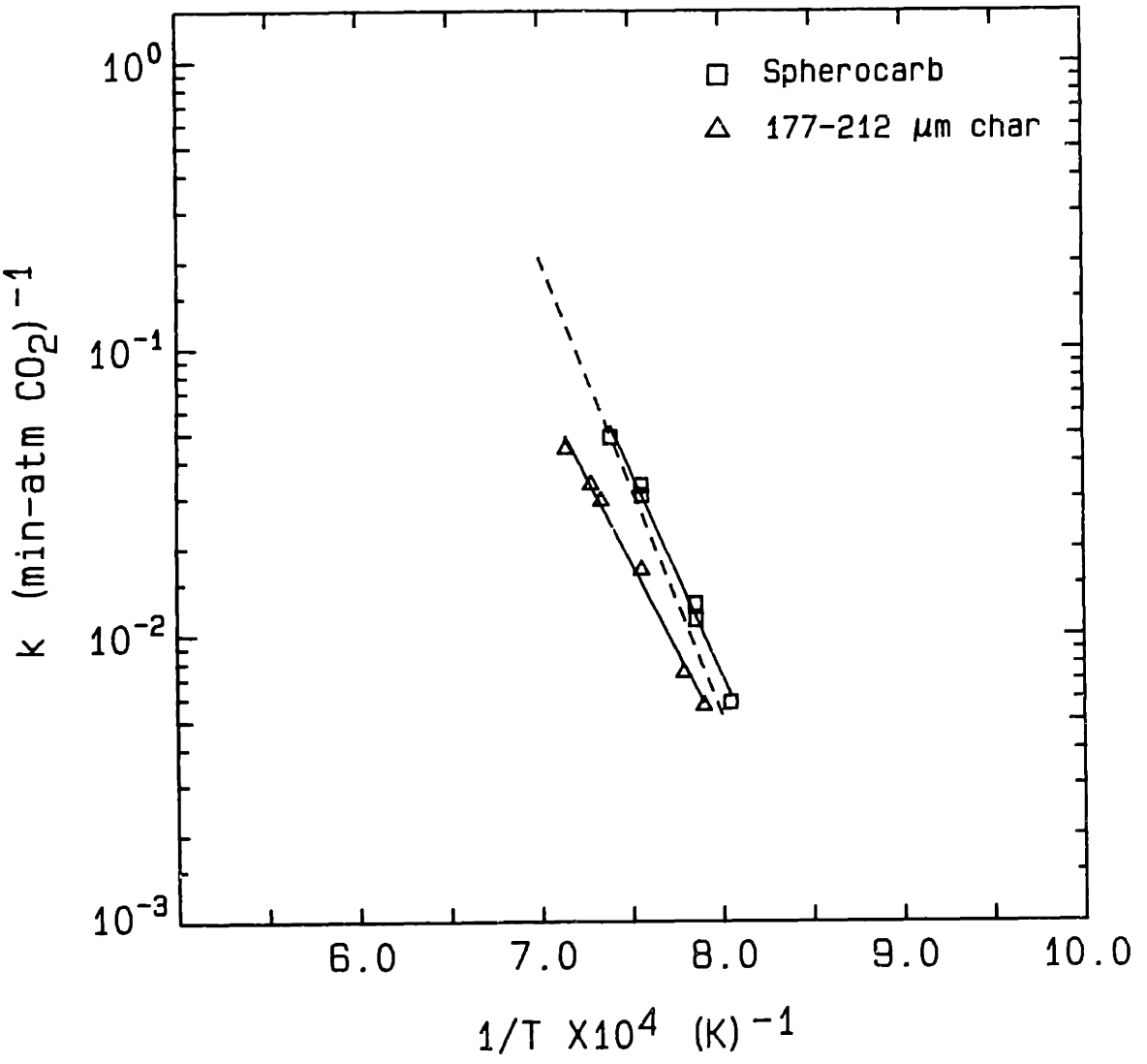

Figure 4.2-14 Arrhenius diagram for the reaction of the C-O char and spherocarb with carbon dioxide (1 atm) at 80% conversion.

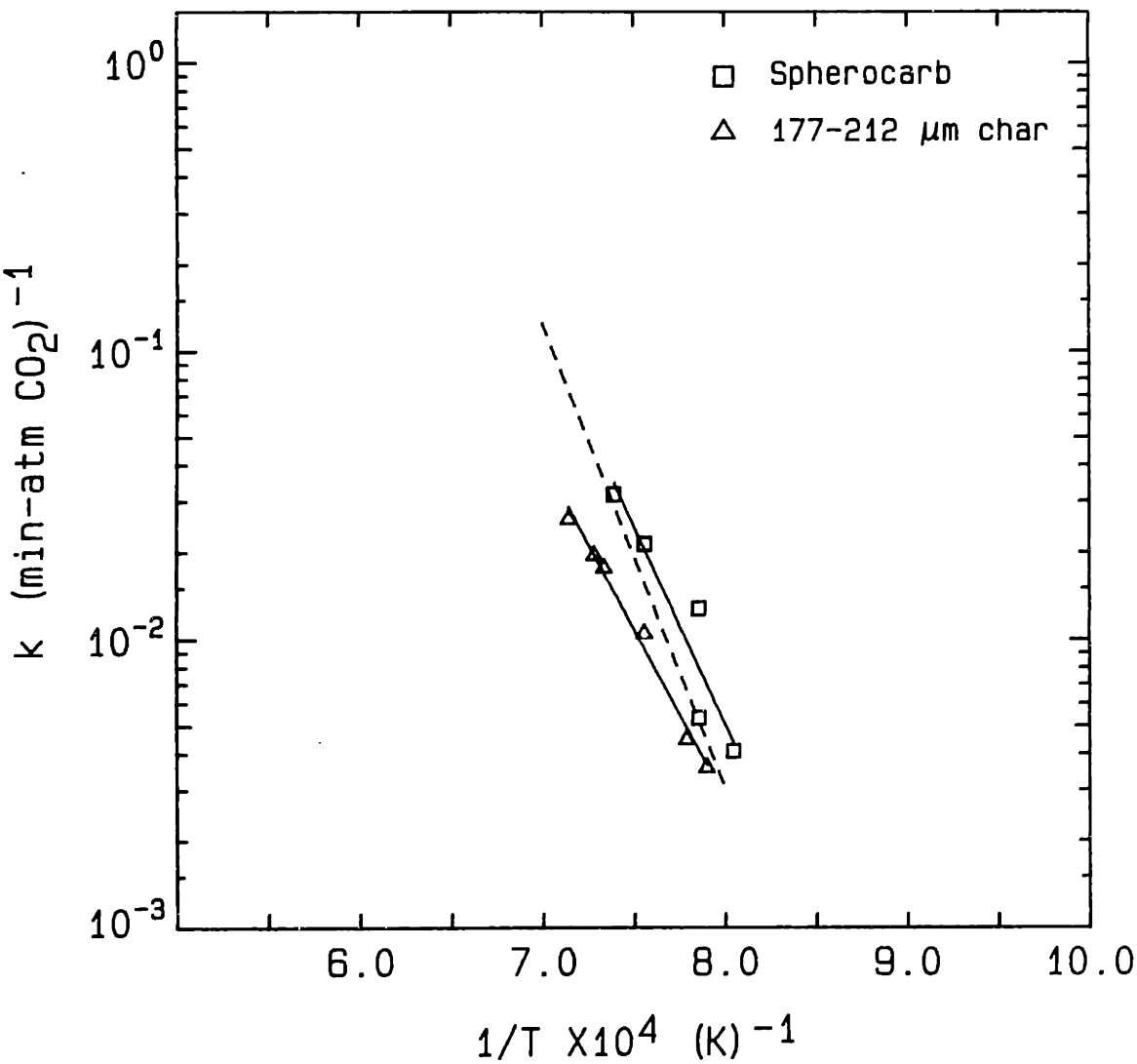

Figure 4.2-15 Arrhenius diagram for the reaction of the C-O char and spherocarb with carbon dioxide (1 atm) at 90% conversion.

Activation energies are listed in Table 4.2-2 and are slightly lower at all conversions. The larger particles were less reactive than the 90-106 μm particles. The difference in rate between the two particle sizes approaches a factor of 1.9, which is greater than was observed with the oxygen reaction. This result indicates that the thickness of the reaction volume is less for the CO_2 reaction. Activation energies (Table 4.2-2) are about 15% lower for the larger particle size.

Graphs of reaction rate versus conversion and normalized time are presented in Figures 4.2-16 to 4.2-17 for the Spherocarb. The rate decreases almost linearly over the entire conversion range. The difference between the oxygen and carbon dioxide reaction conversion curves of the spherocarb is quite noticeable. The reason for this difference is discussed in Section 5.14.

Rate versus time data for the two particle sizes are shown in Figure 4.2-18. The effect of particle size on the rate versus time data are similar to that observed in the oxygen runs.

4.3 Physical and Chemical Characterization of the Chars

4.3.1 Surface Area Measurements

Information on the surface area and porosity of the solids was determined from nitrogen adsorption isotherms, which were obtained at 77K. Adsorption and subsequent desorption measurements were made on the C-O and C-3.6 chars that had been heat treated at 1100 or 1300 K in the usual manner and then

Table 4.2-2. Activation Energy and Pre-Exponential Factors for the Carbon Dioxide Reaction.

Conversion (%)	Pre-Exponential Factor (cc/gmole-sec)	Activation Energy (cal/mole)
C-O Char (177-212 μm)		
20	1.40×10^{12}	63,100
40	7.50×10^{11}	61,400
60	3.40×10^{11}	60,000
80	1.30×10^{11}	58,600
90	4.24×10^{10}	57,000
Spherocarb		
20	1.71×10^{13}	67,200
40	1.33×10^{13}	67,000
60	2.10×10^{13}	68,900
80	8.40×10^{12}	67,700
90	2.52×10^{12}	65,600

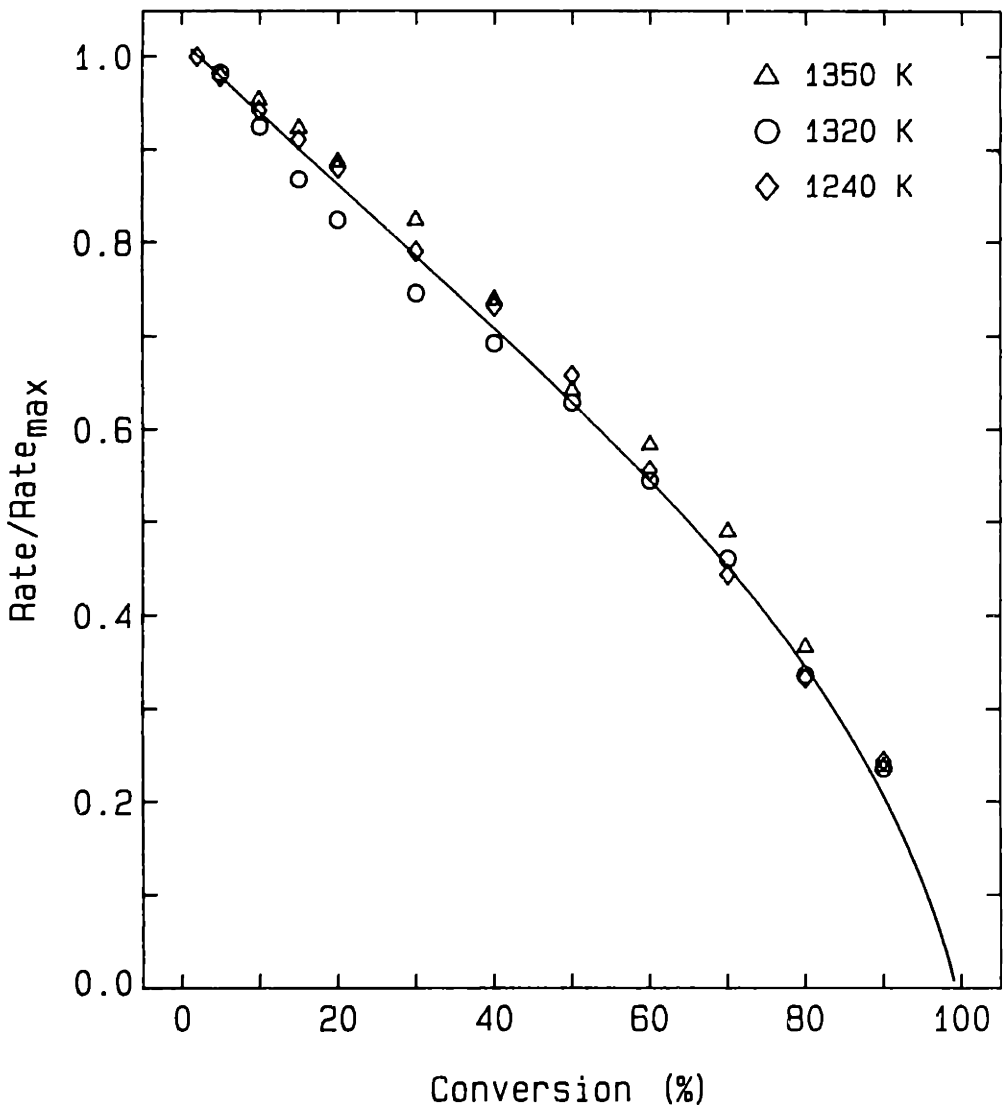

Figure 4.2-16 Reaction rate normalized by the maximum rate plotted against normalized time. Spherocarb-carbon dioxide (1 atm) reaction.

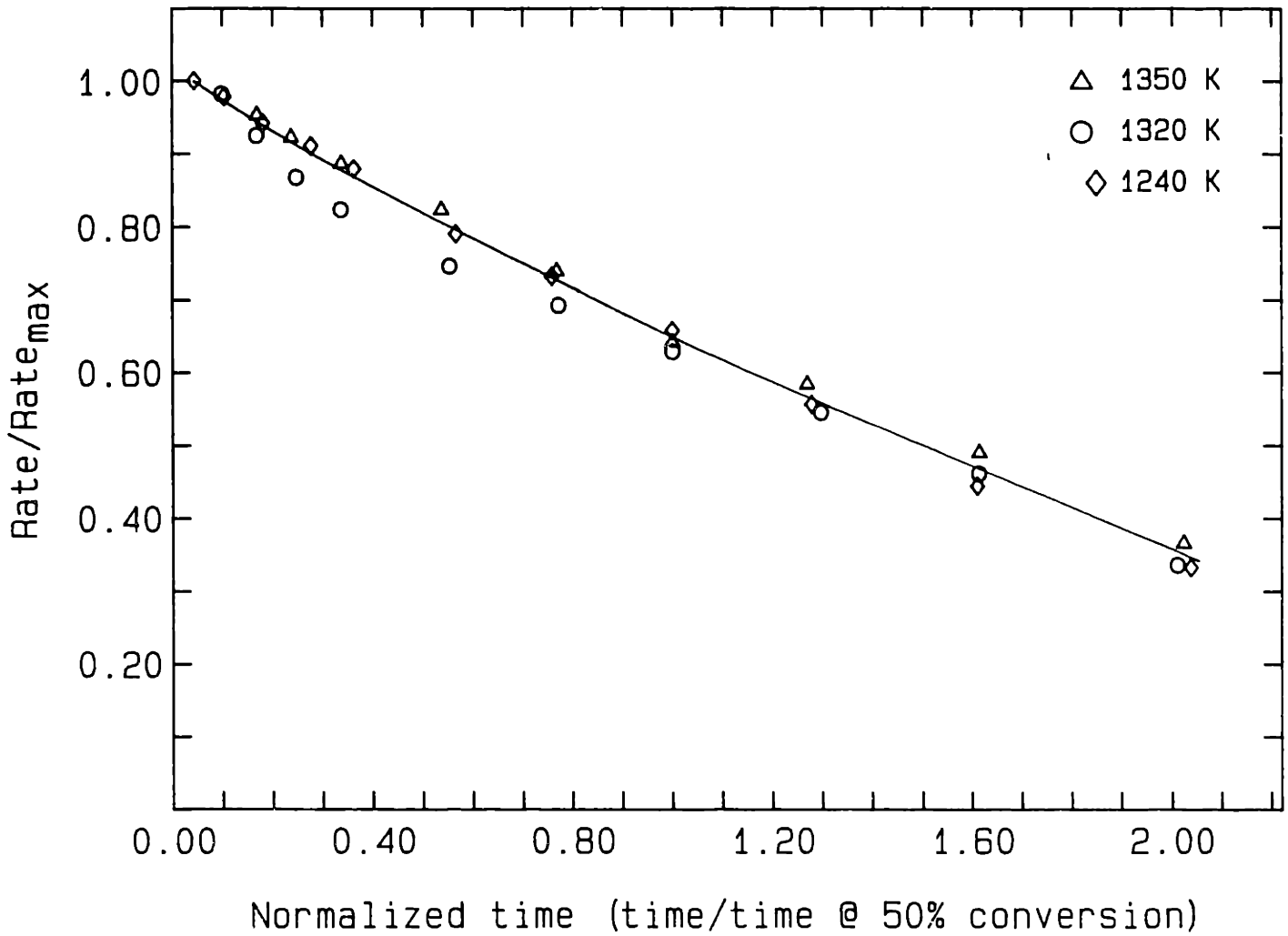

Figure 4.2-17 Reaction rate normalized by the maximum rate versus conversion. Spherocarb-carbon dioxide (1 atm) reaction.

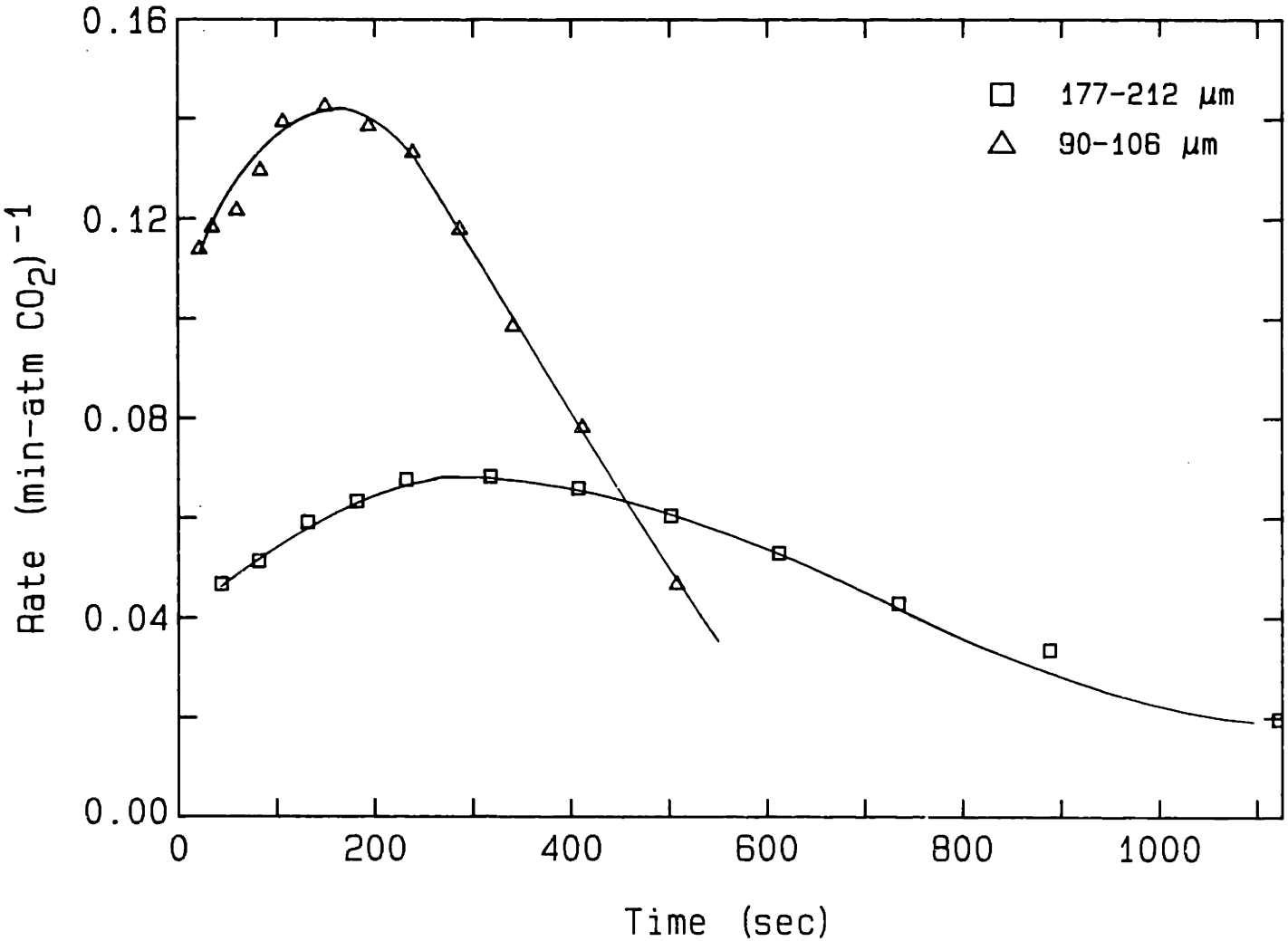

Figure 4.2-18 Reaction rate versus normalized time: effect of particle size C-O char - carbon dioxide (1 atm) reaction at 1370 K.

reacted with air to different extents of conversion. Samples were prepared in either a tube furnace or in the TGA at 760 K for the C-O char and at 615 K for the C-3.6 char. Reaction rates were slow enough at these temperatures to allow the manufacture of a sufficient quantity of sample in a single run. At the end of a run, the gas was switched to nitrogen and the sample was cooled to room temperature. One sample (C-O char; 1100 heat treatment; 40% conversion) was reheated to 1100 K after partial reaction. Reheating the sample resulted in a significant weight loss due to the removal of residual surface oxides (see discussion in Section 4.3.6). The surface area of the outgassed sample is about 25% higher than for the other samples. The reported conversion is in all cases with respect to the final weight of the sample on which the measurement was made.

The adsorption isotherms of the chars, heat treated at two different temperatures and reacted to conversions between 0 and 60%, are shown in Appendix 5. All the isotherms are similar in appearance and correspond to a Type I isotherm in the classificiation of Brunauer (1945), which is characteristic of a microporous solid. Except for the chars at 0% conversion, no hysterisis between the adsorption and desorption curves was observed. It was not possible, however, to desorb all of the nitrogen from the char at 77 K. Even after numerous desorption steps (see for example Figure 4.3-1), appreciable nitrogen remains on the char. The amount remaining corresponds to a quantity just less than the amount at which the isotherm bends

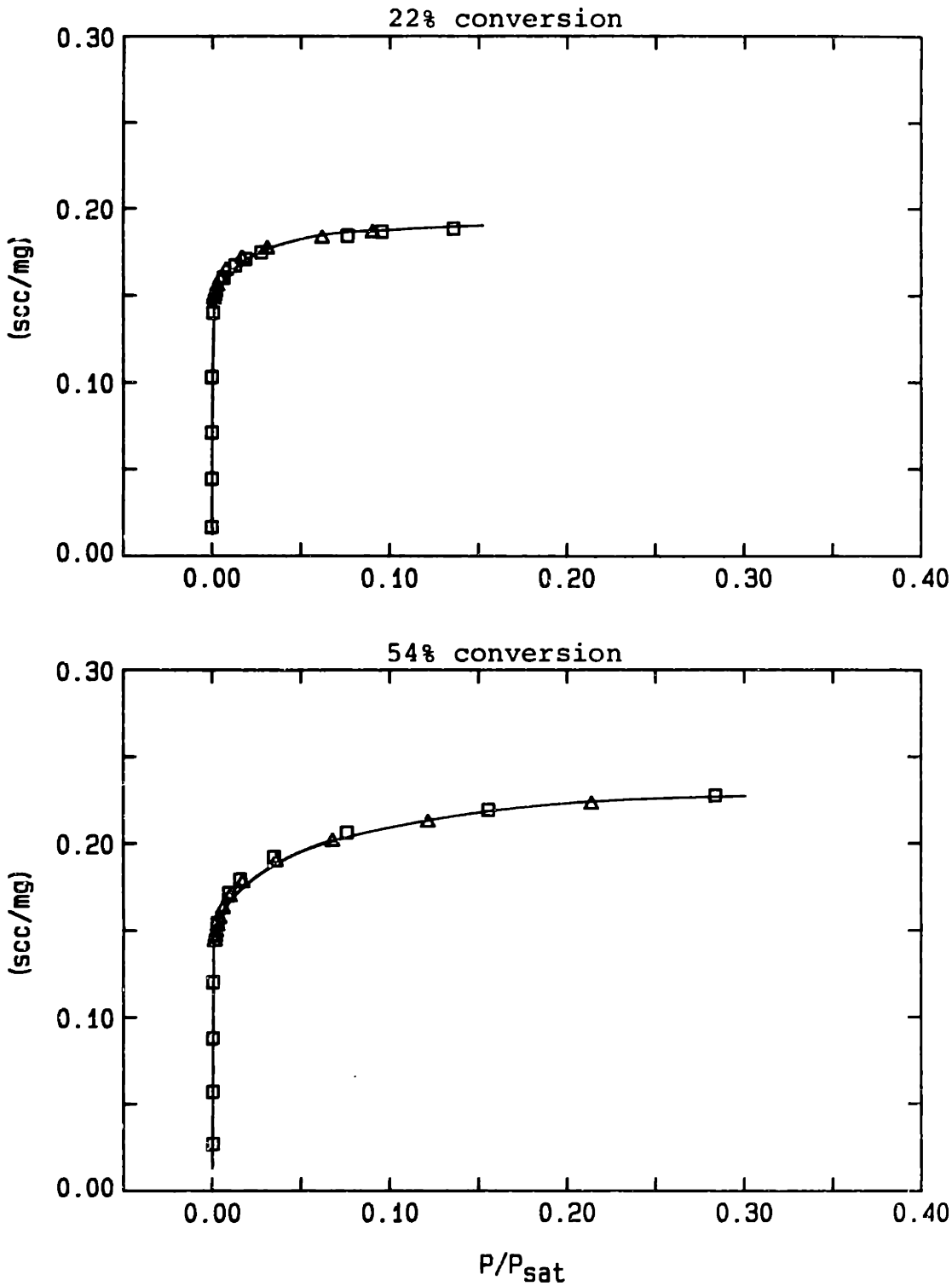

Figure 4.3-1. Nitrogen adsorption and desorption isotherms at 77 K for the C-O char at 22 and 55% conversion. (□)-adsorption; (△)-desorption.

over. The equilibrium adsorption pressure for the nitrogen that was adsorbed in each step below the amount corresponding to the final desportion point is approximately the same. This can be interperted to mean that there is a strong interaction between the adsorbate and adsorbent and that mono-layer coverage is approximately complete prior to multi-layer formation. Therefore, the nitrogen remaining after the last desportion point should correspond closely to a mono-layer coverage.

In a number of experiments, a single point adsorption measurement was also made. In every case, the amount adsorbed at the equilibrium pressure was the same as that obtained by multi-step adsorption.

Except for the chars at 0% conversion, the time required to reach equilibrium at each adsorption step was about 15 sec. A typical plot of pressure versus time is given in Figure 4.3-2. The equilibration time was about the same as that obtained with a non-porous carbon black; however, the equilibrium time was significantly longer than that corresponding to pressure equilibration resulting from a volume expansion (measured with helium at 77K). Equilibration times with helium were typically less than 2 sec. (Figure 4.3-2). Estimation of a characteristic diffusion time from the adsorption transient is not possible since heat effects accompany adsorption, and the 15 second equilibration time may largely reflect heat transfer limitations (Hurt, 1985). This would explain why the equilibration time for the nonporous carbon black was found to be about the same as for the microporous chars. Rapid equilibrium was not observed with

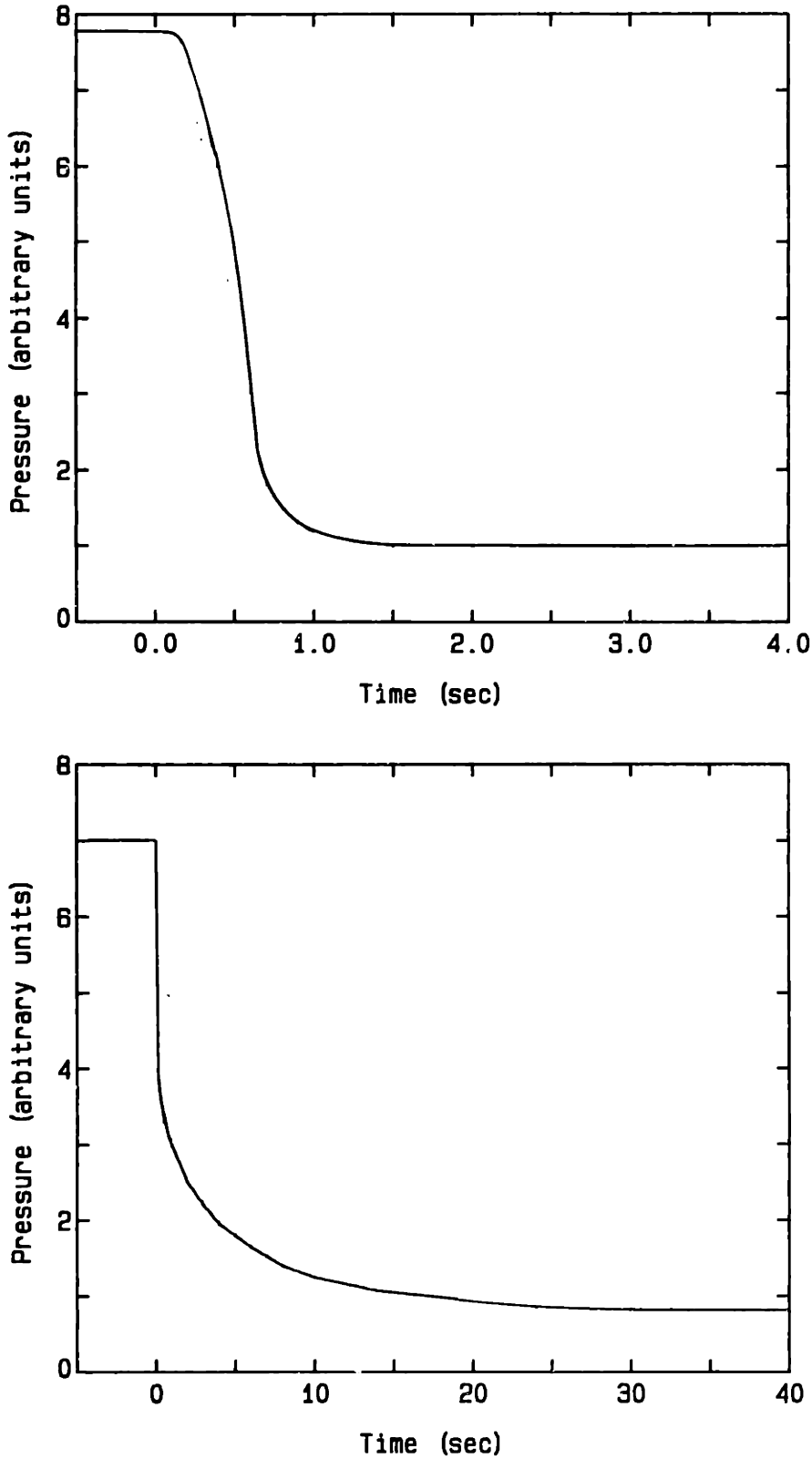

Figure 4.3-2. Equilibration time for helium displacement (top) and nitrogen adsorption (bottom) at 77 K.

the chars at 0% conversion. At 0% conversion, complete equilibrium was not achieved in the time interval between adsorption steps (20 min). As a result, surface areas at 0% conversion are much lower than after some reaction has taken place. The amount of conversion necessary to open up the surface area of the particle was typically about 5%. Because the surface area prior to any conversion was usually very low suggests that the initial pore restrictions must occur principally near the particle surface.

Surface areas were determined from the nitrogen adsorption isotherms by the BET equation. The BET model is an extension of the Langmuir isotherm to a multi-layer adsorption model. The model assumes that the Langmuir isotherm applies to each layer but that the energy of adsorption for the first layer may be different from the subsequent adsorbate-adsorbate layers. The BET equation for the case where adsorption is restricted to n-layers is (Adamson, 1976):

$$v = \frac{v_m cx}{(1-x)} \cdot \frac{(1 - (n+1)x^n + n\,x^{n+1})}{(1 + (c-1)x - c\,x^{n+1})} \qquad (4.3\text{-}1)$$

where v_m is the monolayer coverage (scc/g of solid); v is the amount adsorbed (scc/g of solid) at a given relative pressure; x is P/P_o the pressure relative to the saturation pressure; n is the number of layers; and c is the parameter of the BET model.

The constant c is interperted to be related to the difference in the heat of adsorption between the first layer and the heat of condensation of the vapor to liquid for all other

layers above the first. If it is assumed that the pre-exponential factors for the adsorption and desorption rates are the same for all layers including the first, then (Adamson, 1976):

$$c = \exp[(E_1 - L)/RT] \qquad (4.3.2)$$

Where E_1 is the heat of adsorption of the first layer, L is the heat of condensation, T is temperature, and R is the gas constant. Clearly large values of c suggest that $E_1 > L$.

The parameter c largely governs the shape of the isotherm: increasing c gives an isotherm where the bend in the knee becomes progressively sharper (see Adamson, p 570). For $c \gg 1$, equation (4.3-1) can be rewritten as:

$$\frac{f(n,x)\ x}{v\ (1-x)} = \frac{1}{v_m c} + \frac{1\ (x - x^{n+1})}{v_m} \qquad (4.3.3)$$

where $f(n,x) = (1 - (n+1)\ x^n + n x^{n+1})$. When $n \rightarrow \infty$, this equation reduces to the usual form of the BET equation:

$$\frac{1}{v}\ \frac{x}{(1-x)} = \frac{1}{c v_m} + \frac{x}{v_m} \qquad (4.3.4)$$

where again it is assumed that $c \gg 1$.

The adsorption data are fitted to Equation (4.3-3) for $n = 1.2$, 2 and ∞, as shown in Appendix 5. Usually the best fit is obtained for values of $1.2 < n < 3$. Figure 4.3-3 shows how Equation (4.3-3) changes with the number of layers, n. It is, therefore, not surprising that the BET equation for $1.2 < n < 3$

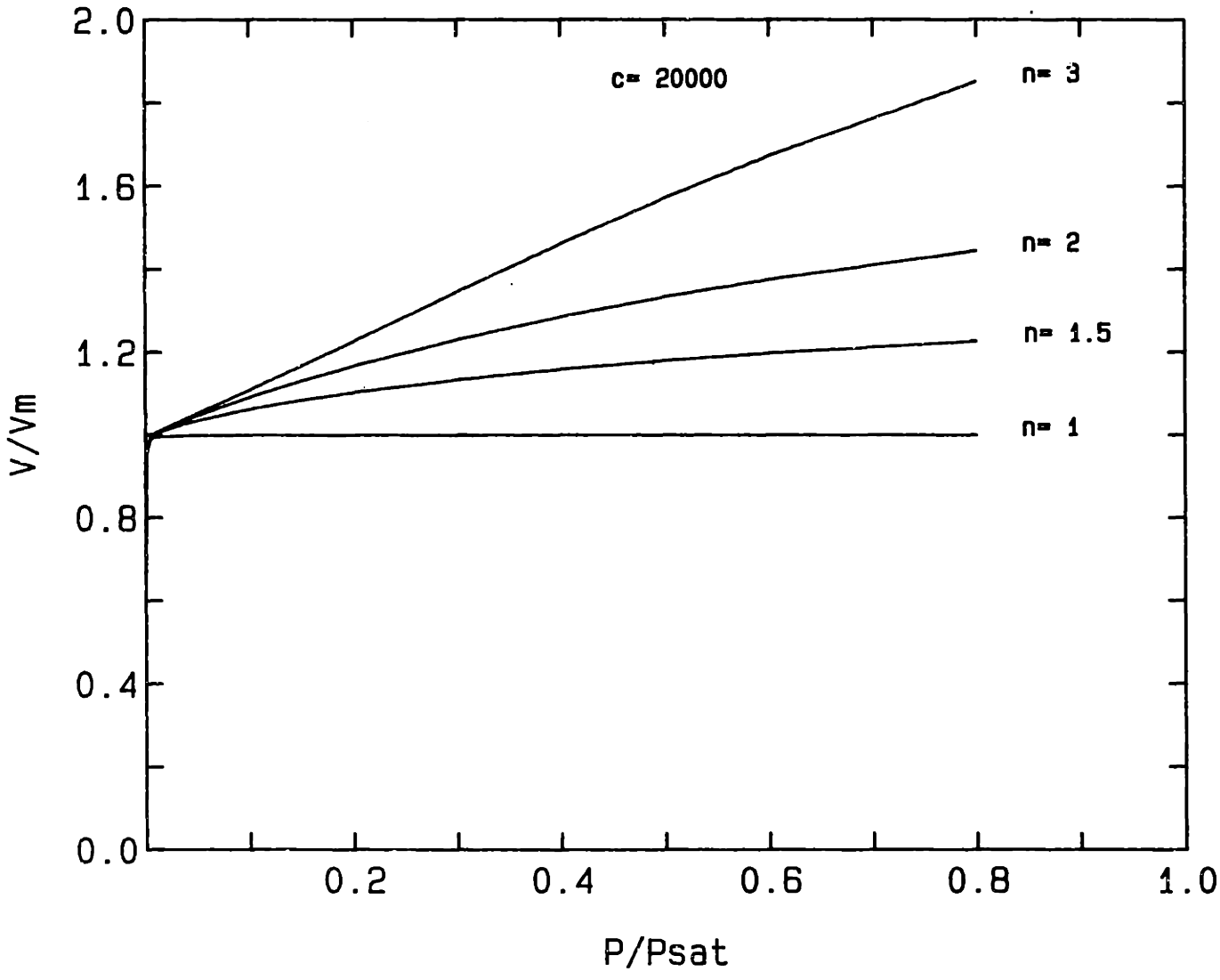

Figure 4.3-3. The BET model for different number of layers.

gives a better fit to the data than the ordinary BET equation. A value for c could not be determined exactly because the relative pressure changed only a little, if at all, with the amount adsorbed at low adsorption levels. Estimates indicate that c>1000. Such a large value of c is in agreement with the experimental observation that the energy of adsorption at low coverage is much greater than at high coverage. The single point BET method will give incorrect values for the surface areas of these chars unless the equilibrium adsorption relative pressure (P/P_o) is less than approximately 0.2. Below about 0.2 the slope (i.e., $1/v_m$) of the BET equation is not very sensitive to the value of n for large values of c.

4.3.2 Pore Volume Determination

The Dubinin-Polanyi equation has been used by numerous investigators to determine either a micropore volume or a monolayer volume from low pressure adsorption data. Whether pore filling or monolayer adsorption occur in a particular adsorbent-adsorbate system depends on the potential energy profile within the pores of a particular solid for a specific adsorbent. Lamond and Marsh (1964) plotted the adsorption data of various adsorbates on microporous chars on a Dubinin-Polanyi potential energy diagram to determine which process is occurring. They conclude that CO_2 adsorption at low relative pressures is probably restricted to monolayer adsorption, whereas nitrogen adsorption seems to result in pore filling. It should be noted at this point that although the Dubinin-Polanyi

equation has been used extensively in recent years to determine surface areas of coal chars from CO_2 adsorption data, the method rests principally on this experimental observation.

The Dubinin-Polanyi equation is derived from Polanyi's potential theory that assumes there is a potential energy field at the surface of a solid (Thomas and Thomas, 1967; Adamson, 1976). The surface of the solid is considered to be homogeneous, and the work done by the adsorption force is assumed to be approximately equal to the work of compression of the gas from the equilibrium pressure, P, to its saturation pressure, P_{sat}:

$$\epsilon = RT \ln\left[\frac{P_{sat}}{P}\right] \qquad (4.3.5)$$

where ϵ is the potential energy at a fixed height above the surface that encloses a volume of adsorbed gas v. Dubinin relates ϵ to v by a semi-empirical equation:

$$v/v_o = \exp[-D'\epsilon^2] \qquad (4.3.6)$$

where D' is a constant and v_o is the total adsorbed volume. Combining equations (4.3.5) and (4.3.6) gives the Dubinin-Polanyi equation:

$$\log(v/v_o) = -D(\log P/P_{sat})^2 \qquad (4.3.7)$$

Plots of $\log(v/v_o)$ versus $[\log(P/P_{sat})]^2$ obtained from the nitrogen adsorption data are also shown in Appendix 5. All the diagrams have a nearly vertical section at low relative pressures and a section where the slope is more nearly

horizontal to the x-axis at higher relative pressures. Thomas and Thomas (1967), based on the analysis of Lamond and Marsh, interpret such behavior to be indicative of pore filling. Therefore, it is expected that extrapolation of the high pressure data to the y-axis intercept will give the micropore volume.

All the data are summarized in Table 4.3-1. Pore volumes were determined from the intercepts of the Dubinin-Polanyi diagrams; the quanitity adsorbed in scc/mg was converted to a pore volume (i.e. cc voids/g solid) by the factor 1.547 as recommended by Barret et al. (1951). Surface areas were determined by two methods: from the volume of v_m calculated from the n-layer BET equation and from the volume of nitrogen remaining on the solid after the last desorption step. Surface areas were calculated from the monolayer volume by assuming an area of 16.2Å^2 per nitrogen molecule. This value for the area of a nitrogen molecule may be incorrect when applied to the volume of nitrogen remaining upon desorption. In this case, localization of the adsorbed molecule on the surface may result in a packing different from the liquid density of nitrogen (Gregg and Sing, 1976). The value of 16.2Å^2 per molecule, however, should represent a lower bound on the molecule area. However, because the surface area calculated from the remaining nitrogen is lower than the BET surface area, it is felt that the desorption end point technique may provide a more accurate estimate of the surface area. Surface areas, determined from the desorption endpoint, of the C-O and C-3.6 chars as a

Table 4.3-1 Surface Areas, Pore Volumes and Average Pore Radii Calculated from the Nitrogen Adsorption and Desorption Isotherms at 77 K.

Conversion (%)	Surface Area (m^2/g of reacted carbon)		Pore Volume (cc/g)	Pore Radius (Å)
	n-BET Equation	Desorption Endpoint		
C-O Char Heat Treatment Temperature 1100 K				
0		282	318	.129	7.1
6.4	(1.5)[1]	580	531	.232	7.1
22	(1.5)	753	645	.300	6.9
24.4	(1.5)	771	671	.303	7.2
24.4[2]	(1.5)	786	657	.309	7.2
40[3]	(1.5)	1000	810	.398	7.1
54.5	(2.0)	870	627	.343	8.2
C-O Char Heat Treatment Temperature 1300 K				
0		∿20	-	-	-
21.2	(1.3)	870	742	.356	7.1
21.2[2]	(1.3)	870	727	.359	7.3
47	(1.7)	1100	806	.464	8.0
51.3	(1.7)	1160	692	.495	9.7

[1] value of n

[2] duplicate point

[3] sample outgassed after reaction

Table 4.3-1 Continued:

Conversion (%)	Surface Area (m^2/g of reacted carbon)		Pore Volume (cc/g)	Pore Radius (Å)
	n-BET equation	Desorption Endpoint		
C-3.6 Char Heat Treatment Temperature 1100 K				
0		104	114	.049	
7	(1.3)	510	374	.192	8.6
22	(3.0)	700	553	.278	7.9
38	(3.0)	725	558	.309	8.5
58	(3.0)	666	483	.278	9.0
58[2]	(3.0)	649	470	.265	8.9
C-3.6 Char Heat Treatment Temperature 1300 K				
0		∿20	-		
26	(1.5)	543	419	.213	8.3
37	(3.0)	580	505	.257	8.1
55	(2.0)	520	449	.240	8.6
Spherocarb				
0	(1.5)	1020	836	.390	6.7

function of conversions are illustrated in Figure 4.3-4. The surface area of both chars is relatively constant between 10 and 70% conversion.

An average pore radius was calculated from the pore volume and surface area using the random pore model to relate surface area to volume. With the assumption that the pores are cylindrical in shape and of uniform radius, this model gives the average pore radius as:

$$\bar{r} = \frac{2(1-\epsilon)}{S_v} \ln(1/1-\epsilon) \qquad (4.3.8)$$

where S_v is the surface area in cm^2/cm^3, ϵ is the porosity (cm^3/cm^3), and $\bar{r}$ is the average pore radius in centimeters. To determine ϵ and the particle density, it was assumed that the true solid density was constant at 2.2 g/cc. This equation becomes identical to the parallel pore model (Satterfield, 1970) when ϵ is small, but it predicts a smaller average pore radius at high porosity since pore intersections cause a decrease in available surface area compared to the non-intersecting or parallel pore model. The models are compared in Figure 4.3-5. Radii calculated by this equation are in general agreement with the values for n determined via the BET equation. The results (Table 4.3-1) show that the average pore radius increases very little with carbon conversion. This is certainly an unexpected result if reaction occurs uniformly throughout the solid. An interpretation of this result is presented in Section 5.1.4.

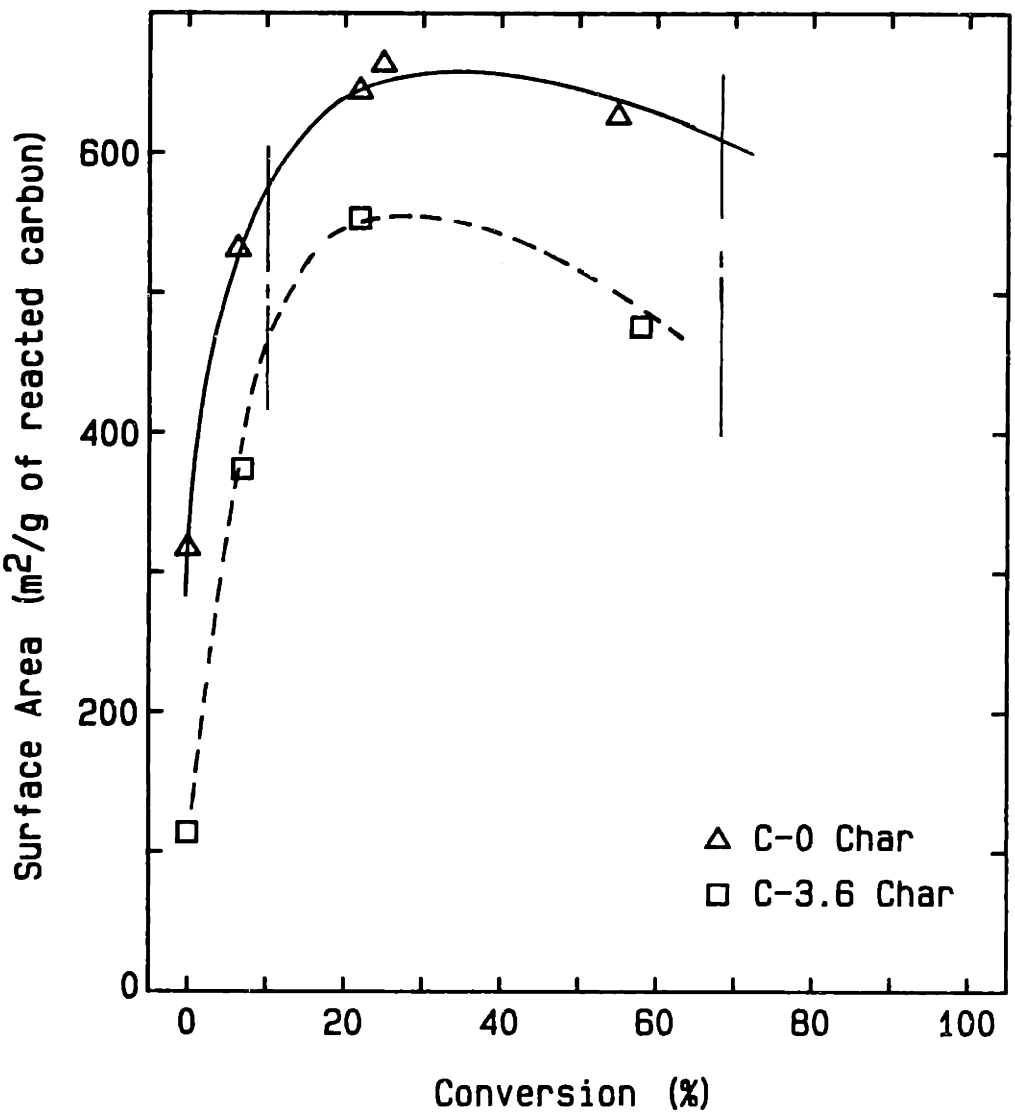

Figure 4.3-4 Surface areas of the C-0 and C-3.6 chars.

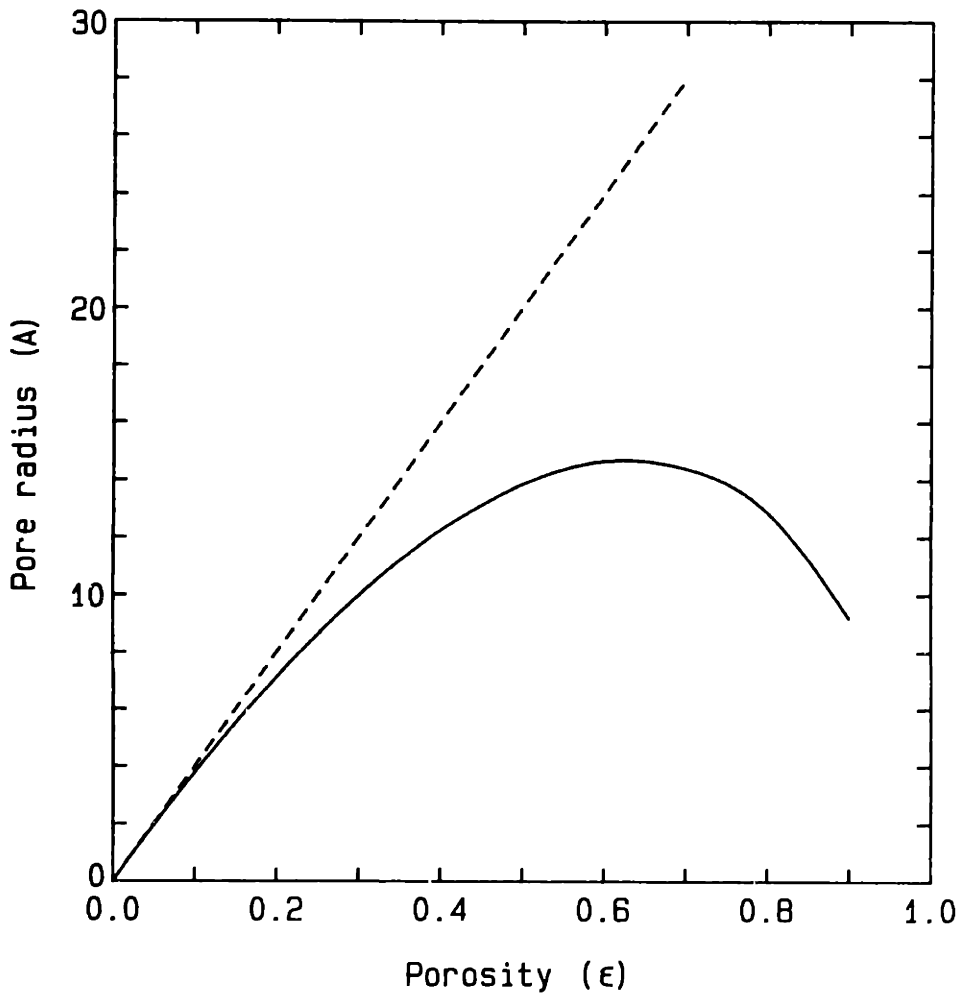

Figure 4.3-5 Comparison of the average pore radius calculated from the random pore (—) and the parallel pore (---) models. ($S_V = 500\ m^2/g$)

4.3.3 Mercury Porosimetry Measurements

Mercury porosimetry measurements of the C-O and C-3.6 chars at 0% conversion showed that the char contained no pores larger than about 100Å (the lower limit of penetration). The results are given in Figure 4.3-6 and 4.3-7. From the porosimetry data, a value of 1.5 g/cc was obtained for the skeletal particle densities (i.e., the density of the microporous char).

4.3.4 True Solid Density

Helium displacement measurements gave a true solid density of 2.0 + 0.05 g/cc for the C-O char at 0% conversion.

4.3.5 Carbon Dioxide Adsorption Isobar

Carbon dioxide is reversibly adsorbed by the calcium free char over a wide temperature range. Although no adsorption isotherms were measured, an isobar at 1 atm. CO_2 was determined for the C-O char at 0% conversion. The isobar is shown in Figure 4.3-8. At all temperatures, CO_2 adsorption and desorption was rapid and completely reversible. The large change in the amount adsorbed with small changes in temperature at 25 C, indicates that precise temperature control is necessary to accurately determine CO_2 adsorption isotherms at room temperature. A smooth curve can be drawn through the isobar even at the critical temperature of CO_2 (304.3 K).

A value of 0.11 scc/mg for v_o was calculated from the data at 298 K by the Dubinin-Polanyi equation. Hurt (1985) reports a value of .095 at 298 K for the gradient, D, in Equation (4.3.7) for this particular char.

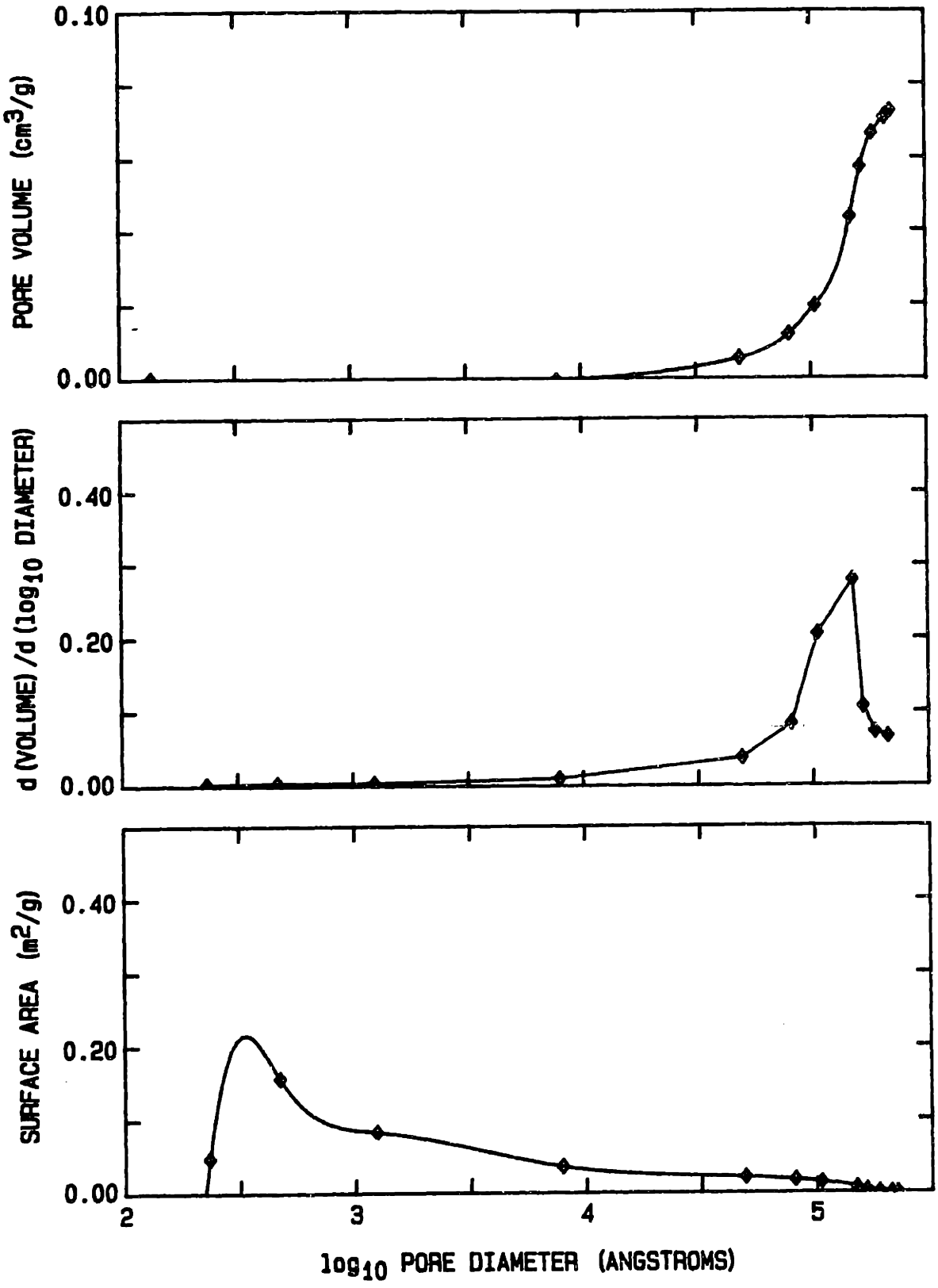

Figure 4.3-6. Mercury porosimetry measurements C-O char heat treated at 1100 K, 0% conversion.

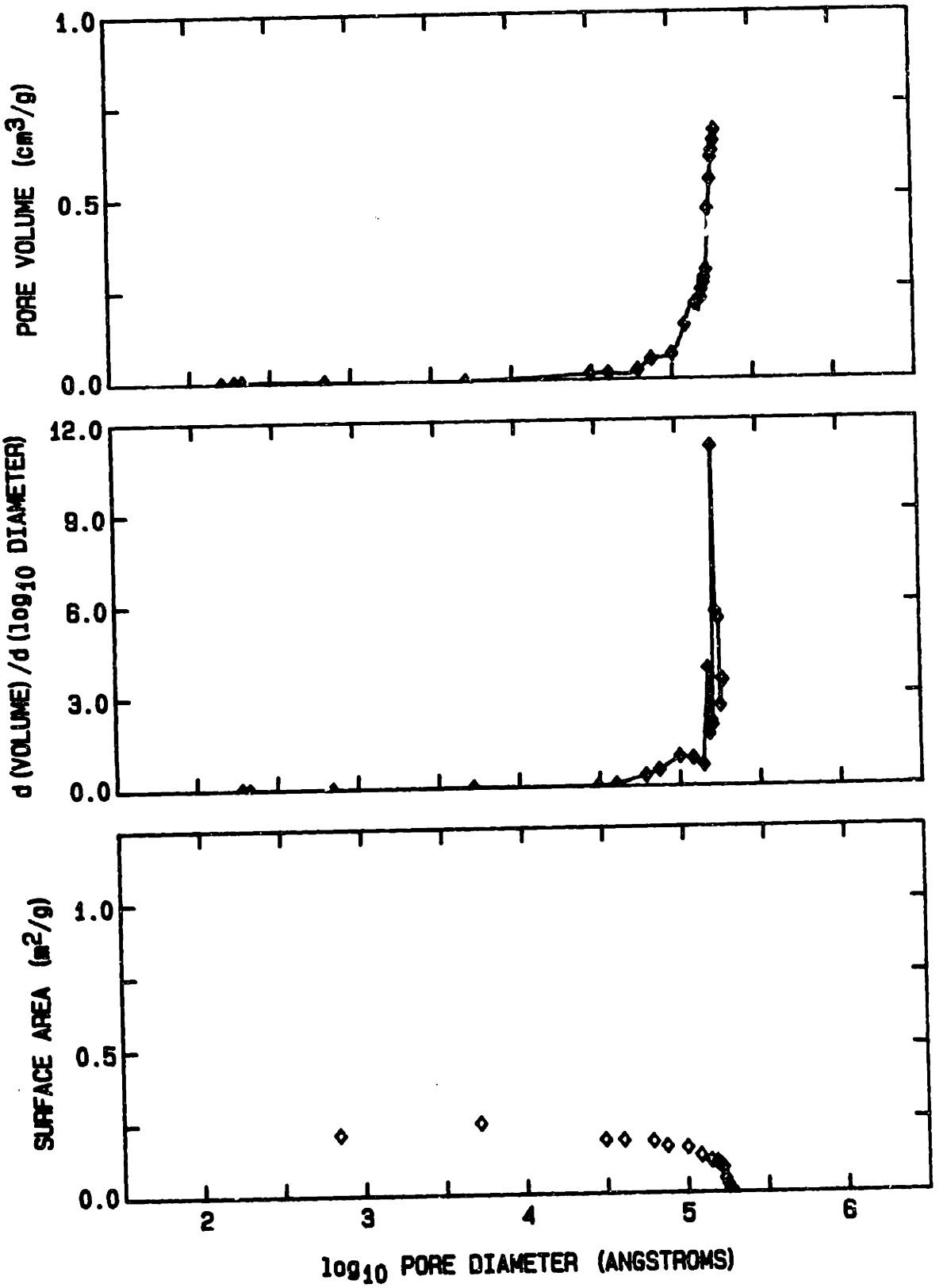

Figure 4.3-7. Mercury porosimetry measurements C-3.6 char heat treated at 1100 K, 0% conversion.

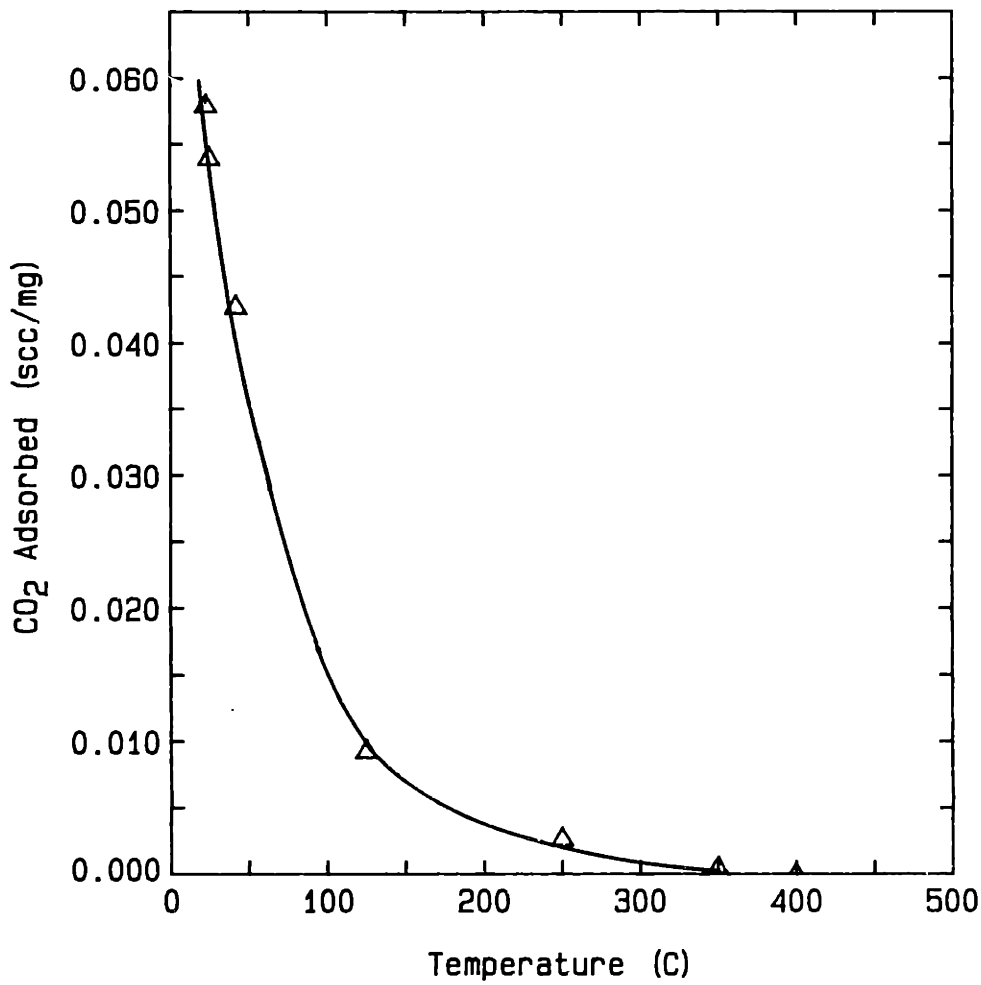

Figure 4.3-8 Carbon dioxide adsorption isobar (1 atm); C-0 char

4.3.6 Elemental Analysis

The samples were analyzed by Huffman Laboratory, Wheat Ridge, Colorado for total carbon, carbonate carbon, hydrogen, and calcium. Duplicate calcium analyses were made by Galbraith Laboratory, Knoxville, Tennessee. In addition, the calcium content of the chars was also determined by the method outlined in Section 3.1.7.

The partially reacted samples were made in the TGA. The samples were heat treated at 1100 or 1300 K in the usual manner prior to reaction and then reacted in air at 760 K for the C-O char and at 615 K for the C-3.6 char. After reaction, most of the samples were brought directly to room temperature. Some samples, however, were reheated to the pretreatment temperature before cooling to room temperature. Reheating the char after the reaction was stopped resulted in a substantial amount of weight loss. Switching the gas composition from air to nitrogen at an intermediate conversion results in an abrupt change in the reaction rate. Some weight loss continues under nitrogen, but the rate is extremely slow. However, subsequent heat treatment results in a large weight loss, indicating that the surface oxides formed during reaction are stable at the reaction temperature. The weight loss of various samples during outgassing is listed in Table 4.3-2. The rate of weight loss after switching from air to nitrogen is also listed in the table. The oxygen content of the char prior to outgassing was calculated from the weight loss data by assuming the CO/CO_2 mole ratio of the desorption products to be 2.0 (64 wt.% oxygen). A

Table 4.3-2 Weight Loss Upon Heat Treatment of Partially Reacted Chars.

CHAR[1]	REACTANT	TEMP. (K)	CONVERSION (%)	RATE[2] (with no oxygen present)	WEIGHT LOSS (%)[3]
C-O	air	760	6.4	.00034	-
			16.	-	26
			19.	0.0010	24
			55.	0.0022	-
C-O	air	875	18.	0.012	-
C-3.6	air	610	7.	0.0005	-
			22.	0.0013	19
			55.	0.0022	29
C-3.6	air	710	20	0.0054	

[1] 1100 K heat treatment temperature

[2] in units of g/g of remaining char

[3] percent of char remaining after reaction

value of approximately 2 for this ratio is reported by Chen and Bach (1979).

The results of the elemental analyses are presented in Table 4.3-3 and Figures 4.3-9 to 4.3-12. The results are reported on a dry-ash free basis. All samples were dried under vacuum at 600 K for 15 minutes prior to analysis. The drying condition was selected to minimize any decomposition of the surface oxides and to assure the decomposition of any $Ca(OH)_2$ and the desorption of any physically adsorbed gases, in particular H_2O. For the C-3.6 char, the carbon and oxygen values were corrected for carbonate CO_2 (Equation 3.1.7). The oxygen content of the char was always determined by difference. The oxygen content calculated from the weight loss during outgassing is also presented in the figures. Conversions are based on the sample weight prior to outgassing, except for the two outgassed samples, where the conversion is based on the final weight.

For both chars, the oxygen to carbon ratio increases with conversion, reaching an amount approximately equivalent to monolayer coverage. The oxygen content relative to the initial sample weight increases rapidly up to 7% carbon conversion, and thereafter rmains relatively constant (Figure 4.3-13). The hydrogen to carbon ratio shows an increase with conversion, except for the two data points (C-3.6 char; 1100 K heat treatment) corresponding to the outgassed samples. In this case, the H/C ratio is approximately constant. This result is quite unexpected. Generally, it is assumed that the hydrogen reacts preferentially to the carbon, resulting in a lower

Table 4.3-3 Elemental Analysis

	C	H	O[1]	Ca[2]	H/C	O/C	H/O
	wt%, dry-ash free basis				(atom ratio)		
C-O (1100 K)[3]	95.9	1.08	3.02	0.0	0.135	0.024	5.7
C-O (1300 K)	96.1	0.40	3.51	0.0	0.050	0.027	1.8
C-1	-	-	-	0.97			
C-3.6 (1100 K)	93.7	1.28	5.07	3.60	0.164	0.041	4.0
C-3.6 (1300 K)	95.0	0.79	4.23	3.60	0.100	0.033	3.0
C-6.2	-	-	-	6.2			
C-ion (1100 K)	91.5	1.06	7.49	2.3	0.139	0.061	2.3
C-$CaCO_3$	-	-	-	6.8			
Spherocarb	96.8	0.73	2.43	-	0.091	0.019	4.8

[1] by difference

[2] Calcium is also reported as wt Ca/wt calcium free char.

[3] heat treatment temperature

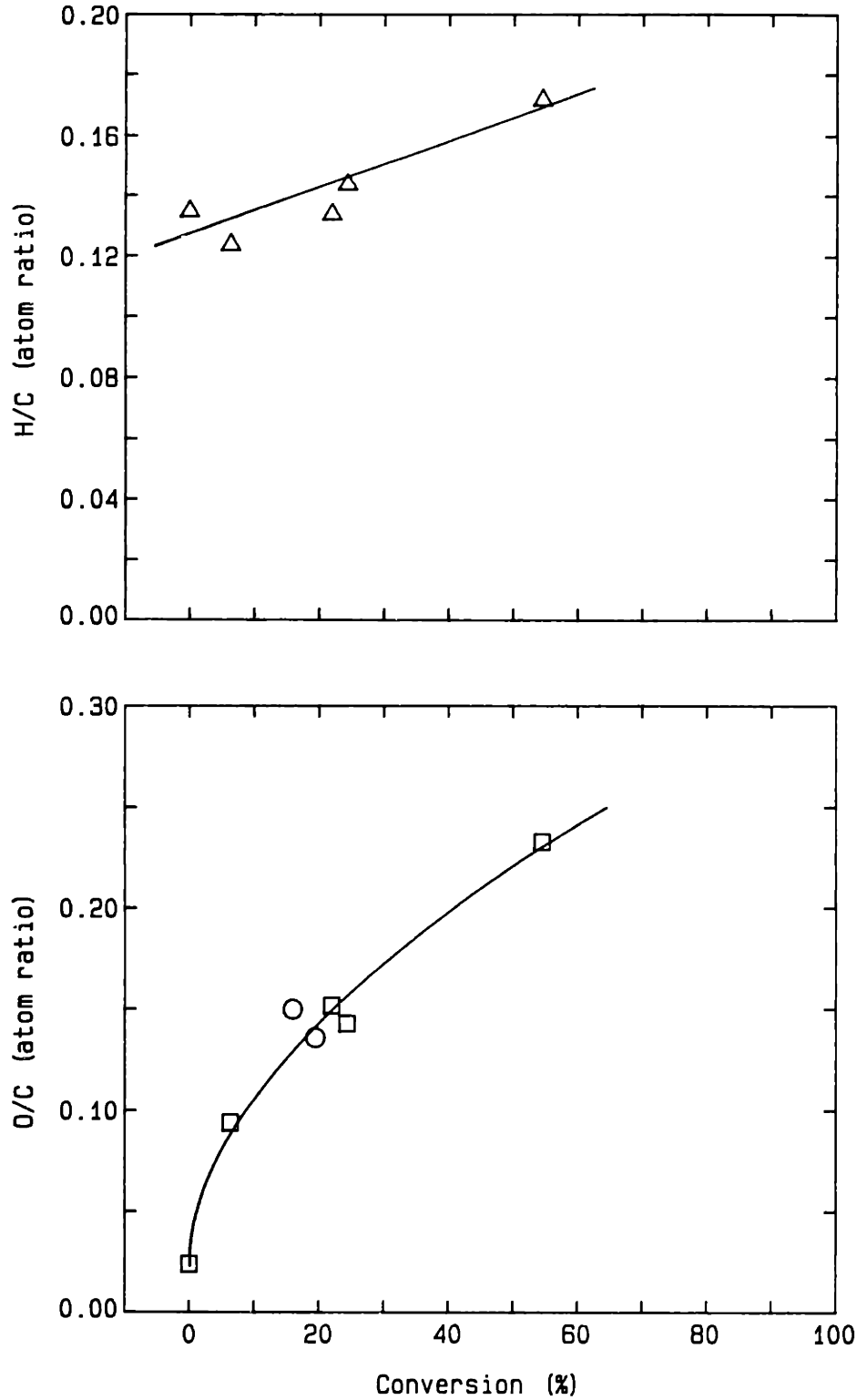

Figure 4.3-9 Hydrogen and oxygen to carbon ratios of the C-O char; 1100 K heat treatment temperature; reacted in air at 760 K; (△, □) - elemental analysis; (O) - calculated from weight loss on outgassing; lines indicate trends.

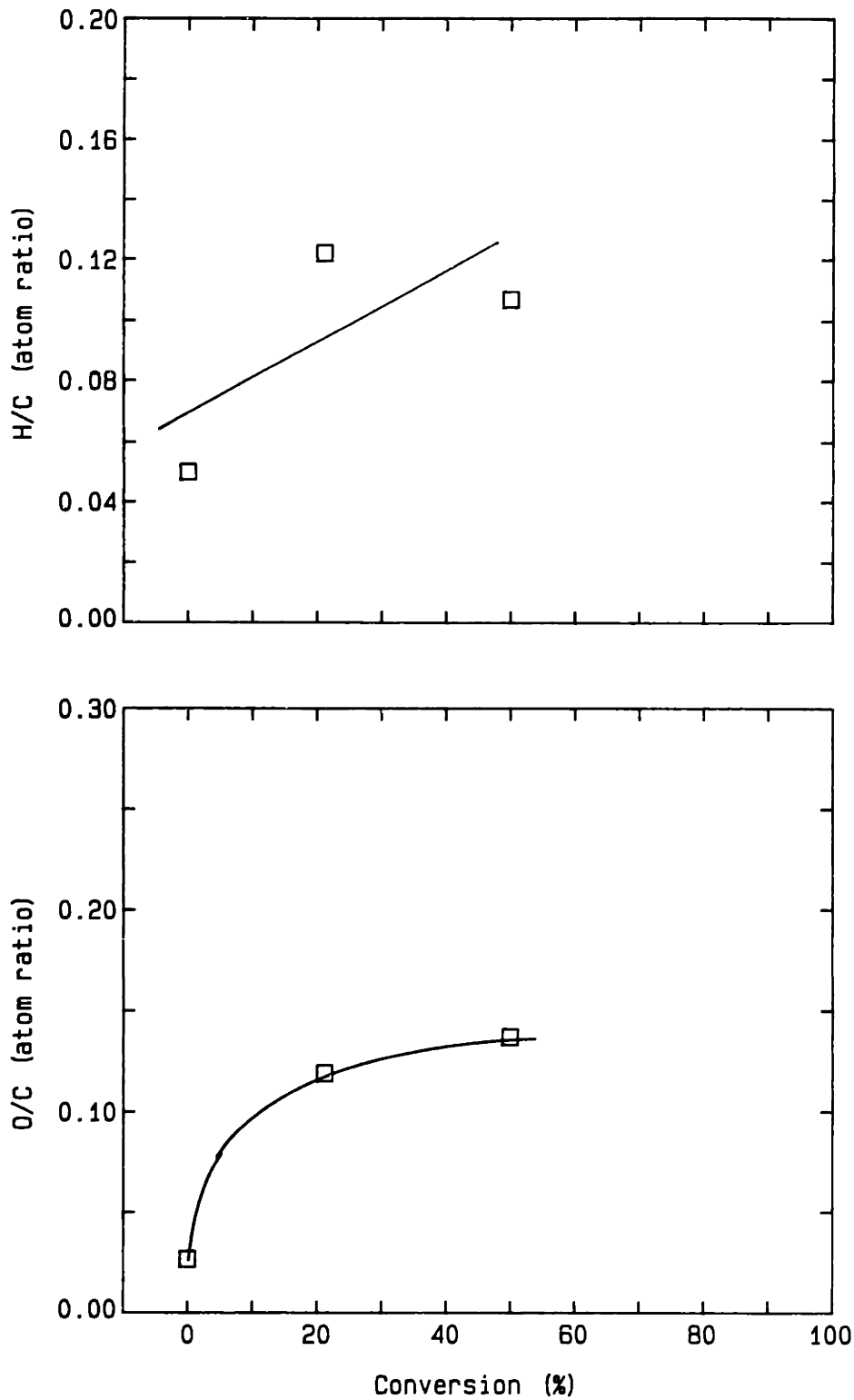

Figure 4.3-10 Hydrogen and oxygen to carbon ratios of the C-O char; 1300 K heat treatment temperature; reacted in air at 770 K; (□) - elemental analysis; lines indicate trends.

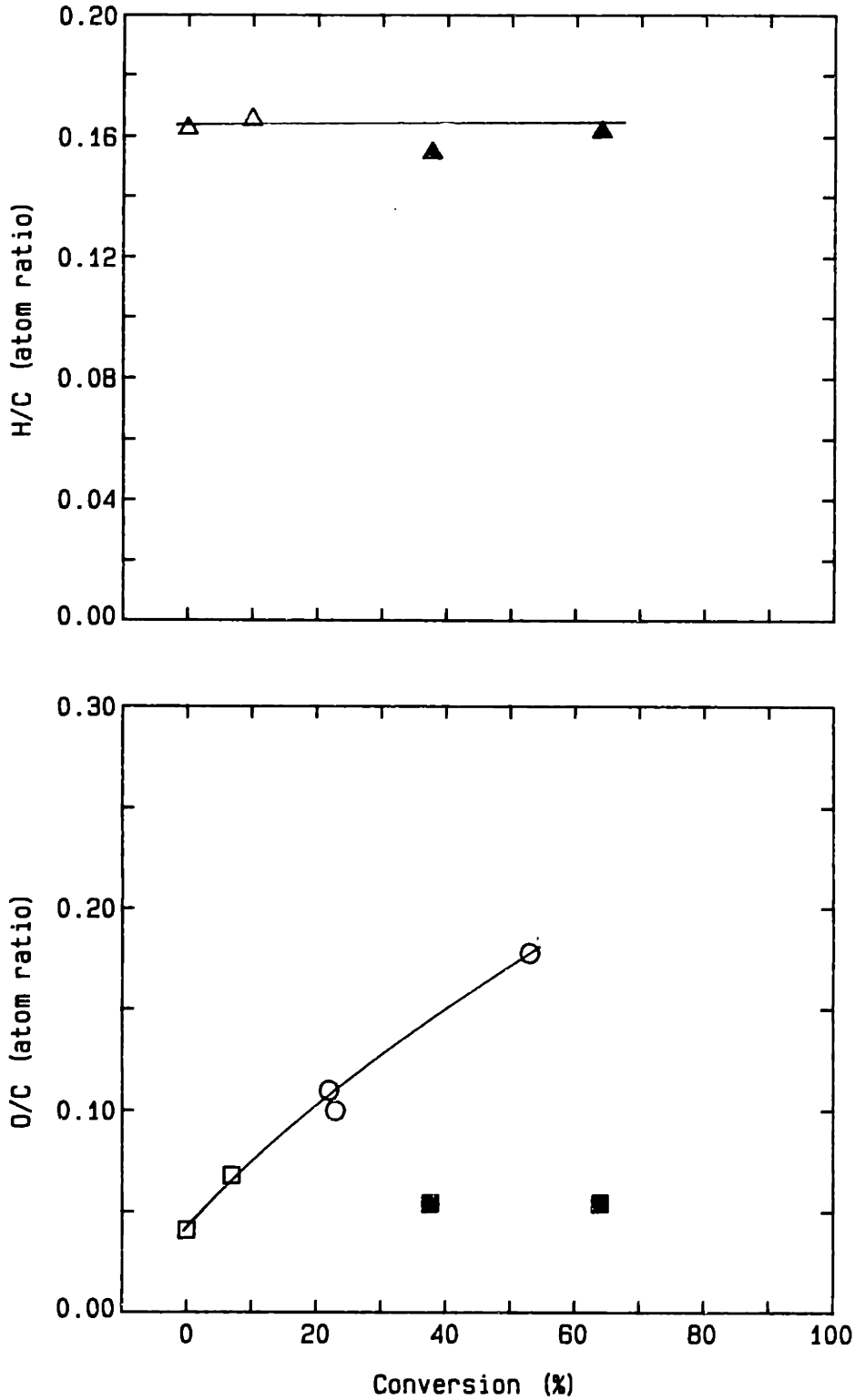

Figure 4.3-11 Hydrogen and oxygen to carbon ratios of the C-3.6 char; 1100 K heat treatment temperature; reacted in air at 615 K; (△,□) - elemental analysis; (▲,■) - elemental analysis of outgassed samples (conversion based on final weight); (O)- calculated from weight loss on outgassing; lines indicate trends.

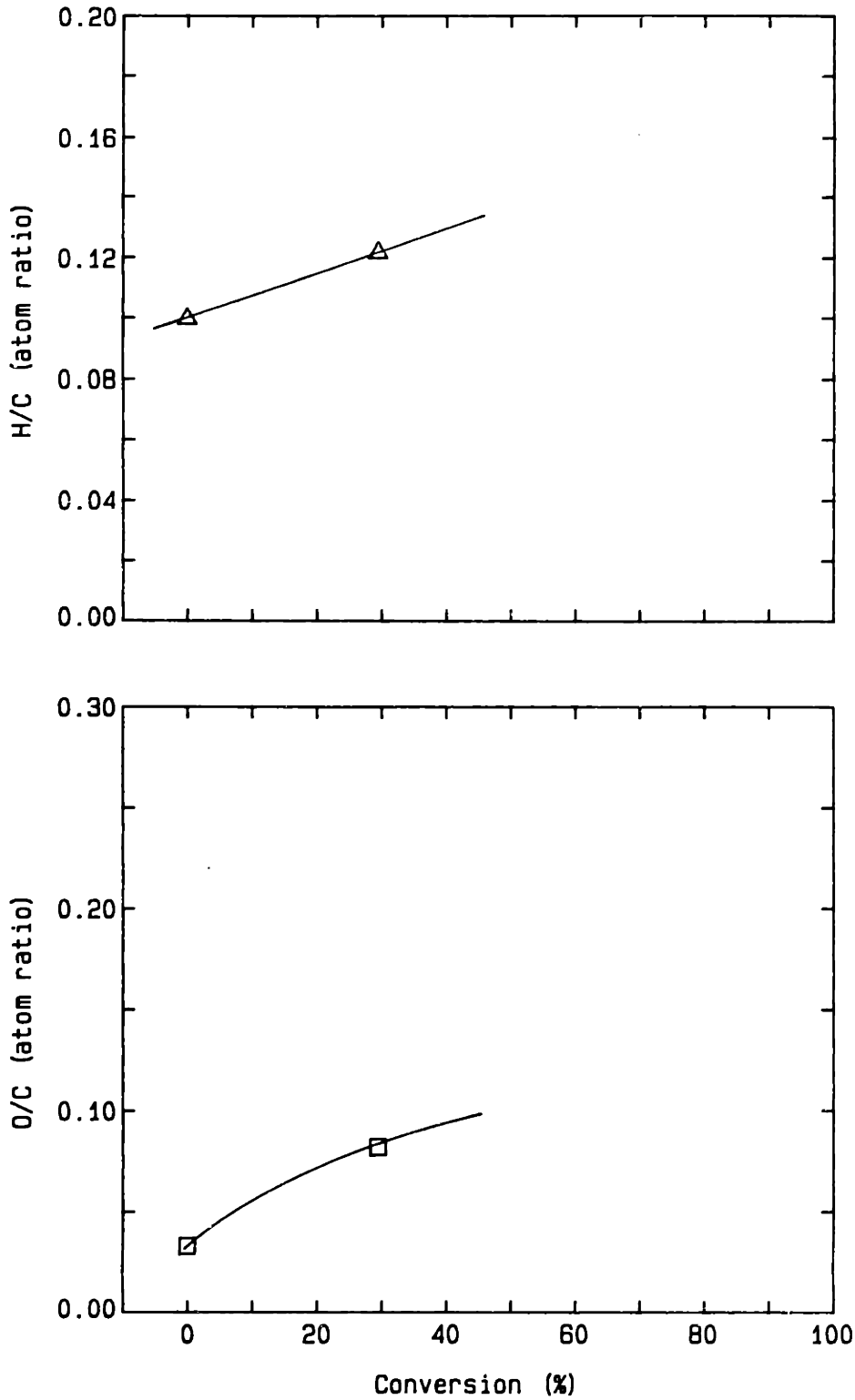

Figure 4.3-12 Hydrogen and oxygen to carbon ratios of the C-3.6 char; 1300 K heat treatment temperature; reacted in air at 620 K; (△, □) - elemental analysis; lines indicate trends.

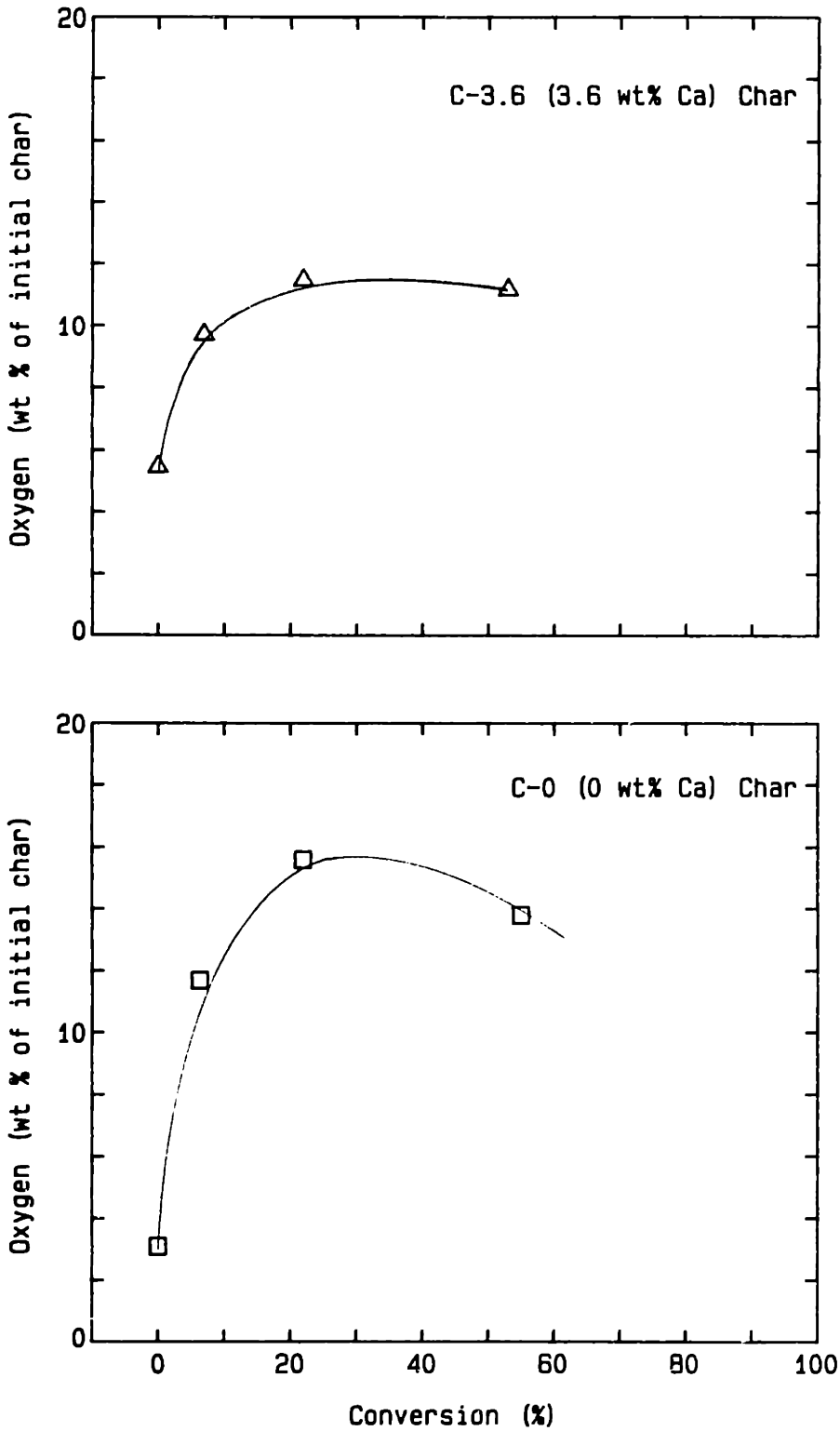

Figure 4.3-13 Oxygen content of the char as a function of conversion (1100 K heat treatment temperature data).

hydrogen content with conversion. It is possible that water, adsorbed during handling and storage of the sample, is responsible for the increased hydrogen content; however, a check of the H/O ratios of the chars show these ratios to be quite variable. Furthermore, it is unlikely that significant amounts of water will chemisorb on the char at room temperature, and any physically adsorbed water should have been removed during vacuum drying of the sample at 60° K. Finally, data reported by Hastings (1984) also show an increase in the H/C ratio of his chars with conversion. These results imply that during reaction the hydrogen oxides are not removed preferentially to the carbon oxides. This suggests that the hydrogen is probably distributed uniformly throughout the graphitic carbon units and that it is present primarily as an aromatic hydrogen.

4.3.7 Electron Spectroscopy Analysis

Some preliminary ESCA (electron spectroscopy for chemical analysis) measurements on the calcium free and calcium added chars were made. Calcium was not detected in any of the calcium chars without ion-sputtering of the surface prior to analysis. No difference in the binding energy of the 1s (core) electrons between the calcium added and calcium-free chars of either the oxygen or carbon atoms was observed; however, high resolution measurements were not attempted in this preliminary investigation. Analysis by Auger electron spectroscopy was not successful due to charging of the sample.

4.3.8 Electron Photomicrographs

Selected electron photomicrographs of the C-O char at 0% conversion, the C-3.6 char at 0, 37, 67, and 100% conversion, and the C-$CaCO_3$ char at 20% conversion are presented in Figure 4.3-14 to 4.3-17. The unreacted chars have a rather smooth surface with no indication of any feeder pores. The angular shape of the particles seems to indicate that the particles undergo brittle fracture when crushed. The C-3.6 char is not distinctly different from the C-O char. Sufficient particle to particle variation was observed so that the hemispherical cavities of the particular particle shown in Figure 4.3-14 are not characteristic of all of the C-3.6 char particles.

Reaction of the C-3.6 char to 37 and 67% conversion did not substantially alter the appearance of the particle. The original angular shape of the particles is still very evident. Cracks and fractures in the particles become more prevalent, but the severity of the fractures varied from particle to particle. Other distinct surface features are present on some particles but not on others. For instance, the circular area of very rough surface features on the particle at the tic marks on Figure 4.3-16 was also observed on a number of other particles. However, usually the surface was as shown in Figure 4.3-15c. The origin of the dust-like specks on the particles is not certain, but may have occurred during preparation and handling of the specimen. Dispersive x-ray measurements gave no indication of calcium agglomeration; measurements continually showed that the calcium remained well distributed.

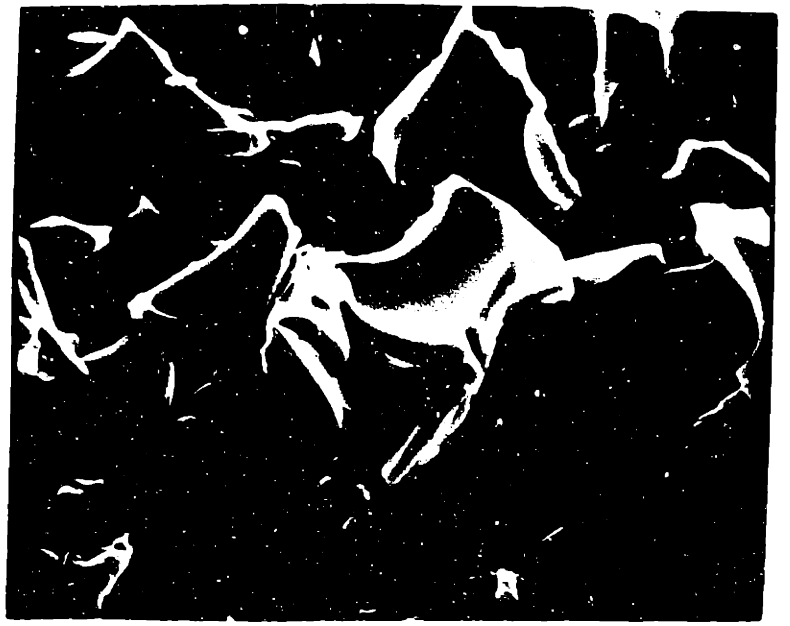

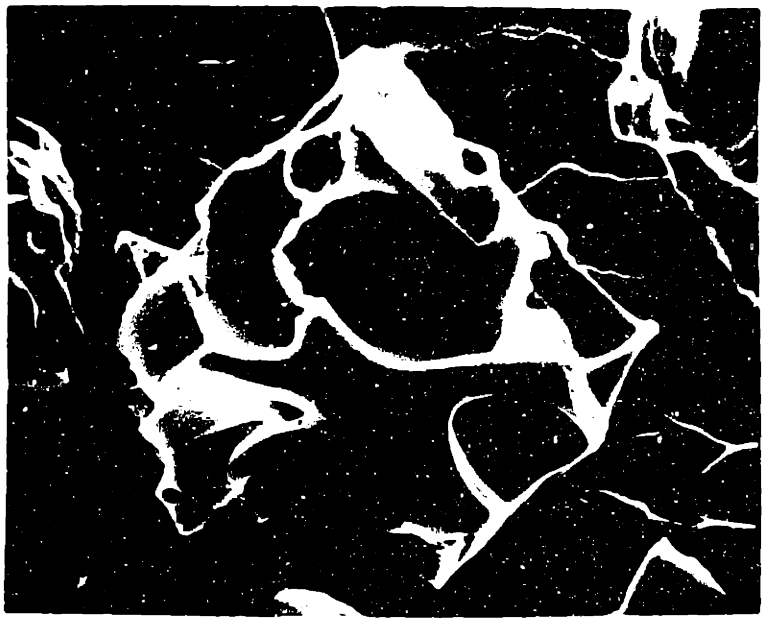

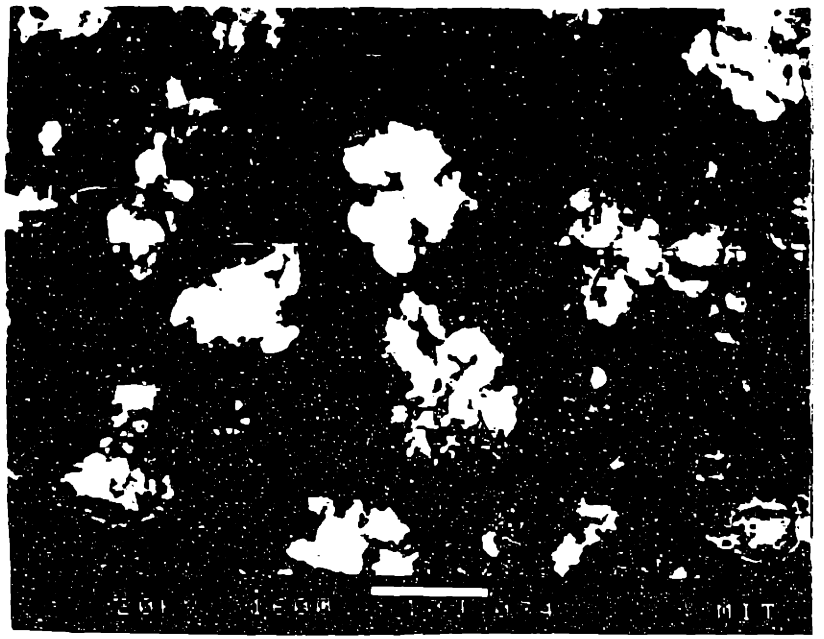

Figure 4.3-14. A. C-O char heat treated at 1300 K; 0% conversion; B. C-3.6 char heat treated at 1300 K, 0% conversion; C. C-$CaCO_3$ char reacted in CO_2 at 1300 K to 20% conversion.

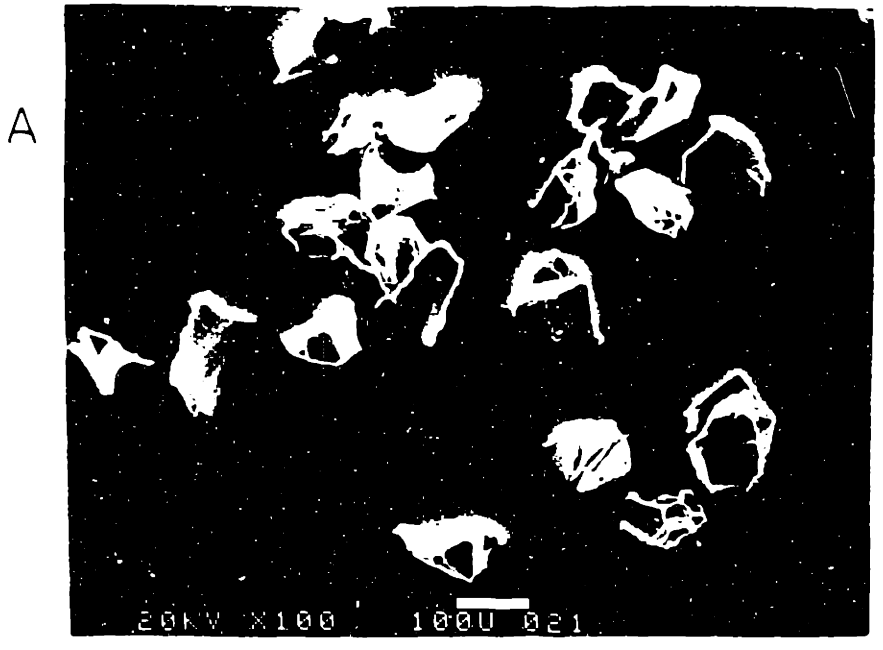

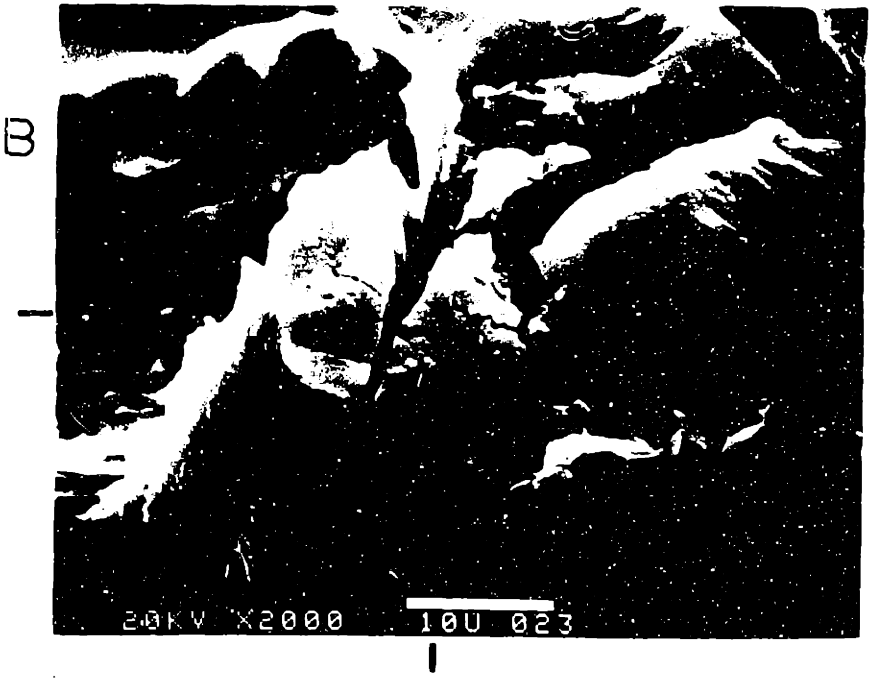

Figure 4.3-15. A, B, and C; C-3.6 char 90-106 μm, heat treated at 1100 K and reacted in air at 615 K to 37% conversion; heat treated at 1100 K after reaction. The tic marks on (B) indicate the area of magnification shown in (C).

Figure 4.3-16. A, B, and C; C.3.6 char 90-106 µm, heat treated at 1100 K and reacted in air at 615 K to 67% conversion; heat treated at 1100 K after reaction. The tic marks on (A) indicate a distinct surface feature noted on some of the particles.

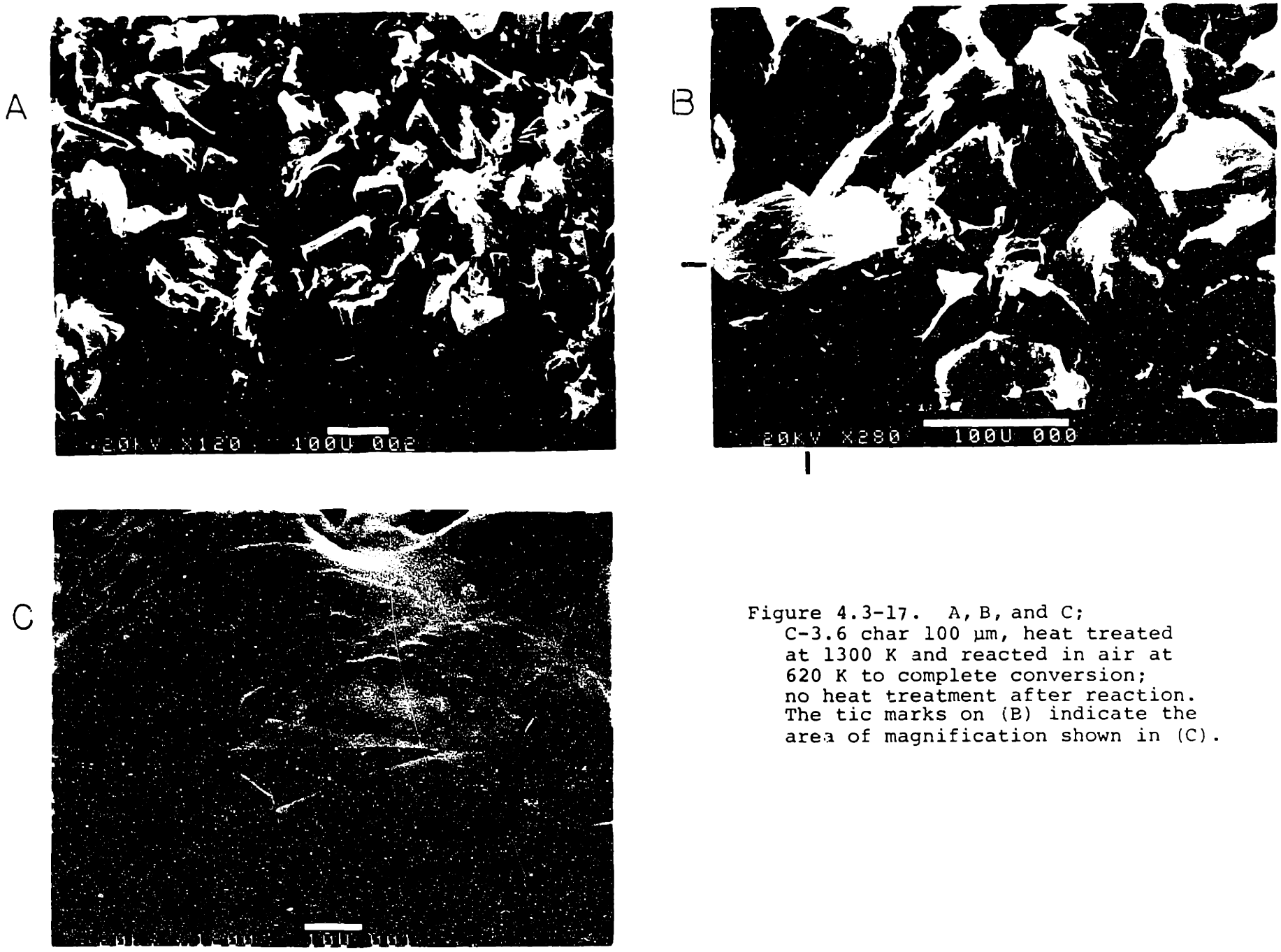

Figure 4.3-17. A, B, and C; C-3.6 char 100 μm, heat treated at 1300 K and reacted in air at 620 K to complete conversion; no heat treatment after reaction. The tic marks on (B) indicate the area of magnification shown in (C).

The most interesting photographs are those obtained at 100% conversion of the C-3.6 char. The residue is probably entirely $CaCO_3$. Examination with an optical microscope showed that the residue consisted of discrete particles of approximately the same size as the original char particle. The residue is an opaque white. The more detailed electron microscope pictures clearly show that the calcium forms a shell-like structure of nearly the same external dimension as the original char particle. Within the main shell, smaller calcium carbonate crystallites are present. The $CaCO_3$ shell appears to be less than 100 Å thick (see Figure 4.3-17). The surface area of the residual calcium must be extremely high. The formation of such a structure can trap residual carbon within an impermeable shell and thus make it inaccessible to the reactant gas. This may account for the failure to successfully burn away the last amounts of carbon in the calcium added chars.

Figure 4.3-14 is a photograph of the C-$CaCO_3$ char. The sample was reacted at 1275 K to 20% conversion in CO_2. The micron sized $CaO/CaCO_3$ particles are well distributed throughout the char. Numerous sub-micron sized holes are present in the carbon surface. The appearance of the surface is quite different from the C-3.6 char. No examination of the same char reacted in air instead of CO_2 was made.

4.4 Calcium Dispersion Measurements

Measurements of calcium dispersion were made in an attempt to relate the extent of dispersion, as a function of carbon

conversion and heat treatment, to reactivity. As the reaction proceeds, $CaCO_3$ (or CaO) formation must occur as carbon is removed. In addition, heat treatment of the char, without reaction, probably causes sintering of the dispersed calcium. Ideally, dispersion measurements could elucidate the behavior of the calcium on the carbon and provide some information on the interaction between the catalyst and the carbon.

The initial calcium dispersion in the unreacted saccharate char is probably high, since reactivity was found to be proportional to the amount of calcium. Had significant agglomeration occurred during pyrolysis of the saccharate and subsequent heat treatment of the char, it is unlikely that a linear relationship between calcium content and reactivity would have been observed.

Radovic (1982) has shown by means of x-ray diffraction studies that CaO formation does occur with heat treatment. Unfortunately, this technique is unlikely to provide a quantitative relationship between reactivity and dispersion when the initial dispersion is on an atomic scale. Determination of grain size by the Scherrer equation is applicable to grains in the range of 100-800 Å. If one assumes that the active calcium atoms are those in direct contact with carbon, x-ray diffraction techniques will provide information only for grains where 1-10% of the total calcium atoms are present as surface atoms. The fraction of surface atoms in a CaO crystallite as a function of diameter is given in Figure 4.4-1. (For this calculation, the cell volume of the fcc CaO crystal was taken as 16.76 cc/gmole

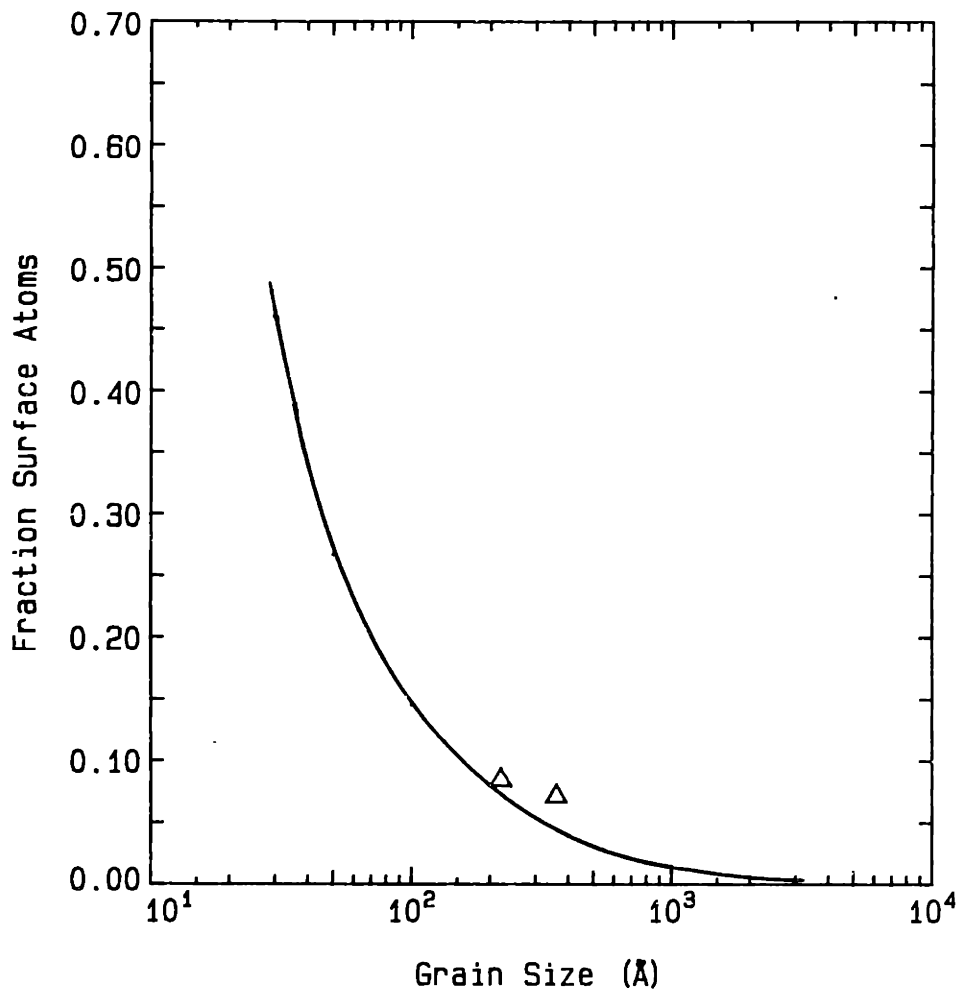

Figure 4.4-1 Fraction surface atoms; (△) calibration points for CO_2 chemisorption at 298 K

(Van Vlack, 1970) and the CaO molecule was assumed to occupy 11.5 $Å^2$ on the crystal surface.) Furthermore, not only is the measurement of calcium dispersion by x-ray diffraction insensitive because the technique is only applicable to grains larger than 100 Å, but also the measured grain size seems to remain essentially constant even as the char undergoes further heat treatment. Results from Radovic's thesis (1982) and measurements obtained in this thesis are summarized in Figure 4.4-2. The data points marked with an (*) are not quantitative; a weak broad peak, just barely distinguishable from the base line, was observed in these cases. With respect to conversion, no CaO or $CaCO_3$ grains were detected by x-ray diffraction measurements below 60% conversion. The results are summarized in Table 4.4-1.

In this thesis, it was attempted to measure calcium dispersion by carbon dioxide chemisorption at 298 K. Preliminary measurements indicated that CO_2 chemisorption at this temperature is probably restricted to the surface molecules of a CaO crystallite. Measurements showed that recarbonation of CaO in the C-$CaCO_3$ char and of the CaO residue after complete conversion of the C-3.6 char was about 7-10%. Crystallite size, calculated by assuming that adsorption is limited to only the surface molecules, was in agreement with the grain size determined by x-ray diffraction. A few calibration points are indicated in Figure 4.4-1.

Although the chemisorption method provided good information on grain size when only CaO was present, it proved to be

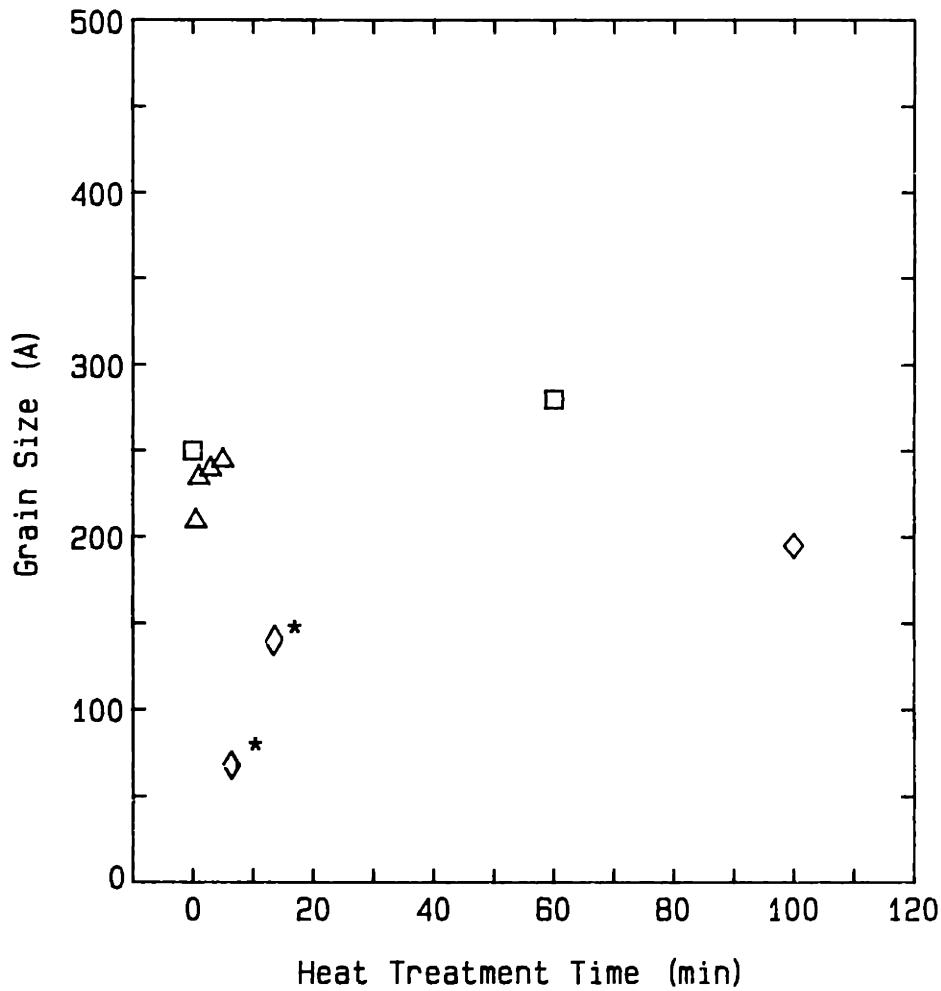

Figure 4.4-2 X-ray diffraction data; (◇) C-3.6 char heat treatment temperature 1300 K; (△, □) data of Radovic (1982), heat treatment temperature 1300 K; (△) rapid heating rate; (□) slow heating rate

Table 4.4-1. Grain Size Determined by X-Ray Line Broadening.

C-3.6 Char (3.6 wt% Ca)

Conversion (%)	Heat Treatment (1100 K)	Temperature (1300 K)
25	no peak	no peak
55	no peak	no peak
100	200 Å (1)	360 Å (2)

(1) 37 $2\theta^{o}$ peak: 238 Å; 54 $2\theta^{o}$ peak: 160 Å

(2) also obtained a $CaCO_3$ peak: 200 Å

difficult to interpret the adsorption data obtained with the C-3.6 char and the ion-exchange char. The total calcium in these chars can be divided into four forms:

$$Ca_T = Ca_C + Ca_I + Ca_S + Ca_g \qquad (4.4.1)$$

where Ca_T is the total calcium in the char; Ca_C is any calcium that may have formed surface complexes with the carbon; Ca_I is inaccessible calcium bound up inside the carbon; Ca_S is calcium on the surface of crystallites; and Ca_g is calcium in crystallites, but not on the surface.

Initially, it was thought that only the calcium as Ca_S would chemisorb CO_2. Then, if Ca_g could be determined, for instance by adsorbing CO_2 at an elevated temperature, a crystallite size could be estimated if a uniform grain size is assumed. Unfortunately, the calcium as Ca_C also reacted with the CO_2. This fact, along with certain other seemingly anamolous results made interpretation of the data, based on only a measurement of weight change, intractable.

Chemisorption measurements with the C-ion char are presented in Figures 4.4-3 to 4.4-4. Ca_I for this char is assumed to be 0. The char was heat treated in situ to 1100 K prior to the adsorption measurement. CO_2 adsorption at 298 K was about 120% (g CO_2 per g CO_2 at 100% recarbonation X 100). About 40% adsorbed almost immediately, whereas the remainder adsorbed over a 30 minute period. At the conclusion of the adsorption measurement, the sample was heated in nitrogen at a rate of 36 C/minute to 1100 K (825 C) and held isothermally at 1100 K for 8 minutes. Weight loss (as a percentage of the weight gained

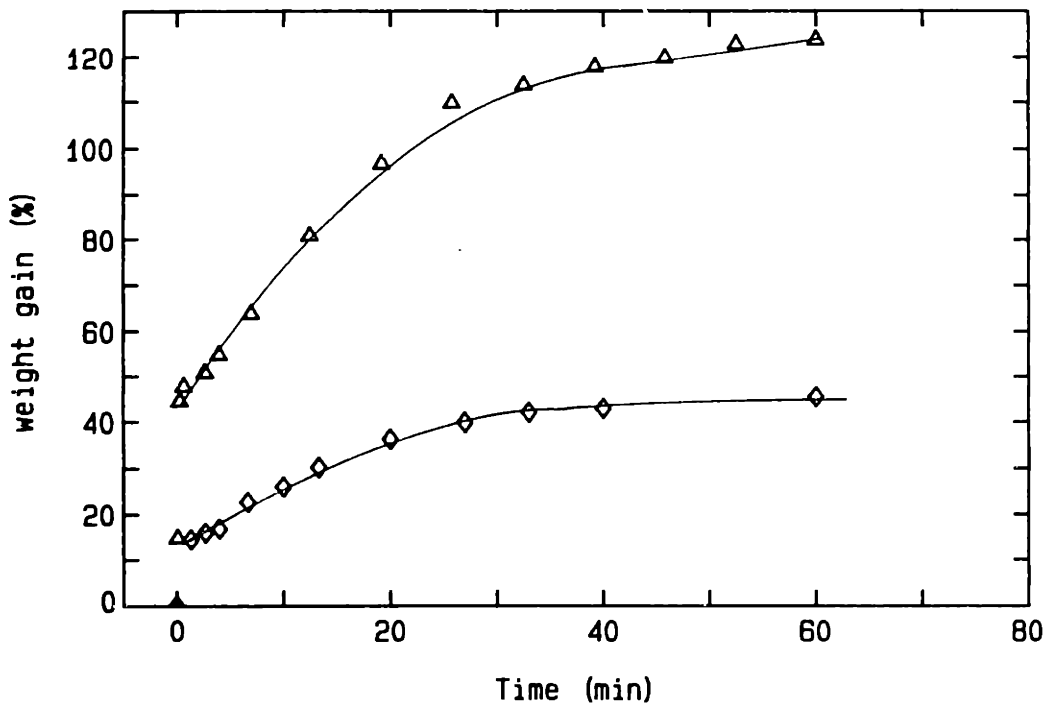

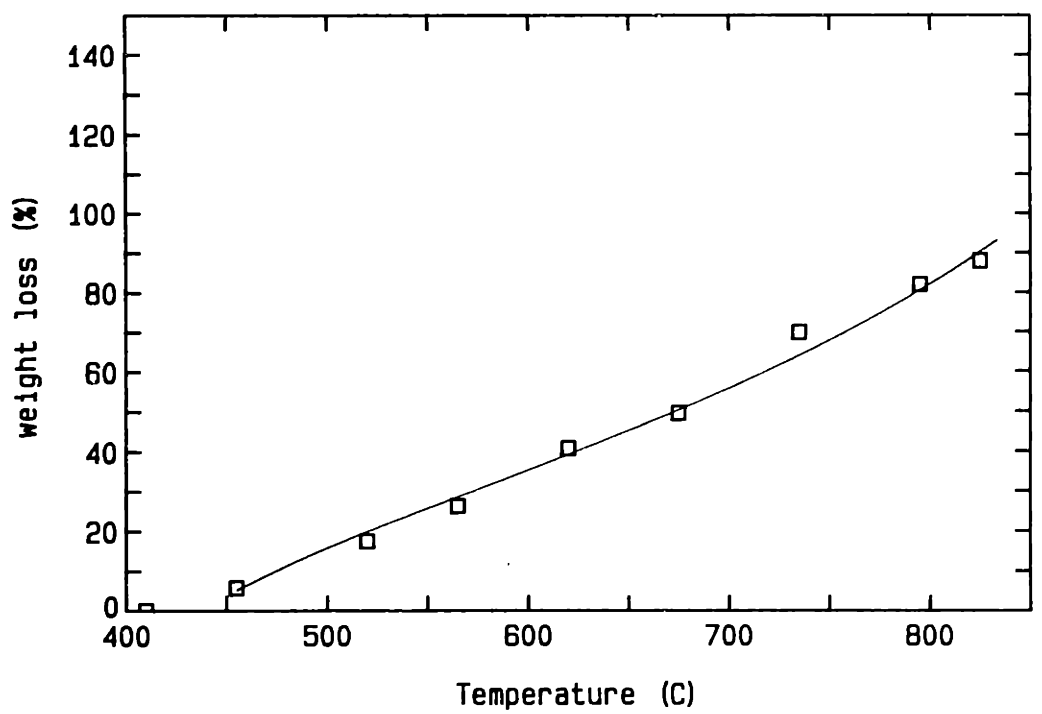

Figure 4.4-3 CO_2 adsorption on the C-ion char at 298 K; heat treatment temperature 1100 K; 0 conversion; adsorption: △ (1^{st} cycle); ◊ (2^{nd} cycle); desorption: (□) (desorption data at a constant heating rate of 36 C/min).

during adsorption) from the sample as a function of temperature is also shown in Figure 4.4-3. (Additional weight loss occurred during the isothermal period, which is not shown in the figure.) After the second heat treatment, another adsorption measurement was made. This time, CO_2 adsorption was only 40%, and both the rapid and gradual adsorptions were less. It is unclear why the difference between the two cycles should be so large. It seems unlikely that sintering or agglomeration of calcium during the second heat treatment cycle can cause such a large difference. One possible explanation is that not all the CO_2 was removed from the calcium that is present as Ca_c during heat treatment after the first cycle. CO_2 adsorption measurements were also done at 700 K with the C-ion char. Figure 4.4-4 presents the data obtained for the first adsorption cycle, desorption, and the second adsorption cycle. Again there is a considerable difference in the amount adsorbed in the two cycles, but adsorption in the first cycle in this case does not exceed 100%. In this case, however, the amount desorbed after the first cycle is greater than the amount adsorbed.

A comparison of CO_2 desorption from chars where calcium is present primarily as calcium carbonate crystallites to the C-ion data shows a marked difference. Figure 4.4-5 shows the adsorption and desorption data obtained with the C-$CaCO_3$ char. Here desorption begins at 875 K (600 C), and it is completed by 925 K (650 C). Weight loss occurs rapidly and over a specific temperature range, and the weight loss is exactly equal to the amount of CO_2 adsorbed. Differences in the desorption curves of

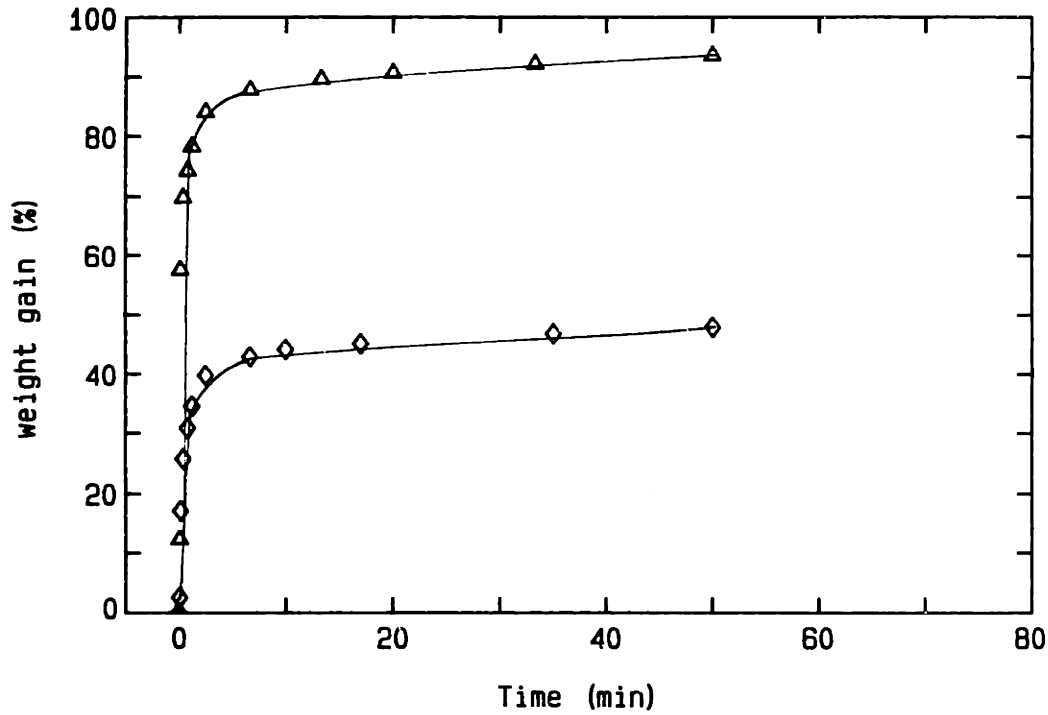

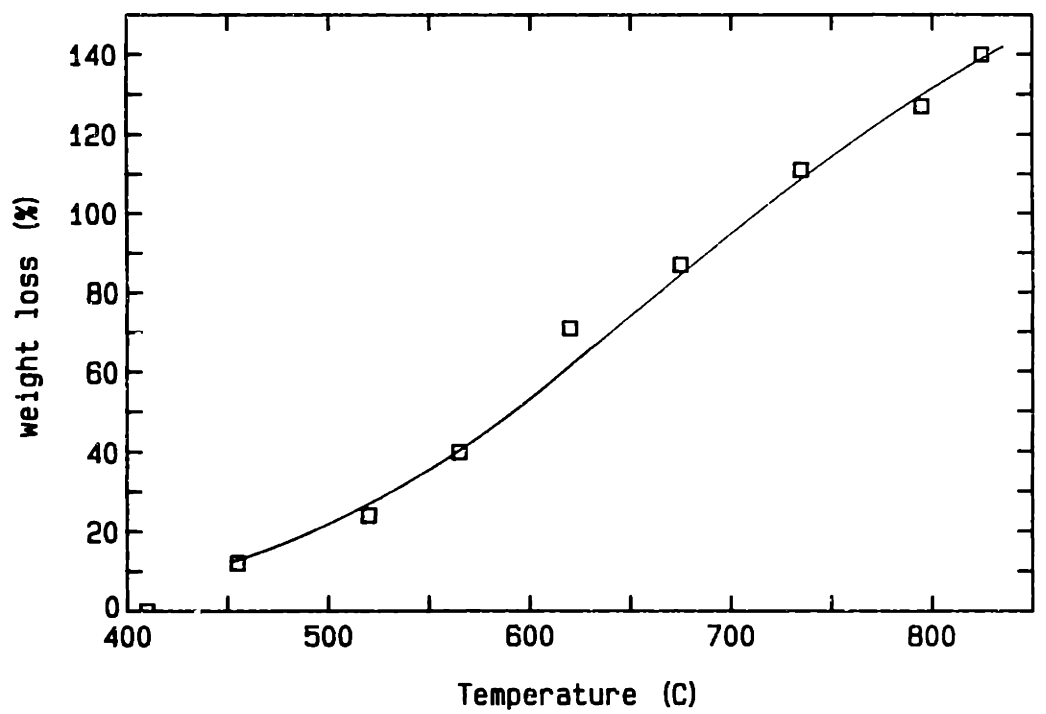

Figure 4.4-4 CO_2 adsorption on the C-ion char at 700 K; heat treatment temperature 1100 K; 0 conversion; adsorption: Δ(1^{st} cycle); ◊ (2^{nd} cycle); desorption: (□) (desorption data at a constant heating rate of 36 C/min).

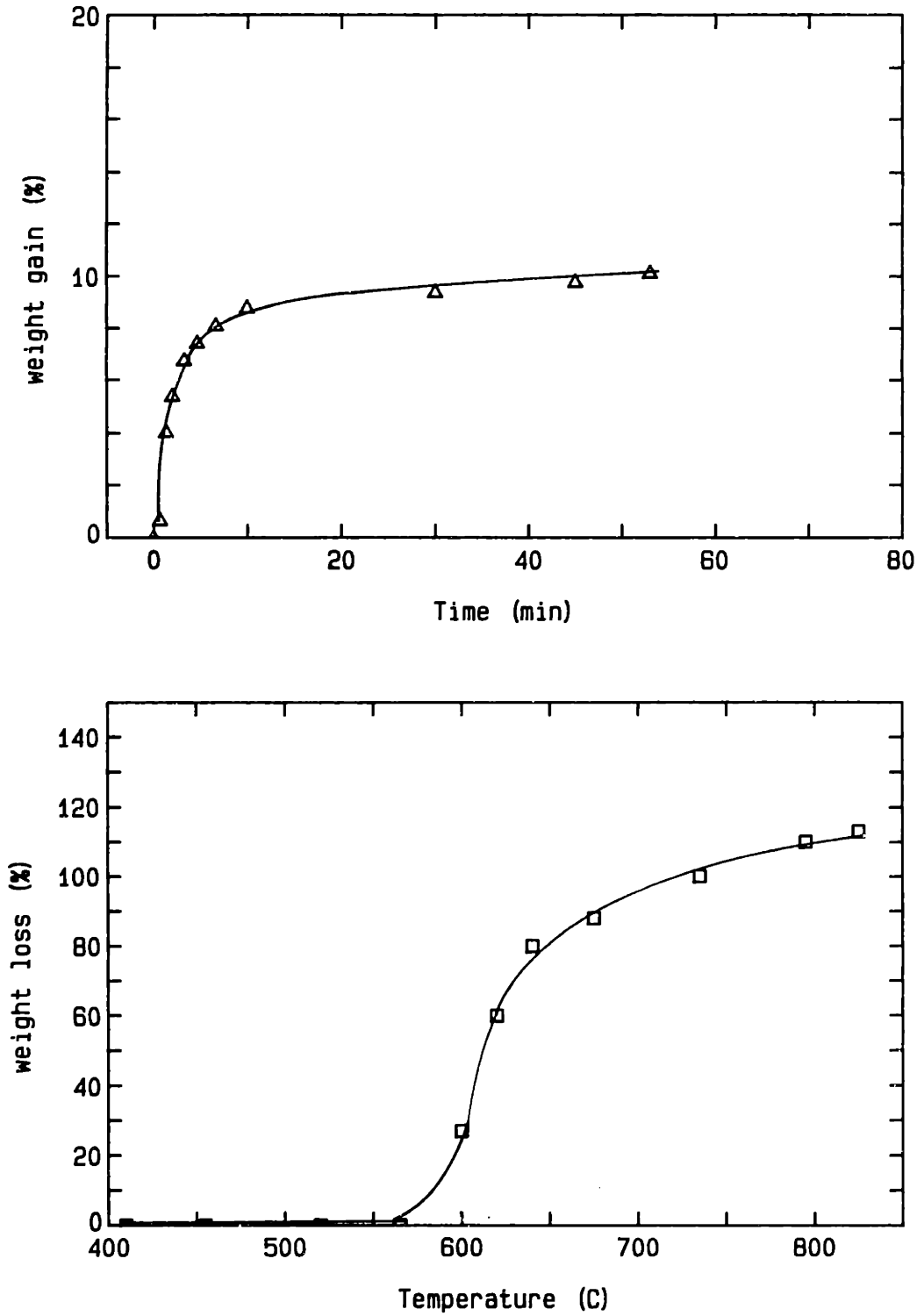

Figure 4.4-5 CO_2 adsorption on the C-$CaCO_3$ char at 298 K; heat treatment temperature 1100 K; 0 conversion; adsorption: (Δ); desorption: (□) (desorption data at a constant heating rate of 36 C/min).

the C-$CaCO_3$ char and the C-3.6 char, in which the calcium is also well dispersed, are further illustrated by adsorption/desorption data obtained at 940 K when the gas composition was switched from nitrogen to CO_2 and back to nitrogen (Figure 4.4-6 and 4.4-7). The C-$CaCO_3$ char lost all of its CO_2 over a short time period, but this occurred only after a lengthy induction period. (The same induction period was also observed when this experiment was conducted with calcined reagent grade $CaCO_3$.) This induction time did not occur because of a failure to reduce the CO_2 concentration in the gas to below its equilibrium value. Gas flow rates were sufficiently high so that the CO_2 partial pressure should have decreased rapidly to below the 0.05 atmosphere equilibrium pressure; rather the induction time apparently represents a true nucleation time (Young, 1966). For the C-3.6 char, the desorption curve is quite different. Weight loss occurs immediately after the gas composition is switched and it continues at a gradual rate over a much longer time period. The total weight loss also exceeds 100%, indicating that the decomposition reaction involves the carbon substrate. Weight loss occurring prior to the switch to nitrogen is probably due to the carbon-CO_2 reaction.

Results obtained with the C-3.6 char, at conversions of 0, 37, 67, and 100% are presented in Appendix 5. All samples were heat treated at 1100 K, reacted in air at 615 K and reheated again (outgassed) prior to the adsorption measurement (conversion is based on the final sample weight). CO_2 adsorption in the second cycle is always less than in the first

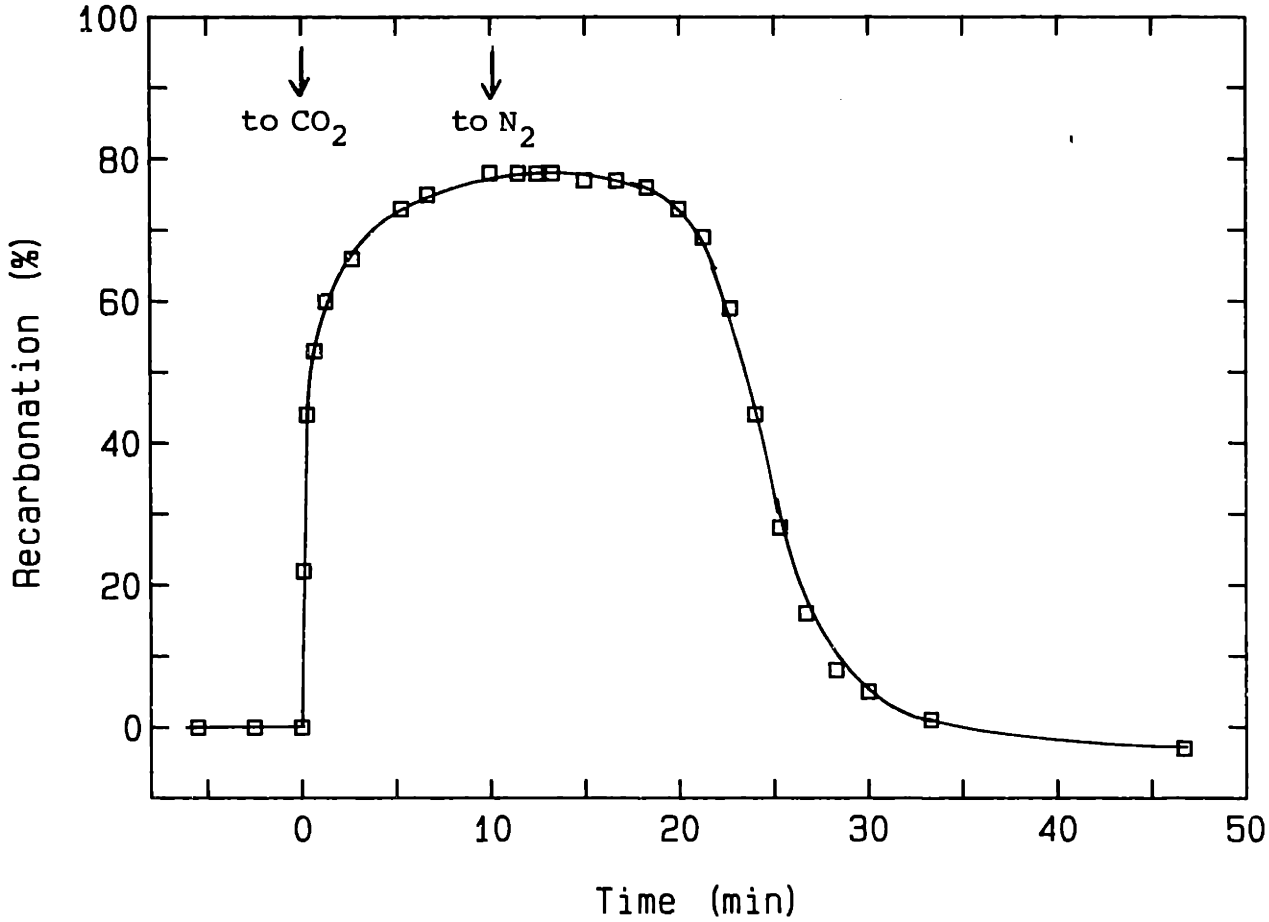

Figure 4.4-6 CO_2 adsorption and desorption at 940 K on the C-$CaCO_3$ char.

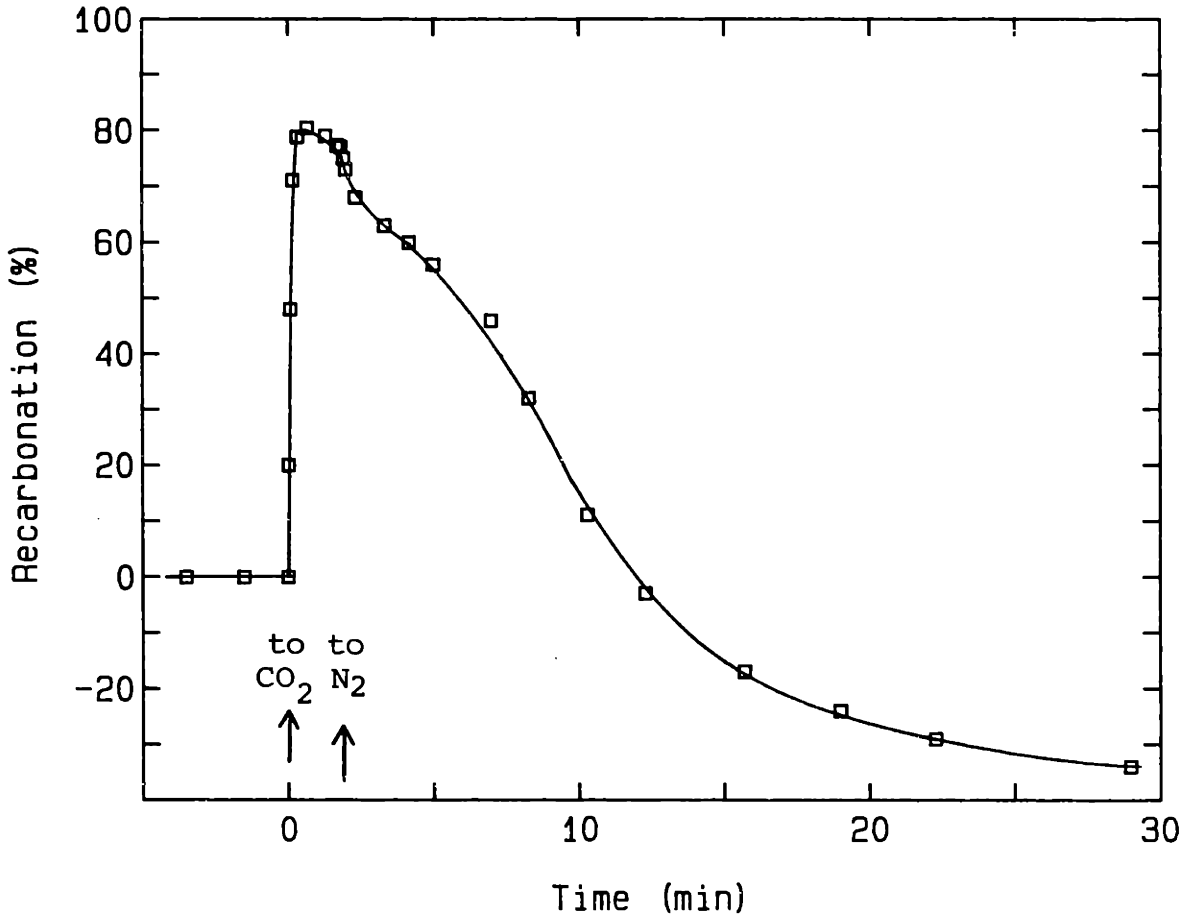

Figure 4.4-7 CO_2 adsorption and desorption at 940 K on the C-3.6 char.

cycle; however with this char, more CO_2 is adsorbed at 700 K than at 298 K. Only a small change in the amount of CO_2 adsorbed with increasing carbon conversion was measured. The shape of the adsorption isotherm change slightly with increasing carbon conversion. Except for the first desorption cycle of the char at zero conversion, the amount desorbed always exceeded the amount adsorbed.

Because of a lack of understanding of the chemistry between CO_2 and calcium present as a complex with the carbon there is some uncertainty in the interpretation of these results. Neither the adsorption or desorption curves provide any information that allows an unambiguous identification of the various calcium species or that even provides some characteristic data that can be correlated with reactivity.

CHAPTER 5. DISCUSSION

The discussion will focus on three main topics, each of which can be treated separately. Together they form an overall picture of intrinsic char gasification. In each case, the relevant experimental data will be summarized to provide a basis for the discussion. The topics are: 1) surface area development in microporous chars and modeling of the rate versus conversion data; 2) kinetic mechanisms for the carbon gasification reactions; and 3) analysis of the reactivity data from both the catalyzed and non-catalyzed chars to test possible mechanisms for catalytic gasification.

5.1 CHAR STRUCTURE AND UTILIZATION OF THE CARBON SURFACE DURING REACTION OF A MICROPOROUS CHAR

5.1.1 Introduction

The principal points addressed in this section are:

1. How do the rate versus conversion data compare to the surface area variations of the char with conversion? Theoretical analysis of the rate versus conversion data generally assumes that the variation in reactivity is due to changes in the surface area of the solid; yet there are few studies in which measurements of both surface area and reactivity with respect to conversion have been made.
2. What is the effect of the pore size distribution of the char on the rate versus conversion profiles? Compared to

most coal chars, the sucrose char used in these experiments contains no macropores and has a relatively uniform pore size distribution. It was, therefore, possible to determine the reaction profiles of the microporous char directly without consideration of a feeder pore network.

Theoretical models have been developed to predict the evolution of surface area with conversion. These models relate the surface area to the pore size distribution of the solid and provide a deterministic description of the surface area in terms of the porosity. Such models can be used to bound surface area variations with respect to changes in the pore volume of either the micropores or macropores or both.

5.1.2 Modeling of the Rate Versus Conversion Data

Theoretical analysis of the rate versus conversion data generally assumes that the variation in reaction rate is due to a change in the surface area on which the reaction occurs. It is assumed that the reaction rate per unit surface area remains constant and that the reactivity is proportional to the surface area of the solid. Usually the surface kinetics are given by the steady state solution of a Langmuir-Hinshelwood rate expression that gives the correct reaction order. Since mass transport of reactant in the solid in the intrinsic reaction regime is not rate limiting, it is postulated that the relative changes in reaction rate with

conversion should be the same for all reactants and reactant concentrations and at all temperatures for which the assumption of intrinsic kinetics is valid.

Formally, this result is obtained as follows. The conversion, x, is only a function of the distance, q, by which the solid surface receeds:

$$x = S(q) \qquad (5.1.1)$$

Note that q may be a function of the position within a particle; it is only assumed that any spatial dependence is independent of temperature in the intrinsic reaction regime. The rate is given as:

$$\frac{dx}{dt} = \frac{dS}{dq} \cdot \frac{dq}{dt} \qquad (5.1.2)$$

where dq/dt is the rate at which the surface receeds. The recession rate does not necessarily have to be a constant, but it is assumed to be independent of conversion. Furthermore, since x is a function of q only, dS/dq can be expressed as a function of x only:

$$\frac{dx}{dt} = G(x) \cdot \frac{dq}{dt} \qquad (5.1.3)$$

Integration of Equation (5.1.3) yields:

$$\int_0^x \frac{dx'}{G(x')} = \int_0^t \frac{dq}{dt}\, dt$$

and

$$I(x) = \int_0^t \frac{dq}{dt}\, dt \qquad (5.1.4)$$

where I(x) is the value of the integral on the LHS of (5.1.4). If the RHS can be scaled with respect to time, then all the data will lie on a single curve that is a function of the scaled variable. This will be the case for certain expressions of dq/dt; for example if

$$\frac{dq}{dt} = k \cdot P_{O_2} \qquad (5.1.5)$$

then

$$I(x) = k\, P_{O_2} \cdot t \qquad (5.1.6)$$

Let $t_{0.5}$ equal the time at 50% conversion, then

$$I(0.5) = k\, P_{O_2}\, t_{0.5} \qquad (5.1.7)$$

and dividing (5.1.6) into (5.1.7) gives:

$$\frac{I(x)}{I(0.5)} = \frac{t}{t_{0.5}} = \tau \qquad (5.1.8)$$

which is independent of temperature or reactant concentration.

Furthermore, because τ is only a function of x, it is possible to express the conversion in terms of τ:

$$x = F(\tau) \qquad (5.1.9)$$

Substitution of (5.1.9) into Equation (5.1.3) gives:

$$\frac{dx}{dt} = G_1(\tau) \cdot \frac{dq}{dt} \qquad (5.1.10)$$

The reaction rate in equations (5.1.3) or (5.1.10) can be scaled with respect to the surface reaction rate constant if G and G_1 are functions of x and τ only, respectively. The Crucial assumptions needed to obtain these scaling laws are that the surface kinetics are independent of conversion, that surface area evolution is the same at different reaction temperatures, and that the surface reaction rate can be adequately represented by a single rate constant over the entire conversion range.

As stated previously, the function G(x) is usually assumed to represent the total surface area of the solid with respect to conversion, although this is not a necessary condition of the analysis. However, it seems reasonable to assume that the reaction rate on all surfaces is the same in the intrinsic reaction regime. Furthermore, the development of deterministic models to describe the surface area in terms of the porosity of the solid allows one to predict changes in surface area with conversion. The conversion is directly related to the porosity of the solid if the total surface area is much greater than the external particle area. In this study, the relationship between the porosity of the solid and the surface area was determined by the random pore model.

5.1.3 Random Pore Model of a Porous Solid

The random pore model is an elegant model that provides deterministic values for geometric quantities that exactly characterize the solid. The porosity of the solid is modeled as overlapping cylindrical pores that are randomly and isotropically orientated in the solid. The mathematical description is identical whether these pores are segments or transverse the entire particle. The random pore model can be considered to be one kind of geometric description of the pores in a solid.

The application of this model to char gasification was first described by Gavalas (1980). In his application, Gavalas assumes the surface reaction rate to be the same in all pores and that no new pores open or become accessible as gasification of the solid occurs.

The random pore model assumes that the solid is intersected by straight lines, randomly orientated in space, which represent the axial center lines of the pores. Such a distribution of lines in space can be described by a Poisson process that can be completely characterized by a single parameter (Gavalas, 1980). It can then be shown that the probability that a point within the solid is at a distance r or larger from each line (i.e., a point is not intersected by a pore of radius r) is (Gavalas, 1980):

$$(1 - \epsilon) = \exp[-2\pi B_o r^2] \qquad (5.1.11)$$

where ϵ is the porosity of the solid, and therefore, $(1 - \epsilon)$ is the probability that a point is not in a pore. B_o is the parameter of the Poisson process and is defined as the number of pores of radius r intersecting a surface element in space. Note that the pores intersect a surface at random angles to the surface normal, and therefore, the pore intersection will appear as an ellipse. The average area of an intersection of the surface is $2\pi r^2$.

The model can be extended to include a distribution of pore sizes (Gavalas, 1980). Let $\lambda(r)\, dr$ be the number of intersections of pores with radius in $(r, r+\Delta r)$ with any surface element. $\lambda(r)$ is a density function characterizing the porosity of the solid. For a distribution of pore sizes, the probability that a point is not in a pore is:

$$1 - \epsilon = \exp[-2\pi \int_{r_*}^{r^*} \lambda(r)\, r^2\, dr] \qquad (5.1.12)$$

r_* and r^* are the lower and upper limits of the distribution, respectively. Or in a terms of a porosity distribution function, instead of the total porosity:

$$\epsilon(r) = 1 - \exp[-2\pi \int_{r}^{r^*} \lambda(R)\, R^2\, dR] \qquad (5.1.13)$$

where $\epsilon(r)$ is the volume occupied by pores of radius r to r^* (or the probability that a point is in a pore of radius r to r^*) and R is the integration variable. This pore volume will

include any overlap volume of pores with radius less than r intersecting pores of radius $\geq$ r.

Now $\epsilon(r)$ is precisely equivalent to the pore volume measured by mercury porosimetry or obtained from the desorption curve of nitrogen adsorption measurements. In each case, the experimental measurements will include the overlap volume of smaller pores intersecting larger pores. The experimentally measured pore volume distribution function is the integral of the pore size density distribution function:

$$\epsilon(r) = \int_{r_*}^{r} -v(R)\, dR \qquad (5.1.14)$$

The negative sign occurs because in each case $d\epsilon$ is the volume of pores between r and $r-\Delta r$.

Differentiation of Equation (5.1.13) by Leibnitz's Rule yields:

$$\frac{d\epsilon}{dr} = -2\pi r^2 \lambda(r) \exp[-2\pi \int_{r}^{r^*} \lambda(R)\, R^2 dR] \qquad (5.1.15)$$

Elimination of ϵ by Equation (5.1.14) gives a relationship between $\lambda(r)$ and the experimental pore size density function $v(r)$ (Gavalas, 1980):

$$\lambda(r) = \frac{1}{2\pi r^2} \frac{v(r)}{1 - \int_r^{r^*} v(R)dR} \qquad (5.1.16)$$

So far it has been shown that the parameter $\lambda(r)$ can be determined exactly from experimental data since the measured pore volume also includes the overlap volume of smaller pores.

As gasification of the solid occurs, the pores will increase in radius by length q(t). However, the parameter (r) is the same as at t = 0. That is, although the radius of the pores increases with time, $\lambda(r)$, the probability density function that characterizes the initial porosity of the solid, does not change with time.

The porosity of the solid, as the pore radius increases by length q, is therefore:

$$\epsilon(q) = 1 - \exp[-2\pi \int_{r_*}^{r^*} (r + q)^2 \lambda(r)dr] \qquad (5.1.17)$$

Expanding the quadratic term and noting that q is not a function of r, one obtains:

$$1 - \epsilon(q) = (1 - \epsilon_T)\exp[-2\pi(B_o q^2 + 2 B_1 q)] \qquad (5.1.18)$$

where $(1 - \epsilon_T) = \exp[-2\pi \int_{r^*}^{r^*} r^2 \lambda(r)dr]$ (5.1.12)

$$B_o = \int_{r_*}^{r^*} \lambda(r)dr \quad (5.1.19)$$

$$B_1 = \int_{r_*}^{r^*} r\,\lambda(r)dr \quad (5.1.20)$$

B_o and B_1 are the zeroeth and first moments of the probability density function, $\lambda(r)$. B_o and B_1, therefore, are not arbitrary parameters of the model, but can be calculated from the initial pore size density distribution function of the solid. Particle shrinkage was neglected in determining conversion since the particle radius is usually much greater than q. Therefore, the change in particle porosity can be identified directly with the conversion of the solid:

$$(1-x) = \frac{1 - \epsilon(q)}{1 - \epsilon_T} = \exp[-2\pi(B_o q^2 + 2B_1 q)] \quad (5.1.21)$$

Differentiation of Equation (5.1.21) gives:

$$\frac{dx}{dq} = 4\pi(B_o\, q + B_1)\exp[-2\pi(B_o q^2 + 2\, B_1\, q)] \quad (5.1.22)$$

Solving equation (5.1.21) for q one obtains:

$$q = \frac{-B_1}{B_o} + \frac{B_1}{B_o}\left[1 - \frac{B_o}{B_1^2 2\pi} \cdot \ln(1-x)\right]^{1/2} \qquad (5.1.23)$$

Finally, substitution of (5.1.21) and (5.1.23) into (5.1.22) yields:

$$\frac{dx}{dq} = 4\pi(1-x)\, B_1 \left[1 - \beta \ln(1-x)\right]^{1/2} \qquad (5.1.24)$$

where $\beta = B_o/2\pi B_1^2$

In terms of conversion:

$$\frac{dx}{dt} = \frac{dx}{dq} \cdot \frac{dq}{dt} = 4\pi(1-x)B_1[1 - \beta \ln(1-x)]^{1/2} \cdot \frac{dq}{dt} \qquad (5.1.25)$$

where dq/dt is the velocity with which the surface receeds. Since the total reaction rate can be written as:

$$\frac{dx}{dt} = S(x) \cdot \rho_s \frac{dq}{dt} \qquad (5.1.26)$$

where S(x) is the available surface area per gC, ρ_s is the density of the solid, and $\rho_s \cdot dq/dt$ is the rate per unit surface area ($g/cm^2.sec$). The surface area from Equation (5.1.25) is therefore:

$$S(x) = 4\pi(1-x)\, B_1 \left[1 - \beta \ln(1-x)\right]^{1/2} \left[(1-\epsilon_T)/\rho_p\right] \qquad (5.1.27)$$

where ρ_p is the initial paricle density and ϵ_T is the initial porosity. Normalization of S(x) to the surface area at 0% conversion yields:

$$S(x)/S_o = 4\pi(1-x)\cdot[1-\beta\ln(1-x)]^{1/2} \qquad (5.1.28)$$

Note that except for a multiplicative constant, the change in surface area with respect to conversion depends on only a single parameter, β. Furthermore, the change of surface area with conversion is independent of the rate at which the carbon surface receeds. The surface reaction rate need not be constant, but it must be the same in all pores and must be independent of conversion. If $\beta < 2$, Equation (5.1.28) predicts that the surface area will monotonically decrease with conversion. Values of $\beta > 2$ will give a curve with a maximum. The location of the maximum will depend on β, but will always be between:

$$0 < x < 1-e^{-0.5} \qquad (5.1.29)$$

This result can be obtained directly by determining the location of the maxima of Equation (5.1.28). Physically, this result means that at conversions above 40%, the loss of surface area because of pore coalescence outweighs the increase in surface area due to pore enlargement. In this model, it is these two competing mechanisms that are responsible for the variations in surface area with

conversion. Equation (5.1.28) for various values of β is shown in Figure 5.1-1. The equation has a high degree of flexibility, changing β yields, in one limit, a straight line, and in the other limit, large maximum values for S(x).

Note also that if the pores are shaped like slits rather than cylinders, no increase in surface area with conversion will occur. In this case, equation (5.1.11) would be $(1-\epsilon) = \exp[-B_o\, m \cdot r\, \Delta\ell]$ where r is the length of the pore, $\Delta\ell$ is the pore width ($r >> \Delta\ell$), and m is a constant that represents an average area of intersection for all angles to the surface normal and pore orientations. Increasing r with conversion, however, will not substantially change the surface area of the pore.

The parameter β is not an empirical parameter but can be determined a priori from the initial pore size density distribution of the char by Equations (5.1.16), (5.1.19) and (5.1.20). This allows one to compare measured surface areas to calculated values, in terms of this model, based on the initial pore size distribution of the char. Such a check can be used to judge the validity of a random pore description of a solid or to provide some guidance for the interpretation of experimental data. A value for β can, of course, also be determined directly from either surface area or rate versus conversion data by plotting $[S(x)/S_o/4\pi(1-x)]^2$ against $\ln(1-x)$.

With the assumption of monosized pores, the parameter β depends only on the initial porosity of the char:

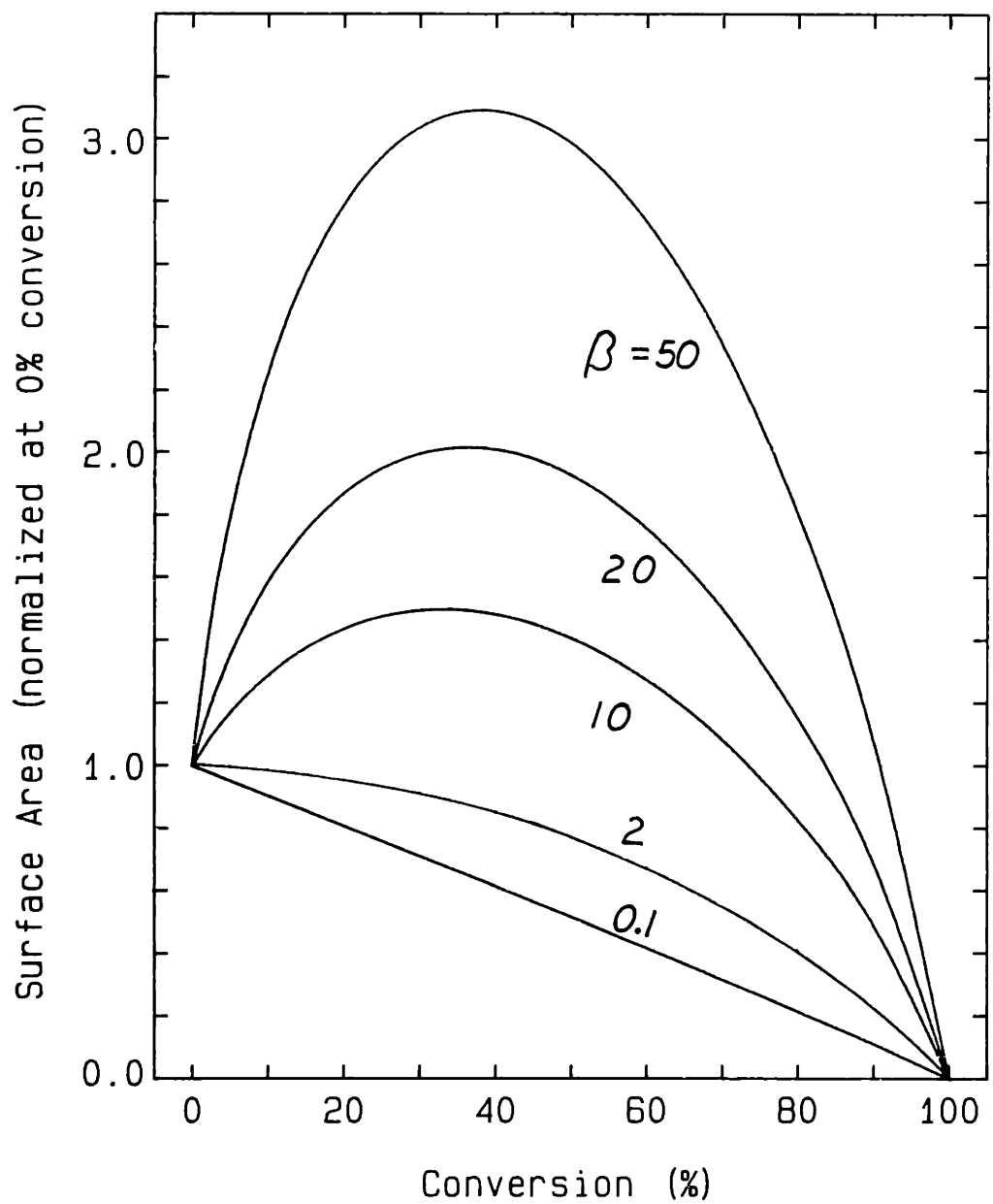

Figure 5.1-1. Random pore model for different values of the parameter β.

$$\beta = \frac{-1}{\ln(1-\epsilon)} \qquad (5.1.30)$$

Therefore, large values of β correspond to a low initial porosity and the maximum surface area near $x = 1 - e^{-0.5}$. In this case, there are few pores and pore enlargement will dominate until the critical conversion is reached. If the initial porosity is greater than 0.4, β is less than 2 and the surface area will monotonically decrease with conversion. Furthermore, percolation theory predicts particle disintegration should occur at a porosity of 0.68 for randomly orientated mono-sized pores (Kerstein and Niska, 1984).

In order to determine the surface area variations predicted by this model for a microporous char, values of β were determined for a number of simple pore size density distributions. Pore size distributions calculated by Barrett et al. (1951) from nitrogen desorption measurements show that the distribution in microporous chars can be adequately represented by simple analytical functions. Because mercury porosimetry measurements gave no indication of any pores larger than 200 Å in diameter in the sucrose char, it was assumed that the pore size distribution for this char is similar to the distributions measured by Barrett et al. The results of these calculations are summarized in Table 5.1-1. Calculations were made at the same total porosity. Constraints imposed by each distribution function gave slightly different values for the surface area and minimum pore radius in each case. In general, the parameter, β, does

Table 5.1-1. Determination of the Random Pore Model Parameter for Different Distribution Functions.

Pore Size Density Distribution Function	Minimum Pore Radius Å	Maximum Pore Radius Å	Total Porosity (cc/cc)	Surface Area (m^2/g)	β
Monosized Pores	8.1	-	0.31	420	2.7
(1/r)	2.5	40	0.31	420	5.4
Exponential	2.5	-	0.31	300	6.0
Linear	2.5	70	0.31	310	5.8
Actual Char Properties	-	100 Å	0.31	$\sim$ 420	-

not depend strongly on the form of these simple distribution functions, but as expected, it is a strong function of the total porosity. The calculations are presented in detail in Appendix 6.

Comparisons of the model prediction for $\beta = 6.0$ to the surface area data and the reaction profiles of the C-O char are presented in Figure 5.1-2. The model predicts, for a moderately porous char, that the surface area will only increase slightly at low conversions, approach a relatively flat maximum around 20% conversion, and decrease rapidly above 40% conversion. The model results give a good, but not exact, fit to the surface area measurements and the reaction profiles. It cannot predict the initial rapid increase in surface area or the initial rise in the oxygen reaction rate based on the TGA measurements, and it tends to overpredict the rate at high conversions. The results also show considerable difference between the surface area determined by nitrogen adsorption and the reaction rate curves. This lack of direct correspondence between the surface area measurements and the reaction rate is perhaps not completely unexpected because of the difficulty in assessing the actual surface area of a microporous char from nitrogen adsorption measurements. Certainly the trend is in agreement, although the nitrogen surface area measurements did indicate that restricted diffusion occurred initially, which disappeared with further carbon conversion, thus indicating that pore opening takes place as carbon conversion proceeds. This is not reflected in

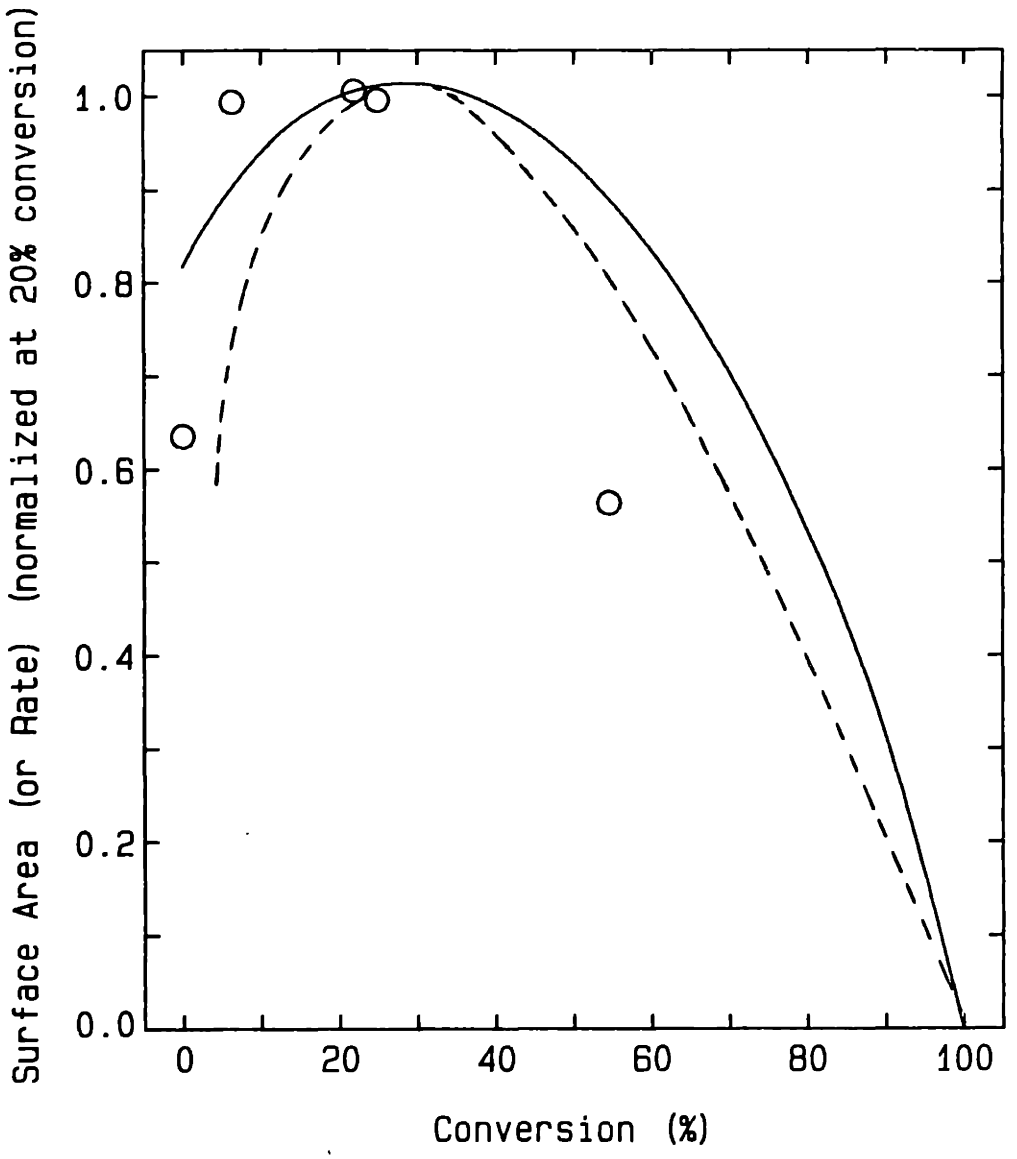

Figure 5.1-2a. Comparison of random pore model (——) to the C-O char - oxygen reaction rate data (---) and surface area measurements (o).

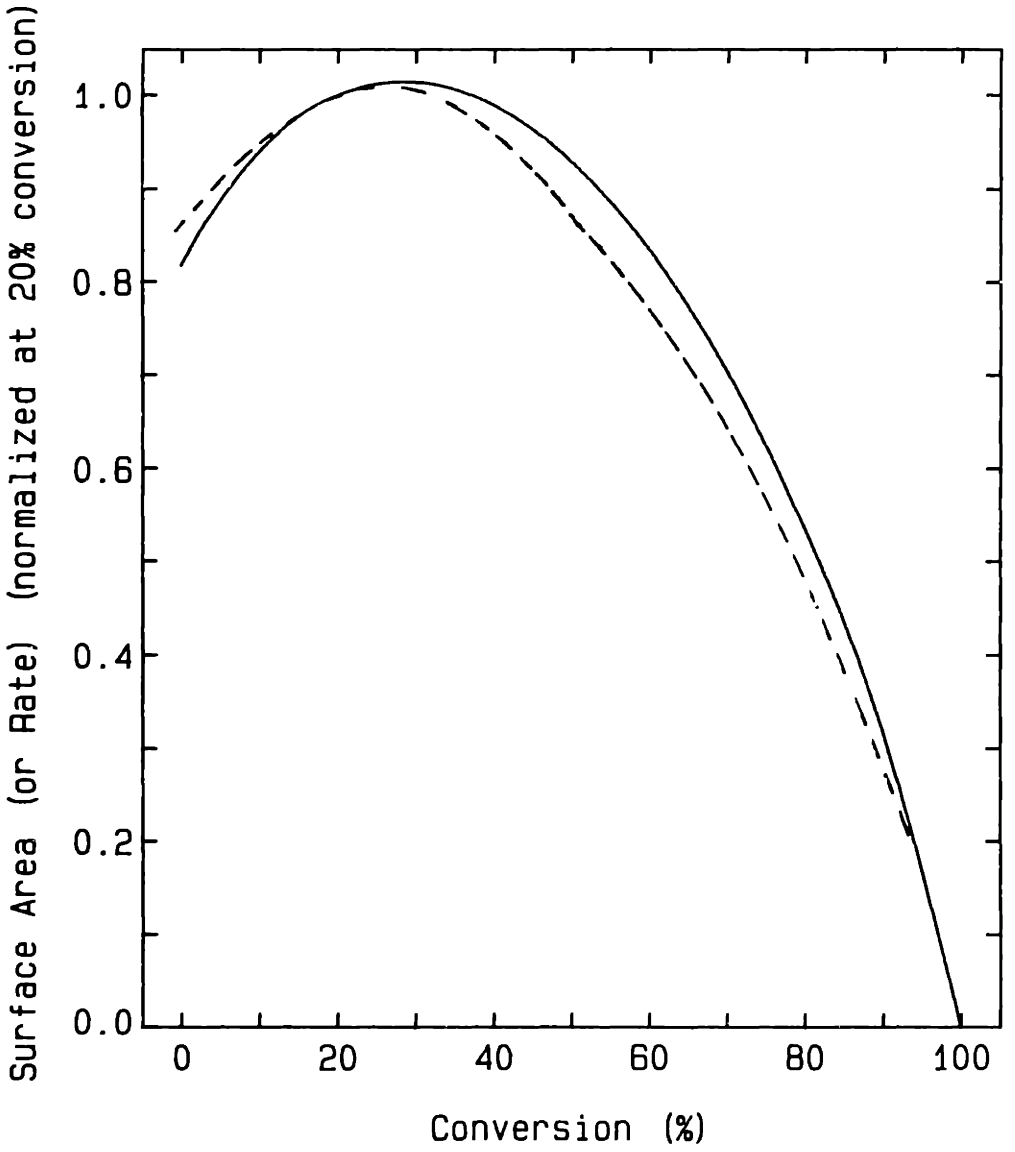

Figure 5.1-2b. Comparison of random pore model (——) to the C-O char - carbon dioxide reaction rate data (----).

the rate versus conversion data of the CO_2 reaction and also probably not reflected in the actual oxygen reaction rate (as compared to the oxygen TGA data). The reason the CO_2 and oxygen TGA data are different over the initial conversion range is further discussed in the next section. Although the model gives a reasonable fit to the rate data, complete assessment of the measurements obtained in these experiments suggests that reaction in a completely microporous particle does not take place exactly as proposed in the random pore model. Rather, the results presented in the next section indicate that a microporous char particle does not react uniformly throughout but instead reacts preferentially near the particle surface. A reason for this phenomenom could not be determined from these data; it seems that the total surface area of a microporous char participates in the reaction only as carbon conversion proceeds. Nevertheless, the random pore model does provide one limit to possible variations in the surface area of the solid with respect to conversion.

5.1.4 Evaluation of the Experimental Results

The particle size effect (Figures 4.1-40 and 4.2-11) shows that the surface area of the C-O char on which the reaction occurs is a function of the particle size. (No nitrogen adsorption measurements were made, however, to determine if the BET surface area is also a function of particle size.) A particle size effect is obtained even though the reactant

gas can access the micropores as indicated by the carbon to oxygen ratios of the partially reacted chars (Figure 4.3-13). The mono-layer oxygen coverage as a function of oxygen content is shown in Figure 5.1-3. Based on the oxygen content of the char during reaction, this figure shows that almost all the carbon surface is covered with oxygen after the initial rise in the oxygen content. Calculations using a first order reaction-diffusion model indicate that the difference in the reaction rate of the two particle sizes cannot be the result of very slow mass transport of the reactant in the small pores. Because the Arrhenius plots of the rate data at different particle sizes are linear and almost parallel over two orders of magnitude, it is not possible to fit this data with such a model. No change in the slope of the Arrhenius diagram is observed at the low temperature end where the rates become almost identical, and at the high temperature end, the reactivity ratio is not proportional to the particle radii.

Further examination of the data also shows that the particles apparently decrease in diameter during reaction. This was determined by comparing the change in particle density with conversion. If reaction occurs uniformly, the particle density at a particular conversion relative to the original particle density is:

$$\frac{\rho_x}{\rho_o} = 1 - x \qquad (5.1.31)$$

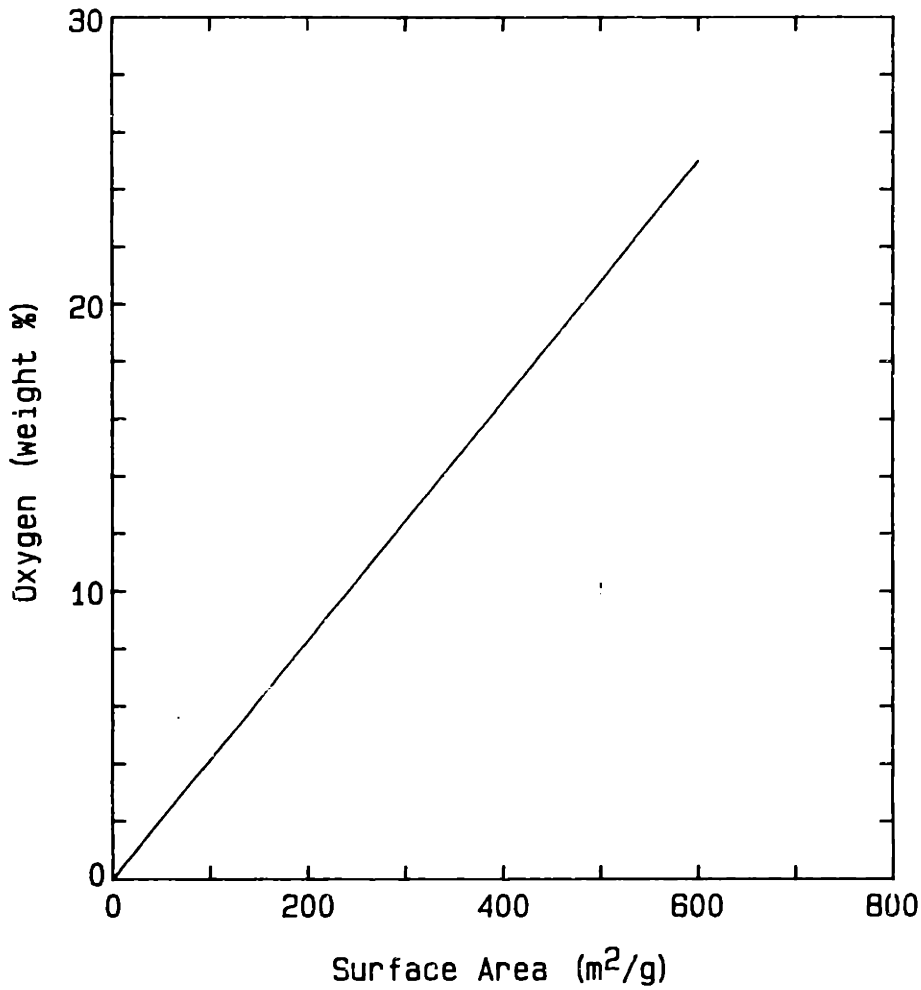

Figure 5.1-3. Weight fraction oxygen as a function of surface area coverage.

where ρ_x is the density at the conversion, x, and ρ_o is the initial particle density. Although the particle density as a function of conversion was not measured in these experiments, it can be calculated from the pore volume and the true solid density:

$$\frac{1}{\rho} = \frac{1}{\rho_c} + V_r \qquad (5.1.32)$$

where ρ is the particle density, ρ_c is the true carbon density, and V_r is the pore volume. Pore volumes were obtained from the nitrogen adsorption isotherms. The true solid density of carbon is approximately 2.2 g/cc. Although a value of 2.0 g/cc was measured for the C-O char at zero conversion, the true solid density apparently rapidly reaches an asymptotic value of about 2.2 g/cc as carbon conversion proceeds. Values reported in the literature are generally between 2.0 and 2.25 g/cc. The higher densities are more usual except for some carbons, which directly after pyrolysis but before reaction, give the lower values.

Calculated particle densities as a function of conversion are listed in Table 5.1-2. The calculated density at zero conversion is in approximate agreement with the skeletal density of the char measured by mercury porosimetry. Equilibrium was not obtained in the nitrogen adsorption measurements at zero percent conversion, suggesting that at low carbon conversion some nitrogen inaccessible porosity exists. From the density data and the initial density, which

Table 5.1-2. Calculation of Particle Density and Size from Porosity Data (C-O Char).

Conversion (%)	Pore Volume (cc/cc)	Carbon Volume (cc/g)	Particle Density $(cc/g)^{-1}$	Conversion (%)	Particle Radius (r/r_o)
0.0	.129	0.50	1.59	-	-
6.4	.232	(0.46)	1.45	6.4	1.0
22.	.300	(0.46)	1.32	14.8	0.97
24.	.306	(0.46)	1.31	15.5	0.96
40	.398	(0.46)	1.17	24.5	0.93
54	.343	(0.46)	1.25	19.4	0.83

was assumed to be equal to the particle density at 6.4% conversion extrapolated back to zero conversion rather than the particle density at 0% conversion, carbon conversions were calculated using Equation 5.1.31. Alternatively, instead of conversion a particle radius can be calculated since a change in mass must result in a decrease in size if the particle density does not change sufficiently. For spherical geometry, the particle radius is given by:

$$\frac{r_x}{r_o} = \left[\frac{\rho_o(1-x)}{\rho_x}\right]^{1/3} \qquad (5.1.33)$$

r_o is the initial particle radius, r_x is the radius at conversion x and density ρ_x, and ρ_o is the initial particle density. The calculated results are shown in Figure 5.1-4. The curve for the shrinking core model (i.e. $\rho_x = \rho_o$) is also shown for comparison. The results demonstrate that either some nitrogen (or even helium) inaccessible porosity exists that is not accounted for because of the assumption of a constant true solid (i.e., nitrogen inaccessible) density or that the the particle size indeed decreases during reaction. However, only the later explanation is consistent with the particle size effect. In addition, a more extensive set of data reported by Culver and Heath (1955), which includes the measurement of particle density, give the same results. (In this case the calculated particle density can be compared to the measured particle density). Table 5.1-3 summarizes the nitrogen adsorption, helium displacement, and mercury

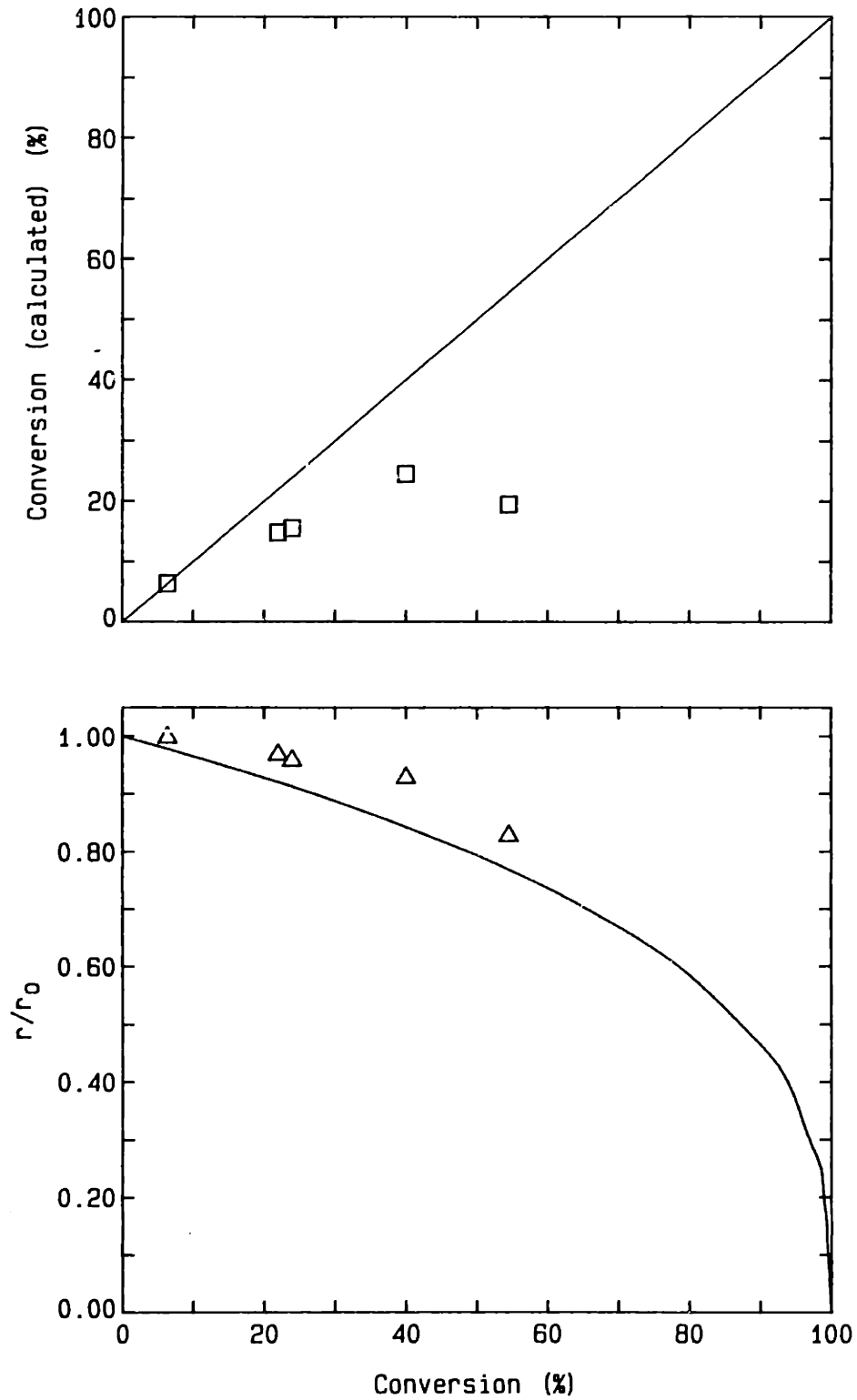

Figure 5.1-4. Conversion and particle radius calculated from porosity data of the C-O char.

Table 5.1-3. Conversion and Particle Radius Calculated from Porosity and Density Data[1]

Conversion (%)	Pore Volume[2] (cc/cc)	Carbon Volume[3] (cc/g)	Particle Density[4] $(cc/g)^{-1}$	Conversion (%)	Particle Radius (r/r_o)
0	.464	.505	1.025	0.0	1.0
33	.603	.455	0.937	8.6	0.89
70	.866	.441	0.761	25.8	0.74
85	-	.435	0.530	48.3	0.66
93	-	.441	0.558	45.6	0.50

[1] Data from Culver and Heath, 1955.

[2] Determined from nitrogen isotherm.

[3] Determined by helium displacement.

[4] Determined by mercury porosimetry.

porosimetry measurements on a steam activated Saran char obtained by Culver and Heath. Conversions and particle radii were calculated from their density data and are shown in Figure 5.1-5.

Qualitative observations made during the course of the experiments agree with these results. Disintegration of a particle was never observed, and particle size did seem to change with the extent of conversion.

Johnson (1975) obtained similar results from his measurements of char densities, but he postulates that shrinkage occurs because of pore collapse and coalesence within a particle. This may be a plausible argument, but it cannot explain why a particle size effect is also observed for these data.

Hashimoto and Silveston (1973) in their analysis of Kawahata and Walker's data (1962) attribute particle shrinkage to attrition of the solid during fluidization. Yet, in this case, the density of the attrited and residual particles should be the same; however, this was not observed.

Similar calculations were made with the C-3.6 char. The data are presented in Table 5.1-4 and are shown in Figure 5.1-6. However, because no significant effect of particle size on the reaction rate was noted for this char, the decrease in particle density should closely follow conversion. This is generally the case except for the data point at 60% conversion. Examination of the Dubinin-Polanyi plots (Figures A.5-7a to 7d) for the C-3.6 char shows that the data

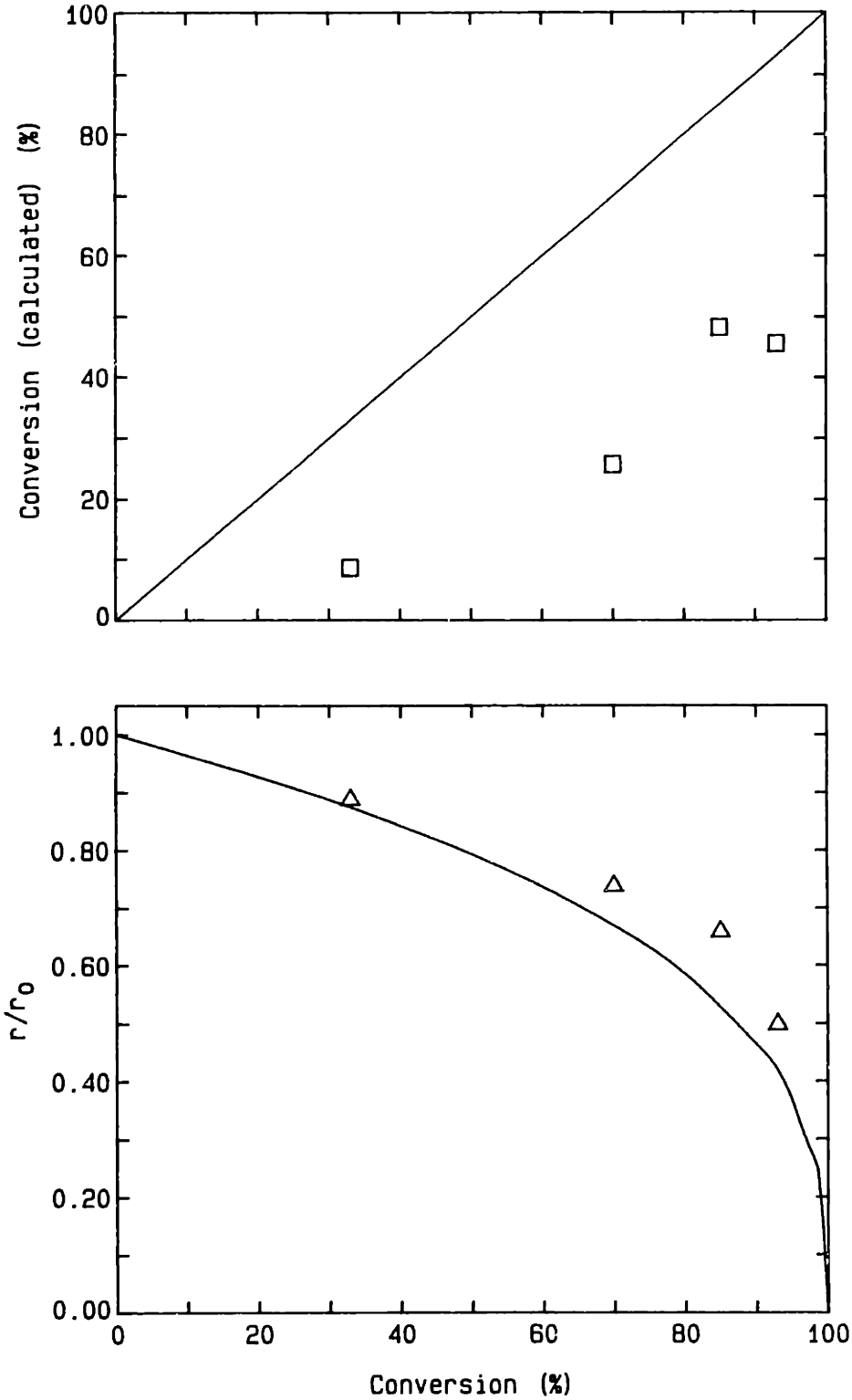

Figure 5.1-5. Conversion and particle radius calculated from porosity and density data (Data of Culver and Heath).

Table 5.1-4. Calculation of Particle Density and Size from Porosity Data (C-3.6 char).

Conversion (%)	Pore Volume cc/cc	Carbon Volume cc/g	Particle Density[1] $(cc/g)^{-1}$	Conversion (%)	Particle Radius (r/r_o)
0.0	.049	(0.50)	1.82	-	
10.3	.192	(0.46)	1.53	10.	1.0
20.4	.278	(0.46)	1.36	20.	1.0
37.7	.309	(0.46)	1.30	24.	0.94
60.	.275	(0.46)	1.36	20.	0.79

[1] All calculations are on an ash-free basis.

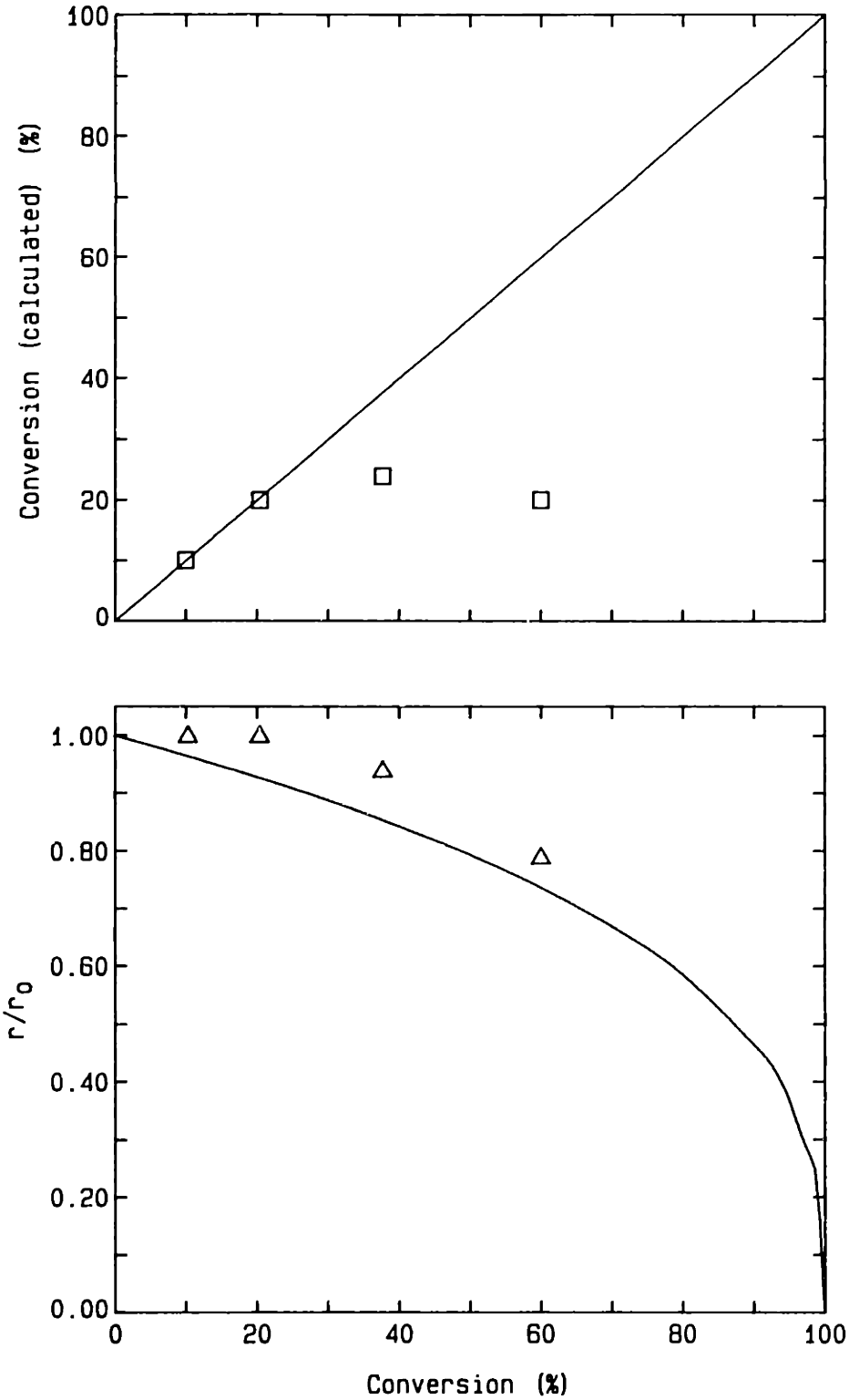

Figure 5.1-6. Conversion and particle radius calculated from porosity data for the C-3.6 char.

points deviate noticeably from a straight line correlation near the y-axis. This may have introduced some error in the determination of the pore volume and therefore in the calculations. The upturn in the Dubinin-Polanyi plots also suggests that a greater amount of pore widening takes place in the catalyzed char than the non-catalyzed char. Overall, the results indicate that particle density non-uniformity is less severe with the catalyzed char. Whether this difference is due to the catalyst or because of a slightly different pore size distribution, since the surface areas are lower and the average pore radii are somewhat larger for the catalyzed char at all conversions, is uncertain.

Additional evidence that reaction in microporous chars is not completely uniform throughout the particle is based on an analysis of intraparticle diffusion in the chars at high reaction rates. Reactivity measurements were made at rates sufficiently fast that a change in the slope of the Arrhenius diagram was observed (Figure 4.1-1 to 4.1-6). The lowering of reaction rates to below the low temperature activation energy correlation was interpreted in terms of the classical reaction-diffusion model of Thiele, Damköhler, and Zeldovitch (Satterfield, 1970). (The calculations are presented in detail in Appendix 3). Analysis of the data at 20% conversion by a first order reaction-diffusion model yields an average pore radius of about 35 Å, if transport in the solid can be described by Knudsen diffusion and the Thiele modulus is taken to be 1 at a reaction rate of 0.35 g/g-carbon, which is just

below the rate at which a change in the activation energy of the rate data is observed. Extending the analysis to higher conversions, one finds that the diffusivity should increase as carbon is reacted away and pores are further opened. Not only will the pores be widened (possibly quite uniformly since for relatively small values of the Thiele modulus no large concentration gradients are present), but in addition, beyond 20% conversion the reaction rate per initial volume of char decreases with further conversion. As a result, the first order reaction-diffusion model predicts an increase in the effectiveness factor to 1 with further conversion. However, this was not observed experimentally; the change in slope in the Arrhenius diagram persists to at least 90% conversion.

This result suggests that the effective reaction depth in the particle is less than the particle radius. If the length scale for intra-particle diffusion is made smaller than the particle radius, a first order reaction-diffusion model gives a possible interpretation of the data over the entire conversion range. The change in slope of the rate data is not believed to be due to a change in the rate controlling step of the reaction because of the low value for the activation energy.

In summary, the gasification of chars or regions (grains) in the char that are microporous appears to proceed in a radially non-uniform manner. This is probably true for both oxygen and carbon dioxide gasification since a particle size effect is noted for each reaction. Therefore, the reactivity

of a grain or particle that is microporous, such as the sucrose char, is a function of particle size. Mercury porosimetry measurements showed that the sucrose char lacks a network of macropores; rather all the porosity is in pores of less than 100 Å in radius. In this case, therefore, the size of the particle is the characteristic dimension of the microporous region. Typical lignite chars, in comparison, have an extensive macropore network which can act as feeder pores to the microporous regions of the char. This makes the determination of the size of the microporous regions difficult. Smith (1972) suggests that if the porosity can be adequately fit by a bimodal pore size distribution, the size of the microporous grains can be calculated. For bituminous coal chars, it is possible that such microporous regions or particles are part of the cenospheric structure that forms during pyrolysis. (This was the case with the sucrose char.) Thus, microporous regions are typical of actual char particles; however, chars that contain extensive feeder pore networks may not exhibit any particle size effect since the microporous regions are substructures (grains) of the larger particle. This is apparently the case for spherocarb, a char that has been highly activated. On the other hand, a particle size effect is observed with some coal chars. For instance, Sears et al. (1980) report a particle size effect for a lignite char and a crushed bituminous coal char. For these chars, the feeder pore network may not be very extensive.

A reaction depth for the microporous particles was calculated from the relative reactivity of the various particle sizes (see Figure 4.1-45). An estimation of the volume of a spherical shell needed for different particle diameters to give the same reaction rate per unit mass yields a reaction depth of 20 μm for the carbon-oxygen reaction and an almost negligible reaction depth for the carbon-carbon dioxide reaction.

It is uncertain if the less pronounced particle size effect obtained with the catalyzed char is a result of the catalysis or a slightly different pore size distribution. Although no distinct particle size effect was noted, which could be indicative of a more effective feeder pore network, a change in the slope of the Arrhenius diagram for the C-1 char persists to high char conversions suggesting that complete penetration into the microporous regions did not occur. However, calculations also show that the average pore radius increases more than the pore radius of the non-catalyzed char with increasing carbon conversion, indicating a greater degree of pore widening.

The reason a microporous (or at least a non-catalyzed) char does not react uniformly throughout the particle is not known. Possible explanations that have been considered include: 1. Pore blockage by chemisorbed oxygen atoms at a pore restriction. It was observed that the oxygen content of the char increases initially, reaching a concentration that is about equivalent to a monolayer coverage on the carbon surface

only after some carbon conversion has occurred. The failure to immediately reach a monolayer coverage suggests that the movement of oxygen molecules into very small pores may be restricted by blockages that are reacted away during gasification. (Most of the nitrogen adsorption measurements were made with chars that contained appreciable amounts of oxygen. The single datum point (Table 4.3-1) for the outgassed char indicates that a higher surface area is obtained for that condition. Pore blockage by chemisorbed oxygen atoms may not be a hindrance to the movement of nitrogen molecules since transport may be augmented by surface diffusion at the temperature of the nitrogen adsorption measurements.) However, pore blockage by chemisorbed oxygen atoms is probably not applicable to the carbon-carbon dioxide reaction. No significant number of surface oxides are present at the temperatures at which this reaction takes place.

2. Pore blockage could be caused by thermal expansion of the solid at the elevated temperatures of the carbon dioxide reaction. This could prevent the movement of reactant molecules past narrow restrictions in the solid. Both of these explanations suggest that incomplete penetration into the solid is caused by physical restrictions that must act as a no-flux boundary condition to mass transport at some point in the solid.

An alternate explanation is proposed in Section 5.2. Here it is suggested that the reaction rate is a function of the pore size. In very small pores, the energy of the gas molecule

is determined by the gas-wall interaction and is therefore different from the energy of a gas molecule striking a free surface. As a result, one would expect the reaction rate to be quite different in 10 Å pores than on an open carbon surface.

Even though the chars do not react uniformly throughout the solid, the rate versus conversion data at different reaction temperatures in the intrinsic reaction regime can, in general, be scaled to a single curve. This suggests that the rate versus conversion data can be scaled by a single rate constant over practically the entire conversion range and that the rate versus conversion curve can be described by a single function of conversion or normalized time. (The data, particularly when plotted against time, do exhibit a slight variation in position with respect to temperature that is particularly evident at low conversions. However, it is not believed that this variation is significant enough to be attributable to one single factor. Possibly it is related to the initial opening of restricted porosity in the solid).

Finally, the experimental results show that the shape of the rate versus conversion curves are slightly different for each reactant gas, primarily at low conversions. It is believed that the rapid increase in the oxygen content of the char at the beginning of the carbon-oxygen reaction is mainly responsible for this difference. Not only is it possible that the reaction rate may depend on the surface oxide concentration of the char, but more importantly, the true

reaction rate of the carbon will not correspond directly to the TGA measurements (see Appendix 7). Dutta and Wen (1977a,b) have also observed that the rate versus conversion data are different for oxygen and CO_2. Examination of their data, however, show that the curves also differ principally in the initial conversion range. On the other hand, a comparison of the Spherocarb reaction data with CO_2 and oxygen show the burn-off curves to be very different. Clearly surface area models, such as the random pore model, would predict a burn-off curve more like the CO_2 data for such a highly porous char. The unusual shape of the TGA oxygen data is probably due to a build-up of oxygen on the char that is stretched over what appears to be a broader conversion range because the remaining carbon only represents a small portion of the total carbon conversion range. That is, the build-up of surface oxides on the carbon, which must include a simultaneous loss of carbon to products, would involve a larger fraction of the carbon initially present with Spherocarb than with a less activated char such as the sucrose char.

5.1.5 An Extension of the Random Pore Model to the Gasification of Microporous Grains

It is proposed that the rate versus conversion curves can be interpreted in terms of a model in which additional reactive surface area in a microporous particle becomes available with increasing carbon conversion. Such a model also introduces an additional parameter that can account for

the fact that the rate versus conversion curves do not depend only on the initial porosity of the solid. A modified version of the random pore model was developed that includes the progressive opening of micropores with carbon conversion. In this model, it is assumed that a fraction of the initial total porosity is inaccessible to the reactant and only participates in the reaction after some carbon has been removed to make the pores accessible. At present the function describing the opening of closed porosity is largely empirical. Additional experimental data are required to relate the properties of the char to the parameters of this function. Although this extended random pore model is exactly correct only if the pore opening is spatially random, it is assumed that the model will give an approximate description of the spatially dependent problem if the porosity variations are not very large, as is the case for the sucrose char.

In the extended model, the parameter $\lambda(r)$, which characterizes the pore size distribution of the solid is divided into two parts. It is assumed that one part represents the pores on which the reaction takes place initially and the other represents pores that participate in the reaction only at a later carbon conversion. It is assumed that the opening of inaccessible pores with conversion can be described by an empirical function, $(1-e^{-\alpha q})$, where α is a constant and q is the distance the surface of an initially accessible pore has receeded. In the notation previously used to describe the random pore model, the porosity of the solid is:

$$-\ln(1-\epsilon(q)) = 2\pi\left[\int_{r_*}^{r^*}(r+q)^2\lambda(r)dr + \int_0^q\int_{r_*}^{r^*}(r+q-s)^2\lambda_I(r)e^{-\tau s}dr\,ds\right.$$

$$\left. + \int_q^{q_\infty}\int_{r_*}^{r^*} r^2\,\lambda_I(r)e^{-\tau s}dr\,ds\right] \qquad (5.1\text{-}34)$$

The second term is the contribution of pores opening at a later time and beginning to grow at q=s. This term is expressed in terms of the Duhamel superposition integral and represents the summation of the fraction of pores that open and expand at $q = s_1, s_2, \ldots$ (Arpaci, 1966). In order to minimize the number of parameters, it is assumed that $\lambda_I = \phi\lambda$, i.e. the inaccessible pores are a fraction of the initially accessible porosity. Note that $\phi\lambda$ is not directly related to the inaccessible porosity, since it includes the section of the inaccessible pores that overlap with accessible pores. This is illustrated in Figure 5.1-7. The initial total porosity of both the accessible and inaccessible pores is:

$$-\ln(1-\epsilon_T) = 2\pi\left[\int_{r_*}^{r^*} r^2\,\lambda(r)dr + \int_0^{q_\infty}\int_{r_*}^{r^*}\phi r^2\,\lambda(r)\,e^{-\tau s}dr\,ds\right] \qquad (5.1\text{-}35)$$

Therefore, the ratio of total to accessible porosity is:

$$\frac{\ln(1-\epsilon_T)}{\ln(1-\epsilon_A)} = 1 + \xi \qquad (5.1\text{-}36)$$

where $\xi = \phi/\pi$. This result is obtained by evaluation of the integral over ds in the second term on the RHS of Equation 5.1-35.

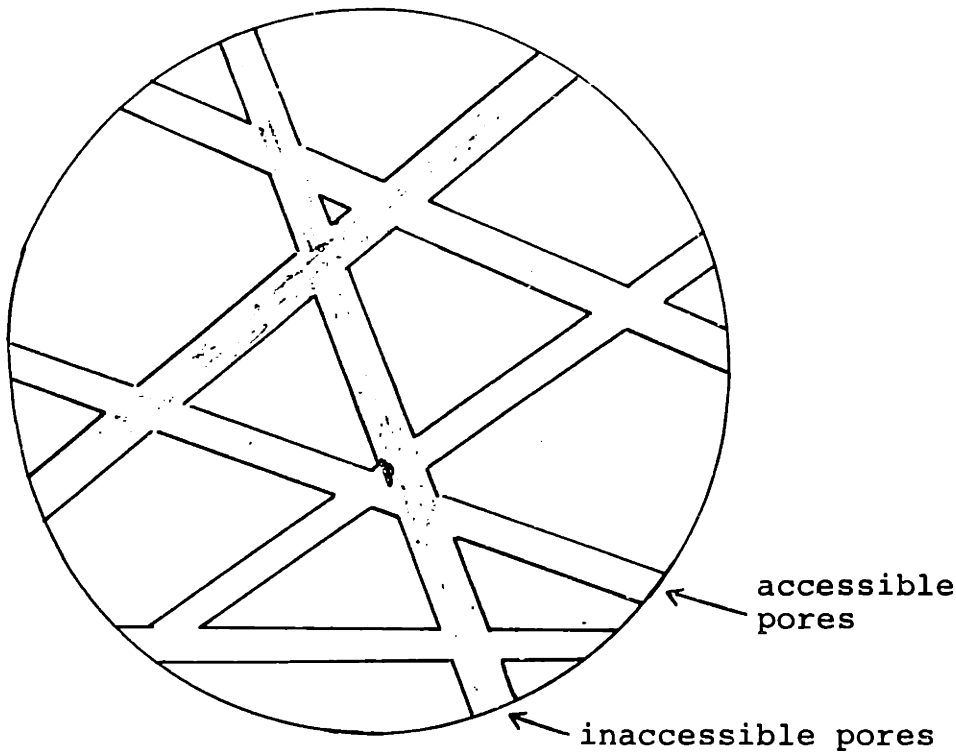

Figure 5.1-7. Accessible and inaccessible pores in the extended random pore model.

Expansion of the quadratic terms in Equation 5.1-34, and substitution of Equation (5.1-35) gives:

$$-\ln \frac{(1-\epsilon(q))}{(1-\epsilon_T)} = 2\pi \left[2B_1 + B_o q^2 + \phi \int_o^q \left[B_o(q^2+s^2-2qs) + B_1(2q-2s)\right] e^{-\tau s} ds\right]$$

$$\text{where } B_o = \int_{r_*}^{r^*} \lambda(r)dr \quad \text{and} \quad B_1 = \int_{r_*}^{r^*} r\,\lambda(r)dr \tag{5.1-37}$$

Evaluation of the integrals and simplification of terms yields:

$$-\ln\left[\frac{1-\epsilon(q)}{1-\epsilon_T}\right] = 2\pi \left[2q\, B_1\left(1+\xi - \frac{\xi}{\tau q}(1-e^{-\tau q})\right)\right. \tag{5.1-38}$$

$$\left. + B_o q^2(1+\xi) - \frac{2\xi}{\tau} B_o q\left(1-\frac{1}{q\tau}(1-e^{-q\tau})\right)\right]$$

or $\quad x = 1 - \exp[-F(q)]$

where F(q) is equal to the RHS of 5.1-38.

The rate is:

$$\frac{dx}{dt} = + \exp[-F(q)] \cdot [F'(q)] \tag{5.1-39}$$

$$= (1-x)[F'(q)] \tag{5.1-40}$$

Evaluation of F'(q) gives:

$$\frac{dx}{dt} = (1-x)\,4\pi\, q'\left[B_1\left(1+\xi - \xi e^{-q\tau}\right) + B_o\left[(1+\xi)q - \xi(1-e^{-q\tau})\right]\right] \tag{5.1-41}$$

Normalization of the rate by the rate at x=0 gives:

$$\frac{r}{r_o} = (1-x)\left[(1+\psi-\psi e^{-\tau q}) + \frac{B_o}{B_1}\left((1+\psi)q - \psi/\tau\,(1-e^{-\tau q})\right)\right] \quad (5.1\text{-}42)$$

Evaluation of the terms must be done numerically. This is best done after substitution of $z = q/r_p$ where r_p is the pore radius and for the assumption of a mono-sized pore distribution. This then gives:

$$\frac{r}{r_o} = (1-x)[1+\psi-\psi e^{-\alpha z}) + (1+\psi)z - \psi/\alpha\,(1-e^{-\alpha z})] \quad (5.1\text{-}43)$$

$$\text{and } x = 1-\exp[-2Ez(1+\psi-\frac{\psi}{\alpha z}(1-e^{-\alpha z}))-E(1+\psi)z^2 \quad (5.1\text{-}44)$$

$$+ 2E(\psi/\alpha)z(1-\frac{1}{\alpha z}(1-e^{-\alpha z}))]$$

where $E = \ln\left[\frac{1}{1-\epsilon_A}\right]$ and $\alpha = \tau r_p$. For monosized pores $B_1/B_o = r_p$, which allowed some simplification of both equations.

The extended model was fit to the C-O char data, and it gives a rather good fit to the data, as shown in Figure 5.1-8. The empirical pore opening function cannot quite match the initial reaction rate, but overall the model provides a better fit than the original random pore model. For a monosized pore distribution, the model parameters yield an initial porosity of 0.35 and an inaccessible porosity which is 23% of the total porosity. The parameter τ is equal to about 0.1 of the pore

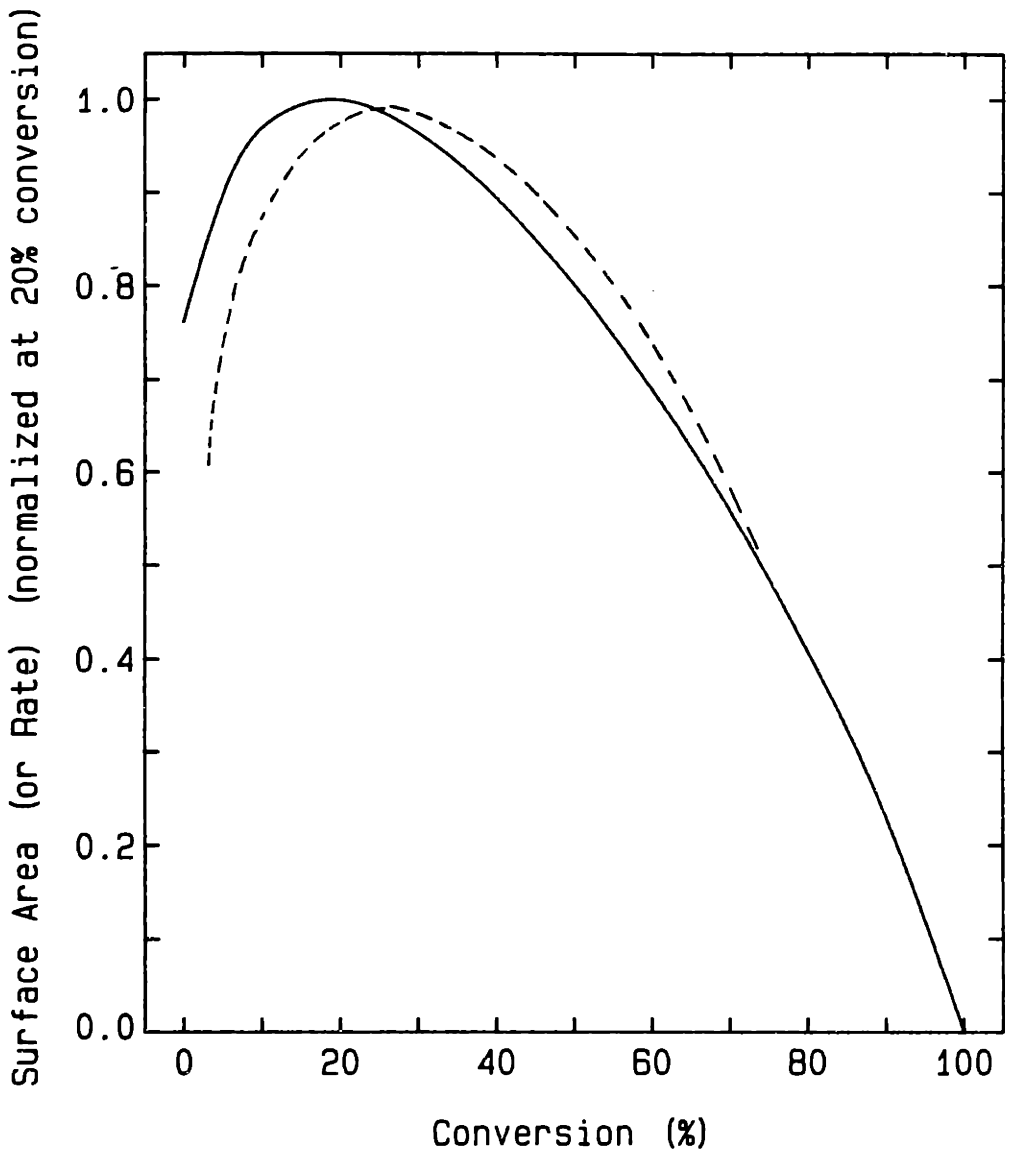

Figure 5.1-8. Comparison of the C-O char rate versus conversion data (---) to the extended random pore model (——).

radius. The initial porosity is in good agreement with the data. The initially inaccessible porosity is a quite reasonable value. If the initially inaccessible porosity is estimated by comparing the difference between the reaction rates of the smallest particles and the 90-106 μm particles, the predicted value agrees quite well with the measurements.

Direct application of the model to the catalyzed char was not successful, because of the large difference between the initial and maximum rates. Furthermore, the more pronounced sigmoidal shape of the weight in conversion data obtained with the catalyzed char suggest that the reaction mechanism for the catalyzed char may involve an initial activation step that is not present, or at least not as important, for the non-catalyzed char. However, it was noted that if it is assumed that the rate constant for the catalyzed char is proportional to the calcium to carbon ratio and if this variation with respect to carbon conversion is taken into account, the rate versus conversion curves are then similar to those of the non-catalyzed char.

With the assumption that the rate constant of the catalyzed char is proportional to the calcium to carbon ratio:

$$k \propto Ca/C$$

$$\text{or} \quad k = k_o \, Ca/C \qquad (5.1\text{-}45)$$

the overall reaction rate of the catalyzed char can then be stated as:

$$r = m_o \, S(x) \cdot k_o [Ca/C_o (1-x)] \qquad (5.1\text{-}46)$$

where m_o is the initial amount of carbon, S(x) is the surface

area variation with conversion, and $Ca/C_o(1-x)$ is the change in the calcium to carbon ratio with conversion. Normalization of this rate with the maximum rate yields:

$$\frac{(1-x)}{(1-x_m)} \frac{r}{r_m} = \frac{S(x)}{S_m} \qquad (5.1\text{-}47)$$

where S_m is the surface area at the maximum rate and x_m is the conversion at the maximum rate.

Values for $S(x)/S_m$ corrected for the calcium to carbon ratio are compared to the rate versus conversion data of the non-catalyzed char for the carbon dioxide and oxygen reactions in Figures 5.1-9 and 5.1-10. The correction of the calcium to carbon ratio brings the rate versus conversion data into good agreement with the non-catalyzed char data. This result implies that the important factor in catalysis is the total calcium to carbon ratio and not the calcium to surface area ratio. Furthermore, it shows that the calcium remains with the carbon and does not deactivate, at least over the first half of the carbon conversion range. The reason the rate of the catalyzed char reaches a maximum at 40% conversion is uncertain. Possibly further increases in the calcium to carbon ratio beyond this point provide no additional increases in reactivity, although other factors must also affect catalyst deactivation at progressively higher carbon conversions. For example, although the maximum rate for the 1% calcium char is displaced to a slightly higher conversion (~50%), this displacement cannot quantitatively account for deactivation only because of calcium saturation.

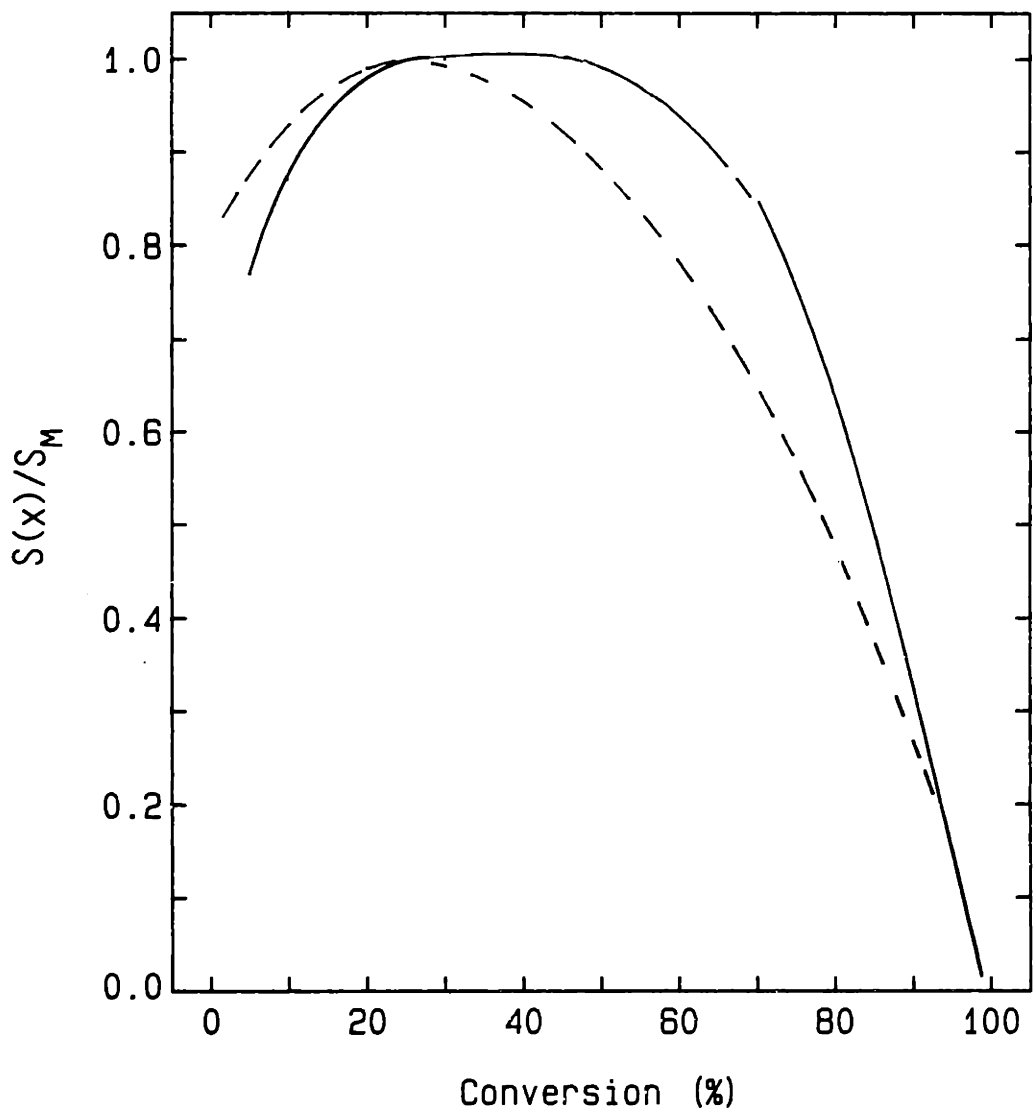

Figure 5.1-9. Normalized rate versus conversion data of the C-3.6 char (—) adjusted for the increase in calcium to carbon ratio for carbon conversions below 30%; carbon dioxide reaction. Rate normalized to the rate at x = 0.3 for the C-0 char (---).

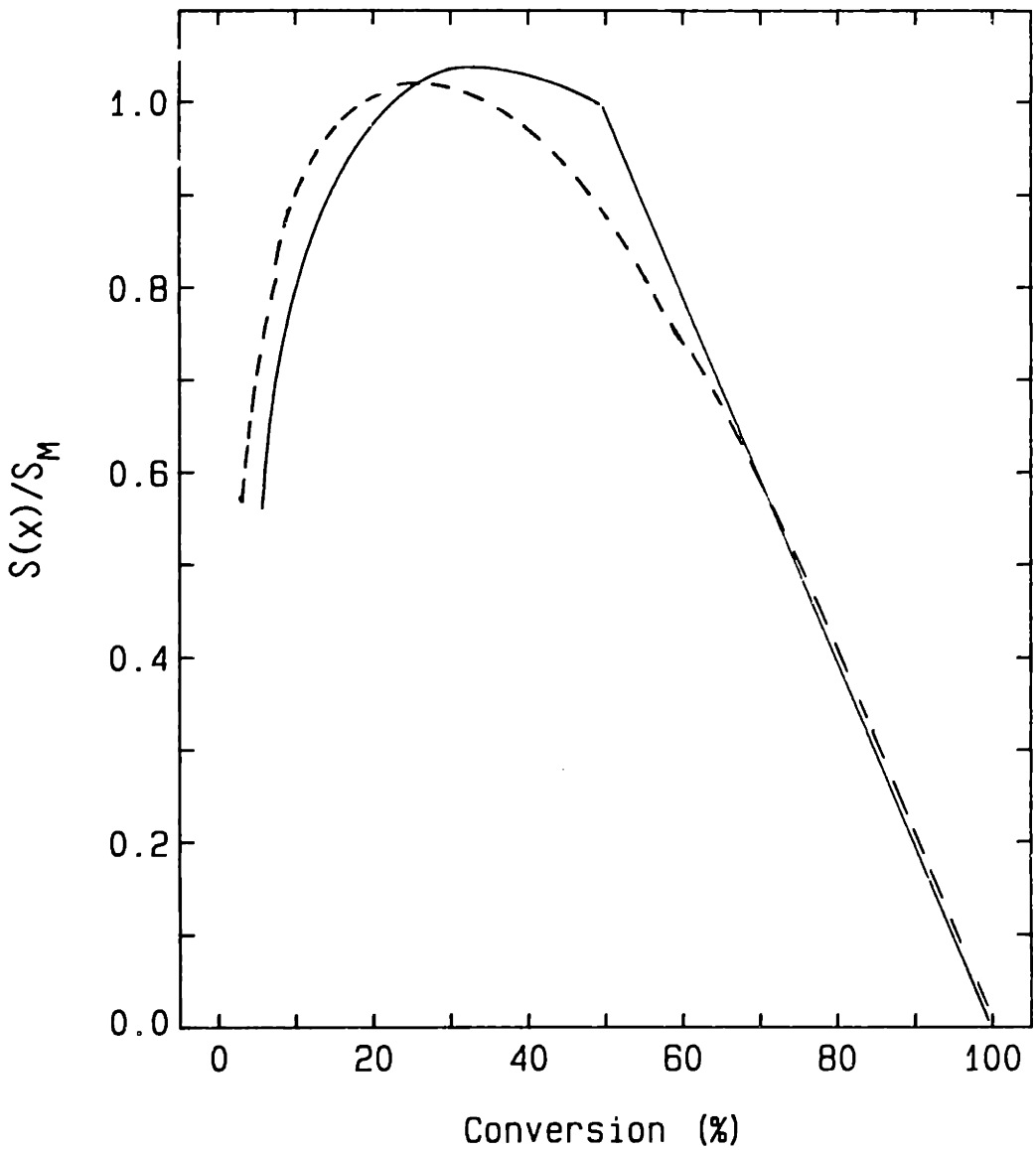

Figure 5.1-10 Normalized rate versus conversion data of the C-3.6 char (——) adjusted for the increase in the calcium to carbon ratio for carbon conversion below 40%. Rate normalized to the rate at x = 0.4 for the C-O char (----).

5.2 RATE MECHANISMS FOR THE GASIFICATION REACTIONS

5.2.1 Introduction

Analysis of the data indicate that the reaction mechanism for the oxygen reaction is different from the Langmuir-Hinshelwood type of mechanism usually proposed for this reaction. The carbon oxygen reaction mechanism cannot be described by a simple adsorption desorption model in which the rate controlling step depends on the extent of oxygen coverage of the surface. Specifically, the high oxygen content of the char and the fact that the reaction is first order eliminate any simple adsorption-desorption mechanism.

Furthermore, it is recognized that the reactivity of a gas molecule in a very small pore (< 10 Å) must be different from the reactivity of a molecule in a pore where molecular flow is in the Knudsen regime or on an open surface. In a pore of less than 10 Å, a gas molecule will have lost two translational degrees of freedom. The energy level of the gas molecule will be largely determined by its interaction with the atoms of the solid and the characteristic vibration frequencies of the atoms in the solid. As a result, a gas molecule within a constricted pore may react at a different rate than a molecule striking a free surface. In a pore in the Knudsen regime, an intermediate situation occurs. Here the energy of a molecule is determined by its accommodation with the surface at each collision with the pore wall. It is postulated from these considerations that for a first order reaction the reactivity of a carbon surface must also depend on the size of the pore associated with the surface.

5.2.2 Reaction Mechanism for the Carbon Oxygen Reaction

Generally, reaction mechanisms for carbon gasification are described in terms of Langmuir-Hinshelwood kinetics. These mechanisms involve obtaining an expression, by means of an adsorption isotherm, for the reactant concentration on the surface and then expressing the rate of formation of products in terms of the concentration of adsorbed species. Surface reaction and product desorption is usually considered together as one single step.

For carbon oxidation, the simplest mechanism that is frequently proposed is (Laurendeau, 1978):

$$2C_f + O_2 \underset{k_{-1}}{\overset{k_1}{\rightleftharpoons}} 2\,C(O) \qquad (A)$$

$$C(O) \xrightarrow{k_2} CO + C_f \qquad (B)$$

$$\text{or} \quad 2\,C(O) \xrightarrow{k_2} CO_2 + C_f \qquad (C) \qquad (5.2.1)$$

where C_f is an available site, C(O) is an occupied site, and $C_T = C_f + C(O)$ is the total number of sites available on the carbon surface. The adsorption of oxygen on the surface is apparently dissociative, and the reverse reaction (desorption to O_2) is not observed ($k_{-1} << k_1$)(Laurendeau, 1978). The steady state assumption for C(O) (Reactions A and C) gives:

$$\frac{dC(O)}{dt} = 0 = 2\,k_1\,C_f^{\,2}\,P_{O_2} - 2k_2\cdot\,C(O)^2 \qquad (5.2.2)$$

where the k_{-1} term was neglected.

The solution for C(O) is:

$$C(O) = \frac{[C_T](k_1 P_{O_2})^{1/2}}{[k_2^{1/2} + (k_1 P_{O_2})^{1/2}]} \qquad (5.2.3)$$

The mechanism assumes that the rate is proportional to C(O). The rate is therefore:

$$r = k_2\,C(O)^2$$

$$r = \frac{k_2\,[C_T]^2\,k_1\,P_{O_2}}{[k_2^{1/2} + (k_1 P_{O_2})^{1/2}]^2} \qquad (5.2.4)$$

For the reaction rate to be first order:

$$k_2 > k_1\,P_{O_2}$$

Equation (5.2.4) then reduces to:

$$r = k_1 C_T^{\,2} P_{O_2} \qquad (5.2.5)$$

This mechanism predicts that the rate controlling step is oxygen chemisorption if the reaction is first order. Since the activation energy for desorption (E_2) is apparently greater than for adsorption (E_1) (Blyholder and Eyring, 1959), this model predicts that the reaction order cannot switch from first to zero order with increasing temperature.

Alternatively, if the reaction is initially zero order, raising the temperature can cause a change to first order. At a fixed temperature, if $P_{O_2} < k_2/k_1$, the reaction is first order, and if $P_{O_2} > k_2/k_1$, the reaction is zero order.

The experimental data (Figure 4.1-13) show that the rate dependence on the oxygen partial pressure does not change with temperature. In terms of the model, this implies that k_2/k_1 is independent of temperature. Therefore, the activation energy of k_2 is equal to the activation energy of k_1 ($E_1=E_2$). Furthermore, since the reaction order changes at an oxygen partial pressure of about 0.1 atm., k_2 at this oxygen pressure must be about an order of magnitude greater than $k_1 P_{O_2}$; i.e.,

$$k_2 \sim 10\, k_1(0.1) \qquad (5.2.6)$$

$$k_2 \sim k_1$$

This result is contrary to the measurements of Blyholder and Eyring (1959) and Tucker and Mulcahy (1969), who show that $k_2 \neq k_1$. In addition, the model predicts that $C(O) \sim 0$ for first order kinetics. However, this is also contrary to the experimental results (Figure 4.3-13). Large quantities of oxides are present on the char, and the surface oxides are stable at the reaction temperature. Although it is possible that the formation of surface complexes may result in inactive sites as suggested by Laine et al. (1963), such an explanation would imply that the reaction rate should decrease with oxide coverage, but this is also inconsistent with the data. It is

obvious that such a simple kinetic model is insufficient to satisfactorily describe the experimental data.

Mechanisms that include surface migration as an intermediate step (e.g., Blyholder and Eyring (1959)) do not provide a rate expression that is better able to explain the experimental data.

Such a mechanism (Laurendeau, 1978) is:

$$\begin{aligned} 2\,C_f + O_2 &\xrightarrow{k_1} 2\,C(O) \quad (A) \\ C(O) &\xrightarrow{k_2} C'(O) \quad (B) \\ C'(O) &\xrightarrow{k_3} CO + C_f \quad (C) \end{aligned} \qquad (5.2.7)$$

If $\theta' = C'(O)/C_T$ and $\theta = C(O)/C_T$, where $C_T = C_f + C(O) + C'(O)$ the steady state approximation for C(O) is:

$$2\,k_1\,C_T^{\,2}(1 - \theta - k_2/k_3\,\theta)^2\,P_{O_2} = k_2\,\theta\,C_T \qquad (5.2.8)$$

A balance on the θ' gives: $\theta' = k_2/k_3\theta$, which is then substituted into the above equation. Expansion of the quadratic to include only first order terms in θ yields:

$$2k_1(1-2(1 + k_2/k_3)\theta)P_{O_2} = k_2\theta$$

$$\theta = \frac{2\,k_1\,P_{O_2}}{4(k_1 + k_1k_2/k_3)\,P_{O_2} + k_2} \qquad (5.2.9)$$

A balance among the terms in the denominator will yield a rate equation with the appropriate reaction order. Since the observed reaction order is independent of temperature, one obtains:

$$\frac{k_1(k_2 + k_3)}{k_2 k_3} \neq f(\text{temperature}) \qquad (5.2.10)$$

In terms of the activation energies of the rate constants, this equation states that:

$$E_1 + E_2 \text{ (or } E_3) = E_2 + E_3 \qquad (5.2.11)$$

If it is assumed that $E_3 > E_2$

then $E_1 + E_3 = E_2 + E_3$

or $E_1 = E_2 \qquad (5.2.12)$

This result is the same as that obtained without the assumption of surface migration. If $k_2 > k_3$ at one temperature, but not at a higher temperature then this conclusion cannot be made. However, it seems unlikely that the pre-exponential factor of the rate constant would be so different that such a shift would occur over a narrow temperature range. This mechanism still predicts that the rate controlling step for a first order reaction is adsorption on a reactive surface site.

Mechanisms based on the Langmuir adsorption isotherm predict that a shift in reaction order results from the extent of coverage of the active sites. But, because the rate constants that determine the extent of coverage are strongly temperature dependent, there should exist only a small temperature range over which the reaction order will change at a fixed oxygen partial pressure; yet it is observed experimentally that the reaction order is the same at 875 and 725 K. In addition, the large quantity of surface oxides that

are present at the reaction temperature demonstrates that the low temperature oxidation reaction is not a simple consecutive adsorption-desorption process. This conclusion was also reached by Chen and Back (1979) who measured both the rate and the amount of surface complex on a pyrolysis carbon as a function of conversion.

In order to maintain agreement with the experimental data, a mechanism is postulated as follows:

$$2\,C_f + O_2 \xrightarrow{k_1} 2\,C(O) \qquad (A)$$

$$C(O) \xrightarrow{k_2} CO + C_f \qquad (B)$$

$$O_2 + C(O) \underset{k_{-3}}{\overset{k_3}{\rightleftharpoons}} C(O)^* + O_2 \qquad (C)$$

$$C(O)^* \xrightarrow{k_4} \text{PRODUCTS} \qquad (D)$$

It is proposed that the formation of a surface complex (A) is a preliminary step. Consecutive desorption of the complex (B) to form CO is assumed to be important primarily only at higher temperatures. The contribution of this reaction to the rate in these experiments was observed to be quite small. Step (C) is postulated in order to obtain the observed pressure dependence and the switch in reaction order. Reactions (C) and (D) are analogous to the Lindemann mechanism for unimolecular gas phase reactions. This may be a quite reasonable analog since the decomposition of a stable surface oxide is also an unimolecular decomposition reaction. (It is assumed that an activated complex results primarily from a

collision with an oxygen atom and not from any third body collision. This may not be an unreasonable assumption in a very narrow pore, where the energy of the gas molecule is governed by interactions with the solid to some degree. Furthermore, even in gas phase reactions, the relative energy transfer efficiency of different molecules varies widely (Gardiner, 1969).)

If it is assumed that $C(O)^* << C(O)$, a steady state balance on $C(O)^*$ gives:

$$\frac{dC(O)^*}{dt} = 0 = k_3 P_{O_2} C(O) - k_{-3} C(O)^* P_{O_2} + k_4 C(O)^* \qquad (5.2.14)$$

The rate is therefore,

$$r = \frac{k_4 k_3 C(O) P_{O_2}}{k_{-3} P_{O_2} + k_4} \qquad (5.2.15)$$

The fact that the oxygen pressure dependence on the rate is independent of temperature, allows one to conclude that $E_{-3} = E_4$. Furthermore, since the linear dependence ends at about 0.1 atm.:

$$10\, k_{-3} P_{O_2} \cong k_4$$

$$\text{or} \qquad k_{-3} \cong k_4 \qquad (5.2.16)$$

That k_{-3} and k_4 are approximately the same is not an unreasonable result. The mechanism predicts that the activation energy for the first order and zero order reactions will be different.

Alternatively, it could be postulated that the reaction order shifts because the fraction of sites covered by $C(O)^*$ increases. Such a model predicts that the activation energy will not be different with the reaction order.

The proposed mechanism consists of two parallel reactions in series with the C(O) formation reaction. The two parallel reactions are proposed to explain the fact that carbon oxides dissociate from the carbon surface at a very slow rate in the absence of oxygen at low oxidation temperatures. At low reaction temperatures, therefore, the mechanism proposes that C(O) formation is independent of the reaction sequence itself. However, experimental evidence suggests that this may not be the actual case. Initial oxygen adsorption on a clean carbon surface represents only a small fraction of the total oxygen content of the char as reaction proceeds. Additional oxide formation, therefore, must be the result of the oxidation reaction itself. The experimental data show that the oxygen level of the char increases from 3 to 15% during the initial reaction period (10% conversion). Thereafter, the total oxygen content remains fairly constant, although the oxygen to carbon ratio increases as carbon is removed by reaction. On the other hand, the initial amount of oxygen adsorbed on a char, which is generally measured at temperatures where the reaction rate is slow, is quite small. Measurements reported by Cheng and Marriot (1985) gave about 1.2 wt% oxygen adsorption on a microporous char. Initial oxygen adsorption apparently involves only a few high energy sites on the carbon.

Additional evidence that further surface oxide formation is the result of the reaction sequence itself rather than a separate reaction step is the observation that the rate data can be approximately scaled by a single rate constant over almost the entire conversion range. This suggests that any transient reaction step involving a rate constant with a much different activation energy must be of short duration. (Although a slight shift in the normalized rate versus conversion data with respect to temperature was observed at low conversions for the C-O char, no such variation was observed with Spherocarb. As a result it is assumed that this shift is probably not due to reaction kinetics. Furthermore, the rate data obtained at different oxygen partial pressures all scale over the complete conversion range. This would not occur if the oxide build-up on the char was governed by a separate non-zero order rate equation.)

Although the overall rate versus conversion curves have been interpreted in terms of a surface area model, it is probable that the initial reaction rate, at least for the oxygen reaction, will also be influenced by the rapid change in the surface oxide concentration at low conversions. This possible interaction between the reaction rate and surface oxide formation is best illustrated by three experiments in which the reaction was stopped at about 20% conversion, the sample was reheated to the initial heat treatment temperature, and the reaction was restarted. In all cases, the rate did not follow the original burn-off curve after heat treatment and

removal of the surface oxides. The results of these experiments are shown in Figures 5.2-1 to 5.2-3 where the rate of the interrupted reaction is compared to the conversion curve obtained without interruption. In both experiments, a substantial amount of weight, corresponding to the amount of carbon oxides on the surface, was lost upon heat treatment after the reaction was stopped. When the reaction was stopped, the rate abruptly changed to a much lower rate; no continuous exponential-like change in the reaction rate was observed when the oxygen flow was turned off. If the reaction was stopped and restarted without reheating the sample, no difference in the rate was obtained. This certainly suggests the reestablishment of surface oxides on the carbon as the reaction once again continues may be responsible for the deviation from the original burn-off curve. However, it is also possible that the second heat treatment can result in some rearrangement of the carbon in small pores such that the surface area on which the reaction occurs after heat treatment of the partially reacted char has also been altered.

5.2.3 Reaction Mechanism for the Carbon-Carbon Dioxide Reaction

The mechanism proposed for this reaction (Walker et al., 1959) is:

$$C_f + CO_2 \underset{k_{-1}}{\overset{k_1}{\rightleftharpoons}} C(O) + CO \qquad (A)$$

$$C(O) \xrightarrow{k_2} CO + C_f \qquad (B) \qquad (5.2.18)$$

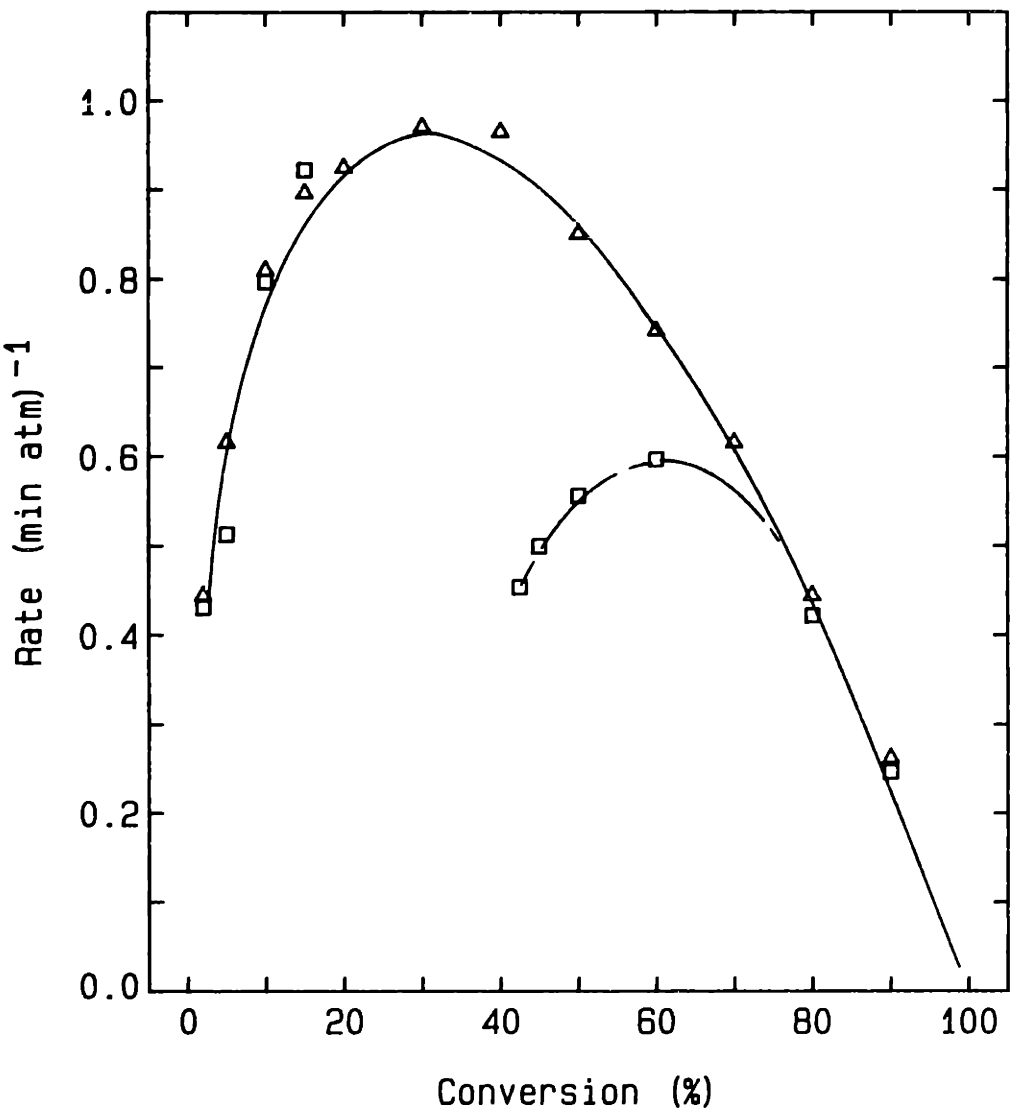

Figure 5.2-1. Rate versus conversion data; (—□—) interrupted reaction (C-O char - oxygen at 875 K).

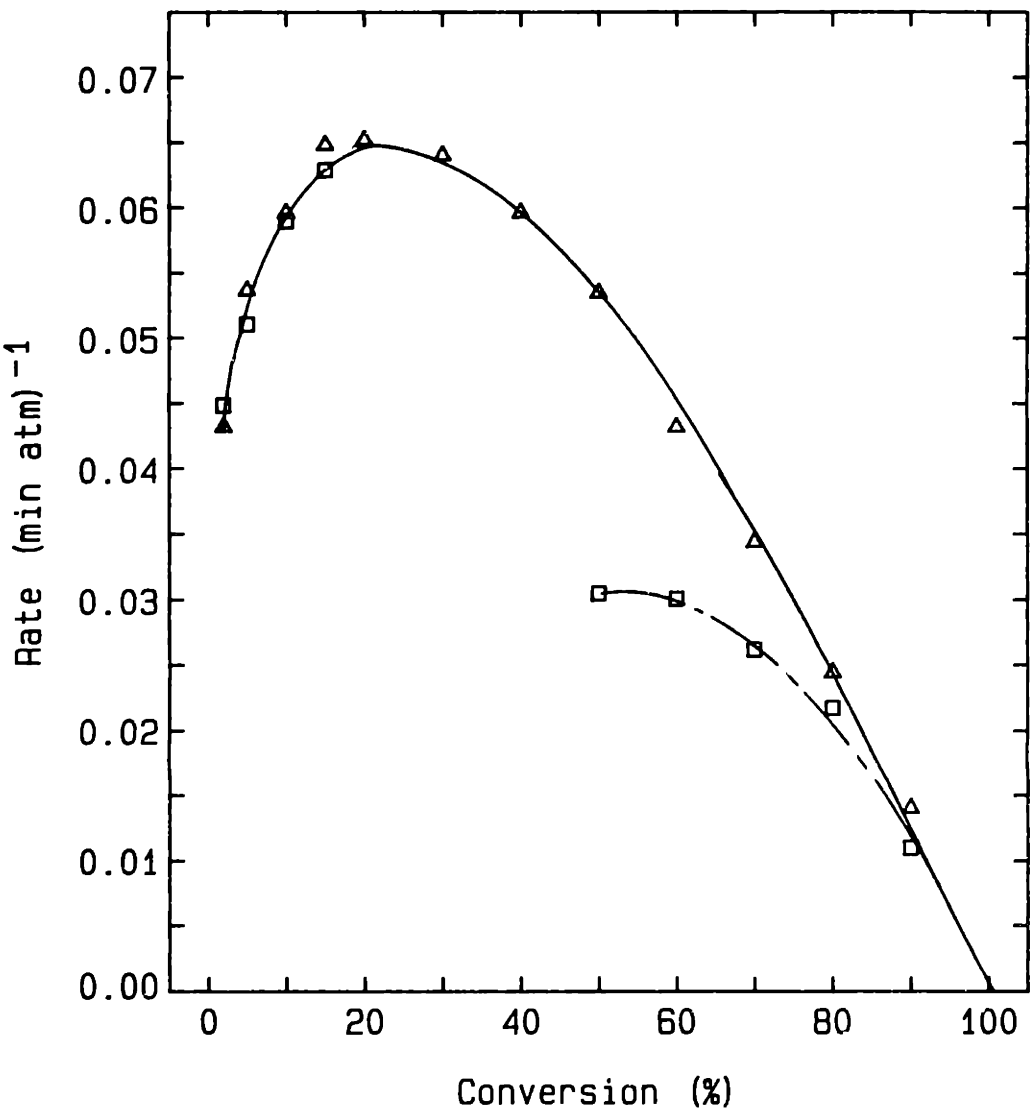

Figure 5.2-2. Rate versus conversion data; (—□—) interrupted reaction (C-O char - oxygen at 760 K).

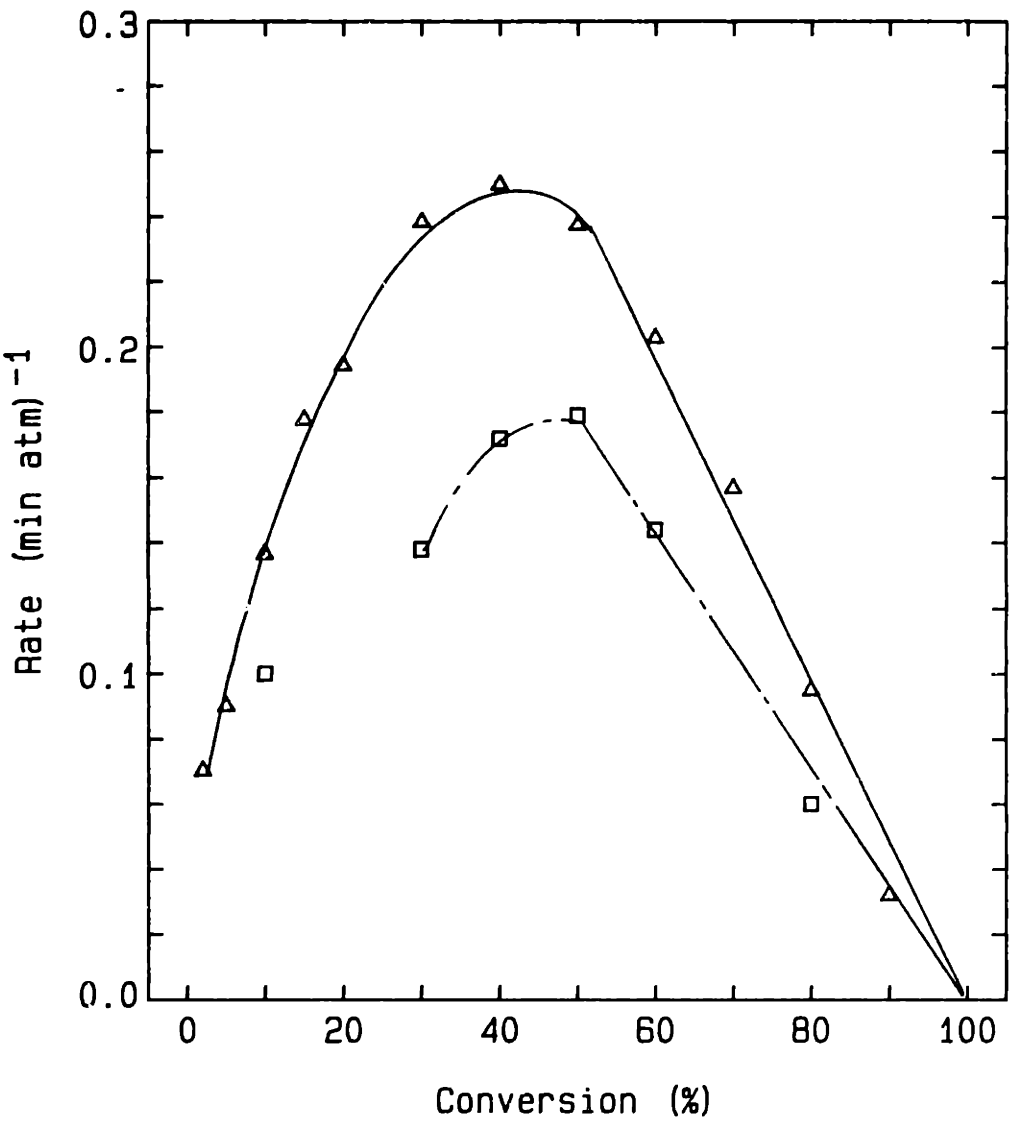

Figure 5.2-3. Rate versus conversion data; (—□—) interrupted reaction (C-3.6 char - oxygen at 660 K).

With the usual steady state assumption on C(O) one obtains:

$$C(O) = \frac{k_1 [C_T] P_{CO_2}}{k_1 P_{CO_2} + k_{-1} P_{CO} + k_2} \qquad (5.2.19)$$

where C_T is the total number of active sites and is assumed to be equal to $C(O) + C_f$ where C_f is a free or available site. P denotes the partial pressure of a particular gas. The rate is given by $k_2 \cdot C(O)$. Substitution of C(O) then gives the final equation. Experimentally it is observed that the rate is proportional to P_{CO_2}/P_{CO}. Studies by Ergun and Mentser (1967) have shown that $k_2 < k_{-1}$, i.e., oxygen exchange is faster than the decomposition reaction, at least at the temperatures of interest in this study. Therefore, the rate expression can be reduced to:

$$r = \frac{k_2 C_T}{1 + \frac{k_{-1} P_{CO}}{k_1 P_{CO_2}}} \qquad (5.2.20)$$

Ergun and Mentser (1965), Freund (1984a), and other investigators have shown that the rate data from the Boudouard reaction can be successfully correlated by this expression.

However, this rate mechanism, which gives the correct reaction order, is probably only an approximation of the actual mechanism. Mims and Pabst (1980b), based on their studies with isotopic compounds, have indicated that the mechanism is not entirely correct.

Efforts to measure the amount of adsorbed oxygen in these experiments were not successful. Because the exchange

reaction is faster than the reaction for oxide decomposition, it should be possible to determine values for k_1 and k_{-1} from an initial transient at the start of a run. However, no weight increase was ever observed at the start of the carbon dioxide-carbon reaction. The sensitivity of the measurement was about 100 ppm (oxygen atom/carbon atom). From Ergun and Mentser's data for the oxygen exchange reaction, it is possible to calculate an upper bound for C_T based on this measurement. They report an equilibrium constant for oxygen exchange between carbon dioxide and carbon monoxide over carbon as:

$$K_{eq} = \frac{[CO][C(O)]}{[CO_2]\ [C_f]} \qquad (5.2.21)$$

where [CO] and $[CO_2]$ are the concentration of carbon monoxide and carbon dioxide, respectively, and $[C_f]$ and [C(O)] are the concentration of free and occupied sites respectively. In their analysis it is assumed that $[C(O)] + [C_f] = [C_T]$, where C_T is defined as the total number of active surface sites. The reported value for K_{eq} is about 0.01 at 900 K. Therefore:

$$\frac{[C(O)]}{[C_f]} = \frac{.01\ [1\ atm\ CO_2]}{[CO]} \qquad (5.2.22)$$

Since no carbon monoxide was introduced with the carbon dioxide, it is not unrealistic to assume that the CO concentration was much less than 1%. Thus, we can conclude that $[C_T] \sim [C(O)]$ and that $C_T < 100$ ppm. Freund (1984b)

measured the decay transient when the reaction was stopped and calculated a value of about 60 ppm for C_T. His measurements were also made on a high surface area non-structured carbon, and his value is within the limit of accuracy of the measurement attempted in this study.

A value of less than 100 ppm for $[C_T]$, however, seems unrealistically low for a high surface area char with structural units on the order of 1000 $Å^3$. For a non-structured carbon, it would seem that almost every surface carbon atom should be capable of participating in the exchange reaction. The average size of a carbon structural unit of this high surface area char can be estimated by calculating the distance between the intersection of pores. The random pore model, with the assumption of uniform sized pores, gives this distance as:

$$L = -r_p/\ln(1-\epsilon) \qquad (5.2.23)$$

L is the distance between intersections, r_p is the pore radius, and ϵ is the porosity of the solid. For typical values of r_p and ϵ for the C-O char, the model predicts an average dimension of 13 Å. This size corresponds to a graphitic structure of about 9 rings and 3 layers.

Ergun and Mentser's value for the equilibrium constant for the exchange reaction was used to determine which term in the denominator of Equation (5.2.20) is dominant when the CO_2 concentration is much greater than the CO concentration. This was done to ascertain that the change in the slope in the Arrhenius diagram obtained with the C-3.6 char was not due to

a shift in the rate controlling step because of a change in the local CO concentration at higher reaction rates. The denominator of Equation (5.2.20) can be rewritten as:

$$K_{eq} \frac{P_{CO_2}}{P_{CO}} + 1 \qquad (5.2.24)$$

K_{eq} is equal to 0.1 at 750 C and about 1.0 at 950 C. This means that the local carbon monoxide concentration had to remain below .01 atm. at 750 C and 0.10 atm. at 950 C for the term on the left to be much larger than 1 (P_{CO_2} was 1 atm in all runs). In all experiments, the rate of weight loss was kept slow enough so that the carbon monoxide concentration remained well below 1%. Furthermore, this 1% limit applies to the fastest reaction rates measured in these experiments. At the lower temperatures, where the reaction rate is correspondingly slower, the back concentration of carbon monoxide was substantially below 1%. The rate equation appropriate for all of the data presented here in terms of the reaction mechanism given by Equation (5.2.18) is therefore:

$$\text{rate} = k_2 [C_T] \qquad (5.2.25)$$

Finally it should be noted that if the other term in the denominator is larger, then:

$$\text{rate} = k_2 K_{eq} [C_T] \frac{P_{CO_2}}{P_{CO}} \qquad (5.2.26)$$

In this case the activation energy will be higher, since the activation energy for K_{eq} is about 32 kcal. Therefore, one

can conclude that the change in activation energy observed in the C-3.6 gasification data at 1080 K is not due to a shift in the reaction mechanism. At higher temperatures, where the non-catalyzed char experiments were made, the dominant term in the denominator of Equation (5.2.19) remains the same.

5.3 AN ASSESSMENT OF THE CATALYTIC GASIFICATION MECHANISMS

5.3.1 Introduction

In this section, the effect of calcium on the gasification rate of a microporous char with both oxygen and carbon dioxide will be discussed. The principal points addressed are:

1. How effective is the calcium catalyst over a broad range of conditions? Most of the previous studies have been conducted only at relatively slow reaction rates, at a single reactant concentration, and over only the initial conversion range. In this investigation, measurements were made at different initial calcium dispersions and calcium to carbon ratios. Experiments were conducted over a broad range of reaction rates, including rates sufficiently high so that intra-particle diffusion was significant, over the entire conversion range, with carbon dioxide, and with oxygen.

2. What is the possible mode of action of the catalyst? The experimental results show that the activation energy of the catalyzed reaction is slightly lower than for the

noncatalyzed char. Calculations using absolute rate theory demonstrate that this decrease in activation energy is exactly sufficient to account for the higher reactivity of the carbon. The data obtained in these experiments does not support a mechanism in which the catalyst acts by increasing the number of active sites on the char at which the reaction takes place.

3. What is the effect of calcium dispersion? The data indicates that the catalyst is only active when it forms a solution or surface complex with the carbon and not when it is present as a separate solid phase.

5.3.2 Summary of Experimental Results

This study was conducted with model chars to eliminate interferences by other inorganic compounds or by the elements of sulfur and nitrogen on the activity of the calcium. The dissolution of calcium oxide in an aqueous sucrose solution or ion-exchanging calcium onto the char gave two flexible and simple methods of calcium addition. The experimental data show that pyrolysis of the saccharate precursor results in a char that contains essentially only atomically dispersed calcium. The similar reactivity to the ion exchange char, and the linear dependence of reactivity on calcium loading, which is also observed when calcium is ion exchanged onto the char, are evidence that calcium dispersion is maintained during pyrolysis of the saccharate precursor. Furthermore, the

electron micrographs of an amorphous skeletal residue after the carbon is removed presents direct visual evidence that the initial dispersion of calcium in the char must have been very high.

Increase in reactivity of almost two orders of magnitude for the carbon oxygen reaction and three orders of magnitude for the carbon-carbon dioxide reaction were obtained with the catalyzed char containing 3.6 wt% calcium. Such an increase in reactivity for the carbon dioxide reaction is almost equal to the increase in reactivity obtained with potassium, which is generally considered to be a much more effective catalyst. Although no comparative measurements were made in this study, the increase in carbon reactivity with calcium addition is in agreement with the relative increase in reactivity obtained by Freund (1984a) for a potassium catalyzed spherocarb. The relative reactivity of the calcium catalyzed char at 910 K (obtained by extrapolation of the data) is compared to Freund's data in Figure 5.3-1. However, to obtain such a large increase in reactivity the calcium must be dispersed in the char on an atomic scale. Incorporation of the calcium as a separate solid phase (either as CaO or $CaCO_3$) directly into the char does not result in an increase in reactivity. The minor increase in the reactivity of the C-$CaCO_3$ char is possibly due to a slight solubility of $CaCO_3$ in a sucrose solution, thereby providing some atomic dispersion. Evidence obtained in this study indicate that calcium in a separate solid phase (i.e., the surface molecules of a $CaCO_3$ or CaO

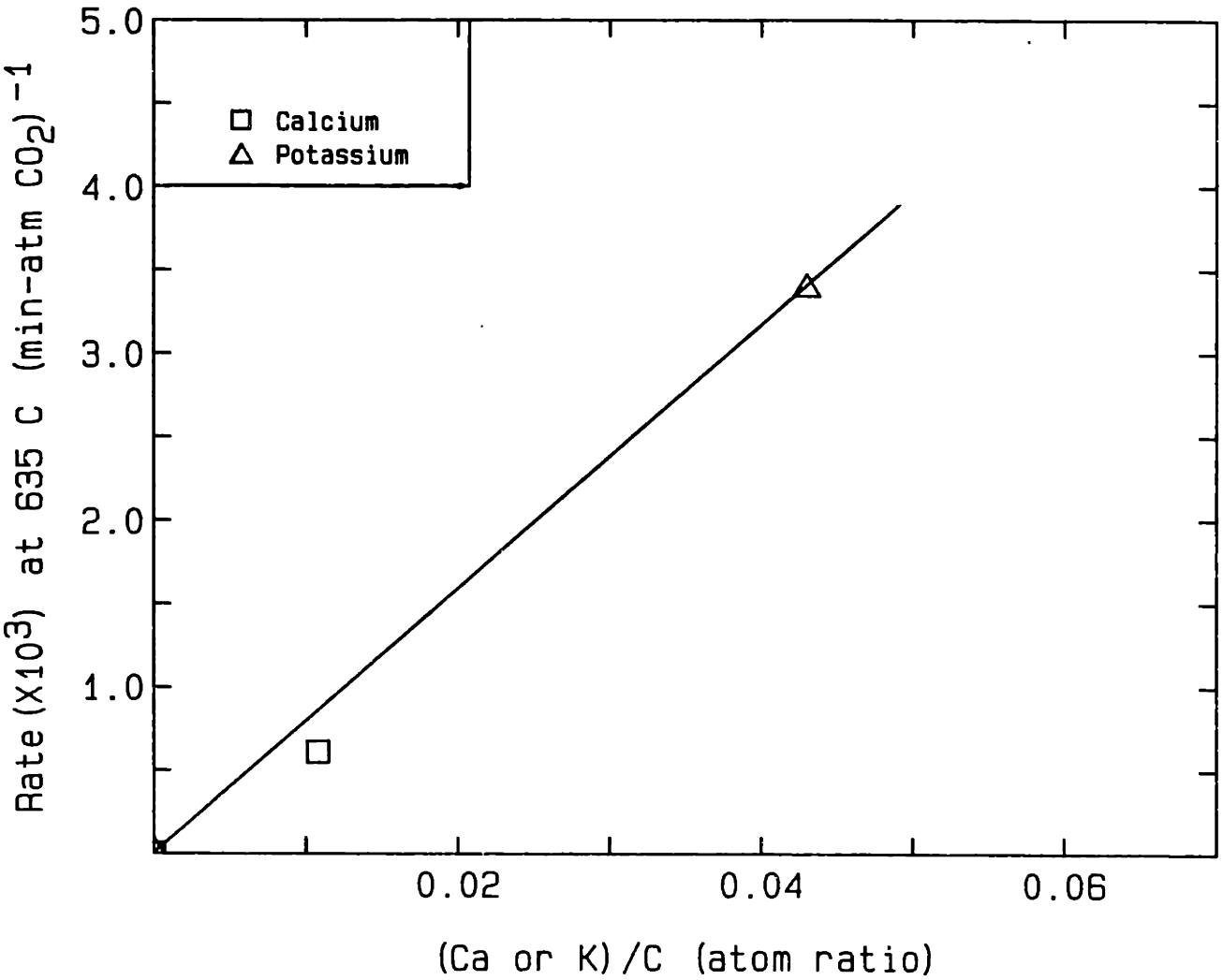

Figure 5.3-1. Comparison of calcium catalysis to potassium catalysis; carbon dioxide reaction (potassium data from Freund, 1984a).

crystallite) does not promote higher carbon reactivity. These results are presented and discussed in Section 5.3. As a result, it must be that calcium will act as a gasification catalyst only when the calcium forms a solution or a direct chemical bond with carbon. This is consistent with the explanation of Mims and Pabst (1983) who have demonstrated that potassium will form a carbon-potassium surface complex and that the number of such complexes correlates with the catalytic activity. Mims and Pabst propose that the complex is similar to a phenolate species. The analogous chemistry of the Group IA and IIA elements makes it likely that such complexes are also formed with calcium, although no direct evidence for a surface complex was obtained in this study. However, unlike potassium carbonate, a cation-carbon solution is not formed by simply heating calcium carbonate with the carbon. It is necessary to provide a separate reaction step to atomically disperse the calcium onto the carbon during preparation of the char. (A small number of surface complexes may also be formed with calcium carbonate. For instance, the increase in reactivity of the C-$CaCO_3$ char, based on only the surface atom calcium content is consistent with the linear relationship between reactivity and calcium loading shown in Figure 4.1-26. The surface atom calcium concentration is 0.144 wt% for 1 μm CaO crystal; therefore, the calcium content of the C-$CaCO_3$ char on this basis is 0.01 wt%. This close correspondence between the surface atom calcium concentration and the catalytic activity suggest that local surface complex

formation at the calcium-carbon interface may take place when the char and $CaCO_3$ are heated together. Either this route or calcium dispersion during sample preparation or both are probably responsible for the slightly higher reactivity of the C-$CaCO_3$ char).

The rate versus conversion (or normalized time) data for the catalyzed char show that the carbon is more reactive over the entire conversion range. The overall shape of the reaction profiles is similar to those obtained with the non-catalyzed char, although the weight versus time curve of the catalyzed char has a more pronounced sigmoidal shape. Both the ion exchange and the calcium-added chars have similar reactivity profiles. This implies that either most of the calcium in the calcium added char is located on the char surface after pyrolysis or that it is not necessary for the calcium to be located at the carbon surface to be effective. The calcium in the C-1 and C-3.6 chars is apparently well distributed throughout the particle. The onset of intra-particle diffusion, which is assumed to be indicated by the change in slope at the high temperature end of the carbon-oxygen Arrhenius diagram, occurs at approximately the same reaction rate for the catalyzed and non-catalyzed chars. In terms of the classical reaction-diffusion analysis this can only occur if the effective diffusivity is the same in all chars. This implies that the calcium must be active in all pores and uniformly distributed throughout the char.

The change in slope of the carbon-carbon dioxide rate data for the C-3.6 char at temperatures above 1075 K is probably the result of more rapid catalyst deactivation at higher temperatures. It is not believed to be due to intra-particle diffusion, since no change in the activation energy is observed with the non-catalyzed char at that rate and since the rate is also below where intra-particle diffusion is observed in the oxygen data. As was shown in Figures 4.1-34, the reaction rate of the catalyzed char decreases rapidly with heat treatment at 1100 K, whereas at 1025 K, no significant decrease in reactivity is observed. (Although the heat treatment data could be correlated by a first order model, the non-Arrhenius temperature dependence of the rate constant demonstrates that the actual deactivation mechanism must involve a number of reactions.) Additional isothermal heat treatment does not alter the reactivity of the non-catalyzed char, suggesting that changes in the char structure alone, which affect reactivity, occur on a time scale that is faster than the heating rate used in these experiments. Furthermore, the results suggest that the decrease in coal char reactivity during heat treatment may be largely caused by a change in the catalytic activity of inherent mineral matter rather than increased graphitization of the carbon structure.

5.3.3 Effect of Calcium Dispersion on Reactivity

The experimental results, which are presented below, show it is probably not small crystallites of calcium oxide or

carbonate that are the catalyst. Rather, it must be calcium that is directly bonded to the carbon that promotes increased carbon reactivity.

The catalytic activity of the calcium is unaltered whether CaO or $CaCO_3$ is the stable phase. As shown in Figure 4.2-1, the catalysis of the Boudouard reaction does not change at temperatures above or below the decomposition temperature of calcium carbonate (1160 K). Likewise, the activity of the catalyst in the oxygen reaction is not altered if the char is initially exposed to CO_2 and the reaction is conducted in air and a CO_2 partial pressure above the $CaCO_3$ decomposition pressure at the reaction temperature. Because the catalyst activity is unaltered whether calcium oxide or calcium carbonate is the stable phase, it is inferred that calcium present in a separate solid phase is not the catalytic agent. If catalysis indeed occurred at the carbon-calcium interface, one would expect the catalytic activity to be a function of the calcium crystal structure. (Cyclic oxidation-reduction cycles involving calcium and the carbon, which have been proposed as a mechanism for carbon catalysis, can only occur at the phase boundary since the calcium phase is specified by the carbon dioxide partial pressure at a fixed temperature.)

Furthermore, if catalysis were effected by small crystallites, the reactivity of the catalyzed char should be governed solely by the behavior of the particles on the carbon surface, since any carbon away from (or not affected by) the

catalyst reacts at such a slow rate that it does not contribute to overall reaction rate. Therefore, such a discrete site model of catalysis should be correlative to models that describe the dispersion of supported metal catalysts. Such models predict that the change in exposed surface area of the catalyst is (Ruckenstein and Pulvermacher, 1973):

$$\frac{dS}{dt} = -kS^n \qquad (5.3.1)$$

where S is a measure of the exposed catalyst surface area. Ruckenstein and Pulvermacher state that the exponent, n, equals 2 or 3 if the reaction is controlled by particle sintering and n > 4 if the reaction is controlled by surface migration. Such dispersion models, therefore, would predict catalysis deactivation to be a function of the catalyst loading. Yet the rate versus conversion data obtained with both the C-1 and C-3.6 chars are almost exactly proportional. The decrease in reactivity beyond the conversion at the maximum rate is best correlated by a first order model. In addition, the heat treatment verus time data (Figure 4.1-34) of the catalyzed char cannot be described by Equation (5.3.1) with n>2. Experiments conducted with the 1% Ca char gave the same type of linear dependence between the rate of decrease in reactivity with heat treatment time as was observed with the 3.6 wt% Ca char. Finally, it would have been expected that the rate versus conversion data of the ion exchange and the

saccharate chars should have been completely different for such a dispersed site model of catalysis since all the calcium in the ion-exchange char is initially located in the surface of the char, but this was also not observed. Direct attempts to measure catalyst dispersion by CO_2 chemisorption indicated that most of the calcium in the catalytic active chars was not present as calcium oxide crystallites, even though quantitative information was not obtained from these measurements.

5.3.4 Mechanism for Calcium Catalytic Gasification

The chemical mechanism by which calcium increases carbon reactivity cannot be determined from this data. In part, this is due to a lack of understanding of the carbon reaction itself, and, therefore, a failure to obtain from the uncatalyzed mechanism an insight into possible modes of action of the catalyst. Efforts to understand carbon catalysis have usually attempted to infer possible pathways for the catalytic reaction from comparative kinetic studies.

Overall, the behavior of the catalyzed and noncatalyzed chars is about the same. The rate versus conversion data, although not identical, are similar for both the catalyzed and non-catalyzed chars, and in each case, can be scaled by a single rate constant over the entire conversion range. The reaction order for the oxygen reaction is not substantially altered by the catalyst, and the amount of surface oxides present on both chars during reaction is quite similar. In

addition, the behavior of the catalyzed char relative to the non-catalyzed char is alike for both the carbon dioxide and oxygen reactions. The primary effect of the catalyst is to lower the temperature at which the reaction occurs. It is also observed that the activation energy of the catalyzed char is lower than the activation energy of the noncatalyzed char in all cases. If the decrease is interpreted in terms of the energy necessary to decompose an activated reaction complex into its products, one finds that the decrease in activation energy is precisely equivalent to the higher reactivity of the catalyzed char. This result is further elaborated on in Section 5.3.5. In that section, calculations using absolute rate theory are compared to the measured reaction rates of the catalyzed and non-catalyzed chars. This action of the catalyst is probably best explained in terms of some modification of the electron distribution in the solid by the catalyst that affects the kinetics of reactions with the carbon. This function of the catalyst has been originally proposed by Long and Sykes (1950), who suggest that the catalyst affects the energy of the bonds in the solid by withdrawing a π-electron from the carbon structure. Although Mims et al. (1982) have established that the potassium (or calcium) cation probably does not form a covalent bond directly with the carbon lattice, as originally proposed by Long and Sykes, the surface complex proposed by Mims et al. is sufficiently nucleophillic in character such that an electron must have been extracted from the carbon structure.

An alternate explanation of the catalyst action, which is frequently proposed, is that the catalyst changes the number of mono-energetic active sites on the carbon at which the reaction takes place. Such an explanation is not supported by the data obtained in this thesis. Because the number of active sites on the catalyzed char is fixed by the calcium content of the char, such a comparison requires that the number of active sites on the non-catalyzed char be a constant. Increasing the reaction temperature will not increase the number of active sites for the catalyzed char; however, it seems unlikely that the active site density of the non-catalyzed char remains constant with increasing temperature. Yet this assumption is necessary to make a meaningful comparison on this basis. Furthermore, since only a small amount of catalyst introduces enough active sites to increase the rate of the carbon dioxide reaction by almost 3 orders of magnitude, one must conclude that only about one carbon surface atom in 10,000 acts as an active site in the noncatalyzed char. It seems highly unlikely that the reaction should be limited to so few active centers on a non-structured carbon.

Finally, if the catalyst increased the number of active sites, one would expect the activation energies to be identical, and the rate versus conversion curves of the catalyzed char to be the same for oxygen and carbon dioxide and the rate versus conversion data of the ion-exchange char, not to have such a large difference between the initial and

maximum rates. Also, one would expect that the duration of any transients at the start or end of a run when the gas composition is changed to be the same for runs at identical temperatures. However, in the oxygen experiments in which a distinct induction time was observed, the duration of the induction period at 725 K with a noncatalyzed char was longer than the entire reaction time for the catalyzed char. In summary, the data is inconsistent with a mechanism whereby the catalyst only increases the active site density on the carbon, without affecting the energy distribution of the sites.

5.3.5 Comparison of Measured Rates to Theoretical Calculations

Since shortly after its development, absolute rate theory has been also applied to surface reactions (Laidler et al., 1940; Laidler, 1954). The theory is an extension of a statistical mechanical description of equilibria to reaction rates; the energy distribution of the reactants and the activated complex is given in terms of the partition functions of the molecules involved in a reaction step. Details of the theory will not be presented here since comprehensive discussions are available in numerous texts (e.g. Laidler, 1965; Thomas and Thomas, 1967). Only the assumptions made in arriving at the final form of the equations as applied to surface reactions will be briefly presented.

Application of this theory to surface reactions requires that certain assumptions be made about the bonding of adsorbed

species on the surface. However, because of a lack of understanding of the nature of the adsorbed species, calculations, which have any hope of correctness, can probably only be made for systems where either adsorption or desorption alone are considered and where some information about the surface complex is available. Even then, the calculation of the activation energy is not possible, and comparison to data is limited to the pre-exponential factor. As a result, the comparison is limited to reactions in which the rate controlling step is either adsorption or desorption. In the few cases where data and theory have been compared, agreement is satisfactory (Laidler, 1965). Accurate comparison of data and theory also requires knowledge of the number of active sites on a surface and a surface on which the sites are homogeneous. Clearly, for the high surface area, nonstructured chars used in these experiments, absolute rate theory provides, at best, limiting values that can be compared to the measured rates. However, as will be shown, by comparing catalytic and non-catalytic rates to the theoretical values, it is possible to infer that the catalyst probably lowers the energy requirement of the rate controlling step in the reaction sequence. The calculations show that the measured decrease in activation energy of the catalyzed reaction gives exactly the higher reactivity observed with the catalyzed char.

A. Adsorption Control

The primary assumptions in the theory are that the reactants and the activated complex are in equilibrium, and that the activated complex is unstable with respect to a single vibration. If v is the frequency of the vibration which leads to the dissociation of the complex to products, then the rate of decomposition is:

$$\text{rate} = v\, c^{\ddagger} \qquad [\text{molecule/cm}^2\text{-sec}] \qquad (5.3.2)$$

where $c^{\ddagger}$ is the concentration of activated complexes per cm^2 of surface.

The assumption of equilibrium between the activated complex and the reactants gives the relationship:

$$\frac{c^{\ddagger}}{c_g c_s} = K^{\ddagger} \qquad (5.3.3)$$

where c_g is the concentration of gas molecules (molecules/cm^3) c_s is the concentration of free sites on the surface (sites/cm^2); and $K^{\ddagger}$ is the adsorption equilibrium constant for the activated complex. The equilibrium constant can be expressed in terms of the appropriate partition functions of the reactants and the activated complex:

$$K^{\ddagger} = \frac{f^{\ddagger}}{f_s F_g} \frac{kT}{hv} e^{-E_o/RT} \qquad (5.3.4)$$

where $f^{\ddagger}$ is the partition function of the transition complex per unit surface area, less the degree of freedom

corresponding to the vibration of dissociation, which is given as kT/hv; f_s is the partition function per unit surface area associated with the free sites; and F_g is the partition function per unit volume of the reactant gas. E_o is the difference in zero point energies between the activated complex and the reactants (on a mole basis); it is identified as the activation energy of the reaction; k is the Boltzmann constant; h is the Planck constant; and T is temperature in Kelvin. Substitution of equations 5.3.3 and 5.3.4 into 5.3.2 gives:

$$\text{rate} = c_g \, c_s \, \frac{kT}{h} \, \frac{f^{\ddagger}}{f_s \, F_g} \, e^{-E_o/RT} \qquad (5.3.5)$$

Calculation of the rate requires evaluation of the partition functions F_g, f_s, and $f^{\ddagger}$. The function, f_s, is assumed to be unity since the surface atoms only undergo restricted vibrations. $f^{\ddagger}$ is assumed to have no translational or rotational degrees of freedom; therefore, $f^{\ddagger}$ includes only vibrational factors. F_g can be factored into partition functions corresponding to the translational, rotational, and vibrational degrees of freedom of the molecule. For a diatomic molecule,

$$F_g = f_t^{\,3} \cdot f_r^{\,2} \cdot f_v \qquad (5.3.6)$$

corresponding to the three translational, two rotational, and one vibrational degrees of freedom. The translational degrees of freedom are given as:

$$f_t^3 = \frac{(2\pi m\, kT)^{3/2}}{h^3} \qquad (5.3.7)$$

where m is the mass of the molecule, and the other terms have been defined previously. The rotational degrees of freedom are:

$$f_r^2 = \frac{8\pi^2\, I\, kT}{h^2} \qquad (5.3.8)$$

where I is the moment of inertia of the molecule.

The rate expression for adsorption is therefore (Laidler, 1965):

$$r = c_g c_s \frac{f^{\ddagger}}{f_r} \frac{h^4}{8\pi^2 I (2\pi m kT)^{3/2}} e^{-E_o/RT}$$

or

$$r = c_g c_s \frac{f^{\ddagger}}{f_r} \frac{B\, e^{-E_o/RT}}{T^{3/2}} \quad \text{molecules/cm}^2\text{-surface-sec} \qquad (5.3.9)$$

where B is a function of the (diatomic) reactant molecule. It is evaluated in Appendix 9 for the oxygen molecule. Equation (5.3.9) is valid for both single and dual site adsorption, depending on how c_s is defined; in addition, c_s will be a function of the extent of coverage.

B. Hertz-Knudsen Equation

An interesting result is obtained if it is assumed that the adsorbed molecules are not localized at an active site. That is, the adsorbed molecule has only one less translational degree of freedom then the free molecule. It still retains

its rotational degrees of freedom and two translational degrees of freedom. The equilibrium between the reactant and the activated complex is (Laidler, 1965):

$$K^{\ddagger} = \frac{c^{\ddagger}}{c_g} = \frac{f^{\ddagger}}{F_g} \frac{kT}{h\nu} e^{-E_o/RT} \qquad (5.3.10)$$

The equilibrium constant does not depend on the concentration of free sites in this case. The difference between $f^{\ddagger}$ and F_g is the loss of one degree of translational freedom. Therefore,

$$\frac{f^{\ddagger}}{F_g} = \frac{h}{(2\pi mkT)^{1/2}} \qquad (5.3.11)$$

The rate is then (Laidler, 1965):

$$r = c_g \frac{kT}{h} \frac{h}{(2\pi mkT)^{1/2}} e^{-E_o/RT} \qquad (5.3.12)$$

or, since $c_g\ kT = p$, the pressure of the gas, and for $E_o = 0$:

$$r = \frac{P}{(2\pi m\ kT)^{1/2}} \qquad (5.3.13)$$

This expression is the classical Hertz-Knudsen equation for the number of molecules striking a surface. This derivation emphasizes the non-localized nature of the adsorption that corresponds to calculations based on collision theory. Application of collision theory directly to reacting

systems usually includes an empirical transmission coefficient, K , to account for the probability that not every collision will result in the formation of an active complex. Absolute rate theory, however, allows one to interpret such an empirical factor in terms of the characteristics of the absorbed molecule.

C. Desorption Control

In this case, the adsorbed species and a transition state of the adsorbed species are considered to be in equilibrium:

$$K^{\ddagger} = \frac{c^{\ddagger}}{c_{ads}} \qquad (5.3.14)$$

where $c^{\ddagger}$ and c_{ads} are concentrations per unit surface area. The equilibrium constant can be expressed in terms of the appropriate partition functions:

$$K^{\ddagger} = \frac{f^{\ddagger}}{f_{ads}} \frac{kT}{hv} e^{-E_o/RT} \qquad (5.3.15)$$

where again $f^{\ddagger}$ is the partition function of the transition complex, less the degree of freedom corresponding to the vibration that allows dissociation of the complex to products.

The rate is therefore:

$$r = c_{ads} \frac{kT}{h} \frac{f^{\ddagger}}{f_{ads}} e^{-E_o/RT} \qquad (5.3.16)$$

Evaluation of the rate requires calculating $f^{\ddagger}$ and f_{ads}. If it is assumed that desorption is immobile $f^{\ddagger}/f_{ads}$ is approximately unity. For this case,

$$r = c_{ads} \frac{kT}{h} e^{-E_o/RT} \qquad (5.3.17)$$

Rates calculated from absolute rate theory applied to adsorption and desorption control and from the experimentally obtained activation energies were compared to the measured reaction rates of the catalyzed and non-catalyzed chars. The results are presented in Tables 5.3-1 and 5.3-2 for the oxygen and carbon dioxide reactions, respectively. Data from the C-0 and C-3.6 chars are compared at equivalent reaction rates, but therefore, at three different temperatures. For desorption control, it was assumed that $f^{\ddagger}/f_{ads}$ is approximately unity, implying immobile desorption. The concentration of adsorbed species for the desorption model was evaluated by comparing the calculated rate to the measured rate. The number of sites, c_s, available for adsorption was taken as 2×10^{15} sites/cm^2 (Blyholder and Eyring, 1957). The calculations show that the difference in activation energy, although less than 15% for the oxygen reaction and about 18% for the Boudouard reaction, between the catalyzed and the uncatalyzed char is exactly sufficient to account for the difference in reactivity between the two chars. It is not necessary to assume a different active site density. One can, therefore, conclude that the catalyst's mode of action is most

Table 5.3-1. Comparison of Measured Reaction Rates to Theoretical Calculations (Carbon-Oxygen Reaction).

	ABSOLUTE RATE THEORY			EXPERIMENTAL
	ADSORPTION		DESORPTION	
C-O Char-Oxygen	Mobile[1]	Immobile		
Temperature (K)	873	873	873	873
Activation Energy (E^*) (cal/mole)	-	-	-	34,000
Pre-Exponential Factor (molecules/cm^2-sec)	3.3×10^{22}	1.3×10^{17}	3.63×10^{28}	-
exp (E^*)	3×10^{-9}	3×10^{-9}	3×10^{-9}	-
Rate (molecules/cm^2/sec)	9.9×10^{13}	3.9×10^{8}	1.1×10^{20}	3.4×10^{13} [3]
C-3.6 Char-Oxygen				
Temperature (K)	700	700	700	700
Activation Energy	-	-	-	28,600
Pre-exponential Factor	3.7×10^{22}	2.2×10^{17}	2.9×10^{28}	-
exp (E^*)	1.2×10^{-9}	1.2×10^{-9}	1.2×10^{-9}	-
Rate (molecules/cm^2/sec)	4.4×10^{13}	2.6×10^{8}	3.5×10^{19}	3.4×10^{13}

[1] Equivalent to the Hertz-Knudsen Equation.

[2] Calculations assume a site density of 2×10^{15} sites/cm^2 (Blyholder and Eyring, 1957).

[3] Surface area for C-O char 640×10^4 cm^2/g; C-3.6 char 550×10^4 cm^2/g; stoichiometry: 0.75 mole O_2/mole C; oxygen partial pressure at 0.21 atm.

Table 5.3-2. Comparison of Measured Reaction Rates to Theoretical Calculations (Carbon Dioxide Reaction).

	ABSOLUTE RATE THEORY		EXPERIMENTAL
	ADSORPTION	DESORPTION	
C-O Char-CO_2	Mobile		
Temperature (K)	1,360	1,360	1,360
Activation Energy (E^*) (cal/mole)	-	-	70,700
Pre-Exponential Factor	1.1×10^{23}	5.7×10^{28}	-
exp (E^*)	4.3×10^{-12}	4.3×10^{-12}	-
Rate (molecules/ cm^2/sec)	4.7×10^{11}	2.5×10^{17}	2.0×10^{13}
C-3.6 Char-CO_2			
Temperature (K)	1,075	1,075	1,075
Activation Energy	-	-	58,000
Pre-exponential Factor	1.2×10^{23}	4.5×10^{28}	-
exp (E^*)	1.6×10^{-12}	1.6×10^{-12}	-
Rate (molecules/ cm^2/sec	2.0×10^{11}	7.2×10^{16}	2.0×10^{13}

Calculations assume a site density of 2×10^{15} sites/cm^2.

Surface area for C-O char 640×10^4 cm^2/g; C-3.6 char 550×10^4 cm^2/g. Carbon dioxide pressure 1 atmosphere.

likely to decrease the energy requirement of the rate controlling step: a reactive carbon-oxygen species can be more readily formed or removed from the carbon lattice.

The trend towards a lower activation energy was observed for all the calcium added chars. For the ion exchange char, the magnitude of the decrease is insufficient to completely compensate for the higher reactivity of the char. However, it is quite possible that this discrepancy is due to an uncertainty in the determination of an activation energy from only three data points. When the activation energy is based on only a few data points, a small error in any one point can easily result in a 10% error in the calculated value. Because differences this small are crucial to these calculations, data of high accuracy are necessary to allow correct conclusions to be drawn.

The experimentally measured rates are as fast or faster than the value calculated even for mobile adsorption, which suggests that the reaction is probably not under adsorption control. The carbon-oxygen rate is almost identical to the value predicted for mobile adsorption. This could be interpreted as support for a mechanism that involves a reaction between an adsorbed complex and a reactant molecule (see Section 5.2.2). The measured rate for the carbon-carbon dioxide reaction is considerably greater than the rate predicted for mobile adsorption. The assumption that the controlling step for this reaction is desorption of a carbon-oxygen complex is, therefore, probably correct.

CHAPTER SIX CONCLUSIONS AND RECOMMENDATIONS

6.1. CONCLUSIONS

1. Calcium is an effective catalyst for carbon gasification when it is present as a complex (or in solution) with the carbon. Calcium in a separate solid phase is inactive. However, the nature of the bond between the calcium and the carbon is uncertain, since the calcium retains its ability to react with carbon dioxide.

2. Approximately 1%(mole/mole) calcium increases carbon reactivity by almost two orders of magnitude for the oxygen reaction and three orders of magnitude for the carbon dioxide reaction. This is comparable to the increase in reactivity obtained with potassium for the Boudouard reaction. For the oxygen reaction, the higher reactivity is comparable to the results obtained by Radovic with calcium ion exchanged lignite chars. The reaction rate increases linearly with calcium content.

3. Calcium increases carbon reactivity over practically the entire carbon conversion range. Only with the ion exchange char was a decrease in reactivity observed at conversions above 80%. Catalyst activity is maintained even at reaction rates where intra-particle diffusion begins to become evident. This implies that the catalyst increases carbon reactivity in all pores about the same. At least up to 1050 K, the activity of

the catalyst is not adversely affected by extensive heat treatment of the char.

4. The catalyst depresses the overall activation energy of the intrinsic reaction. Calculations, using absolute rate theory, show that the decrease in the activation energy gives exactly the higher reactivity observed with the catalyzed char. It is inferred that the catalyst acts through an alteration of the electron distribution in the solid, thereby changing the overall energy level of the solid.

5. The reaction rate of the catalyzed char increases directly with the increase in the calcium to carbon ratio of the char as carbon is removed. This implies that the calcium tends to remain with the carbon and not deactivate at least over the first 50% of the carbon conversion range.

6. Measurements obtained in this study suggest that a microporous char particle reacts preferentially near the particle surface. Microporous particles apparently decrease in size and in density as carbon conversion proceeds.

7. In the intrinsic reaction regime, the rate versus conversion data can be scaled to one common curve. This implies that the rate data can be scaled by a single rate constant over practically the entire conversion range. The normalized rate versus conversion curves are apparently similar for both oxygen

and CO_2. TGA data for the oxygen reaction at the beginning of a run are not equivalent to the reaction rate because of con-current oxygen chemisorption on the char.

8. An extension of the random pore model that includes pore opening as carbon conversion proceeds is proposed to model the rate versus conversion data of microporous chars.

9. A mechanism is proposed for the low temperature carbon-oxygen reaction in terms of a reaction between the oxygen and the surface oxides on the carbon. The reaction is observed to be first order even though the surface oxide concentration is almost equivalent to a monolayer coverage. Furthermore, these surface oxides remain on the carbon, and do not desorb to products at the reaction temperature, in the absence of oxygen in the reactant gas.

6.2 RECOMMENDATIONS FOR FURTHER RESEARCH

1. Quantify the effect of heat treatment on catalyst deactivation.

2. Correct the TGA measurement for the oxygen reaction for the weight increase due to simultaneous oxygen chemisorption on the char. This could readily be done by combining TGA measurements with the measurements of gas composition.

3. Further investigation of the particle size effect in microporous chars. What is the relationship between the total microporous surface area and the surface area on which the reaction actually takes place?

4. Determine if the total surface area of a microporous char is also a function of particle size. This would provide some information on the inter-connectivity of very small micropores in a pyrolyzed carbon.

APPENDIX 1. CALCULATION OF CALCIUM ION-EXCHANGE FROM SOLUTION pH.

It is possible to approximately monitor the calcium uptake on the char by following the pH of the solution during ion exchange. Calculation of calcium uptake from the pH assumes that no acetate ion is removed from the solution through association with the solid, and that the solid does not contribute to the overall charge balance of the solution. For the acetate ion, the equilibria are:

$$Ca(Ac)_2 \longrightarrow Ca^{++} + 2Ac^- \qquad (1)$$

$$H^+ + Ac^- \longrightarrow HAc \qquad (2)$$

From an overall mass balance,

$$[Ac^-] + [HAc] = 2M \qquad (3)$$

where the brackets denote concentration and M is the molarity of the calcium acetate solution. Utilizing the equilibrium constant for Equation (2), one can obtain an expression for the concentration of the acetate ion:

$$[Ac^-] = \frac{2M}{\frac{K}{[H^+]} + 1} \qquad (4)$$

where K is the equilibrium constant.

The calcium ion concentration can then be determined from a charge balance:

$$[Ca^{++}] = 1/2([Ac^-] - [H^+])$$

The calcium ion concentration as a function of pH for a 0.05 M $Ca(Ac)_2$ solution is tabulated below, and the measured pH

of the exchange solution during calcium ion exchange at 298 K as a function of time is shown in Figure A1-1.

pH	Percent Initial Calcium Remaining in Solution
8.5	--
8.0	99.9
7.5	99.8
7.0	99.4
6.0	94.6

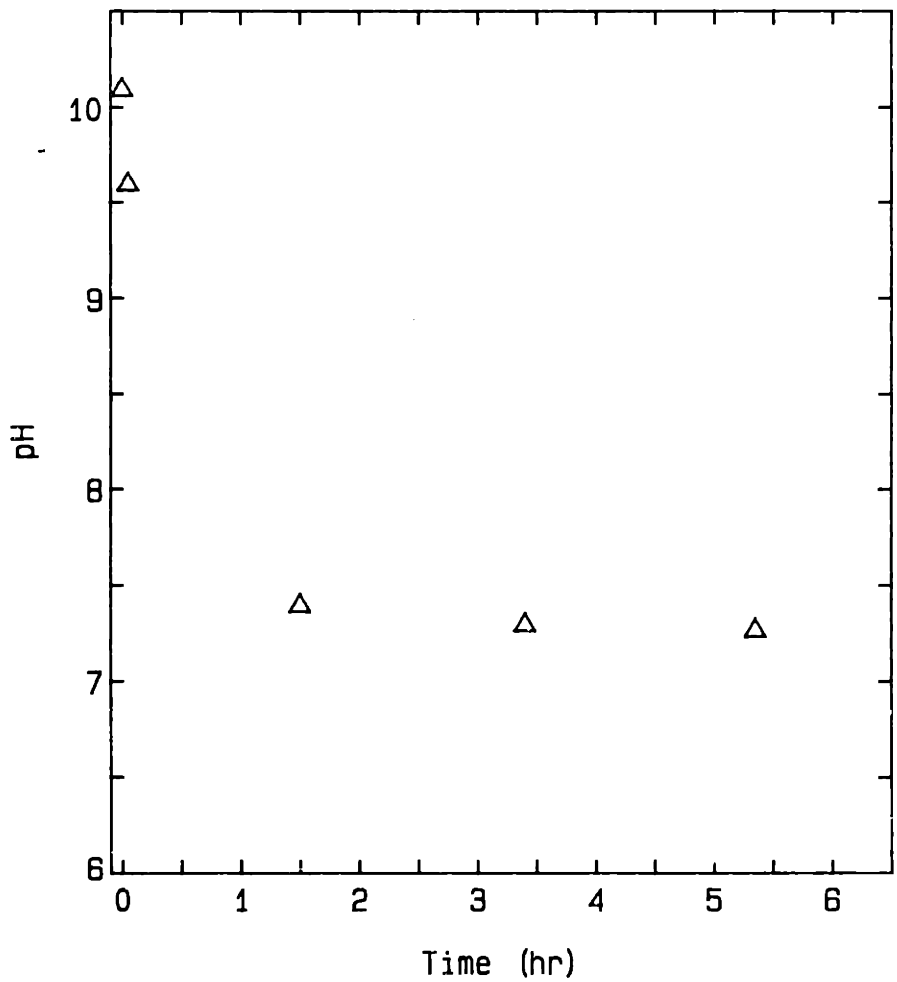

Figure A.1-1. pH of exchange solution versus time.

APPENDIX 2. CALCULATION OF EXTERNAL HEAT AND MASS TRANSFER RESISTANCES TO THE TGA SAMPLE PAN

The effect of bulk phase heat and mass transfer to the agglomeration of particles on the sample pan was determined theoretically, and the theoretical results were checked against experimental measurements in which the sample weight was varied.

The analysis assumes that the reaction is first order, thus allowing the mass transport equation to be readily combined with the reaction equation. It is assumed that the characteristic length scale for heat transfer is the diameter of the sample pan and that the characteristic length scale for mass transfer is the diameter of only the sample cross-section on the pan, since with very small sample amounts, the sample will not completely cover the sample pan. The model includes an empirical variation for the projected sample area with respect to the amount of sample that is based on visual observations made during the experiments. The assumed variation between sample weight and projected surface area is shown in Figure A2-1.

The rate of reaction of the solid is:

$$\frac{dN_C}{dt} = -N_C \ \eta_B \ A(x) \ k_n \ C_s \qquad (1)$$

where N_C is the sample size (gmoles); η_B is the effectiveness factor due to diffusion through the bed of particles; $A(x)$ characterizes the variation in reactivity with conversion; k_n is a rate constant for the reaction; and C_s is the reactant

concentration at the particle surface. A(x) is normalized to the conversion at which k_n is evaluated. The rate of mass transfer to the sample pan is:

$$\frac{dN_G}{dt} = - k_g a_m (C_o - C_s) \qquad (2)$$

where k_g is the mass transfer coefficient (cm/sec); a_m is the cross sectional area for mass transfer; and C_o is the bulk phase concentration of the reactant gas. dN_G/dt is the rate of mass transport. If the reaction is assumed to be:

$$C + O_2 \longrightarrow \text{PRODUCTS} \qquad (3)$$

then $N_C = N_G$. Equations (2) and (1) can be combined to eliminate C_s. The reaction rate expression is then:

$$\frac{-dN_C}{dt} = \frac{C_o}{\frac{1}{k_g a_m} + \frac{1}{N_C \eta_B A(x) k_n}} \qquad (4)$$

In terms of the rate constant, k, reported in this thesis:

$$k_n = k \cdot \frac{RT}{60} \quad \text{(cc-fluid/gmole-sec)} \qquad (5)$$

where the units of k are g/g(initial carbon)-min-atm.

The effectiveness factor for the particle bed is calculated from the Thiele modulus for semi-infinite flat plate geometry and a first order reaction:

$$\phi = L [k_v / D_{eff}]^{1/2} \qquad (6)$$

where L is the bed depth and k_v is the reaction rate per unit volume of the particle bed. D_{eff} is the effective

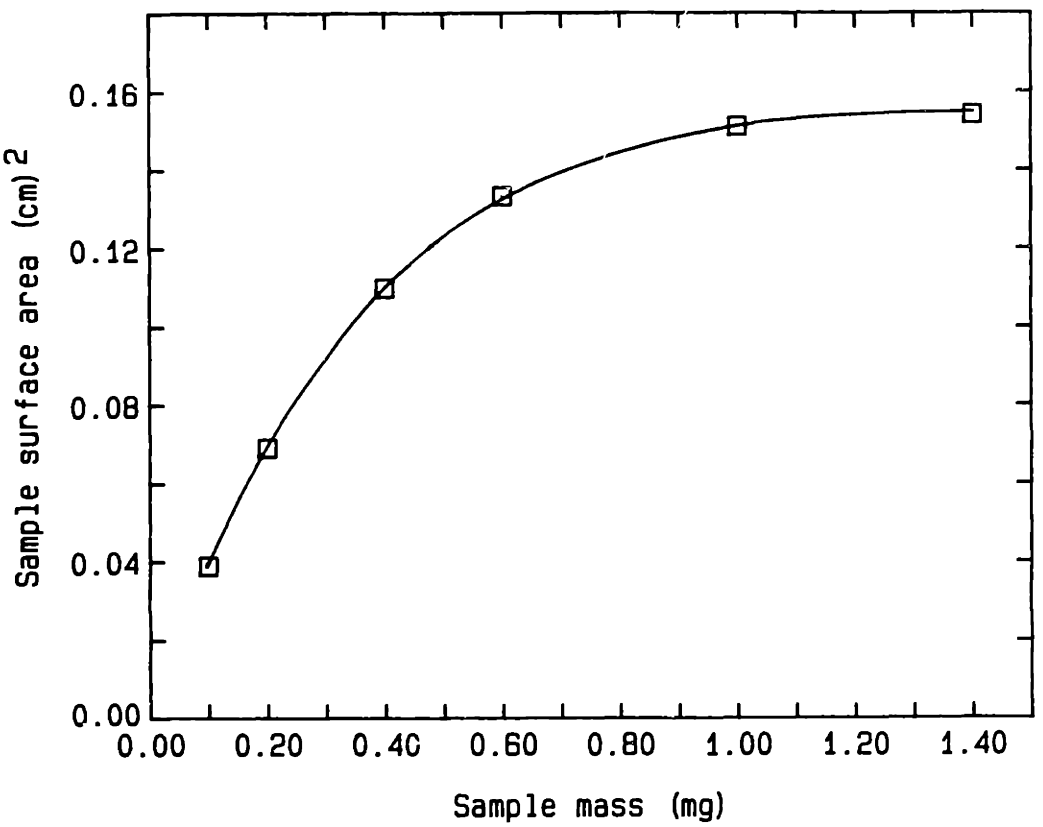

Figure A.2-1. Projected sample surface area on the sample pan.

diffusivity for diffusion between the particles in the bed. In terms of the rate constant k:

$$k_v = k\ A(x)\ \frac{RT}{60}\ .\ \frac{N_C}{V_B} \qquad (7)$$

where V_B is the volume of the particle bed. Substituting Equation (7) into equation (6), expressing D_{eff} in terms of the diffusion coefficient, and expressing L in terms of a multiple of the particle diameter, one obtains:

$$\phi = n \cdot d_p \left[\frac{N_C\ A(x)\ k\ RT \cdot \tau}{60\ V_B\ D_{1,2}\ \epsilon_B}\right]^{1/2} \qquad (8)$$

where n is the multiple of particle diameter, d_p; $D_{1,2}$ is the ordinary binary diffusion coefficient for oxygen in nitrogen; τ is the tortuosity; and ϵ_B is the porosity of the particle bed. The effectiveness factor for the semi-infinite plate Thiele Modulus is:

$$\eta = \tanh \phi / \phi \qquad (9)$$

The mass transfer coefficient was determined from a correlation given by Wigmans et al. (1983). Their correlation was calculated from measurements of the rate of naphthalene sublimation in a Cahn TGA system at 330 K and for gas flowrates up to 1000 scc/min. The results are reported in terms of dimensionless groups as:

$$Sh = \frac{k_g d}{D_{1,2}} = 1.2 + 1.2\ Re^{0.25} Sc^{0.6} \qquad (10)$$

Sh is the Sherwood number; Re is the Reynolds number, and Sc is the Schmidt number. The Reynolds number was defined in

terms of a local velocity.

$$\langle v \rangle = \frac{V}{A_t - A_p} \qquad (11)$$

V is the total volumetric flow rate and A_t and A_p are the cross-sectional areas of the reactor tube and sample pan, respectively. The Reynolds number is then:

$$Re = \frac{\langle v \rangle}{\mu} d \cdot \rho \qquad (12)$$

where d is the diameter of the sample pan. The Schmidt number is defined in the usual manner, $Sc = u/\rho D_{1,2}$.

Extrapolation of this correlation to high temperature is uncertain because the gas flow in the vertical tube furnace is in a transition regime of laminar and free convective flow (Eckert and Drake, 1972). The free convective component will change with temperature and probably dominate at moderately high temperatures. Moreover, because of the dominance of free convection, changing the gas flow rate within the limits of the TGA system is unlikely to greatly change the mass transfer to the sample. The Reynolds number, based on the tube diameter, for the TGA furnace tube is about 5.5 at 1000 K. The Raleigh number is:

$$Ra = Gr\ Pr = \frac{\bar{\rho}\, g\, L_r^3 \Delta \rho}{\mu^2} \cdot Pr \qquad (13)$$

where $\bar{\rho}$ is the average gas density; $\Delta\rho$ is the density difference; g is gravity; Pr is the Prandtl number; and L_r is a characteristic length. Determination of L_r is difficult because of the internal baffle in the tube. However, this baffle is present precisely to reduce the length scale of the

convection eddies. At 1000 K and for a temperature differential of 100 K over a length scale of 5 cm, the Raleigh number is approximately 8000. A comparison of these numbers to the data of Eckert and Drake (Figure A.2-2) show that the flow is well within a mixed flow regime. Minor changes in the Reynolds number (e.g. by increasing the gas flow) will not significantly alter the flow characteristics. Actually, changes in temperature are much more likely to have a significant influence on the flow characteristics in the reactor because of the dominance of free convection.

A heat balance on the sample pan gives:

$$m_p c_p \frac{dT_p}{dt} = h\, a_p (T_o - T_p) + q_r - \Delta H \left(\frac{dN_c}{dt}\right) \qquad (14)$$

where $m_p c_p$ is the mass and heat capacity of the sample pan; T_p is the pan temperature; T_o is the gas temperature; h is the heat transfer coefficient; a_p is the heat transfer area of the pan; q_r is the heat transfer by radiation; and ΔH is the heat of reaction. It is assumed that the char and sample pan temperature are identical. This is probably a reasonable assumption due to the shallowness of the char bed and the high thermal conductivity of platinum. The radiative heat transfer term is:

$$q_r = a_p \epsilon \sigma (T_p^4 - T_{w,eff}^4) \qquad (15)$$

where ϵ_r is the emissivity of the platinum pan and the char sample, σ is the Stefan-Boltzmann constant, and $T_{w,eff}$ is an

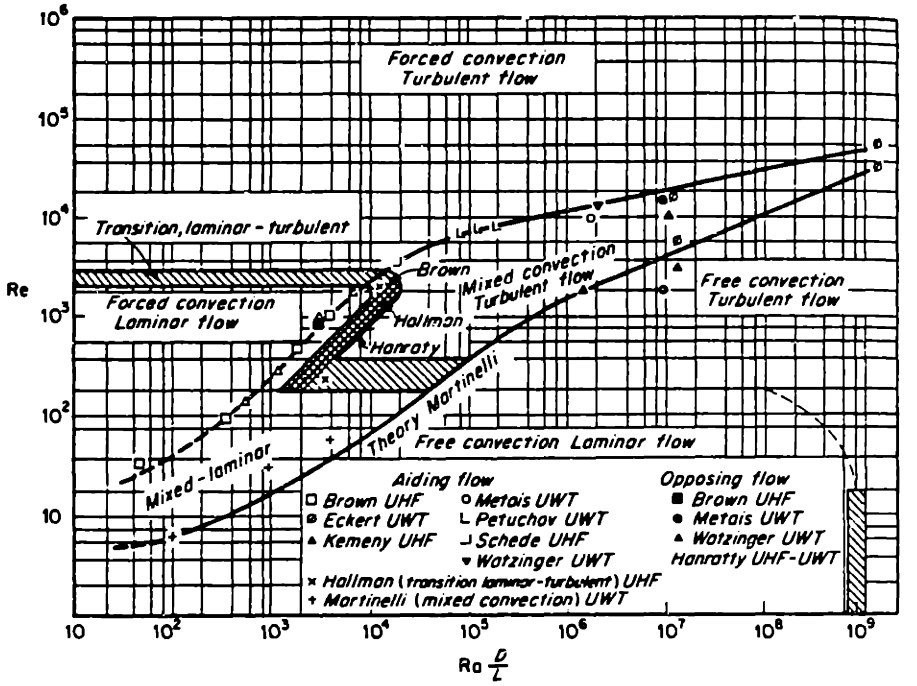

Figure A.2-2. Flow regimes in vertical tubes (Eckert and Drake, 1972).

average temperature characterizing the wall temperature and view factors of different furnace sections radiating to the sample pan. Experimental measurements of the gas and wall temperatures in the furnace by a dual size thermocouple assembly showed the furnace to be nearly isothermal, so that $T_{w,eff} \sim T$. Linearization of the radiation term yields:

$$q_r = a_p \epsilon\sigma \, 4T_{av}^3 \, (T_o - T_p) \qquad (16)$$

where $T_{av} = 1/2(T_o + T_p)$ and the other terms have been defined previously. Note that a_p will be twice the sample pan area since heat transfer occurs from both sides of the pan. (The sample pan diameter was 0.8 cm; its mass about 70 mg). The heat transfer coefficient was obtained by direct substitution of the corresponding heat transfer quantities into the mass transfer correlation (Bird et al., 1960):

$$Nu = \frac{hd}{k} = 1.2 + 1.2Re^{0.25}Sc^{0.6} \qquad (17)$$

The equations that need to be solved are:

$$-\frac{dN}{dt}c = \frac{C_o}{\frac{1}{k_g a_m} + \frac{1}{N_c \eta_B A(x) \, k_n}}$$

$$m_p c_p \frac{dT}{dt}p = h \, a_p(T_o - T_p) + 4a_p \epsilon\sigma \, T_{av}^3 (T_o - T_p) - \Delta H(\frac{dN}{dt}c)$$

(18)

Solution was obtained by a Runge-Kutta-Gill routine. However, in most cases, the characteristic time of the transient for heat transfer was much less than the characteristic reaction time. As a result it was necessary to set dT_p/dt to zero and solve the heat transfer equation algebraically for each integration step of the rate equation to remain within the stability limit of the semi-implicit integration method. That is, the equation set is stiff when the characteristic reaction time is less than about 3 minutes.

Some results of the calculations are presented in Figures A2-3 to A2-5. Figure A2-3 presents the calculated rate at 875 K as a function of the sample weight for different values of emissivity. The calculated results are in good agreement with measurements for $\epsilon_r = 0.45$. This is about the expected value for the emissivity of platinum with carbon on part of one side at 900 K. The reaction rate per unit weight remains constant up to 1.0 mg. Thus rates below about 0.2 mg/min should not be severely influenced by external heat or mass transfer. Note also that the rate deviates in a positive direction from the true rate. This implies that transferring heat away from the sample dominates over mass transfer to the sample. Furthermore, the strong effect of emissivity on the results indicates that radiative heat transfer is important. Since radiative heat transfer depends strongly on temperature, the contribution to heat transfer by radiation in the TGA will change with temperature. The relative

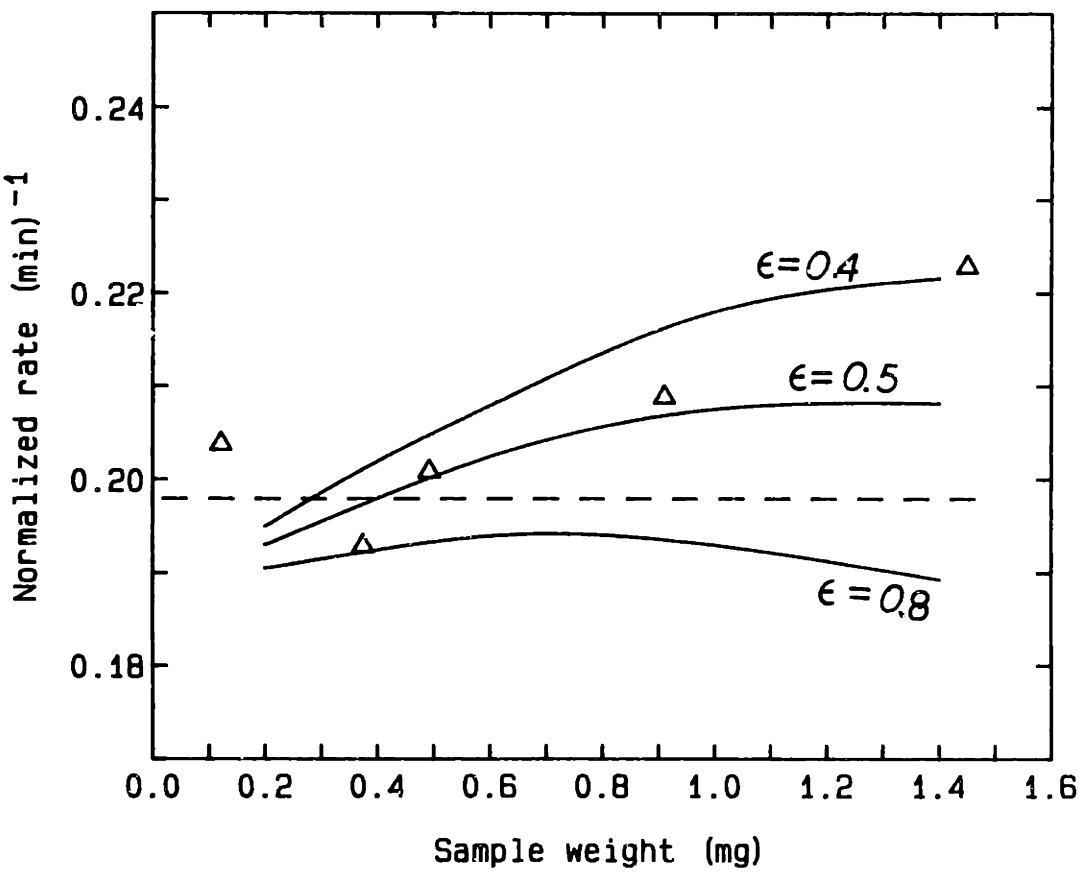

Figure A.2-3. Reaction rate as a function of sample pan loading; reaction rate normalized by initial sample weight; (Δ)-experimental points (C-O char; 875 K; heat treatment temperature 1100 K); (——) calculated for different values of emissivity.

effects of heat and mass transfer are illustrated in Figure A2-4. The overall rate represents a somewhat fortuitous counterbalance of heat and mass transfer effects for an exothermic reaction. Figure A2-5 presents calculated rates as a function of sample weight at 775 and 975 K. The somewhat unusual results obtained at 975 K illustrate the effect of altering the sample cross-section for mass transfer with sample weight. The two additional lines are for the cases where the sample area is kept constant at the area of the 0.40 mg sample.

The effectiveness factor for the particle bed was in all cases approximately 1 because of the shallowness of the bed at such small sample weights.

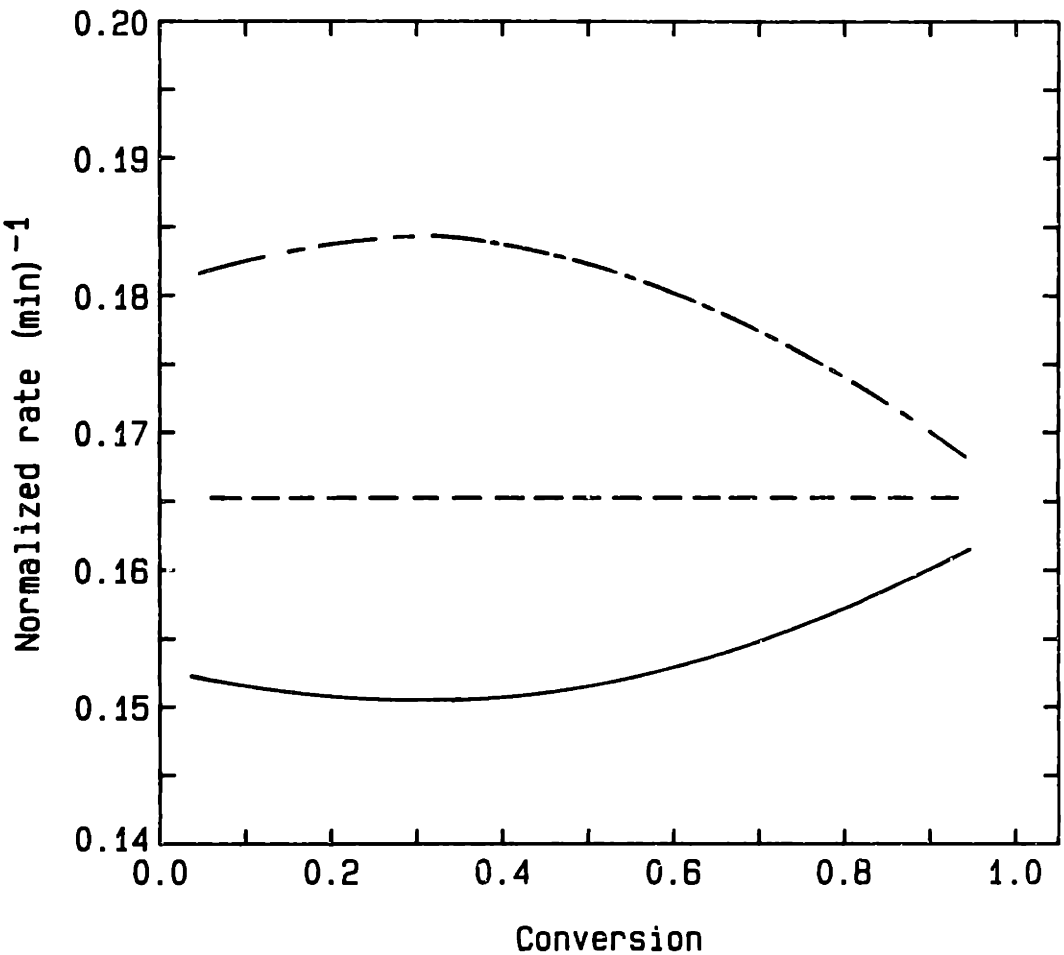

Figure A.2-4. Effect of heat transfer only on reaction rate with respect to conversion (— - —); effect of mass transfer only on reaction rate (——); both heat and mass transfer (– – –). Reaction rate normalized by N_C A(x).

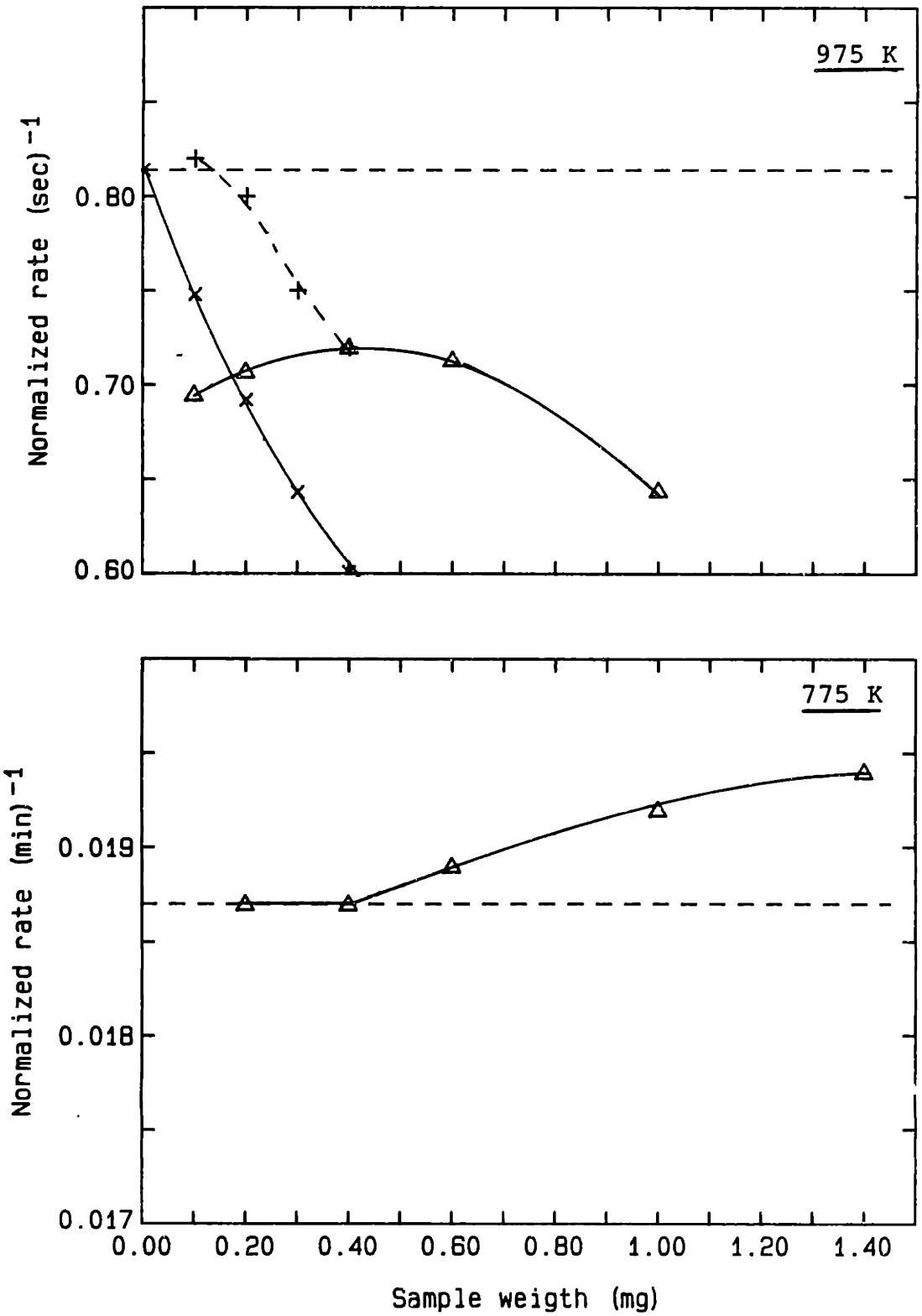

Figure A.2-5. Effect of sample weight on reaction rate. All points calculated. Top figure: (—x—x—)-sample area constant, mass transfer only; reaction temperature constant; (-+-+-)-sample area constant, both heat and mass transfer.

```
      C
      C     PROGRAM HEAT AND MASS TRANFER (HMTTRAN).FORTRAN
      C
      C        THIS PROGRAM CALCULATES THE EFFECTS OF EXTERNAL MASS
      C     AND HEAT TRANSFER ON THE MEASURED REACTION RATE. THE TEMP-
      C     ERATURE EQUATION IS INTEGRATED SIMULTANEOUSLY WITH
      C     THE RATE EQUATION, WHICH HAS INCLUDED IN IT THE MASS TRANSFER
      C     RESISTANCES. THE PROGRAM IS SET UP FOR THE REACTION:
      C                  C + O2 = CO2
      C
      C     ALTHOUGH IT CAN BE READILY MODIFIED TO OTHER REACTIONS
      C     THE PROGRAM IS NOT SET UP IN A COMPLETELY GENERALIZED
      C     FORM
      C
      C     DECLARATION STATEMENTS AND DATA STATEMENTS
      C
0001        REAL MS,MW,MP,NCI
0002        REAL N,K0,M0,K1,M1,K2,M2,K3,M3,N1,N2,N3
0003        REAL NC(502),R1(502)
0004        DIMENSION TIM(502), TEMP(502)
0005        DIMENSION EFF(502),CSO(502)
0006        REAL NRE,NPR,NSC,NU,KG,KT,NUB
0007        XRP(Z1)=(1.-Z1)*SQRT(1.-PSI*ALOG(1.-Z1))
0008        F(Z2)=CO2/(NCI/(KG*AC)+1./(NUB*XRP1*A0*EXP(-ESS/Z2)))
0009        G(Z3)=HT*AT*(TK-Z3)+AT*EPSI*SIG*4.*((TK+Z3)/2)**3*(TK-Z3)
0010        CR(Z5)=KG*AC/(KG*AC+NUB*NCI*XRP1*A0*EXP(-ESS/Z5))
      C     DATA INPUTS
      C
0011        OPEN(UNIT=10,NAME='HMT.DAT',READONLY,TYPE='OLD',
           1CARRIAGECONTROL='FORTRAN')
0012        READ(10,*) A0
0013        READ(10,*) ES
0014        READ(10,*) P
0015        READ(10,*) MW
0016        READ(10,*) Q
0017        READ(10,*) DPAN
0018        READ(10,*) MP
0019        READ(10,*) CP
0020        READ(10,*) RHP
0021        READ(10,*) DP
0022        READ(10,*) NPR
0023        READ(10,*) VIS
0024        READ(10,*) KT
0025        READ(10,*) DELH
0026        READ(10,*) MM
0027        CLOSE(UNIT=10)
0028        SIG=1.354E-12  !S-B const. cal/sec-cm2-K4
0029        ESS=ES/1.987
0030        PSI=6.0
0031        TYPE 202
0032      202 FORMAT('0ENTER VALUE FOR MASS OF SAMPLE (mg)')
0033        ACCEPT*,MS
0034        MS=MS*1.0E-3
0035        NCI=MS/12.
```

```
0036          TYPE 203
0037      203 FORMAT('0ENTER VALUE FOR TEMPERATURE (C)')
0038          ACCEPT*,TC
0039          TYPE 207
0040      207 FORMAT('0ENTER VALUE FOR THE WEIGHTED EMISSIVITY')
0041          ACCEPT*,EPSI
0042          TYPE 208
0043      208 FORMAT('0ENTER STEP SIZE (SEC)')
0044          ACCEPT*,H
      C
      C
      C       CALCULATE THE OVERALL HEAT AND MASS TRANSFER COEFFICIENTS.
      C     CORRELATION OF WIGMAN'S(1980)
      C
      C
0045          TK=TC+273.16
0046          DEN=P*MW/82.06/TK    !g/cc
0047          Q=Q*1.0/P*TK/295./60. !cc/s
0048          VLOC=Q/(3.14*1.1**2-3.14*(DPAN/2)**2)  !cm/s
0049          NRE=DEN*VLOC*DPAN/VIS
      C
      C       CALCULATE DIFFUSIVITY OF O2 IN N2 AND CO2 USING THE APPROXIMATION
      C     GIVEN IN CNS (P12); HOWEVER SINCE YCO2~0 DIM~D12.
      C       ESTIMATE DIFFUSIVITY BY EXPRESSING THE TEMPERATURE DEPENDENCE
      C     BY T**1.65 ABOUT THE VALUE FOR THE DIFFUSIVITY AT 800K
      C
0050          D12=1.092/P*(TK/800.)**1.65  ! cm2/s
0051          NSC=VIS/D12/DEN
0052          SH=1.2+1.2*NRE**.25*NSC**.6
0053          NU=1.2+1.2*NRE**.25*NPR**.6
0054          KG=SH*D12/DPAN  !cm/s
0055          HT=NU*KT/DPAN  !cal/cm2-sec-K
      C
      C
      C       THIS SECTION ESTIMATES THE GEOMETRIC PROPORTIONS OF THE
      C     SAMPLE ON THE PAN
      C
0056          DELD=-0.23E3*MS+0.30
0057          IF(DELD.LT.0.0) DELD=0.0
0059          BD=(-70.*DP+1.6)*MS*1000.+(-168.*DP+2.59)
0060          IF(BD.GT.3.6) BD=3.6
0062          AC=MS*6./3.14/BD/RHP/DP*(1.+DELD)**2
0063          CHECK=0.92*3.14/4.*DPAN**2
0064          IF(AC.GT.CHECK)GOTO 1
0066          GO TO 2
0067        1 AC=CHECK
0068          BD1=MS*6./3.14/AC/RHP/DP*(1+DELD)**2
0069          IF(BD1.LT.BD)BD1=BD
0071          BD=BD1
0072        2 CONTINUE
0073          AT=DPAN**2*3.14/2.
      C
      C     INITILIZE AND BEGIN RUNGE-KUTTA-GILL SCHEME
      C
```

```
0074          A=(SQRT(2.)-1.)/2.
0075          B=(2.-SQRT(2.))/2.
0076          C=-1.*SQRT(2.)/2.
0077          D=1.+SQRT(2.)/2.
0078          PHI1=SQRT(2.*BD*DP/AC/0.52/D12)*(1+DELD)
0079          HP=H/CP/MP
0080          RMS=MS*1000.
0081          WRITE(2,150)
0082          WRITE(2,295) TC,RMS,EPSI,AO,ESS,H,MM
0083          WRITE(2,296) VIS,KT,DP,AC,DELD,BD
0084          WRITE(2,297) NRE,NSC,SH,NU,KG,HT,D12
0085          WRITE(2,310) Q,MW,P,DPAN,MP,CP,DELH
0086          WRITE(2,311) RHP,NPR
0087          WRITE(2,299)
0088          TEMP(1)=TK
0089          T=TEMP(1)
0090          IW=1
0091          XC=0.0
0092          N=XC
0093          XRP1=XRP(N)
0094          CO2=0.21/82.06/T
0095          PHI=PHI1*SQRT(AO*NCI*XRP1*EXP(-ESS/TK))
0096          NUB=TANH(PHI)/PHI
0097          EFF(1)=NUB
0098          CSO(1)=CR(T)
0099          FF=F(T)
0100          R1(1)=-1.*FF*NCI*12000.*60
0101          TIM(1)=0.0
0102          WRITE(2,300) IW,TIM(1),EFF(1),CSO(1),R1(1),TEMP(1),XC,XRP1
      C
0103          DO 20 I=1,MM
      C
0104          KO=H*FF
0105          MO=HP*(G(T)-DELH*FF*NCI)
      C
0106          N1=N+0.5*KO
0107          T1=T+0.5*MO
0108          XRP1=XRP(N1)
0109          FF=F(T1)
0110          K1=H*FF
0111          M1=HP*(G(T1)-DELH*FF*NCI)
      C
0112          N2=N+A*KO+B*K1
0113          T2=T+A*MO+B*M1
0114          XRP1=XRP(N2)
0115          FF=F(T2)
0116          K2=H*FF
0117          M2=HP*(G(T2)-DELH*FF*NCI)
      C
0118          N3=N+C*K1+D*K2
0119          T3=T+C*M1+D*M2
0120          XRP1=XRP(N3)
0121          FF=F(T3)
0122          K3=H*FF
```

```
0123          M3=HP*(G(T3)-DELH*FF*NCI)
      C
0124          II=I+1
0125          NC(II)=N+1./6.*(K0+K3)+1./3.*(B*K1+D*K2)
0126          TEMP(II)=T+1./6.*(M0+M3)+1./3.*(B*M1+D*M2)
0127          TIM(II)=TIM(I)+H
0128          N=NC(II)
0129          XRP1=XRP(N)
0130          T=TEMP(II)
0131          CO2=0.21/82.06/T
0132          PHI=PHI1*SQRT(A0*NCI*XRP1*EXP(-ESS/T))
0133          NUB=TANH(PHI)/PHI
0134          EFF(II)=NUB
0135          CSO(II)=CR(T)
0136          FF=F(T)
0137          R1(II)=-1.*NCI*FF*12.E3*60.
0138          RI=I/20.
0139          IIN=I/20
0140            IW=II
0141          FLAG=ABS(RI-IIN)
0142          IF(FLAG.LT.0.01) GO TO 30
0144          GO TO 40
0145       30 WRITE(2,300) IW,TIM(II),EFF(II),CSO(II),R1(II),TEMP(II),N,XRP1
0146       40 CONTINUE
0147       20 CONTINUE
0148      150 FORMAT(' Version Sept.,1985 HMTTRAN',/)
0149      295 FORMAT(' Temp (C)= ',F8.2,' Mass (mg)= ',F6.2,' Emissivity',
             1F5.2,/,' Ao =',E14.5,' ES/R= ',F8.2,/,' Step size (sec)= ',F5.2,
             2' # of steps = ',I3,/)
0150      296 FORMAT(' Viscosity = ',E12.4,' Thermal conductivity = ',
             1E12.4,/,' Particle diameter (cm) = ',F8.5,
             2/,' Sample area = ',F8.5,' DELD= ',F7.4,' BD= ',F7.3)
0151      297 FORMAT(' NRe= ',F8.3,' NSc= ',F8.3,' NSh= ',F7.4,' Nu= ',
             1F7.4,/,' Mass transfer coeff. (cm/s)= ',E14.5,
             2/,' Heat trans coef. (cal/cm2-sec-K)= ',E14.5,/,' Diffusivity',
             3' (cm2/sec) =',F7.3)
0152      310 FORMAT(' Gas flow=',F6.1,' MW=',F5.1,' Pressure=',F4.1,' Dpan=',
             1F6.3,/,' Mpan=',F8.5,' Cp=',F6.2,' Heat of reaction=',F8.0)
0153      311 FORMAT(' Particle density =',F6.2,'  NPr =',F5.2)
0154      299 FORMAT(/,3X,'I',6X,'TIME',5X,' EFF',7X,'CS/CO ',7X,'RATE',
             17X,'TEMP',6X,'CONV.',4X,' XRP1',/,9X,'(SEC)',27X,'(MG/MIN)',
             26X,'(K)')
0155      300 FORMAT(2X,I3,3X,F7.2,3X,F7.4,4X,F7.4,4X,F8.4,4X,F6.1,4X,F7.4,
             14X,F6.3)
0156          STOP
0157          END
```

APPENDIX 3. CALCULATION OF INTRAPARTICLE DIFFUSION

A Thiele modulus was calculated using a first order reaction-diffusion model to determine the effect of intra-particle diffusion in the solid. The governing equation in spherical coordinates is (Satterfield, 1970):

$$\frac{d^2c}{dr^2} + \frac{2}{r}\frac{dc}{dr} = \frac{S_v\, k_s c}{D_{eff}} \qquad (1)$$

where c is the concentration of the reactant gas; r is the radius of the particle, k_s is a rate constant defined in units of cm^3-fluid/cm^2 of surface-sec; S_v is the surface area per volume of solid (cm^2/cm^3); and D_{eff} is an effective diffusivity of the reactant in the solid. The Thiele modulus for this governing equation is:

$$\phi = r\left[\frac{S_v \cdot k_s}{D_{eff}}\right]^{1/2} \qquad (2)$$

In terms of the rate constant defined for the data reported in this thesis:

$$k_v = k_s \cdot S_v = k \cdot \frac{\rho_p}{MW} \cdot \frac{RT}{60}\cdot\frac{1}{1.5} \qquad (3)$$

where k_v is a rate constant pore unit volume of solid and k is the rate constant defined for this data, gC/gC initial-atm O_2-min; ρp is the initial particle density and MW is the molecular weight of carbon; R is the gas constant in units of 82.06 atm O_2-cc/gmole-K; T is the temperature in Kelvin; 60

is a conversion factor of minutes to seconds; and 1.5 is a stoichiometric factor. Therefore:

$$k_v = k \cdot \frac{1.3\,(gC/cc)}{12\,(g/gmole)} \cdot \frac{82.06\ atm\ O_2\text{-}cc}{gmole\ K} \cdot T(K) \cdot \frac{1\ min}{60\ sec} \cdot \frac{1\ mole\ O_2}{1.5\ mole\ C}$$

$$k_v = (0.103)\, k(T) \qquad (4)$$

To determine the effective diffusivity of the reactant gas, it was assumed that the gas flux can be correctly described by Knudsen diffusion. D_{eff} is therefore (Satterfield, 1970):

$$D_{eff} = 9700 \times 10^{-8}\, \bar{r}_e\, \frac{\epsilon}{\tau} \left[\frac{T}{MW}\right]^{1/2} \qquad (5)$$

where D_{eff} is in units of cm^2/sec; r_e is the average pore radius in Angstroms; ϵ is the porosity of the solid (cc/cc). T is temperature in Kelvin; MW is the molecular weight of the diffusing molecule; and τ is a tortuosity factor. For a non-shrinking particle the porosity is a function of conversion:

$$\epsilon = [1 - (1-x)(1-\epsilon_o)] \qquad (6)$$

where x is the conversion of the solid and ϵ_o is the initial porosity of the particle.

Substitution of equation 4, 5, and 6 into 2 yields:

$$\phi = r \left[\frac{kT^{1/2}}{r_e/\tau}\right]^{1/2} \frac{77.5}{[1-(1-x)(1-0.3)]^{1/2}} \qquad (7)$$

The molecular weight of the diffusing molecule is 32 g/gmole and ϵ_o was assumed to be 0.3.

Rather than calculate ϕ for values of r_e and τ, equation

(7) was fit to the data and a value of r_e/τ was determined from the best fit to the data. The equation was fit to the 90-106 μm C-O char data at 20% conversion. A deviation from the low temperature data appears to begin at about 900 K. The rate at this temperature is 1.65 (min-atm O_2)$^{-1}$.

Therefore:

$$\phi = 1 = \frac{50 \times 10^{-4}[1.65\,(900)^{1/2}]^{1/2}}{[r_e/\tau]^{1/2}} \cdot \frac{77.5}{[1 - (1 - 0.2)(1 - 0.3)]^{1/2}} \quad (8)$$

$$\text{or} \quad \frac{r_e}{\tau} = 16.9 \text{ Å}$$

If τ is assumed to have a value of about 2, then re is approximately 34 Å. The value of r_e calculated from fitting the rate data to the model is larger than the pore radius estimated from the nitrogen adsorption isotherms. Because of the very small pore size, one would have expected the model to underestimate the pore size rather than overestimate it. Alternatively, if a value of r_e/τ equal to 4 is used to calculate an effective particle radius, one obtains a value of 24 μm.

The value of r_e/τ determined at 20% conversion was also used to calculate the Thiele modulus and an effective diffusivity at 60% conversion. Since all the data at 20% conversion were obtained at values of ϕ less than approximately 2, no significant concentration gradient existed in the particle, and as a result the pores in the solid should have widened almost uniformly with gasification of the solid. The enlarged pore diameter at 60% conversion

was estimated from a relationship derived from the random pore model:

$$q = r_e \cdot \left([\, 1 - \beta \, \ln(1-x) \,]^{1/2} - 1 \right) \qquad (9)$$

q is the increase in pore diameter as a function of the conversion, x; and β is the parameter of the random pore model (see Section 5.1-3). With the assumption that the initial pore diameter is about 6 Å (this assumes τ to be about 0.5), a new value for r_e / τ at 60% conversion was estimated as 24. With the value for r_e/τ , and an intrinsic rate constant obtained from the data at 60% conversion, values of ϕ and the effectiveness factor were calculated:

$$k = 1.35 \text{ gC/gC-initial min-atm } O_2 \; ; \; \phi = 0.53 \; ; \; \eta = .98$$

The calculations clearly show that the effectiveness factor should approach one as the reaction proceeds for char particles initially not too far removed from the intrinsic reaction regime. The data however, continue to deviate from the intrinsic reaction regime correlation. Certainly at even higher conversions, the particles should burn in the intrinsic regime, yet the data still remains below the intrinsic rate.

APPENDIX 4. WEIGHT VERSUS TIME TGA DATA.

Typical weight versus time measurements obtained with the TGA are presented in this section for the C-3.6 and C-O chars for the oxygen reaction.

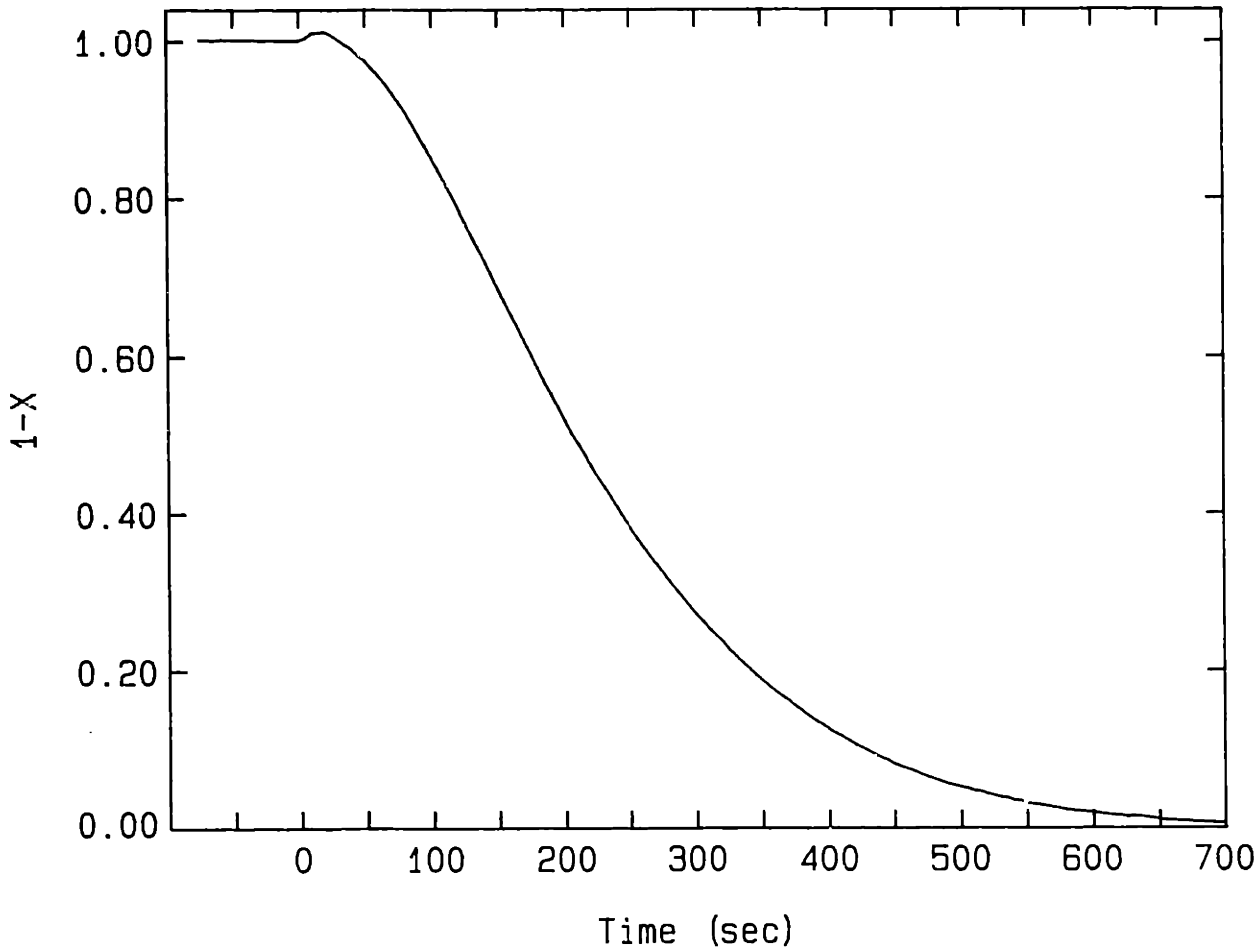

Figure A.4-1. Weight versus time TGA data; C-O char-oxygen (0.21 atm) at 875 K. (1100 K heat treatment temperature, 90-106 μm particles) Sample weight 0.492 mg.

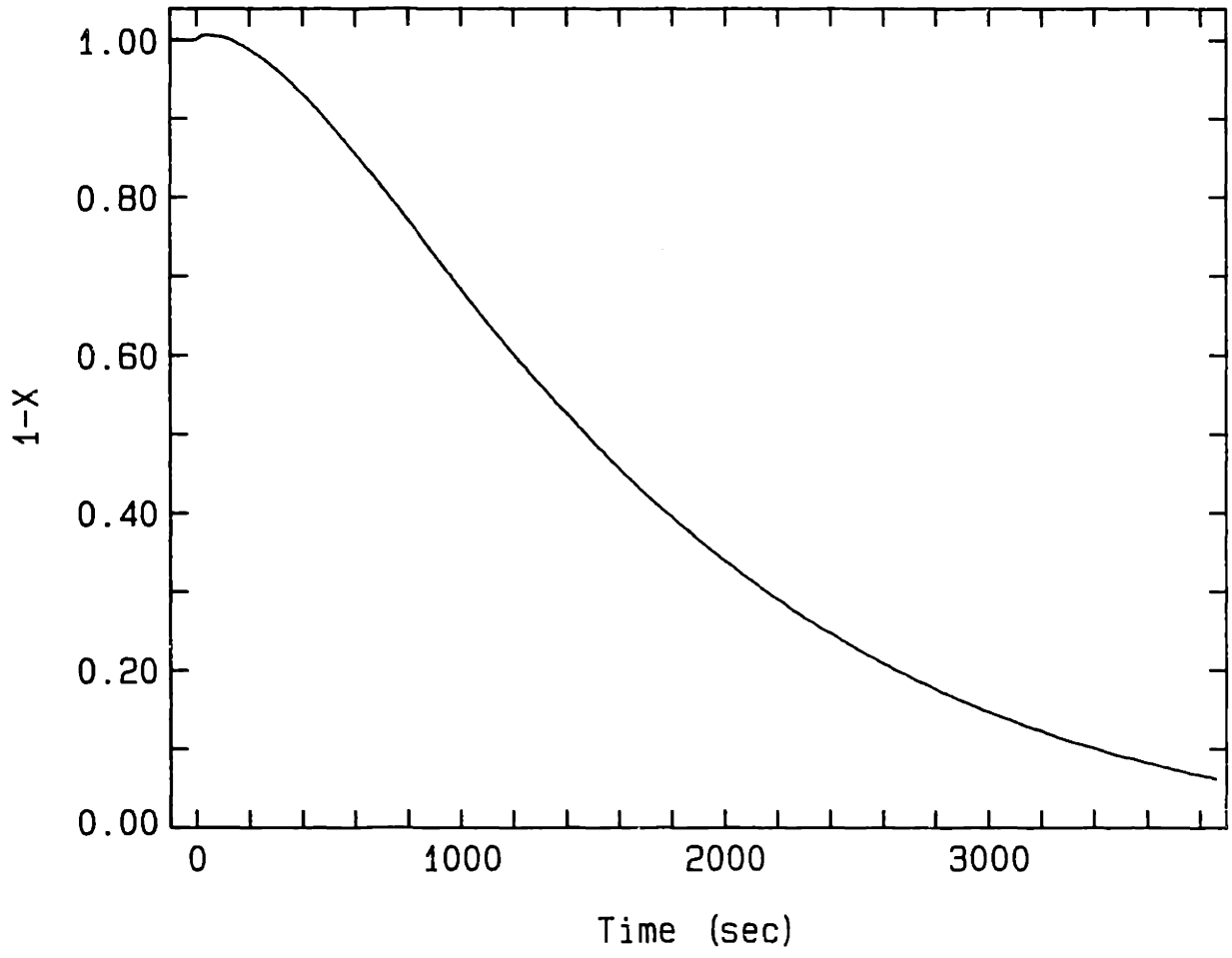

Figure A.4-2. Weight versus time TGA data; C-O char-oxygen (0.21 atm) at 785 K (1100 K heat treatment temperature, 90-106 μm particles) Sample weight 1.203 mg.

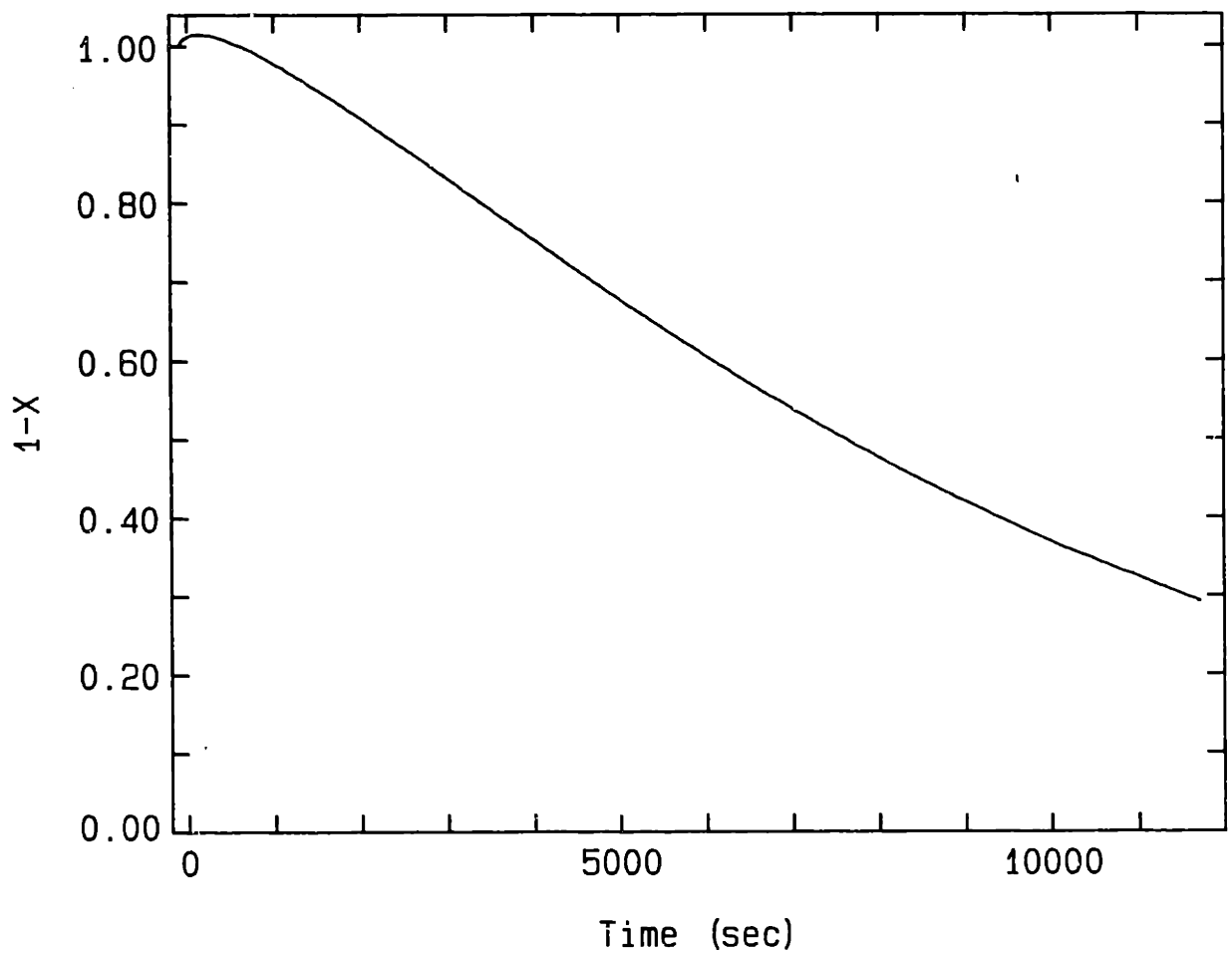

Figure A.4-3. Weight versus time TGA data; C-O char-oxygen (0.21 atm) at 725 K (1100 K heat treatment temperature, 90-106 μm particles) Sample weight 1.237 mg.

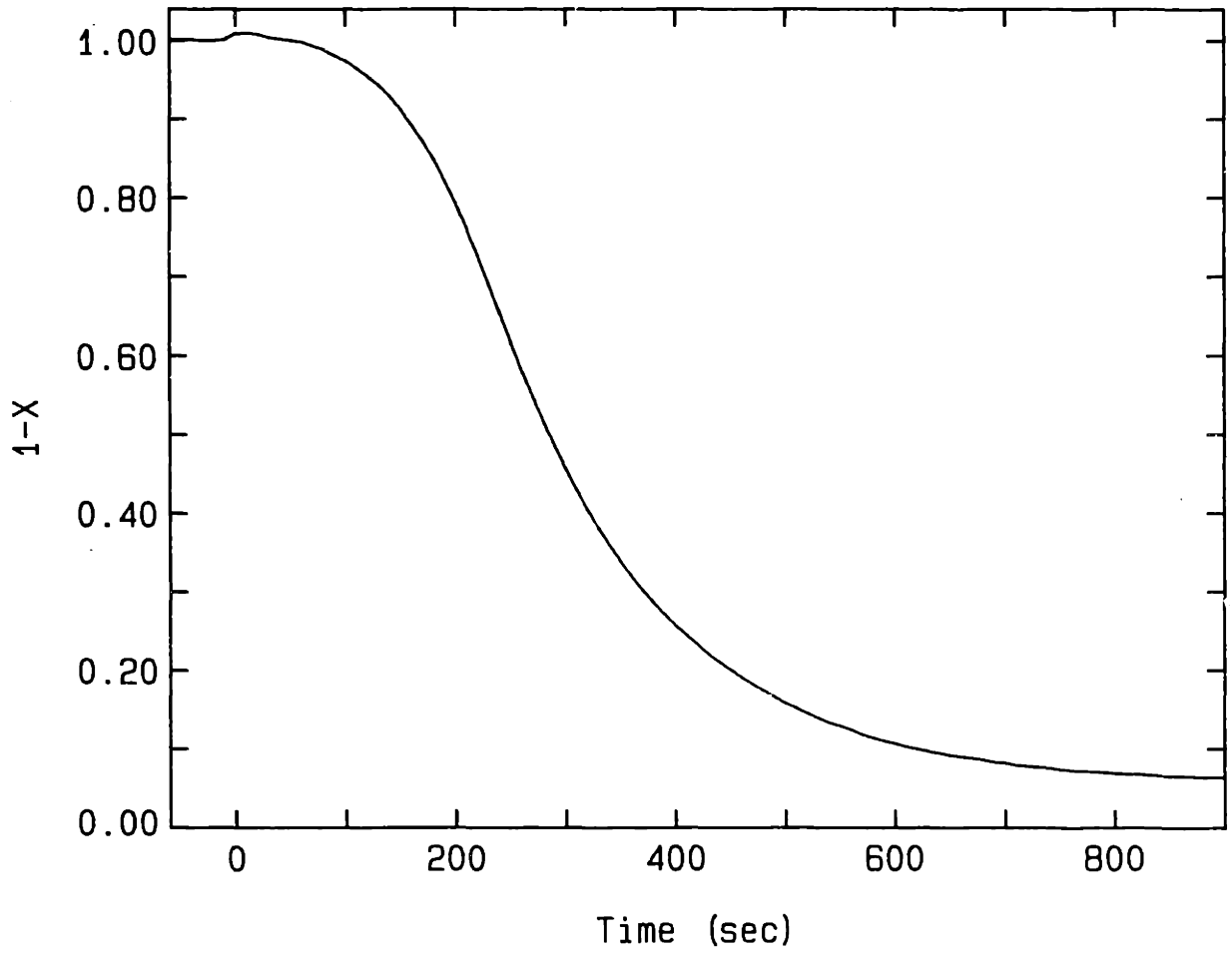

Figure A.4-4. Weight versus time TGA data; C-3.6 char-oxygen (0.21 atm) at 710 K (1100 K heat treatment temperature, 90-106 μm particles) Sample weight 0.525 mg.

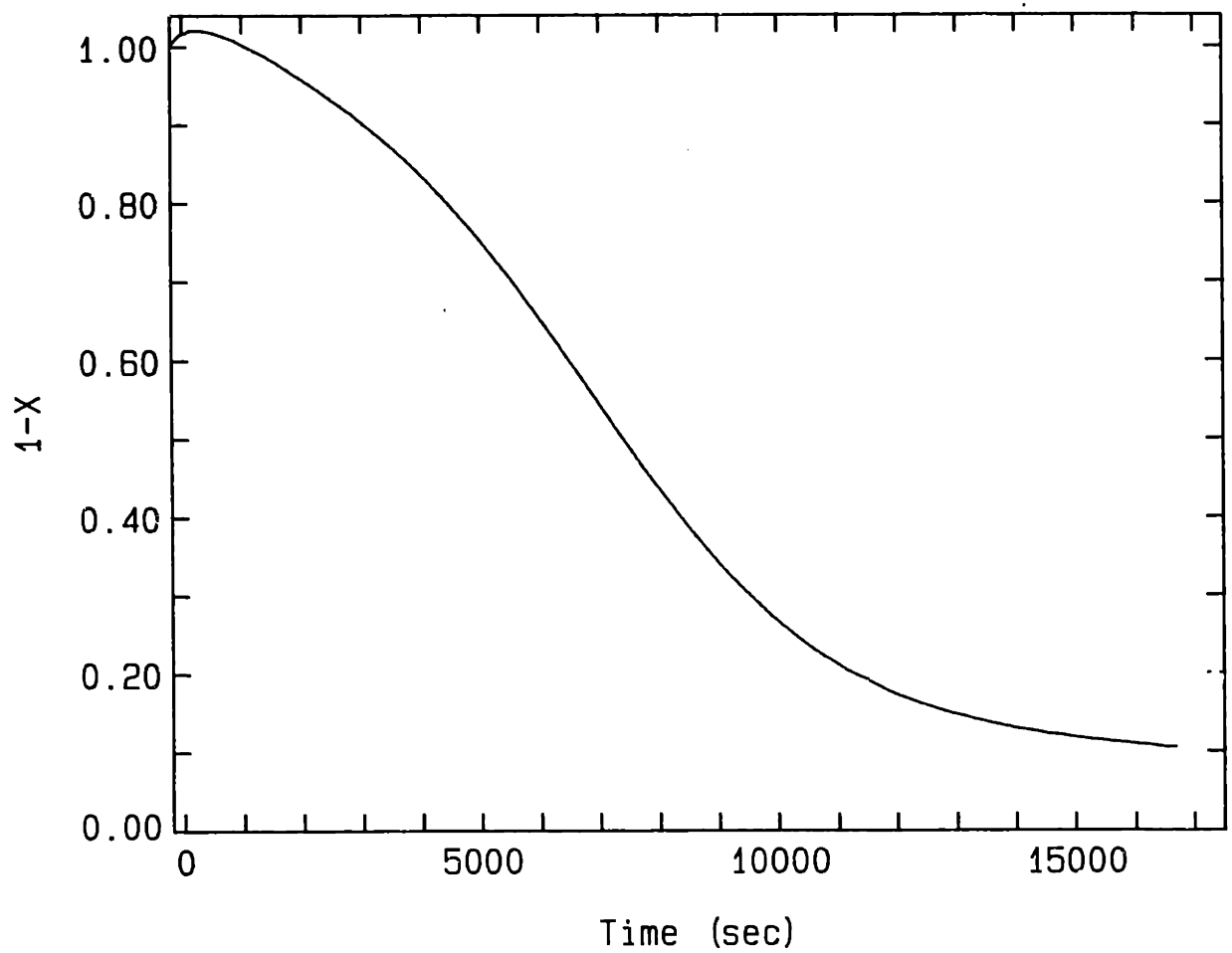

Figure A.4-5. Weight versus time TGA data; C-3.6 char-oxygen (0.21 atm) at 600 K (1100 K heat treatment temperature, 90-106 μm particles) Sample weight 1.24 mg.

APPENDIX 5A. NITROGEN ADSORPTION AND DESORPTION ISOTHERMS AT 77 K AND ANALYSIS OF THE DATA BY THE BET AND DUBININ-POLANYI EQUATIONS.

Figures A5-1 to A5-5 are the nitrogen adsorption and desorption measurements obtained with the C-O and C-3.6 chars and with Spherocarb. The results are discussed in Section 4.3-1. Figures A5-6 to A5-10 present the BET and Dubinin-Polanyi analysis of the nitrogen adsorption data.

APPENDIX 5B. CARBON DIOXIDE CHEMISORPTION ON CALCIUM.

Figurs A5-11a to A5-11e present the results of the carbon dioxide chemisorption measurements on the C-3.6 char. These data are discussed in Section 4.4.

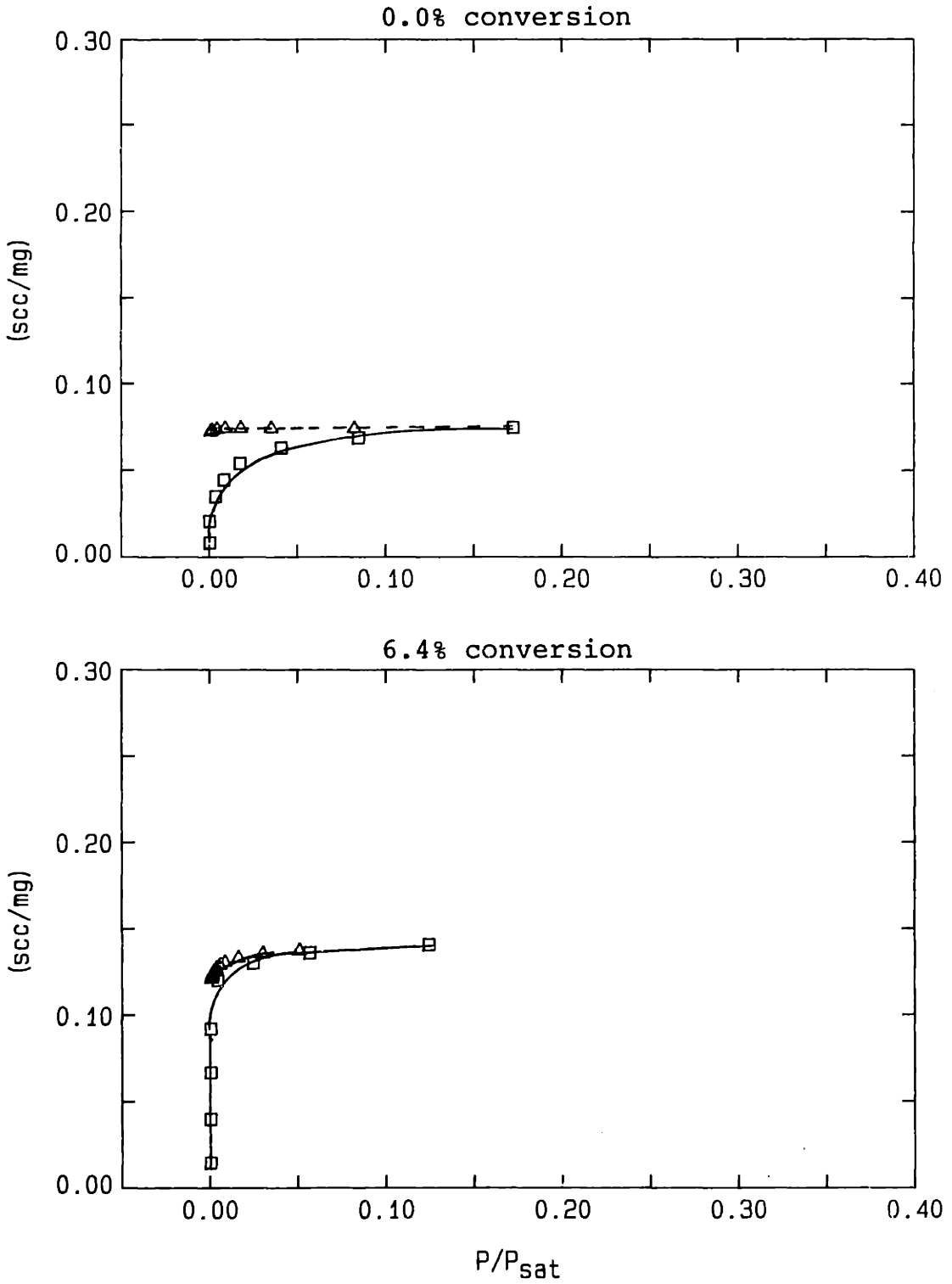

Figure A5-1a Nitrogen adsorption/desorption isotherms for the C-O char; reacted in air at 760 K to the conversion indicated; 90-106 μm particles; heat treatment temperature 1100 K. □ - adsorption; △ - desorption.

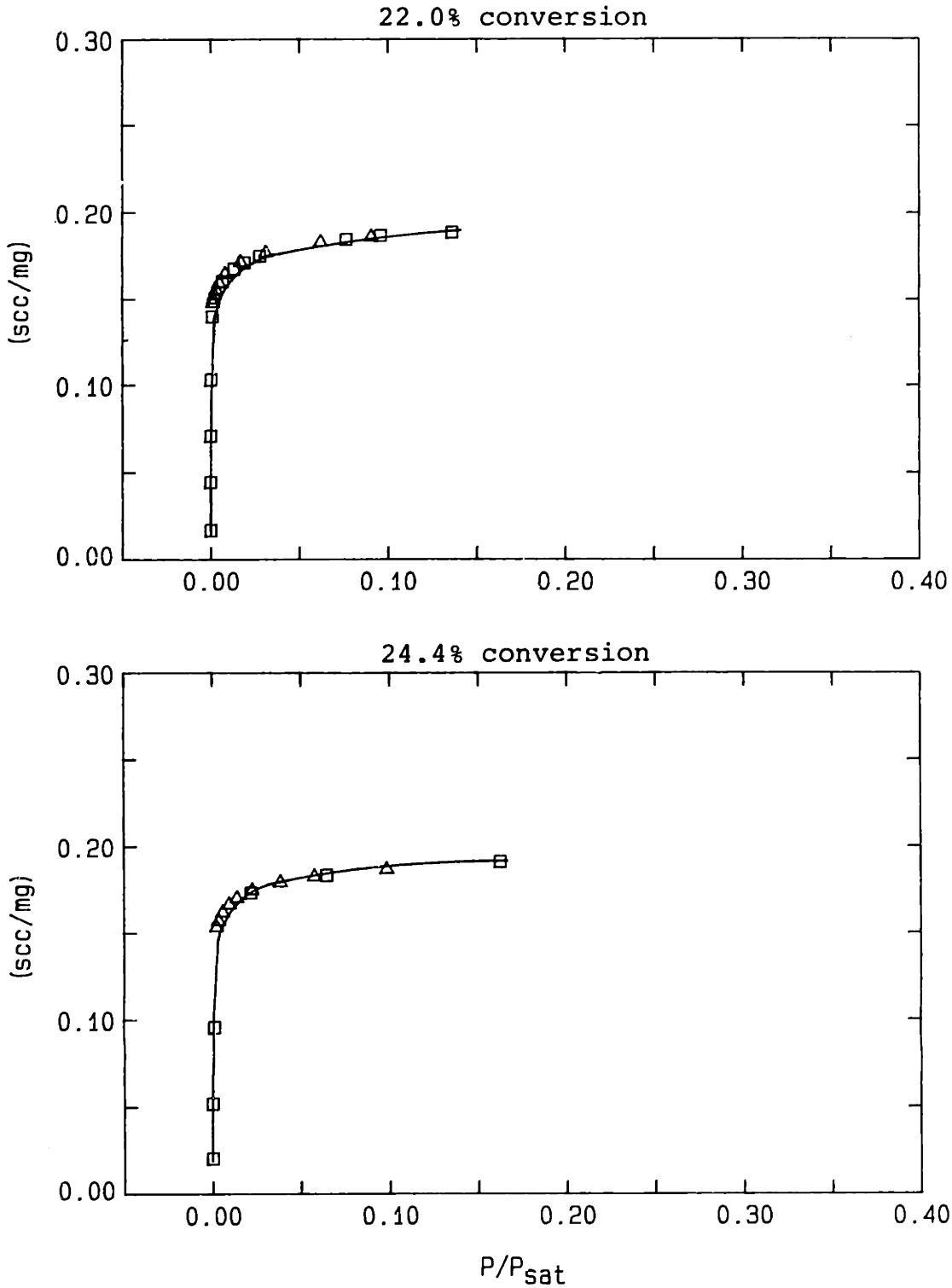

Figure A5-1b Nitrogen adsorption/desorption isotherms for the C-O char. □ - adsorption; △ - desorption.

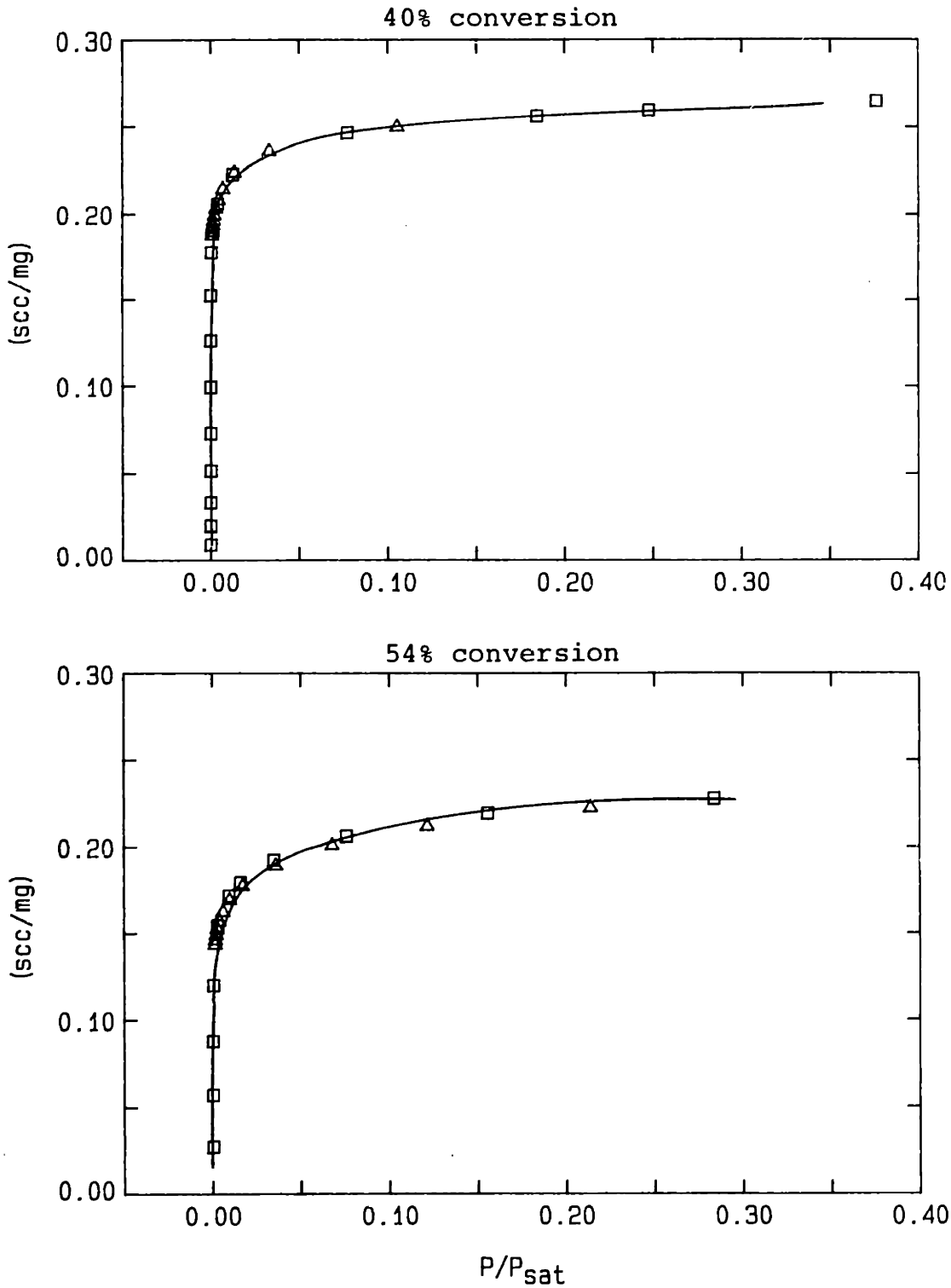

Figure A5-1c Nitrogen adsorption/desorption isotherms for the C-O char. □ - adsorption; Δ - desorption.

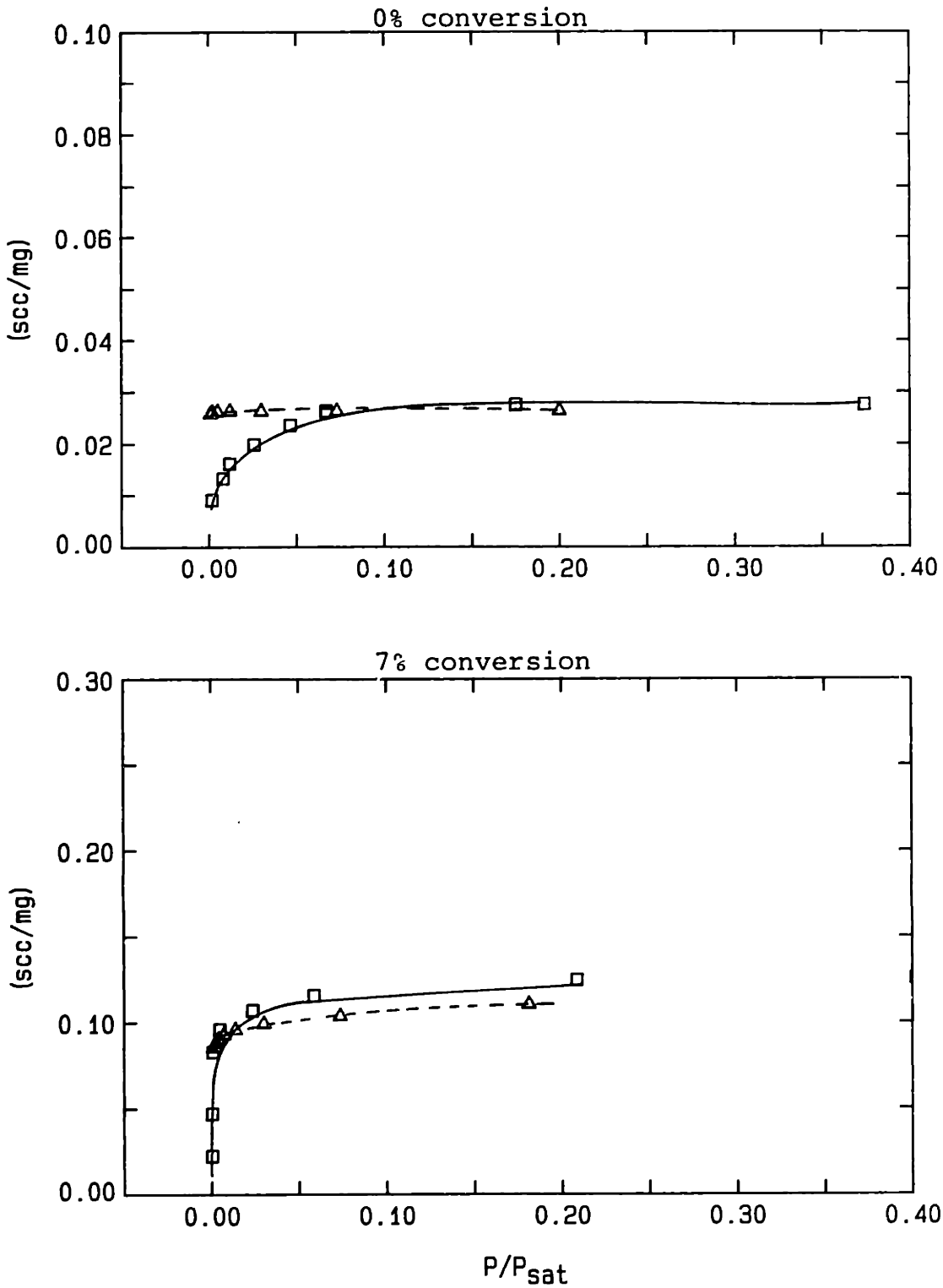

Figure A5-2a Nitrogen adsorption/desorption isotherms for the C-3.6 (3.6 wt% Ca) char; reacted in air at 615 K to the conversion indicated; 90-106 μm particles; heat treatment temperature 1100 K.
□ - adsorption; △ - desorption

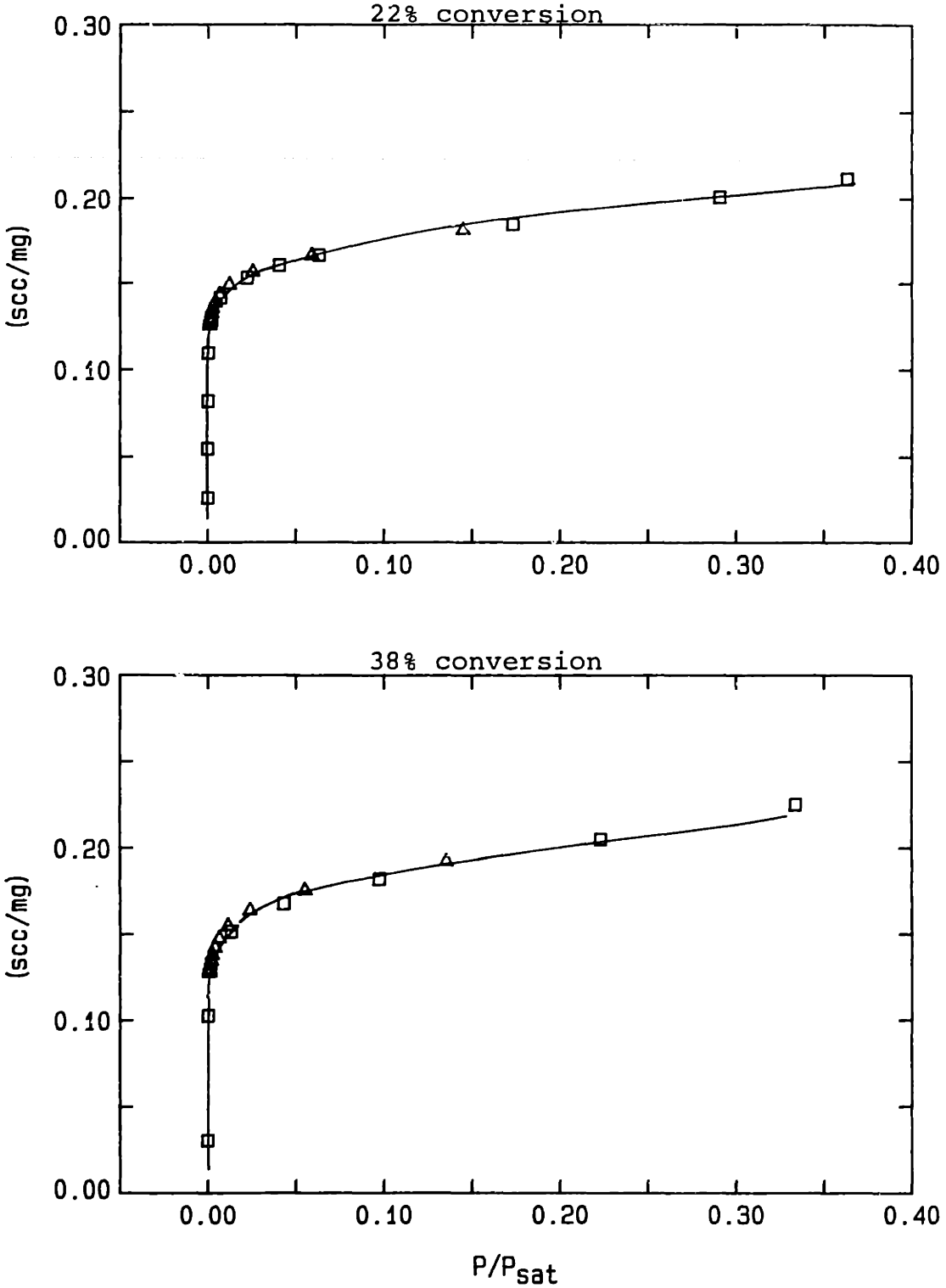

Figure A5-2b Nitrogen adsorption/desorption isotherms for the C-3.6 char. □ - adsorption; △ - desorption.

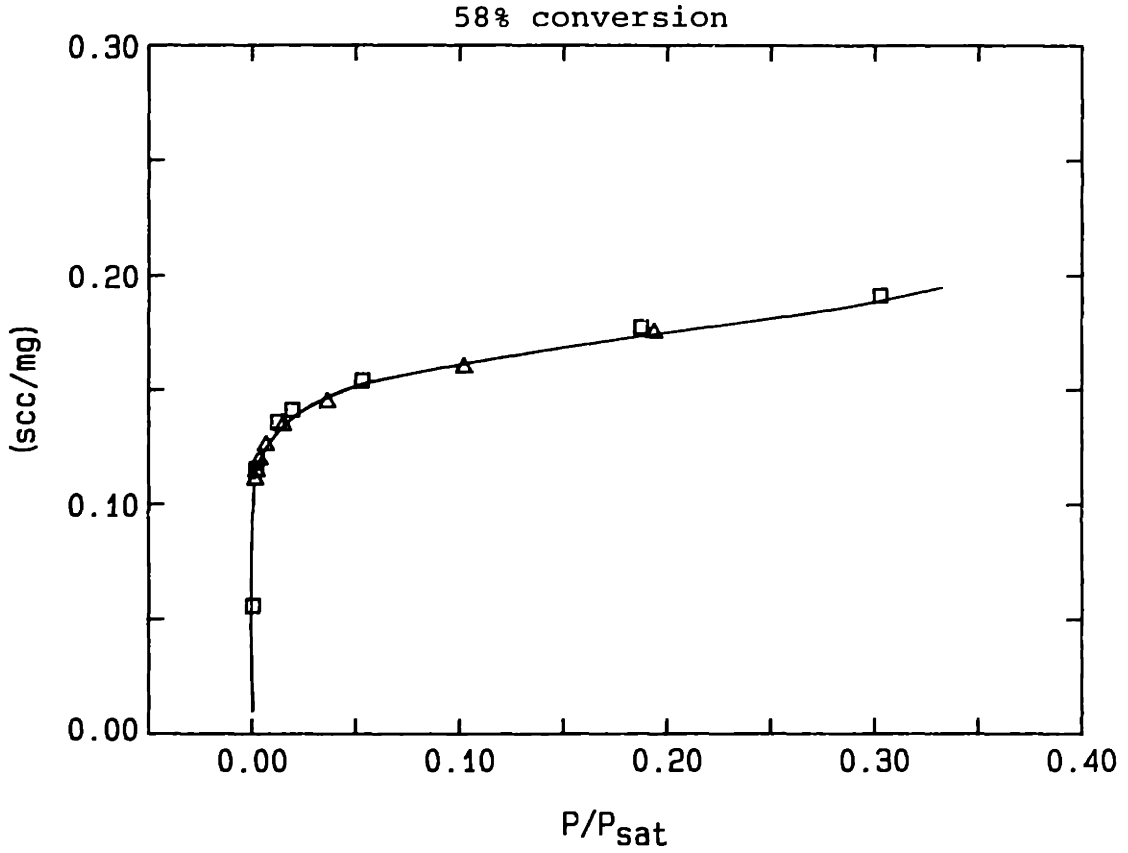

Figure A5-2c Nitrogen adsorption/desorption isotherms for the C-3.6 char. □ - adsorption; Δ - desorption.

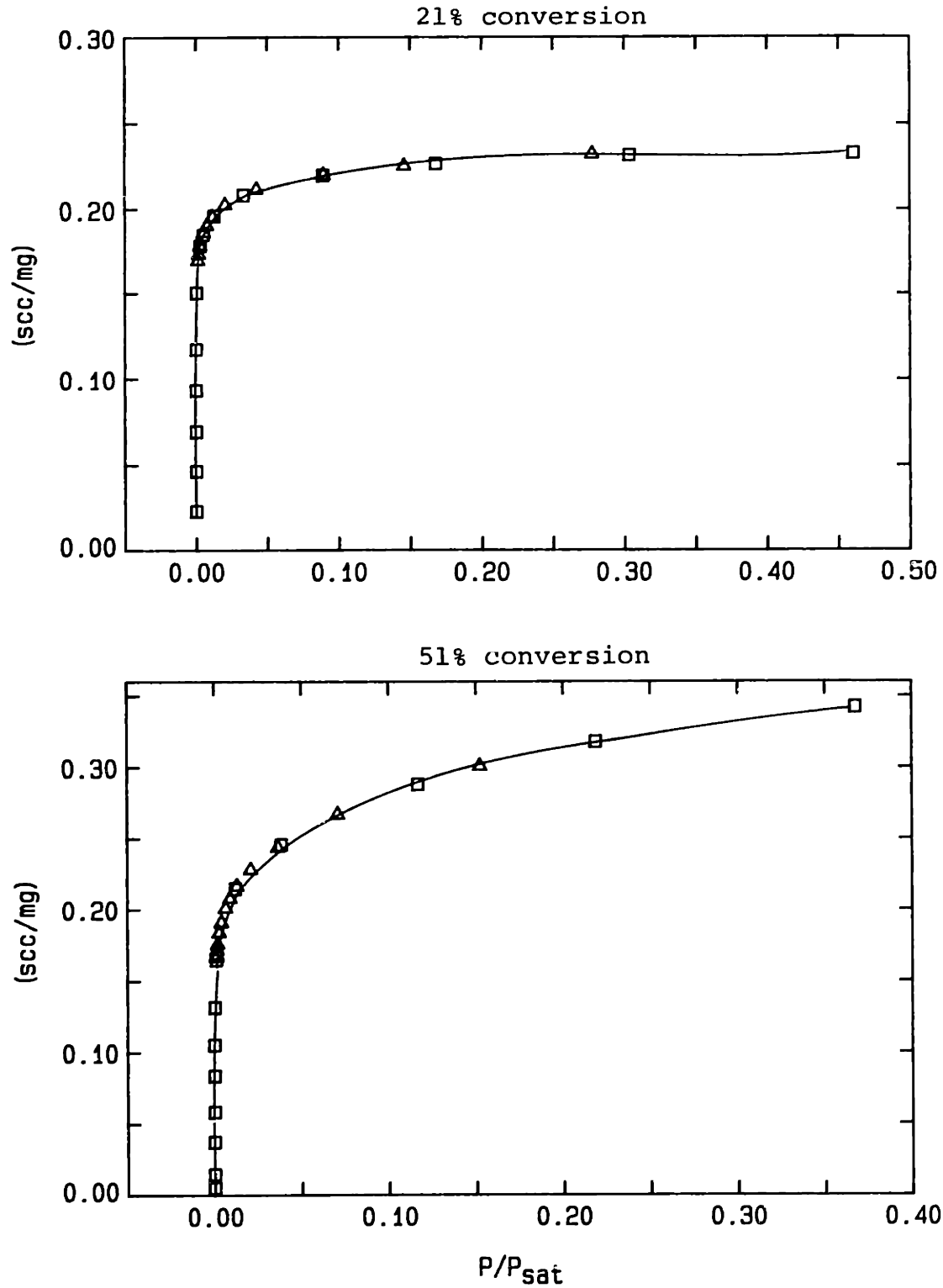

Figure A5-3. Nitrogen adsorption/desorption isotherms for the C-O char reacted in air at 770 K to the conversion indicated; 90-106 μm particles; heat treatment temperature 1300 K. □ - adsorption; △ - desorption.

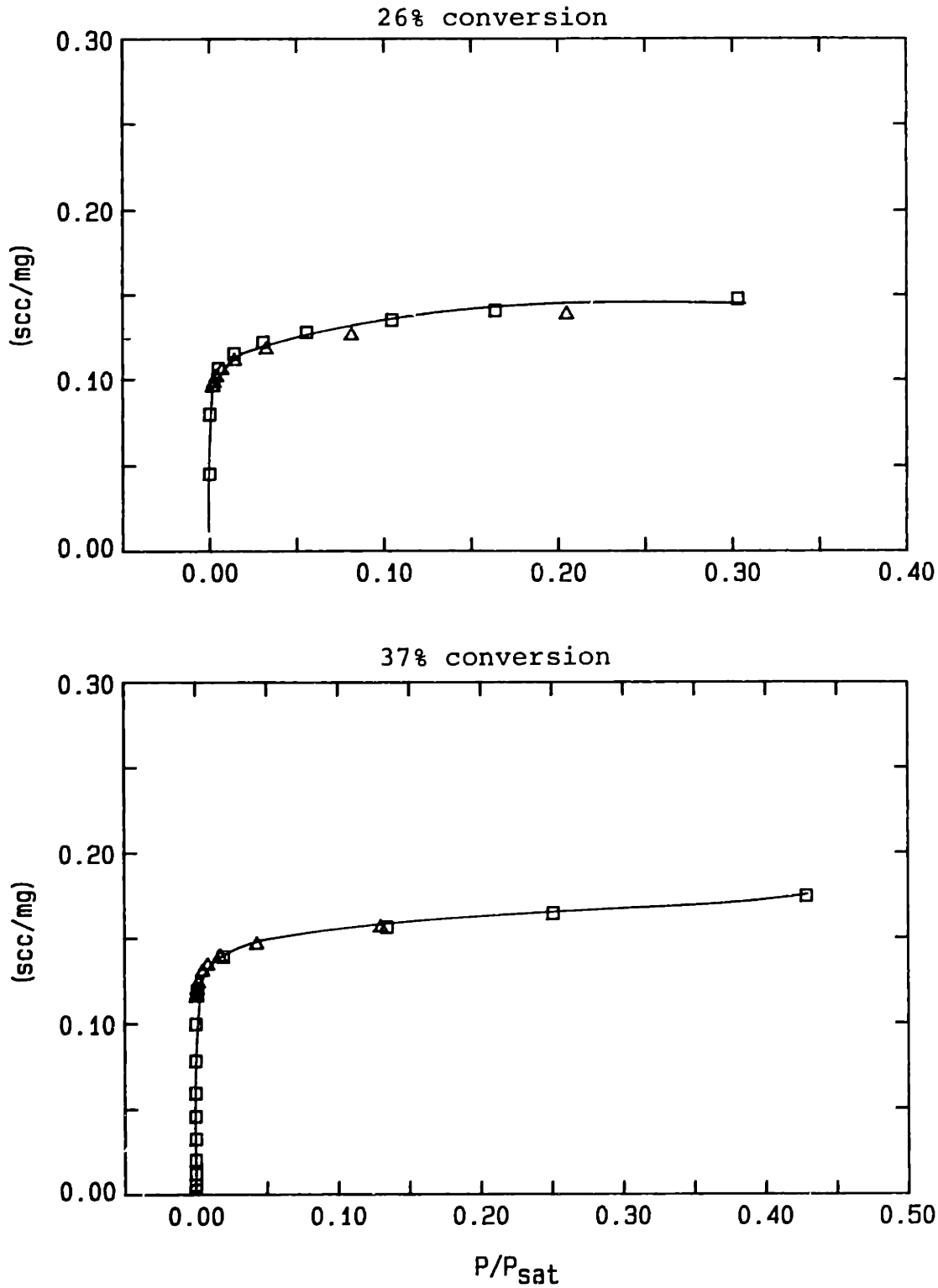

Figure 5-4a. Nitrogen adsorption/desorption isotherms for the C-3.6 (3.6 wt% Ca) char reacted in air at 625 K to the conversion indicated; 90-106 μm particles; heat treatment temperature 1300 K.
□ - adsorption; △ - desorption

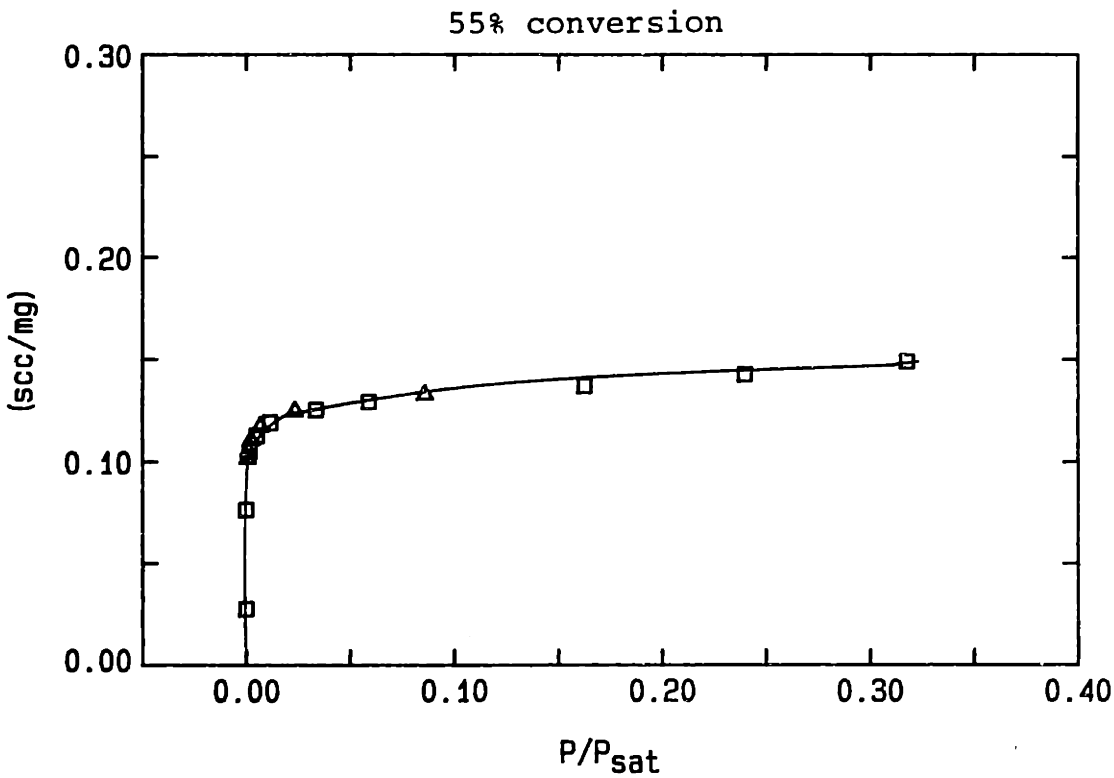

Figure A5.4b Nitrogen adsorption/desorption isotherms for the C-3.6 char. □ - adsorption; Δ - desorption.

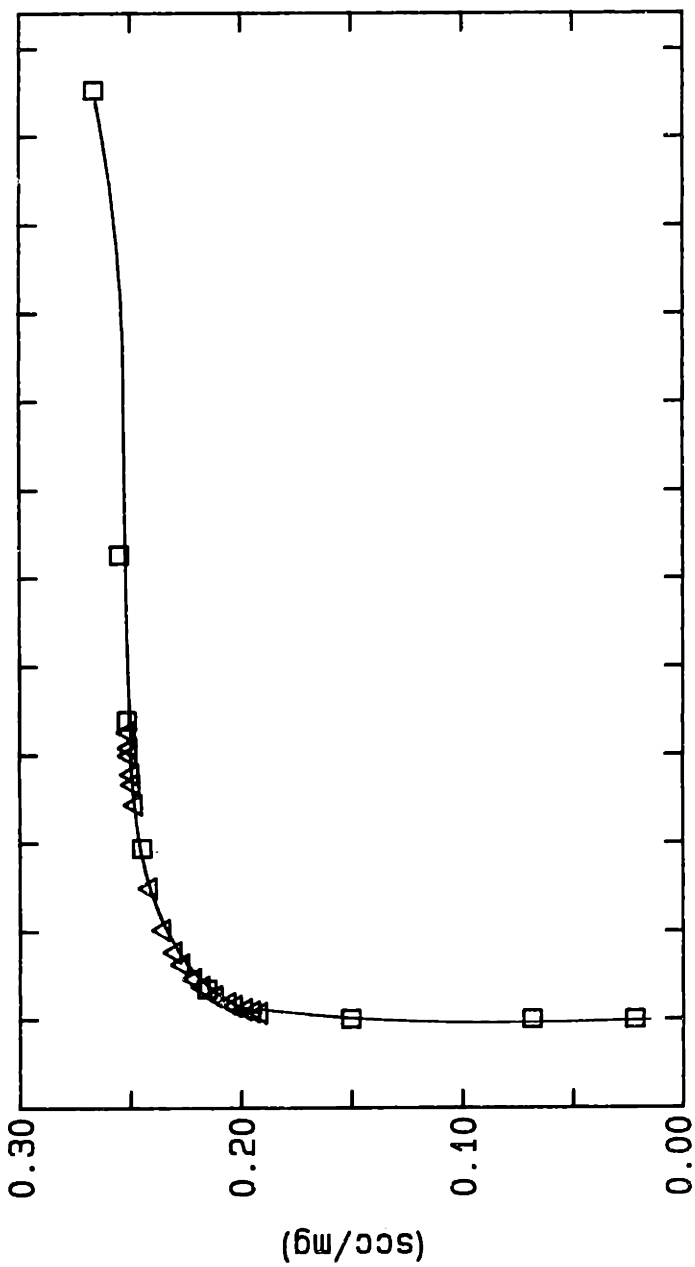

Figure A5-5. Nitrogen adsorption/desorption isotherms for Spherocarb.
□ - adsorption; △ - desorption.

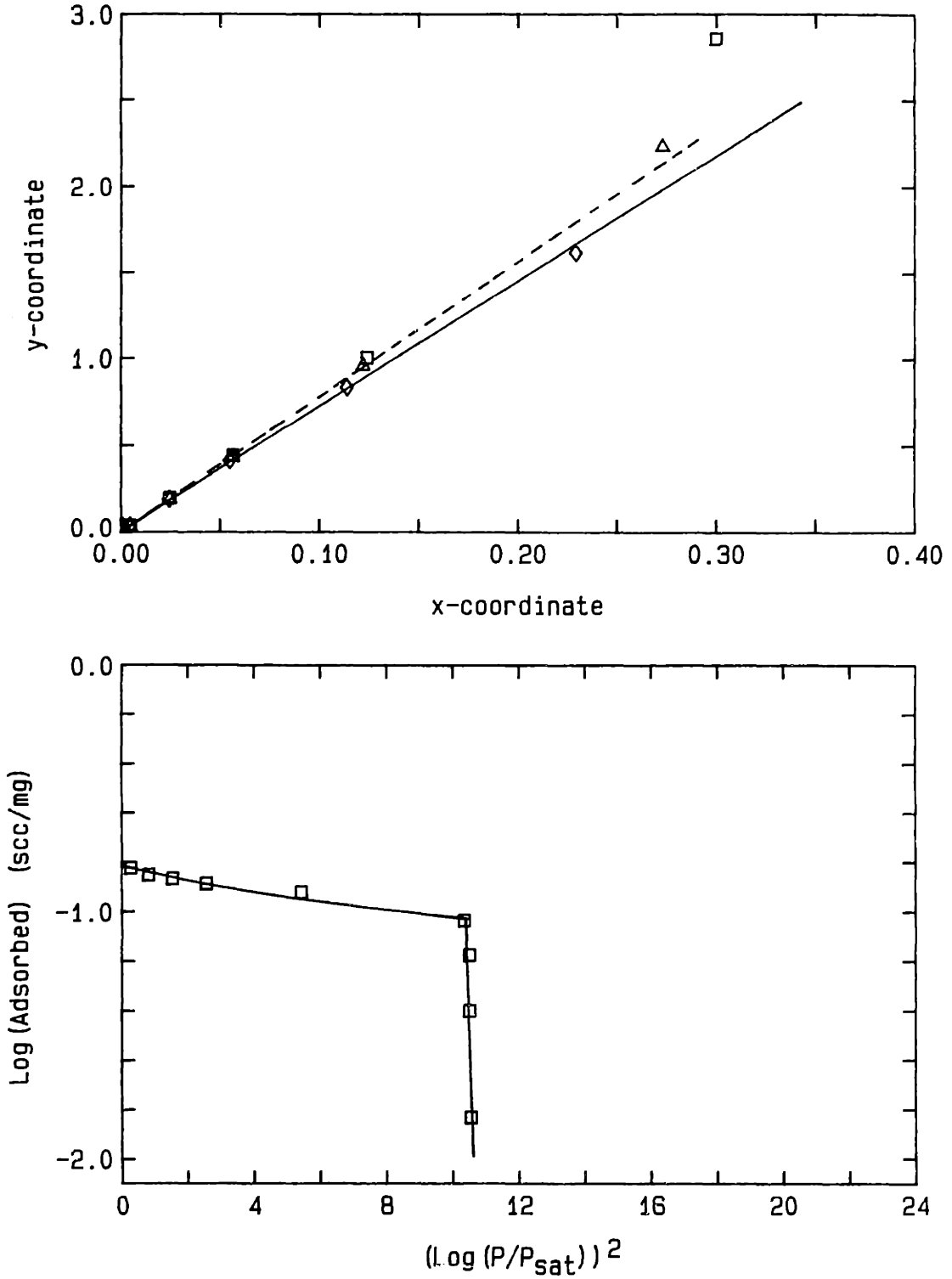

Figure A5-6a. BET plot for n = 1.2(◊); 2(△); and ∞ (□) and Dubinin-Polanyi plot. C-O char 6.4% conversion; heat treatment temperature 1100 K.

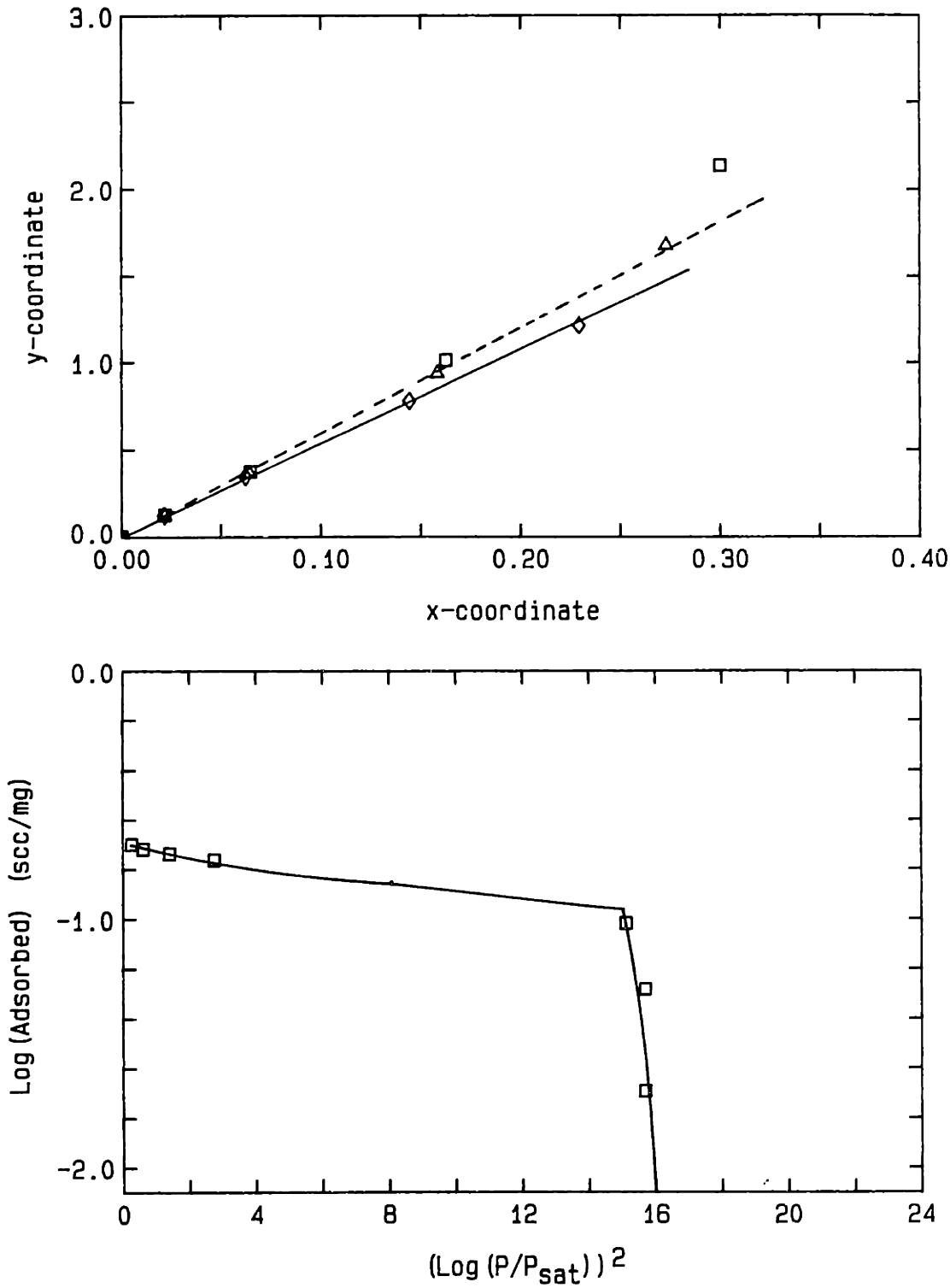

Figure A5-6b. BET and Dubinin-Polanyi plot C-O char; 24% conversion.

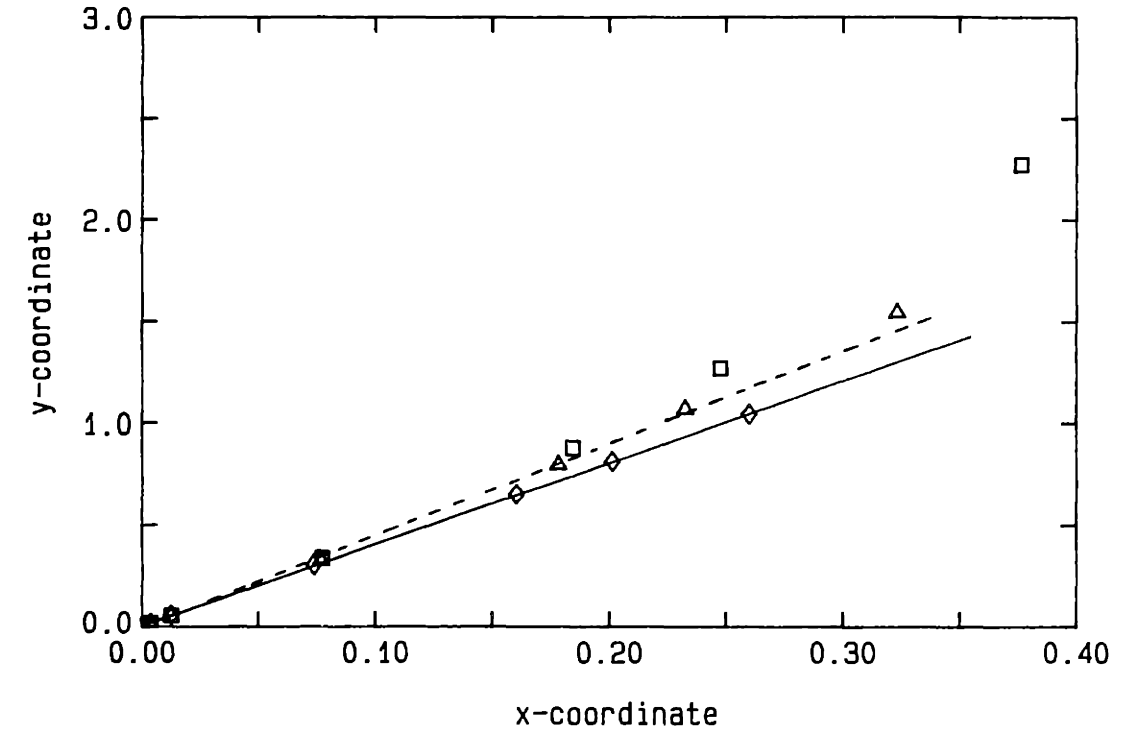

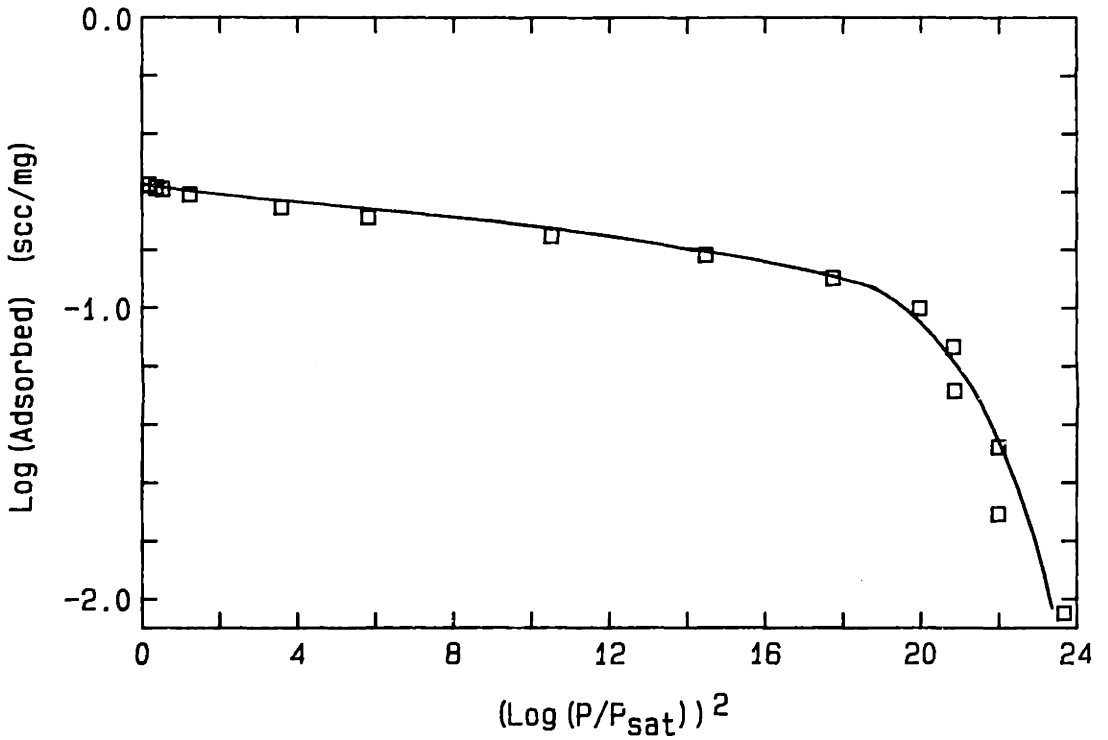

Figure A5-6c. BET and Dubinin-Polanyi plot for C-O char; 40% conversion.

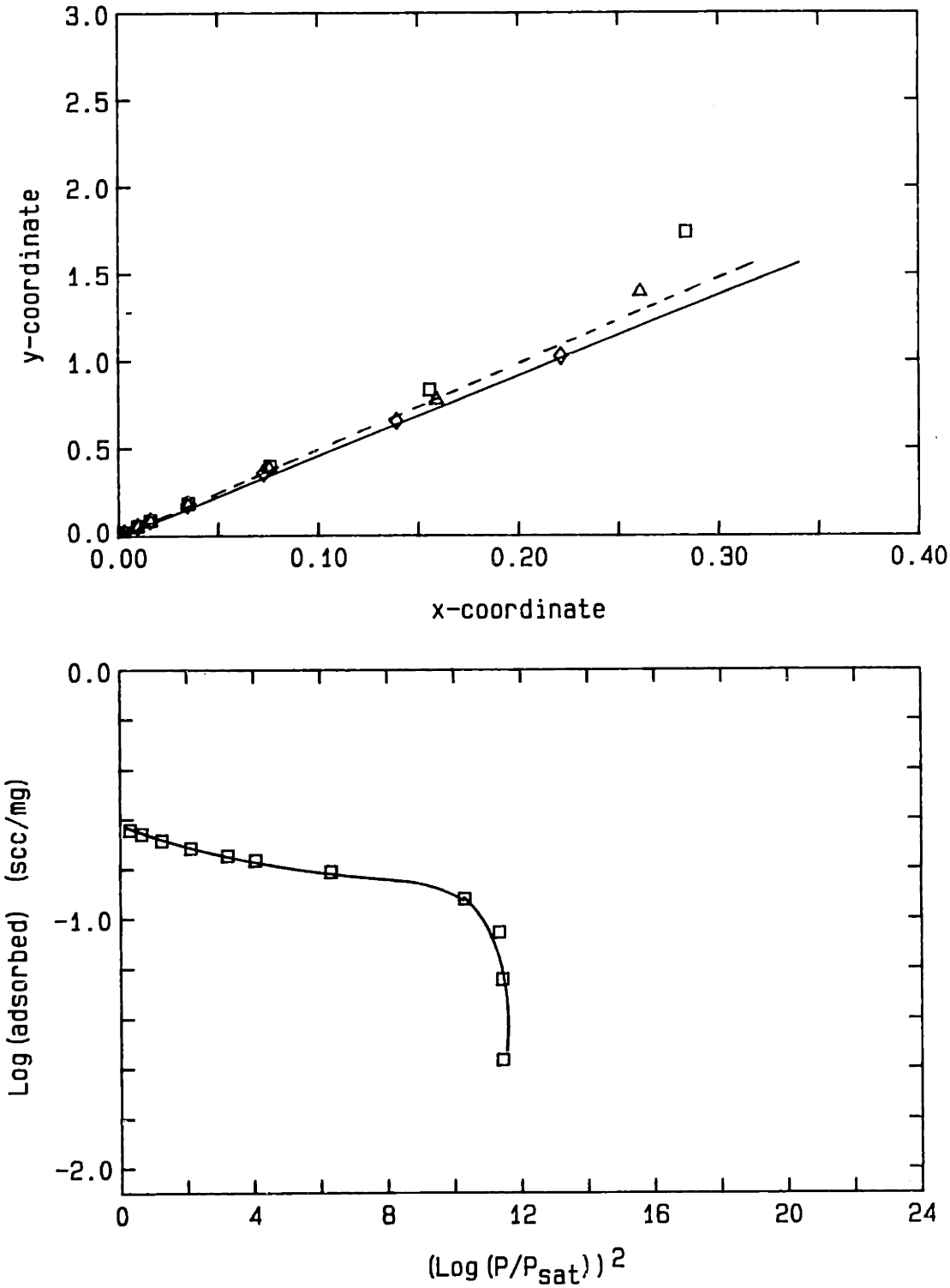

Figure A5-6d. BET and Dubinin-Polanyi plot for C-O char; 54% conversion.

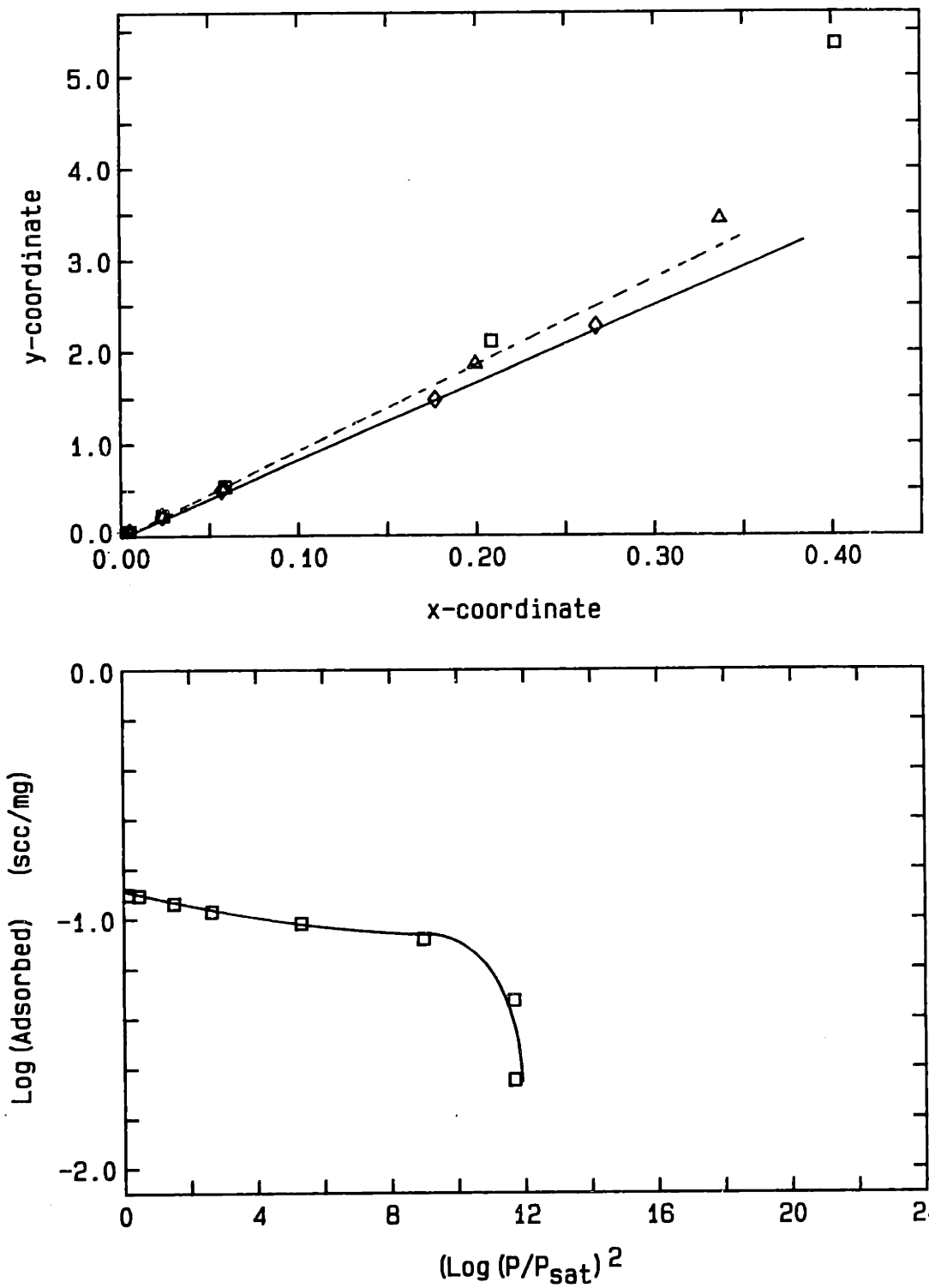

Figure A5-7a. BET plot for n = 1.2 (◊); 2 (Δ); and ∞ (□) and Dubinin-Polanyi plot C-3.6 char; 7% conversion; heat treatment temperature 1100 K.

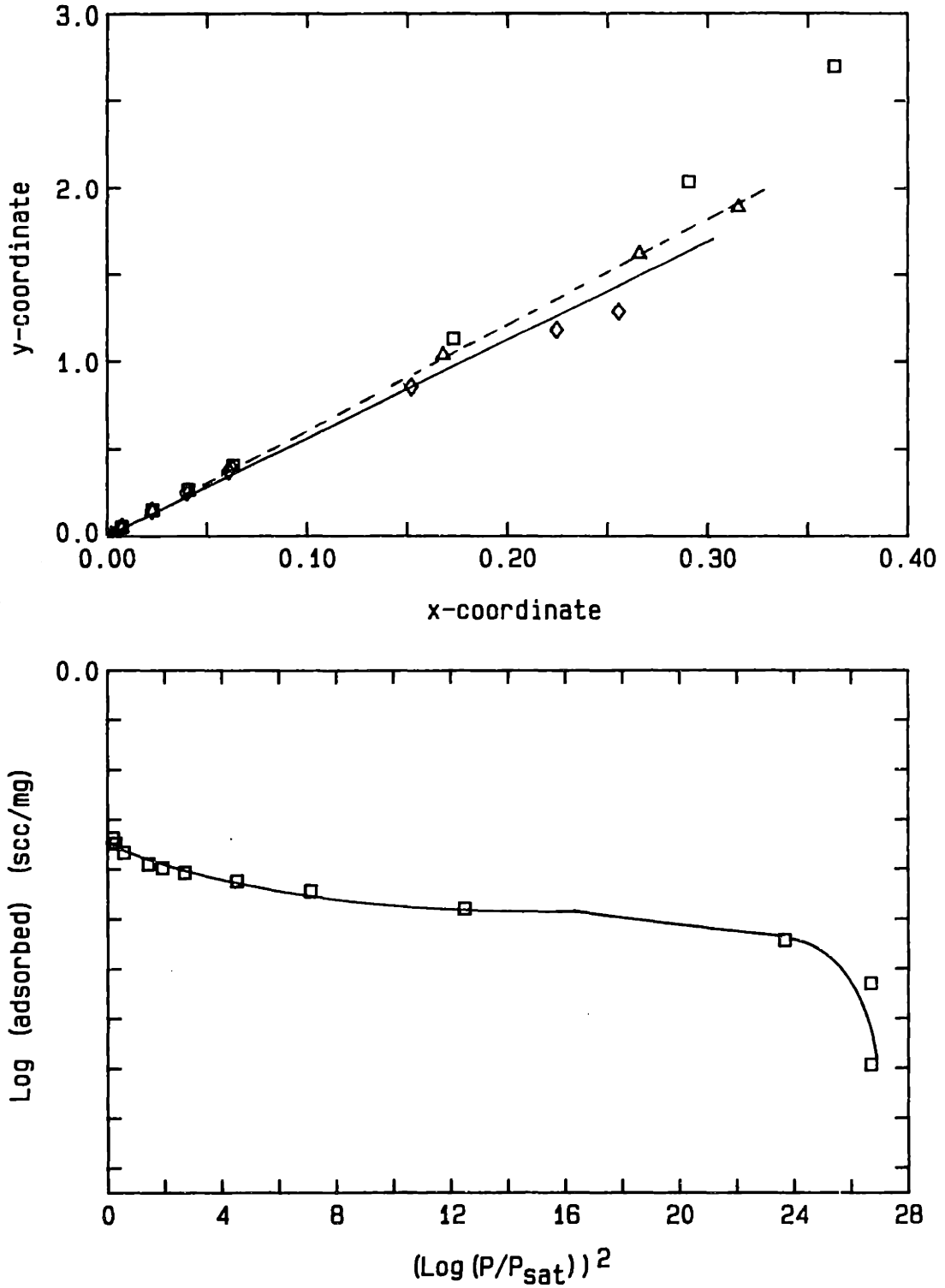

Figure A5.7b BET and Dubinin-Polanyi plot for C-3.6 char; 22% conversion.

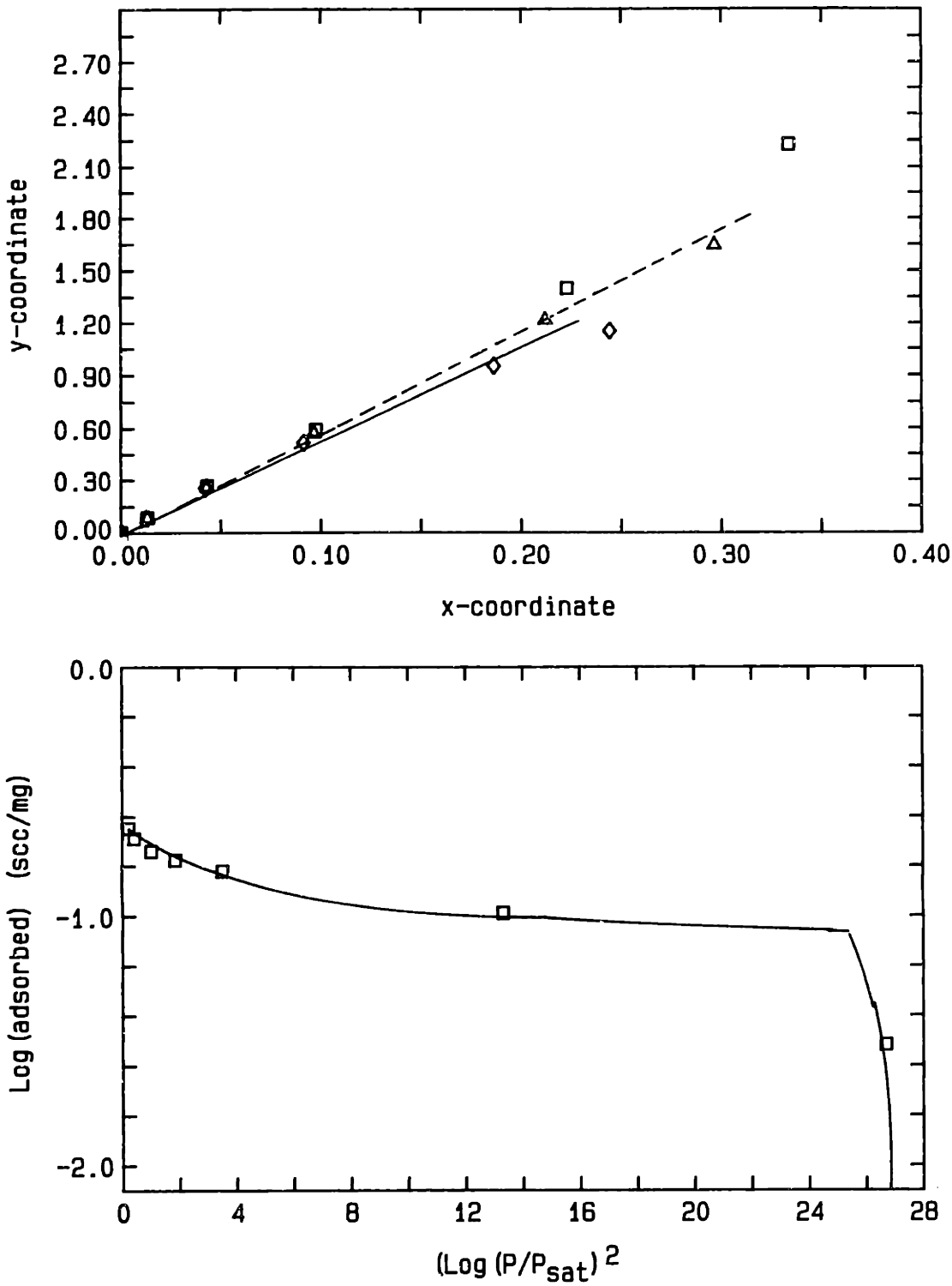

Figure A5.7c. BET and Dubinin-Polanyi plot for C-3.6 char; 38% conversion.

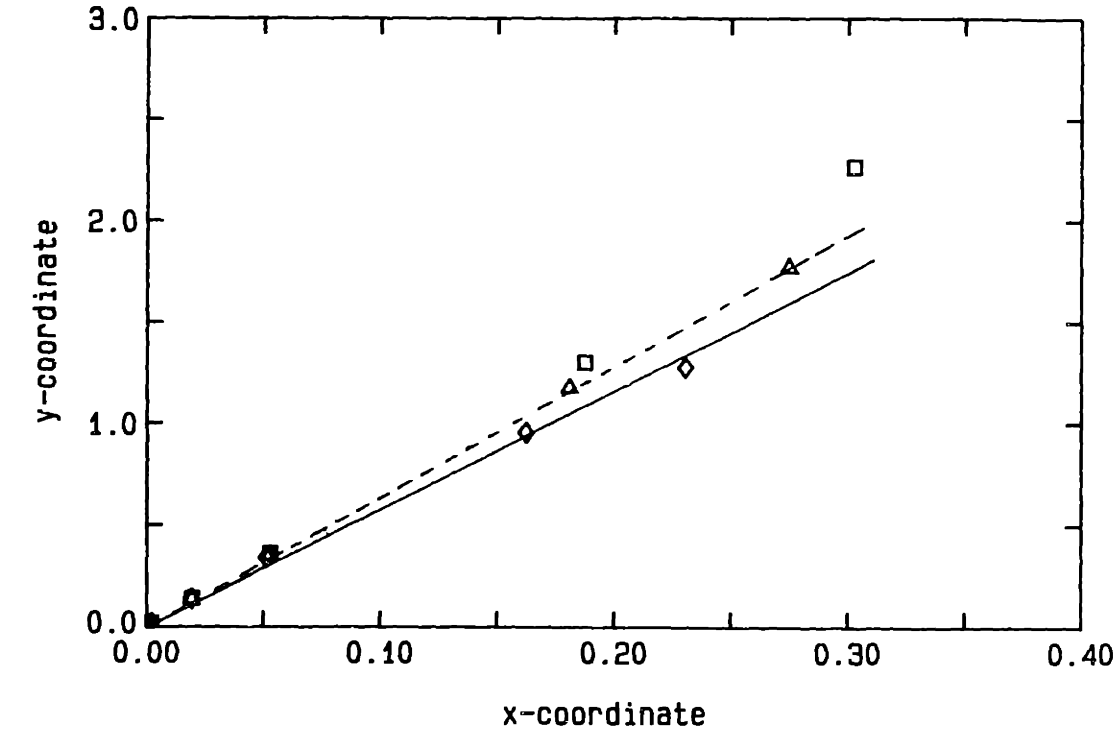

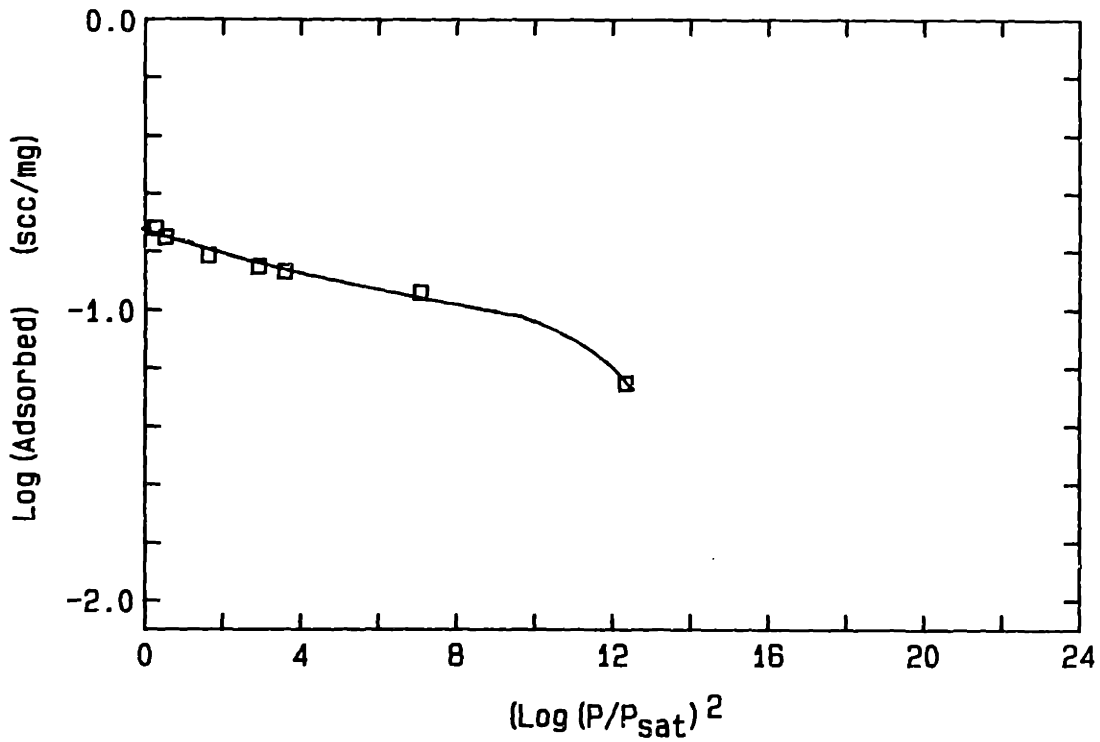

Figure A5-7d. BET and Dubinin-Polanyi plot for C-3.6 char; 58% conversion.

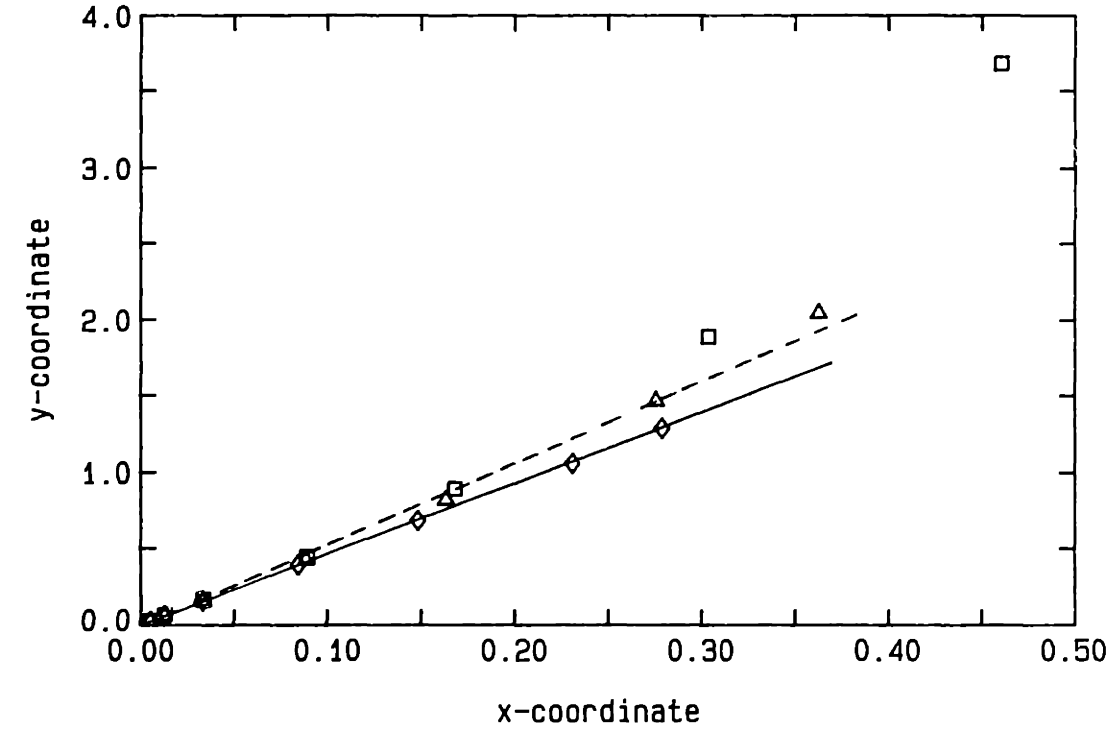

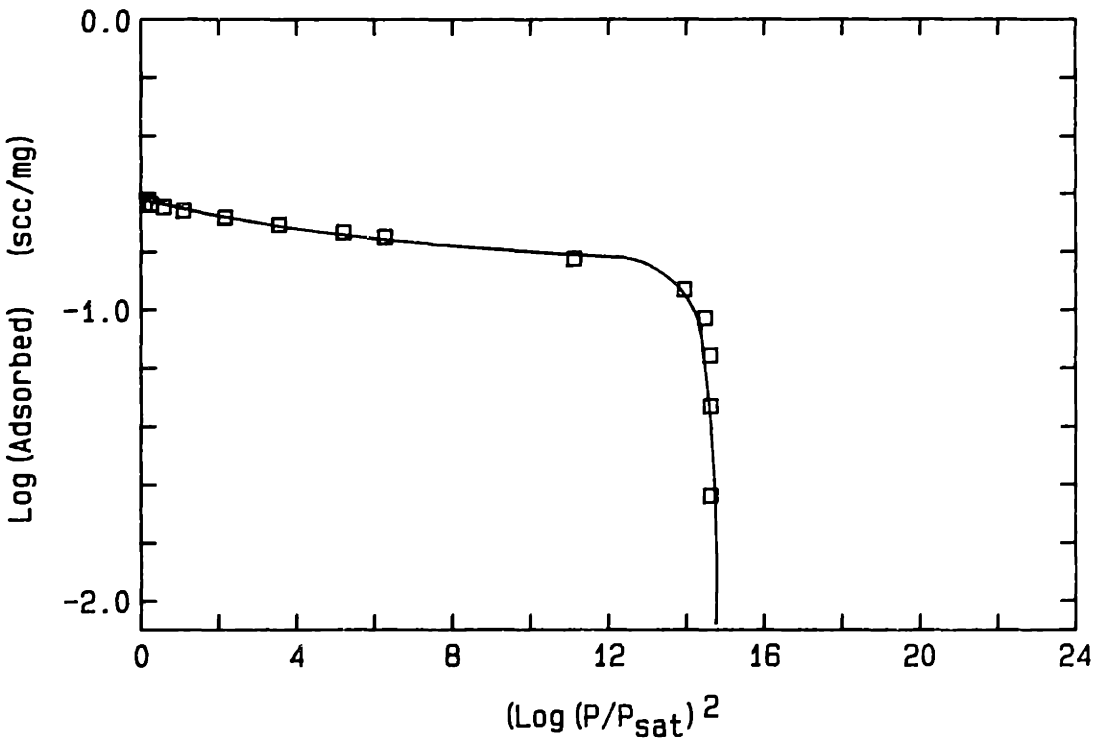

Figure A5-8a. BET plot for n = 1.2 (◊); 2 (△); and ∞ (□) and Dubinin-Polanyi plot for C-O char; 21% conversion; heat treatment temperature 1300 K.

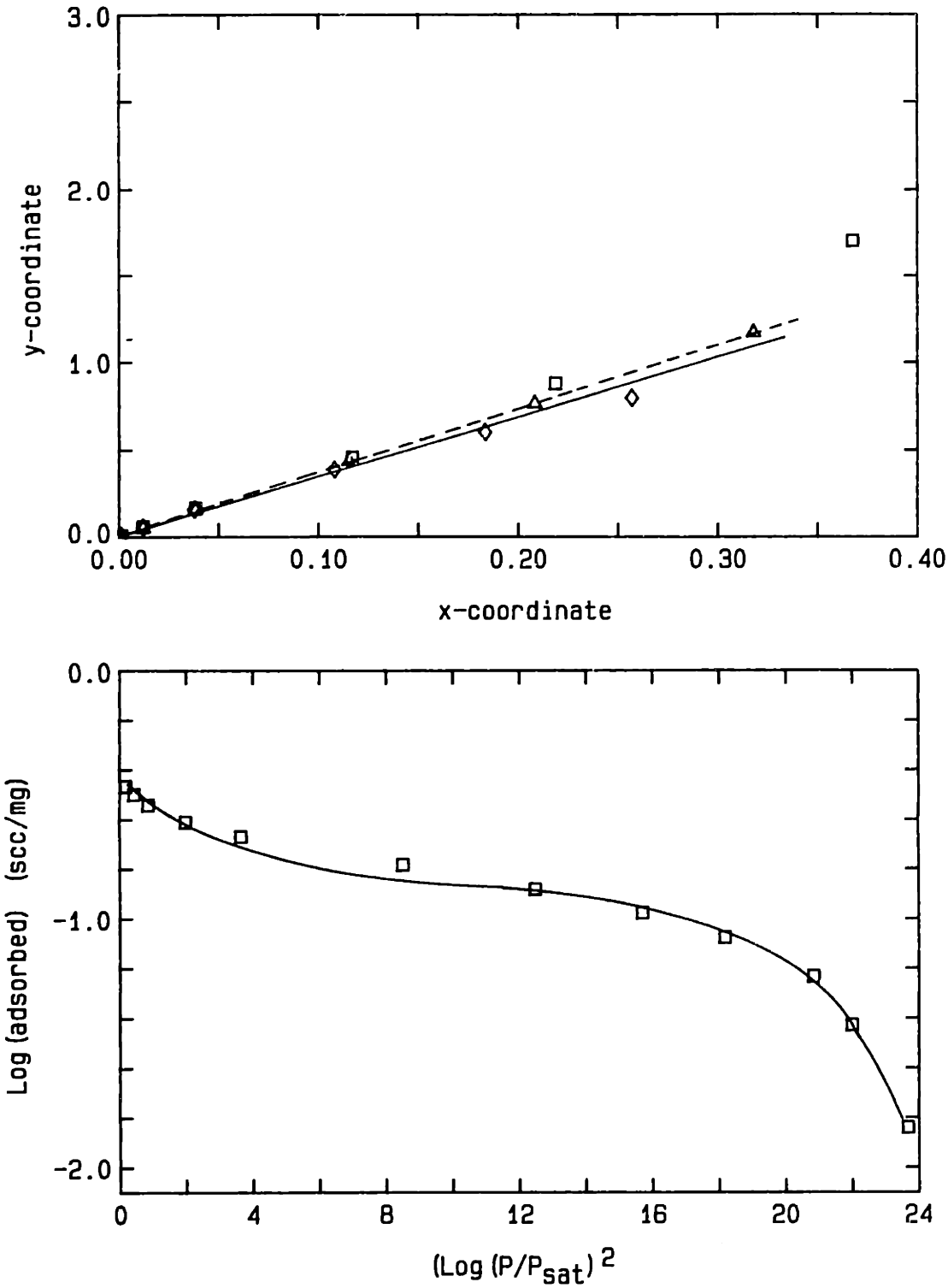

Figure A5-8b. BET and Dubinin-Polanyi plot for C-O char; 51% conversion.

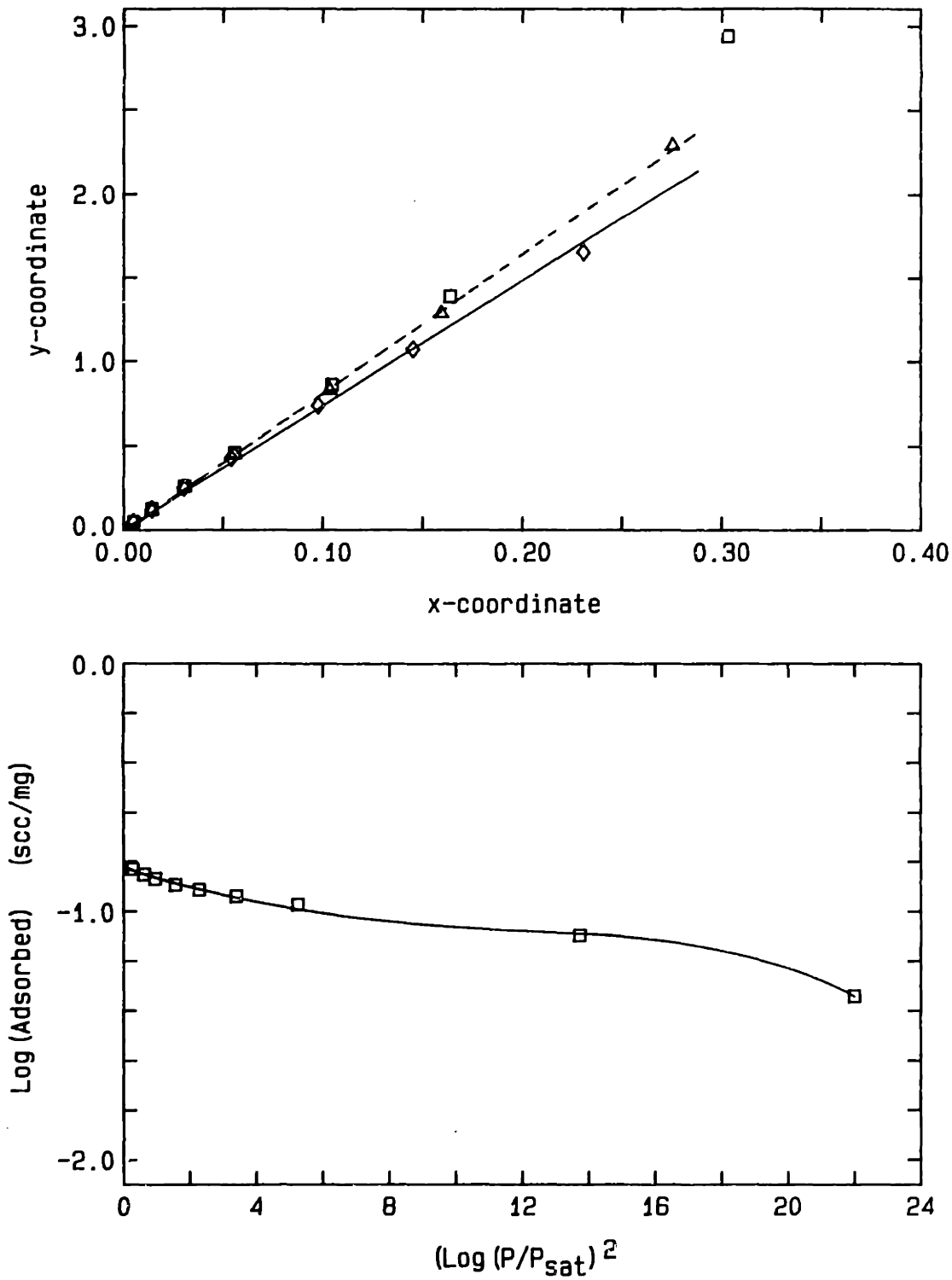

Figure A5-9a BET plot for n = 1.2 (◊); 2 (△); and ∞ (□) and Dubinin-Polanyi plot for C-3.6 char; 26% conversion; heat treatment temperature 1300 K.

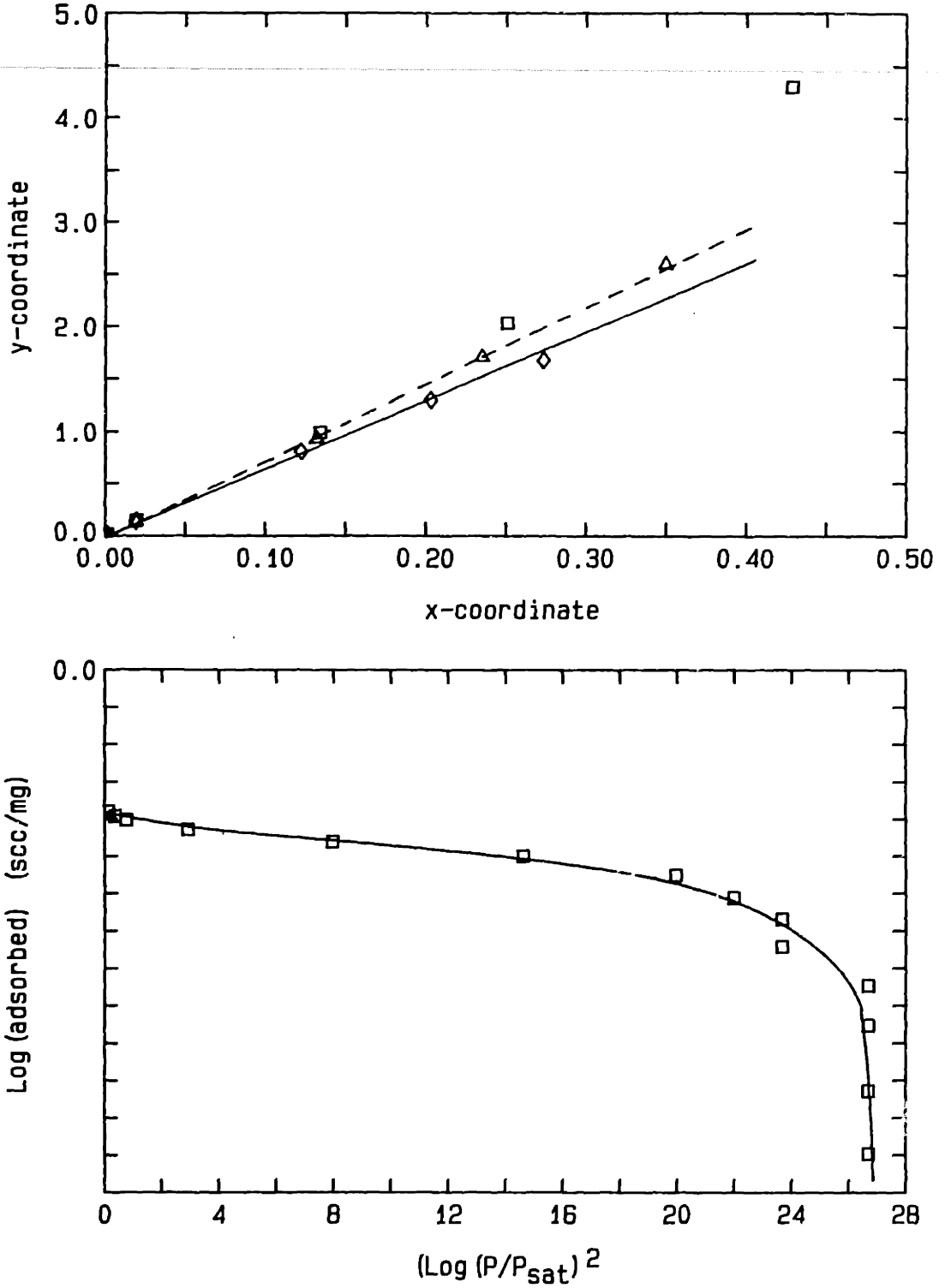

Figure A5-9b BET and Dubinin-Polanyi plot for C-3.6 char; 37% conversion.

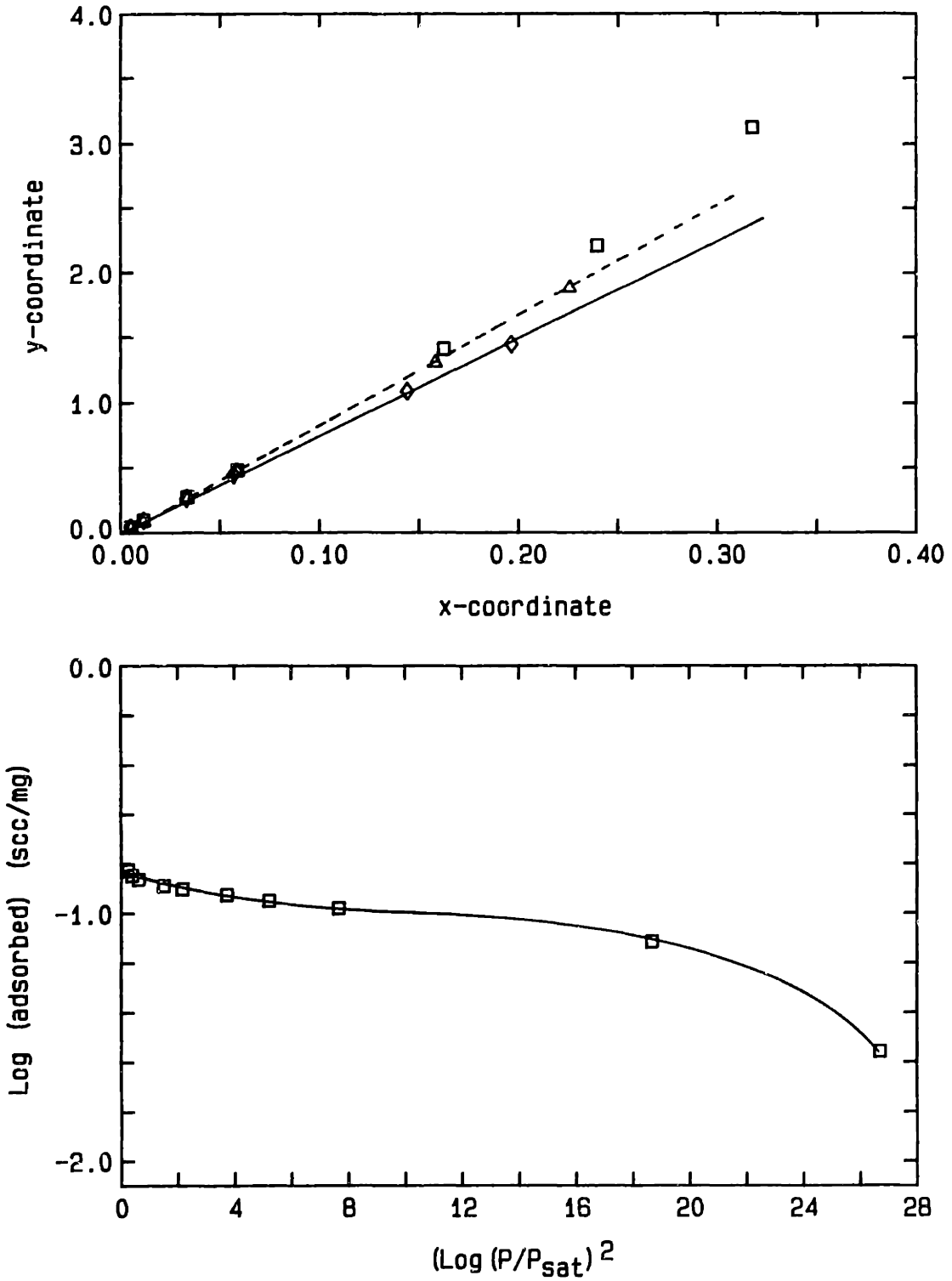

Figure A5-9c BET and Dubinin-Polanyi plot for C-3.6 char; 55% conversion.

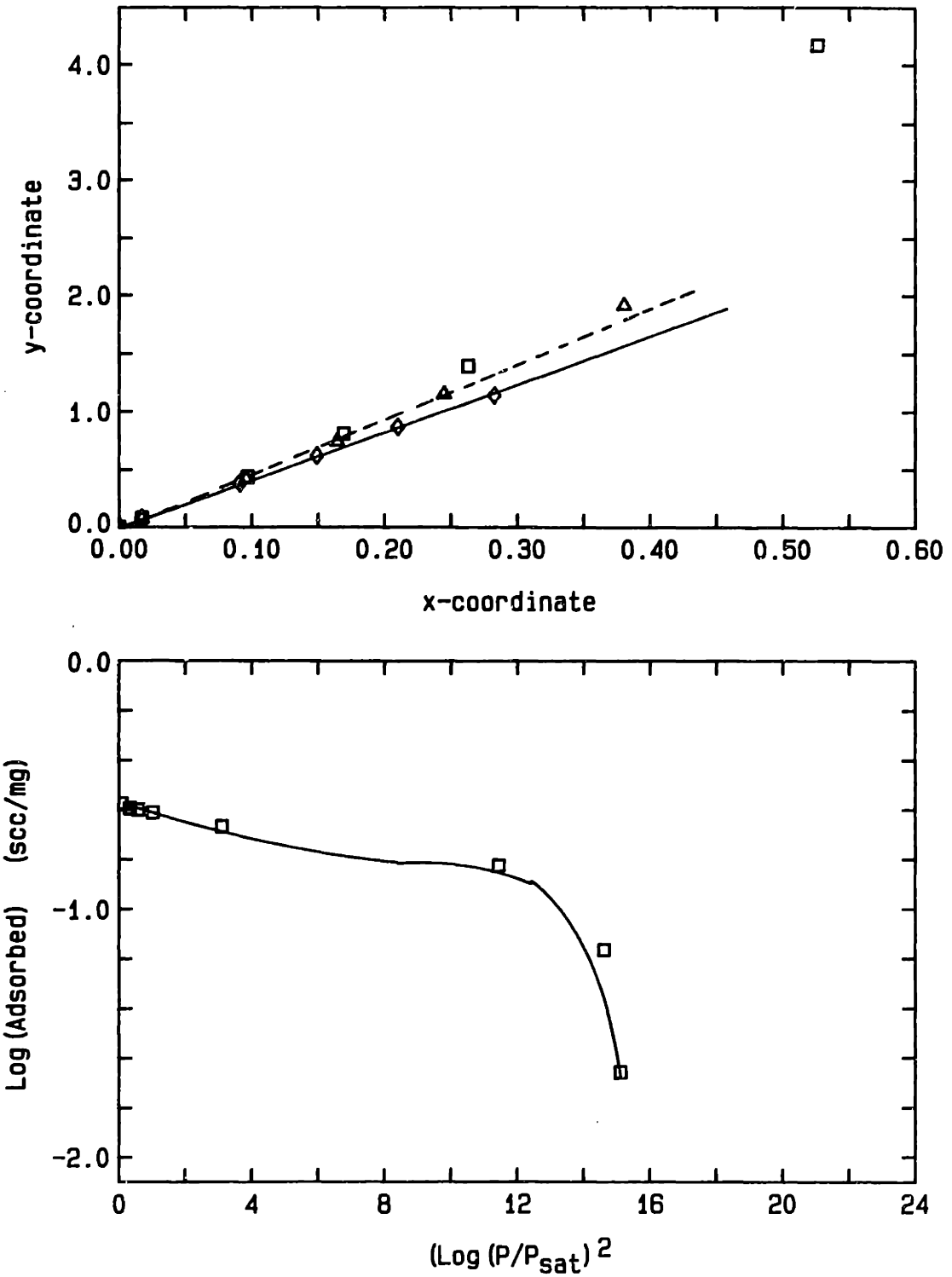

Figure A5-10 BET plot for n = 1.2 (◊); 2 (△); and ∞ (□) and Dubinin-Polanyi plot for Spherocarb.

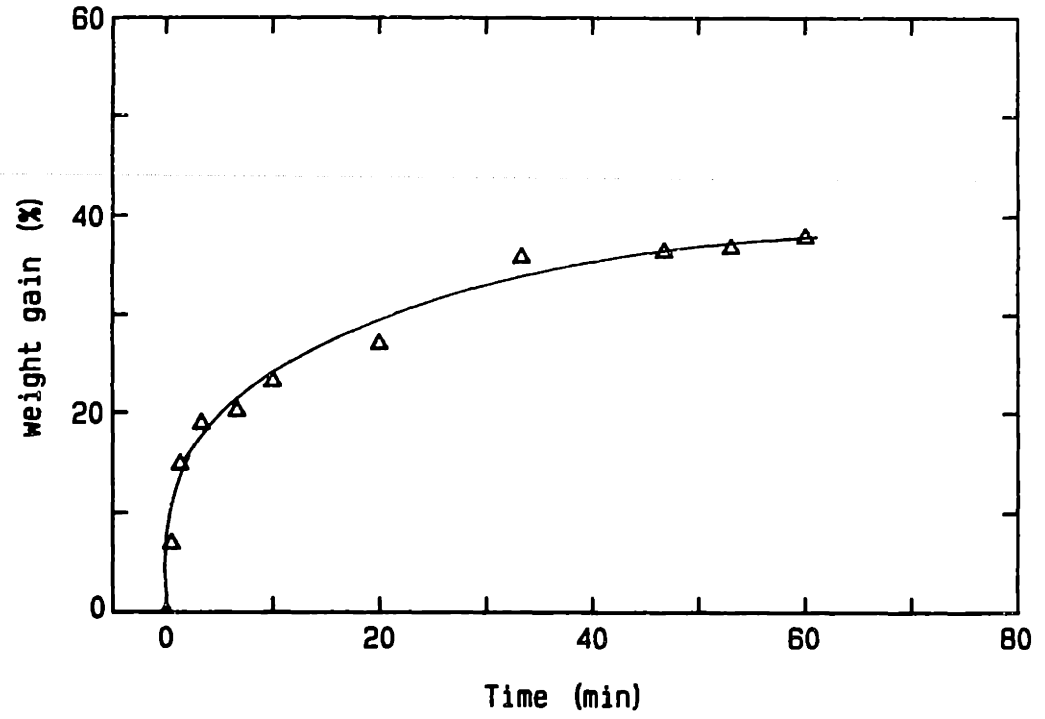

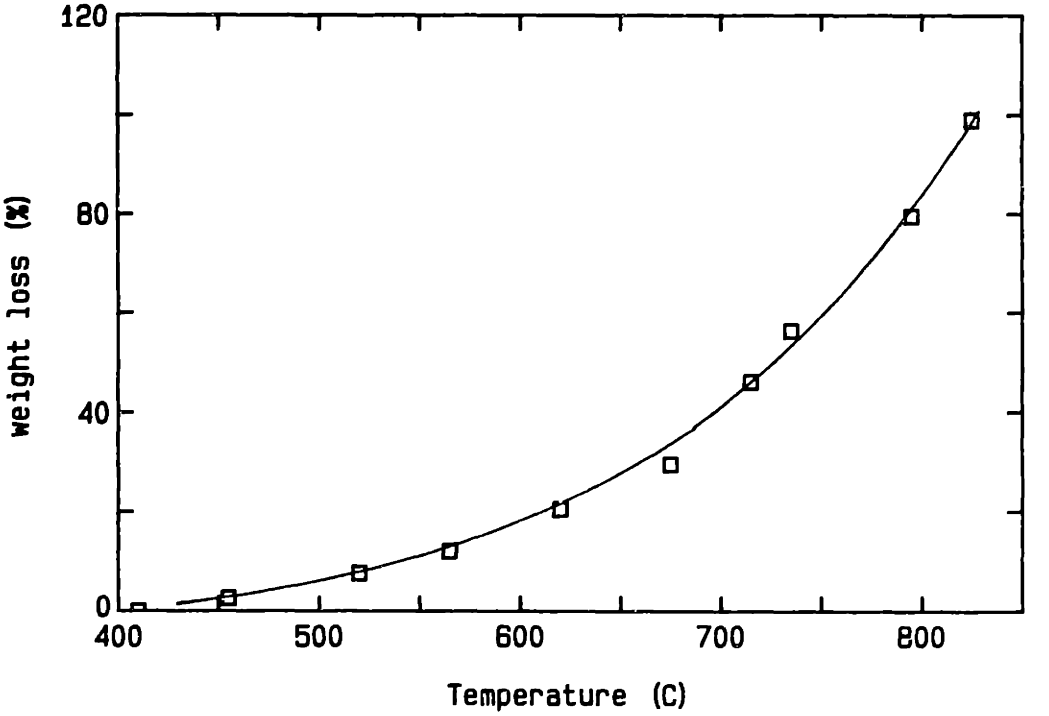

Figure A5-11a First cycle CO_2 adsorption at 298 K on the C-3.6 char; heat treatment temperature 1100 K; 0 conversion; adsorption (Δ); desorption (□) (desorption data at a constant heating rate of 36 C/min).

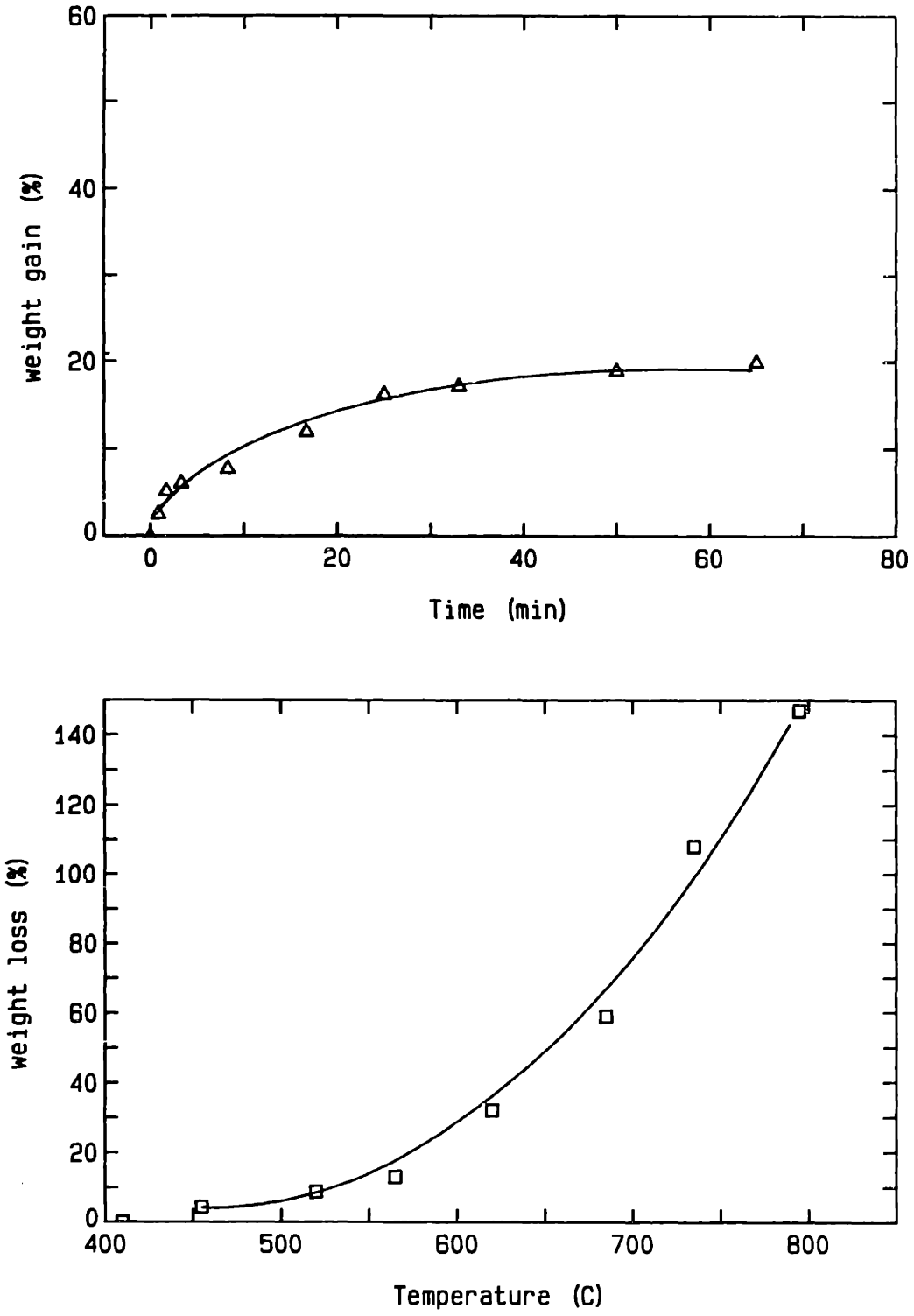

Figure A5-11b Second cycle CO_2 adsorption and desorption at 298 K on the C-3.6 char, 0% conversion.

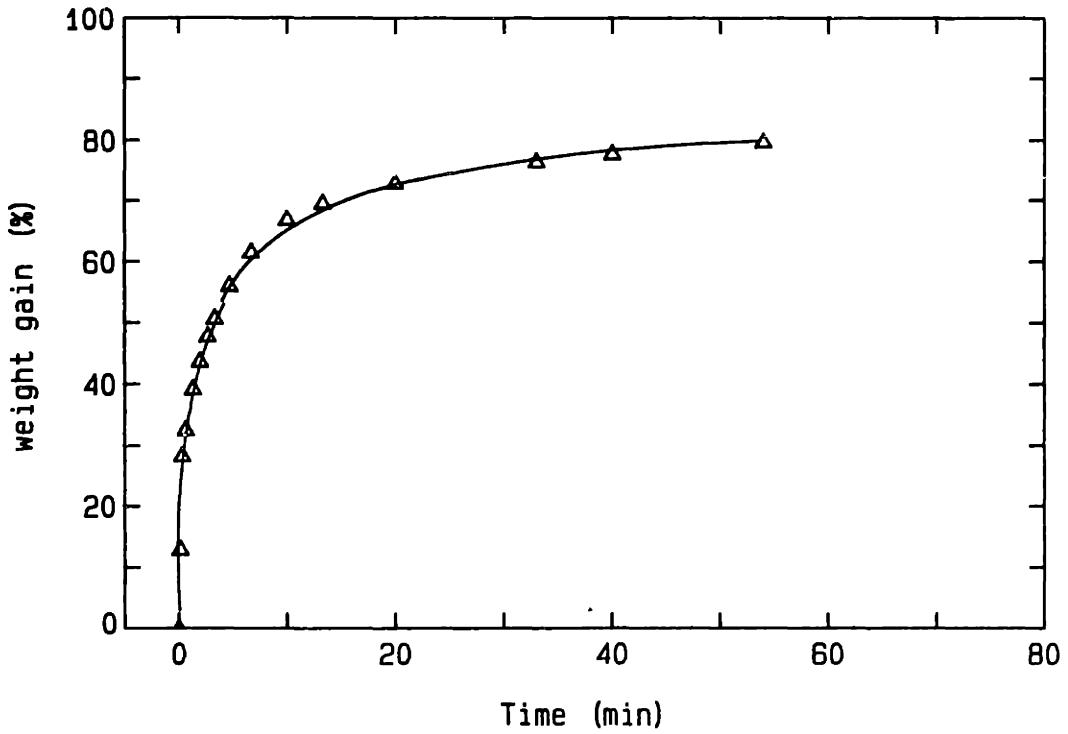

Figure A5-11c CO_2 adsorption at 700 K on the C-3.6 char at 0% conversion.

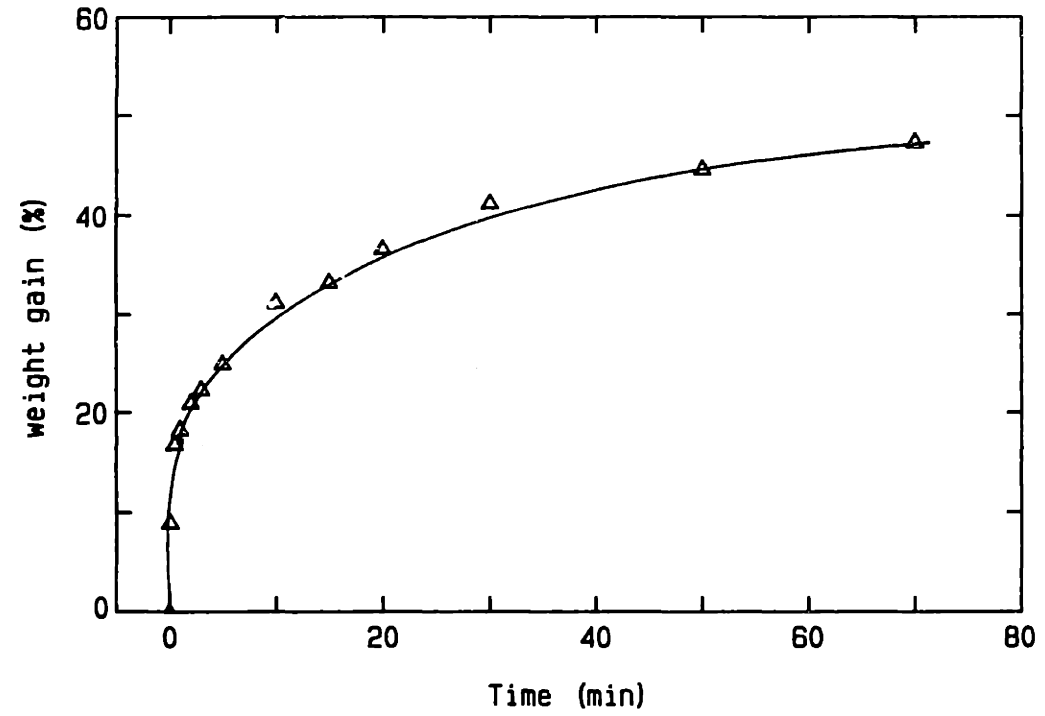

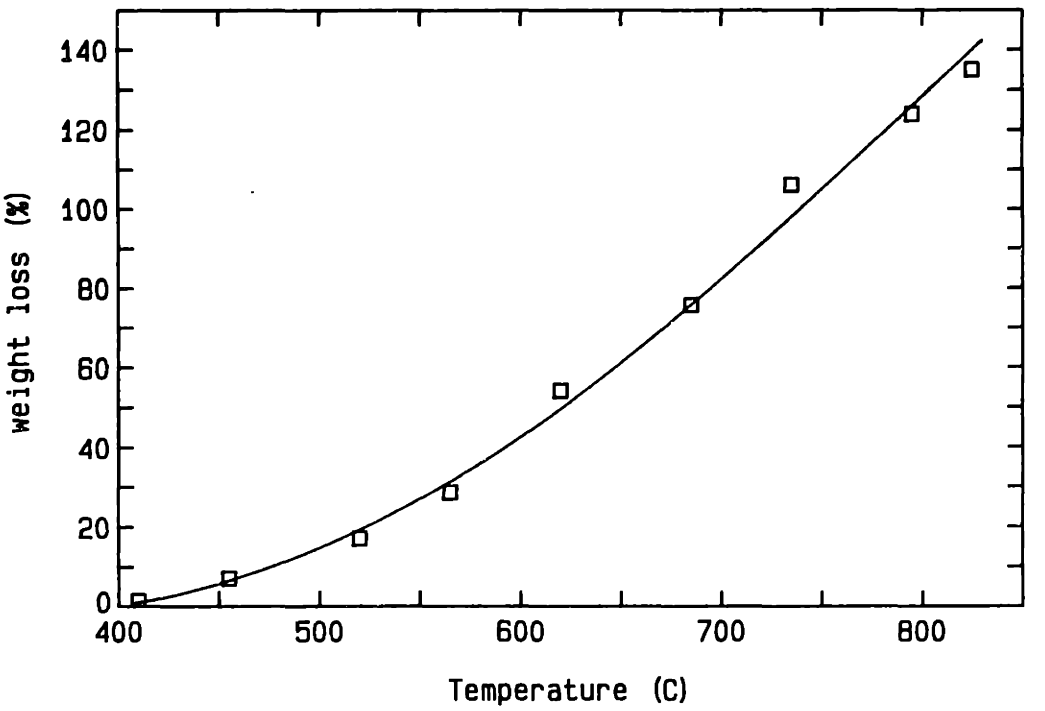

Figure A5-11d CO_2 adsorption and desorption at 298 K on the C-3.6 char at 37% conversion.

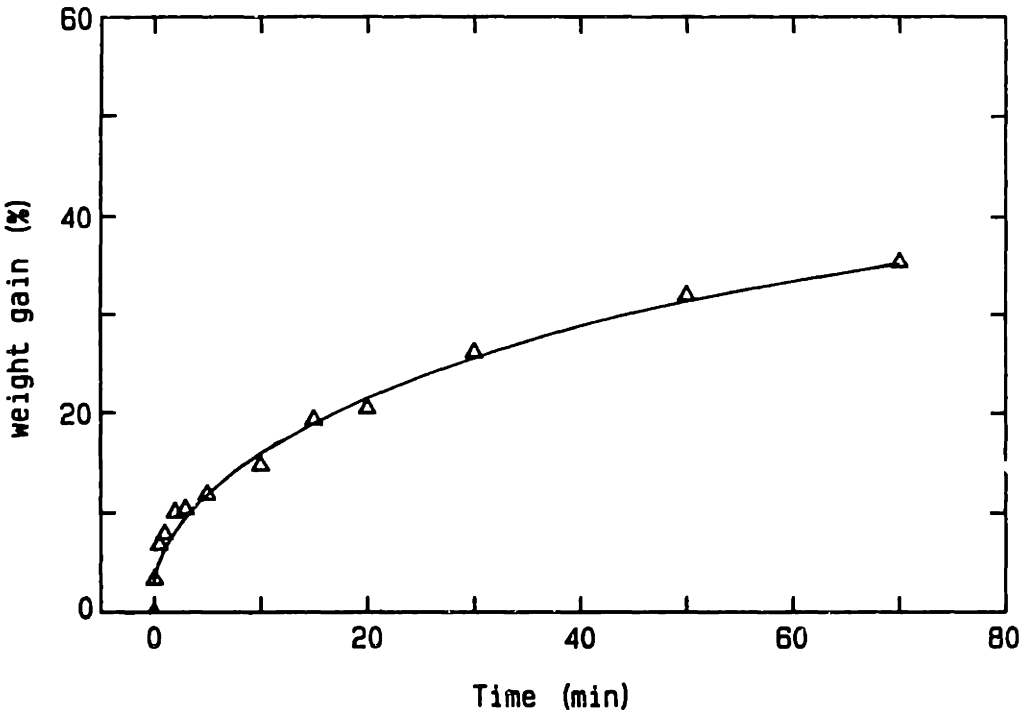

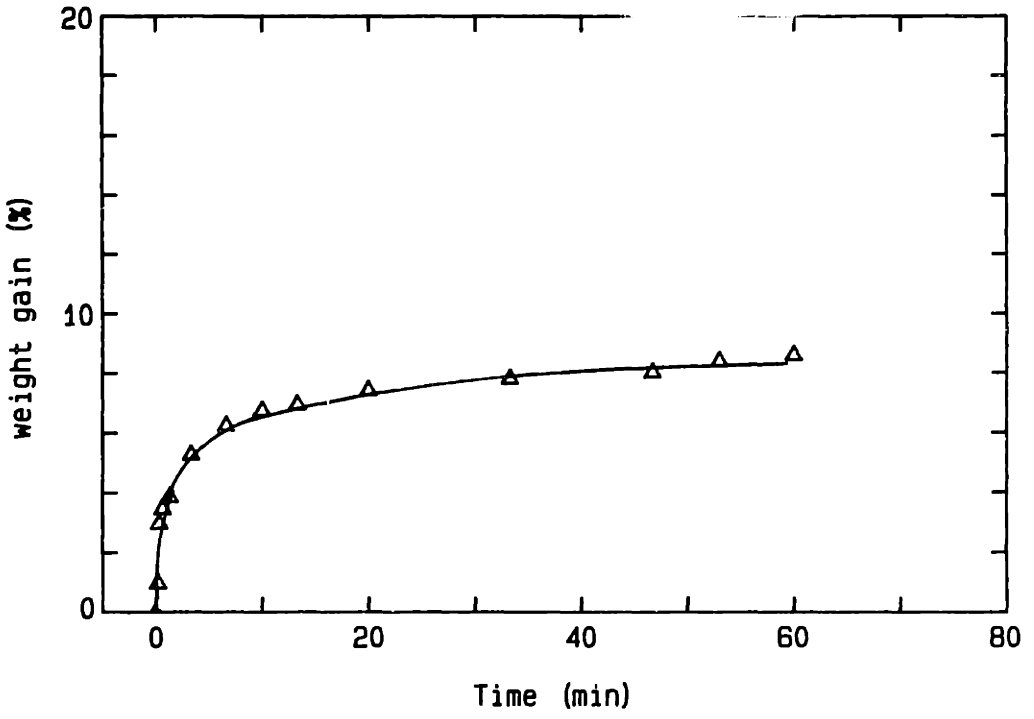

Figure A5-11e CO_2 adsorption at 298 K on the C-3.6 char at 67% conversion (top) and 100% conversion (bottom).

APPENDIX 6. DETERMINATION OF THE PARAMETER β.

The parameter, β, of the random pore model can be determined from the zeroeth and first moments of the pore size density distribution. The parameter was evaluated for three distribution functions: a 1/r distribution, an exponential distribution, and a linear distribution. These functions were selected because of their simple functional form and because they seem to provide an adequate representation of the pore size distribution in microporous chars. Pore size density distributions for microporous chars reported by Barrett et al. (1951) from nitrogen desorption measurements, for example, could be adequately represented by the functions listed. In addition, Simons (1982) has suggested that a 1/r distribution, on average, seems to adequately represent the pore size density distributions of chars.

The relationship between the pore size density distribution $\epsilon(r)$, where $\epsilon(r)dr$ is the pore volume in r and $r + \Delta r$, and $\lambda(r)$ the parameter of the random pore model is (Gavalas, 1980):

$$\lambda(r) = \frac{\epsilon(r)}{2\pi r^2 [1 - \int_r^* \epsilon(r')\, dr']} \qquad (1)$$

Once $\lambda(r)$ is known, β can be calculated from the moments of λ.

$$\beta = \frac{B_0}{2\pi B_1^2} \qquad (2)$$

$$B_o = \int_{r_*}^{r^*} \lambda(r)dr \quad ; \quad B_1 = \int_{r_*}^{r^*} r\lambda(r)dr \qquad (3,4)$$

For the 1/r distribution:

$$\epsilon(r) = C_1/r$$

C_1 is determined by requiring the distribution to satisfy the constraints of total porosity and total surface area respectively:

$$\epsilon_T = \int_{r_*}^{r^*} C_1/r \, dr \qquad (5)$$

$$S_g = 2\int_{r_*}^{r^*} \frac{\epsilon(r)}{r} dr \qquad (6)$$

where S_g is the surface area of the pore size distribution and r^* and r_* are the upper and lower limits of the distribution. Note that the surface area is based on a non-intersecting cylindrical model of the pores. If $r^* >> r_*$, then $S_g = 2\epsilon_T/br_*$ where $b = \ln(r^*/r_*)$. This states that b and r_* are not independent; if one is specified the other is determined. Substitution of $\epsilon(r)$ into Equation (1) and simplification yields:

$$\lambda(r) = \frac{C_1}{2\pi} \frac{1}{r^3} \frac{1}{[1 - C_1(\ln r^* - \ln r)]} \qquad (7)$$

Making the substitution y = ln r, one obtains:

$$B_o = \frac{C_1}{2\pi}\int_{y_*}^{y^*} \frac{e^{-2y}}{(a + C_1 y)}\, dy \qquad (8)$$

$$B_1 = \frac{C_1}{2\pi}\int_{y_*}^{y^*} \frac{e^{-y}}{(a+C_1 y)}\, dy \qquad (9)$$

where $y_* = \ln r_*$; $y^* = \ln r^*$; and $a = (1-C_1 \ln r^*)$.

These integrals can be evaluated in terms of the exponential integrals, yielding finally:

$$\beta = \frac{B_o}{2\pi B_1^{\,2}} = F(\alpha)\cdot\left[\frac{\alpha}{2}\right] \qquad (10)$$

where $\alpha = 1/2 \cdot b(1/\epsilon_T - 1)$ and $F(\alpha)$ is a function of the coefficient, $C(x)$, of the exponential integrals when the integral is expressed as $C(x)e^{-x}/x$. Values for $C(x)$ were obtained from Abramowitz and Stegun (1975). $F(\alpha)$ is shown in Figure A.6-1.

The exponential distribution is:

$$\epsilon(r) = a\, e^{-mr} \qquad (11)$$

The parameters of the distribution are determined from the constraints:

$$\epsilon_T = \frac{a}{m}\left(e^{-mr_*} - e^{-mr^*}\right) \qquad (12)$$

$$S_g = 2a\int_{mr_*}^{mr^*} \frac{e^{-r}}{r}\, dr \qquad (13)$$

Solution of the equation requires knowledge of r_* and r^*; r_* can

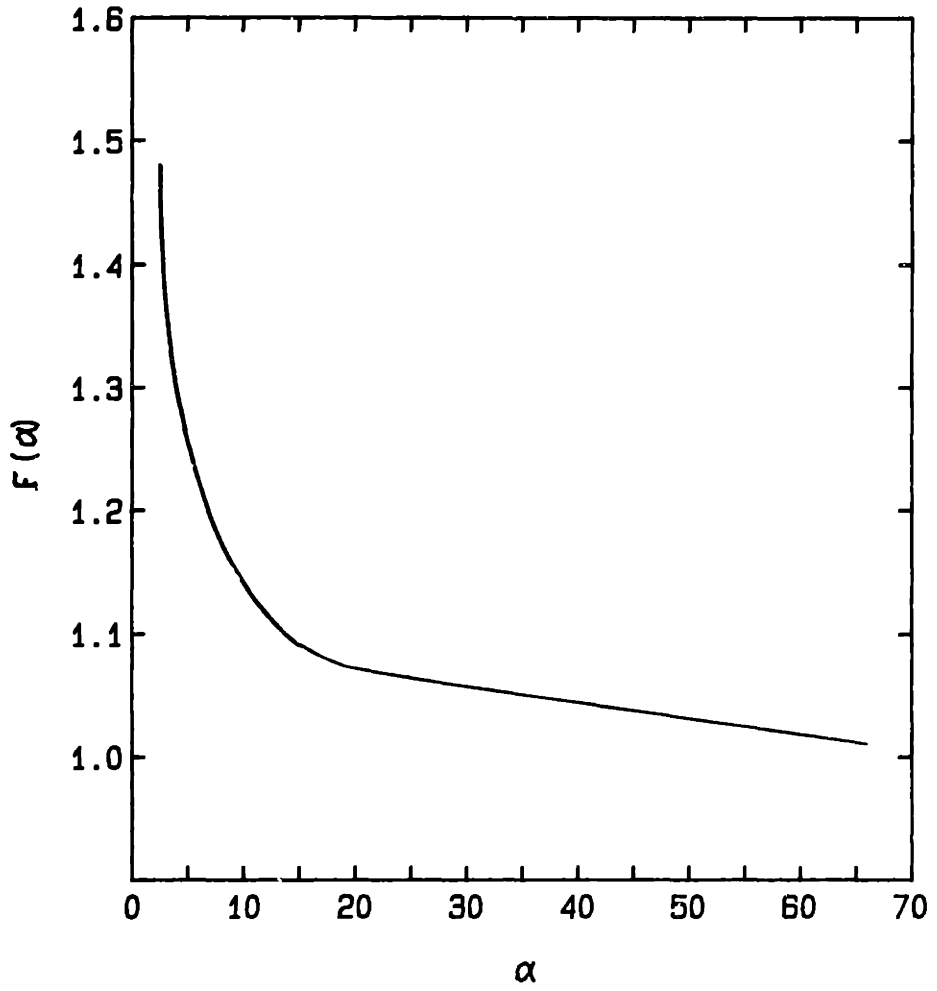

Figure A.6-1. Values for F(α)

be specified as 2.5 Å and r^* as 100 Å. By adding these two constraints, however, the distribution is over specified and a solution will not exist for all values for ϵ_T and S_g. Once the parameters of the distribution are established, β can be calculated. This was done numerically, and the results, as a function of ϵ_T, are summarized in Figure A-2.

. The linear distribution:

$$\epsilon(r) = a + mr \tag{14}$$

requires that all four parameters be specified. The solution for the distribution, where:

$$\epsilon(r) = a[1-r/r^*], \tag{15}$$

was obtained numerically from the equation for $\lambda(r)$:

$$\lambda(r) = \frac{1}{2\pi} \frac{-a(1 - r/r^*)}{\left[\frac{ar^4}{2r^*} - ar^3 - r^2 + \frac{ar^2r^*}{2}\right]} \tag{16}$$

In general, the results of Table 5.1-1 indicate that the parameter β is not very different for these three functional forms, provided the total porosity is identical in each case.

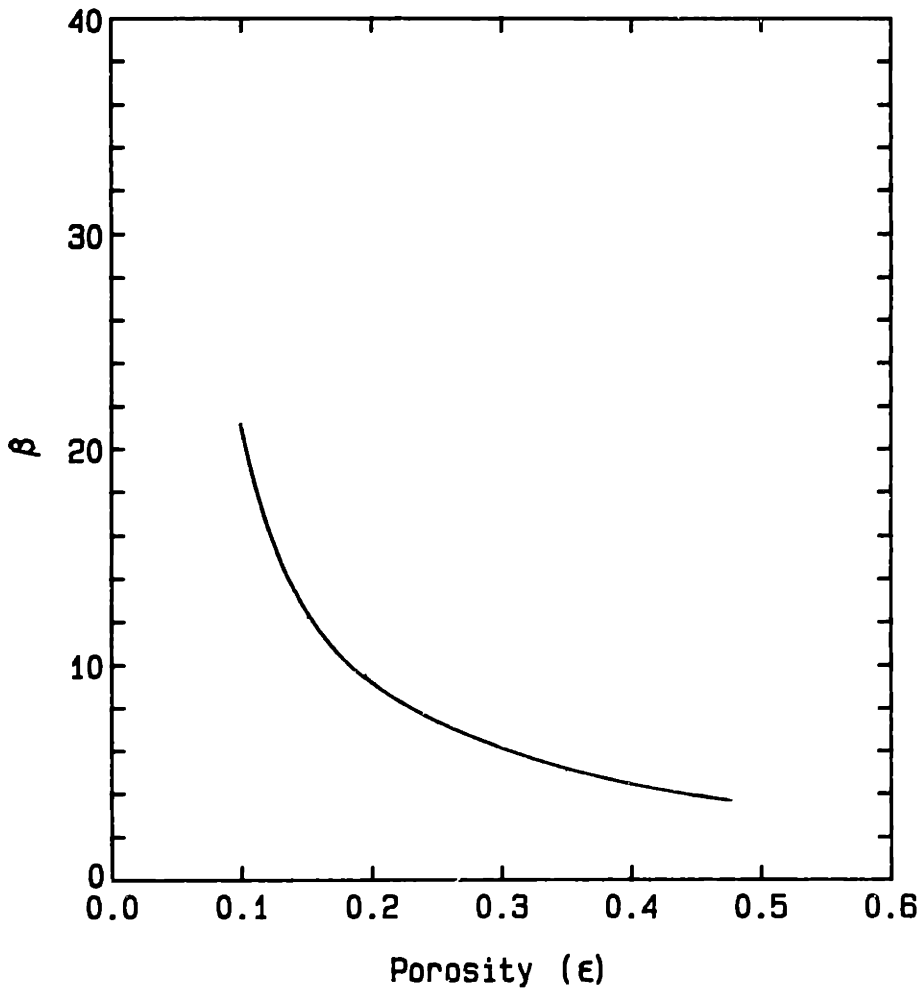

Figure A.6-2. The parameter β as a function of the total porosity for an exponential pore size distribution.

Appendix 7 . CALCULATION OF THE CARBON REACTION RATE FROM TGA DATA.

The experimentally measured rates and conversion are based on the total weight of the sample:

$$x = \frac{w_i - w}{w_i}$$

where w_i is the initial weight of the char sample and w is the measured weight, and x is defined as the conversion. However, w is the weight of the remaining carbon (w_c) and the weight of any adsorbed oxygen (w_o):

$$w = w_c + w_o$$

where w_c refers to the carbon and w_o to the oxygen.

Therefore:

$$\frac{dx}{dt} = \frac{-1}{w_i}\frac{dw_c}{dt} - \frac{1}{w_i}\frac{dw_o}{dt}$$

and since

$$\frac{-1}{w_i}\frac{dw_c}{dt} = \frac{dx_c}{dt}$$

one obtains the result:

$$\frac{dx}{dt} = \frac{dx_c}{dt} - \frac{1}{w_i}\frac{dw_o}{dt}$$

where dx/dt is the experimentally measured rate and dx_c/dt is the carbon reaction rate. The second term on the RHS is probably small compared to the first term, except immediately at the start of the reaction. Analysis of the initial TGA data will require the substitution of a rate equation for oxygen adsorption to determine the actual carbon gasification rate.

APPENDIX 8. NORMALIZATION FACTORS FOR THE RATE VERSUS TIME DATA.

Char	Reactant (atm)	Temperature (K)	$t_{0.5}$ (sec)	r_{max} $(min\text{-}atm)^{-1}$
C-O	O_2 (0.21)	875	202.	0.971
		785	1,466.	0.122
		725	7,650.	0.0226
C-1	O_2 (0.21)	760	207.	1.65
		710	686.	0.423
		650	3,930	0.0617
C-3.6	O_2 (0.21)	710	292.	1.04
		660	1,096.	.250
		600	7,434.	.0311
C-O	O_2 (.136)	875	263.	1.19
	(.055)	875	574.	1.32
	(.103)	725	13,600.	0.0251
C-3.6	O_2 (.124)	710	490.	0.982
	(.056)	710	940.	1.06

Char	Reactant (atm)	Temperature (K)	$t_{0.5}$ (sec)	r_{max} $(min\text{-}atm)^{-1}$
C-ion	O_2 (0.21)	725	192.	1.70
		685	304.	0.826
		625	2,360.	0.0981
Spherocarb	O_2 (0.21)	875	372	0.493
		810	2,304	0.077
		750	17,240	0.010
C-O	CO_2 (1 atm)	1,405	146	0.237
		1,375	239	0.143
		1,250	2,750	0.0115
C-3.6	CO_2 (1 atm)	1,075	488	0.0964
		1,025	1,436	0.0283
		995	3,196	0.0114
Spherocarb	CO_2 (1 atm)	1,350	260	0.127
		1,320	404	0.0890
		1,240	2,160	0.0167

Appendix 9. CALCULATION OF THE QUANTITY B_o

The moment of inertia for a diatomic molecule is:

$$I = d^2 \frac{[m_A m_B]}{[m_A + m_B]}$$

where d is the distance between the centers of the atoms and m_A and m_B are the atomic masses of atoms A and B, respectively. For the oxygen molecule $d = 1.4 \times 10^{-8}$ cm and $m_A = m_B = 16$ amu. Therefore,

$$I = (1.4 \times 10^{-8})^2 \frac{1/2(16)}{6.023 \times 10^{23}} = 2.60 \times 10^{-39} \text{g-cm}^2$$

The factor B for the molecules is:

$$B = \frac{h^4}{8\pi^2 I (2\pi m \cdot k)^{3/2}}$$

where h = Planck constant = 6.62×10^{27} erg-sec

k = Boltzmann constant = 1.38×10^{-16} erg/deg

m = mass of the oxygen molecule = 32 amu

$$B = \frac{(6.62 \times 10^{-27} \text{ erg- sec})^4}{\left[2\pi \cdot 1.38 \times 10^{-16} \frac{\text{erg}}{\text{deg}} \cdot \frac{32}{6.023 \times 10^{23}}\right]^{3/2} \cdot 8\pi^2 (2.60 \times 10^{-39} \text{ g-cm}^2)}$$

since 1 erg = 1 $\text{g-cm}^2/\text{sec}^2$

$$B = 9.46 \times 10^{-13} \text{ cm}^3/\text{sec - deg}^{3/2}$$

REFERENCES

Abramowitz, M. and Stegun, I.A. "Handbook of Mathematical Functions" Academic Press, New York (1975).

Adamson, A.W. "Physical Chemistry of Surfaces" John Wiley, New York (1976).

Amariglio, H. and Duval, X. Carbon 4:323 (1966).

Arpaci, V.S. "Conduction Heat Transfer" Addison-Wesley, Reading, MA (1966).

Arthur, J.R. Trans. Faraday Soc. 47:164 (1951).

Avrami, M. J. Chem. Phys. 8:212 (1940).

Azaroff, L.V. and Buerger, M.J. "The Powder Method" McGraw-Hill, New York (1958).

Barrett, E.P., Joyner, L.G. and Halenda, P.H. J. Am. Chem. Soc. 73:373 (1951).

Bhatia, S.K. and Perlmutter, D.D. A.I.Ch.E. J. 26:379 (1980).

Bird, R.B., Stewart, W.E., and Lightfoot, E.N. "Transient Phenomena" John Wiley, New York (1960).

Blyholder, G. and Eyring, H. J. Phys. Chem. 61:682 (1957).

Blyholder, G. and Eyring, H. J. Phys. Chem. 63:1004 (1959).

Cairns, J.A., Keep, C.W., Bishop, H.E. and Terry, S. J. of Catalysis 46:120-123 (1977).

Campbell, J.H. "The Kinetics of Decomposition of Colorado Oil Shale: II Carbonate Minerals" Lawrence Livermore Laboratory Report UCRL-52089, Part II (1978).

Chen, C-J. and Back, M.H. Carbon 17:495-503 (1979).

Cheng, A. and Marriot, P. "Kinetics of Oxidation and Chemisorption of Oxygen for Porous Carbons with High Surface Area" presented at the AIChE National Meeting (1985).

Culver, R.V. and Heath, N.S. Faraday Soc. Trans. 51:1569 (1955).

Dutta, S. and Wen, C.Y. Ind. Eng. Chem. Process Des. Dev. 16:31 (1977).

Dutta, S., Wen, C.Y. and Belt, R.J. Ind. Eng. Chem. Process Des. Dev. 16:20 (1977).

Eckert, E.R. and Drake, R.M. "Analysis of Heat and Mass Transfer" McGraw Hill, New York (1972).

Ergun, S. and Mentser, M. "Reactions of Carbon with Carbon-Dioxide and Steam" in Chem. and Phys. of Carbon, Vol.1: 203, P.L. Walker, Jr. (editor), Marcel Dekker, New York (1965).

Ergun, S. and Mentser, M. Carbon 5:331-337 (1967).

Essenhigh, R.H., "Fundamentals of Coal Combustion" in Chemistry of Coal Utilization, Second Supplementary Volume, Chapter 19, M.A. Elliot (ed.), John Wiley, New York (1981).

Freund, H. "The Kinetics of Carbon Gasification by CO_2", submitted for publication in Fuel (1984a).

Freund, H. "A Transient Kinetics Experiment on the Gasification of Carbon by CO_2", submitted for publication in Fuel (1984b).

Gardiner, W.C., Jr. "Rates and Mechanisms of Chemical Reactions" W.A. Benjamin, New York (1969).

Gavalas, G.R. AIChE J. 26(4):577 (1980).

Gavalas, G.R. Combustion Science and Technology 24:197-210 (1981).

Gilbert, J.B. and Kipling, J.J. Fuel 41:249 (1962).

Gregg, S.J. and Sing, K.S.W. "The Adsorption of Gases on Porous Solids" Surface and Colloid Science Vol. 9:231, E. Matijevic (editor), John Wiley, New York (1976).

Hashimoto, K. and Silveston, P.L. A.I.Ch.E. J. 19(2):259 (1973).

Hastings, T., "The Effects of Thermal Processing on Lignite Coal Char Structure and Reactivity" Sc.D. Thesis, M.I.T., Cambridge, MA (1984).

Haynes, W.P., Gasior, S.J., and Forney, A.J. "Catalysis of Coal Gasification at Elevated Pressure" ACS Div. of Fuel Chem. 18(2):1 (1973).

Hippo, E.J. and Walker, P.L., Jr. Fuel 54:245 (1975).

Hippo, E.J. and Walker, P.L., Jr. "Effect of Cation Exchange on the Subsequent Reactivity of Lignite Chars to Steam" U.S. Dept. of Energy Report FE-2030-TR4 (March, 1977).

Honig, P. (editor) "Principles of Sugar Technology", Elsevier Publishing Co., Amsterdam (1953).

Hurt, R., personal communication, Cambridge, MA (1985).

Jenkins, R.G., Nandi, S.P., and Walker, P.L., Jr. Fuel 52:288 (1973).

Johnson, J.L. "Relationship between the Gasification Reactivities of Coal Char and the Physical and Chemical Properties of Coal and Coal Char" ACS Division of Fuel Chem. 20(4):85 (1975).

Kawahata, M. and Walker, P.L., Jr. "Mode of Porosity Development in Activated Anthracite" in Proc. Fifth Carbon Conference 2:251-263, Pergamon Press, London (1962).

Kerstein, A.R. and Niksa, S. "Fragmentation during Carbon Conversion: Productions and Measurements" Twentieth Symposium (International) on Combustion (1984).

Laidler, K.J. "Absolute Rates of Surface Reactions" in Catalysis, P.H. Emmett (editor), Reinhold Publishing Co., New York (1954).

Laidler, K.J. "Chemical Kinetics" McGraw-Hill, New York (1965).

Laidler, K.J., Glasstone, S., and Eyring, H. J. Chem. Phy. 8:667 (1940).

Laine, N.R., Vastola, E.J., and Walker, P.L., Jr. J. Phys. Chem. 67:2030 (1963).

Lamond, T.G. and Marsh, H. "The Surface Properties of Carbon-II. The Effect of Capillary Conclerisation at Low Relative Pressures Upon the Determination of Surface Area" Carbon 1:281 (1964).

Lamond, T.G. and Marsh, H. "The Surface Properties of Carbon-III. The Process of Activation of Carbons" Carbon 1:293 (1964).

Lang, R.J. and Neavel, R.C. Fuel 61:621 (1982).

Laurendeau, N.M. Prog. Energy Combust. Sci. 4:221-270 (1978).

Long, F.J. and Sykes, K.W. J. Chim. Phys. 47:361 (1950).

Mahajan, O.P. and Walker, P.L., Jr. "Porosity of Coals and Coal Products" in "Analytical Methods for Coal and Coal Products" Vol.1, C. Karr, Jr. (ed.), Academic Press, New York (1978).

Marsh, H. and Adair, R.R. Carbon 13:327-332 (1975).

Marsh, H. and Wynne-Jones, W.K.F. Carbon 1:269-279 (1964).

Mattson, J.S. and Mark, H.B., Jr. "Activated Carbon: Surface Chemistry and Adsorption from Solution", Chapter 3, Marcel Dekker, New York (1971).

McKee, D.W. Carbon 17:419-425 (1979).

McKee, D.W. Fuel 59:308 (1980).

McKee, D.W. "The Catalyzed Gasification Reaction of Carbon" in Chemistry and Physics of Carbon, P.L. Walker, Jr. (editor), 16: 1 Marcel Dekker, New York (1981).

McKee, D.W. Fuel 62:170 (1983).

Meissner, H.P. "Process and Systems in Industrial Chemistry", Chemical Engineering Department, M.I.T., Cambridge, MA (1971).

Mess, D. personal communication, Cambridge, MA (1985).

Mims, C.A. and Pabst, J.K. "Alkali Catalyzed Carbon Gasification" ACS Div. of Fuel Chem. 25(3): 258 (1980a).

Mims, C.A. and Pabst, J.K. "Alkali Catalyzed Carbon Gasification II. Kinetics and Mechanism" ACS Div. of Fuel Chem. 25(3): 263 (1980b).

Mims, C.A. and Pabst, J.K. Fuel 62: 176 (1983).

Mims, C.A., Rose, K.D., Melchior, M.T. and Pabst, J.K. J. Amer. Chem. Soc. 104(24): 6886 (1982).

Nahas, N.C. Fuel 62: 239 (1983).

Nenniger, R.S. "Determination of Coal and Char Surface Areas" M.I.T. Dept. of Chemical Engineering Report (1982).

Otto, K., Bartosiewicz, L., and Shelef, M. Carbon 17:351-357 (1978).

Otto, K., Bartosiewicz, L., and Shelef, M. Fuel 58:565-571 (1979).

Petersen, E.E. A.I.Ch.E. J. 3:443 (1957).

Puri, B.R. "Surface Complexes on Carbon" in Chemistry and Physics of Carbon, vol. 6, P.L. Walker, Jr. (editor), Marcel Dekker, New York (1970).

Puri, B.R., Singh, S. and Mahajan, O.P. Jour. Indian Chem. Soc. 42(7):428 (1965).

Puri, B.R., Singh, G., and Sharma, L.R. J. Indian Chem. Soc. 34(5):357 (1957).

Radovic, L.R. "Importance of Catalysis and Carbon Active Sites in Lignite Char Gasification" Ph.D. Thesis, Pennsylvania State University (November, 1982).

Ruckenstein, E. and Pulvermacher, B. AIChE J. 19(2):356 (1973).

Satterfield, C.N. "Mass Transfer in Heterogeneous Catalysis", Chemical Engineering Department, M.I.T., Cambridge, MA (1970).

Schafer, H.N.S. Fuel 49:197 (1970).

Sears, J.T., Murralidhara, H.S., and Wen, C.Y. Ind. Eng. Chem. Process Res. Dev. 19: 358-364 (1980).

Simons, G.A. "The Pore Tree Structure of Porous Char" Nineteenth International Symposium on Combustion (1982).

Simons, G.A. and Finson, M.L. Combustion Science and Technology 19: 217-225 (1979).

Smith, I.W. "The Combustion Rates of Coal Chars: A Review" 19th Symposium (International) on Combustion (1982).

Smith, I.W. and Tyler, R.J. Fuel 51:312 (1972).

Snow, M.J. "Sulfation of Limestone and Calcium Oxide: Direct and Series Reactions" Ph.D. Thesis, M.I.T., Cambridge, MA (1985).

Spiro, C.L., McKee, D.W., Kosky, P.G., and Lamby, E.J. Fuel 62:180 (1983).

Squires, A.M. "Cyclic Use of Calcined Dolomite to Desulfurize Fuels Undergoing Gasification" Adv. in Chem. Series 69:205-229 (1967).

Taylor, H.S. and Neville, H.A. J. Am. Chem. Soc. 43:2055 (1921).

Thomas, J.M. and Thomas, W.J. Introduction to the Principles of Heterogeneous Catalysis Academic Press, London (1967).

Tomita, A., Mahajan, O.P. and Walker, P.L., Jr. "Catalysis of Char Gasification by Minerals" ACS Div. of Fuel Chem. 22(1):4 (1977).

Tucker, B.G. and Mulcahy, M.F.R. Faraday Soc. Trans. 65:274 (1969).

Turkdogan, E.R., Olsson, R.G., Wriedt, H.A., and Darken, L.S. Trans. Soc. of Mining Eng. AIME 354:10 (1973).

Van Vlack, L.H. "Materials Science for Engineers" Addison Wesley, Reading, MA (1970).

Walker, P.L., Jr., Rusinko, F., Jr., and Austin, L.G. "Gas Reactions of Carbon" in Advances in Catalysis, Vol. XI:133, D. Eley, P.W. Selwood, and P.B. Weisy (editors), Academic Press, New York (1959).

Walker, P.L., Jr., Shelef, M. and Anderson, R.A. "Catalysis of Carbon Gasification" in Chemistry and Physics of Carbon, P.L. Walker, Jr. (editor), 4:287 Marcel Dekker, New York (1968).

Walker, P.L., Jr., Vastola, F.J., and Hart, P.J. "Oxygen-18 Tracer Studies on the Carbon-Oxygen Reaction" in "Fundamentals of Gas-Surface Reactions" p.307, Academic Press, New York (1967).

Watson, D.J. and Gray, V.R. New Zealand J. of Sci. 23:313-317 (1980).

Wen, W.Y. Catal. Rev. Sci. and Eng. 22(1):1 (1980).

Wigmans, T., v. Cranenburgh, H., Elfring, R., and Moulijn, J.A. Carbon 21:23 (1983).

Winslow, F.H., Baker, W.O., and Yager, W.A. "The Structure and Properties of Some Pyrolyzed Polymers" in Proc. of the Second Conference on Carbon, Buffalo, New York (1956).

Wood, B.J., Brittain, R.D., and Lau, K.H., ACS Div. Fuel Chem. 28(1):55 (1983).

Wood, B.J. and Sancier, K.M. "The Mechanisms of the Catalytic Gasification of Coal Char: A Critical Review", Final Report to U.S. Dept. of Energy, Morgantown Energy Technology Center, Morgantown, W.Va. (1984).

Young, D.A. "Decomposition of Solids" Pergamon Press, Oxford (1966).